ACTA TECHNICA

ACADEMIAE SCIENTIARUM HUNGARICAE

EDITOR-IN-CHIEF: P. MICHELBERGER

VOLUME 101
NUMBER 1

CIVIL ENGINEERING — C/1

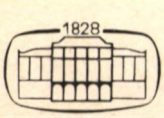

AKADÉMIAI KIADÓ, BUDAPEST 1988

ACTA TECHNICA

A JOURNAL OF THE HUNGARIAN ACADEMY OF SCIENCES

Acta Technica publishes original papers, preliminary reports and reviews in English, which contribute to the advancement of engineering sciences.
Acta Technica is published by

AKADÉMIAI KIADÓ
Publishing House of the Hungarian Academy of Sciences
H-1450 Budapest, Alkotmány u. 21.

Subscription information

Orders should be addressed to

KULTURA Foreign Trading Company
H-1389 Budapest P.O. Box 149

or to its representatives abroad

Acta Technica is abstracted/indexed in Applied Mechanics Reviews, Current Contents–Engineering, Technology and Applied Sciences, GeoRef Information System, Science Abstracts.

ACTA TECHNICA

Volume 101 Nos 1-4

CONTENTS

EDITORS' FOREWORD 3, 111, 229

Bassa, G. - Mao, N.S.: Determination for geometric characteristics of Flames 229

Báder, I. - Berecz, E.: Measurement of the Al_2O_3-content in cryolitic melt by electrochemical method using solid electrolyte. The decomposition voltage of Al_2O_3 and the composition of the anode gas 113

Bognár, L.: Stability of elasto-plastic plane bar systems 5

Csővári, M. - Czeglédi, B. - Stocker, L. - Erdélyi, M. - Egry, R. - Tündök, S. - Horváth, A.: Regeneration of hydrochloric acid in chlorida-hydrometallurgy by anion exchange process 129

Erdősi, P.: Effect of material intensity and energy intensity on the efficiency of development of the national economy 259

Farkas, O.: Determination of coke-natural gas substitution ratio in blast furnaces 143

Füzy, J. - Páti, Gy. - Vas, J.: Conclusion drawn from the analysis of a continuum mechanical model of four degrees of freedom proposed previously for the description of the behaviour of granular materials 49

Gausz, T. - Czédli, Gy.: Examination of flow developing in supersonic diffusers 347

Hegedűs, I. - Kollár, L.P.: Stability analysis of bars elastically restrained from rotation along their entire length 59

Hegedűs, I. - Kollár, L.P.: Generalized bar models and their physical interpretation ... 69

Jermendy, L. - Timashova, L.V.: Results of interference measurements on 400 and 750 kV transmission lines 281

Mikhail, S. - Elbadrawy, S. - Barakat, Y. - Farag, A.: Thermal conversion of paraffins . 295

Oanh, N.: Effect of end restraint upon the strength of steel columns with initial imperfections 97

Paláncz, B. - Benedek, S.: Event recognition by means of a linear model 305

Paláncz, B. - Szabolcs, G.: Solution of inverse heat conduction problem by orthogonal collocation techniques 323

Répási, G.: Results of injection ladle metallurgy in sheet metal production 155

Szepessy, A. - Kékesi, T. - Hertelendi, Á.: Investigation of the parameters of electrolytic opper refining by current reversal 171

Szergényi, I.: Economic growth as a function of changes in energy intensity and production restructuring 339

Tatár, I.: Chordal thickness and span measurement of helical gears 361

Tatár, I.: Chordal thickness and span measurement of conjugate surfaces 379

Tolnay, L. - Tardy, P. - Károly, Gy. - Ghazally, S.: Effect of different technologies of cored wire treatment on the quality of steels 185

Váradi, K. - Poller, R.: Analysis of gears teeth contact by the finite element method ... 397

Voith, M. - Gulyás, J. - Dernei, L. - Zupkó, I. - Herendi, R.: Computer aided roll pass design for I-beams 199

Yosry, W. - Balogh, I. - Molnár, F.: Experimental study of wear of slip differential units 419

BOOK REVIEWS

Berceli, T.: Non-linear active microwave circuits (I. Bozsóki) 110

Mosonyi, E.: Water Power Development. Volume I. Low-head Power Plants (Ö. Starosolszky) . 109

Retter, G.J.: Matrix and spacephasor theory of electrical machines (K. Karsai) 345

CONTENTS

Editors' foreword 3

Bognár, L.: Stability of elasto-plastic plane bar systems 5

Füzy, J.—Páti, Gy.—Vas, J.: Conclusion drawn from the analysis of a continuum mechanical model of four degrees of freedom proposed previously for the description of the behaviour of granular materials 49

Hegedűs, I. —Kollár, L.P.: Stability analysis of bars elastically restrained from rotation along their entire length 59

Hegedűs, I.—Kollár, L.P.: Generalized bar models and their physical interpretation 69

Oanh, N.: Effect of end restraint upon the strength of steel columns with initial imperfections 97

BOOK REVIEWS

Mosonyi, E.: Water Power Development. Volume I. Low-head Power Plants (O. Starosolszky) 109

Berceli, T.: Non-linear active microwave circuits (I. Bozsóki) 110

ACTA TECHNICA

ACADEMIAE SCIENTIARUM HUNGARICAE

EDITOR-IN-CHIEF: P. MICHELBERGER

VOLUME 101
NUMBERS 1—4

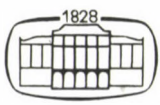

AKADÉMIAI KIADÓ, BUDAPEST 1988

Acta Technica Acad.Sci.Hung., 101(1), pp.3 (1988)

EDITORS' FOREWORD

The Editorial Board has found it necessary to split the "Acta Technica" into four separate series, in order to make the fields of interest more homogeneous. Each series maintains the heading "Acta Technica Academiae Scientiarum Hungaricae", and bears a sub-heading indicating the special field of interest of the series.

The editors hope that the readers will find this new form of the "Acta Technica" easier to survey and more useful than its previous form.

The four series are as follows:

C. Civil Engineering
M. Mechanical Engineering
T. Material Sciences and Technology
E. Energy Engineering

The Civil Engineering series deals with the subjects listed below:

Mechanics of solids
Structural engineering
Geotechnics
Hydraulic engineering
Transportation engineering

An Editorial Commission has been set up to oversee the Civil Engineering series, with the following members:

Lajos KOLLÁR, DSc., Head of the Commission (Structures)
András BÉNYEI, DSc., (Transportation)
Zsolt GÁSPÁR, DSc., (Mechanics)
László RÉTHÁTI, DSc., (Geotechnics)
László SOMLYÓDY, DSc., (Hydraulics)

We hope that by setting up a separate editorial Commission for the Civil Engineering series the professional level and up-to-dateness of the articles can be further improved.

Akadémiai Kiadó, Budapest

Acta Technica Acad.Sci.Hung., 101(1),pp. 5–47 (1988)

STABILITY OF ELASTO-PLASTIC PLANE BAR SYSTEMS

L. Bognár*

(Received: 30 September 1986)

Discussed in this paper is the stability of plane bar systems made of elasto-plastic material. A process for calculation of the critical horizontal load of bar systems is presented, taking into consideration the effect of plastic boundary loads. The calculations are based on the second-order theory and include calculation of the effect of displacements upon internal forces. Cross sections of different type have been investigated. The method presented is suited for direct use in design engineering applications as well as in making design handbooks.

Numerical examples for practical application of the method are presented, the results of which have been compared with the values that can be calculated on the basis of the standard.

1. INTRODUCTION

So called bar systems consisting of cantilevers standing beside each other and two-support beams interconnecting them (Fig. 1) are a supporting system frequently used for industrial buildings. Different methods are known for calculation of such bar systems but (as will be seen later in this paper), these methods are either unsuited for a true representation of the behaviour of structures because of the approximate nature of the starting conditions or neglect of some effects or they are rather sophisticated methods necessitating the use of high-capacity computers.

A method suited for the investigation of bar systems under compression and bending (Fig. 2) is presented in this paper. In the calculations, the bar system has been assumed to function as a plane supporting structure. That means that with given load and rigidity conditions of the bay investigated, no torsional buckling in plane has to be reckoned with.

The structures investigated are made of elasto-plastic material. The investigation is based on calculations according to the second-order theory and it takes into consideration the non-linear behaviour of the material,

*L. Bognár, H–2400 Dunaújváros, Zalka M. u. 1, Hungary

Akadémiai Kiadó, Budapest

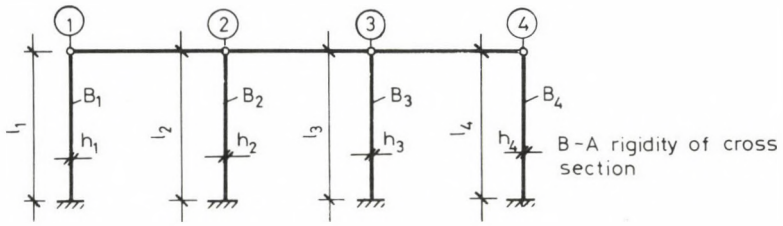

Fig. 1. Bar system

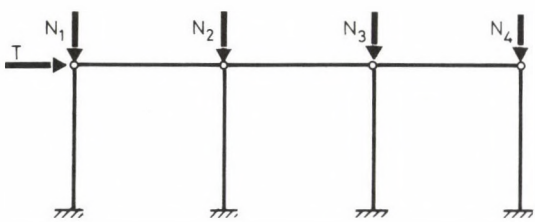

Fig. 2. Bar system under compression and bending

the effect of plastic limit loads as well as the effect of displacements on internal forces. Efforts were made to find a relatively simple method suited for direct use in engineering practice, describing at the same time the true behaviour of the structure accurately.

2. A BRIEF SUMMARY OF METHODS SUITED FOR CALCULATION OF BAR SYSTEMS

Essentially, bar systems can be considered to be a special type of frames and therefore methods suited for investigation of frames can be used to calculate for bar systems.

Investigation of structures of infinitely elastic material on the basis of the first-order and second-order theory can be considered today a problem that has been settled /4/, /6/, /7/, /10/. In case of relatively slender steel bars, the method is accurate provided buckling is taking place in elastic state. However, in case of stubby structures where also the plastic properties of the material contribute to reduction in stability in some cross sections, calculation of the critical load of the structure on the basis of the theory of elasticity may result in a significant error. A remedy can be to calculate for a structure of elastic material and ac-

cordingly, to consider the value resulting in no yield anywhere in the structure to be the maximum permissible load at, however, the expenses of plastic reserve which is surrendered in this case. An interesting phenomenon in the investigation of elastic buckling of bar systems is emphasized, important also in the present case because of later comparability. According to the theorem formulated by Dulácska, the total critical load of a bar system depends only slightly on the distribution of load among the different bars.

Methods offering a better approach to the true behaviour of structures are also available /5/, /8/, /9/. Widely used are first of all methods suited for calculation and investigation of steel frames. The use of an ideally elastic, perfectly plastic model in place of the stress-elongation ($\sigma-\varepsilon$) diagram of steel, suited also investigate plastic instability, proved to be the best approach. However, in investigating any structure, even one single bar, the investigation will become rather complicated and require the use of a computer if the $\sigma-\varepsilon$ conditions corresponding to the bends are taken into consideration in all cross sections. Theoretically, an essential simplification is brought by introducing an approach according to which only perfectly elastic and/or perfectly plastic cross sections are found in the structure and thus the structure is set up essentially of elastic bars and of plastic joints occurring in cross sections of finite number /2/. A further simplification is to replace elastic bars with rigid bars /1/. Today essentially these two methods (elastic-plastic or rigid-plastic structure model) are available for calculation of steel (not perfectly elastic) bar systems.

3. EVALUATION AND CRITICS OF METHODS USED SO FAR, DESCRIPTION OF THE OBJECTIVE IN DETAIL

The difference between theories adopted in investigating a structure (in the present case, a bar system) is demonstratively illustrated in Fig. 3. In the Figure, displacement w of a point of the structure is shown along the horizontal axis while magnitude n of the load intensity (assuming one-parameter load) along the vertical axis of the co-ordinate system. (The problem of one-parameter or two-parameter load will be discussed later.) As seen, modeling of the true behaviour of the structure and within this,

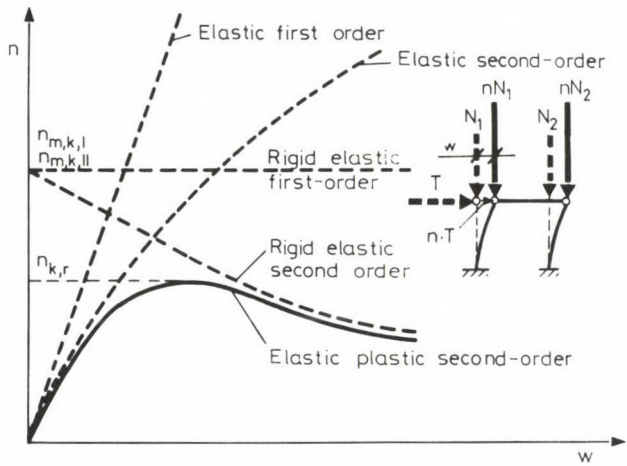

Fig. 3. Investigation of a bar system under compression and bending of the basis of different theories

determination of the critical load intensity are possible only by means of the second-order theory and a non-linear (e.g. elastic-plastic) model.

However, what is not shown in the Figure is that there are restrictions and approximations in the starting conditions of even this, seemingly accurate, calculation method, the effect of which can not be evaluated directly. Namely, in the methods used sor far,

(a) the forces of in general indefinite supporting structures are determined on the basis of first-order elastic theory and also the increase of internal forces in case of increasing load intensity is assumed to be proportional in stability investigation,

(b) the fact that the rigidity of the beam reduces gradually in the course of increase of load intensity (or displacements) is usually not taken into consideration,

(c) the effect of normal forces on moment carrying capacity of the cross sections can not be taken into consideration or if indeed at all, only by use of some iteration process /2/.

In fact, the objective of this work is to eliminate these deficiencies in the investigation of bar systems.

4. THE PROBLEM OF ONE-PARAMETER LOAD AND TWO-PARAMETER LOAD

So called one-parameter loads are usually assumed in the course of stability investigation of supporting structures. This means that the ratio of loads as compared with each other remains unchanged as the load intensity is increased. It can be shown, however, that in non-linear investigations, difficulties are encountered in assuming one-parameter load. Consider the bar restrained at one end shown in Fig. 4. Applied to this bar are vertical compressive force N and horizontal load T. Let cross section K and/or its rigidity be investigated. In accordance with the objective, let us see how does the rigidity of cross section K reduces gradually as the load intensity increases.

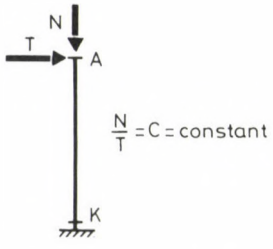

Fig. 4. Cantilever under compression and bending

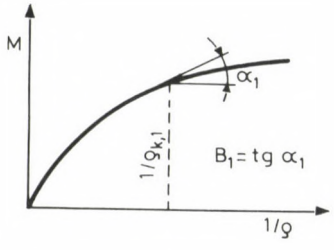

Fig. 5. Determination of moment (M) – curvature ($\frac{1}{\varrho}$) function and rigidity (B)

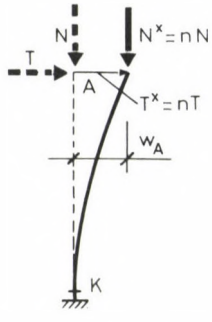

Fig. 6. Clamped bar with one-parameter load acting upon it

Let first the rigidity of a cross section be defined. For this purpose, let the change of moment (M) of the cross section as a function of curvature ($\frac{1}{\varrho}$) be illustrated diagrammatically (Fig. 5). Such a moment-curvature function is associated with a normal force of given magnitude acting upon the cross section. As many functions $M - \frac{1}{\varrho}$ can be produced as many different normal forces have been assumed. By rigidity of a cross section we understand the angular coefficient of a tangential straight e associated with normal force N_1 and curvature $\frac{1}{\varrho_{k,1}}$. Hence:

$$B_1 = \left[\frac{\partial M}{\partial \frac{1}{\varrho}}\right]_{\frac{1}{\varrho_{k,1}}}^{N_1}$$

Consider the case of one-parameter load where $\frac{N}{T} = c = \text{constant}$ ($N^* = n \cdot N$, $T^* = n \cdot T$) when the intensity of load is increased. With increasing displacement of point A at the top of the bar (ω_A in Fig. 6), also curvature $\frac{1}{\varrho_k}$ of cross section K increases from $\frac{1}{\varrho_{k,1}}$ to $\frac{1}{\varrho_{k,2}}$.

Accordingly, the rigidity reduces as the angular coefficient associated with bend $\frac{1}{\varrho_{k,2}}$ (Fig. 7) will be smaller as compared with that associated with $\frac{1}{\varrho_{k,1}}$. However, it is not only the angular coefficient associated with curvature $\frac{1}{\varrho_{k,1}}$ or $\frac{1}{\varrho_{k,2}}$ of given function ($M - \frac{1}{\varrho_k}$) that has to be determined here since normal force N has also changed. The rigidities associated with values $\frac{1}{\varrho_{k,1}}$ and $\frac{1}{\varrho_{k,2}}$ are determined by a different function $M - \frac{1}{\varrho_k}$ each (Fig. 8).

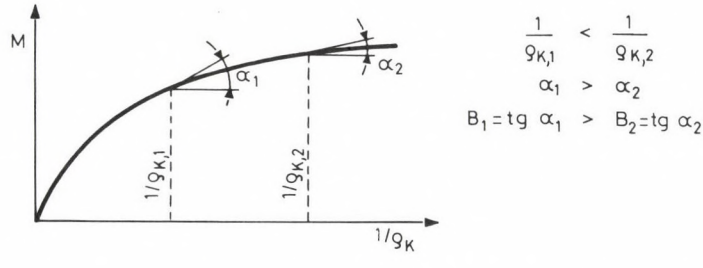

Fig. 7. Rigidity of cross section for different values of curvature

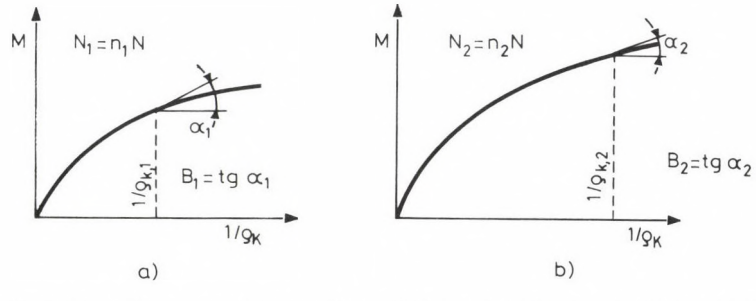

Fig. 8. Rigidity of cross section for different values of the parameter in case of one-parameter load

Hence, in case of one-parameter load, a different moment-curvature function is associated with each step of increase of the intensity of load, on the basis of which the instantaneous rigidity of the cross section can be determined.

The problem can be considerably simplified by assuming the value of N to be constant and increasing only the value of T. In this case, the instantaneous rigidity is merely a value of angular coefficient associated with different points of given function. Such limits set to vertical loads are otherwise a better approach to the actual loading process of structures. The beams experience first the vertical loads (dead weight, effective load etc.) which act upon them independently of the horizontal loads. A possible reduction in stability takes place when the variable horizontal loads (e.g. wind load) reach a certain critical value.

Hence, in investigating the behaviour of the structure (that is function $T - \omega$), the magnitude of forces N loading the bars is assumed to be constant. Of course, the investigations are carried out for forces N of different magnitude.

5. PRINCIPLE OF THE CALCULATION METHOD

The first thing to do is to determine the moment-bend relationship (curve $M - \frac{1}{\rho}$) for a cross section of elastic-plastic material and of given geometry and strength characteristics. The shape of the durve depends, in addition to the magnitude of the normal force acting upon the cross section, largely on the stress-strain conditions of the material(s) used. Except for the simplest cases, plotting of the curve requires that much work be expended on it and thus the use of a computer is necessary. However, for the most frequently used types of cross section, these curves have been numerically determined /1/.

With a view to facilitate handling, analytical functions are used to approximate the numerically plotted curves. On the basis of function $M - \frac{1}{\rho}$, rigidity B can be determined as a function. This functional form of rigidity is used in writing the equilibrium and compatibility equations of the structure. For the sake of safety, the rigidity of the bars is assumed to be identical for each cross section. The magnitude of rigidity along the height of the bar is assumed to be identical with the rigidity of the restraint cross section. The effect of this approach on the accuracy of the results is

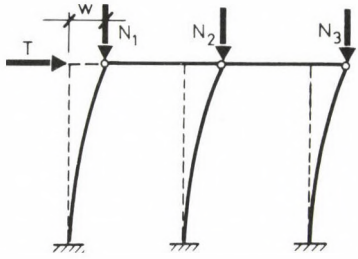

Fig. 9. Displacement (ω) of a bar system under compression and bending as a result of given loads

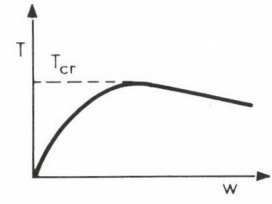

Fig. 10. Determination of critical horizontal load (T_{cr}) on the basis of function $T-\omega$

a question to be investigated on another occasion. In this study, we satisfy ourselves by saying that the effect of this approach depends on the geometry on the cross section as well as on the load conditions and geometry of the bar. However, investigations not described here in detail suggest that even in the most unfavourable case, the contribution of the approach to the inaccuracy of the results lies below 20%.

As the final result of the investigation, the relationship between displacement ω of a top point of given bar system and horizontal force T is obtained (Fig. 9), the maximum value of this function (T_{cr}) being the critical horizontal load of the bar system (Fig. 10). Without impairing generality, the procedure of plotting curve $T-\omega$ is illustrated for a plane system with two bars. The results obtained can be applied also to multibar systems accordingly.

6. MOMENT-CURVATURE FUNCTIONS OF CROSS SECTIONS

To produce the moment-curvature pairs of values, it is necessary that the material characteristics, the cross sectional characteristics as well as the value of normal force be known. Assumption of an ideally elastic-perfectly plastic material model (Fig. 11) leads to appropriately accurate results.

Assumed as a starting point is a concentrically located external force. In the knowledge of the magnitude of the force and of the strength and geometrical characteristics, the compression of the extreme fibre can be calculated. With the force located eccentrically and the value of eccentricity varied, different values of compression of the extreme fibre

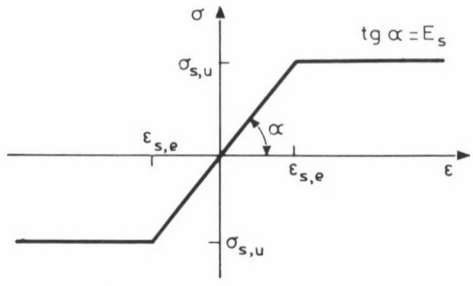

Fig. 11. Stress-strain ($\sigma - \varepsilon$) curve of elasto-plastic material

(strain) are obtained. The value of internal moment and of curvature can be calculated on the basis of deformation of the extreme fibres. To facilitate calculation, this process of the investigation is usually inverted to find the equilibrium state that is the deformation on the side under tension ($\varepsilon_{s,t,i}$) or the place of the neutral axis (x_i) for given normal force, assuming certain extreme fibre compressions $\varepsilon_{s,i}$. After determination of the place of the neutral axis, the values of moment and curvature associated with the normal force and extreme fibre compression $\varepsilon_{s,i}$ can be calculated (Fig. 12). The magnitude of curvature can be determined on the basis of equation

$$\frac{1}{\varrho} = \frac{\varepsilon_{s,i} - \varepsilon_{s,t,i}}{h} \qquad (1)$$

(Fig. 13) while the magnitude of moments can be obtained on the basis of the stress diagrams (Fig. 12).

Moment-curvature functions of different nature are obtained for cross sections of different geometry. Dealt with in this study are sandwich cross sections, I-cross sections, and rectangular cross sections.

6.1 $M - 1/\varrho$ function of sandwich cross sections

The moment-curvature function of the simplest, so called sandwich cross section (Fig. 14) consists of two straights. The functions plotted in Fig. 14 are associated with a different normal force each. So called dimensionless quantities have been measured along the co-ordinate axes and thus the illustrated functions are independent of both the magnitude of the cross section and the strength characteristics. M and M_u in the quantity of relative bending moment $\frac{M}{M_u}$ along the vertical axis are the bending moment

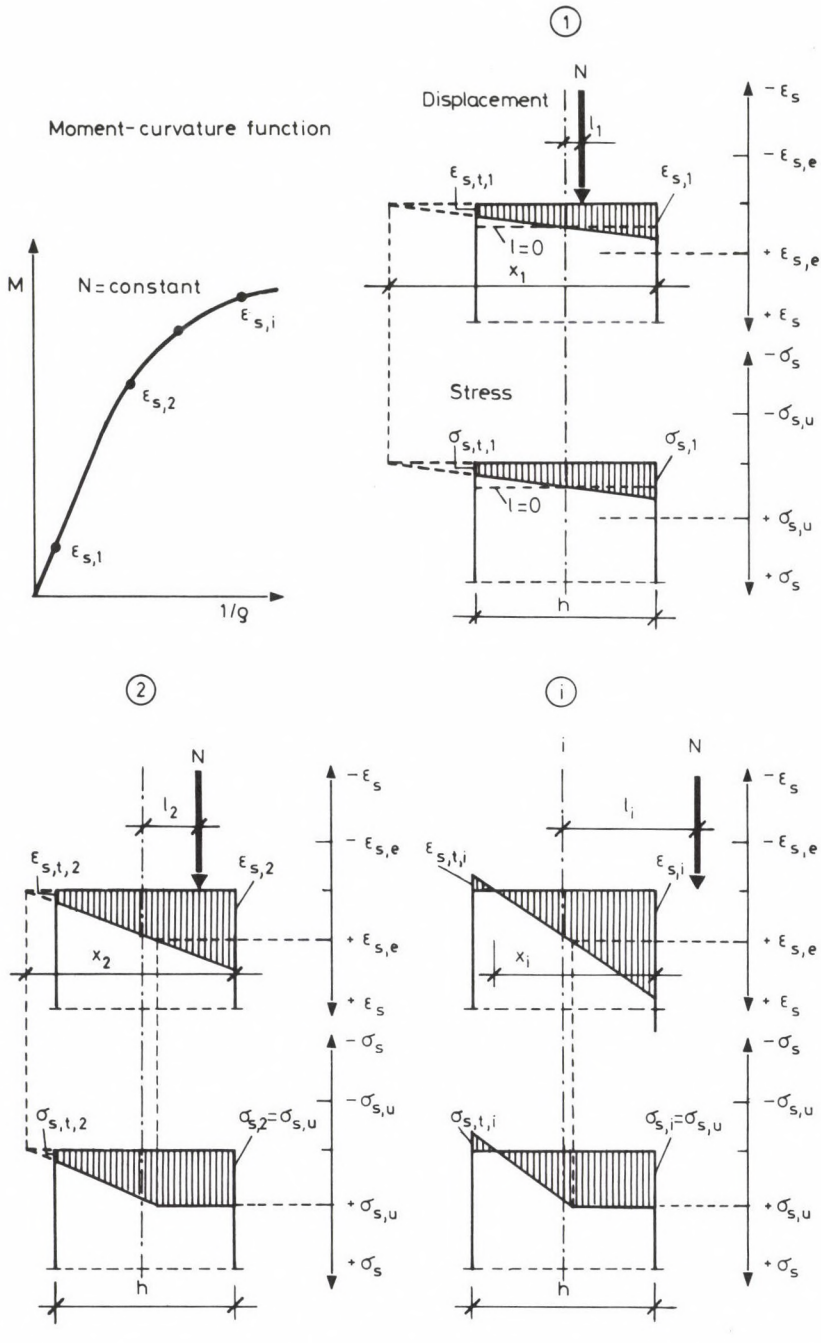

Fig. 12. Procedure of production of moment (M) – curvature ($\frac{1}{9}$) function of a cross section of elasto-plastic material

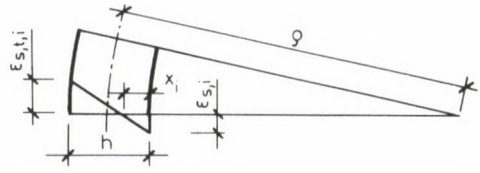

Fig. 13. Curvature of cross section

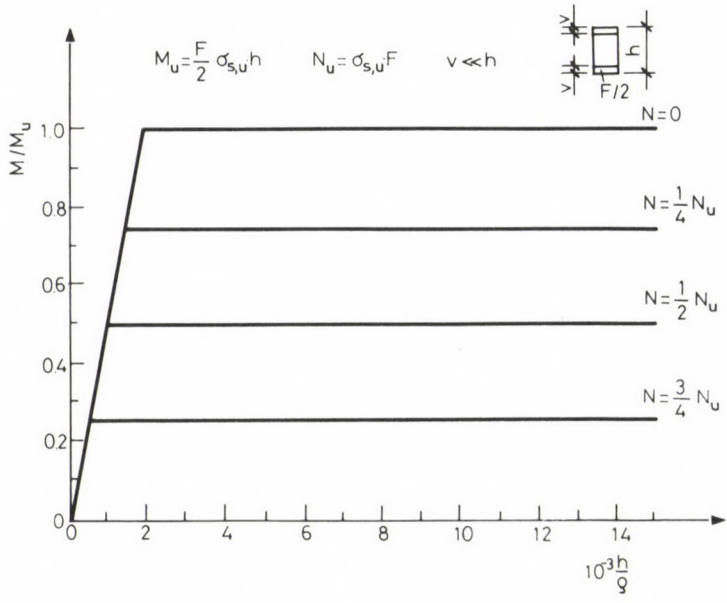

Fig. 14. Moment (M) – curvature ($\frac{1}{\varrho}$) functions of sandwich cross section

associated with curvature $\frac{1}{\varrho}$ and the plastic bending moment of the cross section under pure bending, respectively. In expression $\frac{N}{N_U}$ of the relative normal force, N is the actual normal force while N_U the ultimate force of the cross section under pure compression. The explanation of ϱ and h can be found in Fig. 13. By ultimate force and ultimate moment we understand the force and moment resulting in destruction, respectively. The fact that function $M - \frac{1}{\varrho}$ of the sandwich cross section consists of two straights means at the same time that the rigidity of the cross section is constant below a certain M or $\frac{1}{\varrho}$ while assumed to be zero above this value. The value of bending moment M (or relative bending moment $\frac{M}{M_U}$) which is the end of the

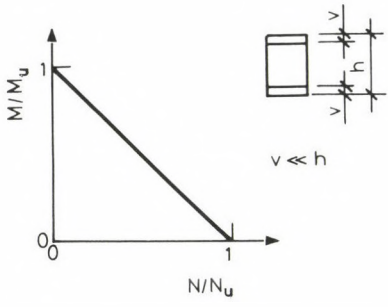

Fig. 15. Function describing the boundary condition of plasticity of sandwich cross section

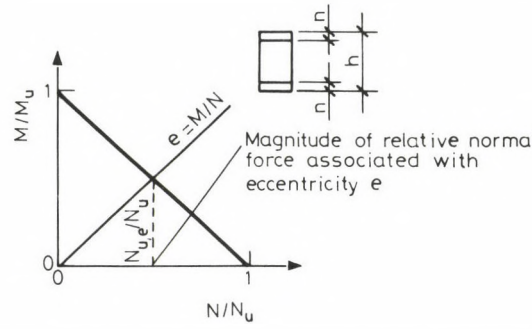

Fig. 16. Determination of boundary force ($N_{u,e}$) associated with eccentricity e on the basis of boundary condition of plasticity in case of sandwich cross section

load capacity of the cross section for given normal force (N or $\frac{N}{N_u}$) where the cross section is incapable of taking up additional moments can be determined on the basis of the boundary condition of plasticity of the cross section under compression and bending /1/.

Function

$$\left|\frac{M}{M_u}\right| + \left|\frac{N}{N_u}\right| - 1 = 0 \qquad (2)$$

expressing the boundary condition of plasticity of the sandwich cross section and/or its part falling within the positive range is illustrated diagrammatically in Fig. 15. For later calculations, the boundary condition of plasticity of the cross section can be expressed practicably as a function of relative normal force acting upon the cross section ($\frac{N}{N_u}$) and eccentricity of normal force to find the value of normal force for given eccentricity where the boundary condition of plasticity of the cross section takes place. Analytically, this value can be obtained as the abscissa of the intersection of a straight $\frac{N}{N_u}$, $\frac{M}{M_u}$ illustrated in co-ordinate system, representing the boundary condition of plasticity, and straight e (Fig. 16). As a result of derivation which is not presented here, the boundary force associated with eccentricity e is expressed in case of a sandwich cross section by equation

$$N_{u,e} = \frac{1}{1+2\frac{e}{h}} \cdot N \quad . \qquad (3)$$

For given ratio $\frac{N}{N_u}$, the value of eccentricity where the boundary condition of plasticity of the cross section takes place:

$$e_u = 0.5\ h \left(\frac{N_u}{N} - 1 \right) \quad . \tag{4}$$

Summing up, for given normal force acting upon the cross section ($\frac{N}{N_u}$ = constant), rigidity B of the cross section can be written as

$$B = EI_o$$

according to the theory of elasticity if eccentricity e of the normal force lies below e_u ($e < e_u$),

where E modulus of elasticity,
I_o moment of inertia of the cross section

and as

$$B = 0$$

for $e \geq e_u$.

In case only bending moment is acting upon the cross section, the rigidity of the cross section will be

$$B = EI_o$$

for $M < M_u$

while

$$B = 0$$

for $M = M_u$.

6.2 Function $M - 1/\varrho$ of I-sections

The moment-curvature function of an I-section is diagrammatically illustrated in Fig. 17. Essentially, like in case of Fig. 14, the function consists of two sections. As long as the cross section is in elastic state, the rigidity of the cross section is constant and the curve rises steeply. As soon as yield is taking place in the flange, the cross section becomes 'soft'. A slight increase in moment results in a significant increase in curvature and after running almost horizontally (practically with zero rigidity) over a short section, the curve approaches the value of the moment

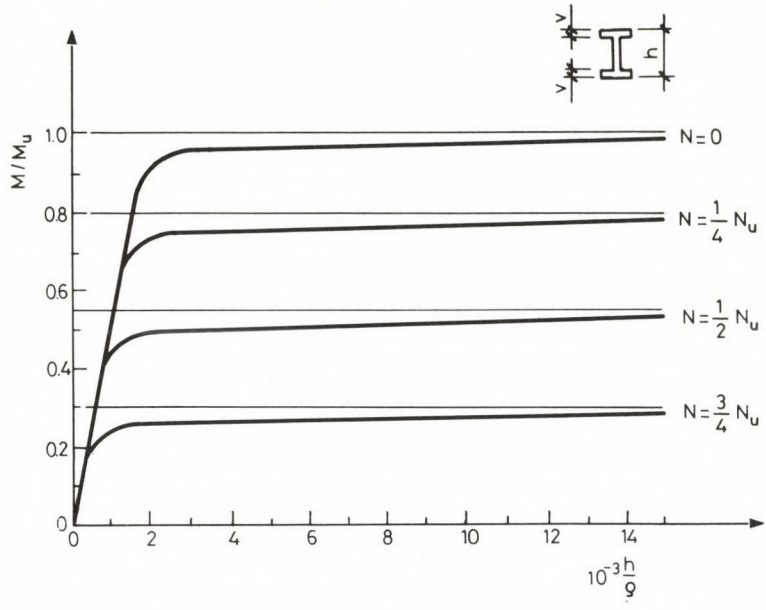

Fig. 17. Moment (M) – curvature ($\frac{1}{\varrho}$) functions of I-section

of plasticity asymptotically. There is a continuous transition between the steep section and flat section of the curve without a sharp break, dissimilarly to the case of the sandwich cross section. Depending on the dimensions of the flanges and/or web, this transition is limited to a longer or shorter domain of the flange.

The curve for boundary condition of plasticity of the I-section (Fig. 18) is a parabole with a straight joining it tangentially, K being a quantity determining the magnitude of the domain confined by the parabola with a value depending on the flange and web dimensions.

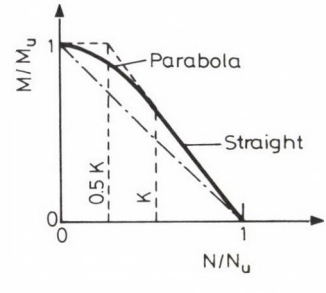

Fig. 18. Function describing the boundary condition of plasticity of I-section

For I-sections used in practice, K = 0.2 . 0.3, which means that the use of a straight characteristic of the sandwich cross section (e.g. the resultant curve in Fig. 18) or of the straights illustrated in Fig. 14 in place of the curve illustrated in Fig. 18 or the moment-curvature function, respectively, is a good approach. This approach will be adopted hereinafter in this study and the design method will be described only for the sandwich cross section as it can be applied to the case of I-sections accordingly.

6.3 Function $M - 1/\varrho$ of the rectangular cross section

In case of rectangular cross sections, the moment-curvature function keeps flattening after an initial steeply rising straight section (in the elastic state of the cross section) to approach then the value of moment of plasticity asymptotically with an approximately horizontal tangent line (Fig. 19). However, it can be seen that, dissimilarly to $M - \frac{1}{\varrho}$ of the sandwich or I section, the cross section is capable of taking up significant additional moments of plasticity after a moment $M_e = W \cdot \sigma_{s,u}$ (that is the upper boundary of the straight section of the function where W = section modulus, essentially the boundary of plastic behaviour, has been reached. An explanation of this phenomenon is that, dissimilarly to the sandwich or I-geometry, the internal parts of the cross section become plastic gradually

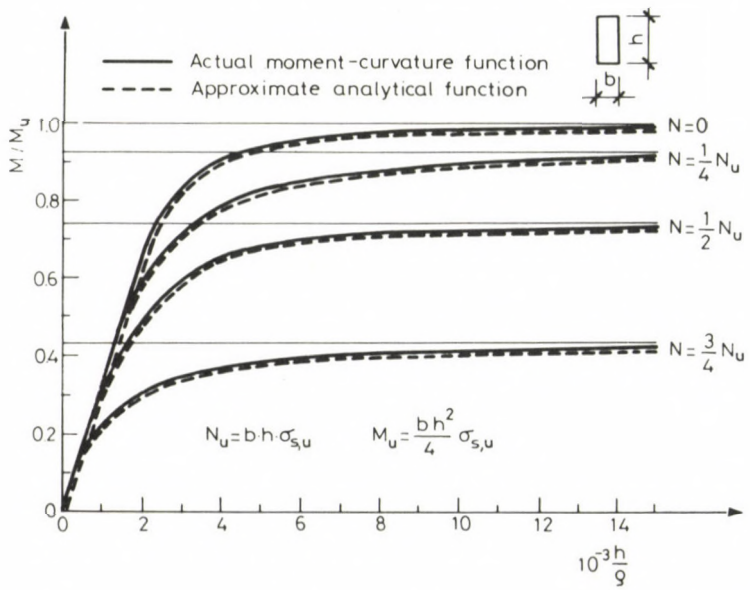

Fig. 19. Moment (M) – curvature $\left(\frac{1}{\varrho}\right)$ functions of rectangular cross section

after yield of the extreme fibre in case of a rectangular cross section and thus an additional increase of the moment is found over a relatively large domain of change of the curvature.

Function

$$\frac{1}{\varrho} = \frac{M}{EI_o}\left[\frac{1}{1-\left(\frac{M}{M_u}\right)^6}\right] \tag{5}$$

is an almost perfect approach also in case of the moment-curvature curve of a rectangular cross section under pure bending /11/. In case of eccentric pressure, this function is written reasonably, as follows:

$$\frac{1}{\varrho} = \frac{M}{EI_o}\left[\frac{1}{1-\left(\frac{N}{N_{u,e}}\right)^6}\right] \tag{6}$$

(for key to the symbols used see the previous chapters). In Fig. 19, full line has been used to illustrate the actual $M - \frac{1}{\varrho}$ relation while dotted line to illustrate the approximate function.

The plastic boundary force ($N_{u,e}$) of a rectangular cross section with a normal force N of eccentricity e acting upon it is given by the co-ordinate of the intersection of the curve illustrating the boundary condition of plasticity and a straight characteristic of eccentricity e (Fig. 20), like in case of the method shown in Fig. 16. Now the boundary condition of plasticity is determined by a parabola the equation of which being

$$\left|\frac{M}{M_u}\right| + \left(\frac{N}{N_u}\right)^2 - 1 = 0 \tag{7}$$

while the value of $N_{u,e}$ is supplied by equation

$$N_{u,e} = \left(\sqrt{4\left(\frac{e}{h}\right)^2 + 1} - 2\frac{e}{h}\right) \cdot N_u \ . \tag{8}$$

With the expression of $N_{u,e}$ according to (8) written into equation (6), the moment-curvature function is obtained, as follows:

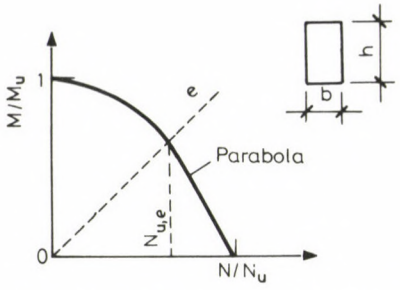

Fig. 20. Determination of ultimate force ($N_{u,e}$) associated with eccentricity e on the basis of boundary condition of plasticity in case of rectangular cross section

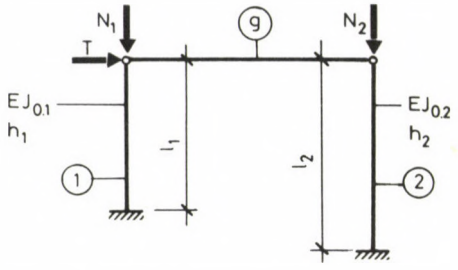

Fig. 21. Static framework of bar system

$$\frac{1}{\varrho} = \frac{M}{EI_o \left\{ 1 - \left[\frac{N}{N_u \left(\sqrt{4 \left(\frac{e}{h}\right)^2 + 1} - 2\frac{e}{h} \right)} \right]^6 \right\}} \quad . \tag{9}$$

The same expression will be obtained if substitution moment of inertia

$$\overline{I} = I_o \left\{ 1 - \left[\frac{N}{N_u \left(\sqrt{4\left(\frac{e}{h}\right)^2 + 1} - 2\frac{e}{h} \right)} \right]^6 \right\} \tag{10}$$

or, in case of pure bending,

$$\overline{I} = I_o \left[1 - \left(\frac{M}{M_u} \right)^6 \right] \tag{11}$$

is used in the calculation, I_o being here the initial 'elastic' moment of inertia.

With this, the problem of writing the rigidity of the cross section as a function of loads acting upon it can essentially be considered solved as, with the expression of bend written in a form

$$\frac{1}{\varrho} = \frac{M}{B} \quad , \tag{12}$$

expression

$$B = E\,\bar{I} \tag{13}$$

is obtained for rigidity B.

7. DETERMINATION OF THE CRITICAL LOAD OF THE BAR SYSTEM

In the previous chapters, the functions of substitution rigidity have been determined for different cross sections. In the knowledge of these functions, the critical load can be calculated for the bar system. First the method of determination of the critical load is presented independently of the different cross section types and then, in the knowledge of the method, the investigations are carried out for actual cases.

7.1 Principle of determination of the critical load

The case to be investigated is schematically illustrated in Fig. 21. The bar system shown in the Figure consists of two clamped bars (1, 2) and a beam (g) interconnecting them in a hinged manner. The bars shall be so numbered that the normal force acting upon bar 2 will not be zero, an essential stipulation in respect of later derivations. The initial rigidity ($EI_{o,1}$, $EI_{o,2}$), length (ℓ_1, ℓ_2), magnitude of normal forces acting upon them (N_1, N_2), width (h_1, h_2) and type of cross section of the bars may be different. The rigidity of the beam is assumed to be infinitely large.

What has to be done now is to produce the function $T - \omega$ (see Fig. 9). In so doing, the structure shall be decomposed into primary beams (Fig. 22). Let the unknown combination force arising in beam g be denoted H. Let the displacements of the end points of the different bars be written:

$$\omega = \omega_T + \omega_N \tag{14}$$

where ω_T – deflection due to the horizontal force,

ω_N – secondary additional deflection due to the normal force /11/. With a sine curve used for approximation of the deflection geometry, equation (14) can be written, as follows:

$$\omega_1 = \omega_{1,T} + \omega_{1,N} = \frac{(T-H)\,.\,\ell_1^3}{3\,EI_1} + \frac{4\,.\,N_1\,.\,\omega_1\,.\,\ell_1^2}{\pi^2\,.\,EI_1} \tag{15}$$

$$\omega_2 = \omega_{2,T} + \omega_{2,N} = \frac{H \cdot \ell_2^3}{3\,EI_2} + \frac{4 \cdot N_2 \cdot \omega_2 \cdot \ell_2^2}{\pi^2 \cdot EI_2} \quad . \tag{16}$$

After reduction of equations (15), (16), we obtain for ω_1 and ω_2

$$\omega_1 = \frac{(T - H) \cdot \ell_1^3}{3\,EI_1 \left(1 - \frac{4 \cdot N_1 \cdot \ell_1^2}{\pi^2 \cdot EI_1}\right)} , \tag{17}$$

$$\omega_2 = \frac{H \cdot \ell_2^3}{3\,EI_2 \left(1 - \frac{4 \cdot N_2 \cdot \ell_2^2}{\pi^2 \cdot EI_2}\right)} \tag{18}$$

The condition of compatibility is that $\omega = \omega_1 = \omega_2$.

To follow the loading process along, an arbitrary value of ω shall be assumed and for this value, the magnitude of H shall be determined from (18). This can be calculated directly. However, as seen, this combination force is not a constant value during the loading process as rigidities EI_1, EI_2 appearing in the equations are given as functions assuming different values in the course of the loading process. In the knowledge of the combination force, H, horizontal load T associated with the assumed displacement can be calculated on the basis of (17). With more values ω assumed one after the other, function $T - \omega$ can be plotted. The critical horizontal load of the bar system (T_{cr}) is given as the maximum of this function.

In case of cross sections made of steel where the assumption of unrestricted yield is acceptable, this value T_{cr} is definitely obtained as the extreme value of function $T - \omega$ (see Fig. 10).

In practice, plotting of function $T - \omega$ in the way described above is a rather tiresome, and because of the functions of the sixth degree, often very complicated job. A method is presented below, which simplifies this job significantly.

The same method is used also for the different actual cross sections.

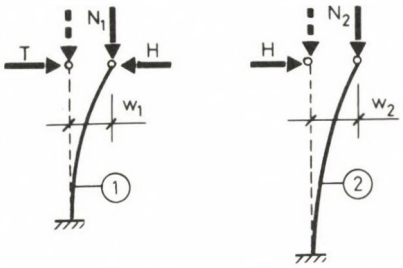

Fig. 22. Primary beam of bar system

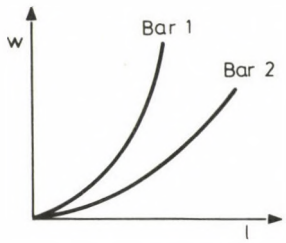

Fig. 23. Displacement (ω) – eccentricity (e) functions of the different bars

Consider first the case where both bars are subjected to normal force. First of all, function $\omega - e$ (displacement-eccentricity) shall be produced for either bar independently (Fig. 23). Production of function $\omega - e$ for a bar upon which given normal force is acting takes place in the following steps (using the notation applying to the i-th bar):

1) Assume an arbitrary value for eccentricity e_i.

2) Calculate rigidity EI_i of the bar as a function of e_i on the basis of the rigidity function applicable to given material and type of cross section.

3) Write value of eccentricity in the restraint cross section of the bar:

$$e_i = \frac{H \cdot l_i + N_i \cdot \omega_i}{N_i} \tag{19}$$

4) By means of equations (18) and (19), express displacement (ω_i) as a function of eccentricity (e_i):

$$\omega_i = \frac{N_i \cdot e_i}{\frac{3\,EI_i}{l_1^2}\left(1 - \frac{4N_i \cdot l_i^2}{\pi^2 \cdot EI_i}\right) + N_i} \tag{20}$$

5) Substitute the value of rigidity EI_i calculated in accordance with par 2 into function (20) to calculate the value of ω_i.

6) Assuming additional values for e_i, function $\omega_i - e_i$ can be plotted. After function $\omega_i - e_i$ has been produced for either bar sub-

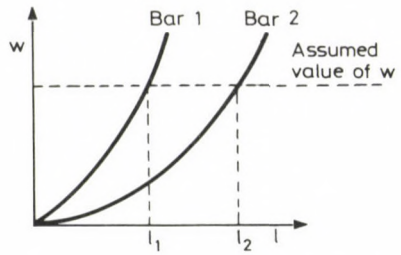

Fig. 24. Determination of eccentricity for the different bars

jected to normal force, relation $T - \omega$ shall be plotted in the following way:

a) Assume an arbitrary value ω .

b) Determine eccentricity (e_1, e_2) for the assumed value of ω for each bar subjected to normal force.

c) Write values of eccentricity for the different bars (the loading and the notation are those used in Fig. 21):

$$e_1 = \frac{(T-H)\ l_1 + N_1 \cdot \omega_1}{N_1} \tag{21}$$

$$e_2 = \frac{H \cdot l_2 + N_2 \cdot \omega_2}{N_2} \tag{22}$$

d) Determine value of H from equation (22).

e) Determine value of T from equation (21).

f) Assuming additional values for ω , plot function $T - \omega$.

If no normal force is acting upon one of the bars, the value of H shall be determined from equation (18) directly (or from equation (26), see later).

Determined below for the different cross section types are the actual $\omega - e$ functions using the method described above. For the sake of general applicability, the equations, functions and diagrams are presented also in a dimensionless form.

For this purpose, the following dimensionless quantities shall be introduced:

$$\frac{H}{N_2} = \vartheta_2 \ ; \qquad \frac{h_1}{h_2} = \nu_1 \ ; \qquad \frac{\omega_i}{h_i} = \xi_i$$

$$\vartheta_1^* = \frac{\overline{H}_1}{N_{u,1}} \quad ; \qquad \frac{N_i}{N_{u,i}} = \varepsilon_i \quad ; \qquad \varepsilon_1^* = \frac{N_{u,1}}{N_2}$$

$$\frac{e_i}{h_i} = \Delta_i \quad ; \qquad \frac{EI_{o,1}}{N_{u,1} \cdot \ell_1^2} = q_1^* \quad ; \qquad \frac{\ell_i}{h_i} = \gamma_i \tag{23}$$

$$\frac{EI_{o,i}}{N_i \cdot \ell_i^2} = q_i \qquad \frac{T}{N_2} = \alpha \quad ; \qquad \frac{N_1}{N_2} = \mu \quad .$$

After introduction of these dimensionless quantities, the problem can be formulated, as follows:

To be determined first is relationship $\xi_i - \Delta_i$ for the different bars upon which normal force is acting (see next chapter). By means of relationship $\xi_i - \Delta_i$ so obtained, function $\alpha - \xi_1$ can be determined from the following equations in case of a system consisting of two bars:

If normal force is acting upon both bars, ϑ_2 can be calculated first by means of (22):

$$\vartheta_2 = \frac{\Delta_2 - \xi_2}{\gamma_2} \tag{24}$$

In the knowledge of ϑ_2, function $\alpha - \xi_1$ to be found can be written directly:

$$\alpha = \frac{\mu}{\gamma_1} (\Delta_1 - \xi_1) + \vartheta_2 \tag{25a}$$

where $\xi_1 = \frac{\xi_2}{\nu_1}$ because of the compatibility condition.

If normal force is acting upon one of the bars (that is upon bar 1 according to agreement), then, for this bar, the resultant of horizontal forces acting upon this bar ($\overline{H}_1$), can be calculated directly from relationship

$$\overline{H}_1 = \frac{3EI_1 \cdot \omega}{\ell_1^3} \tag{26}$$

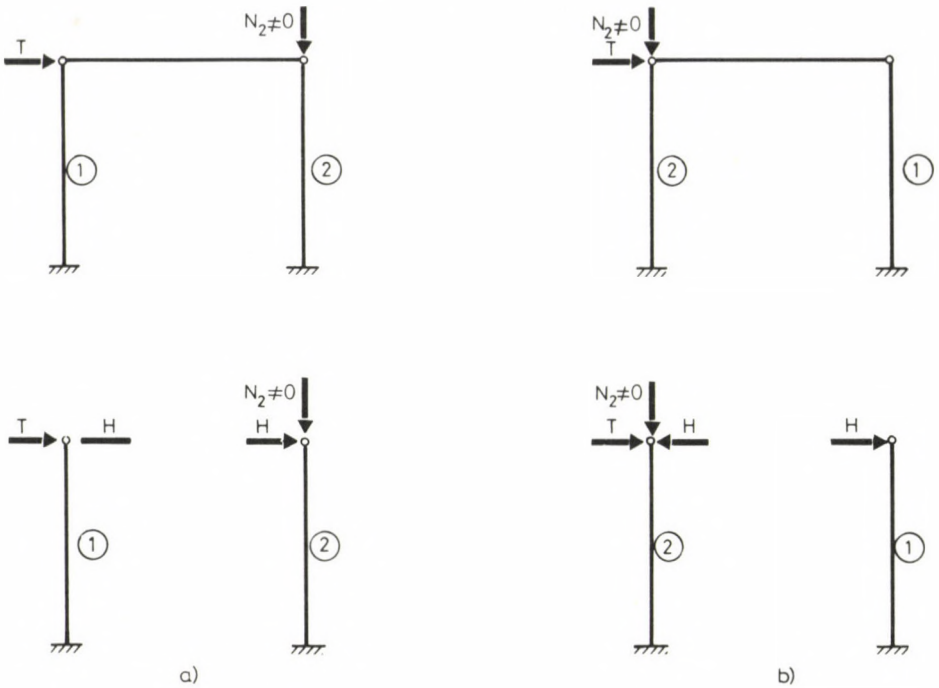

Fig. 25. Bar system with different loads acting upon it

where EI_1 is the function of bending moment acting upon the bar (the dimensionless expression of which, ϑ_1^*, being presented when discussing the different types of cross section). After calculation of ϑ_1^*, relationship $\alpha - \vartheta_1^*$ can be written, as follows (Fig. 25):

$$\alpha = \vartheta_2 + \vartheta_1^* \cdot \varepsilon_1^*$$

for the load illustrated in both Fig. 25a and Fig. 25b, where the value of ϑ_2 is calculated by means of equation (24) also in this case but it means dimensionless quantities $\frac{H}{N_2}$ (Fig. 25a) or $\frac{T-H}{N_2}$ (Fig. 25b) depending on the load.

7.2 Determination of the critical load of elasto-plastic bar systems

7.2.1 Investigation of a system consisting of bars of 'sandwich' cross section

As said in par 7.1, the first thing to do is to produce functions $\omega_i - e_i$ for the different bars. Relationship (20) is used for this purpose. According to the result of investigation described in par 6.1, two values may be assumed by the rigidity in the equation and accordingly, also function $\omega_i - e_i$ is broken in two sections.

If $e_i < e_{u,i}$ (see relationship (4)):

$$\omega_i = \frac{N_i \cdot e_i}{\frac{3EI_{o,i}}{l_1^2} \cdot \left(1 - \frac{4 \cdot N_i \cdot l_i^2}{\pi^2 \cdot EI_{o,i}}\right) + N_i} \quad . \tag{27}$$

If $e_i = e_{u,i}$, then $\omega_i \longrightarrow \infty$.

It is now relationship $\xi_i - \Delta_i$ that shall be written using the notation introduced in (23):

If $\Delta_i < 0.5 \cdot \left(\frac{1}{\varepsilon_i} - 1\right) = \Delta_{i,u}$ (according to relationship 4), then

$$\xi_i = \frac{\varepsilon_i \cdot \Delta_i}{3\, q_i \cdot \varepsilon_i \left(1 - \frac{4}{\pi^2 \cdot q_i}\right) + \varepsilon_i} \tag{28}$$

while if $\Delta_i = 0.5 \cdot \left(\frac{1}{\varepsilon_i} - 1\right) = \Delta_{i,u}$ then

$$\xi_i \longrightarrow \infty \quad .$$

For bars upon which normal force is not directly acting (bar 1), horizontal resultant force $\overline{H}_1$ (ie either combination force H or resultant force T–H) can be calculated directly from displacement ω. Function $\xi_1 - \Im_1^*$ is set up similarly of two sections depending on the magnitude of bending force acting upon the bar. Let first the magnitude of displacement ω or ξ_1 where the bar stops being rigid be calculated. The rigidity of the bar discontinues when the magnitude of bending moment $\overline{H}_1 \cdot l_1$ reaches the value of the boundary moment of the sandwich cross section:

$$\overline{H}_1 \cdot \ell_1 = M_{u,1} \quad . \tag{29}$$

Since $M_{u,1} = \frac{N_{u,1} \cdot h_1}{2}$, thus

$$\overline{H}_1 = \frac{N_{u,1} \cdot h_1}{2 \cdot \ell_1} \quad . \tag{30}$$

With this value substituted into (26) and with the equation reduced, the value of displacement ω where the boundary condition of the cross section takes place (ω_u) can be obtained:

$$\omega_u = \frac{N_{u,1} \cdot h_1 \cdot \ell_1^2}{6\ EI_{o,1}} \tag{31}$$

or in a dimensionless form

$$1, = \frac{1}{6 \cdot q_1^*} \tag{32}$$

Then relationship $\xi_1 - \varrho_1^*$ can be written on the basis of (26).

If $\xi_1 < \xi_{1,u}$, then

$$\varrho_1^* = \frac{3 \cdot q_1^* \cdot \xi_1}{\gamma 1} \tag{33}$$

while if $\xi_1 \geq \xi_{1,u}$, then on the basis of (30):

$$\varrho_1^* = \frac{1}{2 \cdot \gamma_1} \quad . \tag{34}$$

Now with functions $\xi_i - \Delta_i$ and/or $\xi_1 - \varrho_1^*$ determined, the critical load of the bar system can be determined by means of equations (24), (25a) or (24), (25b), respectively, depending on the conditions of load.

7.2.2 Investigation of a system consisting of bars of rectangular cross section

Function $\omega_i - e_i$ of bars with normal force acting upon them is given also in the present case by relationship (20). Rigidity EI_i can be determined in accordance with equation (10). Hence,

$$\omega_i = \frac{N_i \cdot e_i}{\frac{3\ EI_i}{\ell_i^2} \left(1 - \frac{4 \cdot N_i \cdot \ell_i^2}{\pi^2 \cdot EI_i}\right) + N_i} \quad , \tag{20}$$

where EI_i is the value of rigidity:

$$EI_i = EI_{o,i} \left\{ 1 - \left[\frac{N_i}{N_{u,i} \left(\sqrt{4 \left(\frac{e_i}{h_i} \right)^2 + 1} - 2 \frac{e_i}{h_i} \right)} \right]^6 \right\} \tag{10}$$

By introducing reduction factor

$$z_i = 1 - \left[\frac{N_i}{N_{u,i} \left(\sqrt{4 \left(\frac{e_i}{h_i} \right)^2 + 1} - 2 \frac{e_i}{h_i} \right)} \right]^6 , \tag{35}$$

rigidity EI_i is reduced to a simple relationship

$$EI_i = EI_{o,i} \cdot z_i \tag{36}$$

Let now the functions so obtained be written in a dimensionless form. It can be written on the basis of equation (20) that

$$\xi_i = \frac{\varepsilon_i \cdot \Delta_i}{3 \cdot q_i \cdot \varepsilon_i \cdot z_i \left(1 - \frac{4}{\pi^2 \cdot q_i \cdot z_i} \right) + \varepsilon_i} , \tag{37}$$

where the dimensionless values of z_i:

$$z_i = 1 - \left(\frac{\varepsilon_i}{\sqrt{4 \Delta_i^2 + 1} - 2 \Delta_i} \right)^6 . \tag{38}$$

Thus relationship $\xi_i - \Delta_i$ has been determined for the case of bars upon which normal force is acting. It can be seen that, depending on parameters ε_i and q_i, the function takes a different shape for each like in case of sandwich cross sections.

For bars upon which no normal force is acting directly (bar 1), horizontal resultant force $\overline{H}_1$ can be calculated directly from relationship (26). Rigidity EI_1 is obtained from equation (11). Hence,

$$\overline{H}_1 = \frac{3EI_1}{\ell_1^3} \cdot \omega \quad , \tag{26}$$

where

$$EI_1 = EI_{o,1} \left[1 - \left(\frac{M_1}{M_{u,1}} \right)^6 \right] \quad . \tag{11}$$

With boundary moment

$$M_{u,1} = \frac{N_{u,1} \cdot h_1}{4} \tag{39}$$

and effective bending moment

$$M_1 = \overline{H}_1 \cdot \ell_1 \quad , \tag{40}$$

of a rectangular cross section under pure bending, equation (26) will take the following shape:

$$\overline{H}_1 = \frac{3EI_{o,1}}{\ell_1^3} \left[1 - \left(\frac{4 \cdot \overline{H}_1 \cdot \ell_1}{N_{u,1} \cdot h_1} \right)^6 \right] \cdot \omega \; . \tag{41}$$

As seen in relationship (41), the value of $\overline{H}_1$ is given in an implicit form and therefore plotting of function $\overline{H}_1 - \omega$ becomes a rather complicated job. To cope with this difficulty, resultant force $\overline{H}_1$ is considered to be an independent variable while displacement ω a functional value. In this case, no special difficulties are encountered in plotting relationship $\omega - \overline{H}_1$. With equation (41) rearranged accordingly and formulated in a dimensionless form, the following final relationship is obtained:

$$\xi_1 = \frac{\vartheta_1^*}{\frac{3 \cdot q_1^*}{\gamma_1} \left[1 - (4 \, \vartheta_1^* \cdot \gamma_1)^6 \right]} \; . \tag{42}$$

After relationships $\xi_i - \Delta_i$ and $\xi_1 - \vartheta_1^*$ have been determined, the critical load can be determined in the way described above.

8. NUMERICAL EXAMPLES

8.1 Example

Investigated is a system of two bars illustrated schematically in Fig. 26. The bars are made of Grade A 42 steel with sandwich cross section. From among the two bars, it is only bar 2 upon which normal force is acting. Calculate the critical horizontal load of the bar system (T_{cr}).

Specifications:

a) Geometric and cross sectional characteristics:

$$\ell_1 = \ell_2 = 5.00 \text{ m}$$

$$h_1 = h_2 = 0.40 \text{ m}$$

$$F_1 = F_2 = 40 \text{ cm}^2$$

$$I_{1,o} = I_{2,o} = 20 \cdot 20^2 \cdot 2 = 16000 \text{ cm}^4$$

b) Strength characteristics:

Modulus of elasticity: $E = 21000 \text{ KN/cm}^2$

Ultimate strength: $\sigma_{s,u} = 24 \text{ KN/cm}^2$

c) Loads: $N_2 = 600 \text{ KN}$

8.1.1 Calculation of auxiliary quantities

$$N_{u,1} = N_{u,2} = F_1 \cdot \sigma_{s,u} = 40 \cdot 24 = 960 \text{ KN}$$

On the basis of relationship (23):

$$\varepsilon_1 = 0$$

$$\varepsilon_2 = \frac{600}{900} = 0.625$$

$$\gamma_1 = \gamma_2 = \frac{5.00}{0.40} = 12.5$$

$$q_2 = \frac{21000 \cdot 16000}{600 \cdot 500^2} = 2.24$$

$$\nu_1 = \frac{40}{40} = 1$$

$$\varepsilon_1^* = \frac{960}{600} = 1.6$$

$$q_1^* = \frac{21000 \cdot 16000}{960 \cdot 500^2} = 1.4$$

8.1.2 Production of function $\xi_2 - \Delta_2$ of bar 2 (as a bar upon which normal force is directly acting)

According to relationship (28), if $\Delta_2 < \Delta_{2,u}$,

$$\xi_2 = \frac{0.625}{3 \,.\, 2.24 \,.\, 0.625 \left(1 - \frac{4}{\pi^2 \,.\, 2.24}\right) + 0.625} \,.\, \Delta_2 \quad .$$

The result of operation:

$$\xi_2 = 0.153 \;\Delta_2 \quad .$$

Value of eccentricity (see condition before 28):

$$\Delta_{2,u} = 0.5 \left(\frac{1}{0.625} - 1\right) = 0.3 \quad .$$

Function $\xi_2 - \Delta_2$ has been illustrated diagrammatically in Fig. 27.

8.1.3 Production of function $\xi_1 - \vartheta_1^*$ of bar 1 (as a bar upon which no normal force is directly acting)

On the basis of equation (30), if $\xi_1 < \xi_{1,u}$,

$$\vartheta_1^* = \frac{3 \,.\, 1.4}{12.5} \,.\, \xi_1 = 0.336 \,.\, \xi_1 \quad .$$

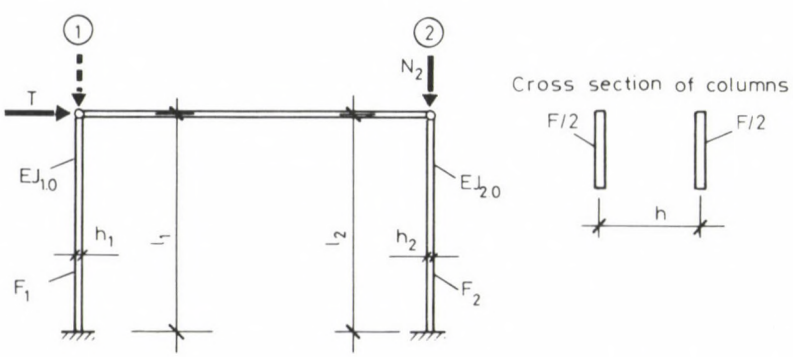

Fig. 26. Bar system consisting of bars of sandwich cross section where normal force is acting upon bar 2

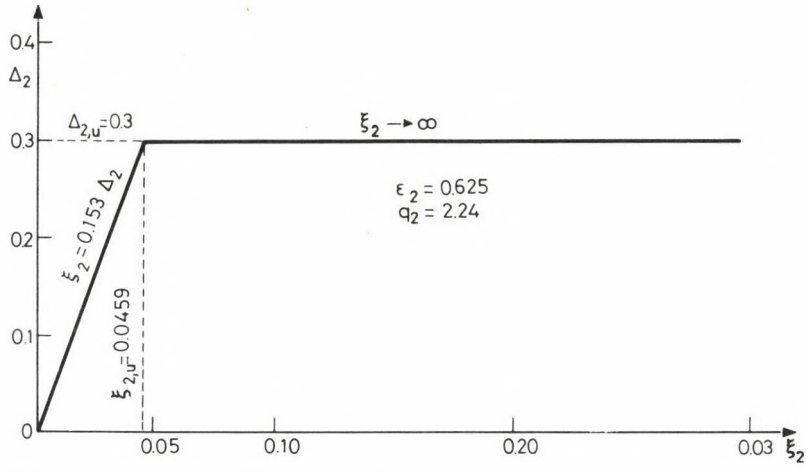

Fig. 27. Function $\xi_2 - \Delta_2$ of bar 2

Value of $\xi_{1,u}$ on the basis of (32):

$$\xi_{1,u} = \frac{1}{6 \cdot 1.4} = 0.119 \quad .$$

Function $\xi_1 - \vartheta_1^*$ has been illustrated diagrammatically in Fig. 28.

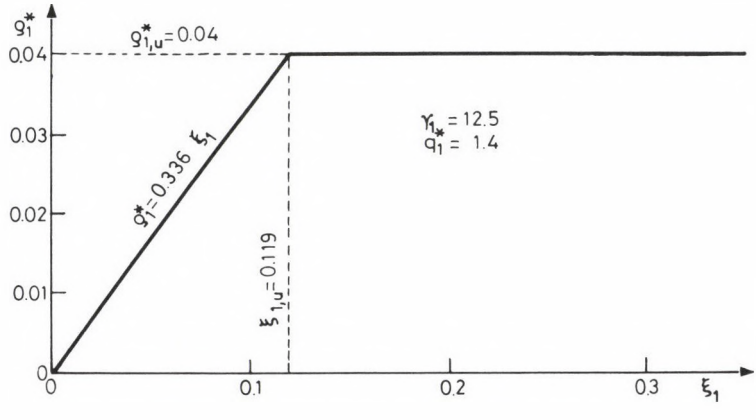

Fig. 28. Function $\xi_1 - \vartheta_1^*$ of bar 1

8.1.4 Determination of the critical horizontal load of the bar system

The different functional values for plotting function $\alpha - \xi_1$ have been determined in Table 1. The tabulated values are diagrammatically illustrated in Fig. 29. $\alpha_{cr} = 0.0784$ has been obtained as the maximum of function $\alpha - \xi_1$. Thus the critical horizontal load:

$$T_{cr} = \alpha_{cr} \cdot N_2 = 0.0784 \cdot 600 = 47.04 \text{ KN} .$$

Table 1 Calculation of critical horizontal load (α_{cr}) of the bar system of example 8.1

Serial No.	Bar 1		Bar 2			Bar system
	ξ_1	ϱ_1^* (Fig. 28)	$\xi_2 = \nu_1 \xi_1$	Δ_2 (Fig.27)	$\varrho_2 = \frac{\Delta_2 - \xi_2}{\gamma_2}$	$\alpha = \varrho_2 + \varrho_1^* \cdot \varepsilon_1$
1	0.02	0.0067	0.02	0.1307	0.0088	0.0195
2	0.0459	0.0154	0.0459	0.3	0.0203	0.0449
3	0.05	0.0168	0.05	0.3	0.0200	0.0468
4	0.1	0.0336	0.1	0.3	0.0160	0.0697
5	0.119	0.04	0.119	0.3	0.0144	0.0784
6	0.15	0.04	0.15	0.3	0.0120	0.0760
7	0.3	0.04	0.3	0.3	0	0.0640

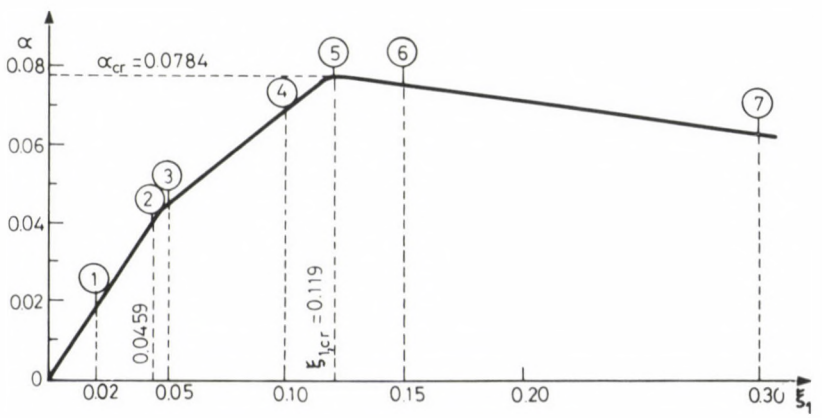

Fig. 29. Determination of the critical horizontal load of the bar system on the basis of function $\alpha - \xi_1$

Displacement of the bar system as a result of force T_{cr}:

$$w_{cr} = \xi_{1,cr} \cdot h_1 = 0.119 \cdot 40 = 4.76 \text{ cm} .$$

8.1.5 Comments

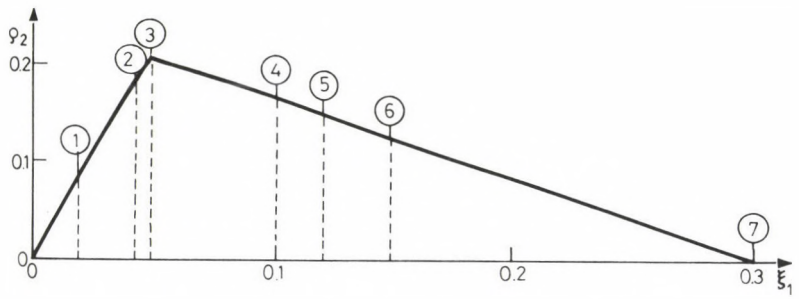

Fig. 30. Function $\xi_1 - \vartheta_2$ of bar system

With function $\xi_1 - \vartheta_2$ plotted on the basis of Table 1 (Fig. 30), the change of the combination force arisen in the horizontal beam is clearly visible in the Figure. At the beginning of the loading process, the combination force (or its dimensionless value ϑ_2) increases approximately in proportion as the horizontal load (α) increases when the load intensity is increased. The value of ϑ_2 is approximately half of the value of α which means that the share of the bars in carrying the horizontal load is approximately identical. A difference occurs because of the second-order effect. This condition will prevail until both bars are in elastic state and their rigidity is identical with the initial rigidity. As soon as a plastic state of bar 2 takes place, the value of ϑ_2 or relative value $\frac{\vartheta_2}{\alpha}$ starts reducing rapidly with the share of bar 2 in carrying the horizontal load continuously reducing. The bar system loses stability when the boundary plastic condition of bar 1 takes place.

With the vertical load acting upon bar 2 increasing, the critical horizontal load of the system reduces rapidly. The results of calculations not presented here in detail are diagrammatically illustrated in Fig. 31.

For the sake of comparison, the value of maximum stress arisen in bar 2 has been determined for a bar system with a horizontal load of T_{cr} = 47.07 KN acting upon it on the basis of Hungarian Standard MSZ

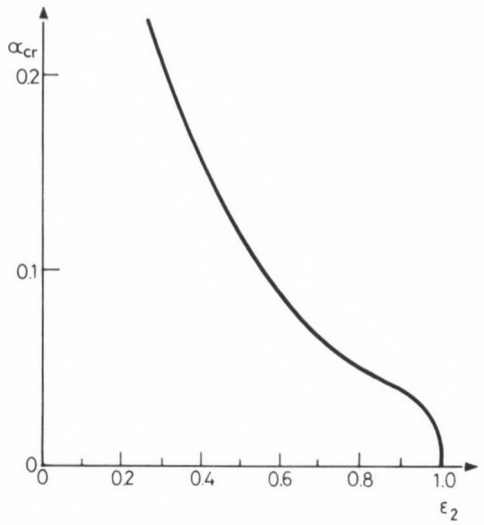

Fig. 31. Change of critical horizontal load of the bar system (α) as a function of vertical normal force (ϑ_2)

15024/1–75. In the calculation according to the standard, the upper limit of load capacity is given, instead of the plastic instability load, by the force resulting in first yield, smaller than the plastic instability load. Thus the investigations takes place in the elastic zone. The ratio of horizontal load per bar can be calculated on the basis of the ratio of elastic rigidities of the bars. The second-order effect is taken into consideration only by multiplying the moment determined for the different bars in accordance with the theory of elasticity with a factor Ψ. A maximum stress of σ_{max} = 33.70 KN/cm^2 has been obtained as a result of calculations. There is a difference of 40% between this value and the value of $\sigma_{s,u}$ = 24 KN/cm^2 used in our calculations, this difference being at the same time an improvement of the safety. This difference increases continuously as the vertical compressive force acting upon bar 2 increases. E.g. if the value of N_2 is increased from 600 KN to 900 KN, the value calculated in accordance with the standard shows a difference of about 55%.

8.2 Example

Consider the bar system schematically illustrated in Fig. 32. This system differs from that of the previous example in that here normal force

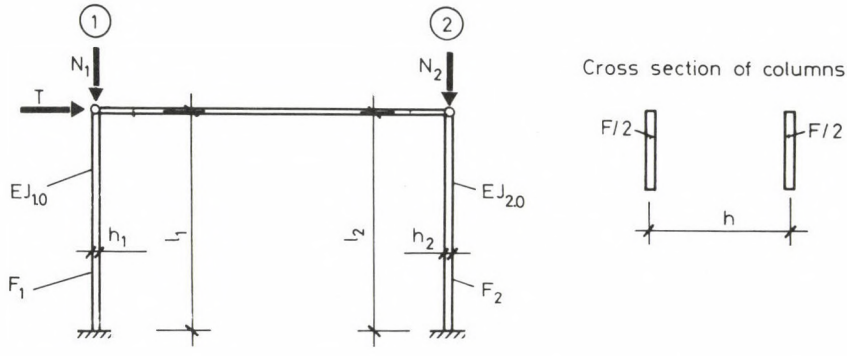

Fig. 32. Bar system consisting of bars of sandwich cross section with normal force acting upon both bars

is acting also upon bar 1. Determine the horizontal critical load (T_{cr}) of the bar system also in this case.

Specifications:

a,b) The geometric and cross sectional characteristics are the same as in case of the bar system of example 8.1.

c) Loads: $N_1 = 300$ KN

$N_2 = 600$ KN.

8.2.1 Calculation of auxiliary quantities

$$N_{u,1} = N_{u,2} = 960 \text{ KN (see example 8.1)}$$

On the basis of relationship (23):

$$\varepsilon_1 = \frac{300}{600} = 0.3125$$

$$\varepsilon_2 = \frac{600}{960} = 0.625$$

$$\gamma_1 = \gamma_2 = 12.5 \text{ (see example 8.1)}$$

$$q_1 = \frac{21000 \cdot 16000}{300 \cdot 500^2} = 4.48$$

$$\left.\begin{aligned} q_2 &= 2.24 \\ \nu_1 &= 1 \end{aligned}\right\} \text{ (see example 8.1)}$$

$$\mu = \frac{300}{600} = 0.5 \quad .$$

8.2.2 Production of function $\xi_2 - \Delta_2$ of bar 2 (as a bar upon which normal force is directly acting)

Function $\xi_2 - \Delta_2$ is identical with the function determined in par 8.1.2 and illustrated diagrammatically in Fig. 27.

8.2.3 Production of function $\xi_1 - \Delta_1$ of bar 1 (as a bar upon which normal force is directly acting)

According to relationship (28), if $\Delta_1 < \Delta_{1,u}$,

$$\xi_1 = \frac{0.3125}{3 \,.\, 4.48 \,.\, 0.3125 \left(1 - \frac{4}{\pi^2 \,.\, 4.48}\right) + 0.3125} \Delta_1 \quad .$$

Result of operation:

$$\xi_1 = 0.0756 \, \Delta_1 \quad .$$

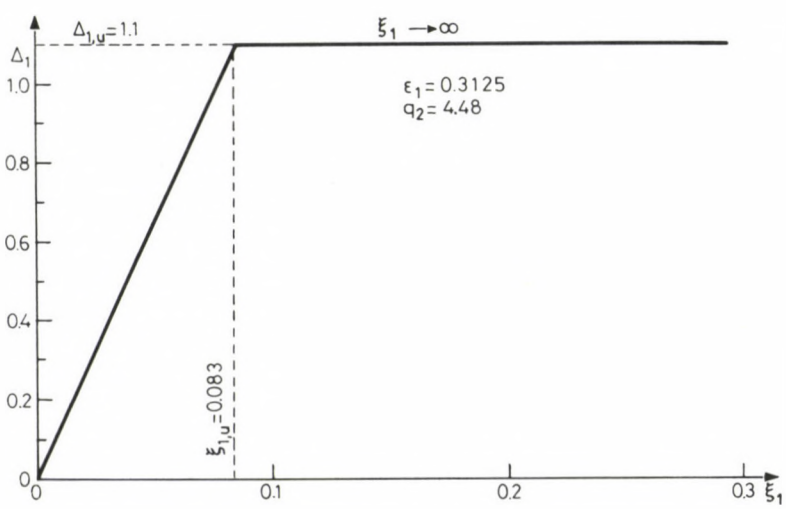

Fig. 33. Function $\xi_1 - \Delta_1$ of bar 1

Value of boundary eccentricity (see condition before 28):

$$\Delta_{1,u} = 0.5\left(\frac{1}{0.3125} - 1\right) = 1.1 \ .$$

Function $\xi_1 - \Delta_1$ has been illustrated diagrammatically in Fig. 33.

8.2.4 Determination of the critical horizontal load of the bar system

The different functional values for plotting function $\alpha - \xi_1$ have been calculated in Table 2 while illustrated diagrammatically in Fig. 34.

$\alpha_{cr} = 0.0579$ has been obtained for the maximum of function $\alpha - \xi_1$. Thus, the critical horizontal load,

$$T_{cr} = \alpha_{cr} \cdot N_2 = 0.0579 \cdot 600 = 34.74 \text{ KN} \ .$$

Displacement of the bar system as a result of critical load:

$$w_{cr} = \xi_{1,cr} \cdot h_1 = 0.083 \cdot 40 = 3.32 \text{ cm} \ .$$

Table 2 Calculation of critical horizontal load (α_{cr}) of the bar system of example 8.2

Serial No.	Bar 1			Bar 2			Bar system
	ξ_1	Δ_1 (Fig. 33)	$\frac{\mu}{\gamma_1}(\Delta_1 - \xi_1)$	$\xi_2 = \nu_1 \xi_1$	Δ_2 (Fig.27)	$\vartheta_2 = \frac{\Delta_2 - \xi_2}{\gamma_2}$	$\alpha = \frac{\mu}{\gamma_1} \cdot (\Delta_1 - \xi_1) + \vartheta_2$
1	0.02	0.2645	0.0097	0.02	0.1307	0.0088	0.0185
2	0.0459	0.6071	0.0224	0.0459	0.3	0.0203	0.0427
3	0.05	0.6613	0.0244	0.05	0.3	0.0200	0.0444
4	0.083	1.1	0.0406	0.083	0.3	0.0173	0.0579
5	0.1	1.1	0.0400	0.1	0.3	0.0160	0.0560
6	0.15	1.1	0.0380	0.15	0.3	0.012	0.0500
7	0.3	1.1	0.032	0.3	0.3	0	0.32

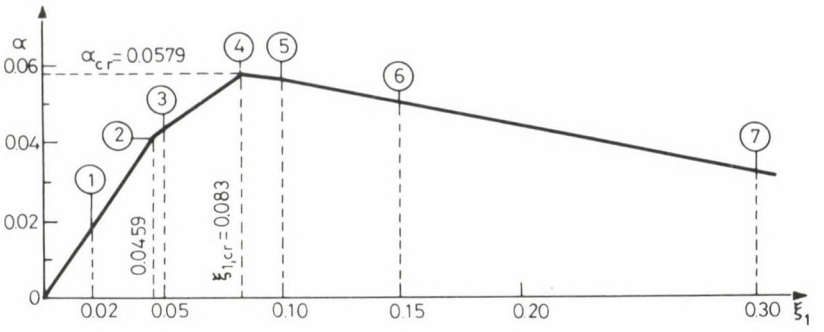

Fig. 34. Determination of the critical horizontal load of the bar system on the basis of function $\alpha - \xi_1$

8.2.5 Comments

The result of the investigation show that the critical load of the bar system reduced considerably because normal load was acting also upon bar 1. The plastic state of bar 2 is the first to take place also in this case.

The supporting power of bar 1 is reduced as compared with that in example 8.1 as bar 1 itself is subjected to normal force and thus its boundary plastic condition takes place sooner which means at the same time the reduction of stability of the entire bar system.

The effect of the ratio of normal forces acting upon the bars on the critical horizontal load has been investigated. With the value of total normal force, $N_1 + N_2 = \sum N$, left unaltered, the values of critical horizontal load was found in the cases investigated.

A difference of about 55% was found for case 1 by use of the method according to Hungarian Standard MSZ 15024/1–75 on steel structures while an almost perfect agreement of the results was found for case 4. Hence, the values according to the standard can be considered accurate if the relative load carried by the bars ($N_i/N_{u,i}$) is approximately identical. However, in case of a significant difference between the loads to be carried as well as in the occurrence of the boundary condition of plasticity, the intersupporting effect of the bars is not taken into consideration by the standard. This means that a significant ratio of the load carrying capacity is practically lost.

Table 3 Effect of $\frac{N_1}{N_2}$ on critical load

Serial No.	$\sum N$ [KN]	N_1 [KN]	N_2 [KN]	T_{cr} [KN]
1	900	0	900	31.79
2	900	150	750	33.19
3	900	300	600	34.49
4	900	450	450	35.39

8.3 Example

In Fig. 35, a rectangular bar system consisting of two bars is illustrated schematically. The initial rigidity of bar 1 is higher than that of bar 1. No normal force is acting upon bar 1. Calculate the magnitude of critical horizontal load:

Specifications:

a) geometric and cross sectional characteristics:

$$\ell_1 = \ell_2 = 5.00 \text{ m}$$

$$h_1 = 0.40 \text{ m}$$

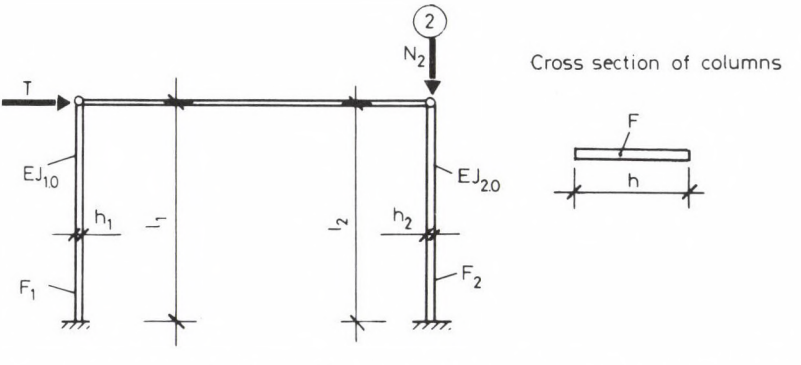

Fig. 35. Bar system consisting of bars of rectangular cross section with normal force acting upon bar 2

$$h_2 = 0.60 \text{ m}$$

$$F_1 = 40 \text{ cm}^2$$

$$F_2 = 60 \text{ cm}^2$$

$$I_{o,1} = \frac{1.40^3}{12} = 53333 \text{ cm}^4$$

$$I_{o,2} = \frac{1.60^3}{12} = 18000 \text{ cm}^4$$

b) strength characteristics:
modulus of elasticity: $E = 21\,000 \text{ KN/cm}^2$
ultimate strength: $\sigma_{s,u} = 24 \text{ KN/cm}^2$
c) loads: $N_2 = 900 \text{ KN}$

8.3.1 Calculation of auxiliary quantities

$$N_{u,1} = 40 \cdot 24 = 960 \text{ KN}$$

$$N_{u,2} = 60 \cdot 24 = 1440 \text{ KN}$$

On the basis of relationship (23):

$$\varepsilon_1 = 0$$

$$\varepsilon_2 = \frac{900}{1440} = 0.625$$

$$\gamma_1 = \frac{5.00}{0.4} = 12.5$$

$$\gamma_2 = \frac{5.00}{0.5} = 8.33$$

$$q_2 = \frac{21.000 \cdot 18.000}{900 \cdot 500^2} = 1.68$$

$$\nu_1 = \frac{40}{60} = 0.667$$

$$\varepsilon_1^* = \frac{960}{900} = 1.067$$

$$q_1^* = \frac{21.000 \cdot 5.333}{960 \cdot 500^2} = 0.466$$

8.3.2 Production of function $\xi_2 - \Delta_2$ of bar 2 (as a bar with normal force directly acting upon it)

Function $\xi_2 - \Delta_2$ is supplied by equation (37):

$$\xi_2 = \frac{0.625}{3 \cdot 1.68 \cdot 0.625 \cdot z_2 \left(1 - \frac{4}{\pi^2 \cdot 1.68 \cdot z_2}\right) + 0.625} \cdot \Delta_2$$

where

$$z_2 = 1 - \left(\frac{0.625}{\sqrt{4\,\Delta_2^2 + 1 - 2\,\Delta_2}} \right)^6 .$$

Result of the operation:

$$\xi_2 = \frac{0.625}{3.15 \cdot z_2 \left(1 - \frac{0.241}{z_2}\right) + 0.625} \cdot \Delta_2 .$$

On the basis of the above equation, function $\xi_2 - \Delta_2$ is plotted in Fig. 36.

8.3.3 Production of function $\xi_1 - \Delta_1$ of bar 1 (as a bar upon which normal force is not acting directly)

According to relationship (42):

$$\xi_1 = \frac{\vartheta_1^*}{\frac{3 \cdot 0.466}{12.5} \left[1 - (4 \cdot \varrho_1^* \cdot 12.5)^6\right]} .$$

Function

$$\xi_1 = \frac{\vartheta_1^*}{0.1118 \left[1 - (50 \cdot \vartheta_1^*)^6\right]}$$

is obtained as a result of the operations.

Function $\xi_1 - \vartheta_1^*$ is plotted in Fig. 37.

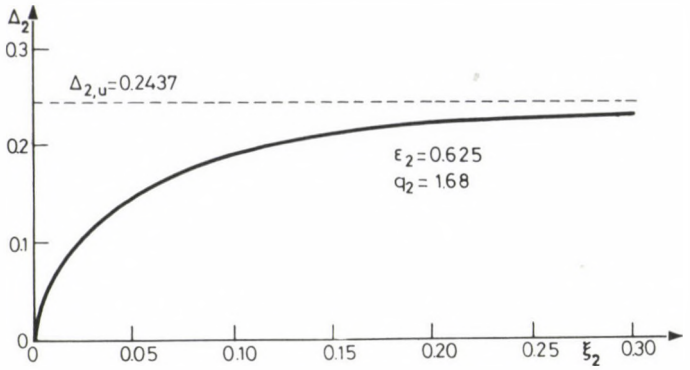

Fig. 36. Function $\xi_2 - \Delta_2$ of bar 2

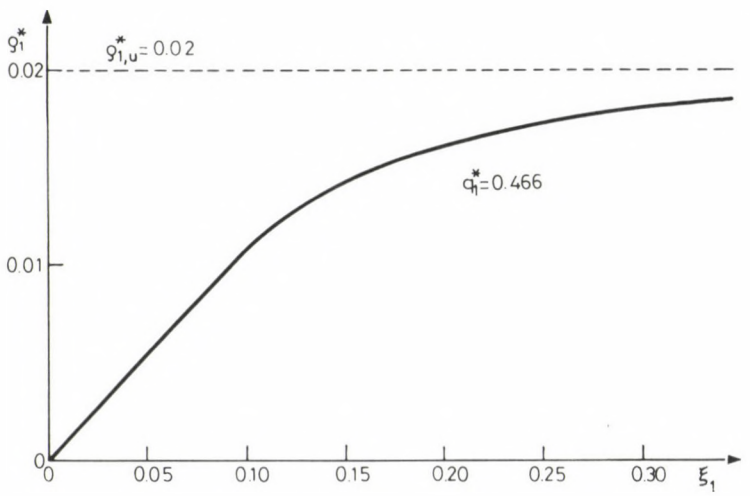

Fig. 37. Function $\xi_1 - \vartheta_1^*$ of bar 1

8.3.4 Determination of the critical horizontal load of the bar system

To plot function $\alpha - \xi_1$, the different functional values have been determined in Table 4. The tabulated values are presented in Fig. 38. Extreme value of function $\alpha - \xi_1$: $\alpha_{cr} = 0.0286$. Thus the critical horizontal load:

$$T_{cr} = \alpha_{cr} \cdot N_2 = 0.0286 \cdot 900 = 25.74 \text{ KN} \quad .$$

Table 4

Calculation of critical horizontal load (T_{cr}) of the bar system of example 8.3

Serial No.	Bar 1		Bar 2			Bar system
	1	$\overset{*}{1}$ (Fig.37)	$2^{=} \; 1^{\cdot} \; \overset{*}{1}$	2 (Fig.36)	$2^{=} \frac{2^{-} \; 2}{2}$	$= \; 2^{+} \; \overset{*}{1}^{\cdot} \; \overset{*}{1}$
1	0.05	0.0055	0.0333	0.123	0.0107	0.01584
2	0.1	0.0108	0.0666	0.170	0.0124	0.0239
3	0.15	0.0142	0.1	0.213	0.0135	0.0286
4	0.2	0.0162	0.1333	0.222	0.0106	0.0278
5	0.25	0.0172	0.1666	0.222	0.006	0.0247

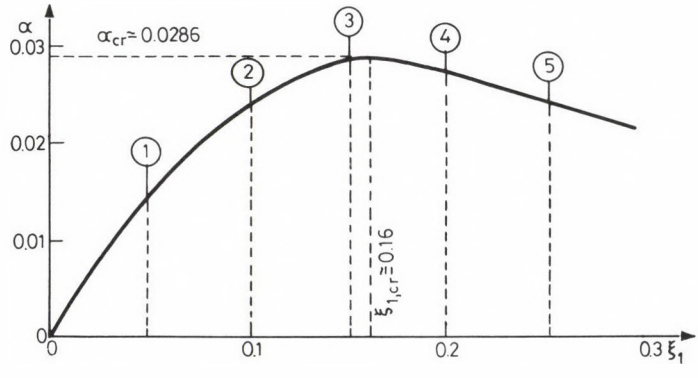

Fig. 38. Determination of the critical horizontal load of the bar system on the basis of function

Displacement of the bar system as a result of force T_{cr}:

$$\omega_{cr} = \xi_{1,cr} \cdot h_1 = 0.16 \cdot 40 = 6.4 \text{ cm} \quad .$$

8.3.5 Comments

Considering function $\xi_1 - \alpha$, it can be seen that there is no sharp break in the curve. This can be attributed to the fact that, due to the nature of the cross section, development of the plastic zones takes place gradually.

A comparison of the result obtained with the final result of calculation according to the standard showed a difference of about 60%, the

critical load according to the standard deviating in favour of safety. If the load acting upon bar 2 is increased, the difference between the two methods of calculation continues increasing. A difference of about 20% is obtained as a result of a comparison of a critical load of a symmetrically arranged bar system with symmetric load with the value according to the standard.

REFERENCES

1. Kaliszky, S.: Theory of plasticity. Theory and applications in enginnering. Akadémiai Kiadó, Budapest, 1975.
2. Halász, O.: Stability calculations of steel structures. Second-order problems (Doctor's Thesis), Budapest, 1976.
3. Halász, O.: Materials and mechanics of light-weight structures. Műszaki Tudomány, Vol. 44, 1971.
4. Korányi, I.: Elastic buckling (stability problems in engineering practice I). Felsőoktatási Jegyzetellátó V., Budapest, 1957.
5. Korányi, I.: Plastic buckling (stability problems in enginnering practice II). Felsőoktatási Jegyzetellátó V., Budapest, 1957.
6. Korányi, I.: Stability problems in engineering practice. Akadémiai Kiadó, Budapest, 1965.
7. Horne, M.R., Merchant, W.: The Stability of Frames. Pergamon Press, Oxford, 1965.
8. Csonka, P.: Contribution to buckling theory. Publications of Department of Technical Sciences, Hungarian Academy of Science, Vol. VI, P. 281, 1951.
9. Ježek, K.: Die Festigkeit von Druckstäben aus Stahl. Verlag von Julius Springer, Wien, 1937.
10. Timoshenko, S.F., Gere, J.H.: Theory of Elastic Stability. McGraw-Hill, New York, 1961.
11. Dulácska, E.: Plastic twist buckling of slender reinforced concrete beams. Architectural Research and Development, 1985/2.
12. Bölcskei, E., Dulácska, E.: Handbook of structural engineers. Műszaki Könyvkiadó, Budapest, 1974.
13. Hungarian Standard MSZ 15024/1–75: Mechanical design of the bearing structure of buildings. Steel Structures, 1975.
14. Korondi, D.: Approximate stability investigation of multiply-supported single-level plane frames. (Postgraduate diploma work), 1972.
15. Stability of frames and bar systems. BVTV–Text Book, 1972.
16. Rabolt, K., Warnstedt, G., Werner, F.: Verfahren der elastischplastischen Berechnung von Stabtragwerken des Stahlhochbaus. Bauplanung-Bautechnik 1986/6.
17. Palotás, L.: Handbook of Engineers. Műszaki Könyvkiadó, Budapest, 1984.
18. Design of steel structures for plasticity. Architectural Sectoral Directives M1–04.188–80, Architectural Information Centre, Budapest, 1980.

Acta Technica Acad.Sci.Hung., 101(1),pp. 49–58 (1988)

CONCLUSION DRAWN FROM THE ANALYSIS OF A CONTINUUM MECHANICAL MODEL OF FOUR DEGREES OF FREEDOM PROPOSED PREVIOUSLY FOR THE DESCRIPTION OF THE BEHAVIOUR OF GRANULAR MATERIALS

J. Füzy*, Gy. Páti**, J. Vas***

(Received: 28 October 1987)

A new microelastic continuum model was developed by two of the authors in a previous paper. This model is based on Mindlin's microelastic continuum theory and it takes into consideration the dilatation of microdeformation only. The model is supposed to be a possible way of simulation of the phenomenon of dilatation of granular materials without isotropic pressure.

In this paper, the proposed model has been studied in detail to find that intrinsic volume change of this type can take place in two dimensional fields such as critical fields or yielding fields but never in the three dimensional space as in case of the mentioned phenomenon.

1. INTRODUCTION

Continuum mechanics is, by definition, a discipline describing the structure of material — discrete in all cases — by continuous functions. The main application of continuum theories of higher degrees of freedom is just to describe the discrete structure of materials more and more accurately with the aid of continuous functions.

The main idea is that structures of inhomogeneous cells recurring in a large number can be replaced by a homogeneous continuum of higher order of freedom /7/. In these theories the elementary point is a finite volume, its dimension defined by the structure of the material investigated. This so called "representative volume" /8/ can not be smaller than over which

*J. Füzy, 1012 Budapest, Márvány u. 1/b, Hungary

**Gy. Páti, Hungarian Institute for Building Science, H–1113 Budapest, Dávid F. u. 6.

***J. Vas, Military Technical Training College, H–2001 Szentendre, Pf. 166, Hungary

Akadémiai Kiadó, Budapest

the macro-stresses can be defined. In case of granular materials the representative volume must consist of so many grains that the volume have the same features of behaviour from macro aspect as the material.

The deformation of the microvolumes is determined by the macro displacement and deformation but inside the microvolume an independent – homogeneous – microdeformation can take place. The number of grains in such a representative volume need not be determined, Cowin and Goodman did not so either /4, 5/, but in the following short introduction we try to give some aspects of it. Our outgoing point will be the deformable director's theory.

An illustrative application of the theory of deformable directors has been given by Eringen /1/ in the following way (see Fig. 1).

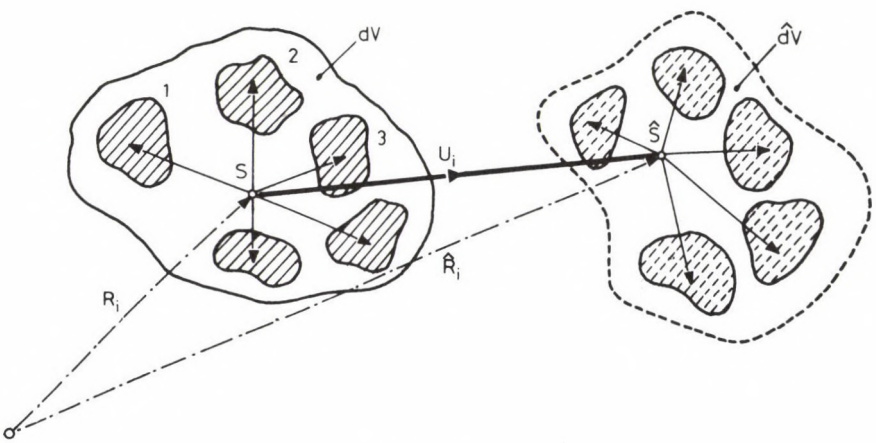

Fig. 1.

In his approach mass points of number "n" "float" in the elementary finite volume "dV". The positions of the mass points are fixed by their position vectors referred to their common centre of gravity "S", which are in this case the deformable directors.

The displacement field of classical continuum theory in this concept is represented by the displacement of the centre of gravity "S". The position vectors describing the relative motion of mass point "n" are independent kinematical variables within the microvolume. Mindlin /2/ reduced the number of deformable directors to three; in this case the elements of motion of the director's tips can be represented as the elements of the so called "micro" deformation tensor (see Fig. 2).

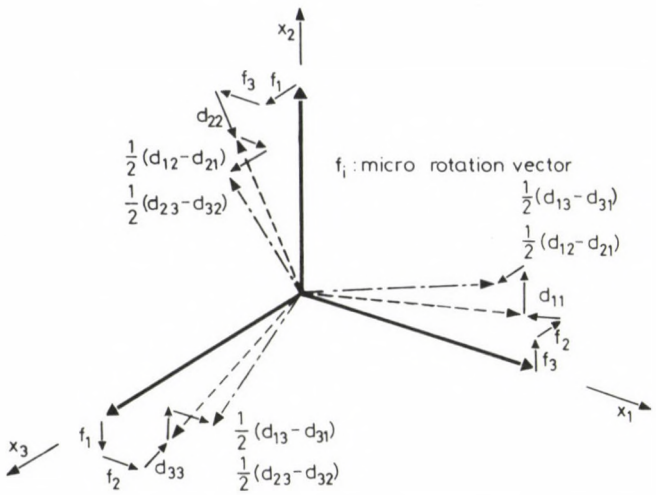

Fig. 2.

This model facilitates the description of the dynamics of granular media in that the finite micro volume contains four grains, one of which being the reference grain, and the motion of the further three grains described by the micro deformation tensor (see Fig. 3).

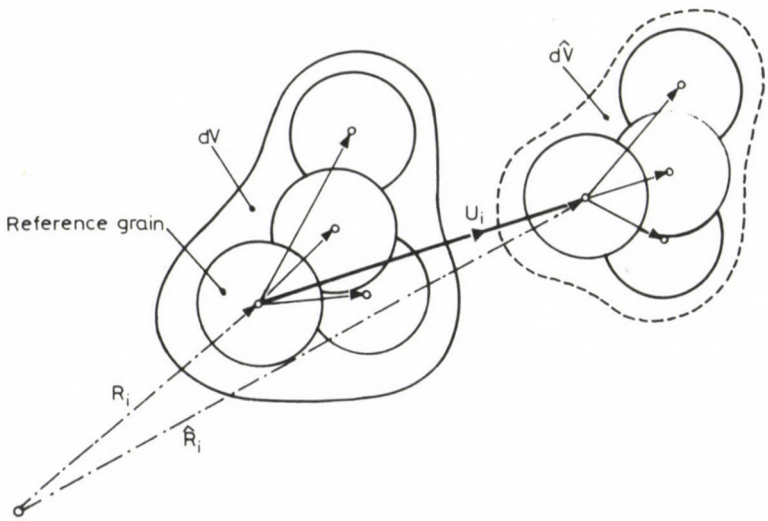

Fig. 3.

In this case the number of kinematically independent variables:

– displacement vector U_i (3 components),

– micro deformation tensor d_{ij} (9 components) and the degree of freedom of the system is 12.

In a previous paper /3/ we have shown that, from this model, we can deduce a system of four degrees of freedom in which, beside the three components of the displacement vector U_i the fourth degree of freedom is represented by an embedded, kinematically independent volumetric function.

In deduction, the micro deformation tensor has been described by a scalar function as follows:

$$d_{ij} = \frac{e}{3} \delta_{ij} \tag{1}$$

From the character of scalar function $e = d_{ii}$ (intrinsic dilatation) we have concluded the model may be suitable for describing and mathematically modelling the dilatational properties of granular media. Therefore, we have carried out detailed investigations into the model /6/ from this point of view, the conclusions drawn being described below.

2. CONCLUSION DRAWN FROM INVESTIGATION INTO THE MODEL OF FOUR DEGREES OF FREEDOM

2.1 Kinematic conclusions

The kinematical variables of the model of four degrees of freedom are essentially identical with the variables of the proposed earlier by Cowin and Goodman /4, 5/. Although they mentioned /5/ that their model was a deduction of Mindlin's model of 12 degrees of freedom, they deduced their relations independently of that model, and we are unable to deduce these relations from Mindlin's basic equations. Cowin and Goodman in their first paper /4/ on the flow of granular media have mentioned that the flow of granular media cannot be taken to be identical with the flow of viscous fluids because of the appearance of "plug regions" in the former. This seems to be in agreement with the relation deduced by us for the volumetric function "e" in /6/:

$$e_{,ii} + C_1 e = C_2 D_{kk} \tag{2}$$

This equation refers undoubtedly to a boundary layer problem, therefore we have studied in detail the physical contents of, and the differences between, "macro" dilatation D_{ii} represented by the gradient field of displacement vector

$$D_{ij} = \frac{1}{2} (U_{j,i} + U_{i,j}) \tag{3}$$

and "micro" dilatation "e" recently introduced.

As the micro deformation tensor has been reduced in this case to a scalar function, the restraint according to Fig. 3 becomes superfluous because it is no longer necessary to describe the motion of the individual grains.

Owing to the restraints imposed on the micro deformation tensor, the third-order tensor, in Mindlin's terminology the hyperstress tensor μ_{ijk}, degenerates to a vector μ_i. This also means, that from among the self-equilibrated double stresses, only those acting coaxially remain (see Fig. 4).

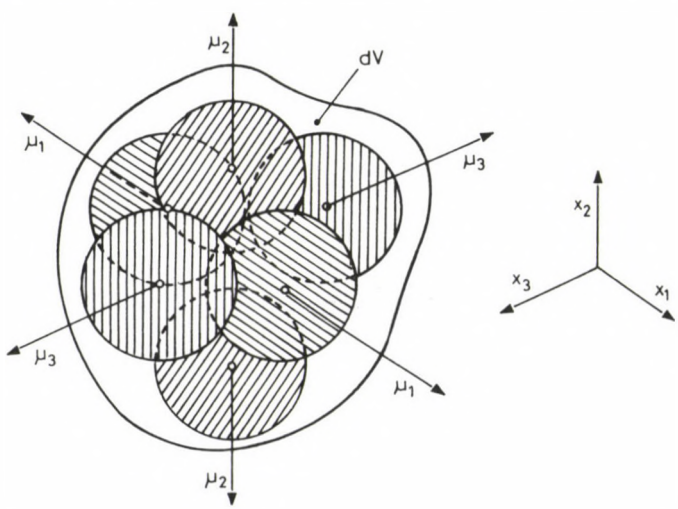

Fig. 4.

On the basis of Fig. 4 the number of grains in the micro volume can be reduced to six if it is necessary to determine their number at all. The physical implication of intrinsic volumetric function "e" is voids that is the changes of voids. In terms applied in soil mechanics, denoting the volume of the solid part in a unit micro volume dV with "m" and the void

with "n", the void varying in time and space can be expressed in the following way:

$$n\left[x_i,t\right] = n_o\left[x_i\right] + D_{ii}\left[x_i,t\right] + e\left[x_i,t\right] \tag{4}$$

where n_o is the initial void varying only in space and D_{ii} is the macro dilatation. This definition also determines the difference between macro dilatation D_{ii} and embedded, micro dilatation "e".

In case of compressible grains isotropic pressure $\mu_1 = \mu_2 = \mu_3 = \mu$ acting on the grains presses them together and the void volume increases. Pressure μ caused by different physical phenomena is independent of the macro stresses. In our case the grains are supposed to be incompressible so many problems are faced.

Accordingly, the dynamics of grains acts in the two following ways:

– in the first case, the grains take part in an affine way in the transformation of volume element dV (see Fig. 5),

– in the second case, however, the motion of grains takes place independently of the variation of volume dV (see Fig. 6).

In Fig. 6, the controversy of the phenomenon can be clearly recognized. Since the grains are incompressible, the voids can increase only such a way that they are shifted to the neighbouring micro-volumes. This, however, is inconceivable in a continuous, three-dimensional field, but is

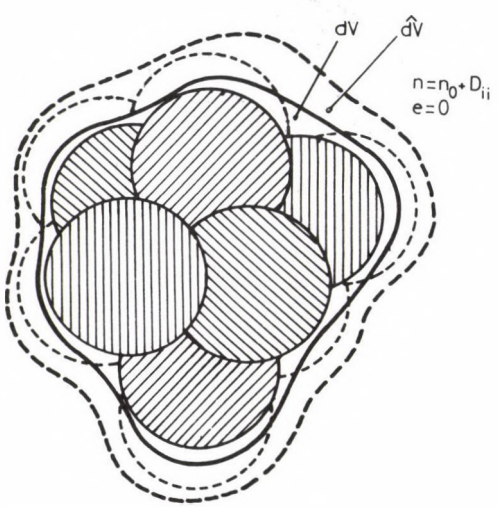

Fig. 5.

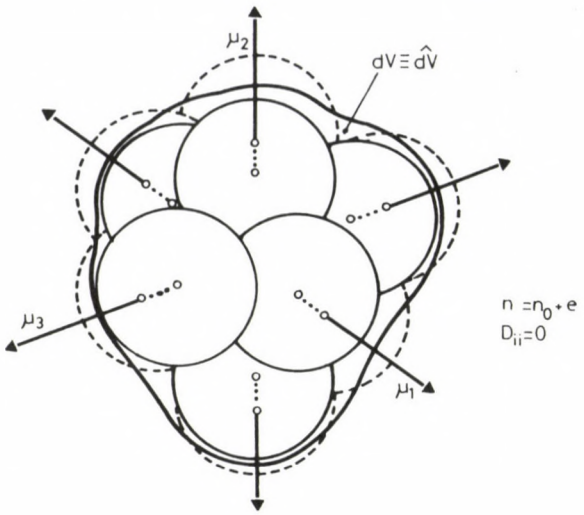

Fig. 6.

conceivable in a continuous layer of one micro-volume thickness, e.g. with dilatancy taking place in that layer while compaction and hardening in the two adjacent layers, also of one micro-volume thickness. This is in agreement with the boundary layer problem character represented by equation (2).

If the initial value of the void in micro-volume dV assumed to be of unit size is n_0, it will change during the process to $(n_0 + e)$, taking into consideration only micro dilatation, and the micro-volume still remains of unit size. Thus, mass distribution function $\mathfrak{Z}$ has only one independent variable:

$$\mathfrak{Z}\left[e(x_i,t)\right] = (1 - n_0 - e)\,\gamma^S = \mathfrak{Z}_0 - e\gamma^S \tag{5}$$

where initial mass distribution:

$$\mathfrak{Z}_0 = (1 - n_0)\,\gamma^S \tag{6}$$

which is determined by initial void n_0 and mass density γ^S = const of the material of grains. In view of what has been said above, the time derivative is

$$\dot{\mathfrak{Z}} = \gamma^S \dot{e} \tag{7}$$

The continuum mechanical field equations (equation of conservation of momentum, geometrical and compatibility equations /6/) remain unchanged but equation of mass conservation is completed by the term (7) and thus takes the following from:

$$\dot{\varrho} + (\varrho V_i)_{,i} + \dot{e}\,\gamma^S = 0 \tag{8}$$

2.2 Constitutive conclusions

Moving the grains closer to or away from each other within the micro-volume determined by the value of "e" influences the work required to bring about shear (deviatoric) deformation. To move the grains away from each other requires work which is linear with "e" while when the grains approach each other energy is released. Near the initial state this energy is also approximately linear, but later, as hydrostatic (or geostatic) pressure in the medium also depends on "e", it increases gradually and tends to infinity at a critical value n_{crit} (see Fig. 7).*

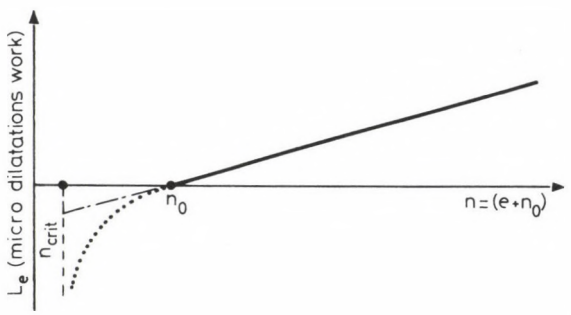

Fig. 7.

The work required to cause shear deformations obviously depends on "e" that is the volume of the void between the grains. The character of the variation of work is shown in Fig. 8.*

With the two types of work added, opposite in the present case (see Fig. 9), there must be a minimum where shear deformation takes place with the smallest possible work input.

*Diagrams taken into consideration by the authors, without experiments

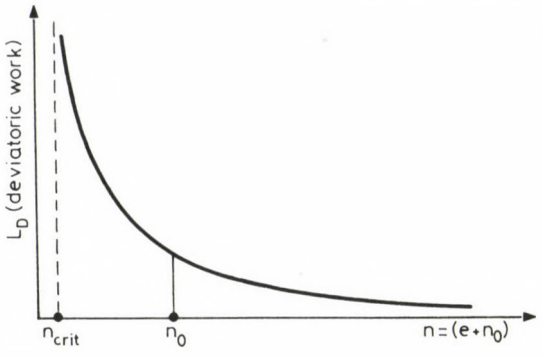

Fig. 8.

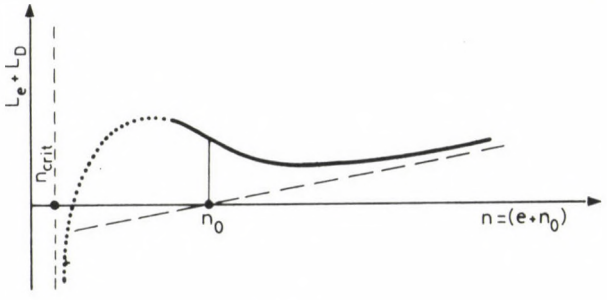

Fig. 9.

This minimum criterion can be formulated as follows:

$$\frac{\partial}{\partial e}\left[L_e + L_D\right] = 0 \qquad \text{a)}$$

$$\frac{\partial^2}{\partial e^2}\left[L_e + L_D\right] < 0 \qquad \text{b)}$$

In summary it can be stated that the theory proposed above is not suitable for the mathematical modelling of the dilatation due to the homogeneous shear deformation of granular materials, but is suitable as a theoretical basis for determination of a new "critical" or, in other words "yielding" surface. The extremum condition shown in (9), however, apply only to magnitude but not to the location of dilatation. After the critical surface will have been located by some accepted theory, the above model can be used to analyse the processes taking place in the immediate vicinity of the

critical surface to assess the magnitude of "e" on the basis of (9) and to characterize its damping with aid of (2).

REFERENCES

1. Eringen, A.C.: Theory of Micropolar Continua. Fracture (Ed. Liebowits, H.) 2, 7. Acad. Press New-York.
2. Mindlin, R.D.: Micro-Structure in Linear Elasticity. Arch. Rat. Mech. Anal. 7 (1964), 51–78.
3. Füzy, J. – Vas, J.: Civil Engineering Applications of Micro-Elastic Continuums. Special Edition of the "Scientific Proceedings" of the Institute of Building Sciences, or a brief summary: Relationships and Application Possibilities of the Theories of Micro-Elastic Continua. Acta Technica Acad. Sci. Hung. 97 (1–4), 69–83.
4. Goodman, M.A. – Cowin, S.C.: Two Problems in the Grawity Flow of Granular Materials. J. Fluid. Mech. 45 (1971), 321–339.
5. Goodman, M.A. – Cowin, S.C.: A Continuum Theory for Granular Materials. Arch. Rat. Mech. Anal. 44 (1971), 249–266.
6. Füzy, J. – Vas, J.: Proposed Continuum Model for Simulating the Behaviour of Granular Materials. Acta Techn. Acad. Sci. Hung. 95 (1982), 49–53.
7. Suquet, P.: Une méthode duale d'homogénéisation: Application aux milieux élastiques. J. Mécanique Théorique et Appliquée, Numéro Spécial (Supplément) 1982, 79–98.
8. Bazant, Z.P. – Oh, B.H.: Crack band theory for fracture of concrete. Matériaux et Constructions. Vol. 16. No. 93, 155–177.

Acta Technica Acad.Sci.Hung., 101(1), pp. 59–67 (1988)

STABILITY ANALYSIS OF BARS ELASTICALLY RESTRAINED FROM ROTATION ALONG THEIR ENTIRE LENGTH

I. Hegedűs[+] – L.P. Kollár[++]

(Received: 5 March 1985)

The paper deals with the buckling of elastically restrained straight bars. It treats two cases: first when the buckling of the bar is restrained by distributed moments which are proportional to the rotation (slope) of the axis, and, second, when the bar is connected to another bar which is capable of shearing deformation only and whose displacements perpendicular to its axis are equal to those of the bar investigated.

The paper shows that the effect on buckling of the two kind of constraint is the same, and, further, that the calculation of the critical load of the restrained bar can be simply reduced to that of a bar without constraint.

1. INTRODUCTION

A kind of restrained bars – different from the well-known case: bars on elastic (Winkler-type) foundation – are those elastically restrained from rotation. This kind of constraint can also be called elastic constraint against rotation. In this case the constraint does not hinder the displacements of the bar, but the rotations of the bar axis induce restraining moments which are proportional to the slope of the axis:

$$m(z) = k(z)\varphi(z) \quad , \tag{1}$$

where $k(z)$ is the coefficient of the constraint and $\varphi(z)$ is the rotation of the bedding surface. This rotation will be considered to be equal to the first derivative of the displacement function $y(z)$ of the bar axis:

$$\varphi(z) = \frac{dy}{dz} = y'(z) \quad . \tag{2}$$

[+]István Hegedűs, H–2083 Solymár, Váci M. u. 10.

[++]László P. Kollár, H–1122 Budapest, Karap u. 9.

Akadémiai Kiadó, Budapest

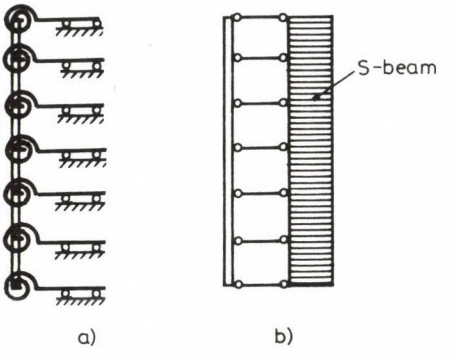

Fig. 1.

In Fig. 1a a possible interpretation of this kind of constraint can be seen.

Csonka has dealt with the stability analysis of this model in the case of concentrated forces at the ends /2/.

The rotation of the axis can also be restrained in another way, namely by bracing the bar by a parallel one (Fig. 1b). The effect of this constraint is similar to the previous case provided that the bending rigidity of the bracing bar is infinite while its shear rigidity is finite. This kind of bar will be called S-bar /3/.

The traditional bars, whose bending rigidity is finite and whose shear rigidity is infinite, will be called B-bars /3/.

Let the shear rigidity of an S-bar be $S(z)$, and its deflection function $y(z)$. In the S-bar shearing forces are induced:

$$Q(z) = S(z)\, y'(z) \quad . \tag{3}$$

As a result, supporting forces $t(z)$ are transmitted to the braced bar from the S-bar, which are equal to the opposite of the loads inducing the shearing forces $Q(z)$ in the S-bar. According to the well-known relationship between the shearing force and the load we obtain:

$$t(z) = \left[S(z)\, y'(z) \right]' \quad . \tag{4}$$

It will be shown in the next chapter that the effects of elastic

constraint against rotation and of bracing by an S-bar are identical, provided $S(z) = k(z)$.

Assumed below are loads acting in vertical direction and small elastic displacements, with changes in length of the bar due to normal forces neglected.

2. STABILITY ANALYSIS OF BARS RESTRAINED FROM ROTATION OR BRACED BY AN S-BAR

First the relationships used in the stability analysis of B-bars restrained from rotation are presented on the basis of Csonka's work /2/. We then derive the analogous equations of buckling of B-bars braced by S-bars. In the derivation the bending rigidity $B(z)$ of the B-bar, the shear rigidity $S(z)$ of the S-bar and the coefficient of the constraint $k(z)$ can be arbitrary functions of z, and the boundary conditions can be arbitrary as well.

Afterwards we shall only deal with the analysis of bars braced by S-bars. (Our results are valid for bars restrained from rotation too.)

Finally, Chapter 2.3 shows that the calculation of the critical load can be reduced to the stability analysis of an unbraced bar.

2.1 Equations of a B-bar restrained from rotation

(B-bar with elastic constraint against rotation)

Let the function of the distributed axial load of a bar be denoted by $\alpha p(z)$, where α is the load parameter (Fig. 2). If the function of the normal force induced in the bar is $\alpha N(z)$, the relationship between the two functions will be:

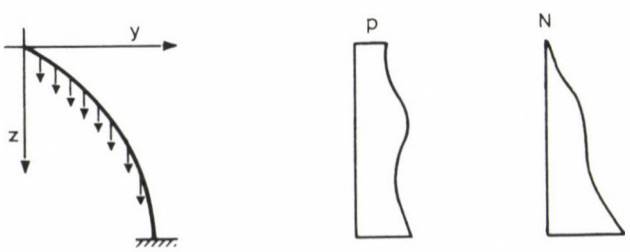

Fig. 2.

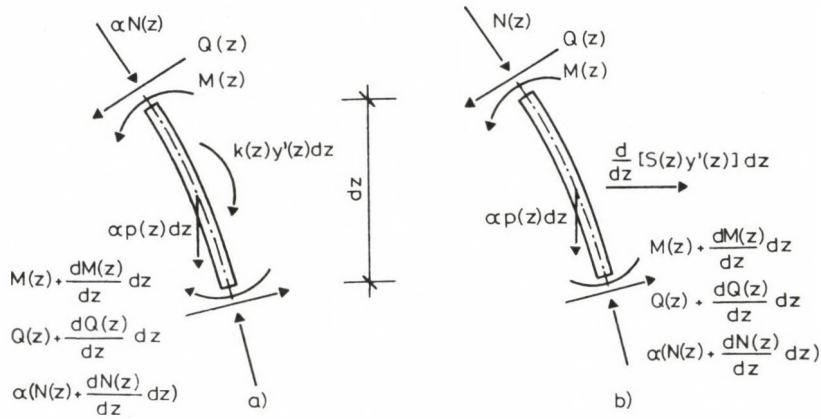

Fig. 3.

$$\left[\alpha N(z)\right]' = \alpha p(z) \quad . \tag{5}$$

In the following analysis we shall use the function of the normal force instead of that of the load because this permits the effect of the boundary conditions to be taken into consideration in a simple way.

The function of buckling shape and those of moments and shearing forces are denoted by $y(z)$, $M(z)$ and $Q(z)$ respectively. The equilibrium equations of moments and transversal forces acting on an infinitely small element of the bar (Fig. 3a) are, as follows:

$$\frac{dM(z)}{dz}\,dz - Q(z)\,dz + k(z)\,\frac{dy(z)}{dz}\,dz = 0 \quad ,$$

$$\frac{dQ(z)}{dz}\,dz - \frac{d}{dz}\left[\alpha N(z)\,\frac{dy(z)}{dz}\right] dz = 0 \quad ,$$

so that

$$M'(z) - Q(z) + k(z)\,y'(z) = 0 \quad , \tag{6}$$

$$Q'(z) - \left[\alpha N(z)\,y'(z)\right]' = 0 \quad . \tag{7}$$

Introducing the function

$$\hat{Q}(z) = Q(z) - k(z)\,y'(z)$$

we obtain:

$$M'(z) - Q(z) = 0 \quad , \tag{8}$$

$$\hat{Q}'(z) - \left[(\alpha N(z) - k(z)) \, y'(z) \right]' = 0 \quad . \tag{9}$$

The moment curvature relationship of the restrained B-bar is

$$M(z) = - y''(z) \, B(z) \quad . \tag{10}$$

Introducing this expression into Eqs (8, 9) and eliminating Q(z) we obtain the differential equation of buckling of a B-bar with elastic constraint against rotation:

$$B(z) \, y''''(z) + \left[(\alpha N(z) - k(z)) \, y'(z) \right]' = 0 . \tag{11}$$

If N(z), k(z) and B(z) are constants, this equation is identical with the basic equation of /2/.

2.2 Equation of a B-bar braced by an S-bar

The equilibrium equations of moments and forces acting on an infinitely small element of a B-bar braced by an S-bar are (Fig. 3b):

$$\frac{dM(z)}{dz} dz - Q(z) \quad dz = 0 \quad ,$$

$$\frac{dQ(z)}{dz} dz - \frac{d}{dz} \left[\alpha N(z) \frac{dy(z)}{dz} \right] dz + \frac{d}{dz} \left[S(z) \frac{dy(z)}{dz} \right] \quad dz = 0 \quad ,$$

so that

$$M'(z) - Q(z) = 0 \quad , \tag{12}$$

$$Q'(z) - \left[(\alpha N(z) - S(z) \, y'(z) \right]' = 0 \quad . \tag{13}$$

The braced bar is a B-bar, therefore, with the aid of (10), we obtain from (12, 13):

$$B(z) \, y''''(z) + \left[(\alpha N(z) - S(z)) \, y'(z) \right]' = 0 \quad , \tag{11a}$$

which – in the case of k(z) = S(z) – is identical with (11).

Thus it was shown that in the calculation of the critical load of a B-bar, the moment constraint against rotation and the bracing by an S-bar are interchangeable. In /3/ the problem of interchangeability is treated in a more general way.

2.3 Determination of the critical load parameter α_{cr}

Let us consider an unbraced bar (Fig. 2) the normal force of which is $\hat{N}(z) = \alpha N(z) - S(z)$. If we write the equilibrium equations of the buckling shape of the bar, we obtain (12, 13).

Hence, the theorem can be stated as follows:

The critical load parameter (α_{cr}) of a bar braced by an S-bar and under the action of the normal force $\alpha N(z)$ is equal to the critical load parameter (α_{cr}) of an unbraced bar under the action $\alpha N(z) - S(z)$.

This theorem can be applied also to S- or sandwich bars and to arbitrary boundary conditions, because of the validity of (12) and (13) is independent of the type of the braced bar and the boundary conditions.

On the basis of the previous theorem the critical load can be determined in the following way:

Let us consider fictitious unbraced bar loaded by distributed axial loads which induce normal forces of the distribution:

$$\gamma\hat{N} = \gamma \left[\alpha_0 N(z) - S(z)\right] \quad ,$$

where α_0 is an arbitrary value, and γ is the load parameter. If the critical value of γ is equal to unity, then α_0 is equal to the critical load parameter of the braced bar: $\alpha_{cr} = \alpha_0$. We can obtain the critical load by trial and error. If $\gamma_{cr} > 1$, then $\alpha_0 < \alpha_{cr}$, so that the result lies on the safe side.

In the special case where the distribution of N(z) is equal to that of the rigidity of the bracing bar, i.e.

$$N(z) = \beta S(z) \quad , \tag{14}$$

the critical load parameter can be calculated without the trial and error procedure. The normal force induced in the unbraced bar is:

$$\hat{N}(z) = \alpha N(z) - S(z) = \left(\alpha - \frac{1}{\beta}\right) N(z) = \alpha' N(z) \quad , \tag{15}$$

where

$$\alpha' = \alpha - \frac{1}{\beta} \quad . \tag{16}$$

With the aid of the critical value (α'_{cr}) of α', the critical load parameter of the braced bar can be calculated by a simple addition:

$$\alpha_{cr} = \alpha'_{cr} + \frac{1}{\beta} \quad . \tag{17}$$

Consequently:

$$N_{cr} = \alpha_{cr} \; N(z) = \alpha'_{cr} \; N(z) + \frac{1}{\beta} N(z) = N^E_{cr} + S \quad , \tag{18}$$

where $N^E_{cr} = \alpha'_{cr} \; N(z)$ is the critical normal force of the unbraced bar.

3. APPROXIMATE CALCULATION OF THE CRITICAL LOAD

Physically, the theorem formulated above can be explained, as follows:

In the state of buckling the load of the braced bar is carried partly by this bar and partly by the bracing S-bar. The distribution of the normal force along the S-bar is equal to that of the rigidity S(z) of the bar, so that shear buckling occurs at every cross-section of the S-bar as a result /1/. The whole S-bar is in an indifferent equilibrium state. Consequently, it has no bracing effect any more, and it is now the bar previously braced that has to carry the residual normal force N(z) − S(z) as if it were unbraced.

We can distribute the loads also in a different way, e.g. by requiring that the distribution of the normal forces along the two bars are identical. In so doing, we obtain an approximate value for the critical normal force:

$$N_{cr} = N^R_{cr} + N^S_{cr} \quad , \tag{19}$$

where $N^R_{cr} = \alpha_R \; N(z)$ is the critical normal force of the unbraced bar and $N^S_{cr} = \alpha_S \; N(z)$ is the critical normal force of the S-bar.

The approximation (19) yields a result that lies on the safe side, and gives the exact result if (14) is satisfied.

In the case of a cantilever loaded by distributed axial load we can obtain a good approximation for the critical load if the section of the bar where $N(z) - S(z) < 0$ is neglected, that is if we investigate the stability of the cantilever reduced by its tensioned top section.

4. NUMERICAL EXAMPLE

Determination of critical load of a braced cantilever in the case of a uniformly distributed axial load.

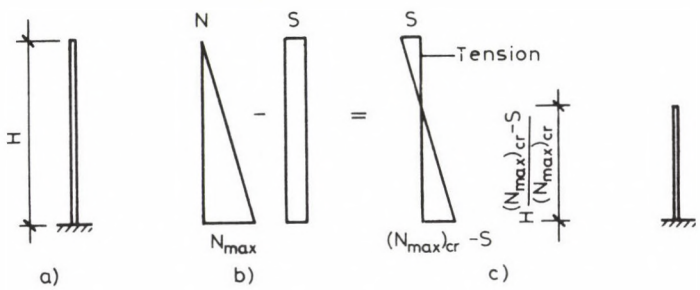

Fig. 4.

In Fig. 4a a cantilever with the total height H and with the constant bending rigidity $B = EI$ is shown. The shear rigidity of the bracing S-bar is constant: $S = 2\frac{B}{H^2}$. The value of the uniformly distributed vertical load is p, and the maximum of the normal force is $N_{max} = p\,H$ (Fig. 4b).

The exact critical value of the normal force is according to /4, 5/:

$$(N_{max})_{cr} = 13.582\,\frac{B}{H^2} \quad .$$

With the aid of (19) we obtain a rough approximation. Using /1/

$$(N_{max})^{E}_{cr} = 7.837\,\frac{B}{H^2} \quad , \qquad (N_{max}(\,{}^{S}_{cr}) = S = 2\,\frac{B}{H^2} \quad ,$$

we obtain

$$(N_{max})^{I}_{cr} = 7.837\,\frac{B}{H^2} + 2\,\frac{B}{H^2} = 9.837\,\frac{B}{H^2} \quad .$$

We obtain a better approximation if we take the compressed part of the column into consideration (as if it were an unbraced one; Fig. 4c):

$$(N_{max})^{II}_{cr} - S = 7.837 \frac{B}{\left[\frac{(N_{max})^{II}_{cr} - S}{(N_{max})^{II}_{cr}}\right]^2} .$$

Hence — solving this equation of the third degree — we obtain:

$$(N_{max}{}^{II}_{cr}) = 12.959 \frac{B}{H^2} .$$

REFERENCES

1. Timoshenko, S. — Gere, I.: Theory of Elastic Stability. McGraw-Hill (1961), New York.
2. Csonka, P.: Buckling of Bars Elastically Built-in Along Their Entire Length. Acta Techn. Hung. 32(3–4), (1961), 424–427.
3. Hegedűs, I. — Kollár, L.P.: Generalized Bar Models and Their Physical Interpretation. Acta Techn. Hung. 101–C/1, (1988), 69–95.
4. Hegedűs, I. — Kollár, L.P.: Buckling of Sandwich Columns With Thick Faces Subjected to Axial Loads of Arbitrary Distribution. Acta Techn. Hung. 97 (1–4), (1984), 123–131.
5. Zalka, K.: Torsional Buckling of a Cantilever Subjected to Distributed Normal Loads. Acta Techn. Hung. 90 (1–2), (1980), 91–108.

Acta Technica Acad.Sci.Hung., 101(1), pp. 69–95 (1988)

GENERALIZED BAR MODELS AND THEIR PHYSICAL INTERPRETATION

I. Hegedűs[+] — L.P. Kollár[++]

(Received: 5 March 1985)

The aim of this paper is to present a simple and visual method for investigation of generalized bar-models (i.e. bars which undergo shear deformation, sandwich bars etc.).

First, the paper defines two basic bar types: the first one develops bending deformation only, while the second one undergoes shear deformation only, furtherly, formal algebraic operations are introduced, with the help of which we define generalized bars. The formal operands of these operations are different basic bars.

The effect of the different rigidities of the generalized bars on their behaviour becomes clearly visible.

We use this method mainly for the stability analysis of bars.

1. FUNDAMENTAL NOTIONS AND ASSUMPTIONS

We assume that the displacements of a vertical bar are elastic and small. The displacement function of the axis of the bar is

$$y = y(z) \quad .$$

The compressive deformation is neglected, so that the function $y(z)$ gives the horizontal deflection of the points of the column.

First, let us consider a traditional (Mohr-type) bar. In this case the deformations are caused by bending moments only. We denote the bending moment function and the curvature function by $M(z)$ and $\kappa(z)$ respectively. Between them the relationship

$$\kappa(z) = \frac{M(z)}{B(z)} \tag{1.1}$$

holds, where $B(z)$ is the bending rigidity, and

$$\kappa(z) = -y''(z) \quad . \tag{1.2}$$

[+]István Hegedűs, H–2083 Solymár, Váci M. u. 10.

[++]László P. Kollár, H–1122 Budapest, Karap u. 9.

Akadémiai Kiadó, Budapest

Second, let us consider a bar whose deformations are caused by shearing force only. The shearing force function and the shearing strain function are denoted by $Q(z)$ and $\gamma(z)$ respectively. The relationship

$$\gamma(z) = \frac{Q(z)}{S(z)} \tag{1.3}$$

holds, where $S(z)$ is the shear rigidity, and

$$\gamma(z) = y'(z) \quad . \tag{1.4a}$$

According to the elastic theory $B(z) = EI(z)$ and $S(z) = GA(z)/\vartheta(z)$, where E and G are the moduli of elasticity and shear respectively, $I(z)$ and $A(z)$ are the moment of inertia and the cross-sectional area respectively, and $\vartheta(z)$ is a factor depending on the shape of the cross-section.

Let us consider a cantilever which is capable of both bending and shearing deformations. It can be set up in two different ways.

First case: the cantilever consists of two parallel bars, one being capable of bending deformation while the other of shearing deformation. The horizontal deflections of the bars are equal to each other, so that they brace each other.

Second case: the cantilever consists of short sections which are alternately capable of bending or shearing deformation only.

We call the bars which are capable of bending or shearing deformation only bars under pure deformation, and the bars which are capable of both types of deformations bars under combined deformation or combined bars. There are two kinds of bars under pure deformation: the bar capable of bending deformation only; these will be called B-bars, and the bars capable of shearing deformation only; these will be called S-bars (see the notation in Figs 1a and 1b, respectively).

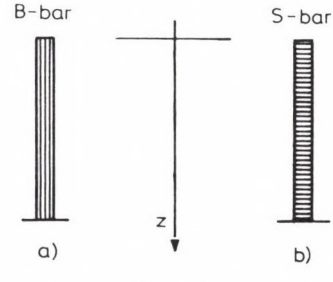

Fig. 1.

We shall investigate in the following how the boundary conditions influence the behaviour of the bars.

It is well-known from the elastic bending theory that we can, and have to, satisfy four boundary conditions for a B-bar to determine the deflections, and from the deflections we can compute the loads and stresses of a bent bar. From (1.1) and (1.2) we obtain

$$M(z) = -y''(z)\, B(z) \quad . \tag{1.5}$$

Deformations of an S-bar allow only the displacements of the cross-sections parallel to themselves, so that a rotation $\varphi(z)$ of the normal of the cross-section will be possible only if the entire bar performs a rigid body rotation. Consequently, if there is no hinge on the bar which allows relative rigid body displacements, then the slope of the bar axis has to be constant, $\varphi(z) = \varphi$. Eq. (1.4a) is valid only if $\varphi = 0$, in other cases the first derivative of the deflection function is

$$y'(z) = \gamma(z) + \varphi \quad , \tag{1.4b}$$

hence, using (1.3), we obtain

$$Q(z) = (y'(z) - \varphi)\, S(z) \quad , \tag{1.6}$$

so that the relationship between the deflection curve and the shearing force is indeterminate, i.e. different functions $Q(z)$ and as a matter of fact, $y(z)$ are associated with the same $y(z)$ and $Q(z)$, respectively.

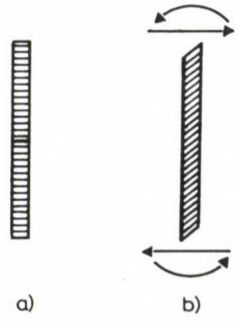

Fig. 2.

For example, the S-bar in Fig. 2a is unloaded and that in Fig. 2b is loaded at the ends. Considering the y(z) functions only, the two cases are undistinguishable. The stresses and strains of a loaded S-bar can be determined only if three boundary conditions are given. These are for example the relationships between the forces and the deflections at both ends and one condition for the normal of one arbitrary cross-section. An example is shown in Fig. 3a, b. The load is identical for both structures, difference lying only in that the slope is not restrained in Fig. 3a while it is restrained in Fig. 3b.

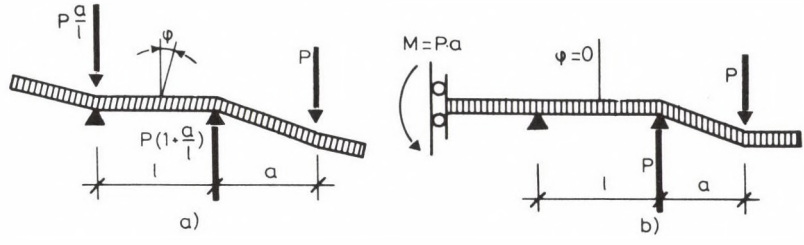

Fig. 3.

In the following we shall deal with bars with combined deformation. These bars are obtained by combining bars with pure deformation. The bars can be combined by parallel and series connections.

2. BARS CONNECTED IN PARALLEL AND IN SERIES

Let us consider two vertical bars denoted by R_1 and R_2 (Fig. 4). Their horizontal deflections are $y_1(z)$ and $y_2(z)$, respectively.

Connection of bars is called parallel when their horizontal deflections are equal to each other at every cross-section of the bars:

$$y(z) = y_1(z) = y_2(z) \quad . \tag{2.1}$$

We denote the resultant bar (consisting of R_1 and R_2) by R, and the connection by ($\parallel$):

$$R = R_1 \parallel R_2 \quad .$$

Connection of bars is called series, when the deflection $y(z)$ of the combined (resultant) bar (R) is the sum of those of the bars R_1 and R_2:

$$y(z) = y_1(z) + y_2(z) \quad . \tag{2.2}$$

We denote the connection in series by $(\asymp)$:

$$R = R_1 \asymp R_2 \quad .$$

To visualize the behaviour of the bar $R = R_1 \parallel R_2$ assume that the bars R_1 and R_2 are connected by horizontal rigid bars with hinged ends (Fig. 4).

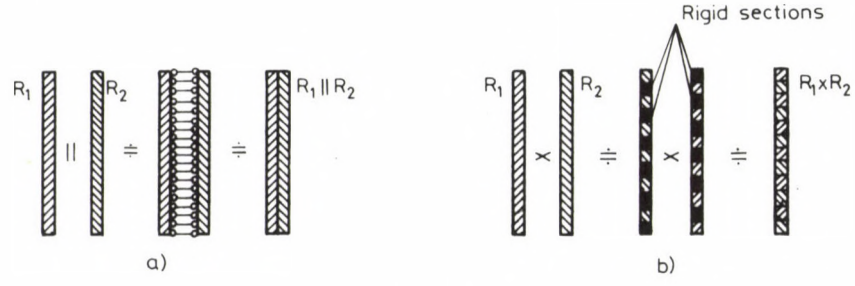

Fig. 4.

The deformation of a bar $R = R_1 \asymp R_2$ can be interpreted as the sum of two deformations: first we consider a bar with the deformability of R_1 and another with that of R_2, then we have to add the deformations developed on the two bars to each others. Some modifications of this definition is necessary when the boundary conditions for the deformation of R do not permit the boundary conditions for the deformations of R_1 and R_2 to be stated independently each.

We can vizualize the behaviour of the bar $R = R_1 \asymp R_2$ also in the following way: We divide the bar R_1 into small elements. We consider every second to be infinitely rigid, while the rigidities of the rest of the elements to be half of those of bar R_1. We fulfil this procedure for the bar R_2 as well. Interconnect now the non-rigid sections of both bars alternately (Fig. 4b). If the length of the sections are infinitely small then the behaviour of the resultant bar R is exactly determined by (2.2).

The connection in parallel and in series are the simplest way of combining bars.

If we connect in parallel more than two bars, then the horizontal deflections of every bar will be the same. Bars can be connected in parallel in an arbitrary order, so that the connection of bars in parallel is commutative and associative. For example, if R_1, R_2 and R_3 are arbitrary (combined) bars:

$$R = (R_1 \parallel R_2) \parallel R_3 = (R_1 \parallel R_3) \parallel R_2 = (R_2 \parallel R_3) \parallel R_1 \quad .$$

Similarly, connection of bars in series is commutative and associative.

In general the distributivity is not valid, that is

$$(R_1 \parallel R_2) \times R_3 \neq (R_1 \times R_3) \parallel (R_2 \times R_3) \quad .$$

2.1 Combination of bars under the same kind of pure deformation

Let us consider two B-bars, denoted by R_{B1} and R_{B2} with the rigidities $B_1(z)$ and $B_2(z)$ respectively. We connect them in parallel:

$$R = R_{B1} \parallel R_{B2} \quad .$$

Hence, using (2.1) and (1.5):

$$-y''(z) = \frac{M_1(z)}{B_1(z)} = \frac{M_2(z)}{B_2(z)} \quad , \tag{2.3}$$

where $M_1(z)$ and $M_2(z)$ are the bending moment functions induced in the bars respectively. Introducing the notation

$$M(z) = M_1(z) + M_2(z) \text{ and } B(z) = B_1(z) + B_2(z) \quad ,$$

after rearrangement we obtain

$$-y''(z) = \frac{M_1(z) + M_2(z)}{B_1(z) + B_2(z)} = \frac{M(z)}{B(z)} \quad , \tag{2.4}$$

so that the resultant bar is a B-bar, whose bending rigidity is equal to

the sum of those of the connected bars. The boundary conditions can be determined on the basis of those of the connected bars.

If we connect two S-bars (R_{S1}, R_{S2}) with the rigidities $S_1(z)$ and $S_2(z)$ respectively, in parallel, then, using (1.6) and (2.1), we obtain

$$y'(z) = \frac{Q_1(z)}{S_1(z)} + \varphi_1 = \frac{Q_2(z)}{S_2(z)} + \varphi_2 \qquad (2.5)$$

where $Q_1(z)$ and $Q_2(z)$ are the shearing forces induced in the bars. Introducing the notation $Q(z) = Q_1(z) + Q_2(z)$ and $S(z) = S_1(z) + S_2(z)$, after rearrangement we obtain:

$$y'(z) = \frac{Q(z)}{S(z)} + \frac{S_1(z)\,\varphi_1 + S_2(z)\,\varphi_2}{S(z)} \,. \qquad (2.6)$$

Consequently, two S-bars connected in parallel cannot be replaced by one S-bar in every case.

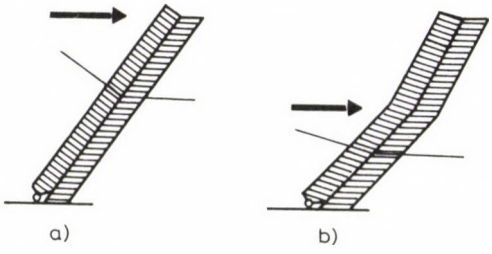

Fig. 5.

For example, in Fig. 5a deflection is not hindered by the bar on the left side, and the behaviour of the structure is the same as in the case of a single S-bar. In Fig. 5b where the difference is only the position of the load as compared with Fig. 5a both bars take part in load bearing.

If the boundary conditions for φ are $\varphi = \varphi_1 = \varphi_2$, then from (2.6) we obtain:

$$y'(z) = \frac{Q(z)}{S(z)} + \varphi \quad ,$$

so that the S-bars connected in parallel can be replaced by an S-bar, whose

shear rigidity is equal to the sum of those of the connected bars, and the boundary conditions can be determined from those of the connected bars.

We can meet the condition $\varphi = \varphi_1 = \varphi_2$ e.g. by requiring that both bars are clamped, i.e. $\varphi_1 = \varphi_2 = 0$.

In the following – if we do not say otherwise – we deal with cantilevers, i.e. bars fixed at the bottom and free at the top, but our results can be generalized for other types of boundary conditions.

If we connect two B-bars in <u>series</u>:

$$R = R_{B1} \times R_{B2} \quad ,$$

then with the aid of (2.2) it is very easy to show that the resultant bar is a B-bar, whose rigidity is equal to the inverse of the sum of the inverses of the rigidities of the connected bars:

$$B(z) = \left\{ \left[B_1(z) \right]^{-1} + \left[B_2(z) \right]^{-1} \right\}^{-1} \quad , \tag{2.8}$$

i.e. the flexibilities have to be added. In the case of two S-bars connected in series the resultant bar is an S-bar with the rigidity:

$$S(z) = \left\{ \left[S_1(z) \right]^{-1} + \left[S_2(z) \right]^{-1} \right\}^{-1} \quad . \tag{2.9}$$

3. BARS UNDER COMBINED DEFORMATIONS

<u>3.1 Connection of bars under different pure deformations</u>

Let us consider an S-bar and a B-bar. We denote them by R_S and R_B, their rigidities by $S(z)$ and $B(z)$, and their deflection functions by $y_S(z)$ and $y_B(z)$ respectively.

<u>3.1.1 Connection of an S-bar and a B-bar in parallel (Csonka-type bar)</u>

From the point of view of the B-bar, its connection with an S-bar is equivalent to an elastic restraint against rotation, so that the two are interchangeable.

Let bar R be clamped, consequently, $\varphi = 0$ at the clamped cross-section and also along the entire length. Let us connect bars R_S and R_B in parallel (Fig. 6a):

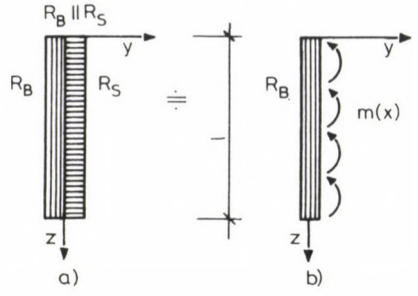

Fig. 6.

$$R_C = R_S \| R_B \quad . \tag{3.1}$$

We can consider the bar R_C as a B-bar braced by an S-bar. The shearing force induced in the bracing bar (R_S) is:

$$Q(z) = S(z)\, y'(z) \quad , \tag{3.2}$$

hence the S-bar restrains the deflections of the B-bar by distributed supporting forces:

$$t(z) = Q'(z) = (S(z)\, y'(z))' \tag{3.3}$$

along the entire length of the bar and by concentrated forces at the ends as follows:

$$Q_0 = S(0)\, y'(0) \quad , \qquad \text{at } z = 0 \quad , \tag{3.4}$$

$$Q_\ell = S(\ell)\, y'(\ell) \quad , \qquad \text{at } z = \ell \quad . \tag{3.5}$$

(In equations (3.3–3.5) we used the condition $\varphi = 0$.) The bending moment acting on the B-bar induced by the supporting forces only, is

$$M(z) = S(0)\, y'(0)\, z + \int_0^z (S(\zeta)\, y(\zeta))' (z - \zeta)\, d\zeta = \int_0^z S(\zeta)\, y'(\zeta)\, d\zeta \tag{3.6}$$

and the resultant of the supporting forces is

$$F = Q_0 + Q_\ell + \int_0^\ell t(z)\, dz = 0 \quad . \tag{3.7}$$

In the following we introduce the concept of elastic constrain against rotation (or bar elastically restrained from rotation), and we shall show that its effect and that of the bracing by an S-bar are interchangeable.

The elastic constraint against rotation does not hinder the deflections, but restrains the slope of the axis of the bar by distributed moments proportional to the rotation of the bar axis:

$$m(z) = k(z)\, y'(z) \quad . \tag{3.8}$$

We shall call the bars restrained from rotation Csonka-type bars, because it was Csonka who used such bars for approximate analysis of frame structures /2/.

The bending moment acting on the B-bar induced by the constraint only is

$$M(z) = \int_0^z m(\zeta)\, d\zeta = \int_0^z k(\zeta)\, y'(\zeta)\, d\zeta \tag{3.9}$$

while the supporting forces are equal to zero and thus also their resultant is zero:

$$F = 0 \quad . \tag{3.10}$$

Let us consider two B-bars one braced by an S-bar, and the other one restrained from rotation. We assume that

$$S(z) = k(z) \tag{3.11}$$

and both the rigidities and the boundary conditions of the two B-bars are identical. In both B-bars bending moments

$$- B(z)\, y''(z)$$

are induced by the loads and by the supports. The bending moments due to the bracing by an S-bar (3.6) and due to the constraint (3.9) are identical, hence, the load has to be the same as well.

Consequently, if the same load acts on the two structures in question, the bending moment curves and the displacement functions will be the same. The shearing force diagrams which, however, result in no deformation, are different.

We will present the conditions of interchangeability for combined (not B-) bars in Chap. 3.2.4.

The results can be generalized for S-bars with the bracing effect where $\varphi = 0$ but in this case the concept of elastic constraint shall be generalized as well. This problem is however, not dealt with here.

3.1.2 An S-bar and a B-bar connected in series

(Sandwich bar with thin faces, i.e. traditional bar, taking shearing deformation also into account)

Let us connect the bars R_S and R_B in series (Fig. 7a):

$$R = R_S \asymp R_B \quad . \tag{3.12}$$

The deflection of the resultant bar consists of two parts

$$y(z) = y_S(z) + y_B(z) \tag{3.13}$$

so that we obtain the bar model presented in Chap. 1, capable of both shearing and bending deformation.

This bar model is also called in the literature "sandwich bar with thin faces" (Fig. 7b), which we obtain by neglecting the bending rigidities of the faces /1/.

It is important to note, that we obtain the total displacement of the bar simply from the sum of the displacements of the B- and S-bar only if the boundary conditions for $y_S(z)$ and $y_B(z)$ are independent from each other.

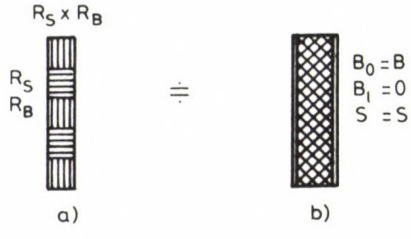

Fig. 7.

3.2 Connection of combined bars in parallel

Let the S-bars be denoted by R_{S1}, R_{S2}, ... the B-bars by R_{B1}, R_{B2}, ..., and their rigidities by S_1, S_2, ...; B_1, B_2, ...; and their deflections by $y_{S1}(z)$, $y_{S2}(z)$, ...; $y_{B1}(z)$, $y_{B2}(z)$, ..., respectively.

3.2.1 Csonka-type bar connected with bars under pure deformation

If a bar under pure deformation (R_{B2} or R_{S2}) and a Csonka-type bar ($R_c = R_{B1} \parallel R_{S1}$) are connected in parallel, the resultant bar will also be a Csonka-type bar. Using the theorem of associativity we obtain

$$R_c \parallel R_{B2} \parallel R_{S2} = (R_{B1} \parallel R_{B2}) \parallel (R_{S1} \parallel R_{S2}) = R_S \parallel R_B \ . \qquad (3.14)$$

The resultant bar is a Csonka-type one, whose rigidities are equal to the sum of the rigidities of the connected bars.

Consequently, if we connect Csonka-type bars in parallel, a Csonka-type bar will be obtained again.

3.2.2 Sandwich bar with thick faces

Connect a B-bar (R_{B2}) in parallel with a bar $R_{B1} \times R_{S1}$ described in Chapter 3.1.2 (Fig. 8a):

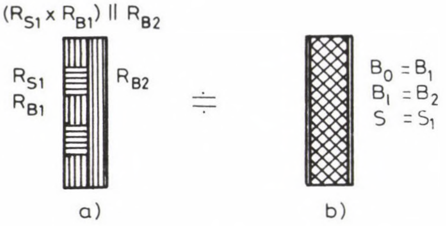

Fig. 8.

$$R = (R_{S1} \times R_{B1}) \parallel R_{B2} \qquad (3.15)$$

This is identical with a sandwich bar with thick faces (Fig. 8b). Among the deflection functions the relationship

$$y(z) = y_{B2}(z) = y_{S1}(z) + y_{B1}(z) \qquad (3.16)$$

hold. The sandwich bar has the local bending rigidity

$$B_{\ell} = B_2 \quad , \tag{3.17}$$

the global bending rigidity

$$B_0 = B_1 \quad , \tag{3.18}$$

and the shear rigidity

$$S = S_1 \quad . \tag{3.19}$$

There are two special cases of a sandwich bar with thick faces:
If the rigidity of bar R_{B2} is equal to zero, i.e.

$$B_2 = 0 \quad ,$$

we obtain the model of a sandwich bar with thin faces:

$$R = R_{S1} \asymp R_{B1} \quad .$$

On the other hand, if the rigidity of bar R_{B1} is infinite, i.e.:

$$B_1 = \infty \quad ,$$

we obtain the model of a Csonka-type bar:

$$R = R_{S1} \parallel R_{B2} \quad .$$

We emphasize that the sandwich bar with thick faces had independent global and local boundary conditions (Fig. 9a–c). For example, the top of the bar in Fig. 9a is "globally free", while the connected bars are "locally clamped", i.e. the slopes of the normals of the bars $R_{S1} \asymp R_{B1}$ and R_{B2} are equal to each other. The bar in Fig. 9b differs from the Csonka-type one in the case of $B_1 = \infty$, since $\varphi \neq 0$.

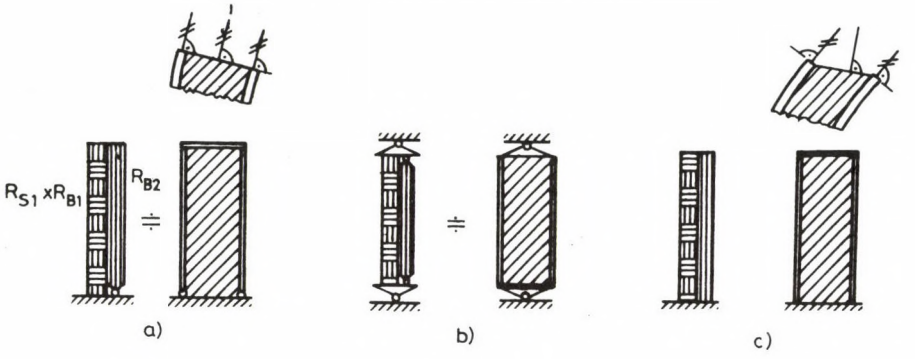

Fig. 9.

3.2.3 Sandwich bar with thin faces connected with an S-bar

Let us connect an S-bar with a sandwich bar with thin faces (Fig. 10a):

$$R = (R_{S1} \times\!\!\!\prec R_{B1}) \parallel R_{S2} \quad , \tag{3.20}$$

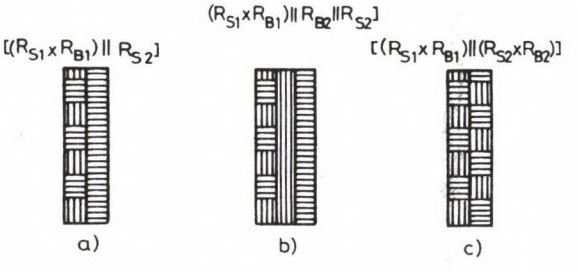

Fig. 10.

so that we obtain a sandwich bar braced by an S-bar. The behaviour of this structure is not identical with the behaviour of a sandwich bar elastically restrained from rotation, because the braced bar is also capable of shear deformation.

3.2.4 Sandwich bar with thick faces connected with an S-bar

Connect an S-bar with a sandwich bar with thick faces (Fig. 10b):

$$R = (R_{S1} \times\!\!\!\prec R_{B1} \parallel R_{B2}) \parallel R_{S2} \quad . \tag{3.21}$$

In this case (if $\Psi = 0$ along the bar R_{S2}), the bracing by an S-bar and elastic constraint against rotation are interchangeable since, due to the principle of associativity:

$$R = R_{S1} \times\!\!\!\!\times R_{B1}) \parallel (R_{S2} \parallel R_{B2}) \quad , \tag{3.22}$$

where the bar in the second bracket is a Csonka-type one.

Using the previous examples, we can state that the bracing by an S-bar and the constraint against rotation are interchangeable provided the braced bar has a B-bar component, i.e.

$$R = R_1 \parallel R_B \quad . \tag{3.23}$$

3.2.5 Sandwich bar with thick faces connected with a B-bar or with a Csonka-type bar

Let a sandwich bar with thick faces be connected in parallel with a B-bar (B_{B3}):

$$R = \left[(R_{B1} \times\!\!\!\!\times R_{S1}) \parallel R_{B2}\right] \parallel R_{B3} \quad . \tag{3.24}$$

Using the principle of associativity we obtain

$$R = (R_{B1} \times\!\!\!\!\times R_{S1}) \parallel (R_{B2} \parallel R_{B3}) \quad , \tag{3.25}$$

so that the resultant bar is a sandwich bar with thick faces.

If we connect a sandwich bar with thick faces with a Csonka-type bar ($R_{B3} \parallel R_{S3}$), then we obtain the model presented in Chapter 3.2.4:

$$\begin{aligned} R &= (R_{B1} \times\!\!\!\!\times R_{S1}) \parallel R_{B2} \parallel (R_{B3} \parallel R_{S3}) = \\ &= (R_{B1} \times\!\!\!\!\times R_{S1}) \parallel (R_{B2} \parallel R_{B3}) \parallel R_{S3} \quad . \end{aligned} \tag{3.26}$$

3.2.6 Connection of two sandwich bars with thin faces

Let us connect two sandwich bars with thin faces in parallel (Fig. 10c):

$$R = (R_{B1} \times\!\!\!\!\times R_{S1}) \parallel (R_{B2} \times\!\!\!\!\times R_{S2}) \quad . \tag{3.27}$$

In the special case where the boundary conditions of the bars are identical, furthermore if the relationship

$$\frac{S_1(Z)}{S_2(Z)} = \frac{B_1(Z)}{B_2(Z)} \tag{3.28}$$

holds, we can replace the bar defined by (3.27) by a sandwich bar with thin faces

$$R = (R_{B1} \parallel R_{B2}) \asymp (R_{S1} \parallel R_{S2}) \ , \tag{3.29}$$

whose rigidities are

$$\begin{aligned} S(z) &= S_1(z) + S_2(z) \ , \\ B(z) &= B_1(z) + B_2(z) \ , \end{aligned} \tag{3.30a,b}$$

because their displacements are equal to each other.

3.2.7 Connection of two sandwich bars with thick faces

Let us connect two sandwich bars with thick faces in parallel. Using the principle of associativity we obtain (Fig. 11a, b):

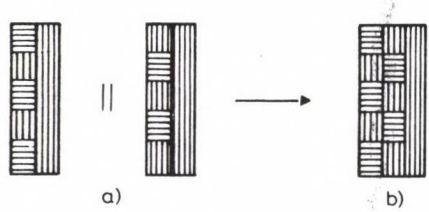

Fig. 11.

$$\begin{aligned} R &= \left[(R_{S1} \asymp R_{B1}) \parallel R_{B2}\right] \parallel \left[(R_{S2} \asymp R_{B3}) \parallel R_{B4}\right] = \\ &= (R_{S1} \asymp R_{B1}) \parallel (R_{S2} \asymp R_{B3}) \parallel (R_{B2} \parallel R_{B4}) \ . \end{aligned} \tag{3.31}$$

We can substitute for R one sandwich bar with thick faces only if

$$\frac{S_1(z)}{S_2(z)} = \frac{B_1(z)}{B_2(z)}$$

and if the boundary conditions of the two bars are identical:

$$R = (R_{S1} \parallel R_{S2}) \times (R_{B1} \parallel R_{B3}) \parallel (R_{B2} \parallel R_{B4}) \ . \qquad (3.33)$$

4. STABILITY ANALYSIS OF COMBINED BARS

The stability analysis of bars under pure deformations can be found in the literature for every important case /9/.

The critical load of Csonka-type bars has been determined for constant rigidities. The solutions can be found for a concentrated force acting on the top in /3/, for a load uniformly distributed along the height in /11/, and for an arbitrary distribution of the load in /6/, which is published simultaneously with this paper.

The critical load of bars taking shear deformation also into account (i.e. sandwich bars with thin faces) has been determined for a concentrated force e.g. in /9/, for a uniformly distributed load in /10/, and for an arbitrary load distribution in /4/.

The stability analysis of sandwich bars with thick faces for different boundary conditions and for differently distributed loads can be found in /1/ and /5/.

The stability analysis of bars braced by an S-bar

$$R = R_1 \parallel R_S$$

(in the case of $\varphi = 0$) can always be reduced to the analysis of an R_1 bar /6/.

We shall deal with the stability analysis of sandwich bars with thick faces connected in parallel in the following:

We connect in parallel n sandwich bars with thick faces (Fig. 12):

$$R = R_1 \parallel R_2 \parallel \ldots\ldots \parallel R_n \ . \qquad (4.1)$$

The rigidities B_{0i}, B_{1i}, S_i of the bars are constant. Let the normal force induced along the i-th sandwich bar be $N \alpha_i(z)$, where N is a constant (the

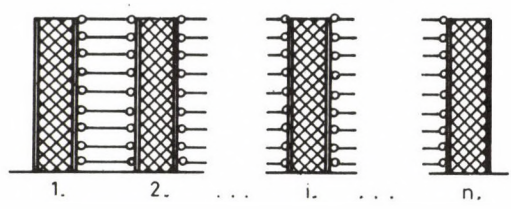

Fig. 12.

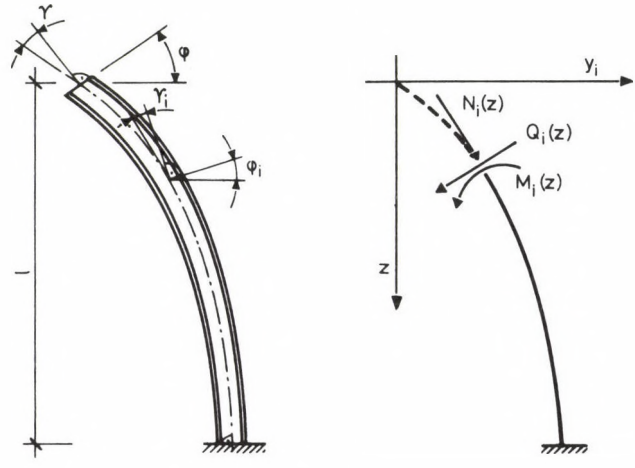

Fig. 13.

normal force), $\alpha_i(z)$ determines the distribution of the normal force. Let us determine the critical value (N_{cr}) of the normal force. Our derivation is based on /5/.

The curvature of the axis of the i-th buckled sandwich bar consists of two parts:

$$y_i''(z) = \left[\varphi_i(z) + \gamma_i(z)\right] \quad , \tag{4.2}$$

where $\varphi_i(z)$ is the slope of the normal of the cross-section and $\gamma_i(z)$ is the shearing strain. According to the two parts of the bending rigidity, the bending moment and the shearing force also consist of two parts each:

$$M_i(z) = - B_{0i}\ \varphi_i'(z) - B_{\ell i}\ y_i''(z) \quad , \tag{4.3}$$

$$Q_i(z) = - B_{0i}\, \varphi_i''(z) - B_{\ell i}\, y_i'''(z) \quad . \tag{4.4}$$

It is only the first part of the shearing force which causes shearing strain:

$$\gamma_i(z) = - \frac{B_{0i}}{S_i}\, \psi''(z) \quad . \tag{4.5}$$

Assuming small displacements we obtain

$$Q_i(z) = N\, \alpha_i(z)\, y'(z) \quad . \tag{4.6}$$

Introducing the sum of functions α_i as

$$\alpha(z) = \sum_{i=1}^{n} \alpha_i(z) \quad ,$$

and using the relations

$$y_1(z) = y_2(z) = \ldots = y_n(z) \quad ,$$

from (4.1–4.6) we obtain a differential equation system of the fourth order:

$$N_{cr}\, \alpha(z) \left(\varphi_i(z) - \frac{B_{0i}}{S_i}\, \varphi_i''(z) \right) + \sum_{j=1}^{n} B_{0j}\, \varphi_j''(z) + \left[\sum_{j=1}^{n} B_{\ell j} \right] \left(\varphi_i''(z) - \frac{B_{0i}}{S_i}\, \varphi_i''''(z) \right) = 0 \quad . \quad (i=1,2,\ldots,n) \tag{4.7}$$

Consequently, the value of N_{cr} is independent of the distribution of the loads among the bars. In the case of n=0 (4.7) is identical with Eq. (7) of /5/.

In the case of n=2 we can substitute a single differential equation of the eighth order for (4.7). In the special case, where the boundary conditions of the two bars are identical and

$$\frac{B_{01}}{B_{02}} = \frac{S_1}{S_2} \quad , \tag{4.8}$$

we can reduce it to an equation of the fourth order. Substituting

$$\varphi(z) = \varphi_1(z) + \varphi_2(z) \quad ,$$

$$B_0 = B_{01} + B_{02} \quad ,$$

$$B_\ell = B_{\ell 1} + B_{\ell 2} \quad ,$$

$$S = S_1 + S_2 \quad ,$$

we obtain

$$N_{cr} \alpha(z) \left(\varphi(z) - \frac{B_0}{S}\varphi''(z)\right) + B_0 \varphi''(z) + B_\ell \left(\varphi''(z) - \frac{B_0}{S}\varphi''''(z)\right) = 0 \tag{4.9}$$

which is the equilibrium equation of the buckled shape of a sandwich bar with the rigidities B_0, B_ℓ and S.

5. APPROXIMATE ANALYSIS OF CONNECTED BARS (Theorem of Southwell and Föppl-Papkovich)

With the aid of the presented bar models we can develop approximate formulas to determine the critical load of the combined bars.

Let the critical load parameter of the bars R_1, R_2 and R be λ_1, λ_2 and λ respectively. In the case of bars connected in parallel (i.e. if $R = R_1 \parallel R_2$)

$$\lambda \approx \lambda_1 + \lambda_2 \quad , \tag{5.1}$$

and in the case of bars connected in series (i.e. $R = R_1 \times R_2$)

$$\lambda \approx (\lambda_1^{-1} + \lambda_2^{-1})^{-1} \tag{5.2a}$$

i.e.

$$\frac{1}{\lambda} \approx \frac{1}{\lambda_1} + \frac{1}{\lambda_2} \tag{5.2b}$$

Relationships (5.1) and (5.2a) are approximations to the benefit of safety i.e. a lower estimate in the sense of the theorems of Southwell and Föppl—Papkovich respectively. Tarnai has given the mathematically sufficient conditions of the validity of the Föppl—Papkovich theorem /8/ for a more general case than ours.

In this chapter some simple conditions are given by which, on the basis of the boundary conditions, it can be simply decided whether or not the theorems are valid. The derivation is based on /8/.

Let us write the strain energy of the bars under pure deformations and that of some combined bars. The total height of the bars is ℓ. Generally, the strain energy of a bar R_j is:

$$U_{Ij} = \frac{1}{2} \int_{(\ell)} \sum_i b_{ji} \, \eta_{ji}(z) dz + \frac{1}{2} \sum_k p_{jk} \, u_{jk} \quad , \tag{5.3}$$

where η_{ji} is a generalized displacement function, b_{ji} is a rigidity, and the second term is the work done by the boundary forces (p_{jk}) on the boundary displacements (u_{jk}) (e.g. in the case of elastic supports or elastic clamping).

For a B-bar:

$$U_I = \frac{1}{2} \int_{(\ell)} B \left[y''(z)\right]^2 dz + \frac{1}{2} \sum_k p_k \, u_k \quad , \tag{5.4a}$$

For an S-bar:

$$U_I = \frac{1}{2} \int_{(\ell)} S \left[y'(z)\right]^2 dz + \frac{1}{2} \sum_k p_k \, u_k \quad , \tag{5.4b}$$

For a Csonka-type bar:

$$U_I = \frac{1}{2} \int_{(\ell)} B \left[y''(z)\right]^2 + S \left[y'(z)\right]^2 dz + \frac{1}{2} \sum_k p_k \, u_k \quad , \tag{5.4c}$$

For a sandwich bar with thin faces:

$$U_I = \frac{1}{2} \int_{(\ell)} B \left[y_B''(z)\right]^2 + S \left[y_S'(z)\right]^2 dz + \frac{1}{2} \sum_k p_k \, u_k \quad , \tag{5.4d}$$

For a sandwich bar with thick faces:

$$U_I = \frac{1}{2} \int_{(\ell)} B_0 \left[y_B''(z)\right]^2 + S \left[y_S'(z)\right]^2 + B_\ell \left[y_B''(z) + y_S''(z)\right]^2 dz + \frac{1}{2} \sum_k p_k u_k \quad . \tag{5.4e}$$

The normal force — induced in the bar prior to buckling — is $N \alpha(z)$, where N is the normal force and $\alpha(z) \geq 0$ is the distribution function of the normal force. The work done by the external forces is

$$U_E = \frac{1}{2} N \int_{(\ell)} \alpha(z) \left[y'(z)\right]^2 dz \quad , \tag{5.5}$$

where y'(z) is the first derivative of the displacement function of the bar axis.

First we examine the bar $\underline{R = R_1 \times R_2}$. The critical load parameter of the bar is equal to the minimum of the Rayleigh quotient:

$$N_{cr} = \min_{y} \frac{\sum_{j=1}^{2} \left\{ \sum_{i} \int_{(\ell)} b_{ji} \left[\eta_{ji}(z)\right]^2 dz + \sum_{k} p_{jk} u_{jk} \right\}}{\int_{(\ell)} \alpha(z) \left[y'(z)\right]^2 dz} . \tag{5.6}$$

The critical load parameters of bars R_1 and R_2 are as follows:

$$N_j = \min_{\hat{y}_j} \frac{\sum_{i} \int_{(\ell)} b_{ji} \left[\hat{\eta}_{ji}(z)\right]^2 dz + \sum_{k} \hat{p}_{jk} \hat{u}_{jk}}{\int_{(\ell)} \alpha(z) \left[\hat{y}'_j(z)\right]^2 dz} \tag{5.7}$$

$$(j = 1,2) \quad .$$

$y_j(z)$ and $\eta_{ji}(z)$ are the deflection and the deformation functions of the j-th bar, if it is a member of the connected bar, $\hat{y}_j(z)$ and $\hat{\eta}_{ji}(z)$ are the deflection and the deformation functions of the j-th bar investigated independently (without any connection). Similarly, $\hat{p}_{jk}$ and $\hat{u}_{jk}$ are the boundary forces and displacements of the independent bar. We chose the boundary conditions of the independent bar in such a way that the relationship

$$\min_{\hat{y}_j} \frac{\sum_{i} \int_{(\ell)} b_{ji} \left[\hat{\eta}_{ji}(z)\right]^2 dz + \sum_{k} \hat{p}_{jk} \hat{u}_{jk}}{\int_{(\ell)} (z) \left[\hat{y}'_j(z)\right]^2 dz} \leq$$

$$\min_{y_j} \frac{\sum_{i} \int_{(\ell)} b_{ji} \left[\eta_{ji}(z)\right]^2 dz + \sum_{k} p_{jk} u_{jk}}{\int_{(\ell)} \alpha(z) \left[y'_j(z)\right]^2 dz} \qquad (j = 1,2) \tag{5.8}$$

holds. (We shall find this to be the sufficient condition of the validity of the Föppl–Papkovich theorem.) On the basis of (5.7) and (5.8) we can give a lower estimate for (5.6) as follows:

$$N_{cr} \geq \min_{y} \frac{N_1 \int_{(\ell)} \alpha(z) \left[y_1'(z)\right]^2 dz + N_2 \int_{(\ell)} \alpha(z) \left[y_2'(z)\right]^2 dz}{\int_{(\ell)} \alpha(z) \left[y'(z)\right]^2 dz} \quad .(5.9)$$

Let us multiply the numerator and the denominator of (5.9) by $(N_1 + N_2)$. After rearrangement and using the positive sign of $\alpha(z)$, we obtain:

$$N_{cr} \geq \min_{y} \left\{ \frac{\left[N_1 \sqrt{\int_{(\ell)} \alpha(z) \left[y_1'(z)\right]^2 dz} - N_2 \sqrt{\int_{(\ell)} \alpha(z) \left[y_2'(z)\right]^2 dz} \right]^2}{(N_1+N_2) \int_{(\ell)} \alpha(z) \left[y'(z)\right]^2 dz} + \right. \quad (5.10)$$

$$\left. + \frac{N_1 N_2 \left[\int_{(\ell)} \alpha(z) \left[y_1'(z)\right]^2 + \alpha(z) \left[y_2'(z)\right]^2 dz + 2 \sqrt{\int_{(\ell)} \alpha(z) \left[y_1'(z)\right]^2 dz \int_{(\ell)} \alpha(z) \left[y_2'(z)\right]^2 dz} \right]}{(N_1 + N_2) \int_{(\ell)} \alpha(z) \left[y'(z)\right]^2 dz} \right\}$$

The first term in the numerator is positive, and using the inequality of Cauchy–Schwartz–Buniakowski:

$$\int_{(\ell)} \alpha(z) \left[y_1'(z)\right]^2 dz \int_{(\ell)} \alpha(z) \left[y_2'(z)\right]^2 dz \geq \left[\int_{(\ell)} \alpha(z)\, y_1'(z)\, y_2'(z)\, dz \right]^2$$

we obtain from (5.10)

$$N_{cr} \geq \frac{N_1 N_2}{N_1+N_2} = \left[N_1^{-1} + N_2^{-1} \right]^{-1} \quad . \quad (5.11)$$

Accordingly, if condition (5.8) is fulfilled, then (5.2) will lie on the safe side.

It can be proved in a simple way that in the case of <u>parallel connection</u>, we have

$$N_{cr} \geq N_1 + N_2 \quad (5.12)$$

provided the boundary conditions of the different bars permit (5.8) to be satisfied.

Condition (5.8) will be satisfied if the boundary conditions for the individual bars do not require a clamping stronger than that of the bars being members of the combined bar. If the boundary conditions for the two cases are identical, then (5.8) will be satisfied as an equality.

If the connected bar is fixed (locally and globally) at the bottom, and free at the top, then we may calculate the critical load parameter of the independent bars as if they were cantilevers. Expression (5.1) and (5.2) then lie on the safe side. In that case the fixing is the real condition at the bottom and the free edge is the softest possible at the top.

If the buckled shapes of the independent bars are identical with that of the combined bar, expressions (5.1) and (5.2) will be satisfied as an equality. Good examples for this are the Csonka-type bar and the sandwich bar with thin faces subjected to concentrated forces.

5.1 Example: Determination of the approximate critical load of a sandwich cantilever with thick faces braced by an S-bar

Let us consider the combined bar presented in Chapter 3.2.4 (Eq. (3.21), Fig. 10b). The bar is fixed (globally and locally) at the bottom and free at the top. Let the critical normal force of the combined bar for an arbitrary distribution be N_{cr}, and that of the independent bars – considered as cantilevers – be N_{S1}, N_{B1}, N_{S2} and N_{B2} respectively. In this case the expression

$$N_{cr} \geq (N_{S1}^{-1} + N_{B1}^{-1})^{-1} + N_{B2} + N_{S2} \tag{5.13}$$

holds. In the case of a concentrated force at the top, (5.13) and (5.8) will be satisfied as equals.

5.2 Example: Plantema's paradox

Tarnai has dealt with the Plantema's paradox /8/ which is the following:

Let us consider a sandwich bar with thin faces $R = R_B \gtrless R_S$ fixed at the bottom and braced (hinged) at the top (Fig. 14a). The load is a concentrated force N, which induces a constant normal force along the entire length of the bar.

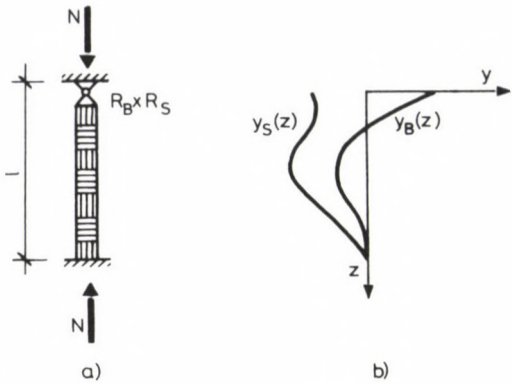

Fig. 14.

The boundary conditions are the following:

$$
\begin{aligned}
y(0) &= y_B(0) + y_S(0) = 0 \quad , \\
y_B(0) &= \frac{Q}{S}\ell \quad , \\
y_B''(0) &= 0 \quad , \\
y_B(\ell) &= 0 \quad , \\
y_S(\ell) &= 0 \quad , \\
y_B'(\ell) &= 0 \quad ,
\end{aligned}
\qquad (5.14a\text{-}f)
$$

where Q is the shearing force induced along the entire length of the bar.

The critical load of a B-bar fixed at the bottom and braced at the top is

$$N_1 = \frac{\pi^2 B}{(0.699\,\ell)^2} \quad , \qquad (5.15)$$

while that of an S-bar is (independently of the boundary conditions):

$$N_2 = S \quad . \qquad (5.16)$$

On the basis of /7/ the exact critical load of the combined bar in question is

$$N < (N_1^{-1} + N_2^{-1})^{-1}$$

i.e. the Föppl–Papkovich approximation lies on the unsafe side.

The visual interpretation of this paradox is the following:

The deflection curves of the bars R_S and R_B (which are the members of the combined bar) are plotted in Fig. 14b. The upper end of the connected bars shift horizontally, because only the sum of displacements has to be equal to zero (5.14a). Consequently the boundary of the connected bar is not braced by hinge, but by "elastic constraint". A softer boundary condition would be for example the free end. Hence, the Föpple–Papkovich theorem remains valid if, instead of (5.15), we use the expression valid for a cantilever:

$$N_1^C = \frac{\pi^2 B}{(2\ell)^2} \quad . \tag{5.17}$$

Hence,

$$N_{cr} > \left[(N_1^C)^{-1} + N_2^{-1} \right]^{-1} \quad . \tag{5.18}$$

(This expression is valid – as an equality – for the sandwich cantilever. Accordingly, it applies also for the model in question.)

Thus, Plantema's paradox results from the assumption of boundary conditions stronger than those applying to connected bars:

$$y_B(0) = y_S(0) = 0 \quad .$$

REFERENCES

1. Allen, H.G.: Analysis and Design of Structural Sandwich Panels, Pergamon Press, Oxford etc. 1969.
2. Csonka, P.: Beitrag zur Berechnung waagerecht belasteter Stockwerkrahmen. Die Bautechnik. 39 (7) (1962), 237–240.
3. Csonka, P.: Buckling of Bars Elastically Built-in Along Their Entire Length. Acta Techn. Hung. 32(3–4), (1961), 424–427.
4. Hegedűs, I.–Kollár, L.P.: Buckling of Sandwich Columns with Thin Faces under Distributed Normal Loads. Acta Techn. Hung. 97(1–4), (1984), 111–122.
5. Hegedűs, I.–Kollár, L.P.: Buckling of Sandwich Columns with Thick Faces Subjected to Axial Loads of Arbitrary Distribution. Acta Techn. Hung. 97 (1–4), (1984), 123–131.
6. Hegedűs, I.–Kollár, L.P.: Stability Analysis of Bars Elastically Restrained from Rotation Along their Entire Length. Acta Techn. Hung. 101–C/1, (1988), 59–67.
7. Plantema, F.J.: Sandwich Construction. Wiley and Sons, New York 1966.
8. Tarnai, T.: A Szerkezeti Stabilitáselmélet Dunkerley-típusú Tételei és Formulái. (The Dunkerley-tpye Theorems and Formulas of the Stability Theory of Structures. In Hung.) Építés- Építészettudomány (1984), (3-4), 427–467.

9. Timoshenko, S.—Gere, I.: Theory of Elastic Stability. McGraw-Hill, New York, 1961.

10. Zalka, K.: Buckling of a Cantilever Subjected to Distributed Normal Loads, Taking Shearing Deformation into Account. Acta Techn. Hung. 89(3—4), (1979), 497—508.

11. Zalka, K.: Torsional Buckling of a Cantilever Subjected to Distributed Normal Loads. Acta Techn. Hung. 90(1—2), (1980), 91—108.

Acta Technica Acad.Sci.Hung., 101(1),, pp. 97–108 (1988)

EFFECT OF END RESTRAINT UPON THE STRENGTH OF STEEL COLUMNS WITH INITIAL IMPERFECTIONS

Nguyen Ngoc Oanh*

(Received: 9 July 1987)

In this study the strength of steel columns in compression with end restraints against rotation and lateral displacement is investigated. The use of the Beer–Schulz method in the investigation has lead to new conclusions in case of non-sway columns. At the same time, the Beer–Schulz method is extended to determination of the strength of sway columns.

NOTATION

A	cross sectional area
a	initial curve amplitude
C_A, C_B	rigidities of rotational springs
E	modulus of elasticity
I	moment of inertia of cross section
K	effective length factor
L	length of column
ℓ_o	effective length ($\ell_o = KL$)
M	bending moment
N	normal force
P	external compressive force
P_{max}	load capacity
r	radius of gyration
v	transversal displacement
v_o	initial deviation of column axis from the straight determined by its end points
β	rigidity of translational spring
σ_y	yield stress
σ_r	residual stress
$\bar{\lambda}$	effective slenderness parameter $\bar{\lambda} = \frac{KL}{r}\sqrt{\frac{\sigma_y}{\pi^2 E}}$

1. INTRODUCTION

As is well known, steel columns of buildings carrying mainly compressive forces, in general, collapse due to loss of their stability.

*Nguyen Ngoc Oanh, Hungarian Institute for Building Science, Budapest, Dávid F. u. 6., H–1113, Hungary

Akadémiai Kiadó, Budapest

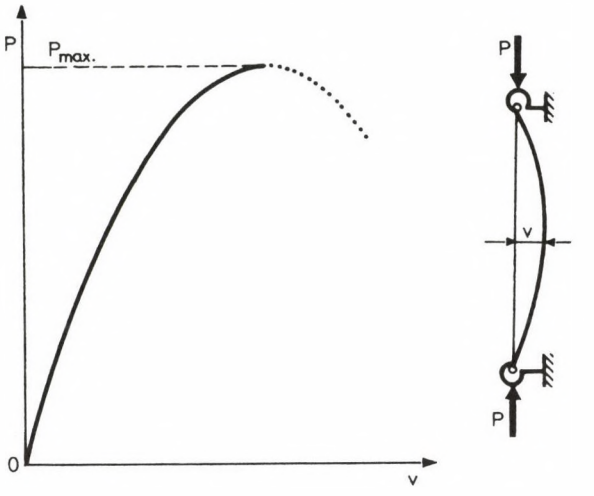

Fig. 1. Load-displacement curve

It is also well known that perfect (that is perfectly straight) columns exist only theoretically. Actually, any column has some initial imperfection, e.g. initial crookedness or residual stress etc., due to manufacture. As a result of the plastic behaviour of the material, these imperfections reduce the strength of the column as compared with that calculated on the basis of Euler's or Engesser's critical load theory. Thus investigation of the strength of a column with initial imperfections involves determination of the load-displacement curve (Fig. 1) where it is the value of load corresponding to the maximum of the curve that shall be considered to be the ultimate load capacity of the column. Almost all important questions concerning load capacity of columns with hinged ends, having initial imperfections, could be answered as a result of international theoretical and experimental research by the 1970s. A still unanswered question is, however, whether the effective length concept according to which the dimensions of columns are calculated on the basis of the dimensions of pin ended columns is acceptable and if indeed at all, to what extent. Therefore, attention of research people had been directed to the investigation of load capacity of steel columns with elastic end restraints /1, 2, 3, 4, 5, 6/ in the late 1970s and results of quite a number concerning the effect of rigidity of end supports on the load capacity of the column were obtained. The question whether in case of identical effective slenderness parameter $\overline{\lambda}$,

the load capacity of end restrained columns with different spring constants or different (symmetrical or asymmetrical) constraint is affected in the same way remains to be answered.

This study has been designed fundamentally to find answer to these questions by means of deterministic investigations using the Beer–Schulz method generalized by Tarnai /5/ in case of non-sway columns and extending the same method to the case of end restrained sway columns. (The Beer–Schulz method or deflection method is based on the principle of elastic loads and it takes into consideration the plastic behaviour of the material, including the effect of residual stresses, as the change in cross sectional rigidity, treating the problem as a problem of elasticity theory. The method is described in /5/ while modification of the method for the case of column end rigidly built in /7/.)

2. EFFECT OF AMOUNT OF RESTRAINT ON LOAD CAPACITY OF THE COLUMN

Investigated are the changes in load capacity of columns with symmetrical equal rotational springs at their ends ($C_A = C_B = C$) as a function of support rigidity B_B ($B_B = CL/EI$) to show the extent to which the load capacity of the column can be increased by increasing the spring rigidity and to see whether the load capacity remains unchanged in case of identical effective slenderness parameter $\bar{\lambda}$ but different spring rigidity.

Let the load capacity of columns in centric compression, with symmetrical constraint at both ends, having an IPBℓ 200 cross section according to DIN, a yield stress of $\sigma_y = 24000\ N/cm^2$, Massonnet-type (parabolically distributed) residual stresses and an initial curve amplitude of a = 0.001 L be investigated for buckling in the weak direction. The spring rigidity shall be kept constant while the length of the column shall be varied. The load capacity of columns of symmetrical end supports of different rigidity ($C = 0,\ 10^7 N.cm,\ 10^8 N.cm,\ 10^9 N.cm,\ \infty$, that is $B_B = 0,\ 2.8563.10^{-1},\ 2.8563.10^{0},\ 2.8563.10^{1},\ \infty$) has been determined by means of a computer program elaborated for this purpose, and illustrated diagrammatically in a dimensionless form as a function of actual column length L (Fig. 2). The diagram shows that the greater the spring rigidity of columns for given length, the higher the load capacity. The load capacity of columns with a less rigid constraint ($B_B \leq 2.8563.10^{-1}$ that is $C \leq 10^7 N.cm$) at the ends increases only slightly as compared with that of pin columns while the load

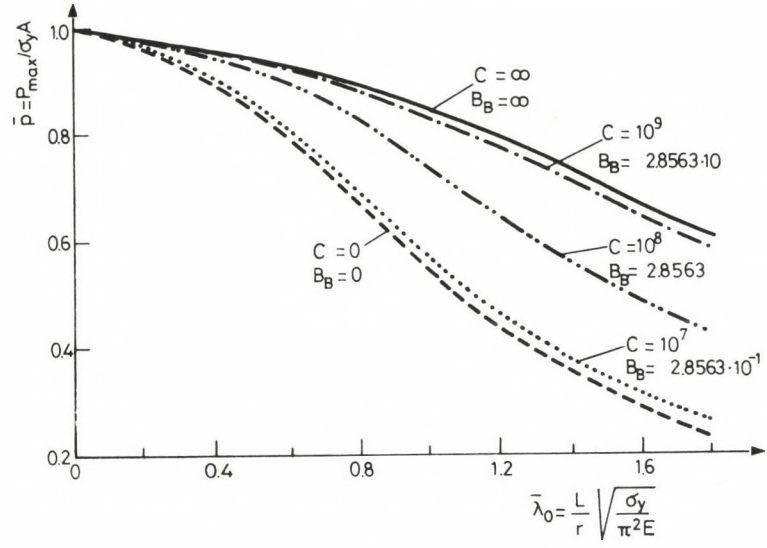

Fig. 2. Change of load capacity as a function of actual length L of the column in accordance with different rotational spring rigidity

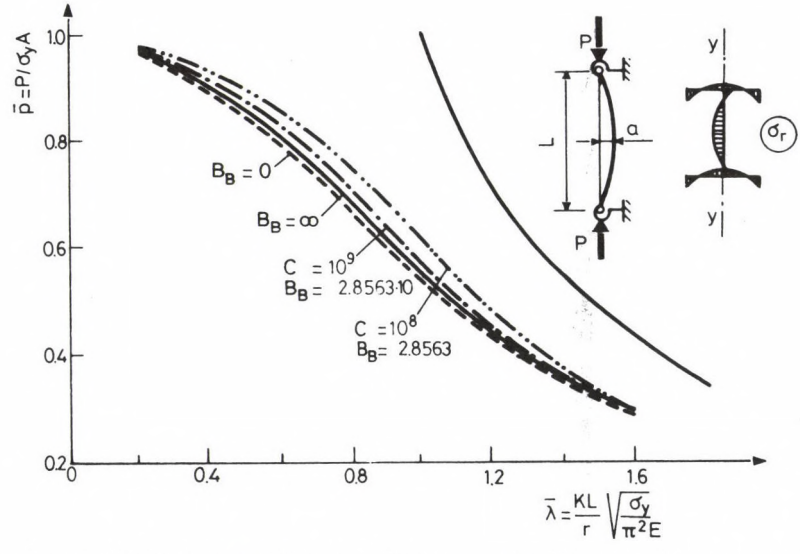

Fig. 3. Change of load capacity as a function of effective length KL of the column in accordance with different rotational spring rigidity

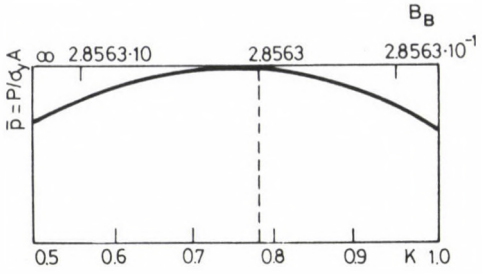

Fig. 4. Change of load capacity as a function of effective length factor K and support rigidity B_B

capacity of columns with a relatively rigid spring at the ends ($B_B \geq 2.8563.10^1$ that is $C \geq 10^9$N.cm) is only insignificantly lower than that of columns with an infinitely rigid spring. As compared with slender columns, the load capacity of the columns is increased to a reduced extent as a result of increasing spring rigidity.

The values of load capacity given in Fig. 2 have been illustrated also as a function of effective length KL and effective slenderness parameter $\bar{\lambda}$ of the column (Fig. 3). Interestingly, the load capacity of columns of identical effective slenderness parameter $\bar{\lambda}$ but with different spring rigidity is not identical. Still more surprisingly, no highest load capacity has been obtained for columns with infinitely rigid spring at both ends, moreover, the load capacity of such columns lies below that of columns with relatively great spring rigidity ($B_B = 2.8563.10^0$ to $2.8563.10^1$ that is $C = 10^8$N.cm to 10^9N.cm). As seen in Fig. 3, the load capacity of columns of an end support rigidity of $B_B \approx 2.8563$ (i.e. $C \approx 10^8$N.cm) is highest from among the columns investigated.

A simple transformation $K = 0.5 + \frac{1}{C + 2}$ and the computer program elaborated helped to more accurately illustrate the change of load capacity of columns as a function of end support rigidity B_B and effective length factor K (Fig. 4). As seen, highest load capacity of columns has been obtained for $K \approx 0.77$ and $B_B \approx 2.8563$.

3. EFFECT OF THE DIFFERENT END SUPPORT TYPES ON THE LOAD CAPACITY OF COLUMNS

Now the load capacity of columns of identical or different (symmetrical or asymmetrical) spring rigidity, an IPBℓ 200 cross section, a

length of L, having Massonnet-type residual stresses and an initial curve amplitude of a = 0.001L, is investigated for buckling in the weak direction.

(a) Column with asymmetrical end supports.

In the extreme case, $C_A = 0$ and $C_B = \infty$. In this case, effective length factor K is independent of the length of the columns and its value is known (K = 0.7). In other cases, the ratio of spring rigidities at the two ends of the column is a finite number other than zero which may also be constant (e.g. $C_A = \frac{1}{5} C_B$). For given lengths L, the values of spring rigidities C_A and C_B have been determined in such a way that the value of effective length factor K of the columns will be 0.7.

(b) Column with symmetrical end supports ($C_A = C_B = C$).

In this case, the values of spring rigidity C have been determined for given lengths L in such a way that the value of effective length factor K of the columns will be 0.7.

The load capacity of the above columns had been calculated by means of the computer program elaborated for this purpose, and on the basis of the results, the load capacity curves of the columns were illustrated diagrammatically in a dimensionless form as a function of effective slenderness parameter $\bar{\lambda}$ (Fig. 5). The following conclusions can be drawn from these curves:

(1) In case of plastic buckling of columns having initial imperfections, with identical effective slenderness parameter $\bar{\lambda}$ but with different (symmetrical or asymmetrical) end support, the load capacity of the columns is not identical. As compared with columns with different spring rigidity at the two ends (asymmetrical end support), the load capacity of columns of identical spring rigidity at both ends (symmetrical end support) is higher, the difference being especially significant in case of columns pinned at one end while rigidly built in at the other end.

(2) There is little difference in load capacity between columns with symmetrical and asymmetrical end supports in case of smaller values ($\bar{\lambda} \leq 0.3$) or greater values ($\bar{\lambda} \geq 1.4$) of effective slenderness parameter while the difference is significant (about 11%) in case of average slenderness.

As a special case, also columns with zero or infinite spring rigidity ($C_A = C_B = 0$, $C_A = 0$ and $C_B = \infty$, $C_A = C_B = \infty$, respectively) have been investigated. The load capacity curves for the three columns are almost identical (Fig. 6), the difference (about 1 to 2%) being insignificant.

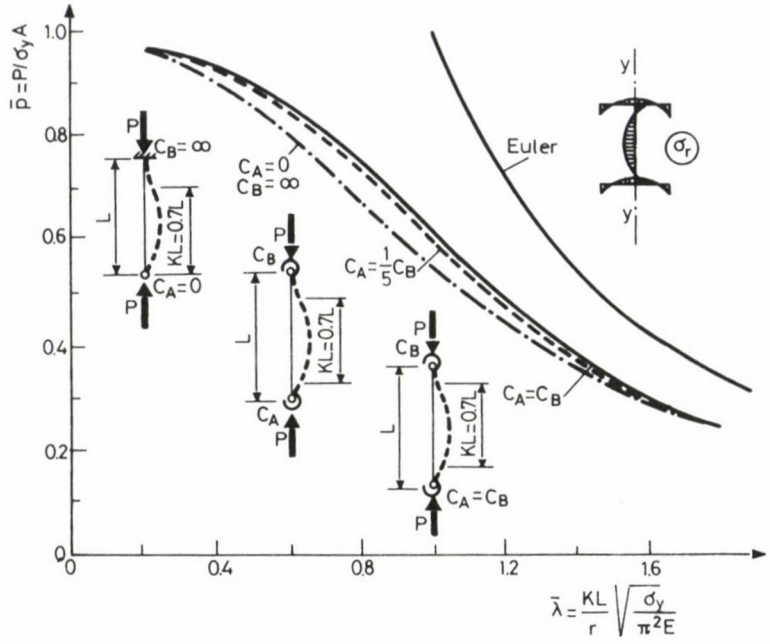

Fig. 5. Change of load capacity in accordance with the different types of end supports

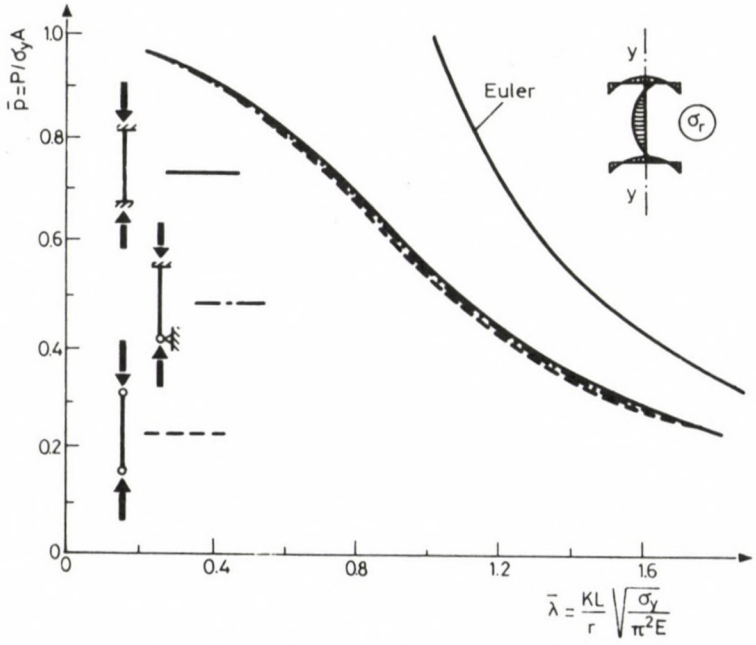

Fig. 6. Load-capacity curves for the three columns

4. EFFECT OF THE TWO AXES OF BUCKLING ON THE LOAD CAPACITY OF COLUMNS

What is now investigated is the load capacity of a column whose cross section rotates about one or the other of the two axes of symmetry (x–x and y–y) of the cross section during buckling to answer the question whether or not the load capacity of columns having buckled around the strong axis (x–x) is always higher than that of columns with a buckling around the weak axis (y–y) in the full range of effective slenderness parameter $\bar{\lambda}$. For this purpose, the load capacity of columns of IPBℓ 200 cross section, Massonnet-type residual stresses, and with an initial curve amplitude of a = 0.001 L and a = 0.002 L has been investigated for buckling around the strong axis and around the weak axis independently.

The load capacity curves of the above columns are illustrated in Fig. 7. Formally, these curves are similar to the load capacity curves plotted for aluminium columns by Chapuis and Galambos /2/. A detailed analysis of this diagram leads to the following conclusions:

(1) As has been known so far, the load capacity of columns having

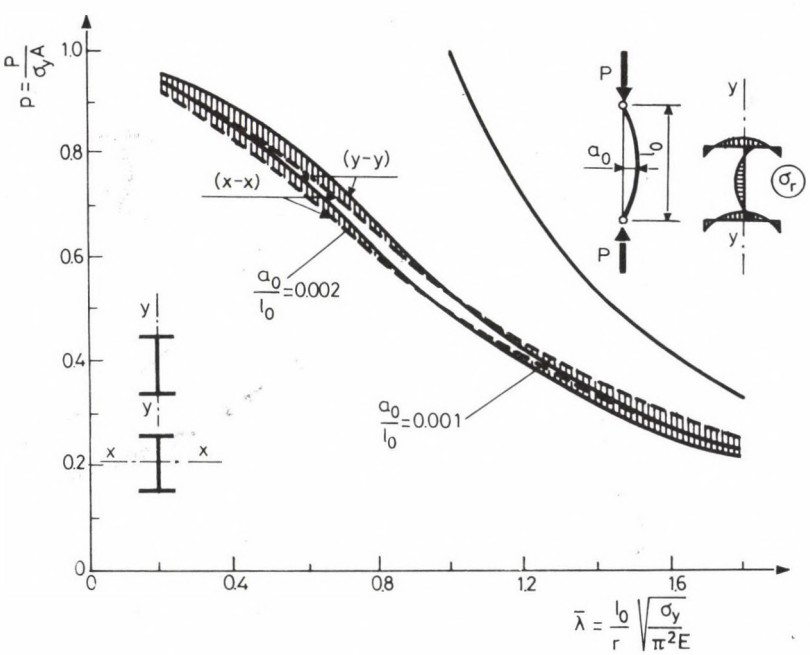

Fig. 7. Change of load capacity according to the two axes of bending

buckled around the two different axes (x—x and y—y) in case of identical effective slenderness parameter $\bar{\lambda}$ and identical initial crookedness is not identical.

(2) Dissimilarly to what has been expected, the load capacity of columns buckled around the strong axis (x—x) is not necessarily higher than that of columns buckled around the weak axis (y—y) over the full range of slenderness investigated. In the case investigated, higher load capacity has been obtained for columns buckled around the strong axis for an effective slenderness parameter of $\bar{\lambda} \geq 1.0$ while just the opposite results have been obtained for $\bar{\lambda} \leq 1.0$.

5. INVESTIGATION OF THE STRENGTH OF SWAY COLUMNS

For sway columns, the effect of lateral restraint and initial out-of-plumb is now investigated using the generalized Beer—Schulz method. This method is described in /8/.

5.1 Effect of lateral spring rigidity

Let columns supported laterally with a spring of different rigidity be investigated first (Fig. 8), with the column length, initial curve amplitude ($amp^{(2)}$) and initial out-of-plumb ($amp^{(1)}$) kept constant while the lateral spring rigidity varied in the course of investigation. On the basis of the calculations made, the values of load capacity of columns of IPBℓ 200 cross section and of an initial out-of-plumb of $amp^{(1)} = 0.01$ L, buckling in the weak direction, have been ilustrated in a dimensionless form for support rigidity $B_C = 20, 40, 60$ (where $B_C = \beta L^3/EI$) as a function of effective slenderness parameter $\bar{\lambda}$ (Fig. 8). It can be seen in the diagram that the load capacity of columns of different lateral spring rigidity is not identical for given slenderness, or more precisely, we might be right in saying that for given slenderness, the greater the lateral spring rigidity, the higher the load capacity of the column, and the load capacity is highest in case of infinite lateral spring rigidity ($\beta = \infty$).

5.2 Effect of initial out-of-plumb

Let now the load capacity of columns according to par 5.1 be investigated. What is varied now is the initial out-of-plumb of the columns. The load capacity of the columns has been calculated for an initial out-of-

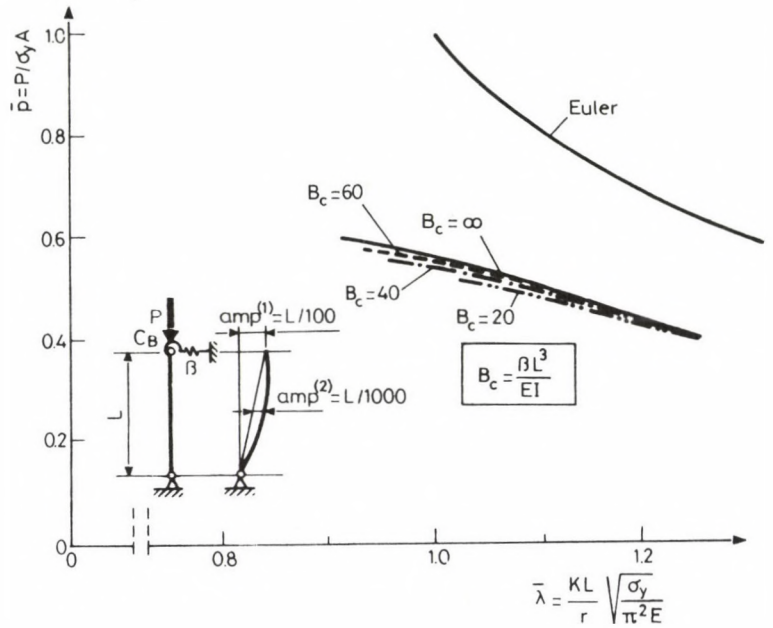

Fig. 8. Change of load capacity according to different lateral spring rigidity

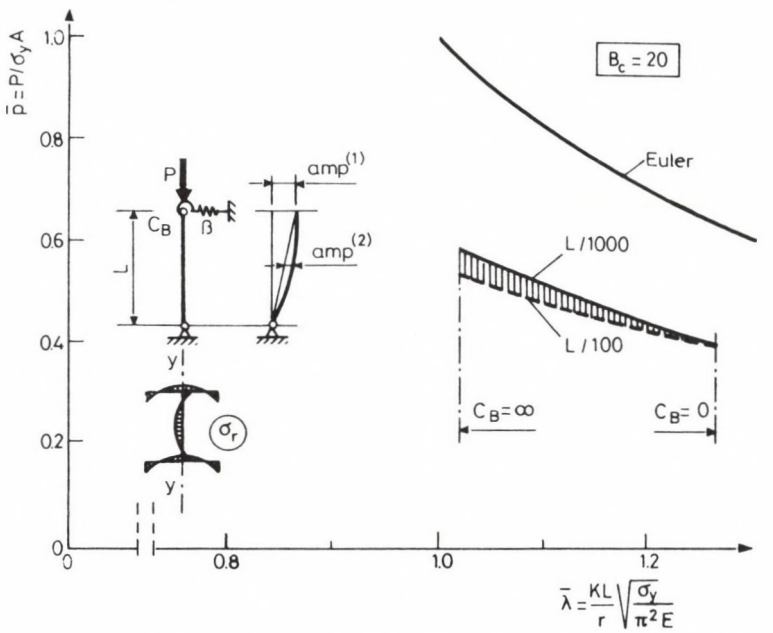

Fig. 9. Change of load capacity according to different initial out-of-plumb in case of $B_C = 20$

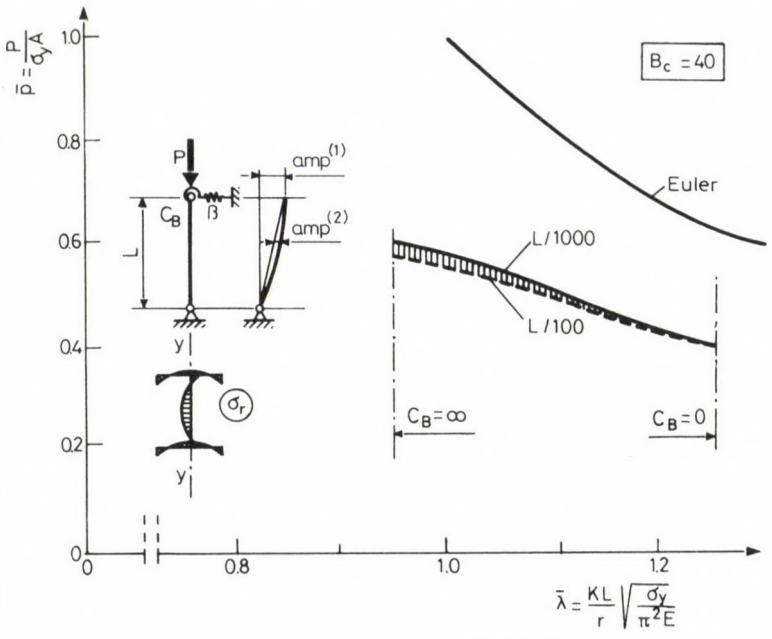

Fig. 10. Change of load capacity according to different initial out-of-plumb in case of B_C = 40

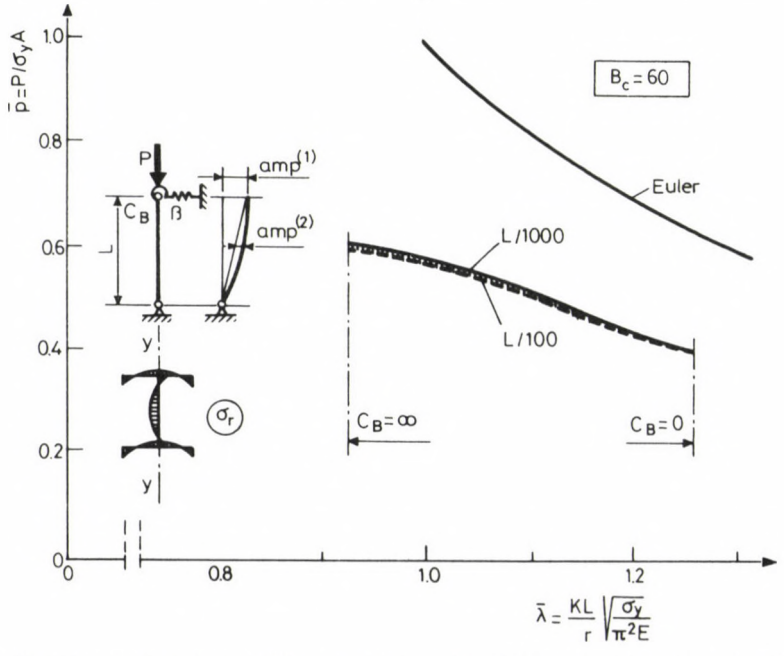

Fig. 11. Change of load capacity according to different initial out-of-plumb according to B_C = 50

plumb of amp$^{(1)}$ = L/1000 and L/100. Figure 9 shows the change of load capacity for an initial out-of-plumb of L/1000 to L/100 in case of B_C = 20 while Figs 10 and 11 show the same change in case of B_C = 40 and B_C = 60. As shown by these three diagrams,

(1) in case of given support rigidity, the load capacity of the columns reduces more significantly as a result of an increase of the initial out-of-plumb from L/1000 to L/100 for columns of a great rotational spring rigidity C_B while less significantly for columns of less rotational spring rigidity C_B.

(2) In case of identical effective slenderness parameter $\bar{\lambda}$, the load capacity of columns of less lateral spring rigidity reduces more significantly as a result of an increase of the initial out-of-plumb from L/1000 to L/100 and vice versa.

REFERENCES

1. Bergquist, D.J.: Tests on Columns Restrained by Beams with Simple Connection. Report No. 1, American Iron and Steel Institute, Project No. 189, Department of Civil Engineering, The University of Texas, Austin, Texas (1977).
2. Chapuis, J. and Galambos, T.V.: Design Criteria for Aluminium Columns and Beam-Columns. Research Report No. 58, Structural Division, Washington University, St. Louis (1980).
3. Chen, W.F.: End-Restraint and Column Stability. Journal of the Structural Division Proc. of the ASCE, Vol. 106 (1980), pp. 2279–2295.
4. Jones, S.W., Kirby, P.A. and Nethercot, D.A.: Effect of Semi-Rigid Connections on Steel Column Strength. Journal of Constructional Steel Research, Vol. 1, No. 1, London (1980), pp. 38–46.
5. Tarnai, T.: Strength of End Restrained Steel Columns (in Hungarian). Építési Kutatás Fejlesztés, Vol. 18 (1985), pp. 136–152.
6. Tarnai, T. and Nagy, Sz.: Parametric Study of the Strenght of Non-Sway End Restrained Steel Columns (in Hungarian). Közlekedésépítés- és Mélyépítéstudományi Szemle, Vol. 37 (1987), pp. 58–70.
7. Nguyen Ngoc Oanh and Tarnai, T.: Strength of Non-Sway Steel Columns, Rigidly Built in at their Ends (in Hungarian). Közlekedésépítés- és Mélyépítéstudományi Szemle, Vol. 38 (1988), 274–276.
8. Nguyen Ngoc Oanh: Investigation of the Strength of Steel Columns with Elasto-plastic Material Behaviour and Initial Imperfections (in Hungarian). Candidate's Thesis, Budapest (1987).

Acta Technica Acad.Sci.Hung., 101(1), pp. 109–110 (1988)

BOOK REVIEWS

E. Mosonyi: Water Power Development. Volume I. Low-head Power Plants. Akadémiai Kiadó, Budapest 1987. Third, revised edition (1074 pages, 726 figures, 7 supplements)

The book was published first in Hungarian language in 1952. At that time, the book contained 353 pages. On the basis of this first edition, the book appeared in German language in 1956 and in English language in 1957. A second edition in English language came out in 1963. In the special field of water power utilization, the book has been known and used all over the world and it has been reviewed as a most comprehensive work many times.

Research and development in planning and construction of water power plants and innovations in engineering necessitated that the book be revised and modernized. A considerable contribution ot this new modernized edition has been the recent increasing interest in the uses of water power. The author, retired as Professor of the University of Karlsruhe, Department of Water Power Engineering, has added much to his knowledge and experience in the course of research, pilot experiments, planning and construction of water power plants, multipurpose water power utilization projects in many countries of the world since 1963.

In addition to a general revision of the book many chapters have been rewritten in accordance with the state of art, among others, the discussion of construction and engineering of tubular turbines and the wide field of application of such turbines. Numerical examples of quite a number have been added.

The first volume which has been published recently consists of two parts, the first part dealing with the fundamental principles of utilization of water power (125 pages) while the second part presents a discussion of low-head water power plants in seven chapters subdivided into 75 subchapters (861 pages).

Two chapters of the first part are devoted to the mechanical energy sources of water and to the history of water power utilization. Chapter IV deals with wave energy as a new source of water power while Chapter VI presents up-to-date world statistics on the utilization of water power, data on largest dams and barriers, reservoirs and water power plants relating to the year of revision of the book.

The second part of five chapters includes estimation of water power resources, general layout of water power utilization, water power plant with process water duct, types of water power plants including machinery and engine house. Essentially, the chapter on economical utilization of water power and technical-economical parameters is designed to establish the use of water power plants. Like in the book in general, new problems and issues of quite a number are discussed also in this part, e.g. water intake losses, stability of process water duct, classification of turbines, efficiency and regulation of turbines, scroll, operation at variable head, permissible suction head, static calculation and structural test of water power plants, axial turbines and many other details.

Given in appendix are an updated bibliography, unified conversion chart in internationally accepted units of measurement, index for authors, water power plants, institutions and subject matter. 7 appendices are attached to the text to be the readers' help in practical work, especially in the design of steel constructions.

Since many papers had contributed to the development of water power

utilization in the recent 25 years, it must have been quite a job to select the works to be included among references even within water power utilization in a narrower sense. By way of instruction, the author comments on this problem by saying that all the results and contributions could not be presented in this book but this was not necessary either as the details were found in the literature. Thus e.g. a report on the hydraulics on non-permanent motion with the numerical results of computer calculations could not be included in the book. A report on the development in the field of hydroelectric ministrations is expected to appear in the second volume.

The book is rich in photographs part of which being made by the author himself as well as in graphic illustrations of existing power plants. The projects presented emphasize the international background of the book. Understandably, the author's methods and the application of these methods are privileged in the book.

There are many details in the book which, beyond the narrow sense expressed by the title, can be used also in other field of hydraulic engineering.

Although written for the experts of water power utilization or in other words, for engineers designing, constructing and operating hydroelectric power plants and thus its content and scope go far beyond what is taught at university, the book is a useful reading also of university students.

The author can certainly expect the same international response to this third edition as he was happy to experience in case of the previous two editions.

Ö. Starosolszky

T. Berceli: Nonlinear active microwave circuits. Akadémiai Kiadó, Budapest 1987. (271 pages)

Active circuits are widely used in microwave systems. Their behaviour is described by models. Selection of a model depends on whether a general idea of the characteristics of the circuit or accurate circuit is required. In the latter case, it is not easy to find an appropriate model of the electromagnetic field surrounding the active element of the circuit. A more sophisticated model is acceptable only if the gain in computational accuracy is not questioned by the neglected parameters.

After a brief general introduction (Ch1), the description of negative conductance (free running and injection locked) oscillators, negative conductance amplifiers (Chs 2–4); varactor up-converter and frequency multiplier, divider, parametric amplifiers (Chs 5–8); nonlinear resistance mixers (Ch9) and large signal FET amplifiers follows. Throughout the book, the author's intention is clearly reflected by the approach he uses: by selection of well defined but limited characteristics for the nonlinear device, the circuits can be handled analytically. This enables a surprisingly detailed understanding and description of the circuit behaviour. Where necessary, the analytical treatment is completed by numerical or graphical methods. Emphasis has been laid on clear understanding of the main points.

The book is essentially a monograph with the author's contribution to each group of circuits. The circuit examples are properly selected and not only the results of the design process are correct but also the circuit operation can be clearly understood, an explanation of why did the author omit PIN diode circuits (limiters, attenuators, switch).

The book can be equally used as a textbook in postgraduate studies and as a design help for engineers in practical design work.

I. Bozsóki

INFORMATION BULLETIN

PRESS RELEASE

We are pleased to announce the publication of our 1988 Edition of our Sensitizing Dye Catalog. Our catalog lists over 100 Dyes including their structures, absorption characteristics, solubility information and other details.
Dye production is in the USA and Sands also does Custom Synthesis in this product range. Also available are catalogs for Dye Intermediates and Anti-Halation products.

H.W. SANDS CORP.
International Sales Manager

Telex: 261057
Fax No. (516) 348-0637

1324 Motor Parkway
Hauppauge, N.Y. 11788
USA

PRINTED IN HUNGARY
Akadémiai Kiadó és Nyomda Vállalat, Budapest

NOTICE TO CONTRIBUTORS

Papers in English* are accepted on condition that they have not been previously published or accepted for publication.

Manuscripts in two copies (the original type-written copy plus a clear duplicate one) complete with figures, tables, and references should be sent to

Acta Technica
Münnich F. u. 7. I. 111 A
Budapest, Hungary
H-1051

Although every effort will be made to guard against loss, it is advised that authors retain copies of all material which they submit. The editorial board reserves the right to make editorial changes.

Manuscripts should be typed double-spaced on one side of good quality paper with proper margins and bear the title of the paper and the name(s) of the author(s). The full postal address(es) of the author(s) should be given in a footnote on the first page. An abstract of 50 to 100 words should precede the text of the paper. The approximate locations of the tables and figures should be indicated on the margin. An additional copy of the abstract is needed. Russian words and names should be transliterated into English.

References. Only papers closely related to the author's work should be referred to. The citations should include the name of the author and/or the reference number in brackets. A list of numbered references should follow the end of the manuscript.

References to periodicals should mention: (1) name(s) and initials of the authors(s); (2) title of the paper; (3) name of the periodical; (4) volume; (5) year of publication in parentheses; (6) numbers of the first and last pages. Thus: 5. Winokur, A., Gluck, J.: Ultimate strength analysis of coupled shear walls. American Concrete Institute Journal 65 (1968), 1029–1035.

References to books should include: (1) author(s) name; (2) title; (3) publisher; (4) place and year of publication. Thus: Timoshenko, S., Gere, J.: Theory of Elastic Stability. McGraw-Hill Company, New York, London 1961.

Illustrations should be selected carefully and only up to the necessary quantity. Black-and-white photographs should be in the form of glossy prints. The author's name and the title of the paper together with the serial number of the figure should be written on the back of each print. Legends should be brief and attached on a separate sheet. Tables, each bearing a title, should be self-explanatory and numbered consecutively.

Authors will receive proofs which must be sent back by return mail.

Authors will receive 50 reprints free of charge.

*Hungarian authors can submit their papers also in Hungarian.

Periodicals of the Hungarian Academy of Sciences are obtainable at the following addresses:

AUSTRALIA
C.B.D. LIBRARY AND SUBSCRIPTION SERVICE
Box 4886, G.P.O., *Sydney N.S.W. 2001*
COSMOS BOOKSHOP, 145 Ackland Street
St. Kilda (Melbourne), Victoria 3182

AUSTRIA
GLOBUS, Höchstädtplatz 3, *1206 Wien XX*

BELGIUM
OFFICE INTERNATIONAL DES PERIODIQUES
Avenue Louise, 485, *1050 Bruxelles*
E. STORY-SCIENTIA P.V.B.A.
P. van Duyseplein 8, *9000 Gent*

BULGARIA
HEMUS, Bulvar Ruszki 6, *Sofia*

CANADA
PANNONIA BOOKS, P.O. Box 1017
Postal Station "B", *Toronto, Ont. M5T 2T8*

CHINA
CNPICOR, Periodical Department, P.O. Box 50
Peking

CZECHOSLOVAKIA
MAD'ARSKA KULTURA, Národni třida 22
115 66 Praha
PNS DOVOZ TISKU, Vinohradská 46, *Praha 2*
PNS DOVOZ TLAČE, *Bratislava 2*

DENMARK
EJNAR MUNKSGAARD, 35, Nørre Søgade
1370 Copenhagen K

FEDERAL REPUBLIC OF GERMANY
KUNST UND WISSEN ERICH BIEBER
Postfach 46, *7000 Stuttgart 1*

FINLAND
AKATEEMINEN KIRJAKAUPPA, P.O. Box 128
00101 Helsinki 10

FRANCE
DAWSON-FRANCE S.A., B.P. 40, *91121 Palaiseau*
OFFICE INTERNATIONAL DE DOCUMENTATION ET LIBRAIRIE, 48 rue Gay-Lussac
75240 Paris, Cedex 05

GERMAN DEMOCRATIC REPUBLIC
HAUS DER UNGARISCHEN KULTUR
Karl Liebknecht-Straße 9, *DDR-102 Berlin*

GREAT BRITAIN
BLACKWELL'S PERIODICALS DIVISION
Hythe Bridge Street, *Oxford OX1 2ET*
BUMPUS, HALDANE AND MAXWELL LTD.
Cowper Works, *Olney, Bucks MK46 4BN*
COLLET'S HOLDINGS LTD., Denington Estate,
Wellingborough, Northants NN8 2QT
WM DAWSON AND SONS LTD., Cannon House
Folkstone, Kent CT19 5EE
H. K. LEWIS AND CO., 136 Gower Street
London WC1E 6BS

GREECE
KOSTARAKIS BROTHERS INTERNATIONAL BOOKSELLERS, 2 Hippokratous Street, *Athens-143*

HOLLAND
FAXON EUROPE, P.O. Box 167
1000 AD Amsterdam
MARTINUS NIJHOFF B. V.
Lange Voorhout 9–11, *Den Haag*
SWETS SUBSCRIPTION SERVICE
P.O. Box 830, 2160 Sz Lisse

INDIA
ALLIED PUBLISHING PVT. LTD.
750 Mount Road, *Madras 600002*
CENTRAL NEWS AGENCY PVT. LTD.
Connaught Circus, *New Delhi 110001*
INTERNATIONAL BOOK HOUSE PVT. LTD.
Madame Cama Road, *Bombay 400039*

ITALY
D. E. A., Via Lima 28, *00198 Roma*
INTERSCIENTIA, Via Mazzé 28, *10149 Torino*
LIBRERIA COMMISSIONARIA SANSONI
Via Lamarmora 45, *50121 Firenze*
SANTO VANASIA, Via M. Macchi 58
20124 Milano

JAPAN
KINOKUNIYA COMPANY LTD.
Journal Department, P.O. Box 55
Chitose, *Tokyo 156*
MARUZEN COMPANY LTD., Book Department
P.O. Box 5050 Tokyo International, *Tokyo 100-31*
NAUKA LTD., Import Department
2-30-19 Minami Ikebukuro, Toshima-ku, *Tokyo 171*

KOREA
CHULPANMUL, *Phenjan*

NORWAY
TANUM-TIDSKRIFT-SENTRALEN A.S.
Karl Johansgata 43, *1000 Oslo*

POLAND
WĘGIERSKI INSTYTUT KULTURY
Marszalkowska 80, *00-517 Warszawa*
CKP I W, ul. Towarowa 28, *00-958 Warszawa*

ROUMANIA
D. E. P., *Bucuresti*
ILEXIM, Calea Grivitei 64–66, *Bucuresti*

SOVIET UNION
SOYUZPECHAT — IMPORT, *Moscow*
and the post offices in each town
MEZHDUNARODNAYA KNIGA, *Moscow G-200*

SPAIN
DIAZ DE SANTOS Lagasca 95, *Madrid 6*

SWEDEN
ESSELTE TIDSKRIFTSCENTRALEN
Box 62, *101 20 Stockholm*

SWITZERLAND
KARGER LIBRI AG, Petersgraben 31, *4011 Basel*

USA
EBSCO SUBSCRIPTION SERVICES
P.O. Box 1943, *Birmingham, Alabama 35201*
F. W. FAXON COMPANY, INC.
15 Southwest Park, *Westwood Mass. 02090*
MAJOR SCIENTIFIC SUBSCRIPTIONS
1851 Diplomat, P.O. Box 819074,
Pallas, Tx. 75381-9074
READ-MORE PUBLICATIONS, INC.
140 Cedar Street, *New York, N. Y. 10006*

YUGOSLAVIA
JUGOSLOVENSKA KNJIGA, Terazije 27, *Beograd*
FORUM, Vojvode Mišića 1, *21000 Novi Sad*

HU ISSN 0001-7035 Index: 26.025

ACTA TECHNICA

ACADEMIAE SCIENTIARUM HUNGARICAE

EDITOR-IN-CHIEF: P. MICHELBERGER

VOLUME 101
NUMBER 2

MATERIAL SCIENCES AND TECHNOLOGY–T/1

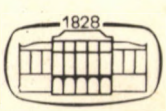

AKADÉMIAI KIADÓ, BUDAPEST 1988

ACTA TECHNICA

A JOURNAL OF THE HUNGARIAN ACADEMY OF SCIENCES

Acta Technica publishes original papers, preliminary reports and reviews in English, which contribute to the advancement of engineering sciences.
Acta Technica is published by

AKADÉMIAI KIADÓ
Publishing House of the Hungarian Academy of Sciences
H-1450 Budapest, Alkotmány u. 21.

Subscription information

Orders should be addressed to

KULTURA Foreign Trading Company
H-1389 Budapest P.O. Box 149

or to its representatives abroad

Acta Technica is abstracted/indexed in Applied Mechanics Reviews, Current Contents–Engineering, Technology and Applied Sciences, GeoRef Information System, Science Abstracts.

CONTENTS

EDITORS' FOREWORD 111

Báder, I. - Berecz, E.: Measurement of the Al_2O_3-content in cryolitic melt by electrochemical method using solid electrolyte. The decomposition voltage of Al_2O_3 and the composition of the anode gas 113

Csővári, M. - Czeglédi, B. - Stocker, L. - Erdélyi, M. - Egry, R. - Tündök, S. - Horváth, A.: Regeneration of hydrochloric acid in chloride-hydrometallurgy by anion exchange process 129

Farkas, O.: Determination of coke-natural gas substitution ratio in blast furnaces ... 143

Répási, G.: Results of injection ladle metallurgy in sheet metal production 155

Szepessy, A. - Kékesi, T. - Hertelendi, Á.: Investigation of the parameters of electrolytic copper refining by current reversal 171

Tolnay, L. - Tardy, P. - Károly, Gy. - Ghazally, S.: Effect of different technologies of cored wire treatment on the quality of steels 185

Voith, M. - Gulyás, J. - Dernei, L. - Zupkó, I. - Herendi, R.: Computer aided roll pass design for I-beams 199

Acta Technica Acad.Sci.Hung., 101(2), pp. 111--112 (1988)

EDITORS' FOREWORD

The recent decades are often called the age of technical-scientific revolution as never in history has so much been added to scientific knowledge and technical development. To this revolutionary development, the contribution of materials science and technology has been significant if not decisive as proved also by the increasing number of periodicals published to report on the results of development in the field of materials science and technology.

The booklet you are holding in your hand is a result of the efforts of the Hungarian Academy of Sciences, Section of Technical Sciences, to encourage research in the field of materials science and technology in the country by offering a possibility of publication of the results not only in the country but also in international scientific world.

At the same time, the new international results are also published in the periodical. New papers are welcome from every part of the world and the Editorial Board is happy to publish also contributions to, and comments on, the papers published.

Papers published in the periodical are designed to directly contribute to progress in the field of materials science and technology. Speaking of technology, some explanation seems to be necessary to make clear what is meant by technology. According to Anglo—Saxon terminology, 'technology, the application of science to the practical aims of human life or, as it is sometimes phrased, to the change and manipulation of human environment' (Encyclopaedia Britannica 1985), technology comprises all the technical results including an airplane or a computer, a new machining process or a new material etc.

In Europe and first of all in Hungary, the term 'technology' is used only for knowledge and activity in relation to processing of materials. We say that 'technology is a comprehensive theory of all the scientific and practical results by means of which raw materials available as natural resources as well as semi-finished products resulting from these raw materials can be converted into materials for use by man'. Of course, this category

includes any equipment, device, tool etc. serving for materials processing while results having no bearing upon production are excluded from it.

Why did we define 'technology' so exactly? Because we expect papers reporting on the new results of materials and technological sciences in the sense of the European approach. Authors of the papers submitted will receive professional advisers' opinion of the works.

The Editorial Board hopes the proceedings 'Materials Science and Technology' will be a useful aid and an efficient contribution to research in this field.

Acta Technica Acad.Sci.Hung., 101(2), pp. 113—127 (1988)

MEASUREMENT OF THE Al_2O_3-CONTENT IN CRYOLITIC MELT BY ELECTROCHEMICAL METHOD USING SOLID ELECTROLYTE. THE DECOMPOSITION VOLTAGE OF Al_2O_3 AND THE COMPOSITION OF THE ANODE GAS

BÁDER, I., BERECZ, E.*

(Received: 25 April 1988)

A method and a measuring system using ZrO_2 solid electrolyte have been developed and suggested by the authors for the measurement of the concentration of dissolved Al_2O_3 in the cryolitic melt of alumina electrolysis. The data obtained from the measurements and calculations made possible to calculate some thermodynamic functions (e.g. the free enthalpy of formation) of dissolved Al_2O_3, their dependence on the Al_2O_3-content of the cryolitic melt, as well as the concentration dependence of the primary anode gas on the anode potential.

1. Introduction

In the analytical and thermodynamic studies at high temperatures in general the unipolar ionic conductivity of solid electrolytes is used for the measurements. Recently, the solid electrolytes containing ZrO_2 and conducting by O^{2-}-ion has the most wide area of employing these ones, but the number of the different types of solid electrolytes, which are employed for the realization of other practical problems is increasing continuously.

The main advantage of the unipolar solid electrolytes from point of view of the utilization in the electrochemical measurement technics is the possibility of the application of new analytical and measuring technics both for the analytical and thermodynamic studies, when well defined electrical signs can be got from "in situ" measurements. The sensors consisting of solid electrolytes are especially important in those fields where the controlling of the technology requires much shorter time of analysis than the classical methods. Recently e.g. the automatic heating regulation based on the continuous measuring of the oxygen content of flue gases of furnaces, as well as the direct, eventually quasi-continuous measurement without sampling of the dissolved oxygen in high-temperature metallic melts are

Báder, I., H—3515 Miskolc-Egyetemváros, Hungary
Berecz, E., H—3515 Miskolc-Egyetemváros, Hungary

Akadémiai Kiadó, Budapest

practically solved, and promising results appeared for the determination of oxygen content and oxygen activity in nonmetallic melts, e.g. also in the circumstances of the cryolitic alumina electrolysis /1—3/.

The method gives a new way mainly for the thermodynamic studies because using solid electrolyte the possibility arises for the electrochemical — and in many instances more accurate — determination of the thermodynamic data measuring the cell potentional — in this case practically the electromotive force — instead of that of the earlier calorimetric method.

Nowadays, in general, the Hall-Héroult method is used for the aluminium production where the cryolitic melt of the alumina is electrolysed by means of C-anode. During the electrolysis the alumina content of the melt decreases, therefore it must be supplied. Although the quantity of the alumina going to the supply can be calculated from the mass of the Al forming in the process, but the conditions of electrolysis could become more effective, if a fast and reliable method were available for the "in situ" determination of the alumina.

The effort to decrease the specific energy consumption requires also the keeping of the Al_2O_3-concentration at an optimal level, because — on one hand — one of the components of the applied bath voltage is the decomposition potential of the dissolved Al_2O_3, and — on the other hand — some physico-chemical characteristics of the elctrolyte — e.g. the electrical conductivity, the liquidus temperature, the measure of the redissolution of the aluminium, the interfacial phenomena etc. — also depend on it strongly.

The fast determination of the alumina concentration and the knowledge of the concentration dependence of the decomposition potential are required also in the studies directed to the forming of more suitable electrodes than the actual (i.e. indifferent) ones.

As known, the decomposition voltage of the components depends also on their concentrations in the systems containing more than one or two several components. It follows directly from this fact that the deposition (electrode) potentials depend on the activity of the ions depositing on the electrodes.

In the case of the alumina electrolysis carried out in cryolitic melt between indifferent — e.g. Pt-electrodes the following series of equation can be written, which are simplified, but expressing well the nature of the process:

$$Al_2O_3(s) \overset{1}{\rightleftharpoons} Al_2O_3(sol) \overset{2}{\rightleftharpoons} 2Al^{3+} + 3O^{2-} \overset{3}{\rightleftharpoons} 2Al + 1.5\ O_2 \qquad (1)$$

This series of reactions expresses the decomposition of the solid Al_2O_3 into aluminium and oxygen through the part processes, dissolution and dissociation.

When at a constant temperature the system reaches the equilibrium state according to the series of reaction (1) the chemical potential of the Al_2O_3 dissolved in the cryolite becomes equal to that of pure solid Al_2O_3, and so, as a matter of course, its activity in the melt will also be equal to that of the pure solid Al_2O_3. At this moment the decomposition voltage can be expressed by the relation:

$$E_{(1)} = E^{\ominus}_{(1)} - \frac{RT}{6F} \ln \frac{a_{Al_2O_3(s)}}{a^2_{Al}\sqrt[3]{p_{O_2}}} = E^{\ominus}_{(1)} - \frac{RT}{6F} \ln \frac{a_{Al_2O_3(sol)}}{a^2_{Al}\sqrt[3]{p_{O_2}}} =$$

$$= E^{\ominus}_{(1)} - \frac{RT}{6F} \ln \frac{a^2_{Al^{3+}} \cdot a^3_{O^{2-}}}{a^2_{Al} \cdot \sqrt[3]{p_{O_2}}} \ , \qquad (2)$$

where the a-s denote the adequate (relative) activities (and $a^{\ominus}_i = 1$), $E^{\ominus}_1$ is the decomposition voltage in standard state at a given temperature-suitably in alumina/cryolite melt saturated with Al_2O_3 or in that containing 1 mass % Al_2O_3-measured in the presence of pure Al_2O_3 and oxygen, and P_{O_2} is the partial pressure of the oxygen in the gas (which can be used instead of the fugacity because of the small pressure values, and when $p^{\ominus} = 1$).

At constant temperature and pressure the lowest decomposition voltage can be measured in the melt saturated in Al_2O_3. In the melt non-saturated with Al_2O_3 the decomposition potential increases in proportion to the logarithm of the Al_2O_3 activity, resp. depending on the activity of Al^{3-} and O^{2}-ions.

Similar conclusion can be drawn for non-indifferent electrodes, e.g. C-electrodes. In this case the over-all process can be expressed by the following equations (3), (4) and (5):

$$Al_2O_3(s) \rightleftharpoons Al_2O_3 \text{ (dissolved)} \qquad (3)$$

and

$$Al_2O_3(\text{dissolved}) + 3C(s) \rightleftharpoons 2Al(l) + 3CO(g) \ , \qquad (4)$$

or

$$Al_2O_3(\text{dissolved}) + 1.5\ C(s) \rightleftharpoons 2Al(l) + 1.5\ CO_2(g) \ . \qquad (5)$$

For the solution of practical problems the equations

$$Al_2O_3(sol) + xC \rightleftharpoons 2Al(l) + (2x-3)CO + (3 - x)\,CO_2 \quad , \tag{6}$$

and

$$Al_2O_3(sol) + \frac{3}{1+y}\,C \rightleftharpoons 2Al(l) + \frac{3(1-y)}{1+y}\,CO + \frac{3y}{1+y}\,CO_2 \tag{7}$$

obtained by summarizing the equations (4) and (5) are more suitable. The inequality $1.5 < x < 3$ is valid for the equation (6). In equation (7) y means the stoichiometric coefficients, instead of the molar fraction of the CO_2 in the gas mixture.

It is clear that at high temperature, studying the equilibrium conditions of above reactions the Boudouard reaction

$$2CO(g) \rightleftharpoons C(s) + CO_2(g) \quad , \tag{8}$$

taking place in the anode chamber can not be neglected as well, because it considerably affect the composition of the primary forming anode gas.

Under the conditions identical with the above mentioned ones, i.e. that is on the basis of the equations (4) and (5) the decomposition potential of the Al_2O_3 can be expressed in the following manner:

$$E_{(4)} = E^{\ominus}_{(4)} - \frac{RT}{6F} \ln \frac{a_{Al_2O_3(sol)} \cdot a_C^3}{a_{Al}^2 \cdot p_{CO}^3} \quad ; \tag{9}$$

and

$$E_{(5)} = E^{\ominus}_{(5)} - \frac{RT}{6F} \ln \frac{a_{Al_2O_3(sol)} \sqrt{a_C^3}}{a_{Al}^2 \cdot \sqrt{p_{CO_2}^3}} \quad . \tag{10}$$

In the case of the reaction (9) and using similar principles the relation

$$E_{(7)} = E^{\ominus}_{(7)} - \frac{RT}{6F} \ln \frac{a_{Al_2O_3(sol)} \cdot (a_C)^{\frac{3}{1+y}}}{a_{Al}^2 \cdot (p_{CO_2})^{\frac{3y}{1+y}} (p_{CO})^{\frac{3(1-y)}{1+y}}} \tag{11}$$

will be valid for the decomposition potential.

The analysis of the above relations raises two principal questions, namely:

a) how the decomposition potential depends on the Al_2O_3-content of the electrolyte; and

b) what is the composition of the primary forming anode gas?

Let us study further these two problems in detail.

2. On the dependence of the decomposition potential on the Al_2O_3-content of the electrolyte melt

Summing up the research activity dating back more than half a century and directing to the determination of the decomposition voltage it becomes clear that the data published relate nearly exclusively to the decomposition voltage of the melt saturated with Al_2O_3 and being in equilibrium with the solid Al_2O_3. The reasons of this fact can be found in the following factors and experimental difficulties:

a) The knowledge of the concentration dependence of the activity of the dissolved Al_2O_3 is also needed for the calculation of the concentration dependence of the decomposition voltage, but these data are hardly available;

b) The ceramic material of the galvanic cell — mainly that of the reference electrodes — constructed for experimental purposes and used until now generally contained Al_2O_3, therefore accurate measurements could only be carried out in melt saturated with Al_2O_3.

The pioneers of the research works of this kind Drossbach /4/, Treadwell and Terebesi /5/, Baimakov and coworkers /6/, Mashovets and Revazian /7/, and lately Thonstad /8/, Vetiukov and Van Ban /9/, as well as Ghosh and Kay /10/ performed their measurements in such systems.

Rolin and Gallay /11/ were the first researchers who measured the cell potential depending on the dissolved Al_2O_3-content in the cryolitic melt in galvanic cells containing several metal oxides and a C-electrode. The experimental data of measurements performed by electrodes containing SnO_2 and Cr_2O_3 in cells with relatively complicated construction showed an unambiguous interconnection with the Al_2O_3-content dissolved in the melt.

Vetiukov and Van Ban applied BN ceramic material and determined the concentration dependence of the activity of Al_2O_3 in cryolitic melt between 980 and 1060 ^{o}C.

The use of solid electrolytes with good ionic conduction made possible a radically new measuring method for the thermodynamic study of

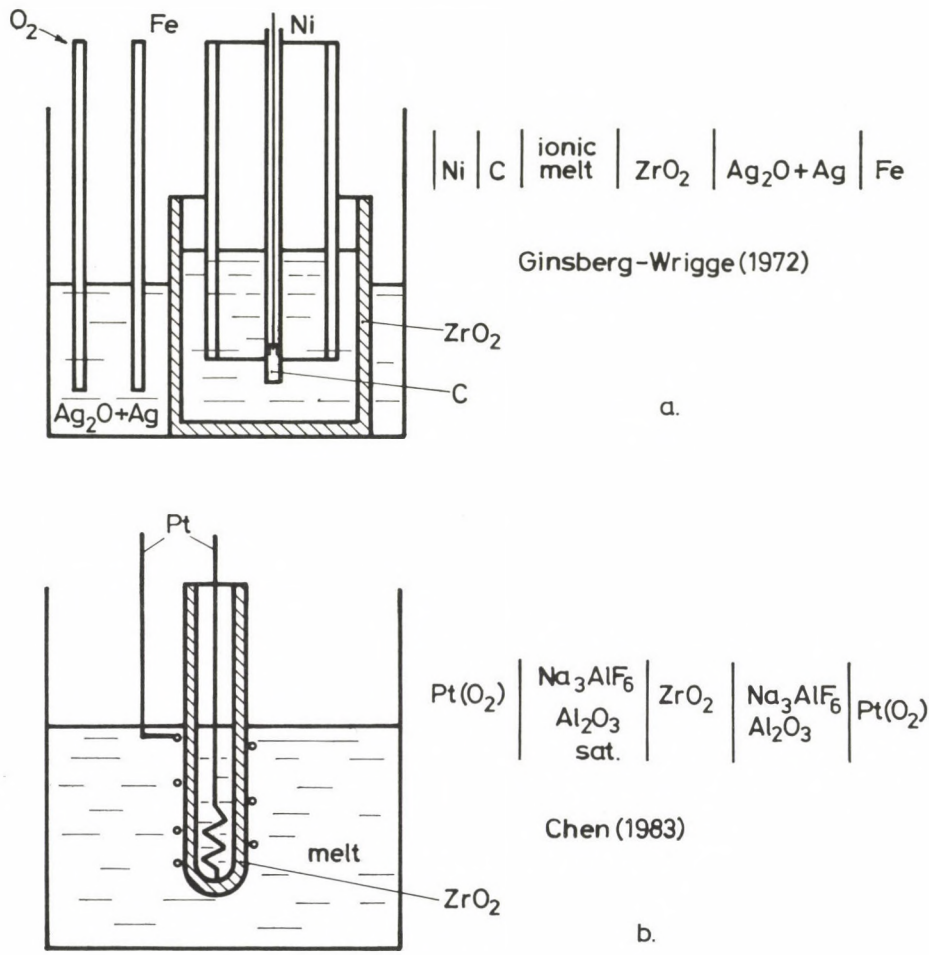

Fig. 1. Solid electrolyte galvanic cells: a) Ginsberg and Wrigge /12/; b) Chen /13/

the alumina-cryolite melt. The solid electrode based an ZrO_2 and conducting by oxyde ions was first used by Ginsberg and Wrigge /12/ for the separation of the anodic and cathodic spaces in the cell for electrolysis, as well as for the study of the cathode current efficiency (Fig. 1/a).

In the last years such galvanic cell constructions based also on the ionic oxygen conductivity of the solid electrolytes with ZrO_2 matrix were developed, where the reference electrode was enclosed in the tube itself formed from the solid electrolyte and the measuring electrode was either

Pt/O_2, or Mo/MoO_2, respectively Al/Al_2O_3 /1—3, 13/. The cell potential, resp. practically the E_{MF} in our case developing in such oxygen concentration cells can be expressed by the generalized Nernst-equation:

$$E_{MF} = -\frac{RT}{6F} \ln \frac{a_{Al_2O_3}\ (measuring)}{a_{Al_2O_3}\ (ref)} \qquad (12)$$

In Fig. 1/b the galvanic cell construction developed by Chen /13/ is shown, in which he measured the activity of the dissolved Al_2O_3 in the alumina-cryolite melt at 1020 ^{o}C chosen the $a^{\ominus} = 1$ value as standard state, where $a^{\ominus}$ is the activity of the melt saturated with the Al_2O_3.

Using this solution and improving it in a suitable way and using also the ZrO_2 solid electrolyte a procedure making possible several technical solutions was developed by the authors for the measurements of the Al_2O_3-content of the cryolitic melt /1—3/. As it is shown in Fig. 2, reference electrodes were prepared in the inner part of the ZrO_2 (stabilized with CaO) closed at one end so that in the tube either a mixture of powder of

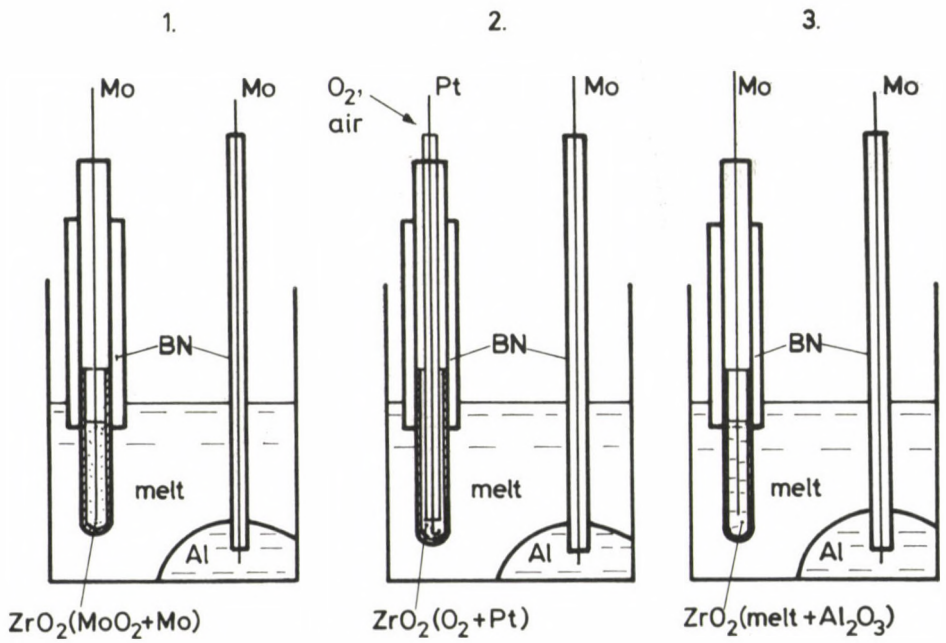

Fig. 2. The experimental galvanic cells used by authors

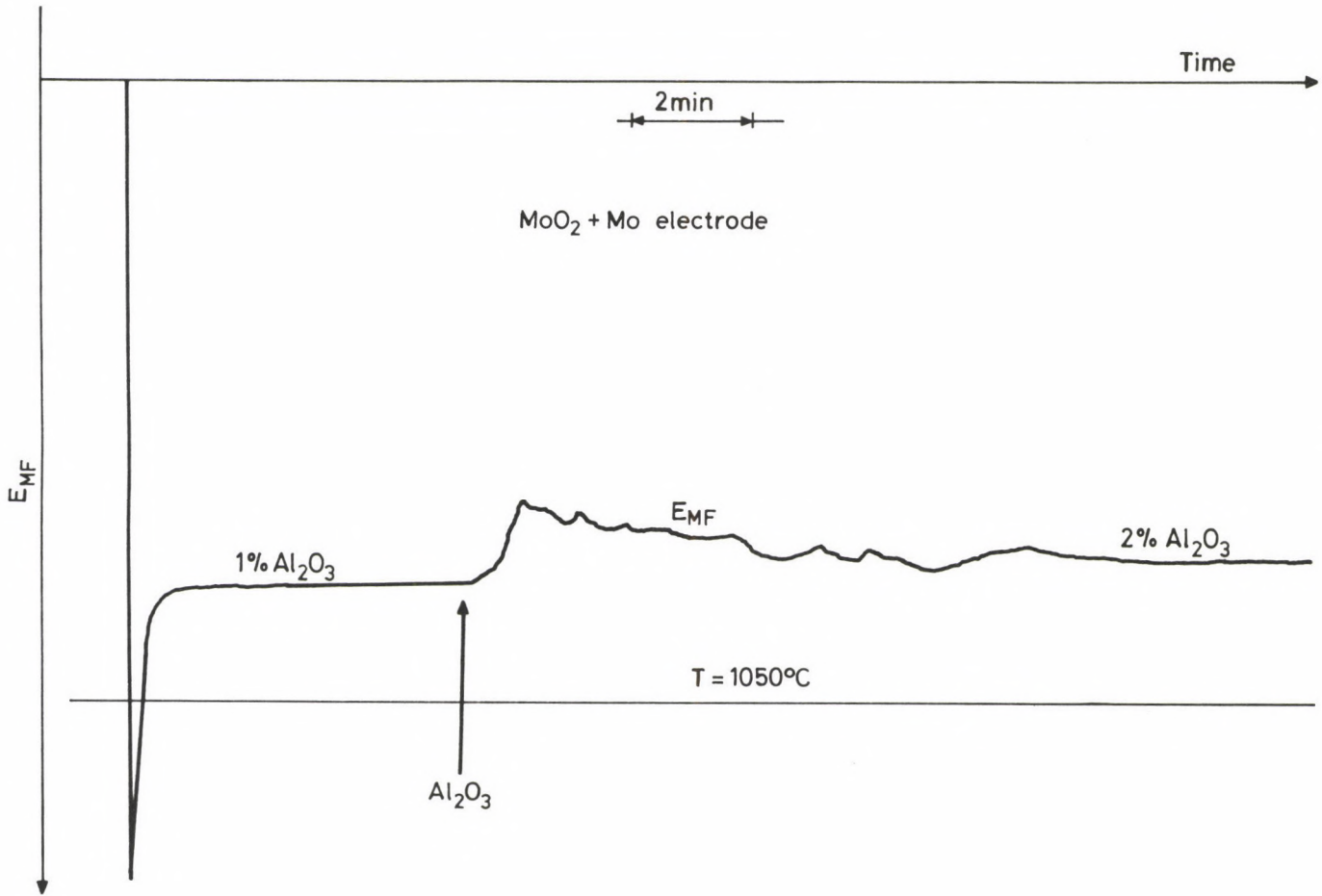

Fig. 3. The change in time of the EMF and the temperature in the course of the experiments

of Mo and MoO_2, or oxygen or air, respectively, or — as an essential development —, a cryolitic melt containing 1 mass % Al_2O_3 dissolved in the melt were.

According to the above solutions the cell diagrams of each galvanic cells can be given as follows:

$$Mo(s) \mid MoO_2(s) \mid ZrO_2(s) \mid \begin{matrix} Na_3AlF_6(melt) \\ Al_2O_3 \end{matrix} \mid Al(melt) \mid Mo(s), \qquad (13)$$

$$Pt(s) \mid O_2(g) \mid ZrO_2(s) \mid \begin{matrix} Na_3AlF_6(melt) \\ Al_2O_3 \end{matrix} \mid Al(melt) \mid Mo(s), \qquad (14)$$

$$Mo(s) \mid Al(melt) \mid \begin{matrix} Na_3AlF_6 \ (melt) \\ 1\%\ Al_2O_3 \end{matrix} \mid ZrO_2(s) \mid \begin{matrix} Na_3AlF_6(melt) \\ Al_2O_3 \end{matrix} \mid Al(melt) \mid Mo(s) \qquad (15)$$

Systematic experiments were carried out by authors for the determination of the concentration dependence of the Al_2O_3 activity of the cryolitic melt. Using anal. puriss. materials alumina-cryolite mixture containing 1% Al_2O_3 was prepared, then it was melted in a BN crucible and kept at $1050 \pm 3\ ^{0}C$ during the experiment. After melting, the suitable reference electrode prepared also in own laboratory was immerged into the melt and the cell potential and the temperature were measured and recorded by means of a two-channel Philips PM 8222 recorder. The life-time of the reference electrodes developed in the inner part of the ZrO_2 tube was about half an hour at the temperature of the measurement. In time-interval the Al_2O_3-content was increased by adding gradually Al_2O_3 powder into the melt until saturation.

3. Discussion of experimental results

As an example Fig. 3 represents the change in the function of time of the measured and recorded values for the case of the increase of the Al_2O_3-content from 1 mass percent to 2 mass percent using Mo + MoO_2 reference electrode.

Similar experiments were also performed using alumina-cryolite reference electrode containing 1 mass percent Al_2O_3, and we convinced of the working ability of the air reference electrode as well.

Table 1 Measured E_{MF}-s at 1050 °C, mV

Al_2O_3 mass%	Reference electrodes	
	MoO_2 + Mo	alumina-cryolite containing Al_2O_3 1%
1	1365	0
2	1340	25
3	1321	43
4	1308	59
5	1295	70
6	1285	82
7	1277	91
8	1270	98
9	1264	103
10	1260	107
12	1253	113
14	1249	116
sat. 16.5	1247	119

Table 1 represents the experimental data for 1050 °C in the cases of Mo + MoO_2, alumina-cryolite melt containing 1% Al_2O_3 reference electrodes.

After analysing the experimental data it can be concluded that the experiments performed by both reference electrodes gave nearly the same results for the difference of cell potential measured in the alumina-cryolite melt containing 1% Al_2O_3 and in that saturated with Al_2O_3. The difference was 120 mV, which is in good agreement with the 117 mV obtained by Chen /13/ at 1020 °C.

The above mentioned experimental results — in contrary of the measurements until now giving results for the solid Al_2O_3 — can give a possibility to calculate the free enthalpy of formation and — in the knowledge of this value — the decomposition potential of Al_2O_3 dissolved in the melt in the case of its different concentrations.

For the free enthalpy of formation of the solid Al_2O_3 and MoO_2 on the basis of analysis of data of JANAF Thermochemical Tables /14/ the following functions.

$$\Delta G^{\ominus}_{Al_2O_3}(s) = -1690.710 + 0.3291\ T;\ (kJ.mol^{-1}) \tag{16}$$

$$\Delta G^{\ominus}_{MoO_2}(s) = -574.626 + 0.1655\ T;\ (kJ.mol^{-1}) \tag{17}$$

were used from which the free nethalpies of formation are the following:

$$\Delta G^{\ominus}_{Al_2O_3}(s,\ 1050\ ^{o}C) = -\ 1255.31\ kJ.mol^{-1}$$

and

$$\Delta G^{\ominus}_{MoO_2}(s,\ 1050\ ^{o}C) = -\ 533.50\ kJ.mol^{-1}\ .$$

Using the above data and the relation

$$\Delta G = \Delta G^{\ominus}_{1\%} + RT\ \ln \frac{a_{\%}}{a_{1\%}} = -\ 6FE_{MF}\ , \qquad (18)$$

as well as on the basis of the experiments performed in the cryolitic melt containing 1% Al_2O_3 we could calculate the difference of standard free enthalpies of formation (from its elements) of the Al_2O_3 dissolved in the alumina-cryolite melt containing 1 mass % Al_2O_3, then the activity of the Al_2O_3 in the melt with different composition, the activity coefficients referring to the composition expressed in mass %, as well as the decomposition potential of the Al_2O_3 dissolved in the alumina-cryolite melt. The calculated data are given in Table 2.

Table 2 Calculated thermodynamic data

Al_2O_3 mass %	E^{1323}_{decomp} V	ΔG_{1323} kJ.mol^{-1}	$a_{\%}$	$\gamma_{\%}$
1	2.286	1323.4	1	1
2	2.261	1308.9	3.73	1.86
3	2.241	1297.4	9.61	3.20
4	2.229	1290.4	22.3	5.57
5	2.216	1282.9	39.8	8.0
6	2.206	1277.1	74.9	12.5
7	2.198	1272.5	120.2	17.2
8	2.191	1268.4	173.8	21.7
9	2.185	1264.9	226	25.1
10	2.181	1262.6	279	27.9
12	2.174	1258.6	383	31.9
14	2.170	1256.3	448	32.0
sat. 16.5	2.168	1255.1	525	31.8

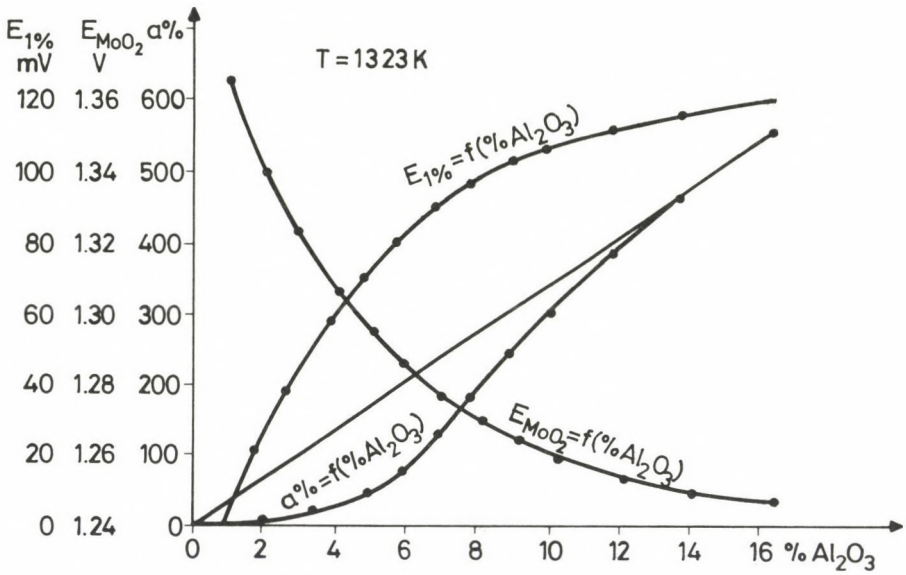

Fig. 4. The dependence of the E_{MF} and the activity of the Al_2O_3 on the Al_2O_3-content of the melt

The composition dependence of the cell potentials measured at 1050°C and the calculated activity data are represented in Fig. 4.

The shape of the activity curve shows that the alumina-cryolite melt system represents a very negative deviation from the ideal behaviour. This must obviously be connected to the chemical reactions taking place in the fused state, which refer to the very large interconnections between Al_2O_3 and cryolite. It supports also in this way the results obtained earlier by other researchers who used different research methods and supposed the presence of a lot of complex ions containing Al, O and F in different compositions, i.e. AlF_4^-, $AlOF_4^{3-}$, $Al_2O_2F_4^{2-}$, etc.

4. The anode potential dependence of the composition of anode gas

During the alumina electrolysis one of the components of the electrolysing voltage is the decomposition potential. The decomposition potential and through it the specific electric energy consumption can be lowered by carrying out the electrolysis with carbon anodes instead of in different electrodes. According to this fact the oxyde ions lose their charges, react with the anodes, so, the anode is consuming, as it follows from the over all reactions (4) and (5).

Therefore one of the important working characteristics of the electrolysis is the specific anode consumption, which — on the basis of the two given equations — is a value falling into the interval 330—660 kg/t Al depending on the consumption of the anode gas forming primarily.

From the point of view of the effort to achieve a specific anode consumption as low as possible it is very important to study the factors influencing the composition of the anode gas.

From the relations it is absolutely clear that we can reach a more economical anode consumption when the ratio of process (5) is higher and the process (8) shifts towards the right hand side to the largest extent. If the reaction between C and O_2 were influenced by the equilibrium conditions of the (8) Boudouard reaction — taking into consideration that the temperature equals to 950—1000 ^{o}C — the anode gas would be practically pure CO. But it is well known in practice that 50—80 % of the anode gas is CO_2! It can be concluded from this fact, that the composition of the anode gas is obviously determined not only by the equilibrium of the Boudouard-reaction. Moreover, the experiments of Ginsberg and Wrigge /12/ gave evidence that the composition of the anode gas forming primarily during the electrolysis contains practically 100% CO_2 and this CO_2 can only be transformed into CO in the way of a secondary reaction, i.e. only in a non-electrochemical process.

If we study from electrochemical point of view the process between the C anode and the O_2 developing there it can be determined as a function of the anode potential, in which measure the composition of the gas will be shifted compared to the equilibrium data predicted by the Boudouard-reaction. Starting from the fact that the C will be oxidized in the process (8) in an electrochemical process the compositions will be determined not only by the chemical potentials, but by the electrochemical ones as well.

The equilibrium conditions of the (8) Boudouard-reaction under the electrolysing voltage (polarisation) can be determined on the basis of the relation.

$$\Delta G = \Delta G^{\ominus} + RT\ln I = 2F\Delta E \qquad (19)$$

where I expresses the quotient of the given momentary compositions (in volume percents of in mole fractions):

$$I = \frac{y_{CO_2}}{y_{CO}^2} = \frac{\%CO_2}{(\%CO)^2} = \frac{y_{CO_2}}{(1-y_{CO_2})^2} = \frac{\%\ CO_2}{(100-\%\ CO_2)^2}\ , \qquad (20)$$

and ΔE denotes the difference between the decomposition and the electrolysing voltage (i.e. the polarisation potential).

The CO_2-percentage can be expressed after replacing (20) into (19), in this way the CO_2 content of the primary anode gas can be calculated.

For the calculations the JANAF thermochemical data /14/ were also used, from which we could determine the standard free enthalpy of the reaction (8) at different temperature. The data obtained are represented in Table 3.

Table 3. ΔG_T^o-values of the reaction: $2CO \rightleftharpoons CO_2 + C$

Temperature K	ΔG_T^o , kJ
1000	4.563
1100	22.043
1200	39.420
1300	50.724
1400	73.933
1500	91.062

For further calculations ΔE was chosen as a parameter between 0 and 1 V and the mixed quadratic equation obtained for the CO_2 percentage was solved.

Figure 5 represents the CO_2 content of the anode gas forming primarily as a function of the temperature in the case of different constant values of the polarisation potential chosen as a parameter.

It can also be seen from Fig. 5 that in the case of electrolysis performed under working conditions (at 950—1000 ^oC) the primary anode gas must be pure CO_2. But in practice there is only 50—80 percent of CO_2, in this gas. This difference is the consequence of the fact that CO_2 will be reduced after forming by the reaction (8) increasing the undesirable consumption of the anode.

This secondary reaction is enhanced by the not adequate solidity and strength of the anode, by the long retention time of the gases under the anode, and at last but not least the higher working temperature.

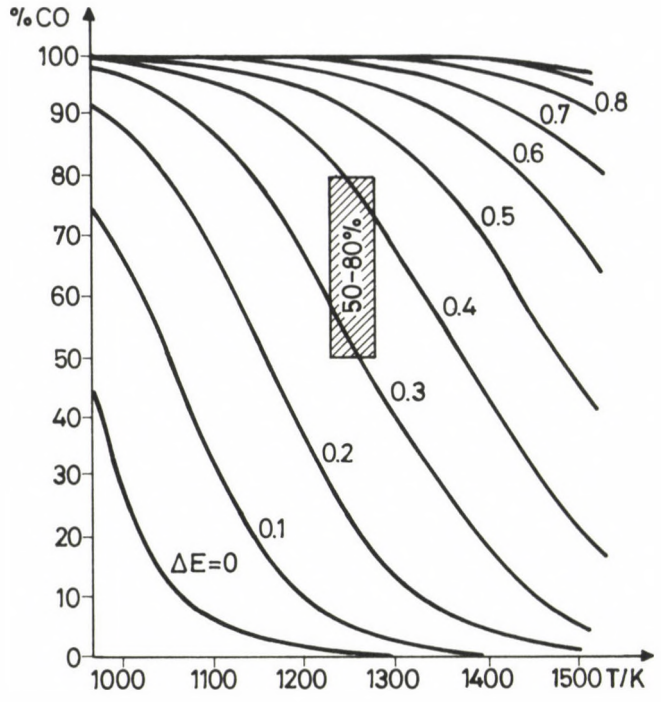

Fig. 5. The dependence of the CO_2-content of anode gas on the temperature in case of various polarization potentials

REFERENCES

1. Báder, I.-Berecz, E.: BKL Kohászat. **119**, 1986, 127–31.
2. Báder, I.-Berecz, E.: Publ. Techn. Univ. Heavy Ind. (Miskolc), Ser. Metallurgy. **37** (1) 1987, 21–33.
3. Báder, I.-Berecz, E.-Szina, G.-Horváth, J.: USA Pat. 4 639 304 (1984); Hung. Pat. 191 839 (1987). Can. Pat. 1 230 923 (1987).
4. Drossbach, P.: Z. Electrochem. **40**, 1934, 605–608.
5. Treadwell, W.D.-Terebesi, L.: Helv. Chim. Acta. **16**, 1933, 922–934; Z. Electrochemie. **40**, 1934, 744.
6. Baimakov, J.V.-Mashovets, V.P.-Kilj, I.G.: Legkie Metalli. **1**, 1937, 22.
7. Mashovets, V.P.-Revazian, A.A.: J. Prikl. Khimii. (1957), 1006–1012.
8. Thonstad, J.: Electrochim. Acta. **13**, 1986, 449–489.
9. Vetiukov, M.-Van Ban, N.: Tsvetnye Metally. **44**, 1971, 31–33.
10. Ghosh, G.-Kay, D.A.R.: J. Electrochem. Soc. **124**, 1977, 1836–45.

11. Rolin, M.-Gallay, J.: Bull. Soc. Chim. France. (1960) 2043—96, 2096—2100, 2101—2104.

12. Ginsberg, H.-Wrigge,H.Ch.: Metall. **26**, 1972, 997—1007.

13. Chen, S.: Dongbei Congxueyuan Xuebao **37**, 1983, 37—44.

14. JANAF Thermochemical Tables. 2nd ed. U.S.Dep. of Commerce. Nat. Bur. Stand., Washington (1971).

Acta Technica Acad.Sci.Hung., 101(2), pp. 129—141 (1988)

REGENERATION OF HYDROCHLORIC ACID IN CHLORIDE-HYDROMETALLURGY BY ANION EXCHANGE PROCESS

CSŐVÁRI, M. - CZEGLÉDI, B. - STOCKER, L. - ERDÉLYI, M. - EGRY, R. - TÜNDÖK, S. - HORVÁTH, A.*

(Received: 25 April 1988)

Regeneration of hydrochloric acid in chloride-hydrometallurgical processes is usually carried out by using pyrolytic decomposition of the concentrated solutions of the chlorides obtained. If the chloride-hydrometallurgical process includes anion exchange process it is possible to regain the main part of the hydrochloric acid spent by treatment of anion exchange resin with sulphuric acid. In the paper some experimental results are given dealing with the producing of hydrochloric acid by anion exchange process. It has been proved that hydrochloric acid solution with low sulphate concentration (<1 g/dm^3) can be produced by column technics. It has also been established that the sulphuric acid bound on anion exchanger in form of hydrosulphate ions can be partially removed by treating ion exchanger with water. The sulphuric acid solution obtained during this process can be reused and thus the overall specific consumption of sulphuric acid is at the level of 1.4—1.5 kg/kg HCl. The developed technology has been used for many years at Mecsek Ore Mining Enterprise.

LEGENDS

R-H	cation exchange resin in hydrogen-form
R-Cl	anion exchange resin in chloride-form
V_r	flowrate of resin, m/h
V_s	flowrate of solution, m/h
τ	retention time
r	resin (in index)
s	solution (in index)

*Csővári, M., H—7635 Pécs, Csortos Gy. u. 16/c, Hungary
Czeglédi, B., H—7633 Pécs, Ybl M. u. 7/3, Hungary
Stocker, L., H—7633 Pécs, Dandár u. 7/b, Hungary
Erdélyi, M., H—7634 Pécs, Ércbányász u. 36, Hungary
Egry, R., H—7632 Pécs, Hajas I. u. 2, Hungary
Tündök, S., H—7633 Pécs, Dandár u. 1/a, Hungary
Horváth, A., H—7633 Pécs, Bihari J. u. 5/b, Hungary

Akadémiai Kiadó, Budapest

Introduction

It is known that in chloride-hydrometallurgy pyrolytic decomposition of concentrated solutions of chlorides obtained during the process is widely used on industrial-scale for regeneration of hydrochloric acid /1, 2, 3, 4/. However, if dilute solutions are obtained, this method is rather expensive because of preliminary concentration of solution. Nevertheless, it is possible to regain the main part of hydrochloric acid spent if the chloride-hydrometallurgical process includes anion exchange step. Investigations, presented in this paper, are connected with the producing of dilute hydrochloric acid by anion exchanger, aiming at its regeneration and as a result at decreasing the wastes and making such processes more economical.

First of all it should be mentioned that hydrochloric acid is synthetized generally using H_2 and Cl_2 gases. However, hydrochloric acid can be produced by other methods, too. Thus, Osborn /5/ has described an original method in which cation exchange resin is used. Basic equations of the process are:

$$R - H + NaCl = R - Na + HCl \quad (1)$$

$$R - Na + H_2SO_4 = R - H + NaHSO_4 \quad (2)$$

In this process for 1 mol HCl 1 mol H_2SO_4 is needed. Our investigations have aimed at using anion exchanger instead of cation exchanger for producing dilute hydrochloric acid suitable for technological purposes.

Process, based on using anion exchange resin in some cases has great advantage over the process using cation exchanger. This is the situation e.g. when in the basic ion exchange technology anion exchange resin is used for the sorption of metal species and a dilute hydrochloric acid solution is used in elution step. In such cases anion exchanger in chloride-form is obtained and at the end of the process chloride-containing waste solutions are formed, too. Obviously, it would be expedient to produce the hydrochloric acid to be used in elution step from the chloride-containing products of the main process. In this case large part of the chloride can be circulated in the system and in this way a considerable amount of concentrated hydrochlorid acid can be saved.

According to this philosophy a method has been developed for the producing of hydrochloric acid solution using anion exchanger in chloride-

form and solution of sulphuric acid. The method has been used for years in large scale in Hungary in milling uranium ores.

Some data of the developed process have been described in our previous paper /6/. In present paper some further experimental results are presented first of all concerning the continuous counter-current tests carried out in columns of pilot-scale.

Experimental results

In all experiences Hungarian-made anion exchange resin, type Varion AP, was used. The continuous counter-current tests were performed in a column of 7 m height and 0.2 m diameter. The ion exchanger in appropriate form was fed on the top of the column and the liquid phase was added on the bottom of it. The solution and the ion exchanger were removed from the column continuously or quasi continuously. The tests were carried out at temperature 25 $\pm$ 2 ^{o}C.

1. Process of producing hydrochloric acid

Process is based on the following reaction:

$$R - Cl + H_2SO_4 \rightleftharpoons R - HSO_4 + HCl \qquad (3)$$

i.e. on the treatment of anion exchanger in chloride-form by sulphuric acid solution.

From the practical point of view it is very important to know whether it is possible to obtain in this way hydrochloric acid solution with low sulphate concentration, because the sulphate in solution can disturb the use of the hydrochloric acid solution obtained. To determine the efficiency of conversation of chloride to hydrochloric acid and the sulphate content of produced hydrochloric acid solutions experiments using continuous counter-current technics were performed.

Tests were carried out using sulphuric acid solutions of different concentrations. After achieving the equilibrium, solutions were taken from different height of the column and analysed for HCl and H_2SO_4. The results obtained are summarized in Table 1.

The data show that in counter-current process product solutions with very low sulphate concentration are obtained. The concentration of hydro-

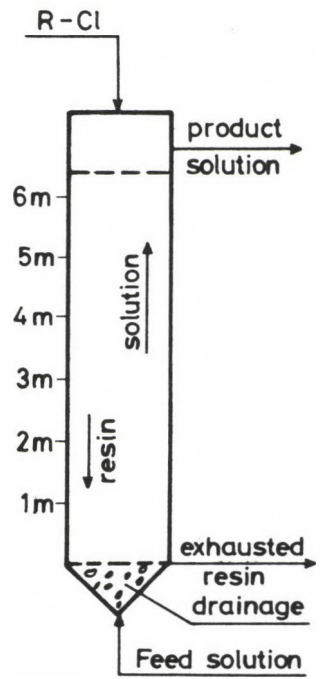

Table 1 Experimental data

Solution or ion exchanger		Concentration, mol/dm^3					
		HCl	H_2SO_4	HCl	H_2SO_4	HCl	H_2SO_4
Product solution		1.01	0.03	0.86	0.01	0.55	0.005
Solution in column	6	0.99	0.05	0.86	0.01	0.55	0.01
	5	0.93	0.09	0.86	0.02	0.53	0.02
	4	0.82	0.20	0.85	0.03	0.50	0.03
	3	0.59	0.42	0.77	0.11	0.40	0.13
	2	0.34	0.66	0.57	0.33	0.25	0.28
	1	0.11	0.91	0.32	0.58	0.16	0.38
Exhausted resin*		0.03	1.36	0.05	1.30	0.10	1.25
Feed solution (H_2SO_4)		0.00	1.02	0.00	0.87	0.00	0.50

*Data are presented as Cl and SO_4 concentration on the ion exchanger

chloric acid in solution is almost the same (in mol/dm^3) as that of the sulphuric acid fed in the column. This fact verifies that the main process can be described by the equation (3), and the reaction:

$$2R - Cl + H_2SO_4 \rightleftharpoons R_2SO_4 + 2HCl \qquad (4)$$

takes place only in negligible degree especially when the concentration of sulphuric acid is high (1 mol/dm^3). As the concentration of sulphate in product solution is low, the solution is suitable for technological purposes, for instance in elution step of milling uranium ores.

On Figure 1 chloride- and sulphate-front profiles are shown. The data have been obtained by examining an industrial-scale operating column. The presented data show that the most part of the ion exchanger in column is in chloride-form which ensures the very low concentration of sulphate (< 1 g/dm^3) in product solution. Comparing the results presented in Table 1 and Figure 1 a conclusion can be drawn that the "wall-effect" in an industrial-scale column is lower than that of a pilot-scale one and as a result the fronts of ion-profiles are sharper in industrial-scale column.

2. Process of removing sulphuric acid, sorbed on anion exchanger

From the equation (3) and the results presented in Table 1 it is evident that the exhausted resin contains first of all hydrosulphate ions.

From the economic point of view it is an important question whether certain part of the HSO_4^- can be dissociated according to equation:

$$2R - HSO_4 \xrightarrow{water} R_2SO_4 + H_2SO_4 \qquad (5)$$

i.e. whether some quantity of the sulphuric acid spent in process (3) can be removed and in this way the specific consumption of sulphuric acid can be reduced. On Fig. 1 a characteristic elution curve is presented when anion exchange resin obtained in previous experiments was eluted by destilled water. The data of Tables show that the concentration of sulphuric acid in solution obtained can reach the value of 0.4 mol/dm^3.

Continuous counter-current experiments were also performed in a column similar to the previously described. The experimental results are listed in Table 2.

Using different quantities of water for treating, solutions of

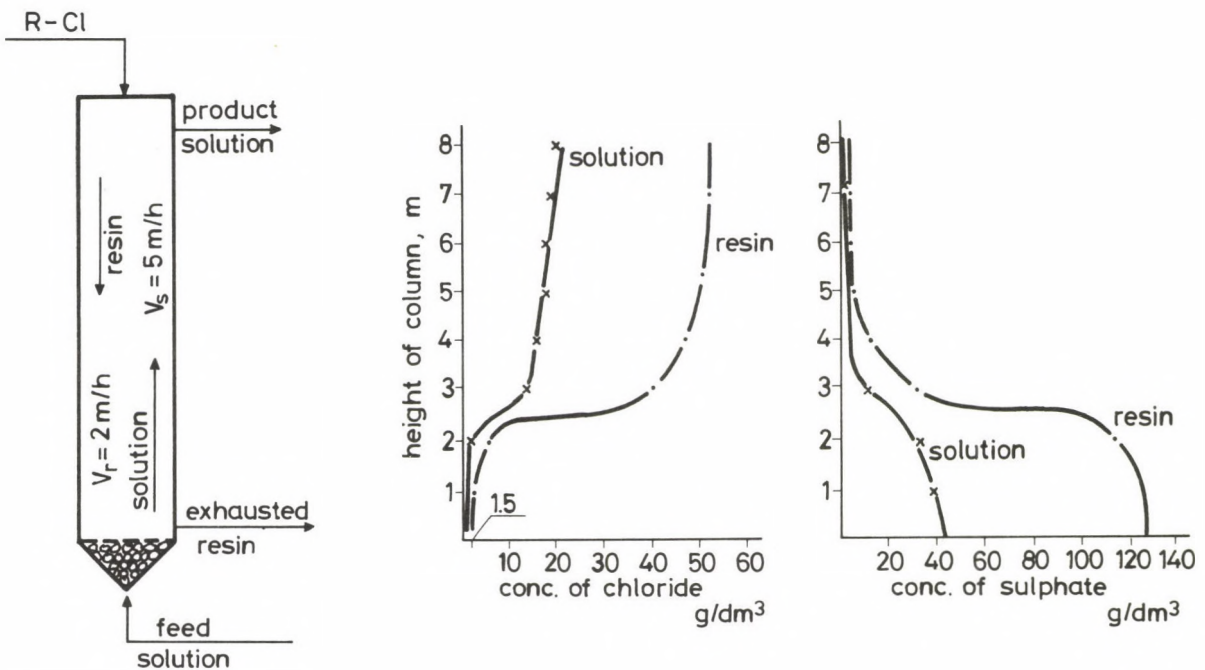

Fig. 1. Chloride and sulphate front profile in operating industrial-scale column

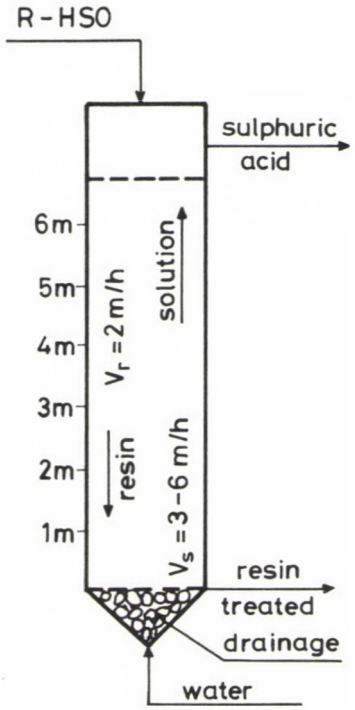

Table 2 Experimental results of removal of sulphuric acid in counter-current process

Volume of water W_w/V_r	Concentration, g/dm^3					
	Ion exch. fed in		Ion exch. treated			Sulphuric acid sol.
	Cl	HSO_4	Cl	HSO_4	ΣSO_4	H_2SO_4
1.5	5.5	118	3.3	32	76	27
2	5.5	118	3.0	28	72	23
3	5.5	118	2.8	23	70	16

τ_r = 1.5 h

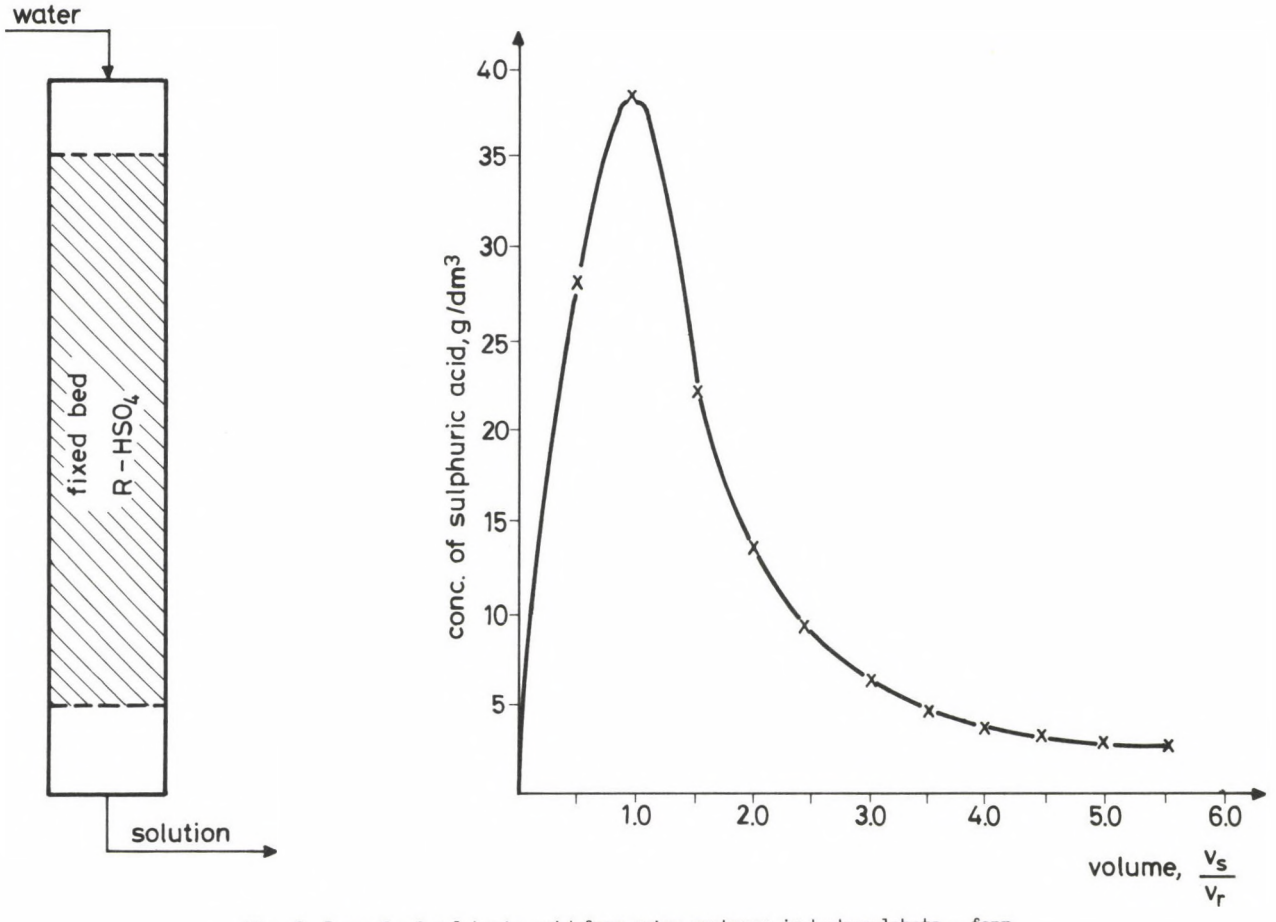

Fig. 2. Removal of sulphuric acid from anion exchange in hydrosulphate - form

sulphuric acid of different concentration were obtained in range 27—16 g/dm^3. At the ratio $V_{resin} : V_{water} = 1:3$ the treated resin contains only about 23 g/dm^3 hydrosulphate ions. So, from practical point of view, in real conditions most part of the hydrosulphate ions bound on anion exchanger can be dissociated and a sulphuric acid solution is obtained which can be reused (after adding appropriate amount of sulphuric acid) in process (3).

3. Fields of use of dilute hydrochloric acid obtained

As previously shown dilute hydrochloric acid can be obtained by anion exchange process. It should be mentioned that such a process is worth to be organized when in a plant dilute hydrochloric acid is needed for some purposes: this is the case for example in uranium mills where dissolved uranium is sorbed by anion exchange resin and hydrochloric acid solution is used for elution of loaded resin. In this case dilute hydrochloric acid producible in the elution system itself can be reused instead of preparing diluted acid from concentrated one and as a matter of fact operation of such an installation is highly advantageous both from economic and environmental point of view.

To produce dilute hydrochloric acid in uranium mill where chloride-containing solution is used for elution of uranium is a rather simple problem: for this only one column is needed with appropriated vessels in which chloride-hydrosulphate exchange process takes place in counter-current operation mode: anion exchange resin in chloride form obtained during the elution of uranium is treated in the installed column with dilute sulphuric acid and as a result of process (3) dilute hydrochloric acid is formed.

To show the reasonability of the above mentioned technology, two principal technological schemes are presented. To be more understandable the whole ion exchange circuit, i.e. sorption and elution of uranium, is given below.

Conventional scheme

The sorption system generally consists of 4—8 series-connected reactors in which anion exchange resin and solution or pulp are mixed and uranium is sorbed on the resin during the counter-current process, then the loaded resin is eluted by solution of appropriate composition.

The principal scheme of such an ion exchange circuit is presented on Fig. 3.

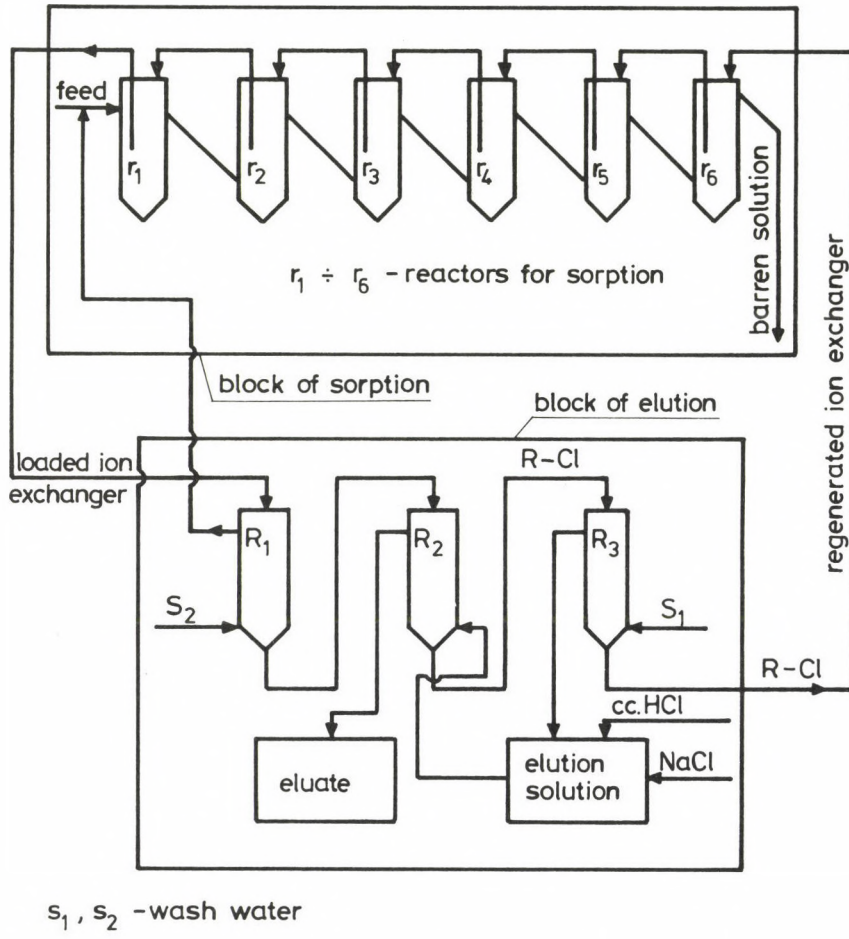

Fig. 3. Principal scheme of sorption and elution in processing uranium ores

The sorption system in this particular case is made of 6 reactors. The regenerated resin is fed into the r_6 reactor and the loaded resin is removed from r_1 reactor. Feed solution or pulp is led to r_1 reactor and leaves the sorption system from r_6 reactor. The loaded resin is put in the elution system which mainly consists of some columns (reactors r_1, r_2,...) operating in counter-current mode. The loaded resin in reactor r_1 is washed by water or in some cases by solutions of suitable composition (dilute hydrochloric or sulphuric acid solution, etc.) for removing solids (particles of sand, clay, etc.) and for desorbing some impurities. The solution obtained during this process is usually fed back to the sorption system as it contains

some amount of uranium. The pretreated resin is added to the elution column r_2, where the uranium is eluted by eluent prepared from concentrated hydrochloric acid and sodium chloride. Usually the hydrochloric acid content of the eluent is at the range of 10—20 g/dm^3, the sodium chloride content is on the level of 30—40 g/dm^3.

The eluted resin is fed into column r_3 for washing, then is led back to the sorption system in reactor r_6.

Improved scheme with producing dilute hydrochloric acid

As it was just mentioned in the conventional scheme hydrochloric acid needed is obtained by dilution of concentrated one. By installation of a further column in the elution system a great part of hydrochloric acid can be obtained to be used for elution.

The proposed principal scheme of such a technology is shown on Fig. 4.

The sorption system of the recovery of the dissolved uranium is the same as previously described, but the elution system is extended with one column r_4, in which the anion exchange resin is treated by sulphuric acid solution in counter-current operation mode, and an appropriate storing tank for preparing sulphuric acid solution. It is evident that in such a system from every m^3 resin about 45 kg HCl can be obtained taking into account the chloride capacity of the resin. In some cases this amount of hydrochloric acid is enough for elution, in the other ones some more acid is needed.

It should be emphasized that in this case the efficiency of the elution of uranium is much higher, because using the proposed tehcnology, the column r_4 is operated not only as a hydrochloric acid "producer", but as an elution column, too.

To illustrate the advantage of the producing of dilute hydrochloric acid as a by-product in uranium mill, some results of an industrial-scale installation — which has been operating for years in the uranium mill of Mecsek Ore Mining Enterprise — are summarized.

The total consumption of sulphuric acid for the producing of 1 t HCl is about 1.4 t. The efficiency of removing chloride from the resin in column r_4 is above 95%.

The sulphate concentration is less than 1 g/dm^3 in the hydrochloric acid obtained. As a consequence of circulation of the great part of the chloride ions in the elution system itself, the solutions on the tailing

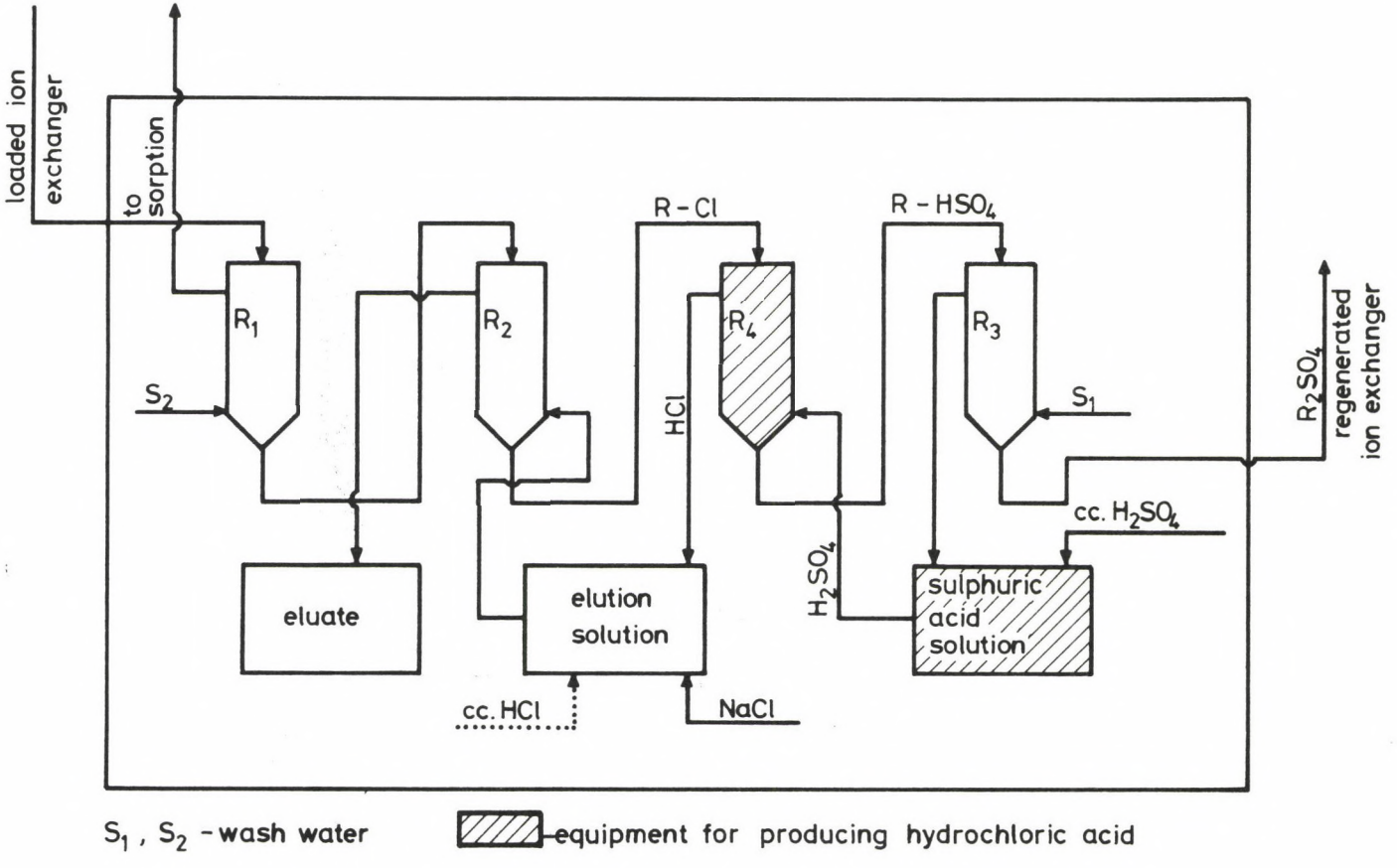

Fig. 4. Principal scheme of elution with producing hydrochloric acid

pound are much less contaminated by chloride than before the regaining of chloride in form of hydrochloric acid from the regenerated anion exchange resin. Efficiency of the elution of uranium has increased, i.e. uranium content remained in the anion exchanger and circulated back to the sorption system has significantly decreased. The price of hydrochloric acid obtained at the installed system is only about 50% of the price of concentrated acid.

Summarizing our experience it should be underlined that the technology has proved perfectly reliable and highly economical.

REFERENCES

1. Jedlicka, H.: New Applications of the Spray Process in the Chloride Hydrometallurgy. Series of technical reports on developments and processes. ANDRITZ, Ruthner Division, Wien.

2. Bierbach, H. — Hohmann, K.: Umweltfreundliches Verfahren für die kontinuierliche Regenerierung salzsäurer Beizbäder und anderer Metallchloride. Lurgi Schnellinformation. Frankfurt am Main.

3. Köhler, J.: Salzsäure-Regeneration umweltfreundlich bei hoher Leistung. Keram Chemia, Siershahn.

4. Stocker, L. — Czeglédi, B. — Riederauer, Sz.: Chlormetallurgie in der Buntmetallverhüttung. Bányászati és Kohászati Lapok Kohászat, vol. 120. No. 2 (1987), p. 87.

5. Osborn, G.H.: Synthetic ion exchangers. Moscow, 1964. p. 199. Mir. Izd.

6. Csővári, M. — Czeglédi, B. — Csukás, B. — Szomolányi, I.: Use of chloride-containing hydrometallurgical waste-waters for production of dilute hydrochloric acid. Env. Prot. Eng., Vol. 8 (1982) No. 1—4, 87—92.

Acta Technica Acad.Sci.Hung., 101(2), pp. 143—153 (1988)

DETERMINATION OF COKE-NATURAL GAS SUBSTITUTION RATIO IN BLAST FURNACES

FARKAS, O.*

(Received: 17 May 1988)

The mathematical formula for determination of coke-natural gas substitution ratio under different operating conditions in blast furnaces is presented in this work. The theoretical basis for the formula includes analysis of the enthalpy conditions changing in the course of partial oxidation of natural gas and coke carbon and reduction of the gas products as well as the relationships thereof. The H_2-balance is presented, and the mathematical model suited to determine the amount of H_2 contributing to reduction of FeO that is to calculate H_2 utilization is outlined in detail. Simplified calculations are given for actual determination of the coke-natural gas substitution ratio.

1. Introduction

Because of the difference in price between coke and natural gas in favour of natural gas as well as the favourable metallurgical effect of hydrogen resulting from natural gas, natural gas blast is preferred in our blast furnaces as far as possible.

Of course, the economic efficiency of utilization of natural gas depends on the efficiency of contribution of hydrogen, liberated from natural gas, to reduction that is the higher the coke-natural gas substitution ratio the higher the economic efficiency. Unfortunately, this ratio lies only exceptionally above 0.9 at present. That means that 1 m^3 of natural gas of a heat value of 35 000 kJ cannot replace 1 kg of coke of a heat value of 27 000 kJ/kg.

It follows from what has been said that optimization of natural gas blast both quantitatively and technically as well as the development of a mathematical model to determine the coke-natural gas substitution ratio for given conditions of reduction are important research problems. Of course, the mathematical model not only offers the possibility of calculation of the substitution ratio but at the same time it describes the basic parameters

*Farkas, O., Technical University of Heavy Industries, Department of Ferrous Metallurgy, H—3515 Miskolc-Egyetemváros, Hungary

Akadémiai Kiadó, Budapest

describing the substitution ratio directly, moreover, these parameters serve as a basis for research into optimization of factor affecting the process indirectly.

2. Development of the method to determine the coke-natural gas substitution ratio

In development of the calculation model suited to determine the coke-natural gas substitution ratio, the following facts shall be taken into consideration:

— Although the heat value of natural gas is higher than that of coke, this advantage is hardly appreciable in the blast furnace or if indeed at all, only in a blast furnace where the efficiency of gas is significant.

— Limits are set to heat generation in the partial oxidation process of natural gas by heat consumption in thermal dissociation of methane. This unfavourable effect can be offset by a simultaneous proportional increase of the blast temperature (or oxygen content of the blast or, possibly, both) but, as a matter of fact, not only the combustion and thermal conditions of natural gas but also those of the C. Content of coke are affected by these blast parameters.

— CO produced in partial oxidation of natural gas and in partial oxidation of coke (with oxygen present in air or ore) contributes to the reduction process practically identically independently of the different range of temperature at which CO is generated.

— Carbonization of the pig iron takes place indirectly (with CO) or directly (with C). Presumably, the contribution of natural gas and coke to carbonization complies with their quantitative ratio.

— There is a close relationship between CO and H_2 utilization. The degree of gas-utilization — in addition to the heat-value — determines the coke/natural gas substitution ratio, and by this the maximum specific blowable quantity of natural gas, taking into consideration the aspects of energy-utilization.

— The calculation method and/or the mathematical model suited for determination of the coke-natural gas substitution ratio can be worked out only on the basis of thermal engineering considerations in relation to pig iron.

2.1 Thermal effects per 1 m^3 of natural gas blast

According to reaction equation

$$CH_4 + 0.5\ O_2 = CO + 2H_2 \quad ,$$

the quantity of heat generated by partial oxidation of C in natural gas will be

$$\Delta H^{CO}_{298} = -\ 1606.33\ kJ/m^3\ CH_4 \quad .$$

Hydrogen liberated in the course of partial oxidation of the natural gas contributes to reduction of the iron oxides to an extent determined by the utilization of hydrogen and it results in heat generation according to formula

$$H_2 + 0.5\ O_2 = H_2O \quad , \qquad \Delta H_{298} = -\ 119\ 617.0,\ kJ/kg\ H_2 \quad .$$

For hydrogen present in 1 m^3 of natural gas, this quantity of heat is

$$\Delta H^{H_2O}_{298} = \frac{4}{22.46} \cdot (-\ 119\ 617.0) = -\ 19\ 561.24\ kJ/0.178\ kg\ H_2$$

or 1 m^3 CH_4 ,
22.46 being the molar volume of gas at 298 K in l/mol.

Of course, less heat is generated by the hydrogen contributing to reduction and this quantity of heat can be calculated by means of expression

$$\Delta H^{H_2O}_{298} = -\ 19\ 561.24 \cdot \eta_{H_2} \ , \ kJ/m^3\ CH_4 \quad .$$

Theoretically, the utilization of hydrogen according to the formula can be calculated in the knowledge of the constituents of the blast furnace gas by means of the following formula:

$$\eta_{H_2} = \frac{H_2O\%}{H_2\% + H_2O\%} \quad .$$

However, it can be calculated to the required accuracy only by means of relationship

$$\eta_{H_2} = \frac{H_2^r}{H_2^{fg} + H_2^l + H_2^k}$$

based on the H_2-balance,

where H_2^r — H_2 contributing to reduction, m^3/t pig iron

H_2^{fg} — H_2 introduced by natural gas, "

H_2^l — H_2 introduced by humidity in air, "

H_2^k — H_2 introduced by coke, "

Also CO produced in partial oxidation of the natural gas results in an indirect reduction as a function of the current CO utilization, according to basic reaction

$$CO + 0.5\ O_2 = CO_2 \qquad \Delta H_{298}^{CO_2} = -\ 10\ 112.62\ kJ/kg\ CO\ .$$

Thus energy of

$$\Delta H_{298}^{CO_2} = \frac{28}{24.46} \cdot (-\ 10\ 112.62) \cdot \frac{CO_2\%}{CO\% + CO_2\%} = -\ 11\ 576.18 \cdot \eta_{CO}, kJ$$

is produced by carbon monoxide produced in oxidation of 1 m^3 of natural gas (at 298 K).

2.2 Thermal effects per 1 kg of coke carbon

Quantity of heat generated in partial oxidation of the carbon is:

$$\Delta H_{298}^{CO} = -\ 2917.94\ kJ/kg\ C$$

according to reaction

$$C + 0.5\ O_2 = CO\ .$$

Additional reduction results from CO developed in partial oxidation of carbon due to combustion or reduction to an extent determined by the utilization of CO. On the basis of process

$$CO + 0.5\ O_2 = CO_2 \qquad \Delta H_{298}^{CO} = -\ 10\ 112.62\ kJ/kg\ CO\ ,$$

the quantity of heat generated here per 1 kg of coke carbon will be

$$\Delta H_{298}^{CO_2} = \frac{29}{12} \cdot (-\ 10\ 112.62) \cdot \frac{CO_2\%}{CO\% + CO_2\%} = -\ 23\ 596.11 \cdot \eta_{CO}\ kJ/kg\ C\ .$$

2.3 Comparison of thermal effects of oxidation of natural gas and coke carbon, determination of relationship expressing coke-natural gas substitution ratio

The thermal effect of oxidation of natural gas (with oxygen present in air and ore) can be described, as follows:

$$\Delta H_{fg} = - (1606.33 + 19\,561.24 \cdot \eta_{H_2} + 11\,576.18 \cdot \eta_{CO}) \cdot V_{gf} =$$

$$= - X \cdot V_{fg} \quad .$$

Oxidation of coke carbon (with oxygen in air and ore):

$$\Delta H_C = - (9217.94 + 23\,596.11 \cdot \eta_{CO}) \cdot C = - Y \cdot C \quad .$$

Since equality

$$X \cdot V_{fg} = Y \cdot C$$

is assumed by the equivalent replacement of coke carbon for natural gas, the coke carbon substitution ratio is given by relationship

$$\frac{C}{V_{fg}} = \frac{X}{Y} \quad .$$

It is rather coke than carbon, the substitution ratio of which is important in practice in first line. The coke substitution ratio can be calculated on the basis of what has been said above by means of equation

$$\frac{K}{V_{fg}} = \frac{1606.33 + 19\,561.24 \cdot \eta_{H2} + 11\,576.18 \cdot \eta_{CO}}{9217.94 + 23\,596.11 \cdot \eta_{CO}} \cdot \frac{100}{C_k} \quad ,$$

where

K quantity of coke that can be replaced by the quantity V_{fg}, kg/m^3

η_{CO} carbon monoxide utilization $= \frac{CO_2}{CO\% + CO_2\%}$, where the gas components are the constituents of the blast furnace gas

η_{H_2} hydrogen utilization = $\frac{H_2^r}{h_2^{fg} + H_2^l + H_2^k}$ (definitions given earlier)

C_k C-content of coke in per cents. (The substitution ratio applies to dry coke or wet coke depending on whether the C-content of dry coke or wet coke is taken into consideration in calculations.)

As it has been mentioned earlier, the exact determination of the coke-natural gas substitution ratio requires the knowledge of the actual value of hydrogen utilization, while the numerical values for H_2^r/H_2 contributing to reduction, m^3(t pig iron) in relationship

$$\eta_{H_2} = \frac{H_2^r}{H_2^{fg} + H_2^l + H_2^k}$$

suited for accurate calculation of the hydrogen utilization can be determined only on the basis of hydrogen balances.

2.4 Determination of the quantity of hydrogen contributing to reduction by means of H_2 - balance

H_2-balance:

$$H_2^{fg} + H_2^l + H_2^k = H_2^{tg} + H_2^r \quad , \qquad m^3/t \text{ pig iron}$$

where

H_2^{tg} H_2 escaping with blast furnace gas, m^3/t pig iron.

In detail:

$$H_2^{fg} = 2\, V_{fg} \qquad m^3/t \text{ pig iron}$$

$$H_2^l = V_l \cdot n_l \frac{22.41}{18} \cdot 10^{-3} \qquad "$$

$$H_2^k = k \cdot H_{2_k} \cdot \frac{22.41}{2} \cdot 10^{-2} \qquad "$$

$$H_2^{tg} = V_{tg} \cdot H_{2_{tg}} \cdot 10^{-2} \qquad "$$

The quantity of H_2 consumed in reduction cannot be determined directly, but only on the basis of the H_2-balance. Accordingly:

$$H_2^r = 2 \cdot V_{fg} + V_1' \cdot n_1 \frac{22.41}{18} \cdot 10^{-3} + k . H_{2_k} \frac{22.41}{2} \cdot 10^{-2} - V_{tg} \cdot H_{2_{tg}} \cdot 10^{-2} \ , \ m^3/t \text{ pig iron.}$$

In the formulas,

V_{fg}	quantity of natural gas	m^3/t pig iron
V_1'	quantity of wet air	m^3/t pig iron
n_1	humidity in air	g/m^3
k	coke consumption	kg/t pig iron
H_{2_k}	H_2 content of coke	mass %
V_{tg}	quantity of blast furnace gas	m^3/t pig iron
$H_{2_{tg}}$	H_2 content of blast furnace gas	volume %

The following quantities included in the equation, expressing the quantity of H_2 contributing to reduction are to be calculated:

$$V_1' = \frac{(k \cdot 0.75 \cdot C_k \cdot 10^{-2} + V_{fg} \frac{12}{22.41}) \cdot \frac{0.5 \cdot 22.41}{12}}{O_{2_1} \cdot 10^{-2} (1 - n_1 \frac{22.41}{180} \cdot 10^{-2}) + 0.5 \, n_1 \frac{22.41}{180} \cdot 10^{-2}} = \frac{(k \cdot 0.0075 \cdot C_k + V_{fg} \cdot 0.535) 0.934}{O_{2_1} \cdot 10^{-2} (1 - n_1 \cdot 0.001\,245 (+ n_1 \cdot 0.000\,6225} \ ,$$

m^3/t pig iron

$$V_{tg} = \frac{V_1' \left\{ 1 - 10^{-2} \left[O_{2_1} \left(1 - n_1 \frac{22.41}{180} \cdot 10^{-2} \right) + n_1 \frac{22.41}{180} \right] \right\} + 0.008 \cdot k \cdot N_{2_k} + V_{fg} \cdot N_{2_{fg}} \cdot 10^{-2}}{N_{2_{tg}} \cdot 10^{-2}} =$$

$$= \frac{V_1' \left\{ 1 - 10^{-2} \left[O_{2_1} (1 - n_1 \cdot 0.001\,245) + n_1 \cdot 0.1245 \right] \right\} + 0.008 \, k \cdot N_{2_k} + V_{fg} \cdot N_{2_{fg}} \cdot 10^{-2}}{N_{2_{tg}} \cdot 10^{-2}} \ ,$$

m^3/t pig iron

Definition of new symbols in these formulas:

C_k	C-content of coke	mass %
O_{2_1}	O_2-content of air (dry)	volume %
N_{2_1}	N_2-content of coke	mass %
N_{2_K}	N_2-content of natural gas	volume %
$N_{2_{fg}}$	N_2-content of blast furnace gas	volume %
$N_{2_{tg}}$		

$$H_2^{\Gamma} = 2V_{fg} + \frac{(k\cdot 0.0075\cdot C_k + V_{fg}\cdot 0.535)\ 0.934}{O_{2_l}\cdot 10^{-2}(1-n_1\cdot 0.001\ 245)+n_1\cdot 0.000\ 6225}\cdot n_1\cdot 0.001\ 245 + k\cdot H_{2_k}\cdot 0.112\ 05 -$$

$$-\frac{\frac{(k\cdot 0.0075\cdot C_k + V_{fg}\cdot 0.535)\ 0.934}{O_{2_l}\cdot 10^{-2}(1-n_1-0.001\ 245)+n_1\cdot 0.000\ 6225}\cdot\left\{1-10^{-2}\left[O_{2_l}(1-n_1\cdot 0.001\ 245)+n_1\cdot 0.1245\right]\right\}+0.008\cdot k\cdot N_{2_k} + V_{fg}\cdot N_{2_{fg}}\cdot 10^{-2}}{N_{2_{tg}}\cdot 10^{-2}}\cdot H_{2_{tg}}\cdot 10^{-2} =$$

$$= 2V_{fg} + k\cdot H_{2_k}\cdot 0.112\ 05-(0.008\ k\cdot N_{2_k} + V_{fg}\cdot N_{2_{fg}}\cdot 10^{-2})\cdot\frac{H_{2_{tg}}}{N_{2_{tg}}} +$$

$$+\frac{(k\cdot 0.0075\cdot C_k + V_{fg}\cdot 0.535)0.934}{O_{2_l}\cdot 10^{-2}(1-n_1\cdot 0.001\ 245)+n_1\cdot 0.000\ 6225}\left[n_1\cdot 0.001\ 245-\left\{1-10^{-2}\left[O_{2_l}(1-n_1\cdot 0.001\ 245)+n_1\cdot 0.1245\right]\right\}\cdot\frac{H_{2_{tg}}}{N_{2_{tg}}}\right] =$$

$$= 2\ V_{fg} + 0.112\ 05\cdot k\cdot H_{2_k}-(0.008\cdot k\cdot N_{2_k} + V_{fg}\cdot N_{2_{fg}}\cdot 10^{-2})\frac{H_{2_{tg}}}{N_{2_{tg}}} +$$

$$+\frac{(0.0075\cdot k\cdot C_k + 0.535\cdot V_{fg})\ 93.4}{O_{2_l}(1-0.001\ 245\cdot n_1) + 0.062\ 25\cdot n_1}\left\{0.001\ 245\cdot n_1 - \left[1-10^{-2}\cdot O_{2_l}(1-0.001\ 245\cdot n_1) - 0.001\ 245\cdot n_1\right]\cdot\frac{H_{2_{tg}}}{N_{2_{tg}}}\right\},\quad m^3/t\ \text{pig iron}$$

Substituting the expressions "V_1" and "V_{tg}" into the earlier equation serving for the determination of H_2-quantity contributing to the reduction and reducing this equation, the relationship shown on page 150. is obtained.

On the above basis, the following expressions serve to determine the quantities given in the denominator of the formula for hydrogen utilization (η_{h_2}):

Quantity of H_2 introduced by natural gas:

$$H_2^{fg} = 2\ V_{fg}, \qquad m^3/t \text{ pig iron.}$$

Quantity of H_2 introduced by air:

$$H_2^1 = \frac{(k \cdot 0.0075 \cdot C_k + V_{fg} \cdot 0.535)\ 0.934}{O_{2_1} \cdot 10^{-2}(1-n_1 \cdot 0.001\ 245) + n_1 \cdot 0.000\ 6225} \cdot n_1 \cdot 0.001\ 245,$$

m^3/t pig iron.

Quantity of H_2 introduced by coke:

$$H_2^k = k \cdot H_{2_k} \cdot 0.11205\ , \quad m^3/t \text{ pig iron.}$$

In the knowledge of these quantities (definitions given above) as well as of H_2^r (quantity of H_2 contributing to reduction in m^3/t pig iron), the utilization of hydrogen can be exactly calculated by means of the equation presented. Accurate result is thus supplied also by determination of the coke-natural gas substitution ratio (k/V_{fg}).

To avoid the tiresome procedure of determination of the H_2-balance, the utilization of H_2 can be calculated in the knowledge of CO-utilization (which can be easily determined on the basis of composition of the blast furnace gas by means of relationship

$$\eta_{CO} = \frac{CO_2\%}{CO\% + CO_2\%}\ ),$$

using the author's equation

$$\eta_{H_2} = 0.8575\ \eta_{CO}^{0.8276}$$

which gives satisfactory results especially in case of calculation of comparative values for the substitution ratio.

3. Actual determination of coke-natural gas substitution ratio

Assume a CO-content of 25.7% while a CO_2-content of 14.3% in blast furnace gas. Thus the CO-utilization will be

$$\eta_{CO} = \frac{CO_2\%}{CO\% + CO_2\%} = \frac{14.3}{25.7 + 14.3} = 0.357 \quad .$$

Use formula

$$\eta_{H_2} = 0.8575 \ \eta_{CO}^{0.8276}$$

to determine H_2-utilization (as no H_2-balance is available). Accordingly:

$$\eta_{H_2} = 0.8575 \cdot 0.357^{0.8276} = 0.366 \quad .$$

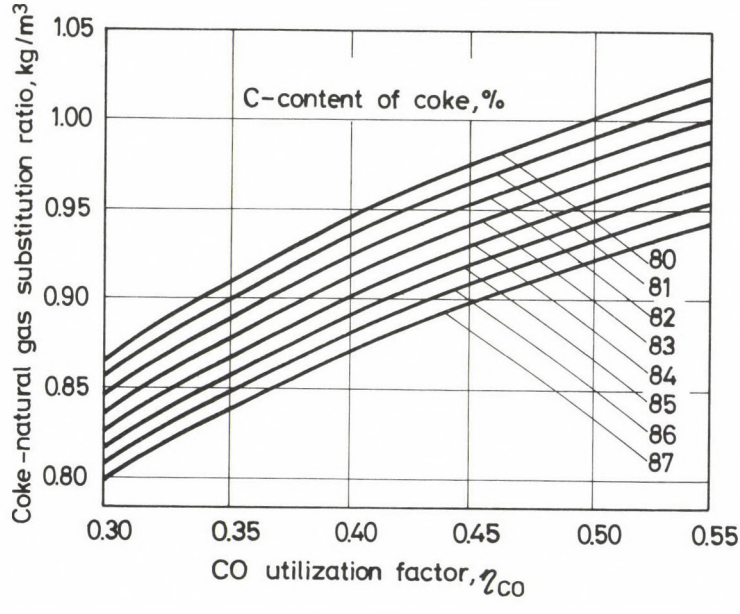

Fig. 1. Relationship between CO-utilization and coke-natural gas substitution ratio for cokes of different C-content

Assuming a C-content of 82.3% in wet coke while 86.1% in dry coke, 1 m^3 of natural gas substitutes for

$$\frac{K}{V_{fg}} = \frac{1606.33 + 19561.24 \cdot 0.366 + 11576.18 \cdot 0.357}{9217.94 + 23596.11 \cdot 0.357} \cdot \frac{100}{82.3} = 0.888 \text{ kg}$$

and

$$\frac{K}{V_{fg}} = 0.731 \cdot \frac{100}{86.1} = 0.849 \text{ kg}$$

of wet coke and dry coke, respectively.

The significant effect of CO and H_2 utilization on coke substitution ratio is shown by the fact that e.g. in case of a CO_2 content of 16.2% and a CO-content of 23.8% in blast furnace that is $\eta_{CO} = 0.405$ and thus $\eta_{H_2} = 0.406$, 1 m^3 of natural gas is capable of replacing 0.921 kg of wet coke (C = 82.3%) while 0.881 kg of dry coke (C = 86.1%) as seen in Fig. 1.

A change in the quantity of natural gas per unit time or 1 t of pig iron results in a simultaneous change in gas utilization. Namely, the quantity of gas in the hearth increases gradually as the quantity of natural gas increases and due to increasing gas flow rate with invariable campaign intensity (for coke plus natural gas), the utilization of H_2 and CO and thus also the coke-natural gas substitution ratio reduce.

Acta Technica Acad.Sci.Hung., 101(2), pp. 155—170 (1988)

RESULTS OF INJECTION LADLE METALLURGY IN SHEET METAL PRODUCTION

RÉPÁSI, G.*

(Received: 29 January 1987)

In the production process of steel for high-strength heavy plates and cold rolled thin sheets, injection ladle metallurgical methods are used for deoxidation and desulphurization. As a result, both the technology and the properties of the finished product are affected favourably in that the number of non-metallic inclusions is reduced and the inclusion morphology is modified. CaSi is injected into steels for heavy plate production while CaO + CaF_2 + Al into steel for thin sheet production. The success of deoxidation and desulphurization depends on the appropriate slag composition. Synthetic slag is fed for this purpose during tapping.

Introduction

In Hungary, ladle metallurgical processes are finding use in three important fields, such as

(1) production of high-strength heavy plates and tube steel suited for direct rolling, weldable, and having spatial isotropy,

(2) production of low-silicon or non-silicon continuously cast steel slabs suited for direct rolling to produce thin sheets,

(3) production of square billets deoxidized with aluminium.

Vacuumless injection processes are used in any of the above three cases in application with converters, open-hearth furnaces and arc furnaces.

The following results have been obtained in efforts to meet the different objectives:

Preparation of liquid steel for injection

The success of the injection processes depends on quantity, chemical composition, and physical condition of the slag on the surface of liquid steel in the ladle. Namely, the slag is intensively mixed with the steel in

*Répási, G., H—2400 Dunaújváros, Kisdobos u. 1, Hungary

Akadémiai Kiadó, Budapest

the course of scavenging with inert gas and it shall be capable of absorbing the products of reactions taking place at the slag-steel phase boundary. This applies first of all to the sulphur capacity of the slag. Since the desulphurization reaction sequence depends on the oxygen activity of the liquid steel, also this requirement shall be met during tapping.

The synthetic slag produced in the course of tapping consists of the following components:

— A mixture of CaO and CaF_2 or CaO, CaF_2, Al (or some other deoxidizer) fed to the ladle during tapping in a quantity determined as a function of tapping temperature so that the slag will be liquid,

— deoxidation products, first of all Al_2O_3 and SiO_2,

— products of reactions taking place between the steel-slag system and the ladle lining,

— primary slag particles emulsified in the steel bath,

— erosion of the ladle lining.

This synthetic slag of a ratio of 16—20 kg/t gets into intensive contact with steel in the course of injection.

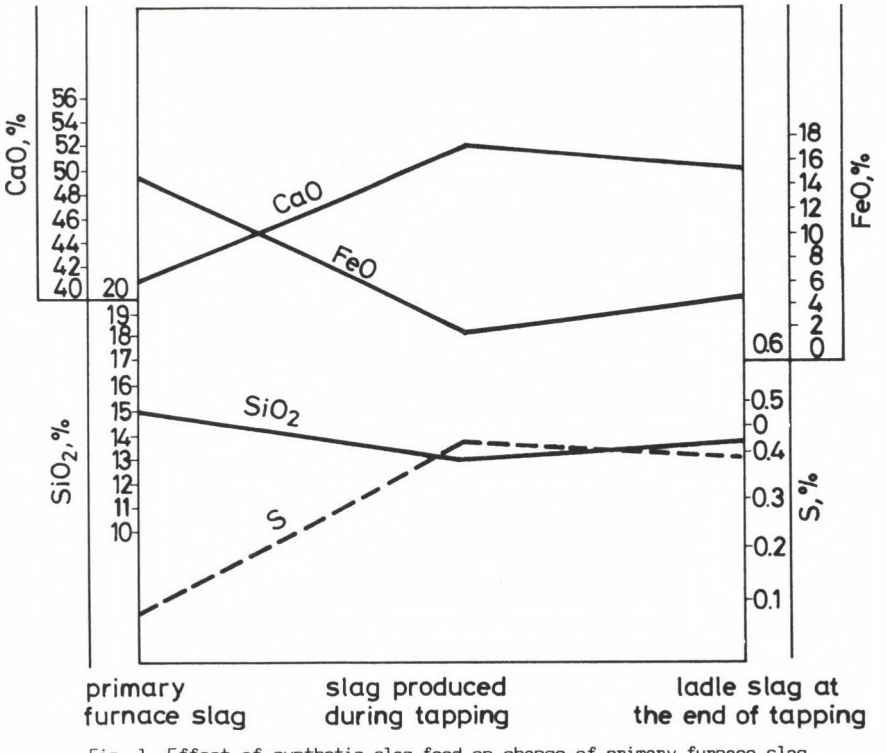

Fig. 1. Effect of synthetic slag feed on change of primary furnace slag

The chemical composition of slag produced during tapping differs significantly from that of primary slag and of the slag developing after tapping as shown in Fig. 1.

The literature considers the ideal ratio in respect of sulphur dissolving capacity to be

$$\frac{CaO}{SiO_2} : Al_2O_3 = 0.35 \quad .$$

Production of slag of the above characteristics in the ladle during tapping means that the most important condition for a successful injection has been created.

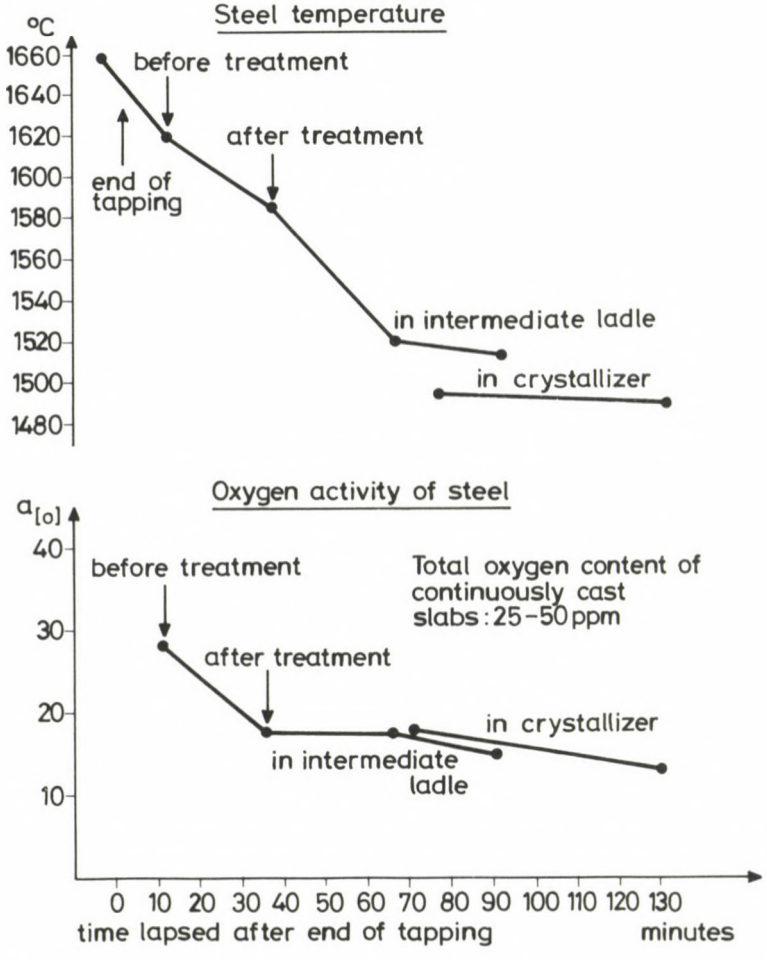

Fig. 2. Effect of CaSi injection on oxygen activity of steel as a function of temperature and time in the production process of grade 62 and 62 steels

High-strength heavy plate production

In a ladle with basic lining, the synthetic slag described above is produced during tapping. Then calcium-silicon is injected into the liquid steel in a ratio of 2 to 3 kg/t at a rate of 40 to 50 kg/min by means of Ar of a feed rate of 400 to 600 l/min.

As a result of this treatment, also the oxygen content of steel reduces in the way shown in Fig. 2, often to a value of 10 ppm or less.

Also the total oxygen content of the slabs reduces to a value of 25 to 50 ppm (according to neutron activation analysis).

As a result, the number of sulphide and oxide inclusions reduces significantly to a degree of 0.67 on the average for sulphid inclusions while 1.9 to 2 for oxide inclusions according to Jernkontoret (Table 1).

Fig. 3. Magnification: 5000 x
Chemical composition of steel, %:
C - 0.11; Mn - 1.45; Si - 0.41; S - 0.008; Al - 0.018; V - 0.06; O - 70 ppm
Chemical composition of inclusion, %:
Mn - 51; S - 48.5; V - 0.5

Table 1 Number of inclusions in finished product after desulphurization during tapping

Batch No.	Sample No.	Degree			
		A	B	C	D
26502	295	1.4	2.3	-	0.8
	296	1.4	1.9	-	0.6
	297	1.6	2.3	-	0.8
	298	1.6	2.2	-	0.7
	299	1.5	2.0	-	0.6
	300	1.1	1.5	-	0.7
	301	1.7	2.0	-	0.9
	302	1.6	1.8	-	0.8
	303	1.6	2.0	-	0.7
	304	1.1	1.6	-	0.6
	305	1.6	2.2	-	0.6
	306	1.5	2.1	-	0.6
	Average:	1.47	1.99	-	0.7
26503	271	1.5	1.9	-	0.5
	272	1.5	2.3	-	0.6
	273	1.3	1.9	-	0.5
	274	1.7	2.2	-	0.6
	275	1.6	2.0	-	0.7
	276	1.3	1.9	-	0.8
	277	1.4	1.8	-	1.0
	278	1.3	1.9	-	0.6
	279	1.5	0.5	-	0.6
	280	1.4	2.5	-	0.5
	281	1.4	2.0	-	0.8
	282	1.3	2.1	-	0.7
	283	0.9	2.2	-	0.9
	284	1.3	2.3	-	0.7
	285	1.5	1.9	-	0.5
	Average:	1.33	1.96	-	0.67

Sulphur appears in the shape of manganese sulphide dendrites or spheroidal manganese sulphides (Fig. 3). Chemical composition:

Sulphur	40 to 58 %
Manganese	30 to 50 %
Ferrum	10 to 20 %.

Figure 4 shows the Baumann print of a continuously cast slab of a sulphur content of 0.004 %.

In steels of a manganese content above 1%, oxide inclusions always appear as spheroical calcium aluminates or calcium-manganese aluminates. Such an inclusion is shown in Fig. 5.

Fig. 4. Baumann print of CaSi-injected continuously cast slab
Chemical composition of steel, %
C - 0.12; Mn - 1.06; Si - 0.36; P - 0.022; S - 0.004; Al - 0.040; O - 30 ppm

Batch No.: 15419

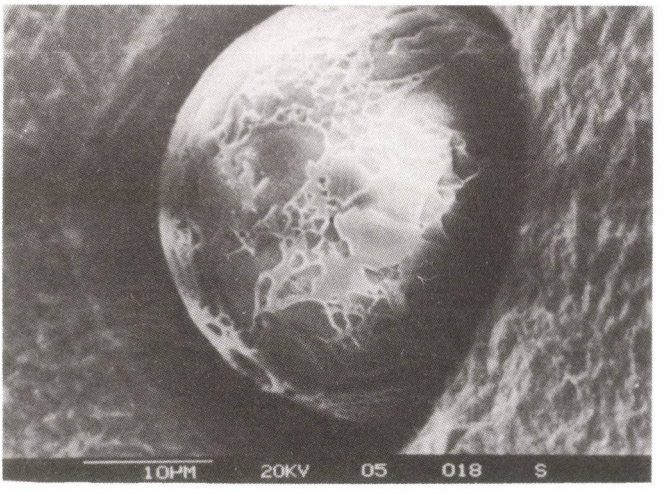

Fig. 5. Spheroidal calcium aluminate inclusion
Chemical composition of steel, %
C - 0.10; Mn - 1.38; Si - 0.3; S - 0.005; Al - 0.042; O - 35 ppm
Chemical composition of inclusion, %

Bright area:		Dark Area:
Al	74.5	64
Mg	16.5	-
Ca	6	35
S	1	1

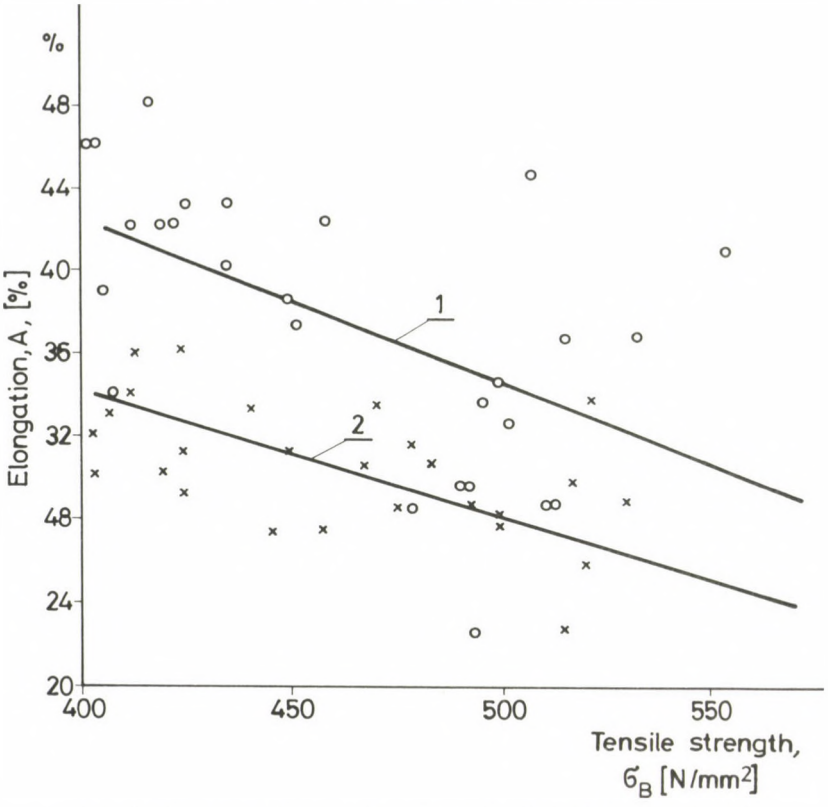

Fig. 6. Elongation of heavy plates as a function of tensile strength
1 - SL process: $A = -0.085\ \sigma_B$, N/mm^2 + 76.4 (%)
2 - Conventional process: $A = -0.051\ \sigma_B$, N/mm^2 + 53.34 (%)

As a result of contact with air, the nitrogen content of the steel increases by a value of 10 to 20 ppm during injection. Increase in hydrogen content has also been experienced in some cases (this latter taking place only in case of a high moisture content of the calcium silicon used). The hydrogen content of steel amounts to 0.4 to 1.0 ppm at present.

As seen, a reduction in sulphur and oxygen content and a modification of the inclusion morphology have taken place as a result of calcium silicon injection.

The effect of modified inclusion morphology on the quality of heavy plates and tube steels has been tested by means of multiple technological tests to find that CaSi-injected products are superior to conventional products in that

(a) the danger of the well-known staggered fracture is avoidable,

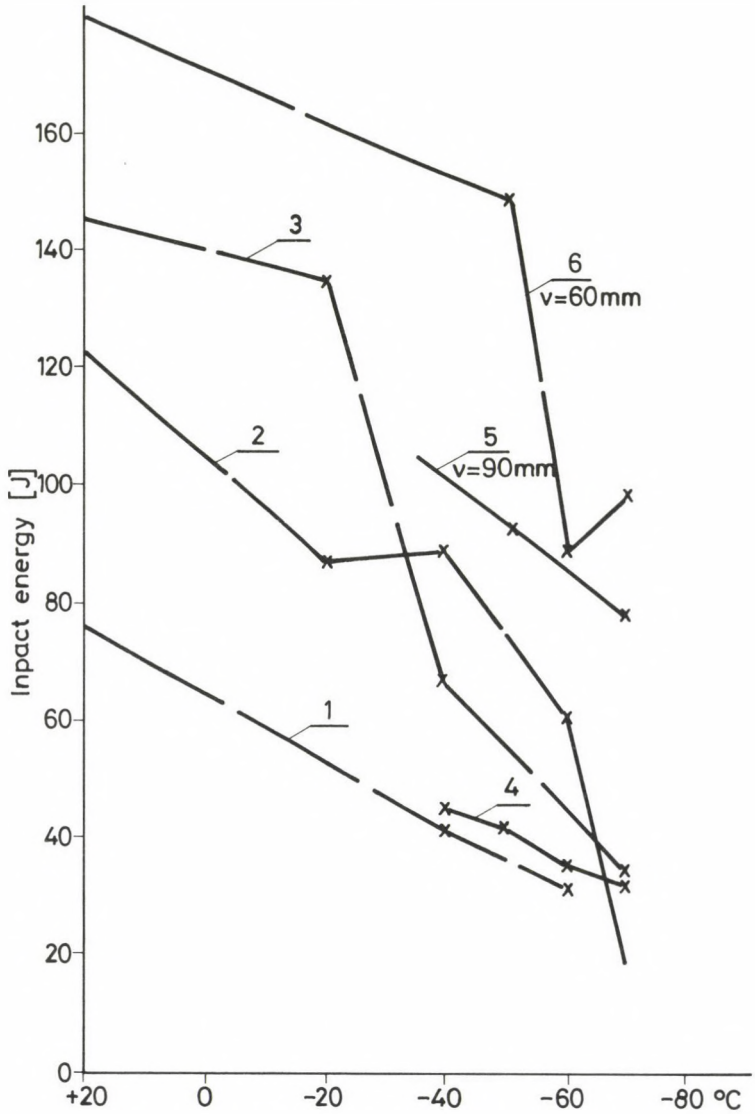

Fig. 7. Effect of sulphur content on intermediate temperature of high-strength steels

Notation	C	Mn	Si	P	S	Al	Ni	V	Nb
1	0.16	0.90	0.33	0.014	0.015	0.04	0.5	0.16	-
2	0.17	1.39	0.35	0.021	0.013	0.04	-	-	-
3	0.14	1.35	0.28	0.016	0.016	-	-	0.13	-
4	0.14	1.30	0.35	0.035	0.035	0.04	-	-	0.04
5	0.13	1.32	0.34	0.025	0.005	0.02	-	-	-
6	0.13	1.32	0.34	0.025	0.005	0.02	-	-	-

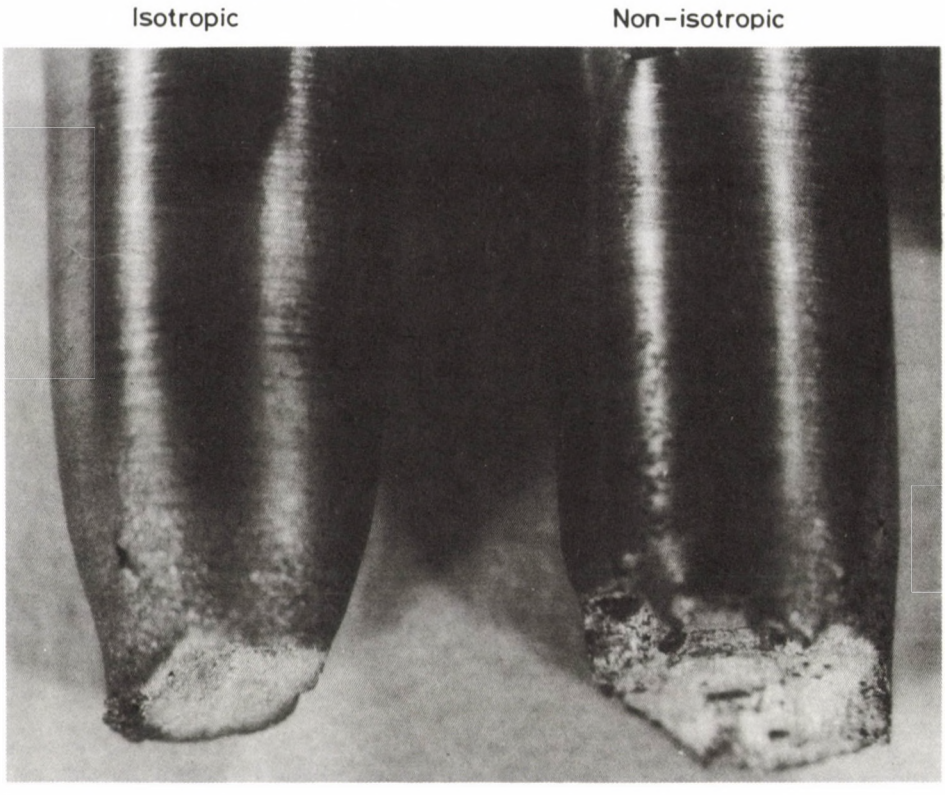

Fig. 8. Contraction of tensile test specimens of isotropic and non-isotropic heavy plate in the direction of thickness

Chemical composition of isotropic steel (%)

C	Mn	Si	S	P	Al
0.10	1.36	0.30	0.005	0.025	0.037

Mechanical characteristics of isotropic steel

R_m N/mm^2			Contraction		
H	K	V	H	K	V
534	531	526	70.0	60.2	63.3

H = in longitudinal direction
K = in transversal direction
V = in the direction of thickness

Table 2 Anisotropy of boiler plates in longitudinal and transversal direction (contraction)

Batch No. S content, %		12 — 15	16 — 20	22 — 30	35 — 55	60 — 80	85 — 100
		thickness, mm					
	L	73	72	69.8	-	-	-
15874	Q	67.4	67.7	70.7	-	-	-
S=0.006	L/Q	0.92	0.94	1.01	-	-	-
45716	L	74.1	72.0	72.0	70.7	-	-
	Q	69.8	68.6	70.7	69.8	-	-
S=0.005	L/Q	0.94	0.95	0.98	0.99	-	-
	L	69.1	-	66.5	-	61.6	58.0
35451	Q	65.4	-	61.6	-	51.0	44.0
S=0.005	L/Q	0.95	-	0.93	-	0.83	0.6

L = longitudinal direction

Q = transversal direction

(b) there is an improvement of 20 to 30 % in the elongation figures (A%) in any strength range (measured in a range of up to 700 MPa) as shown in Fig. 6.

(c) there is a reduction of 30 to 50 ^{o}C in transition temperatures, the basic material keeping its toughness even at lower temperatures (Fig. 7),

(d) the contraction ratio of heavy plates measured in both longitudinal and transversal direction lies between 0.92 and 1.01 for plates of a maximum thickness of about 50 mm (Table 2),

(e) as proved by Table 3, contraction of heavy plates in the direction of thickness has become a standardizable (warranted) technological characteristic. The same is proved also in Fig. 8 showing that the results of technological tests made in three different directions are almost identical as compared with the tensile test of a conventional heavy plate in the direction of thickness.

As is well known, the technological properties of rolled products are affected by more rolling parameters in case of broad strip rolling as compared with heavy plate rolling mills (e.g. rate of rolling and cooling,

Table 3 Contraction of boiler plates in the direction of thickness

Batch No. S content, %	Thickness, mm											
	12 — 15		16 — 20		22 — 30		35 — 55		60 — 80		85 — 100	
	M	A	M	A	M	A	M	A	M	A	M	A
15874 S=0.006	-	-	29.0	31	-	-	53.6	60.5	-	-	-	-
45716 S=0.005	-	-	34.5	40	-	-	36.5	46.0	58.0	61.0	-	-
35451 S=0.005	37.5	44.3	-	-	22.5	25.8	38.8	42.8	-	-	21	30.3
15560 S=0.009	-	-	-	-	21.5	23.7	-	-	-	-	-	-
/1/ S = 0.035	-	-	-	-	11.8	11.8	-	-	-	-	-	-
/2/ S = 0.022	-	-	-	-	13.0	13.0	-	-	-	-	-	-
/3/ S = 0.022	-	-	-	-	11.4	13.3	-	-	-	-	-	-

M = Minimum

A = average

coiling temperature etc.) in one direction. Therefore, it had to be tested whether the results obtained for heavy-plate rolling mills were reproducible also in case of broad-strip rolling. The result of the comparative test has been illustrated diagrammatically as the correlation between strength and elongation figures using internationally accepted curves (Fig. 9). It is proved definitely by the diagram that the change in inclusion morphology accompanied with a reduction of the sulphur content below 0.005 % results in an increase of the value of elongation associated with given strength, a fact affecting especially the conditions of construction of the steel framework of motor vehicles favourably.

Use of injection methods in the production of cold rolled thin sheets

The objective has been to use the injection technology for the production of continuously cast slabs equivalent to rolled ingots cast in unkilled steel, an important requirement because, as is well known, continuous casting in unskilled steel has not been successfully realized so far.

After research for two years, the composition and manufacturing parameters permitting the above objective to be met could have been de-

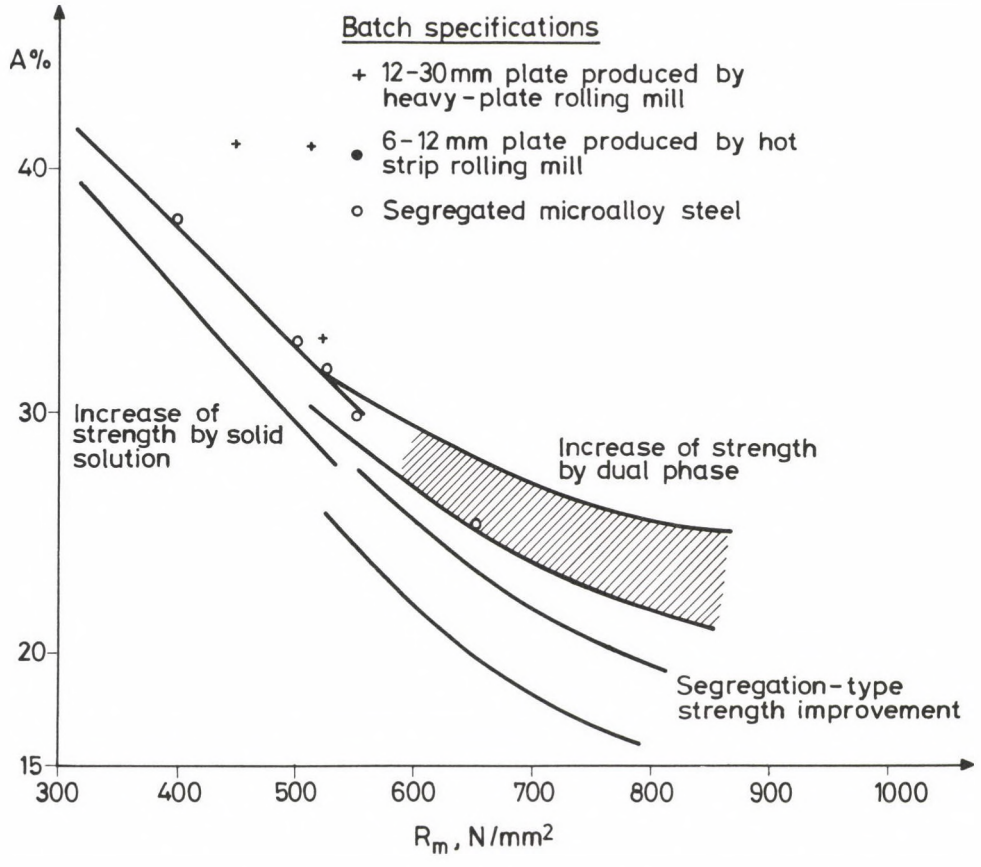

Fig. 9. Relationship between tensile strength and elongation of high-strength hot-rolled steels

termined. The part of injection in the technology is predominant. As a result of the process developed, 100% continuous casting is possible at our largest sheet production plant.

The use of CaSi is out of question because the slabs so cast must not contain silicon or if indeed at all, only a small amount. At the same time, the development of Al_2O_3 inclusions can be expected if the deoxidizer is aluminium alone, resulting in troubles in casting and a poor surface quality as compared with the desirable quality. Thin sheets of appropriate surface quality can be produced only if the surface of the slabs is entirely scraped.

Efforts were made to find the minimum deoxidation which is enough to prevent the C+O=CO reaction from taking place but still insufficient to result in the development of Al_2O_3 inclusions. On the basis of evaluation of the results obtained for full-scale experimental batches of a large number, the following composition and casting parameters were found to meet the requirements:

Chemical composition, %:

C	max. 0.10
Mn	0.30 to 0.45
Si	max. 0.08
P	max. 0.10
S	max. 0.015
Al	0.004 to 0.010
Casting temperature:	1550 to 1560 ^{o}C
Casting rate:	0.6 m/min
Oxygen activity in tundish:	40 to 60 ppm
Total oxygen in slabs (on the basis of neutron activation analysis):	100 to 120 ppm

Synthetic slag of a composition of CaO + CaF_2 + Al (80—85 %, 15—20 %, 1 kg/t, respectively) shall be injected to cope with the problem. In this way, the sulphur content of the steel can be reduced to a value below 0.010 % that means that less sulphur is present in the entire cross section than in the skin of ingots cast in unskilled steel. Al_2O_3 inclusions are not developing or, if indeed at all, their number is small because calcium aluminates are formed also in this case. The Al content of steel ranges between 0.006 and 0.010 %. The metallurgical process is diagrammatically illustrated in Fig. 10.

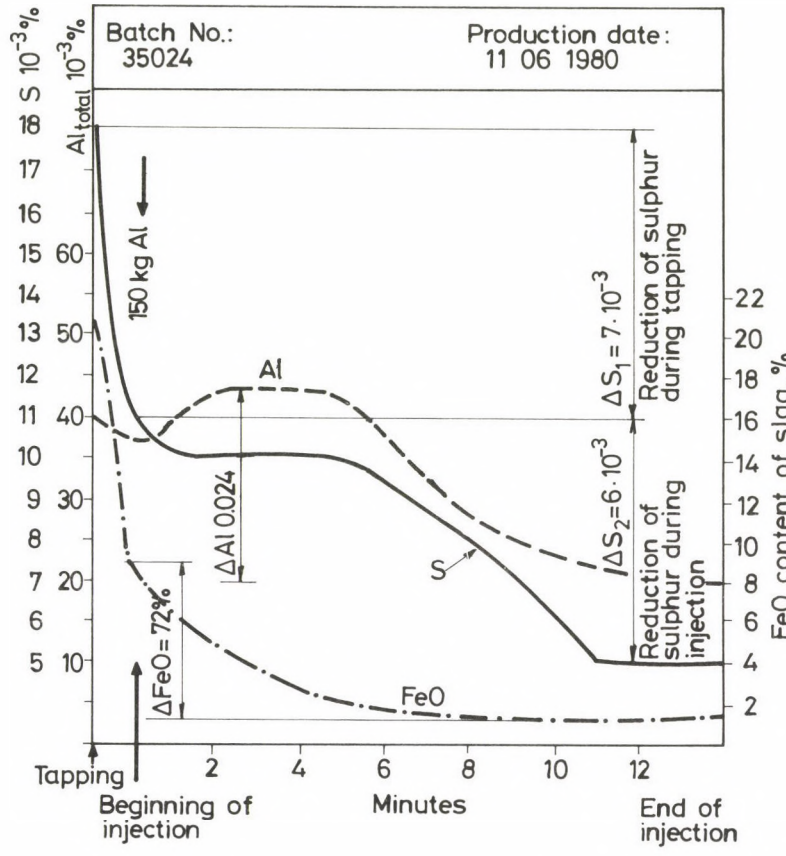

Fig. 10. Desulphurization process vs time in case of injection of CaO + CaF_2 at a rate of 3.0 kg/t

According to Fig. 10, the sulphur content of the steel reduces from 0.011 % to 0.005 % while the iron oxide content of the slag from 8 % to 2 %. Aluminium is used in a ratio of 0.024 % for deoxidation of the steel. The typical Baumann print of continuously cast slabs produced by means of this technology is shown in Fig. 11.

The process is controlled on the basis of oxygen activation measurements in the intermediate ladle. Correction of the extent of deoxidation is possible on the basis of the results of measurement by adding aluminium wire to the steel (Fig. 12).

The metallurgical process consists of two parts. The first phase includes feed of synthetic slag during tapping with proper adjustment of

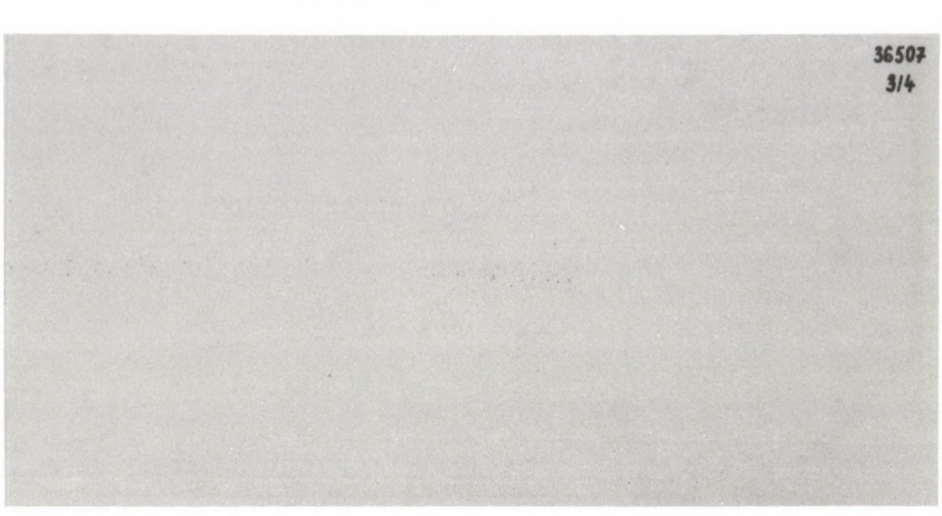

Fig. 11. Baumann print of $CaO+CaF_2$+Al injected continuously cast slab

the quantity and composition of the slag required for sulphur absorption. Then the injection parameters are determined on the basis of temperature and oxygen activity measurements.

It is also possible to work without silicon. In this case, the Al content shall be adjusted to a value between 0.010 and 0.020 % at, however, the expenses of an increasing danger of development of Al_2O_3 inclusions. This danger can be reduced by adding CaO + CaF_2. As has been found also by other research workers, an

$$m(CaO) + n(Al_2O_3) = m\ CaO\ .\ n\ Al_2O_3$$

reaction may take place under these conditions.

The texture of the slab is affected also by the casting rate. It was found e.g. that a reduction of the casting rate from 0.5 m/min to 0.3 m/min resulted in the development of CO-draws in the skin.

The surface quality of thin sheets produced in accordance with the technological instructions meets the requirements imposed upon cold roller thin sheets in every respect and also the requirement of suitability for direct rolling.

The total amount of thin sheets is produced by means of this technology in Hungary today.

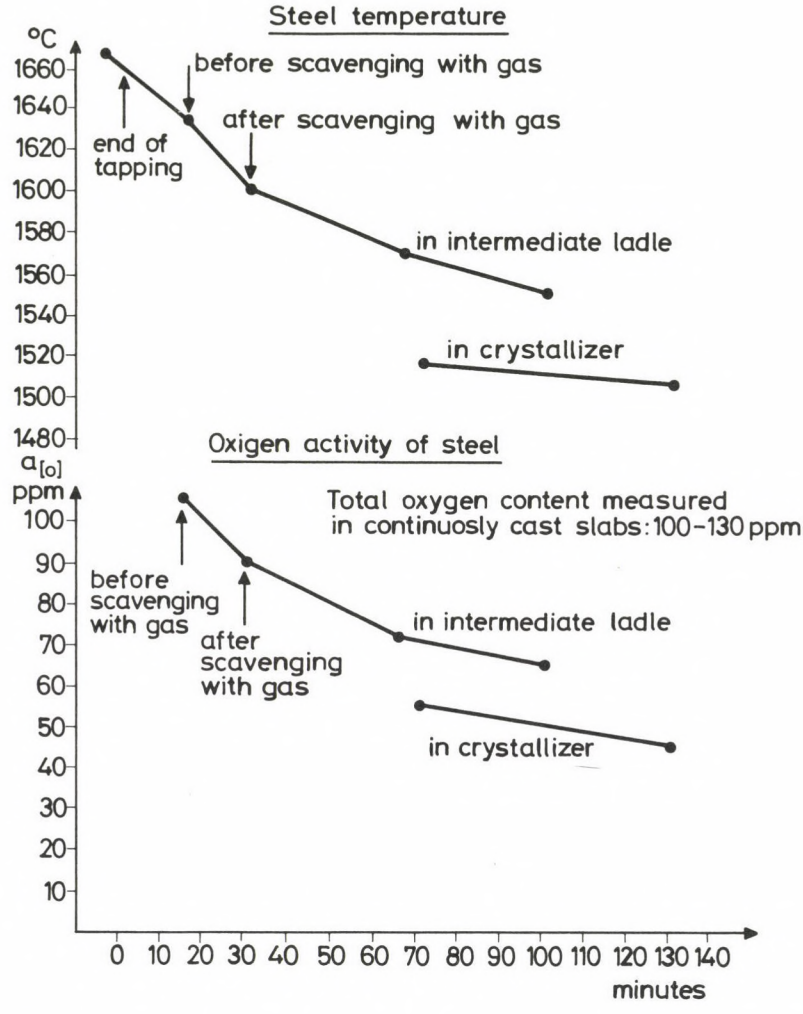

Fig. 12. Change of oxygen activity and temperature as a function of time in steels scavenged with gas and partly deoxidized with Al

Because of the reduced sulphur content, the workability of thin sheets so produced is facilitated. Due to the favourable values of elongation as well as $\bar{r}$ and $\bar{m}$, the sheets are easy to bend, work, flange, and deep draw.

Acta Technica Acad.Sci.Hung., 101(2), pp. 171—183 (1988)

INVESTIGATION OF THE PARAMETERS OF ELECTROLYTIC COPPER REFINING BY CURRENT REVERSAL

SZEPESSY, A. — KÉKESI, T. — HERTELENDI, Á.*

(Received: 25 April 1988)

The authors investigated the effect of current density, anode-cathode distance, times and current intesity ratios of forward and reverse current periods on polarization voltage, cell voltage and specific energy consumption in electrolytic copper refining by current-reversal. Incomplete four-variable interpolation polynomials were used to describe the relationships between the above variables. On the basis of evaluation using the methods of mathematical statistics, the current density and the anode-cathode distance were found to affect the specific energy consumption significantly in the range of variation investigated.

Electrolytic copper refining plants with conventional box-type multiplex-system DC tanks use a current density of 200—220 A/m^2 the electric efficiency being 93—96 %. The productivity at these plants lies at 1.65—2.00 t Cu/m^2a /1/.

To increase the economic efficiency of electrolytic copper refining, first thing to do is to improve productivity. The quantity of copper deposited cathodically depends on the time of electrolysis, utilization of current and on current density determining the rate of deposition of the metal.

In case of given operating time and current efficiency, limits are set to increase the current density by the consequences of increasing overvoltage on the electrodes.

As a result of concentration polarization taking place on the cathode, the cathode potential reduces at a current density of 250—300 A/m^2 to an extent complying with the potential at which impurities (As, H) in the electrolyte are deposited. The codeposition of impurities with copper results in a poor quality, purity and texture of cathodic copper.

---

*Mrs. Szepessy, A., H—3515 Miskolc-Egyetemváros, Hungary
Kékesi, T., H—3532 Miskolc, Tátra u. 13, Hungary
Hertelendi, Á., H—3211 Gyöngyösoroszi, Altáró u. 2, Hungary

Akadémiai Kiadó, Budapest

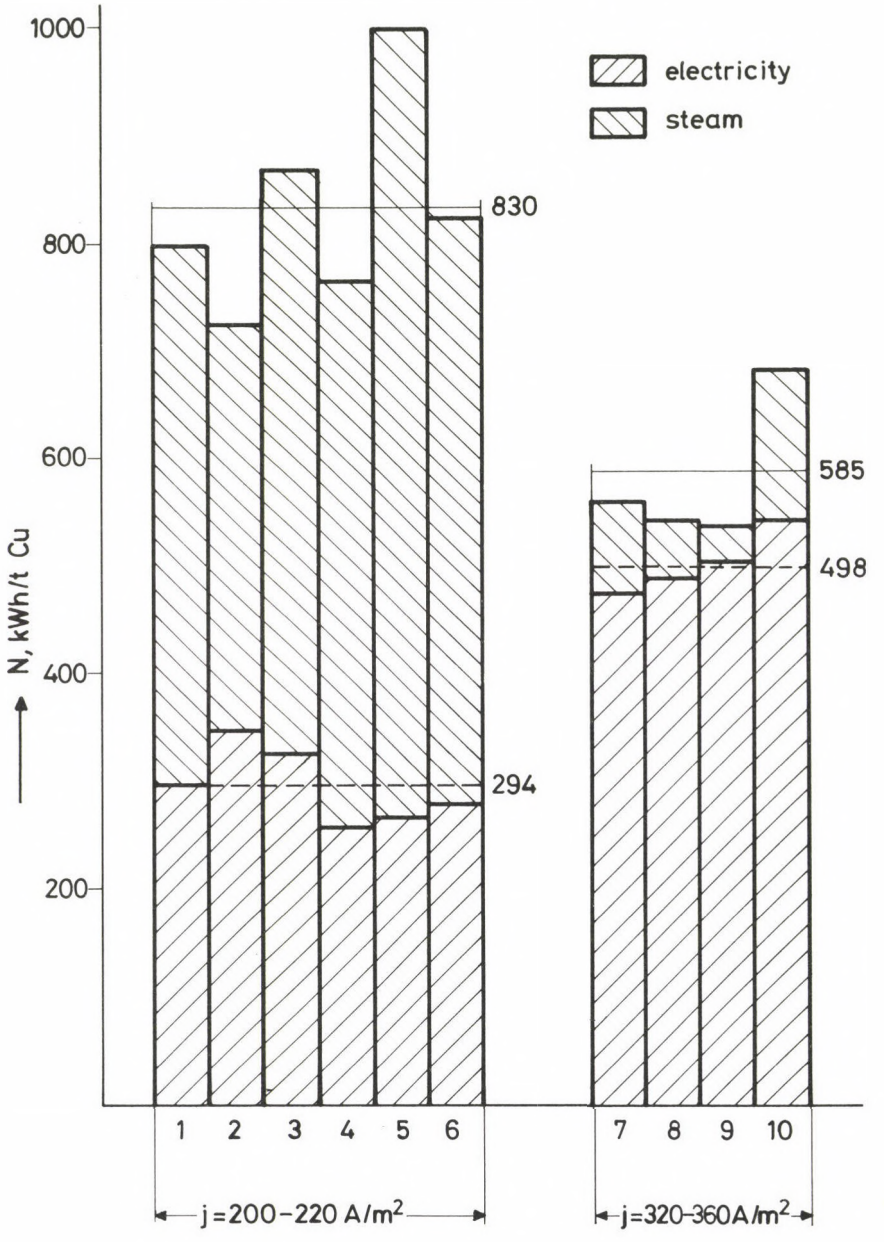

Fig. 1. Specific energy consumption of electrolytic copper refining plants (/1/, Tables 1-2)

Increasing cathodic and anodic polarization results in increasing tank voltage and specific electricity consumption. As shown in Fig. 1 indicating the parameters of the different plants, the electric energy consumption of tanks using a current density of 200—220 A/m^2 amounts to about 250—350 kWh/t Cu while that of tanks using a current density of 320—360 A/m^2 to about 470—540 kWh/t Cu. However, the significant gain in Joule heat accompanying the increase in current density results in significant savings in steam which compensate for the increase in electricity consumption. At the plants investigated, the average value of gross energy consumption lies at 830 kWh/t Cu in case of a conventional current density while at only 585 kWh/t Cu in case of increased current density.

In electrodeposition, electrolysis by current of periodically alternating polarity or periodically interrupted current has been used to reduce undesirable overvoltages resulting from high current density in electrolytic metal deposition has been used since the early 1900s. The process found a wide industrial use for electrolytic copper refining only after the early 1960s. At present, more than 16% of the world's cathodic copper production is produced by means of the PCR (periodical current reversal) process. The PCR process patented by Montanwerke Brixlegg, Austria, was introduced at the Electrolytic Copper Plant of Csepel Metal Works in 1986.

In the current-reversal technology, the polarity of the current is reversed periodically in accordance with a programme. The electrochemical process is controlled by a train of square-wave current pulses of alternating polarity and different length. Change of the cathode current as a function of time is illustrated in Fig. 2. During the longer forward current

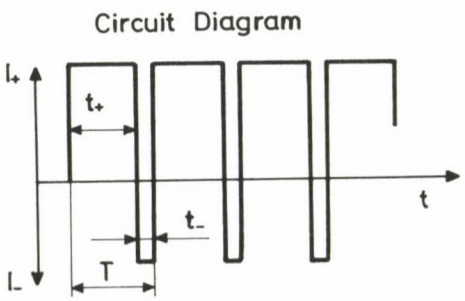

Fig. 2. Circuit Diagram of current-reversal technology (/3/, Fig. 1)

periods of time (t_+), copper and impurities more electronegative than copper are dissolved on the anode while copper is deposited on the cathode. During the shorter reverse current periods of time (t_-), the electrodes change roles with the cathodes functioning as anodes while the anodes as cathodes. The time of a cycle (T) is the sum of forward current period of time and reverse current period of time. Proper selection of the length and ratio of the forward and reverse current periods of time, as well as that of the ratio and magnitude of the corresponding current intensities results in a reasonable electric efficiency of the PCR-technology not reducing it significantly as compared to the efficiency of DC copper refining.

Investigations described in this work have been designed to determine parameters for current supply and technology which are most favourable in respect of specific energy consumption. The effect of factors affecting numerical characteristics proportional to specific energy consumption has been investigated by evaluation of the results of laboratory experiments based on a complete factorial experiment programme of type 2^n, using the methods of mathematical statistics.

The effect of factors on specific energy consumption has been evaluated on the basis of measured values of cathodic polarization (y^e_{kp}), anodic polarization (y^e_{ap}) and cell voltage (y^E) as well as of calculated values of the specific energy consumption (y^N). The effective current efficiency averaged at 92.40% in the investigated range of factors and this value was not affected significantly by the change of the factors.

From among factors considered to be important on the basis of preliminary information, the following factors have been varied:

— current density (x_1),
— time of the forward and reverse current periods (x_2),
— ratio of the forward and reverse current intensities (x_3), and
— anode-cathode distance (x_4)

the variation interval of the factors investigated being tabulated in Table 1.

The experimental set-up is schematically illustrated in Fig. 3. In determining the dimensions of the model equipment, the criterion of similarity has been to ensure the same current density as that under operating conditions. The dimensions of the experimental anode, cathode and tank are 1/100 of the electrodes and tanks used at the Electrolytic Copper plant of Csepel Works. Other factors affecting the numerical characteristics investigated have been fixed at a constant value in the course of measurements.

Table 1 Range of variation of the factors investigated

j	factor, $\tilde{x}_j$	$\tilde{x}_{ja}$	$\tilde{x}_{jo}$	$\tilde{x}_{jy}$	I	unit of measurement
		$x_j=-1$	$x_j=0$	$x_j=+1$		
1	current density	250	300	350	50	A/m^2
2	time of the forward and reverse current periods	10(0.5)	15(0.75)	20(1)	5(0.25)	s(s)
3	ratio of the forward and reverse current intensities	2.35	2.425	2.5	0.075	A/A
4	anode-cathode distance	30	35	40	5	mm

Table 2 Average value of numerical characteristics

i	x_1	x_2	x_3	x_4	y^e_{ap}	y^e_{kp}	y^E	y^N
					y_i	y_i	y_i	y_i
1	-	-	-	-	11.36	18.01	109.06	104.54
2	+	-	-	-	11.50	12.09	137.00	128.66
3	-	+	-	-	7.99	11.20	99.76	93.41
4	+	+	-	-	9.19	14.15	136.79	128.24
5	-	-	+	-	8.79	12.87	101.60	95.21
6	+	-	+	-	10.53	12.69	136.48	124.00
7	-	+	+	-	8.55	11.51	101.70	93.03
8	+	+	+	-	8.07	12.21	103.80	124.63
9	-	-	-	+	7.34	12.54	116.37	113.88
10	+	-	-	+	11.05	19.36	154.69	146.80
11	-	+	-	+	6.84	13.74	116.36	114.49
12	+	+	-	+	10.32	12.63	153.12	141.35
13	-	-	+	+	7.73	10.84	115.99	110.21
14	+	-	+	+	8.73	12.96	157.02	148.82
15	-	+	+	+	6.98	10.73	117.82	113.82
16	+	+	+	+	8.64	13.21	158.72	150.13

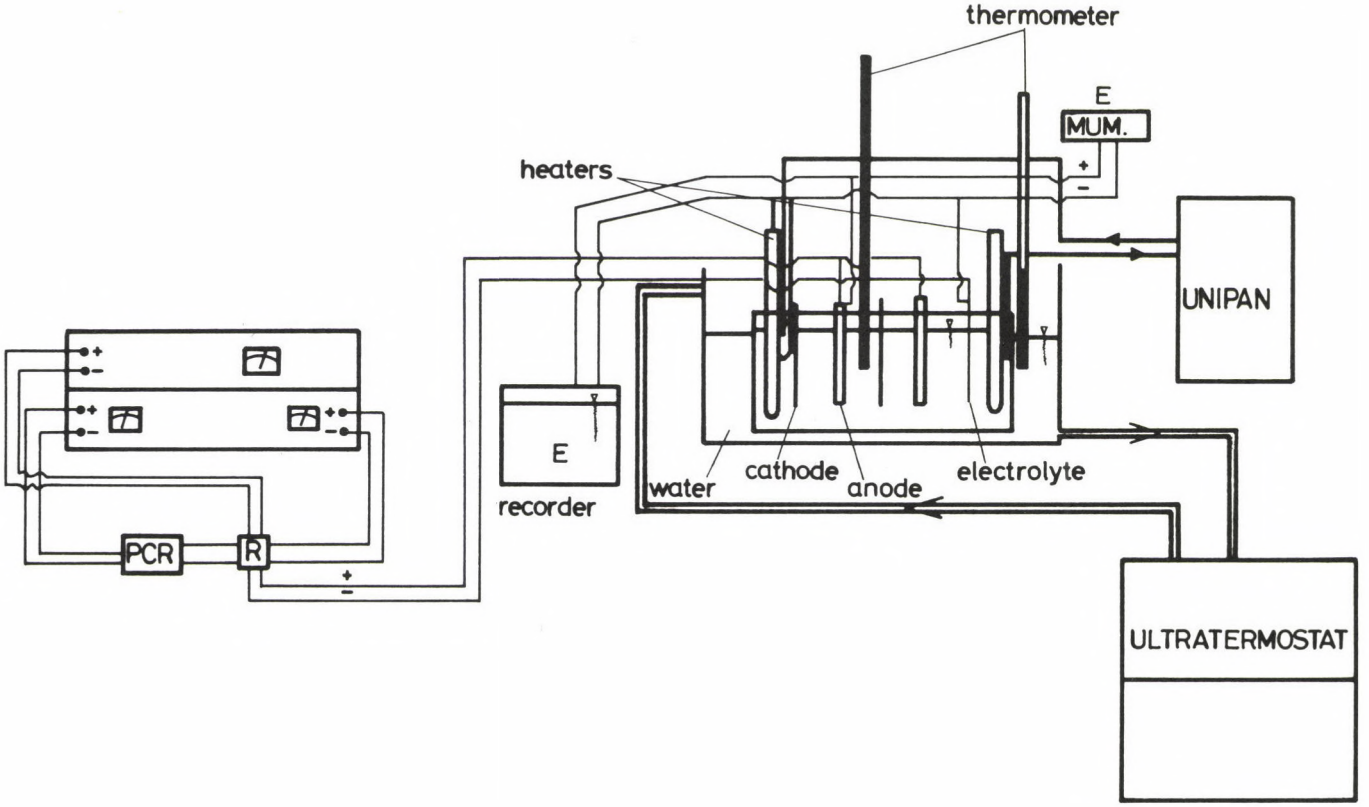

Fig. 3. Schematical illustration of experimental set-up (/4/, Fig. 9)

The material of the experimental anode and cathode is the same as the material of the industrial-size electrodes. The copper content of the electrolyte has been adjusted to 40 g/dm^3 while the sulphuric acid content to 190 g/dm^3. The electrolyte has been circulated by means of UNIPAN micro-pump. In the tank, the electrolyte has been heated to 55 ^{o}C by means of a tubular resistance heater. Constant operating temperature has been ensured by water bath heated by a circulation thermostat. The current of the supply operating in current generator mode has been converted into square-wave current by an electronically controlled relay.

Each measurement has been repeated once. The integral mean values in time, referring to the different experimental settings of the numerical characteristics investigated are tabulated in Table 2.

Agreement of variances has been tested using Cohran's hypothesis test. A comparison of values G and G_{kr} in Table 3 indicating the results of calculation shows that the assumption concerning the agreement of the variances has been correct.

In evaluating the results of measurement, regression equation

$$y = b_o + b_1x_1 + b_2x_2 + b_3x_3 + b_4x_4 + b_{12}x_1x_2 + b_{13}x_1x_3 + \\ + b_{14}x_1x_4 + B_{23}x_2x_3 + b_{24}x_2x_4 + b_{34}x_3x_4 + b_{123}x_1x_2x_3 + \\ + b_{124}x_1x_2x_4 + b_{134}x_1x_3x_4 + b_{234}x_2x_3x_4 + b_{1234}x_1x_2x_3x_4 \quad (1)$$

was used to describe the relationship between numerical characteristics and transformed values of the factors. The coefficients of four-variable polynomials were determined by means of the least squares method. The values so obtained are tabulated in Table 4.

The significance of the coefficients was tested by means of Student's statistical test. Values t used as a measuring variable are tabulated in Table 5, from among which those corresponding to the significant coefficients are marked with an asterisk.

Fisher's test was used to make sure that the models were adequate. Values F in Table 6 prove that models containing significant coefficients only, described by incomplete biquadratic polynomials

$$y^{e}_{ap} = 8.98 + 0.78\ x_1 - 0.65\ x_2 \quad , \quad (2)$$

Table 3 Standard deviation of the values of numerical characteristics
$G_{kr}(1;16) = 0.4546$

S_i^2	y_{ap}^e	y_{kp}^e	y^E	y^N
S_1^2	1.39	17.18	0.63	8.95
S_2^2	0.19	0.70	0.00	0.63
S_3^2	0.24	2.20	0.57	24.71
S_4^2	0.43	0.73	5.85	14.85
S_5^2	0.90	22.78	2.64	0.00
S_6^2	2.31	2.28	3.48	10.21
S_7^2	0.10	10.41	3.35	4.29
S_8^2	3.17	10.11	8.04	41.59
S_9^2	0.56	0.61	0.01	8.78
S_{10}^2	6.12	2.20	1.57	12.05
S_{11}^2	1.02	20.43	5.38	20.87
S_{12}^2	2.25	3.21	0.00	5.99
S_{13}^2	0.00	0.13	0.08	58.21
S_{14}^2	0.73	1.69	1.53	40.41
S_{15}^2	0.04	2.20	0.28	0.99
S_{16}^2	0.07	0.72	0.50	0.16
ΣS_i^2	19.54	97.58	33.92	252.69
G	0.31	0.23	0.24	0.23

$$y^E = 127.71 + 17.87\,x_1 - 0.82\,x_2 + 8.56\,x_4 + 1.75\,x_1x_4 + \\ + 1.06\,x_2x_4 + 1.31\,x_3x_4 - 0.84\,x_1x_2x_3 + 1.02\,x_1x_2x_3x_4 \quad , \tag{3}$$

$$y^N = 120.70 + 15.88\,x_1 + 9.24\,x_4 \quad , \tag{4}$$

showed good fit in case of the numerical characteristics except for cathodic polarization. Change of cathodic polarization in the factor space investigated is described adequately by the following equation:

$$y_{kp}^e = 13.17 + 0.49\,x_1 - 0.75\,x_2 - 1.04\,x_3 + 0.08\,x_4 + \\ + 0.13\,x_1x_2 + 0.15\,x_1x_3 + 0.80\,x_1x_4 + 0.53\,x_2x_3 - 0.27\,x_3x_4 +$$

$$+ 0.02\, x_1x_2x_3 - 1.08\, x_1x_2x_4 - 0.29\, x_1x_3x_4 + 0.17\, x_2x_3x_4 + \quad (5)$$

$$+ 1.02\, x_1x_2x_3x_4$$

where only b_0 is significant.

Table 4 Coefficients of interpolation polynomials

b_j	y^e_{ap}	y^e_{kp}	y^E	y^N
b_0	8.98	13.17	127.71	120.70
b_1	0.78	0.49	17.87	15.88
b_2	-0.65	-0.75	-0.82	-0.81
b_3	-0.47	-1.04	-0.19	-0.72
b_4	-0.52	0.08	8.56	9.24
b_{12}	-0.05	0.13	0.10	0.32
b_{13}	-0.29	0.15	0.37	1.03
b_{14}	0.45	0.80	1.75	0.96
b_{23}	0.21	0.53	0.56	1.23
b_{24}	0.39	0.07	1.06	0.82
b_{34}	0.04	-0.27	1.31	1.53
b_{123}	-0.15	0.02	-0.84	-0.26
b_{124}	0.10	-1.08	-0.31	-1.37
b_{134}	-0.28	-0.29	0.50	0.85
b_{234}	-0.16	0.17	0.07	-0.01
b_{1234}	0.26	1.02	1.02	0.73

Polynomials 2 through 5 permit the following conclusions to be drawn:

— Cathodic polarization is not affected significantly by any of the factors investigated because, as compared with the measuring error, changes of the numerical characteristic in the investigated range of factors is small. Under the given circumstances, y^e_{kp} as a numerical characteristic of the current-reversal technology is not sensitive enough.

— As shown by equations 2 thru 4, the numerical characteristics are most affected by changes in current density (x_1). Increasing current density affects the process unfavourably in each case. On a probability level (95%), an increase of current density from 250 A/m^2 to 350 A/m^2 results in an increase of 1.56 mV in anodic polarization, 35.56 mV in cell voltage and 31.75 kWh/t in specific energy consumption. The significant effect of current density is clearly shown by the fact that the above changes of the numerical characteristics are 17.1%, 55.1% and 31.75% of the overall change resulting from the factors in general.

Table 5 Significance test of the coefficients of interpolation polynomials
$t_{kr}(16) = 2.12$

t_j	y^e_{ap}	y^e_{kp}	y^E	y^N
t_0	32.49*	21.33*	350.81*	121.49*
t_1	2.82*	0.79	49.19*	15.98*
t_2	2.37*	1.22	2.26*	0.82
t_3	1.72	1.69	0.52	0.73
t_4	1.89	0.13	23.50*	9.30*
t_{12}	0.17	0.22	0.27	0.32
t_{13}	1.04	0.24	1.00	1.04
t_{14}	1.64	1.29	4.82*	0.97
t_{23}	0.76	0.86	1.55	1.24
t_{24}	1.43	0.12	2.92*	0.83
t_{34}	0.14	0.44	3.61*	1.54
t_{123}	0.54	0.03	2.31*	0.26
t_{124}	0.36	1.75	0.86	1.38
t_{134}	1.01	0.47	1.34	0.86
t_{234}	0.59	0.28	0.20	0.01
t_{1234}	0.94	1.65	2.80*	0.73
$S^2_{\{y\}}$	1.22	6.10	2.12	15.79
$S_{\{b_j\}}$	0.28	0.62	0.36	0.99

Table 6 Test of the goodness of fit of the model

	y^e_{ap}	y^e_{kp}	y^E	y^N
S^2_{ill}	2.93	0.39	3.85	27.13
$S^2_{\{y\}}$	1.22	6.10	2.12	15.79
f	13	1	7	13
F	2.30	0.06	1.82	1.72
F_{kr}	2.38	4.50	2.65	2.38

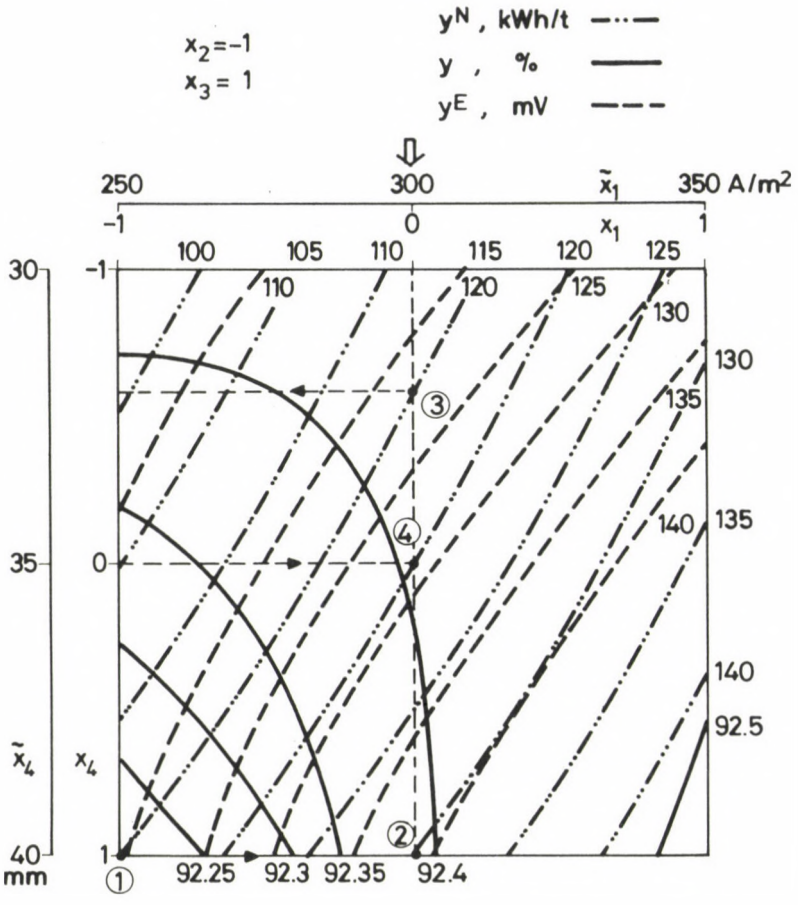

Fig. 4. Change of cell voltage, current efficiency and specific energy consumption as a function of current density and anode-cathode distance

— Only the values of anodic polarization and cell voltage are affected significantly by changes in the cycle time (x_2). In case of a constant ratio of times for forward and reverse current periods (20:1), increase of the value of cycle times results in reduction of the voltages investigated.

— The anode-cathode distance affects only the cell voltage and specific energy consumption significantly. Increase of the anode-cathode distance from 30 mm to 40 mm results in an increase of 17.11 mV in cell voltage while 17.47 kWh/t Cu in specific energy consumption.

Given in Fig. 4 are iso-y curves for a cycle time of 10 sec (0.5 sec) and a forward to reverse current ratio of 2.5 A/A. The Figure permits the following conclusions to be made:

— A current density of 250 A/m^2 and an anode-cathode distance of 40 mm are used at the PCR plant of Csepel Works at present (1 in Fig. 4). Accordingly, the value of cell voltage is about 120 mV. In case of a current efficiency above 92.2%, this cell voltage results in a specific energy consumption of 115 kWh/t Cu.

— With the current density increased to 300 A/m^2 but with constant anode-cathode distance the specific energy consumption increases to 130 kWh/t Cu in case of η = 92.35 — 92.40 % (2 in Fig. 4), which is an increase of 13%.

— This increase in specific energy consumption resulting from increased current density can be avoided only by reduction of the anode-cathode distance to 32 mm (3 in Fig. 4).

— If, for fear of short circuit, the anode-cathode distance can be reduced to only 35 mm, the specific energy consumption will increase to 120 kWh/t Cu, which is an increase of about 4.5% (4 in Fig. 4).

At the Electrolytic Copper Plant, PCR cell voltages of 218 mV, 333 mV and 450 mV were measured per cathode cycles while the average value for the entire anode cycle was 337 mV.

The average value of cell voltage (128 mV) measured under laboratory conditions is comparable only with the value measured in the first cathode cycle, the difference resulting from voltage drops on conductors and contacts which are not independent from the current density.

Under operating conditions, the specific energy consumption amounts to 204 kWh/t in the first cathode cycle while to 316 kWh/t over the entire anode cycle in case of an electric efficiency of 90%. An increase of the current density from the present value of 250 A/m^2 to 300 A/m^2, a value determined by the capacity of the rectifier, is expected to result in a specific energy consumption of about 230 kWh/t in the first cathode cycle while about 320 kWh/t over the entire anode cycle.

As suggested by the results of laboratory and industrial-scale experiments, it seems reasonable to continue also industrial-scale experiments because significant savings in energy are promised by the results.

REFERENCES

1. Horváth, Z.: Change in specific energy consumption in electrolytic copper refining (in Hungarian). 4th Metallurgical Days, Balatonaliga, Oct. 5—7, 1983

2. Mrs. Szepessy, A., Majoros, M., Mihalik, A.: Investigation of a possible increase of current efficiency in electrolytic refining of copper. Development of electrolysis (in Hungarian). 5th Metallurgical Days, Balatonaliga, Oct. 1—3, 1986

3. NME, Department of Metallurgy: Investigation of electrolytic copper refining by pole reversal. Miskolc, 1986 (Final Report, in Hungarian)

4. Hertelendi, Á.: Diploma Work. Miskolc, 1987

5. Wöbking, H.: Kupferratinationelectrolyse mit Umkehrstrom. Elektrolyse Nichteisenmet. Paper No. 11. Met. Smin. Lüneburg, January 22—24 1981, Weinhaeim, 1982. 201—213

6. Petrescu, N.: Cercetari privind rafinarea cuprulni prin metoda electrolizei cu curent inversat periodic. Metalurgia. (RSR) 37, 1985 (7), 343—348

Acta Technica Acad.Sci.Hung., 101(2), pp. 185—197 (1988)

EFFECT OF DIFFERENT TECHNOLOGIES OF CORED WIRE TREATMENT ON THE QUALITY OF STEELS

TOLNAY, L. - TARDY, P. - KÁROLY, GY. - GHAZALLY, S.*

(Received: 30 April 1988)

Experiments carried out in the combined steelmaking shop of Lenin Metallurgical Works in Hungary proved the increasing importance of cored wire treatment in secondary metallurgy. From among the different possibilities the combination of CaSi-filled wire treatment in the ladle with Ca-cored wire treatment in the tundish offered the best solution. Efficiency of the treatment was strongly influenced by the control of oxygen level as well as by protection against reoxidation.

Introduction

Many different variations of complex ladle metallurgy treatment suitable for the quality improvement of steels have been developed in the last years, and many reference data dealing with this treatment can be found in the metallurgical periodicals too. Obviously it is no doubt, that in case of grades, where the very low C-content, the low gas-content or a special kind of alloying are desirable, we cannot renounce the using of vacuum during ladle metallurgy treatment; however, in case of making so called quality mass steels of lower value it is necessary to use the cheaper ladle metallurgy treatment (i.e. the powder blowing without vacuum and the feeding of Al-wire, the cored wire treatment or their combination) simply because of economical causes. It is considered, that in certain cases — i.e. during dephosphorization of steels of super low C-content or during microalloying — the powder blowing into the vacuum cannot be considered a fantastic method, however nowadays the most important question in Hungary on the field of ladle metallurgy is: Is it reasonable the general use of end-deoxidation with Al-wire as well as the cored wire treatment in operational conditions besides (or instead of) the Scandinavian lance powder blowing units becoming

*Tolnay, L., H—3540 Miskolc-Diósgyőr, Lenin Kohászati Művek, Hungary
Tardy, P., H—1025 Budapest, Galán u. 43/b, Hungary
Károly, Gy., H—3525 Miskolc, Szepesi P. u. 4, Hungary

Akadémiai Kiadó, Budapest

widespread in a short time and standing on a high technical level? The possibilities of the cored wire treatment, applied in a greater and even greater extent all over the world because of its optimal production-costs, are manifold in itself, first of all because their results can be extraordinarily influenced by the local circumstances. Therefore our purpose in Diósgyőr — where the steel is tapped from a 80 t LD-converter or from a 80 t UHP-furnace into a ladle lined with a so-called Stirodur-lining containing 47—48 % ZrO_2 — is to investigate the effects of different variations of cored-wire treatment, as an important part of the complex ladle metallurgy treatment, besides the strict oxygen-level-control, during making of steels microalloyed with B, or of low alloyed, case-hardened steels.

Role of cored wire treatment during casting of billets

Among the well-known and investigated variations of the cored wire treatment, the wire-feeding into the casting ladle is one of the most frequent methods, its different effect are suggestively summarized by T. Ototani in his book under the title: "Calcium Clean Steel", published not long ago /1/.

However, during casting of □-billets of ≤ 150 mm, — taking into consideration the fact, that technological difficulties arise during casting by using dip tubes, and the desoxidation by means of Al can be only limited because of the dangers of nozzle-blocking — the cored wire treatment can play a certain role in the course of continuous casting too, mainly in case, if steels microalloyed with elements showing a great affinity to the oxygen (i.e. B) are made. This method was used in Diósgyőr in the course of such a comparing test, when ⌀ 120 mm billets were casted; in this case Ø 4 mm wires were fed into the impact point of inpouring stream by a speed of 8—10 m/min, and by free direction, in the following way: an Al-wire was directed to one of the strands, a wire filled with CaSi to the other, and a wire filled with BTi to the third one.

On the basis of investigation results it has been proved /2/, that even during continuous casting, if the quantity of Al is <0.007% and ~ 400 g/t of CaSi is fed, an improvement of the inclusion-morphology can be detected, but this effect is strongly sensitive to the oxygen-level. As a result of it the Ca can be built in the aluminate-inclusions and it forms

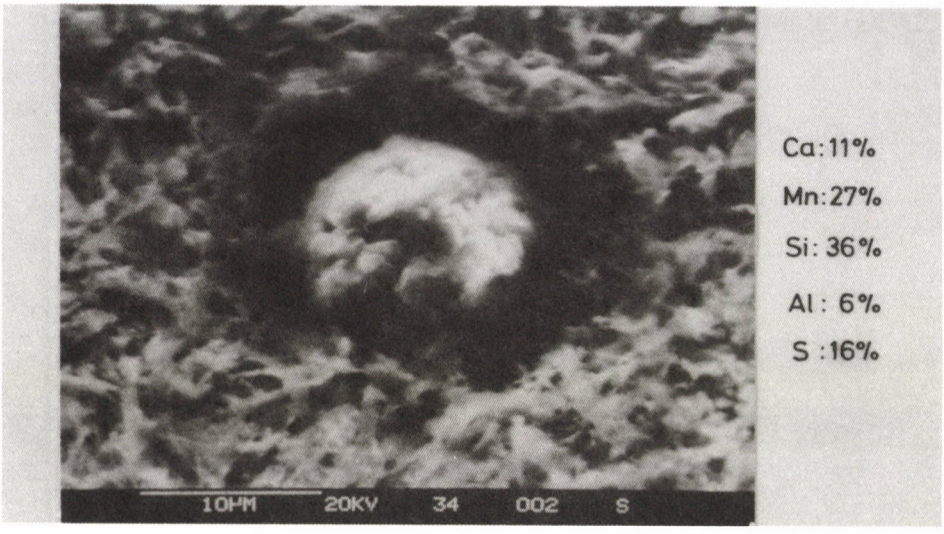

Fig. 1. Effect of CaSi fed into the □120 mm crystallizer in a quantity of ~400 g/t on the inclusion-morphology of AlSl 100 grade steels

complex oxisulphide inclusions (Fig. 1), however a significant part of them does not reach the size (20—30 μ), which is able to float to the slag-foam.

Unfortunately, as the control of oxygen-level is not satisfactory, the effect of adding BTi can be detected only in the Mn-silicates, the angular Ti-carbide (carbonitride) inclusions do not appear, dissolved B-content does not remain in the steel. After all — in order to improve the accuracy of microalloying with B — these investigations give us an inspiration to control strictly the oxygen-level even in the casting ladle, i.e. to develop such variations of the control of oxygen-level, in case of which the CaSi-wire can be fed into the casting ladle.

Role of cored wire treatment in the casting ladle

One of the difficulties of using this method considered as a classical one nowadays, that the results are extraordinary influenced by the local circumstances. In our paper — apart from the details of adaptation experiments — we describe, that the best results of cored wire treatment in the casting ladle have been obtained /3/, when a Ø 13 mm wire, filled with CaSi, has been fed into the bath of the 80 t ladle lined with

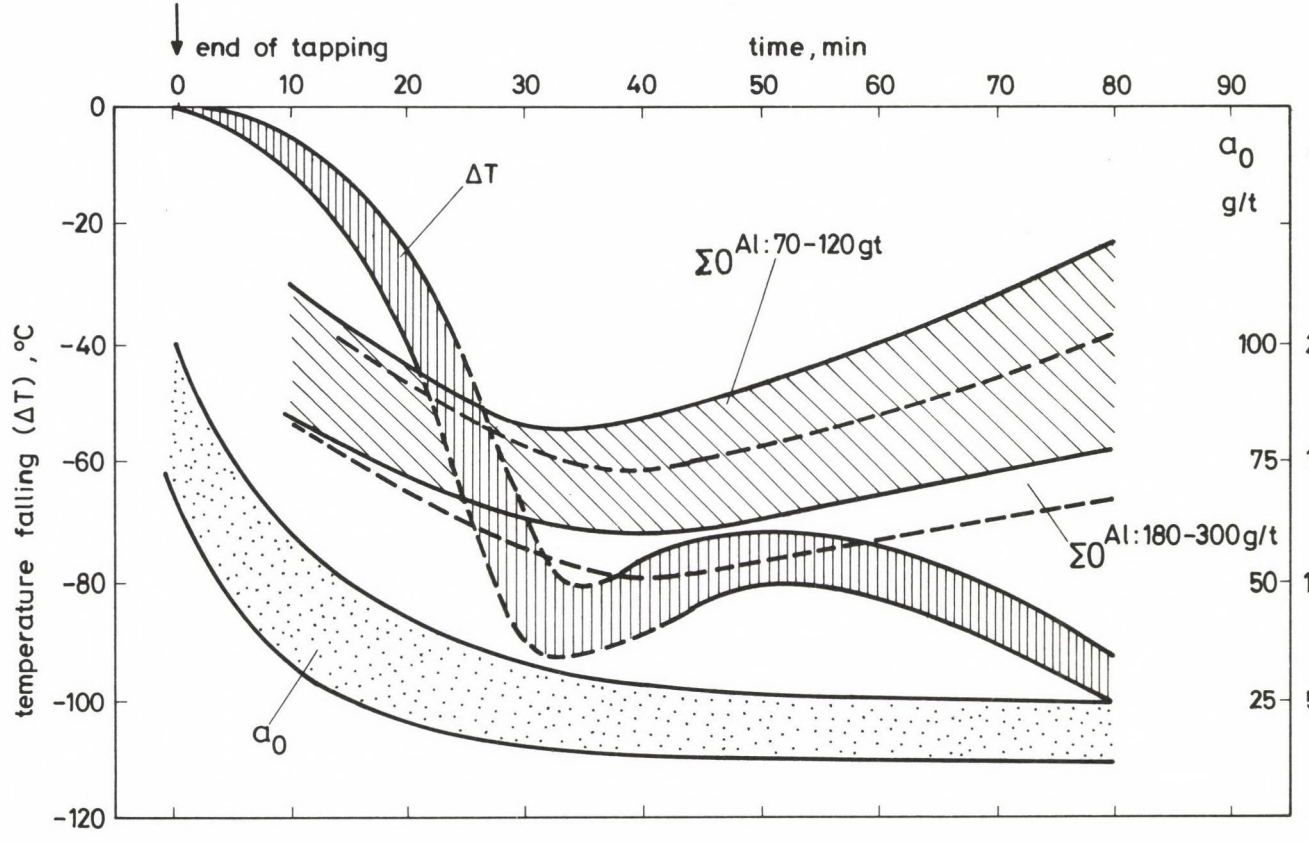

Fig. 2. Temperature-change of steels and the dissolved as well as Σ oxygen-contents from the end of tapping in the ladle, in the course of cored wire treatment with 0.7 kg/t of CaSi

ZrO_2, by a nominal speed of 100 m/min, for about ~5 min (in a quantity of 0.7—0.8 kg/t), during argon-bubbling. In this case (Fig. 2) the effect of CaSi cored wire treatment on controlling the oxygen level can be precisely detected, till the ΣO-content does not increase. Unfortunately, during casting without protective tube and dip tube the reoxidation has such an extent, that the increase of Σ-oxygen-content can be detected both in the presence of Al of a quantity of ϕ120 g/t and 180—300 g/t. Therefore there are 3 possible variations:

1. In case of $\left[Al_{dissolv.}\right]$ = 0.007% and of greater billet sections, it is necessary to add 15—30 kg of Al to the 80 t charge, following the predeoxidation with Mn+Si, then it is necessary to ensure the entire protection against reoxidation by using protective and dip tubes. Otherwise, for example if 20XH3A Cr-Ni case-hardened steels are continuously casted with a full protection (i.e. a protective tube between the ladle and tundish and a dip tube between the tundish and the crystallizer), our experience is, that the cored wire treatment does not play a direct role in controlling the oxygen-level, because the measured dissolved oxygen level is under the value of 3 g/t even without using this treatment in normal circumstances. Of course, the entire protection is economical merely if steels of greater value are made with a section of □ ≥150 mm.
2. According to our investigations, in case of $\left[Al_{dissolv.}\right]$ = 0.005—0.007% and of greater billet-sections, the quantity of Σ Al necessary of making the Al-deoxidation can be calculated as follows:

$$\Sigma\,Al,\ kg/t = (a+b\ .\ [a_o]_{converter} + [Al_{dissolv.}])\ .\ G_{ladle}\ .\ 10^{-2}$$

where:

G_{ladle} — the capacity of the ladle (t)

$[a_o]_{converter}$ — oxygen-level in the converter during tapping (ppm)

a, b — constants depending on the steel-grade (at BCMo2-grades, according to our measurements $a=1.6 \cdot 10^{-2}$, $b=1.6 \cdot 10^{-4}$)

This means, it is necessary a quantity of 1.2—1.4 kg/t of steel. This quantity, which is about the 2/3 part of the calculated, relatively great amount of Al, can be added into the steel-bath in the ladle during tapping, after that the 1/2—3/4 part of the ladle had been be filled with steel; the rest of the calculated amount can be fed into the bath

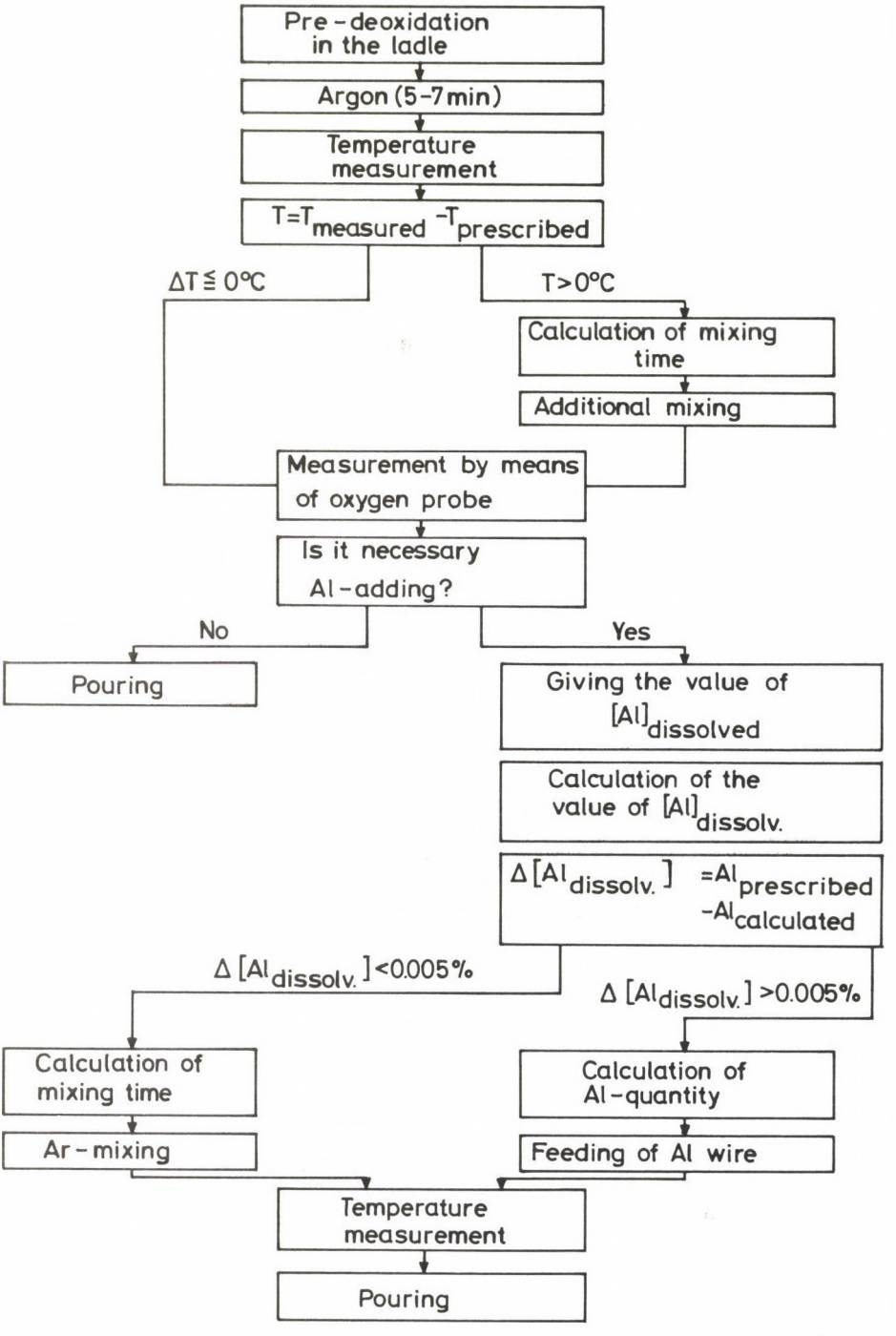

Fig. 3. Flow-diagram of oxygen-level control with Al-deoxidation by means of a computer

only by means of Al-wire-feeding, after the oxygen-probe-measurements according to Fig. 3, — during intensive or less intensive Al-bubbling — through a furnace slag tapped into the ladle only in a small quantity, and corrected satisfactorily with slag-forming materials. Though Fig. 3 does not show, but if the value of desired $[Al_{dissolv.}]$ cannot be guaranteed on the basis of the results of oxygen-probe-measurements, then — besides the additional feeding of Al-wire — the following favourable effects can be obtained by feeding a wire filleg with CaSi into the ladle, in a quantity of 0.6—1.0 kg/t calculated for Ca:

- the satisfactory degree of cleanliness (the low value of $[a_O]$)
- the satisfactory value of $[Al_{dissolved}]$
- the further improvement of desulphurization
- the further improvement of η_{Al}.

3. If the section of billets is $\square \leq 150$ mm, the protection against reoxidation is strongly limited, therefore it is necessary to use the cored-wire treatment in the tundish too, within the limits of economy. Namely if our purpose is to make the microalloying process with a good efficiency at the end of a really complex ladle metallurgy treatment, then the ΣO-content cannot be increased if the active oxygen level is decreased.

Role of cored wire treatment in the tundish

In Diósgyőr, our tundishes, used at the 5-strand CCM, have a fireclay lining, with a coating containing MgO. It has been proved by practice, that if the basic coating is suitable, then the lining — as a reoxidation resource — has no special influence, even in case of many sequence-castings. In order to maintain the uniform temperature- and composition-distribution when the cored wire is fed into the bath in the tundish, it was established, that it is necessary to feed the wire of Ø 8 mm into the bath by a speed of 8—10 m/min in the surroundings of the inpouring stream; in this case the wire immerses into the bath to 40—45 cm, till it is fully melted, the quantity of material to be fed corresponds to a value of 0.6—0.65 kg/min, or ~0.3 kg/t. Though it is a well-known fact, that wires filled with CaSi are used in this case in many steelworks, according to our investigations CaSi cannot be fed into the tundish; here the treatment with a wire filled with metallic Ca can be merely reasonable in order to reach the value of Ca/Al $\geq$0.015 /4, 5/. However, it is very favourable both from the point of view of temperature- and oxygen-level-change.

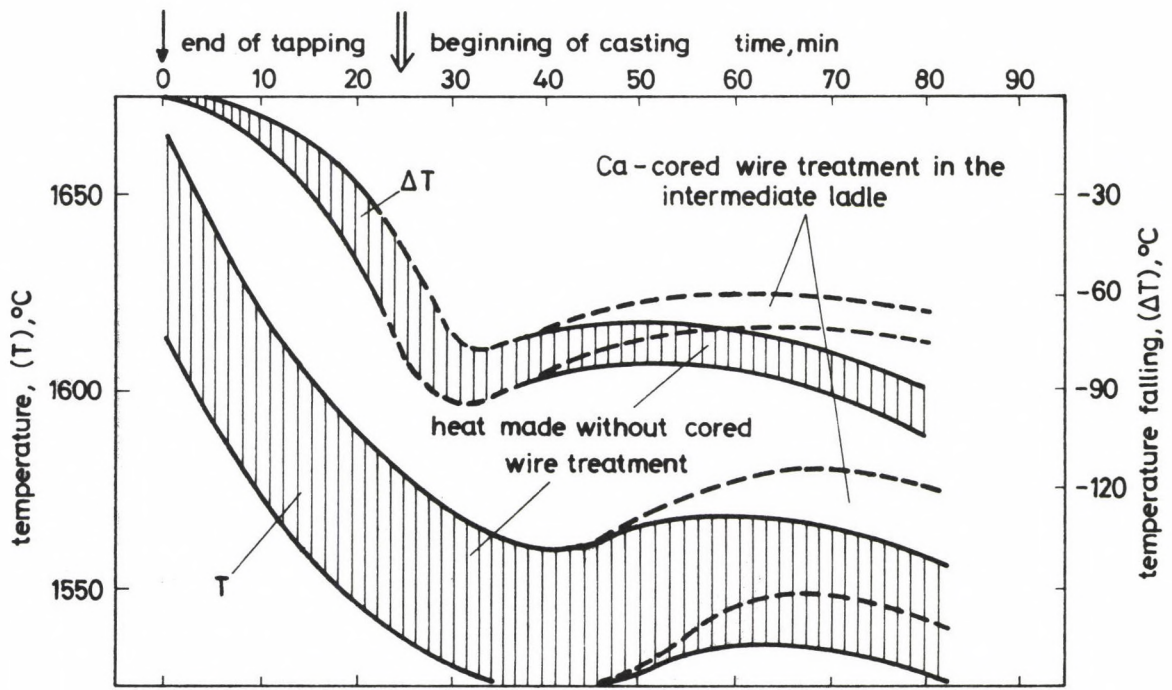

Fig. 4. Changes of temperature in the ladle from the end of tapping, during traditional steel-making, as well as in the course of Ca-cored wire treatment in the intermediate ladle

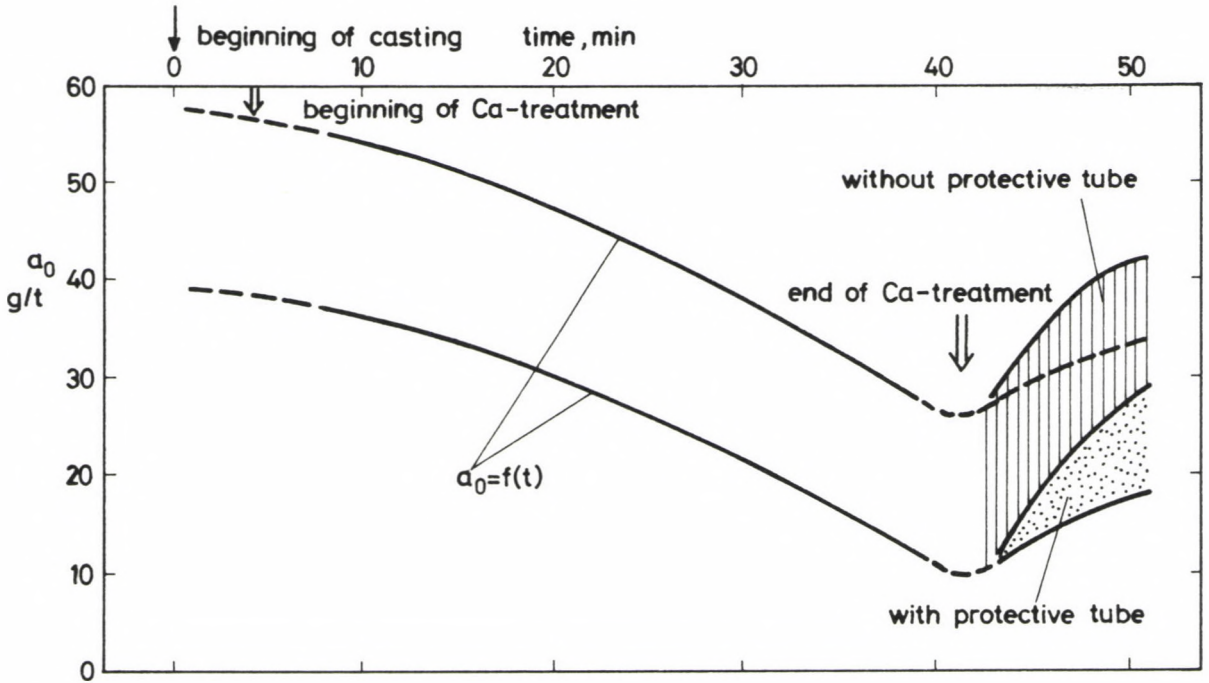

Fig. 5. Change of the dissolved oxygen-content (a_o) depending on the time passed from the beginning of casting during Ca-cored wire treatment with protective tube, as well as following the treatment

It is a well-known fact, that the heat-loss is $2.5 \pm 0.2^{\circ}C$/min during the average 20—25 min passed from the end of tapping till the beginning of casting (Fig. 4). In the tundish — mainly at the first heat of the sequence-casting — the cooling is strong, especially in the first minutes, then, after the heat-equalization, a small re-heating can be observed, after, in the course of the further casting, the value of temperature-decrease is in average $0.9 \pm 0.2\ ^{\circ}C$/min during the 50—60 min passed till the end of casting. The same or similar temperature-change can also be observed in case, if the steel is treated with a CaSi-cored wire of Ø 13 mm for 5 min, in the casting ladle.

However, the situation is much favourable, if a wire filled with Ca, is used in the tundish. As the feeding of Ca into the bath is a strongly exothermic process, the reheating period takes place later and the cooling during casting becomes slower if the mentioned quantity of Ca (~ 0.3 kg/t) is fed into the bath, so a temperature-difference of about 25—30 $^{\circ}C$ can be observed to the advantage of the Ca-wire. Its favourable utilization results obviously in significant energy-savings even so far as the entire charge-production is concerned; it is not necessary to analyse it here, however it has to be utilized by all means as a very important metallurgical advantage.

As to the oxygen-level control (Fig. 5), the dissolved oxygen content can be decreased to a value of 10—12 g/t under the influence of the cored wire treatment in the tundish, in spite of the fact, that evidently greater oxygen-contents belong to temperatures greater by 25—30 $^{\circ}C$. However, it is also true, that it is necessary to add Al in a quantity of min. 350—500 g/t for the reoxidation, in order to avoid the increase of ΣO-contents. By all means it is a very interesting observation, so far as the effect of Ca-treatment is concerned, that if the Ca-treatment is stopped and the steel is not protected with a so-called protective tube between the ladle and intermediate ladle, the oxygen level immediately increases by a value of 6-10 ppm under the influence of the reoxidation.

Conclusion

Naturally, the application of the cored wire treatment at the tundish increases the costs and it is a complicated solution from technical aspects too, however — for the suitable controlling of oxygen-level — the

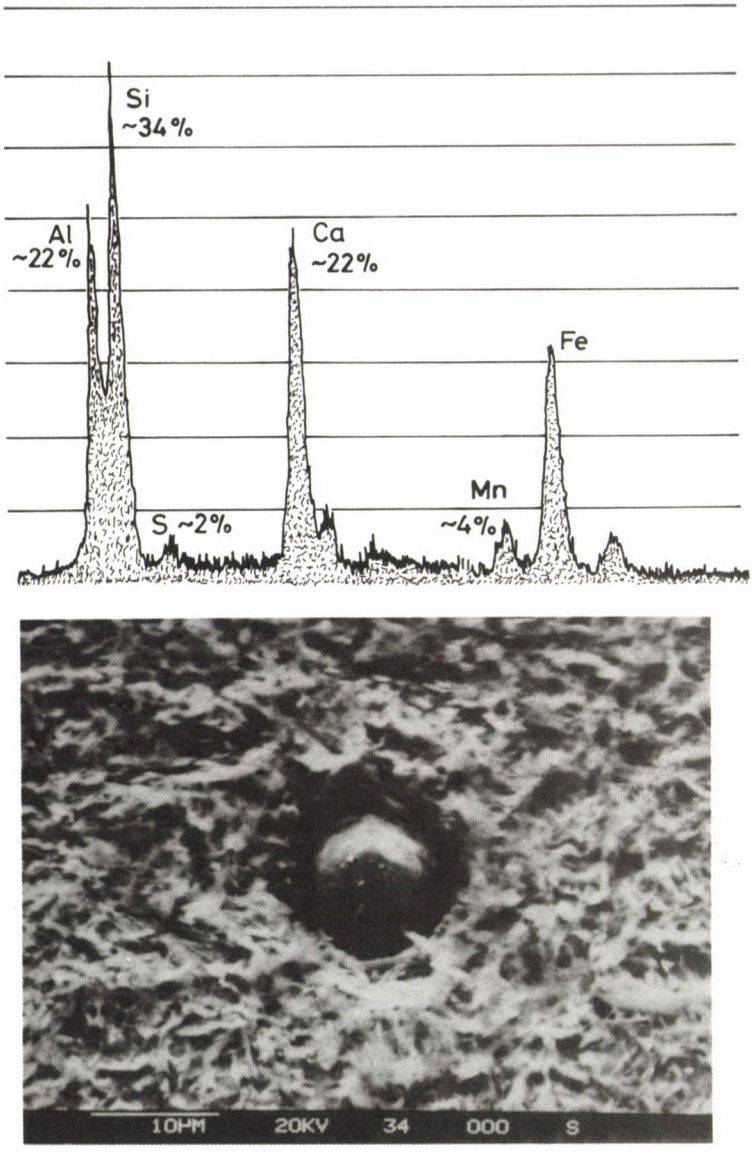

Fig. 6. The image and composition of the characteristic complex inclusion in the AlSi 100 grade steelbillet treated with CaSi cored wire in the ladle, and with Ca-cored wire in the intermediate ladle

CaSi cored wire treatment in the casting ladle + Ca-wire treatment in the tundish guarantee the optimal complex ladle-metallurgy solution, from both economical and technical point of view. Of course, in case of unalloyed steels refined with Ca/Al = 0.02—0.05% — in order to avoid the nozzle-narrowing — it is also very important in the future to ensure the satisfactory pre-deoxidation (possibly slag-free tapping or in the absence of it a satisfactory slag-reduction, then the precise feeding of deoxidation materials into the bath), to influence favourably the inclusion-morphology (to guarantee the value of Ca/Al >0.15 in the ladle by means of a CaSi cored wire treatment), and at last to protect the steel against the end-deoxidation (by means of a Ca-treatment in the tundish, and perhaps by an Al-wire treatment at the crystallizer). In this case the remaining inclusions (Fig. 6) are characteristic globulitic complex inclusions with a relatively high Ca-content. In case of alloyed steel — i.e. in case of CrNi case hardened steels — besides the protective tube between the casting ladle and tundish it is necessary to use a dip tube too at the crystallizer in order to protect the steel against reoxidation; the application of at least the protective tube seems to be necessary in case of making unalloyed steel too. It gives a guarantee for the industrial application of the cheaper, but suitable effective technology of cored wire treatment for microalloying.

Making ⌀ ≦150 mm billets, the results of treatment are uncertain, because the route between the tundish and the crystallizer causes a significant reoxidation resource, if dip tube is not used in the system (this can be only partly compensated by the Al-wire feedable into the pool), therefore in Diósgyőr nowadays a method has been being developed, according to which pre-billets would be made instead of small billets during making quality steels; in this case the formation causes extra-costs, however the production of billets of excellent quality can be guaranteed by the perfect protection against reoxidation.

REFERENCES

1. Ototani, T.: Calcium Clean Steel, Springer-Verlag, Berlin. 1986.

2. Tolnay, L.- Károly, Gy.- Tardy, P.: Experiments for Feeding Cored Wires into the Mold of CCM, "Clean Steel", Balatonfüred, 2—4 June, 1986.

3. Tolnay, L.- Károly, Gy.: Improvement of cleanliness of steels made in UHP-furnaces with increased intensity of oxygen-blowing, by means of complex ladle-metallurgy treatment, "Fifth Int. Congress", Washington, 6—9 April, 1986

4. Tolnay, L. - Varga, S. - Károly, Gy. - Szegedi, J.: Improvement of cleanliness of electric steels by complex ladle-metallurgy treatment, La metallurgia italiana 6/87, 453—460

5. Tolnay, L. - Mezei, J. - Tardy, P. - Károly, Gy.: Improvement of costability of continuously cast billets by cored wire treatment, "Int. Steelmaking Conference", Pittsburg, 1987, 97—102

Acta Technica Acad.Sci.Hung., 101(2), pp. 199—225 (1988)

COMPUTER AIDED ROLL PASS DESIGN FOR I-BEAMS

VOITH, M. - GULYÁS, J. - DERNEI, L. - ZUPKÓ, I. - HERENDI, R.*

(Received: 13 May 1988)

The technology of rolled sections is based on groove design. This process implies a great number of partly iterative calculations and constructions. Describing the design of a rolling schedule for an I-beam the present work exemplifies a computer system enabling the construction of consecutive grooves and partial areas of them in accordance with the permanent physical aspects concerning the plastic deformation; in addition to the computer a plotter unit can trace each grooves in an optional scale.

The present study also implies the changes of temperature of the rolled sections and the loading limits of the mill within the ranges and possibilities of the computer aided technology taking into consideration the conditions accompanied by the geometry of the groove design and tracing accomplished by means of a proper software.

Establishing resp. modifying a roll pass design for various finishing passes is a highly recurrent job. This designing and constructing work implies a regular succession of logical steps to be exactly formulated with a view of mathematics and therefore a computer aided carrying out of the required numerical and graphical analyses is highly recommended.

The mechanization and computerization of the above-mentioned task of computing and constructing is reinforced by the great volume and scope of this work as well: e.g. theoretically in a given case a finished section can be rolled set out from optional blooms of various sizes requiring a selection of the proper technology; a given finished section implies a great number of roughing passes and shaping grooves as well; the roll pass design has to be in accordance with the general layout of the mill (e.g. in an other mill a different amount of passes is practicable); in fact, modifying an existing technology would be justifiable also in the case when the loading level of a stand within the range of a rolling schedule exceeds the average one. The last-mentioned modification, i.e. reducing the peak-load

*Voith, M., H—3515 Miskolc-Egyetemváros, Hungary
Gulyás, J., H—3515 Miskolc-Egyetemváros, Hungary
Dernei, L., H—3515 Miskolc-Egyetemváros, Hungary
Zupkó, I., H—3515 Miskolc-Egyetemváros, Hungary
Herendi, R., H—1158 Budapest, Körvasút sor 110, Hungary

Akadémiai Kiadó, Budapest

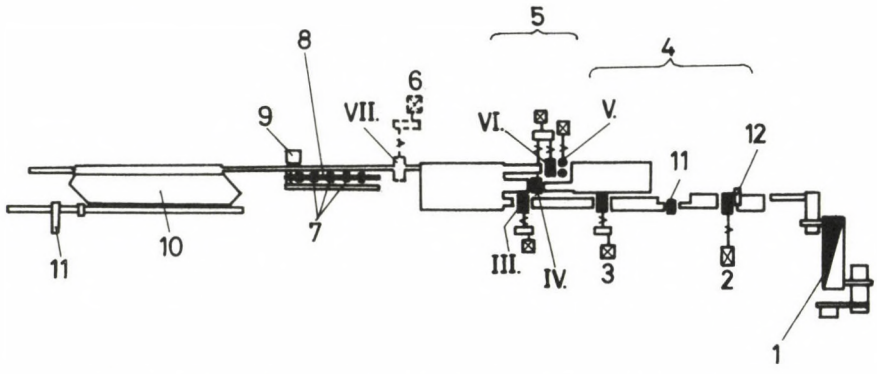

Fig. 1. Layout of the medium-size profile rolling mill is question
1. heating furnace, 2. I. reversing (two-high) stand, 3. II. (three-high) stand, 4. roughing stands, 5. (two-high) finishing train, 6. new universal stand to be inserted, 7. saws, 8. saw-track, 9. crops, 10. cooling bed, 11. shears

resp. passing this load to the adjacent passes and grooves is beneficial not only to the maintenance of an equal safety but enables a more intensified reduction of the initial temperature of rolling, reducing the specific energy consumption as well /1, 2, 3/.

A computer program performing the above-mentioned general tasks has to be developed in a practicable manner for each section-group resp. for each section (e.g. beams, girders, angle bars, pit rails etc.) too.
A program adaptable for the design of roll passes for I-beams within the 80—120 mm range of web height is presented as a model as follows. This program version has been developed by us for the roll pass design of both the normal (IN — tapered flange) beams and for the parallel-flanged (IPE) ones. The studies have been accomplished by us for a given rolling mill established for medium-size products (Fig. 1). The mill is supplied by a walk-beam heating furnace and consists of two groups of stands; the first stand of the roughing line is a two-high reversing stand and the second stand is a three-high one. The finishing section consists of two-high stands implying open passes (in cross-country arrangement); three of these stands have horizontal axis and the fourth stand (No. V) is an edging one. The stands No. IV and No. VI have a common geared motor.

1. Relations required for roll pass design

Our computer program developed for the design and tracing the grooves concerning the 80, 100, 120 and 140 mm parallel-flanged (IPE) beams (according to the German standard DIN 1025-5) and configured for each typical grooves (resp. finishing pass, leader pass, roughing-shaping pass) in accordance with the rules and laws of plastic deformation regarding the consecutive grooves as follows.

1.1 Finishing pass

The shaping pass of parallel-flanged I-girders can be performed only in an universal mill. According to some sources /4--9/ the small-size parallel-flanged (IPE) beams can be rolled by means of edging rolls integrated additionally in a two-high stand, i.e. by so-called roll-cases forming an auxiliary mechanism with edging rollers fit in replaceable and adjustable frame-beams.

Designing the rolls forming a finishing pass of universal type made by a roll-case the following aspects shall be considered (Fig. 2).

The dimensions of the web between the flanges of an I-beam are de-

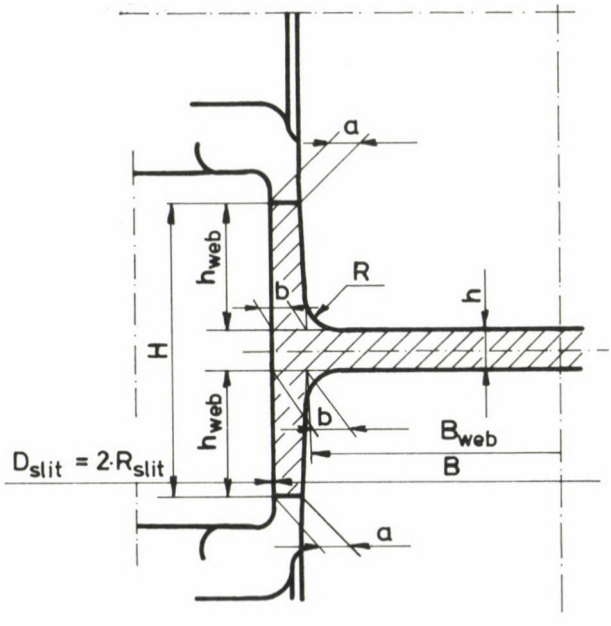

Fig. 2. Dimensions of the finishing groove

terminable by the "collars" (ribs or rings) formed on the horizontal rolls opposed with the grooves of finishing passes of normal joists in which the groove defines the whole height of web. Accordingly the breadth of shaping collars or ribs belonging to the horizontal roll (B_{web}) has to be dimensioned with an enlargement of 1.2% equivalent to the corresponding contraction of the section running out with a temperature of approx. 1000 ^{o}C, even as with an approximated reduction of 0.3% corresponding with the thermal expansion of the cold-machined collar expected in attaining the working temperature, i.e. designing shall be accomplished with a resulting multiplication factor of 1.009.

In addition an other dimensional change caused by roll wear may occur: diameters and breadths concerning the rolls can decrease during a remachining. The reduction of the roll diameter can be compensated by adjusting but the reduction of breadth shall appear in the reduction of the height of web concerning the finished section.

Owing to the mechanism of this wear phenomenon the new rolls have to be machined with a breadth augmented with a (for security reasons only) 50% value of positive rolling margin concerning a given IPE-beam:

B_{web} = 1.009 (nominal height of web -- double thickness of flange + half value of the positive rolling margin) =

$$= 1.009 \left[B - 2b \left(\frac{+\Delta}{2} \right) \right] .$$

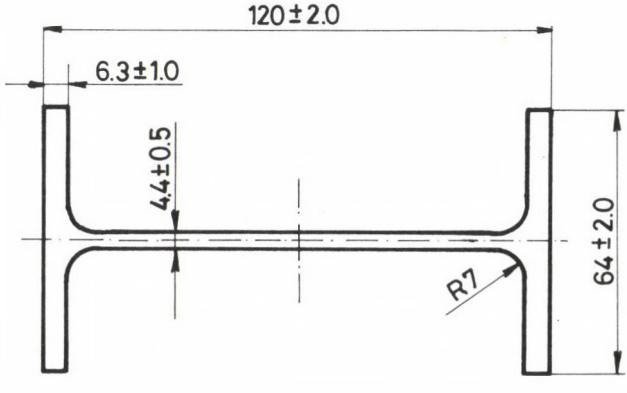

Fig. 3. Dimensions of an 120 IPE-beam

The normal dimensions of the exemplified 120 mm IPE-beams and the relating rolling margins are presented in Fig. 3.

The nominal thickness of flange and its tolerance range are controllable by adjusting the edging rollers fit in the roll-case. The rounding radius (R) set between the web and the flange is identical with the concerning normal radius of the finished beam-section.

The height of the flange (H) can be established by adjusting the roll gap of the leader (symmetrizing) groove, respectively — in the case when it is staying in the range of rolling margin — it will be possible by reducing the thickness of flange (b) or by enlarging (i.e. by adjusting the edging rollers) of it. Edging rollers are the same in the case of rolling of each section.

1.2 Leader (symmetrizing) pass

The dimensions of the rolled product leaving the leader grooves (Fig. 4) have to be enabling themselves to form in the finishing stand a parallel-flanged beam-section with dimensions presented in Fig. 3 — with an identical and constant elongation factor for all elements of section if possible. The elongation factor concerning the finishing pass is as follows:

$$\lambda_{web} = \lambda_{fl} = \frac{0.5(a' + b')\, h'_{fl}}{0.5(a + b)\, h_{fl}}$$

where the comma symbolizes the input dimensions of the sections further on too. The above average elongation factor has been assumed in such a way the reduction of the height of web to amount to a numerical value cut down to a round sum of one place of decimals and not to exceed the values of 0.6... 0.7 mm even in the case of the largest girder as follows:

$$\Delta h_{web} \leq 0.6...0.7 \text{ mm} \quad \text{and}$$

$$\lambda_{web} = \frac{h'_{web}}{h_{web}} = \frac{h_{web} + \Delta h_{web}}{h_{web}} \quad .$$

It is possible to equate the elongation factors concerning the areas of the web and the areas of the flanges, however the deformation within the area of a flange cannot be homogeneous. Assuming a value of $\lambda_a = 1.1$ for the elongation factor ($a' = \lambda_a \cdot a$) concerning the end of a flange, the

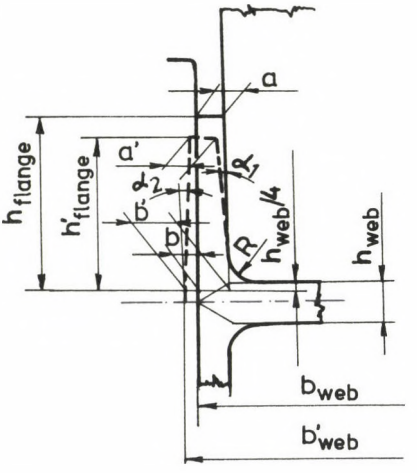

Fig. 4. Dimensions of the leader groove

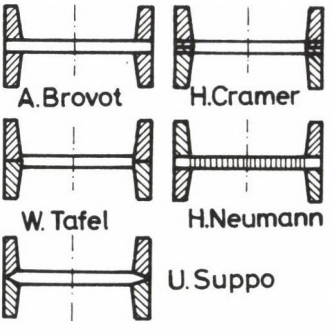

Fig. 5. Interpretation concerning the height offlange according to various authors

numerical value for λ_b concerning the transition of a flange has to be greater than the aforementioned one in the case when the designing features of the section-shaped stretching grooves are not of universal pass type having both the open and closed flanges a well-defined taper in the two-high rolls and in the three-high ones as well.

The elongation factor of the transition section of flange can be determined by the following formula:

$$\lambda_b = \vartheta \cdot \lambda_a \quad (\vartheta > 1.1)$$

performing it in such a way that the existent cutting pass remains unchanged as much as possible after varying the concerning values. The appropriate

numerical values are as follows:

in the case of minor dimensions: $\lambda_b \approx 1.35$ and

in the case of major dimensions: $\lambda_b \approx 1.2$.

The height of flange is defined in the practice in many ways /10/ (Fig. 5). In our calculations carried out for pass design we have proceeded according to the methode of U. Suppo: considering the aspects of the plastic deformation the flanges were separated from the web by a straight line intersecting the outer centre of the height of flange and the line of intersection of the web and the transition line of the flange. In this way one half of the continuum will be belonging to the flanges (further on a quarter of it will belong to the closed flanges and an other quarter to the open ones) and the other half will be conform to the principles of deformation concerning the web. According to this definition the height of flange shall be measured set off from the point marking the quarter of the height of web.

The height of the flanges running into a finishing pass must be smaller than the height of flange concerning the finished product, the flanges having been exposed to a direct thrust and pression generated by the edging roll. Under the influence of this effect the spreading of the flanges i.e. the increase of the height of flange will be according to the formula of Siebel modified by Goutscher:

$$\Delta b_{fl} = 0.25 \frac{\frac{a'+b'}{2} - \frac{a+b}{2}}{\frac{a'+b'}{2}} \cdot \sqrt{R_{beam} \cdot \left(\frac{a'+b'}{2} - \frac{a+b}{2}\right)} \quad .$$

The initial height of flange i.e. the total height of the leader groove amounts as follows:

$$h' = h_{finish} - \Delta b_{fl} \quad .$$

The outer inclination and the inner one of the flanges concerning the leader pass are either equal ($\alpha_1 = \alpha_2$) in the case when each of the angles is smaller than 1.4^o, therefore

$$\alpha_1 = \alpha_2 \leq 1.4^o \quad ,$$

where

$$tg(\alpha_1 + \alpha_2) = \frac{b-a}{h} \; ;$$

or in the other case when the sum of the two angles exceeds 2.8^o, the outer

angle, i.e. $\alpha_2 = 1.4^o$ and the inner one figures out the following difference:

$$\alpha_1 = \text{arc tg} (\alpha_1 + \alpha_2) - 1.4^o \quad .$$

The transition radius concerning the groove of symmetrization measured at the flange top (R) resp. the other radius measured at the flange bottom (r) are in direct proportion to the correspondent radii of the finished section as follows:

$$R = \nu . R_{finish} + m_1(n-1) \quad ;$$

$$r = r_{finish} + m_2(n-1) \quad ,$$

where

n — serial number of the pass (taking the finishing pass as its starting point);

m_1 and m_2 — invariables valid in a pass sequence from beginning to the cutting groove.

At the factor ν the increase of the radius has been considered yet to be greater in the breaking-down passes ($n \geq 3$).

In the case of the flange bottom concerning the parallel-flanged beams no transition radius will occur (in the Fig. 3: $r \approx 0$). To occur a transition radius in the preceeding grooves with appropriate dimensions, a value of $r_{finish} = 1.5$ mm has been supposed as a base for calculations, on the other hand the transition radius concerning the leader pass has been limited to r = 1 in all cases. In the case of deforming this flange bottom of r = 1 with an alongation factor of $\lambda = 1.1$ it could be assumed the edges of the finished section to be sharpened. In the case when the required transition radius (however not specified in the standard on the subject) in the finished section would be extremely large even after accomplishing this, the relative radius could be reduced either by remachining or by machining the collar and the bottom of groove shaping the flange bottom in this way.

The scheme of calculation is the following: having assumed an elongation factor (λ_b) and two proportionality factors (m_1 and m_2) the value of λ_{fl} will be determined: it will be equal with λ_{web}. Having assumed the dimensions of the leader groove obtained in this way as a base, the calculation shall be continuing through the construction process (Chap. 1.3) until making out the dimensions of the cutting groove. Having then the intention of maintaining the two-high rolls and the rolling technology

followed in the two-high stands not to be varied, this computing will be continued having assumed different values of λ_b and occasionally with other proportionality factors (m) until obtaining an appropriate profile for the designed cutting groove either coinciding with the dimensions of the actual one having inclined flanges and presenting an appropriate height of web or approximating to it.

1.3 Shaped breaking-down passes

Each of shaped breaking-down passes and grooves preceeding the leader (symmetrizing) ones and preceeding each of them are principally characterized by deforming and shaping by means of closed and opened flanges alternately applied. The principal shceme concerning the breaking-down passes indicating the relative dimensions is presented in Fig. 6. The average width of the web is also made out proceeding from the widths of flange tops. In respect of the relative pass or the outgoing section:

$$b_{web,m} = b_{web} - 0.5(b_{l.fl} + b_{d.fl})$$

and in the case of the entry one:

$$b'_{web,m} = b'_{web} - 0.5(b'_{l.fl} + b'_{d.fl}) \quad .$$

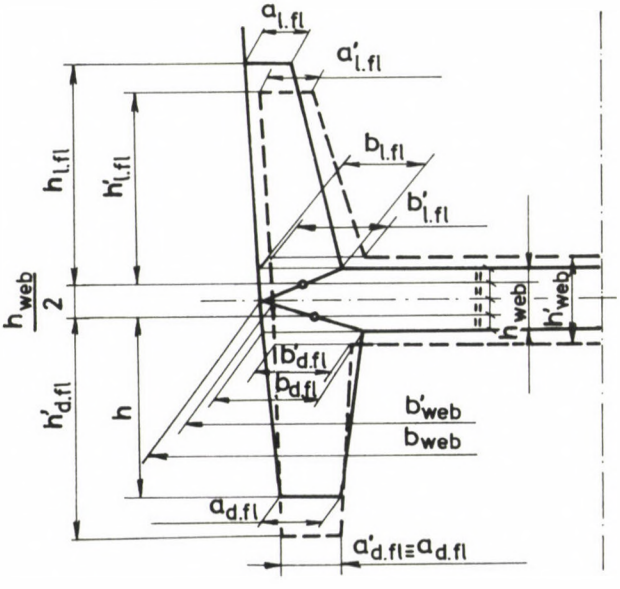

Fig. 6. Dimensions of the shaping roughing grooves

The computation of the dimensions of breaking-down passes is started from selecting the partial spreading concerning the web. The maximum permissible spreading (inferior to the not contained one) is a function of the serial number of pass (i.e. n=1 in the finishing pass) and the width of web ($b_{web,finish}$) concerning the finished section will be as follows /11/:

$$b_{web} = \xi \cdot \left[0.015 \quad b_{web,finish} + 0.6(n-3)\right] \quad .$$

To comment the conception for the factor (n-3): n-1 signifies the finishing pass and n=2 is the same for the symmetrizing one; computations concerning these factors will be accomplished in another way.

The constants implied in the above equation are to some extent differing from the data published in the literature on the subject; the relative difference could be influenced by the effect of the factor ξ. The reason for this can be explicated by the different widths of sections of the parallel flanged beams and standard ones running into the finishing grooves i.e. the parallel flanged beams shall be edged in the finishing passes in consequence of the principles concerning the rolling operations accomplished by universal stands and therefore and decreasing their total width as well, while the standard beams having inclined flanges and rolled by two-high rolls are spreading during the last pass too. This leader section having relatively considerable differences of width is able to be rolled starting from a cutting pass only in the case when the spreading concerning each break-down pass would be selected as greater (but of course smaller than in the case of not contained spreading).

Therefore the width of the sections running into a considered breaking-down groove will be the following:

$$b'_{web} = b_{web} - \Delta b_{web}$$

and the thickness of web of the section running in will be as follows:

$$h'_{web} = \lambda_{web} \frac{b_{web,m} \cdot h_{web}}{b'_{web,m}} \quad .$$

Determining the dimensions concerning the entry section will be accomplished by a successive approximation or iteration method; assuming in the first step appropriate elongation factors for the web (λ_{web}) and for

the flange (λ_{fl}) as well, the following equations will be obtained:

$$\lambda_{web} = \xi \cdot \psi \cdot \eta \left[1.1785 + 0.14\sqrt{(n-3)}\right] \quad \text{and}$$

$$\lambda_{fl} = 0.65(\lambda_{web} - 1) + 1 \quad ,$$

where

ξ — by putting in the appropriate figures related to this factor the depth of the cutting groove (subsequently the sape of this groove as well) can be appropriately influenced;

ψ — the value of this factor makes out 1 on the starting point; in the case when iterating the conditions of contact should be corrected, i.e. $\psi < 1$;

η — multiplying factor ($\eta \lesssim 1$) applied by the computer starting from an acceptable serial number of pass (n) following the size of section running in. The introduction of this factor has been necessitated because during a pass design in practice following on the cutting pass the elongation factor of the web has to be different from the factor computable applying the base function.

Determination of the running-in dimensions concerning the open flange will be accomplished by application of an assumed initial value of the elongation factor, subject to calculation of the above mentioned value of h'_{web} being done. Width of the flange top running into the open flange will be generated according to the following formula:

$$b'_{1fl} = \frac{\lambda_{1fl}(a_{1fl} + b_{1fl})\dfrac{h_{1fl}}{h'_{1fl}} - 0.4\, a_{1fl}}{1 + 0.65\dfrac{a_{1fl}}{b_{1fl}}} \quad ,$$

where the resulting elongation factor concerning the open flange can be originated either from the following product of vertical elongation factor ($\lambda_{1fl,vert}$) and the horizontal one ($\lambda_{1fl,hor}$):

$$\lambda_{1\,fl} = \lambda_{1fl,hor} \cdot \lambda_{1fl,vert} \quad ,$$

or in terms of geometrical dimensions as follows:

$$\lambda_{lfl,hor} = \frac{a'_{lfl} + b'_{lfl}}{a_{lfl} + b_{lfl}}$$

$$\lambda_{lfl,vert} = \frac{h'_{lfl}}{h_{lfl}} = \frac{h_{lfl} - \Delta h_{lfl}}{h_{lfl}} \quad .$$

The spreadlike deformation proceeding in the open groove will be expressed by Δh_{lfl} inserted in the latter relationship and therefore can be determined by the following formula:

$$\Delta h_{lfl} = 0.25 \frac{b'_{lfl} - b_{lfl}}{b'_{lfl}} \cdot \sqrt{\frac{D_o}{2} \cdot (b'_{lfl} - b_{lfl})} \quad .$$

In the practice of pass design for I-beams the deformation of flange bottoms is in a general way inferior to the deformation concerning the flange top depending on the average flange thickness as follows:

$$\frac{a'}{a} < \frac{b'}{b} \quad .$$

An empirical equation for that:

$$\frac{a'}{a} = 0.65 \frac{b'}{b} + 0.4 \quad ,$$

or expressed for an open flange:

$$a'_{lfl} = a_{lfl} \left(0.65 \frac{b'_{lfl}}{b_{lfl}} + 0.4\right) \quad .$$

Considering a known Δh_{lfl} the height of the section running into a groove having been considered should be at the open flange bottom as follows:

$$h'_{lfl} = h_{lfl} - \Delta h_{lfl} \quad .$$

Two of the characteristic dimensions of the running-in section ensuring an appropriate groove filling, i.e. b'_{lfl} and h'_{lfl} will be given with application of a common solution concerning a system of equations consisting

of two equations including them. The set of equations has been solved by us by means of an iteration process in view of computing technique. In the first step of successive approximation process the numerical value of $\lambda_{1\,fl}$ determined by the above mentioned empirical formula has been made equal to the resulting elongation factor $\lambda_{1\,fl}$ and the values of $b'_{1\,fl}$ and $h'_{1\,fl}$ have been determined from that factor. The iteration process was considered to be complete and the obtained values of $b'_{1\,fl}$ and $h'_{1\,fl}$ were considered to be acceptable only in the case when the deviation concerning the successively computed figures of $b'_{1\,fl}$ was inferior to 0.1 mm as follows:

$$\left| b'_{1\,fl} - b'_{1\,fl,(i+1)} \right| \leq 0.1 \text{ mm} \quad .$$

Computation of the running-in dimensions concerning a closed flange would be initiated assuming the following relationship (Fig. 6):

$$a'_{d.fl} = a_{d.fl} \quad .$$

The resulting elongation factor concerning a closed flange will be as follows:

$$\lambda_{d.fl} = \lambda_{d.fl,hor} \cdot \lambda_{d.fl,vert} \quad ,$$

where

$$\lambda_{d.fl,hor} = \frac{a'_{d.fl} + b'_{d.fl}}{a_{d.fl} + b_{d.fl}} \qquad \text{and}$$

$$\lambda_{d.fl,vert} = \frac{h'_{d.fl}}{h_{d.fl}} \quad .$$

Height of section entering a closed part of groove will be as follows:

$$h'_{d.fl} = 0.5\, h_{d.fl} - (a_{d.fl}+b_{d.fl}) + \sqrt{(a_{d.fl}+b_{d.fl} - 0.5h_{d.fl})^2 + 2h_{d.fl}\, \lambda_{fl}(a_{d.fl}+b_{d.fl})}$$

resp. its width:

$$b'_{d.fl} = 0.5(h'_{d.fl} - h_{d.fl}) + b_{d.fl} \quad ,$$

where the value 0.5 concerning the empirical factor is selected according to Bachtinow.

Control of the elongation factor. Having known the concrete dimensions given by assumed elongation factors the surfaces of the entering sections resp. grooves can be calculated (without considering the rounding-off radii) as follows:

$$A = (a_{l.fl}+b_{l.fl})\,h_{l.fl} + (a_{d.fl}+b_{d.fl})\,h_{d.fl} + h_{web}\left[b_{web} - 0.5(b_{l.fl}+b_{d.fl})\right] + \\ + \frac{h_{web}}{4}(b_{l.fl}+b_{d.fl});$$

(in this case the entering value of A' being the same but calculated with values indexed by commas). The resulting elongation factor will be as follows:

$$\lambda_{result} = \frac{A'}{A} \quad .$$

Verification of entry conditions inc. conditions of bite. Having entered the closed flange of the open groove the conditions of threading have to be controlled. The computer is performing the control (Fig. 7) with an analysis of the point x_{12} of roll section resp. the interval of itself reduced by a third of the actual radius to be inferior to the interval concerning the straight section to be entered as follows:

$$x'_5 > (x_{12} - \tfrac{1}{3} R_{l.fl}) \quad .$$

In the case when this condition would be unsatisfied, the assumed valued of λ_{web} should be iterated by a reduced ψ. The successive approximation shall be continued up to the reestablishment of the given condition of bite.

Determining the rounding-off radii of each part of section will be accomplished according to the principles and relationships outlined in chapter 1.2. We outlined in chapter 1.2 the principles and formulas concerning the calculation of the angle of inclination of a closed part of groove. Theoretically the inclination of an open part of groove (α_4, Fig.8) could be calculated by the same method but with the difference that an opportunity would be presented itself to incline the open part of groove so

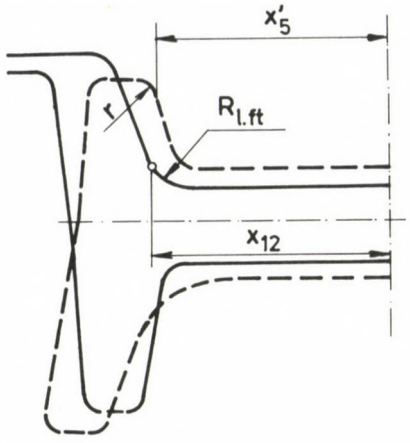

Fig. 7. Examinations and analysis of the conditions of bite

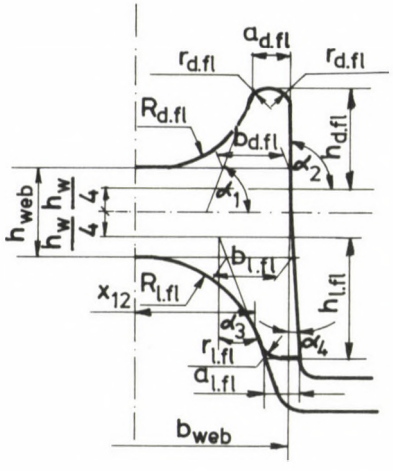

Fig. 8. Interpretation concerning the geometrical notations of a groove

that the given angle have a value of $\Delta\alpha_{l.fl}$ to be arbitrarily determined and imprinted as well (Chapter 2).

The calculation concerning the breaking-down passes should be iterated assuming a number of passes arbitrarily put in and the grooves successive preceeding each other would be plotted in this way. The amount of passes is limited by the prevailing conditions of a given rolling train operating in an actual plant. A pass sequence can be considered as "finished"

only in the case when the rolls with closed grooves according to a value n_{all} would be satisfying the conditions of a cutting groove as well.

Starting from the fact of a principled conception that both the given plant conditions and a set of rolls belonging to a two-high stand should be maintained, the following aim was set by us: the shape and dimensions of the designed groove should be corresponding to the ones concerning the current cutting grooves (applied to the normal I-beams).

In this way the computer-aided roll pass design would be continued by changing the possible parameters (Chapter 2) up to a correspondence both of the existent cutting groove and the closed part of another cutting groove concerning a possible total number of passes (n_{all}) as well. At this point the groove in question should be "symmetrized" by the computer program: in this way the dimensions of the closed groove will be applied instead of the dimensions of the half groove containing an open flange (by reason of the given two-high roll arrangement) and the figures for the width of flange will be averaged as well as follows:

$$a_{cutting} = 0.5(a_{d.fl} + a_{l.fl}) \qquad \text{and}$$

$$b_{cutting} = 0.5(b_{d.fl} + b_{l.fl}) \quad .$$

1.4 The ultimate shaped breaking-down groove

A specific intermediate groove has to be arranged between the breaking-down groove sequence of same configuration in principle (i.e. sequence changing both the closed flanges and the open ones) and the leading groove performing the symmetrizing pass (Fig. 9). This groove is characterized by containing both an open flange and a closed one however they have to imply a specific geometry to be enabled to be bitten by the symmetrizing leading groove. The condition of bite (i.e. that of bending) is the following: the maximum width of the part of section outgoing from the open part of flange (b'_{max}) has to be inferior to the sum of the width of groove (b_{web}) and a figure not greater than the third of the outer rounding-off radius (R_{out}) as follows:

$$b'_{max} < (b_{web} + 0.5\ R_{out}) \quad .$$

The leading groove has a symmetrizing character (by name it is also symmetrizing), therefore the dimensions of both the lower roll and the

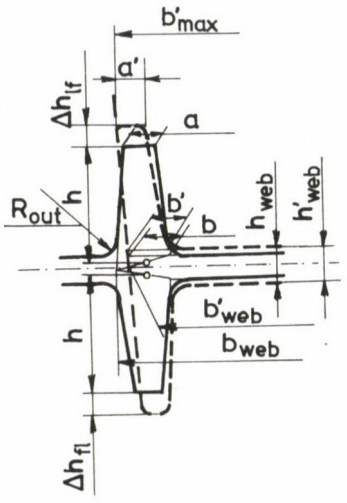

Fig. 9. Dimensions of the last shaping roughing groove

upper one are the same. It was required by us the shape of the section entering the leading groove — i.e. the section of the ultimate shaped breaking-down one — to be of such a character that as a result of this fact the deformations of each part of section within the symmetrizing groove have to be identical as follows:

$$\lambda_{web} = \lambda_{fl} \cdot$$

The closed flange and the open one running from the ultimate shaped breaking-down groove will enter an identically closed part of groove situated within a given symmetrizing pass, therefore both flanges of the ultimate breaking-down groove should have to be narrower and higher than the flange shaped within the symmetrizing groove. In our method of calculation a value of Δh_{fl} was assumed according to the technical literature in question. By doing so for each flange an edging of a discrete amount of material with a section of Δh_{fl} would occur at the flanges. Having taken into consideration the elongation and the spread to be equal, the section with a value of

$$\frac{1}{2} \cdot \Delta h_{fl} \cdot a$$

would generate a spread of

$$\frac{1}{2} \frac{\Delta h_{fl} \cdot a}{h} ,$$

in the flange having a height of h.

The total width of web of the ultimate breaking-down groove (Fig. 9) will be as follows (two flanges are to be taken into consideration):

$$b'_{web} = b_{web} - 2 \cdot 0.5 \cdot \frac{\Delta h_{fl} \cdot a}{h} \quad .$$

The widths of flanges situated within the ultimate breaking-down groove will be of following values:

$$a' = a - 0.5 \frac{\Delta h_{fl} \cdot a}{2} \quad \text{and}$$

$$b' = b - 0.5 \frac{\Delta h_{fl} \cdot a}{h} \quad .$$

The elongation factor of the flanges will be as follows:

$$\lambda_{fl} = \frac{a' + b'}{a + b} \quad \frac{h + \Delta h_{fl}}{h} \quad .$$

According to the identical values of the elongation factors of each part of section the thickness of web could be calculated in the following manner:

$$\lambda_{web} = \lambda_{fl} \quad \text{and}$$

$$h'_{web} = \lambda_{web} \cdot h_{web} \quad .$$

The calculation of the rounding-off radii and the "straightening/closing" of the parts of sections i.e. that of the angles of inclination will be performed according to the principles outlined in the previous chapter.

2. A computer program for groove designing

According to the principles, functions and methods of calculation summarized in the chapter 1.1 to 1.4 we developed a computer algorithm made appropriate and suitable for designing the successive grooves arranged both for the beams with inclined flanges (normal ones) and for the parallel flanged (IPE) girders resp. to calculate the principal dimensions of the grooves in question. Starting from the dimensions of the finished section

having computed the required dimensions of the section entering the groove in question the shape of section would be designed and plotted by the given program. Computing the successive sections would be performed on a discrete program instruction. The program designs the section exclusively. The type of the train (either a two-high or a three-high one) and the roll gap having been different, the required clearance between collars has to be marked on the designed and plotted section.

The program version taken into consideration for the inclined flange (i.e. normal) beams was tested according to a pass designing currently applied in a rolling mill indicated in Fig. 1: each pass sequence containing grooves for four normal I-beams (with heights 80, 100, 120 and 140 mm) designed by a computer was compared with the actual ones. As a result of comparing a possibility could be established for an analogue computer simulation concerning the roll pass designing of every single beams resp. the groove configurations applied to themselves for a relatively exact reproduction of that one.

According to the above mentioned anaylses and tests a program version suitable to the roll pass calculations concerning the IPE-beams has been developed by us. This program verifies the finishing pass (i.e. the groove n=1) having assumed a "universal" stand. The leading groove (n=2) is performing a task of symmetrizing and its dimensions have to be determined according to the formulas inserted in chapter 1.2. The principal dimensions of the so-called ultimate shaped breaking-down groove (n=3) preceeding the leading pass would be calculated also by a discrete subroutine (v.s. chapter 1.4). A sequence calculation concerning the shaped breaking-down grooves would be performed in the case of $n > 3$.

Calculation shall be continued up to the point where the total number of passes should have been in accordance with the total number of passes (n_{all}) applied to the current normal I-beams of equivalent heights of web. This restriction had to be done because only by this way would have every reason to hope to maintain the existent roughing and breaking-down technology concerning the two-high stands, its roll sets and in addition the current initial dimensions of billets resp. the cutting groove configurations as well.

In the case of maintaining the general principles of roll pass design assumed inserting a determined amount of grooves between a finished IPE-section and an assumedly given cutting groove designing the pass sequence of IPE-beams observing every limiting condition (load and stress

level, conditions of bite, a uniform deformation for each portion of section etc.) could be performed only by the aid of a computer.

3. Section drawings and profile sketches

A pass sequence excluding the finishing groove calculated and designed by means of the computer program has been shown relating to the IPE 120 section (Fig. 10). In Fig. 11 have been compared the shape of the cutting groove designed by means of a computer and the shape of the cutting groove used currently also for normal beams of type 120 with inclined flanges. On the basis of slight deviations it can be established the fact that a section leaving the present cutting groove (used for normal beams) enclosed in the reversing two-high stand of the 120 I-beam could be threaded securely into the newly designed first shaping breaking-down groove established in the three-high stand built for IPE-beams.

A decision concerning the question if a number of passes corresponding to the present one were satisfying in the course of rolling the IPE-beams could be made after a load test of a rolling train (Chapter 4).

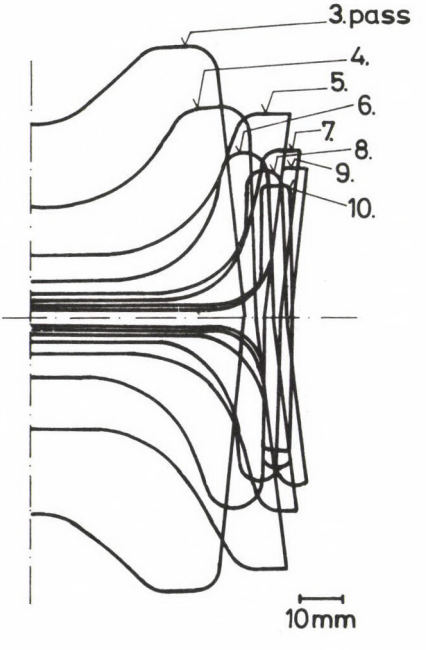

Fig. 10. Calculated series of grooves of the 120 IPE-beam

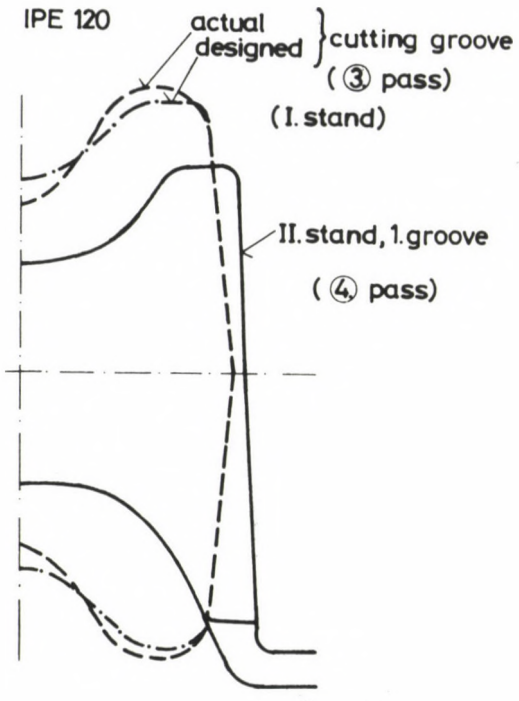

Fig. 11. Transition of the cutting groove and the first shaping one

The profile sketches calculated by means of the above mentioned explained in detail and designed also by means of a computer program and drawn by a plotter have been drawn separately and have been transported also the values of the roll clearance and roll gap considering the number of stands and the rolling schedule as well (Fig. 12). The series of profile sketches is starting with the grooves of the three-high roll set because the cutting groove resp. the breaking-down one will be integrated in the technology concerning the IPE-beams.

4. Control of the load level

Load level characterizing each stand of a rolling train may be deviated from the existing ones in accordance to the newly designed technology. The load capacity of a newly "universalized" stand will be unchanged from the point of view both of the torque and of the power (having been both

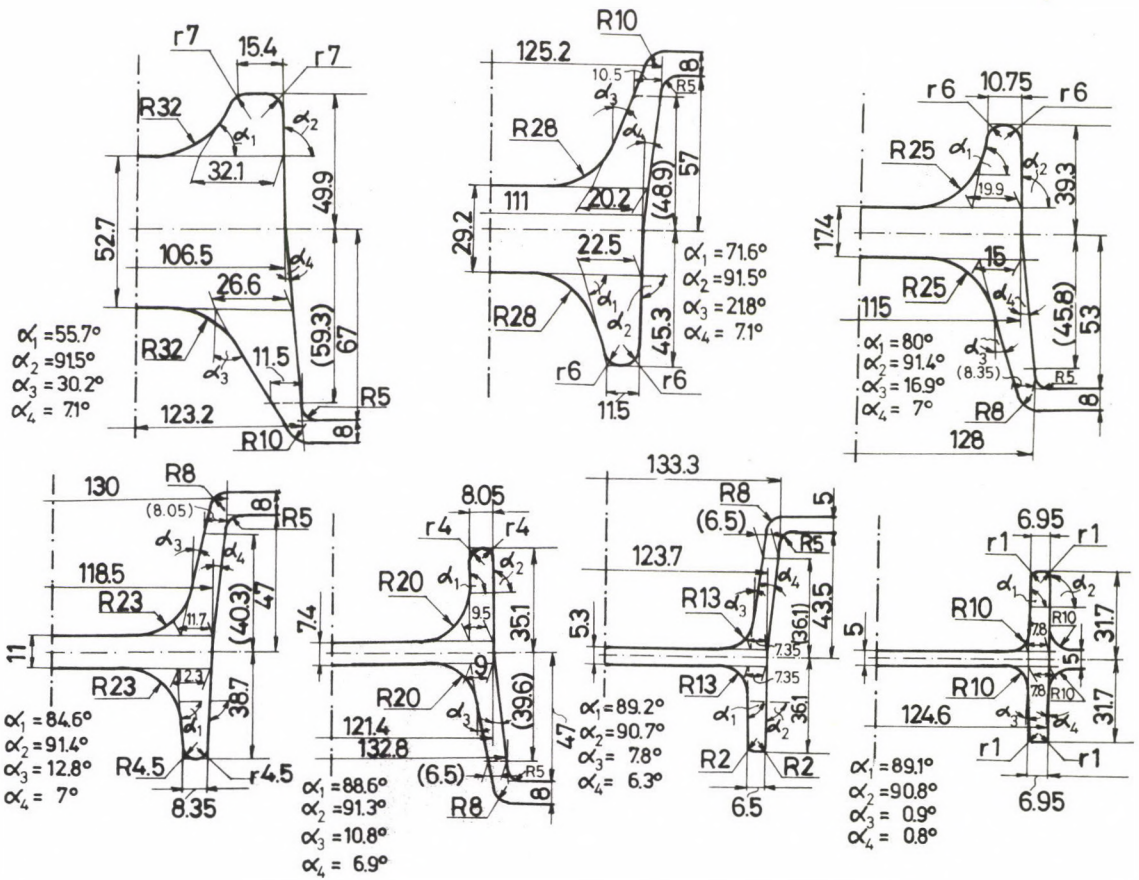

Fig. 12. Series of groove designed by means of computer for the 120 IPE-beam

the driving motor and the drive the same) and as regards roll force the values of load capacity are as follows:

for horizontal rolls: F_{max} = 800 kN;

for vertical edging rolls: F_{max} = 700 kN.

In the case of hot rolling proceeded in a shaping groove we established previously a methodology of computing and an operating machine program /1—3/ having run on a computer.

The appropriate mathematical model contains the following sub-routines and calculations:

— a chronology of holding the rolled piece or pieces in the rolling train;

— calculation of the cooling conditions and actual temperature values of the rolled piece;

— calculation of the deformation resistance;

— calculations for the roll force, torque and power;

— determination and estimation of various specific technological values.

Roll force resp. forming resistance and temperature of a piece leaving a groove will be determined by the data processing machine model using an iteration method concerning both of the starting point and of the end of a beam separately.

In the case of cutting in two roll force and power demands concerning both halves will be calculated by the data processing machine separately according to the different cooling conditions as well.

Using the above mentioned and explained data processing machine model we determined the parameters of rolling technology concerning all the passes proceeded in the course of rolling an IPE 120 beam. To make clear the obtained results temperature values of a rolled piece have been plotted in a line diagram and roll force, torque and power data have been described in a column diagram by means of a plotter subroutine (Fig. 13). Beams having been cut-off in two halves between two roughing stands the calculated resp. plotted data are concerning the second cut-off piece having been coller therefore representing a greater load.

Permissible roll force, both nominal and actual driving motor torques and power values have been plotted in with dotted and dashed lines (where the scales of diagrams have allowed it). When estimating the allowable overloading it should be taken in consideration that a simultaneous rolling of two piece takes place in the stand No. II.

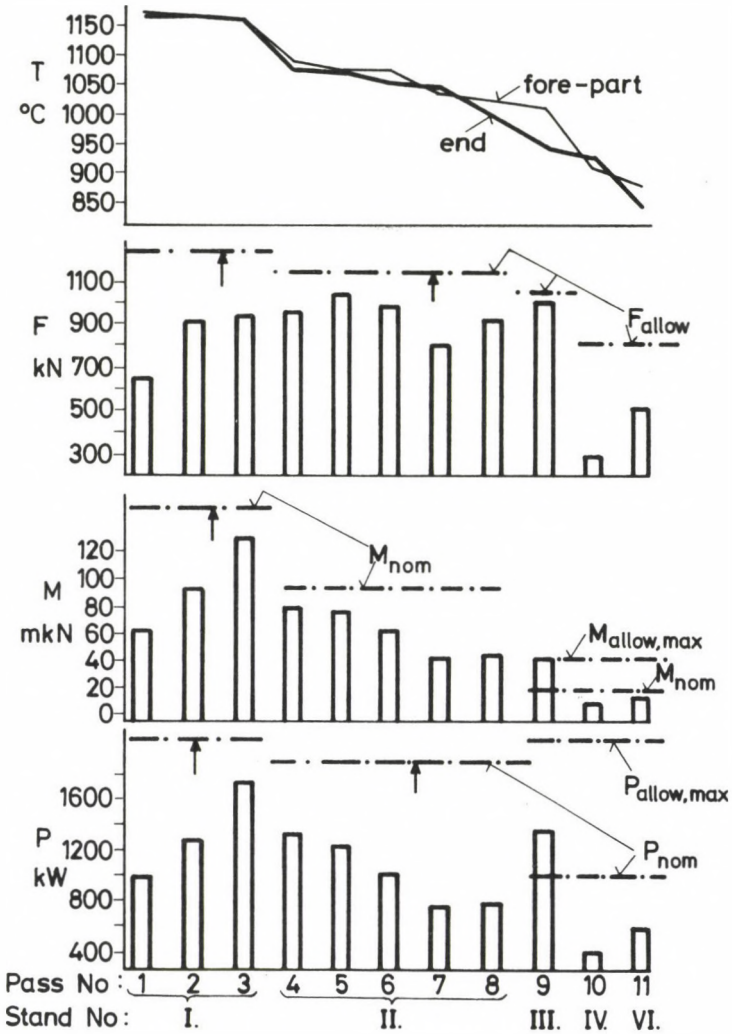

Fig. 13. Calculated rolling parameters

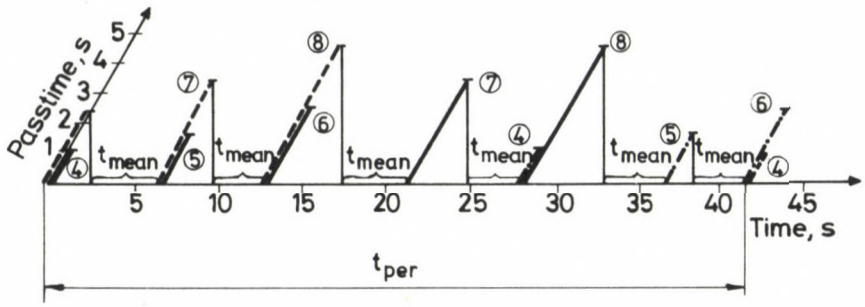

Fig. 14. Rolling schedule for the stand No. II (IPE 120)

Warming up of driving motors can be calculated on the basis of estimated data and of the rolling schedule. On this basis a roughing stand doesn't present any bottleneck factor having (could be) rolled a single piece only in each case in it. In the stands of open passes No. III, IV and VI even a total power slightly exceeding the nominal one couldn't result in an overheating of the driving motor having presented the time intervals remarkable values.

We subjected however the three-high stand No. II to a separate test in course of which a simultaneous rolling of two beams took place systematically on the bais of the rolling shcedule demonstrated in Fig. 14. It is worth mentioning that even a simultaneous rolling of three beams could be proceeded theoretically, however it has to be avoided by means of efficient measures, even in order to prevent an overloading from the point of view of roll forces.

The effective power of the driving motor can be estimated by means of the following formula:

$$P_{eff} = \sqrt{\frac{\Sigma P_i^2 t_i + (P^2_{\text{idle int.}} \cdot t_{\text{idle int.}})}{t_{per}}} \leq P_{nom}$$

where

i — number of passes run in the stand No. II under discussion;

P_i — calculated mean power demand concerning the pass No. i;

t_i — rolling period of the pass No. i;

$P_{idle\ int}$ — no-load power demand of the three-high stand;
$t_{idle\ int}$ — no-load time interval (within the total rolling period);
t_{per} — duration of the rolling period (total rolling period in stand No. II).

The effective driving motor power calculated on the basis of the above described formula doesn't exceed the nominal power of the driving motor of the three-high stand.

5. Conclusion

Roll sets can be designed and established on the basis of profile sketches and load level concerning it as well as the layout of a given rolling mill. Arrangement of the grooves resp. determining the number of passes proportionate to the groove wear can take place in the usual manner. On the basis of known profile sketches and roll drawings appropriate technological instructions concerning the rolling of an 120 IPE-beam can be established as well.

In the case of an optional number of passes (i.e. of a given rolling mill layout) resp. taken in consideration various initial bloom sections and dimensions the adapted computer-aided system will provide an opportunity to remodel the groove sequence, to examine the load level as well as to modernize the technologies concerning a given mill train. Having modified the given functions, the above mentioned and explained method could be applicable and useful for modelling and designing groove series concerning other profiles as well.

REFERENCES

1. M. Voith, L. Dernei and R. Herendi: Estimation of optimum conditions for energy consumption of profile rolling. Freiberger Forschungshefte B 231. (1982) 41—59
2. R. Herendi, M. Voith and L. Dernei: The effect of the initial temperature of rolling upon the specific energy demand. BKL - Kohászat 113. (1980) 17—25
3. Th. Spittel, B. Schieferdecker and M. Voith: The specific energy demand and energy consumption in profile-, fine- and wire rolling mills. BKL - Kohászat 116. (1983) 217—224
4. V.N. Grinavtsev et al.: Rolling of I-beams in a stand 650 using box-type grooves in driven rolls. Stal. (1976) 432—434
5. V. Najzar: Rolling of I- and U-profiles in two-high stands using box-type grooves with vertical rolls. Hutnik. 27. (1977) 261—264

6. H. Menne: Groove designs for straight-flange beams in rolling mills with and without universal stands. Der Kalibreur. No. 15. (1971) 3—221

7. H. Menne and H. Koch: Comparative examinations concerning the rolling of I NP 100 beams using two up-to-date continual rolling trains. Der Kalibreur, No. 12. (1970) 3—18

8. P.H. Reuter: Modern Mill Layout and Design for Rolling Structural Steels. Iron and Steel Engineer, (1970 May) 73—87

9. W. Kolbmüller: Factors exerting influence on projecting of beam mills. Technische Mitteilungen, 74, (1981) 563—571

10. J. Vesčičik: Influence of roll pass design of IPE-beams exerted on rolling in universal stands. Hutnické Listy, No. 2. (1977) 133—137

11. A.P. Tchekmarev: Roll pass design. Metallurgya. Moscow, 1971

PRINTED IN HUNGARY
Akadémiai Kiadó és Nyomda Vállalat, Budapest

NOTICE TO CONTRIBUTORS

Papers in English* are accepted on condition that they have not been previously published or accepted for publication.

Manuscripts in two copies (the original type-written copy plus a clear duplicate one) complete with figures, tables, and references should be sent to

Acta Technica
Münnich F. u. 7. I. 111 A
Budapest, Hungary
H-1051

Although every effort will be made to guard against loss, it is advised that authors retain copies of all material which they submit. The editorial board reserves the right to make editorial changes.

Manuscripts should be typed double-spaced on one side of good quality paper with proper margins and bear the title of the paper and the name(s) of the author(s). The full postal address(es) of the author(s) should be given in a footnote on the first page. An abstract of 50 to 100 words should precede the text of the paper. The approximate locations of the tables and figures should be indicated on the margin. An additional copy of the abstract is needed. Russian words and names should be transliterated into English.

References. Only papers closely related to the author's work should be referred to. The citations should include the name of the author and/or the reference number in brackets. A list of numbered references should follow the end of the manuscript.

References to periodicals should mention: (1) name(s) and initials of the authors(s); (2) title of the paper; (3) name of the periodical; (4) volume; (5) year of publication in parentheses; (6) numbers of the first and last pages. Thus: 5. Winokur, A., Gluck, J.: Ultimate strength analysis of coupled shear walls. American Concrete Institute Journal 65 (1968), 1029–1035.

References to books should include: (1) author(s) name; (2) title; (3) publisher; (4) place and year of publication. Thus: Timoshenko, S., Gere, J.: Theory of Elastic Stability. McGraw-Hill Company, New York, London 1961.

Illustrations should be selected carefully and only up to the necessary quantity. Black-and-white photographs should be in the form of glossy prints. The author's name and the title of the paper together with the serial number of the figure should be written on the back of each print. Legends should be brief and attached on a separate sheet. Tables, each bearing a title, should be self-explanatory and numbered consecutively.

Authors will receive proofs which must be sent back by return mail.

Authors will receive 50 reprints free of charge.

*Hungarian authors can submit their papers also in Hungarian.

Periodicals of the Hungarian Academy of Sciences are obtainable at the following addresses:

AUSTRALIA
C.B.D. LIBRARY AND SUBSCRIPTION SERVICE
Box 4886, G.P.O., *Sydney N.S.W. 2001*
COSMOS BOOKSHOP, 145 Ackland Street
St. Kilda (Melbourne), Victoria 3182

AUSTRIA
GLOBUS, Höchstädtplatz 3, *1206 Wien XX*

BELGIUM
OFFICE INTERNATIONAL DES PERIODIQUES
Avenue Louise, 485, *1050 Bruxelles*
E. STORY-SCIENTIA P.V.B.A.
P. van Duyseplein 8, *9000 Gent*

BULGARIA
HEMUS, Bulvar Ruszki 6, *Sofia*

CANADA
PANNONIA BOOKS, P.O. Box 1017
Postal Station "B", *Toronto, Ont. M5T 2T8*

CHINA
CNPICOR, Periodical Department, P.O. Box 50
Peking

CZECHOSLOVAKIA
MAD'ARSKA KULTURA, Národni třida 22
115 66 Praha
PNS DOVOZ TISKU, Vinohradská 46, *Praha 2*
PNS DOVOZ TLAČE, *Bratislava 2*

DENMARK
EJNAR MUNKSGAARD, 35, Nørre Søgade
1370 Copenhagen K

FEDERAL REPUBLIC OF GERMANY
KUNST UND WISSEN ERICH BIEBER
Postfach 46, *7000 Stuttgart 1*

FINLAND
AKATEEMINEN KIRJAKAUPPA, P.O. Box 128
00101 Helsinki 10

FRANCE
DAWSON-FRANCE S.A., B.P. 40, *91121 Palaiseau*
OFFICE INTERNATIONAL DE DOCUMENTATION ET LIBRAIRIE, 48 rue Gay-Lussac
75240 Paris, Cedex 05

GERMAN DEMOCRATIC REPUBLIC
HAUS DER UNGARISCHEN KULTUR
Karl Liebknecht-Straße 9, *DDR-102 Berlin*

GREAT BRITAIN
BLACKWELL'S PERIODICALS DIVISION
Hythe Bridge Street, *Oxford OX1 2ET*
BUMPUS, HALDANE AND MAXWELL LTD.
Cowper Works, *Olney, Bucks MK46 4BN*
COLLET'S HOLDINGS LTD., Denington Estate,
Wellingborough, Northants NN8 2QT
WM DAWSON AND SONS LTD., Cannon House
Folkstone, Kent CT19 5EE
H. K. LEWIS AND CO., 136 Gower Street
London WC1E 6BS

GREECE
KOSTARAKIS BROTHERS INTERNATIONAL BOOKSELLERS, 2 Hippokratous Street, *Athens-143*

HOLLAND
FAXON EUROPE, P.O. Box 167
1000 AD Amsterdam
MARTINUS NIJHOFF B. V.
Lange Voorhout 9–11, *Den Haag*
SWETS SUBSCRIPTION SERVICE
P.O. Box 830, 2160 Sz Lisse

INDIA
ALLIED PUBLISHING PVT. LTD.
750 Mount Road, *Madras 600002*
CENTRAL NEWS AGENCY PVT. LTD.
Connaught Circus, *New Delhi 110001*
INTERNATIONAL BOOK HOUSE PVT. LTD.
Madame Cama Road, *Bombay 400039*

ITALY
D. E. A., Via Lima 28, *00198 Roma*
INTERSCIENTIA, Via Mazzé 28, *10149 Torino*
LIBRERIA COMMISSIONARIA SANSONI
Via Lamarmora 45, *50121 Firenze*
SANTO VANASIA, Via M. Macchi 58
20124 Milano

JAPAN
KINOKUNIYA COMPANY LTD.
Journal Department, P.O. Box 55
Chitose, *Tokyo 156*
MARUZEN COMPANY LTD., Book Department
P.O. Box 5050 Tokyo International, *Tokyo 100-31*
NAUKA LTD., Import Department
2-30-19 Minami Ikebukuro, Toshima-ku, *Tokyo 171*

KOREA
CHULPANMUL, *Phenjan*

NORWAY
TANUM-TIDSKRIFT-SENTRALEN A.S.
Karl Johansgata 43, *1000 Oslo*

POLAND
WĘGIERSKI INSTYTUT KULTURY
Marszalkowska 80, *00-517 Warszawa*
CKP I W, ul. Towarowa 28, *00-958 Warszawa*

ROUMANIA
D. E. P., *Bucuresti*
ILEXIM, Calea Grivitei 64–66, *Bucuresti*

SOVIET UNION
SOYUZPECHAT — IMPORT, *Moscow*
and the post offices in each town
MEZHDUNARODNAYA KNIGA, *Moscow G-200*

SPAIN
DIAZ DE SANTOS Lagasca 95, *Madrid 6*

SWEDEN
ESSELTE TIDSKRIFTSCENTRALEN
Box 62, *101 20 Stockholm*

SWITZERLAND
KARGER LIBRI AG, Petersgraben 31, *4011 Basel*

USA
EBSCO SUBSCRIPTION SERVICES
P.O. Box 1943, *Birmingham, Alabama 35201*
F. W. FAXON COMPANY, INC.
15 Southwest Park, *Westwood Mass. 02090*
MAJOR SCIENTIFIC SUBSCRIPTIONS
1851 Diplomat, P.O. Box 819074,
Pallas, Tx. 75381-9074
READ-MORE PUBLICATIONS, INC.
140 Cedar Street, *New York, N. Y. 10006*

YUGOSLAVIA
JUGOSLOVENSKA KNJIGA, Terazije 27, *Beograd*
FORUM, Vojvode Mišića 1, *21000 Novi Sad*

HU ISSN 0001-7035 Index: 26.025

ACTA TECHNICA

ACADEMIAE SCIENTIARUM HUNGARICAE

VOLUME 101
NUMBER 3

ENERGY ENGINEERING — E/1

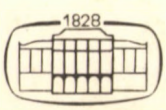

AKADÉMIAI KIADÓ, BUDAPEST 1988

ACTA TECHNICA

A JOURNAL OF THE HUNGARIAN ACADEMY OF SCIENCES

Acta Technica publishes original papers, preliminary reports and reviews in English, which contribute to the advancement of engineering sciences.
Acta Technica is published by

AKADÉMIAI KIADÓ
Publishing House of the Hungarian Academy of Sciences
H-1450 Budapest, Alkotmány u. 21.

Subscription information

Orders should be addressed to

KULTURA Foreign Trading Company
H-1389 Budapest P.O. Box 149

or to its representatives abroad

Acta Technica is abstracted/indexed in Applied Mechanics Reviews, Current Contents–Engineering, Technology and Applied Sciences, GeoRef Information System, Science Abstracts.

CONTENTS

EDITORS' FOREWORD 227

Bassa, G. - Mao, N.S.: Determination for geometric characteristics of flames 229

Erdősi, P.: Effect of material intensity and energy intensity on the efficiency of development of the national economy 259

Jermendy, L. - Timashova, L.V.: Results of interference measurements on 400 and 750 kV transmission lines 281

Mikhail, S. - Elbadrawy, S. - Barakat, Y. - Farag, A.: Thermal conversion of paraffins . 295

Paláncz, B. - Benedek, S.: Event recognition by means of a linear model 305

Paláncz, B. - Szabolcs, G.: Solution of inverse heat conduction problem by orthogonal collocation techniques 323

Szergényi, I.: Economic growth as a function of changes in energy intensity and production restructuring 339

BOOK REVIEW

Retter, G.J.: Matrix and spacephasor theory of electrical machines (K. Karsai) 345

Acta Technica Acad.Sci.Hung., 101(3), pp. 227 (1988)

EDITORS' FOREWORD

Taking into consideration the opinion of Acta Technica readers, editorial and formal modifications are being introduced in the next editions of the journal, expected to be a significant aid in the work of readers interested in different professional fields. While the old heading 'Acta Technica' remains unchanged, each special field will have its own series including papers in a narrower and more homogeneous range with a view to contribute to a more reasonable arrangement. You are now holding in your hand one of these series,

Energy Engineering,

an issue comprising a wide professional field considering all what is implied in energy, among others, fuel engineering, energy engineering, electrical engineering, economic implications of energy etc. as Energy Engineering is designed to treat the energy issue in a most complex way.

Efforts are made to increase the scientific value of the papers by requiring a more rigorous reader's job and publication of papers from the most timely professional fields. Practical applicability and contribution to energetic development are the most important point in our publications. You are requested to submit papers of this type.

Although the number of pages available for this purpose is limited, advertisements offering high-quality information for publication in Acta Technica Energy Engineering are welcome.

We hope all this effort will contribute to the popularity of our journal as well as to information exchange in the energy field.

Acta Technica Acad. Sci. Hung., 101(3), 229–257 (1988)

DETERMINATION OF GEOMETRIC CHARACTERISTICS OF FLAMES

BASSA, G. – NGUYEN SI MAO*

(Received: 20 April 1988)

In combustion and heat transfer calculation, it is very important to reliably define the flame and establish its physical and geometrical characteristics more exactly. In this paper, the analysed problem is how to explain the geometrical structure of flames formed in the combustion chamber, and how to establish the relationship between geometrical characteristics and flow parameters at the burner's orifice. On the basis of our experimental data we made a regression analysis to present numerical equation for practical use.

Introduction

The construction and characteristics of the flames formed in the combustion chamber of boilers play a decisive role in developing the conditions of combustion. Besides the physical and chemical characteristics of flames, the geometrial characteristics are of great importance from this point of view, and are particularly determined by the very complicated and interacting physical and chemical processes inseparable from each other in the case of turbulent diffusion combustion either in space or time.

The geometrical characteristics of flames (dimensions, volume, surface, shape) provide information on the spatial progress of combustion, impose a limit on the scope of application, and determine the proper harmony between the firing equipment and the combustion chamber. The knowledge of the flame volume as geometrical characteristic is indispensable for the determination of one of the most important combustion characteristics, i.e. intensity of combustion (= energy released in the volume unit of flame during the unity of time), independently from the most complicated physical-chemical processes taking place in it. Furthermore, the knowledge of the flame surface is also important – in addition to the knowledge of combustion temperature and emissivity – for the calculation of the amount of heat transferred by radiation, especially in cases the flame can be considered approximately as a detached radiant "body".

*Bassa, G. and Nguyen Si Mao, Department of Heat Engines, Technical Unviersity Budapest, H–1111 Műegyetem rkp. 3, Hungary

Akadémiai Kiadó, Budapest

For the combustion process to be controlled as required for pursuing the given objective (flame shape and temperature, intensity of combustion heat transfer, efficiency of combustion etc.), the full knowledge of the conditions influencing the combustion can be achieved mainly in an experimental way.

Furthermore, it should be mentioned that the dimensions and volume of the individual flames, as well as the characterization of the boundaries for multiflame systems can be established or performed, respectively, in several ways differing from each other (e.g. visually, by photographic method, by measuring the ionic conductivity, the CO component and by Schlieren exposure).

To determine the composition of flame structure, examinations have been carried out to detect the temperature, concentration, pressure, velocity, ionization- and emission-fluctuations etc. Some of the researchers lay a great stress upon extending the laws of the turbulent free-jet flow — — under certain conditions — over to the turbulent diffusion flames, and due to this endeavour, the information on the turbulent diffusion combustion has been widened beyond any doubt to a great extent.

The aim of our examinations was to contribute to the determination of the trends of geometrical changes as yielded from the interactions due to the changes in the geometrical dimensions (shape) and the geometrical position of the laminar and turbulent diffusion flames with the homogeneous gas-phase combustion by means of different measurement methods.

In this case, the methods of ionization, local gas analysis and temperature distribution were applied to carry out our experiments.

Formation of diffusion flames under flow conditions

The flow- and combustion processes of turbulent flames are generally described by using the knowledge and laws of turbulent free jets. In many cases, there are applied burners through which fuel-jets of high velocity are injected into the combustion chamber together with a relatively slow flow of air. In such cases, flames of free jet are in question approximately, especially if the combustion chamber is relatively large in comparison with the jet. The interest in the laws of free-jet — when analysing the processes of combustion — originates in the fact that the process of reaction can be directly concluded from the process of mixing (in case of dif-

fusion flames) since the time-demand of the chemical reaction can be generally neglected — especially in engineering practice — as compared with the time-demand of mixing process, and as a consequence, the termination of the combustion process, i.e. the contour of flames is provided theoretically by the stoichiometric mixing-line.

In order to analyse the process taking place in the flame, the knowledge of concentration-distribution is also required in addition to that of velocity-distribution.

The longitudinal- and cross-section-distribution of velocity in the jet can be described by the following formula:

$$u = u_o \frac{6.4}{\frac{x}{d_o}} \sqrt{\frac{\varrho_o}{\varrho}} \exp\left[-82\left(\frac{y}{x}\right)^2\right]$$

where:

- u — the flow velocity in the jet,
- u_o — the output velocity of the nozzle,
- ϱ_o — the density of the medium,
- ϱ — the density of the jet,
- x — the co-ordinate of the main direction of flow,
- y — the co-ordinate perpendicular to x.

While the distribution of mass-concentration is:

$$c = c_o \frac{5.26}{\frac{x}{d_o}} \sqrt{\frac{\varrho_o}{\varrho_k}} \exp\left[-54\left(\frac{y}{x}\right)^2\right]$$

The cone-angle of the free-jet without swirl is constant, and the cone-angle will be of 19^o.

The energy released in combustion will be higher by several orders of magnitude than the mechanical energy of the jet in which the reaction takes place.

The formulae set out above can be applied to the free-jet flames in case the average density of the flames is taken for the density of the surrounding material.

Due to the differences in density, buoyancy force will arise. The buoyancy force is of flow direction in case the burning is taking place upwards from below. Consequently, the momentum flow will not remain constant

but it may increase essentially. The mixing along the length of the jet is the more intensive the more rapid the momentum flow of the jet is. Consequently, the buoyancy force acting in the direction of the jet accelerates the mixing process and reduces the flame. The researchers have proved the fact that in case the Froude-number is above value 10^5 (concerning the conditions prevailing within the nozzle), no remarkable action of the buoyancy force upon the length of flame can be observed. With the horizontal flames, the action of the buoyancy force is more compllicated but the mixing process is accelerated in this case, too.

In combustion chambers, the heat- and density-differences between the flame and the neighbouring material are essentially smaller than with the flames burning freely. Therefore, the buoyancy forces are also smaller but they can not be neglected especially at the ends of flames.

In turbulent diffusion flames, the fuel- and air-flows are mixing to a decisive extent as moving away from the mouth of burners due to the turbulent momentum- and mass-transfers. With the neglection of the time-demand of chemical reaction, the progression of combustion can be determined approximately as a function of the mixing process. The characteristics of turbulent flames can be calculated with the help of the following equations:

Momentum flow:

$$\dot{I} = 2\pi \int_0^r \varrho u^2 y dy = \dot{I}_o \quad ,$$

Mass flow:

$$\dot{M} = 2\pi \int_0^r \varrho c u y dy = \dot{M}_o \quad ,$$

Reduction in concentration of the jet along the axis:

$$c_m = \frac{1}{x} \quad \frac{\dot{M}_o}{\sqrt{\dot{I}_o \varrho}} \quad k_2 \quad ,$$

Reduction in velocity of the jet along the axis:

$$u_m = \frac{1}{x} \quad \frac{\dot{I}_o}{\sqrt{\varrho k_1}} \quad ,$$

where:

$$\dot{M}_o = [\rho cu]_o \frac{\pi}{4} d_o^2$$

$$\dot{I}_o = [u^2 \rho]_o \frac{\pi}{4} d_o^2$$

k_i is a constant to be determined epxerimentally.

Simultaneously,

$$\frac{c_m}{c_o} = k_3 \frac{k_o}{x} \sqrt{\frac{\rho_o}{\rho}}$$

If a fuel-flow of density ρ_o is mixing with ambient air of density ρ_k, then:

$$\frac{c_m}{c_o} = k_3 \frac{d_o}{x} \sqrt{\frac{\rho_o}{\rho_k}}$$

If the fuel-air mixture enters into reaction within the components, then density ρ_L should be used in the similarity region.

$$\frac{c_m}{c_o} = k_3 \frac{d_o}{x} \sqrt{\frac{\rho_o}{\rho_L}}$$

which means that the concentration is reducing slower in the flame — dependently from the density-ratios in it — than in a not burning jet ($\rho_k > \rho_L$).

The flame ends at the point where the concentration along the axis is stoichiometrical $[c_m = c_{st}]$.

The length of the flame is yielded from equation:

$$\frac{x_1}{d_o} = k_3 \frac{c_o}{c_{st}} \sqrt{\frac{\rho_o}{\rho_L}}$$

where:

x_1 is the distance from the end of flame to the flame front.

The flame-front does not generally coincide with the output cross-section of the jet (mouth of burners). According to our experiences, the following statements can be made:

— With smaller Reynold's numbers, the similarity region starts earlier and draws closer to the output hole.

— With double-concentring jets, the relative velocity between the two jets is reduced, and as a consequence, the beginning of the jet is shifted into flow direction due to the turbulent transfer processes.

— In case of swirl, the mixing process taking place at the beginning of the jet is accelerated, and as a consequence, the beginning of the jet is shifted dependently from the changes in density ratios.

The single-concentring jet is influenced also by the moment of momentum-flow in addition to the axial momentum-flow bringing about the mixing due to the superimposed rotary motion, and this, in turn, will involve the acceleration of mixing.

The reduction in concentration within the single concentring jet with swirl will develop according to the equation deducted for the single concentring axial jet:

$$\frac{c_m}{c_o} = k_4 \frac{d_o}{x + k_5 D}$$

where:

k_i — constant to be determined experimentally,

D or $\frac{D}{d_o} = \vartheta$ is the parameter of swirl.

The flame ends when the stoichiometrical mixture has been reached, the position of which can be calculated from the following equation:

$$\frac{x_1}{d_o} = k_4 \frac{c_o}{c_{st}} \sqrt{\frac{\varrho_o}{\varrho_L}} - k_6 \vartheta$$

Description of experiment

The experimental equipment consists of the following main parts:

— burner group

— Schlieren equipment

— device for measuring electric conductivity

— device for measuring components CO, CO_2 and the temperature.

The photo taken of the experimental equipment is shown in Fig. 1, while the block diagram and the operational scheme of it can be seen in Fig. 2.

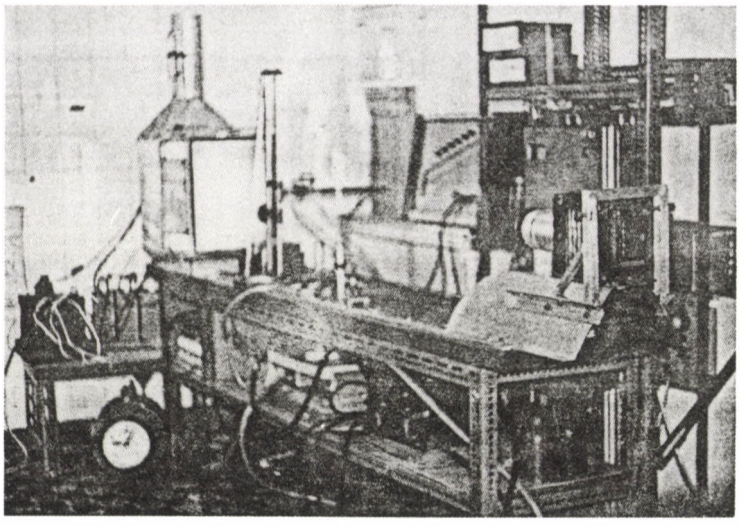

Fig. 1. Experimental equipment

Burner group

The drawings of the gas burners used in the experiments are shown in Fig. 3, while the photo of a gas burner can be seen in Fig. 4. In accordance with the aim of experiments, the burners chosen are gas burners of diffusion type, the nozzles of them can be replaced as it is represented in Fig. 3.

With a layout according to Fig. 2, the gas and air should be of such quality which is identical with that of the gas-air mixture blown into the combustion chamber of Bunsen-burners. In order to develop a proper nozzle, relatively numerous preliminary experiments were carried out. Since one of the main requirements was that the shape of flames could be varied essentially during later experiments because this fact will expectedly play an important role in the interactions.

The experimental equipment consists of 5 burner-groups each containing several burners. The burners are positioned along a straight line parallel to each other with their axis, and being at an equal but variable distance from each other.

For the purpose of taking proper photos with the help of the Schlieren equipment, the height of burners can be altered by means of a holding frame.

The measuring devices belonging to the equipment, and the block diagrams are shown in Fig. 2. Accordingly, the gas is supplied from the

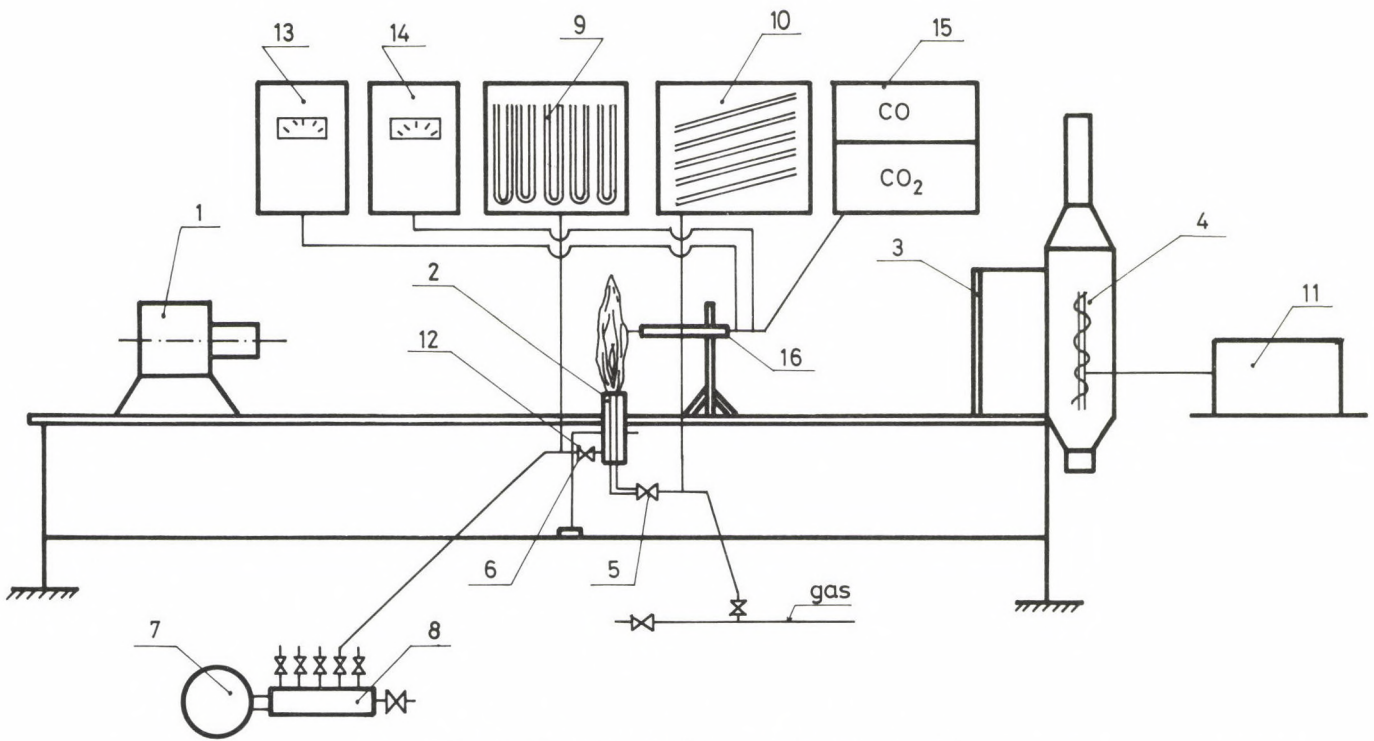

Fig. 2. Block diagram of the experimental equipment
1. Picture-forming unit, 2. Burners, 3. Lamp, 4. Flash-lights, 5. Gas valve, 6. Air valve, 7. Exhauster, 8. Air reservoir, 9. U-tubes, 10. Gas manometers, 11. Flash-lights, 12. Burner-holders, 13. Temperature-measuring device, 14. Device for measuring electric conductivity, 15. Device for measuring CO, CO_2, 16. Sounds (T, E, CO, CO_2)

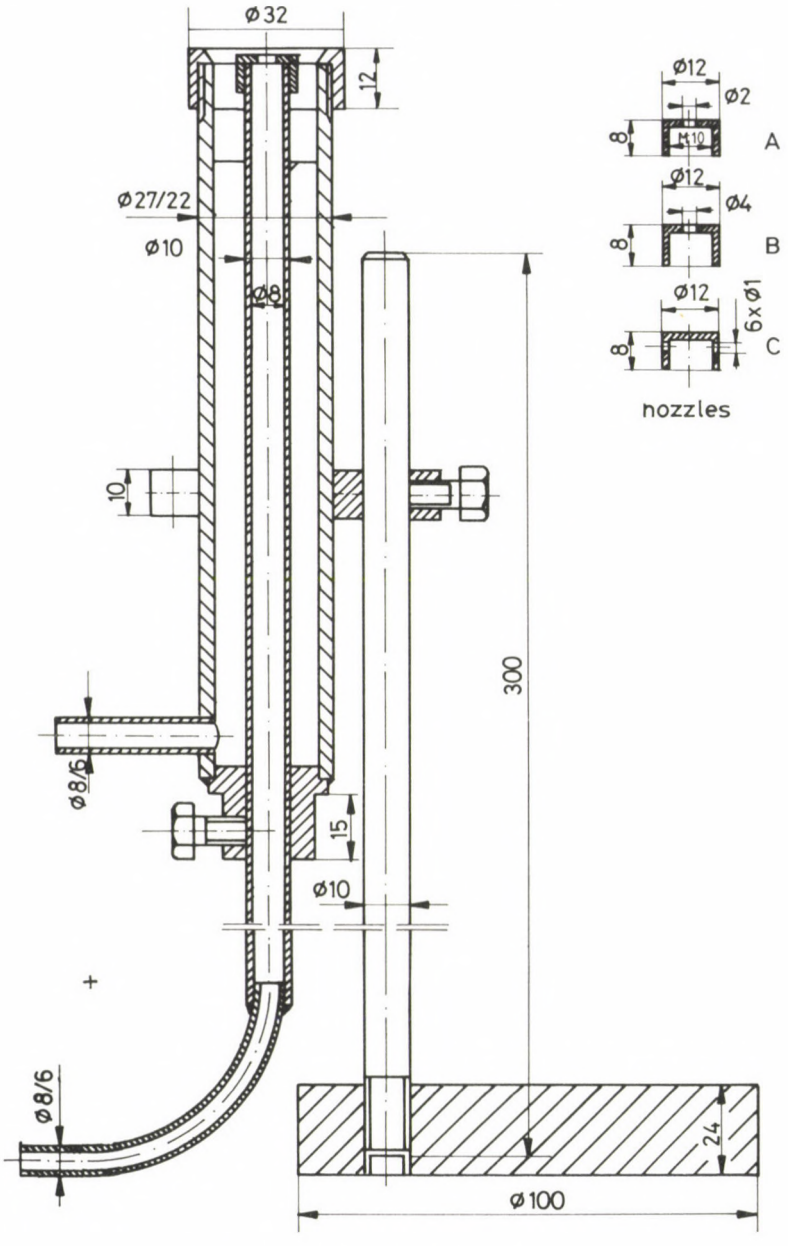

Fig. 3. Drawings of experimental burners

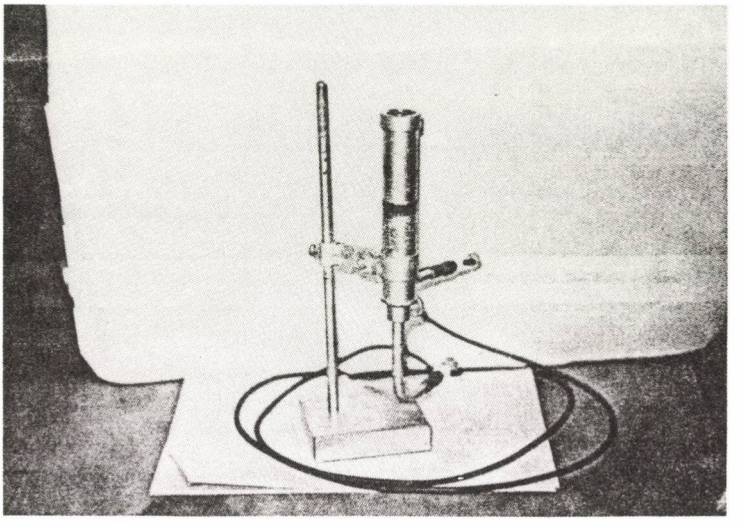

Fig. 4. Experimental burner

network into the distributing reservoir, and reaches the nozzles through stop-cocks and a flow-meter. The air was compressed into the nozzle by an industrial exhauster through the distributing reservoir, the flow-meter and stop-cocks. After the stop-cocks, there are manometers inserted to determine the volume of gas and air per burners by reading off the values shown on the manometers having been calibrated previously.

Schlieren equipment

To assemble the experimental equipment, the available 4.5/300 Tessar objective was used, and the raster constant was selected as e = 2 mm. The primary raster had a dimension of 30x40 cm, while the negative had a dimension of 6.5x9 cm including a field of sight of 15x20 cm onto the object positioned in the middle between the objective and the primary raster, and so the transformation-ratio of the object was N=0.5. The sensitivity achieved in this way was approximately 10 sec of arc calculated by means of the following formula:

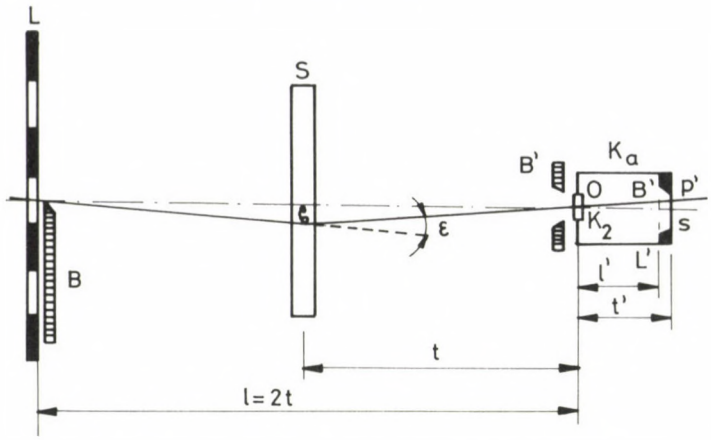

Fig. 5. Operational scheme of Schlieren equipment

$$\varepsilon_{min} = \frac{e}{40 \cdot f} \quad \frac{N}{N+1} \quad \text{(rad)}$$

The source of light applied in the Schlieren equipment consisted of two parts: normal source of light and a momentum-source of light. The lamp-matrix of the normal one contained 6x5=30 units of opal spherical krypton lamps of 60 W each. The momentum source of light was made up of 3 flash-tubes and 6 spherical krypton lamps of 60 W each. In the tubes of 400 torrs filled with argon, the discharge takes place in the form of a spark running along the ignition electrodes. The operation of the Schlieren equipment can be seen in Fig. 5.

Device for measuring electric conductivity

The measurement of electric conductivity is performed by means of 550 Hz frequency current, and in this way, the fluctuation of conductivity can be examined up to 225 Hz. In the flame, a detector of cylindrical-capacitor-type was used having a small diameter, which was made in the work-shop of the Department of Heat Engines at Budapest Technical University (BME). The drawing of the sound is shown in Fig. 6. The sound is a cylindrical capacitor of a capacitance 1-2 pF. Its internal electrode is a bar of 1 mm in diameter, the length of the external cylinder is 3 mm, while its minor diameter is 2 mm. Accordingly, the signal was measured as resulting from the ionic and electron-concentration of the medium flowing through the cylinder of a volume 9.42 mm^3, and having a surface area of 3.14 mm^2. The

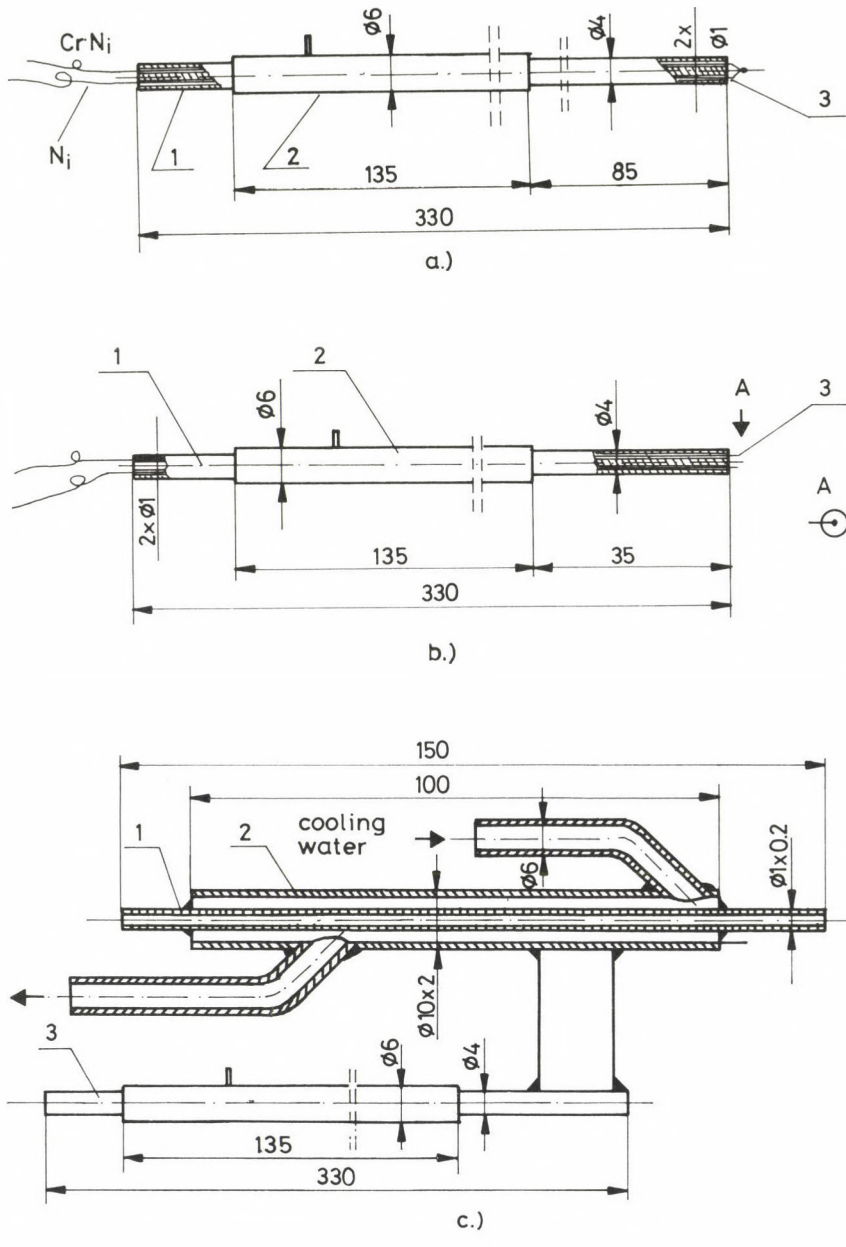

Fig. 6. Measuring Sounds

a) Temperature-measuring sound - 1. Ceramic tube, 2. Copper tube, 3. Thermocouple N_i - CrN_i Ø 0.5; b) Sound for measuring electric conductivity - 1. Ceramic tube, 2. Copper tube, 3. Copper sound for measuring conductivity; c) Gas sampler - 1. Sampling tube (heat-resistant needle), 2. Cooling-water tube, 3. Holder for the measuring-coordinator

matching of the signal to be measured to the input amplifier was provided by the measuring unit. The connection of the sound was implemented by a twin-hole ceramic tube to avoid failure caused by glowing. The experimental sounds were mounted on a holding frame movable in three different directions, due to which the sounds can be positioned accurately at the required measuring point in the flame.

Temperature-measuring device

The measurement of the temperature along the flame is carried out with the help of the thermocouple made in our workshop. The thermocouple was made of "Ni - CrNi" which can be applied within a temperature range 0—1400^{o}. The signals coming from the matching device were transmitted to the digital display. The temperature-matching device is shown in Fig. 6.

Analysis of local gas

In order to measure the composition of combustion products in the flame, a particular sound is applied whose picture is shown in Fig. 6. The gas sampler is connected with measuring unit "URAS" operating on the principle of absorption of infrared radiation.

Experimental results

After the experimental equipment had been constructed, a great number of experiments were carried out with the help of different measurement methods: photography, measurement of components CO, CO_2, measurement of electric conductivity, and measurement based on schlieren exposure. The photos shown in Figs 7, 8 represent the shape of flames in different combustion regions (laminar, transient and turbulent). The measurement results of the temperature, components CO, CO_2-, and electric conductivity distributions are represented in Figs 9—13.

From the above mentioned results it can be seen that there is a relatively wide zone within the diffusion flames beyond which the gas compositions are liable to changes. Within this area beyond the wide zone, changes are effected between the reactions and combustion products on the principle of interdiffusion.

On the basis of more than 2000 photos and the gas analyses performed at several points, the relations between the geometrical characteristics of

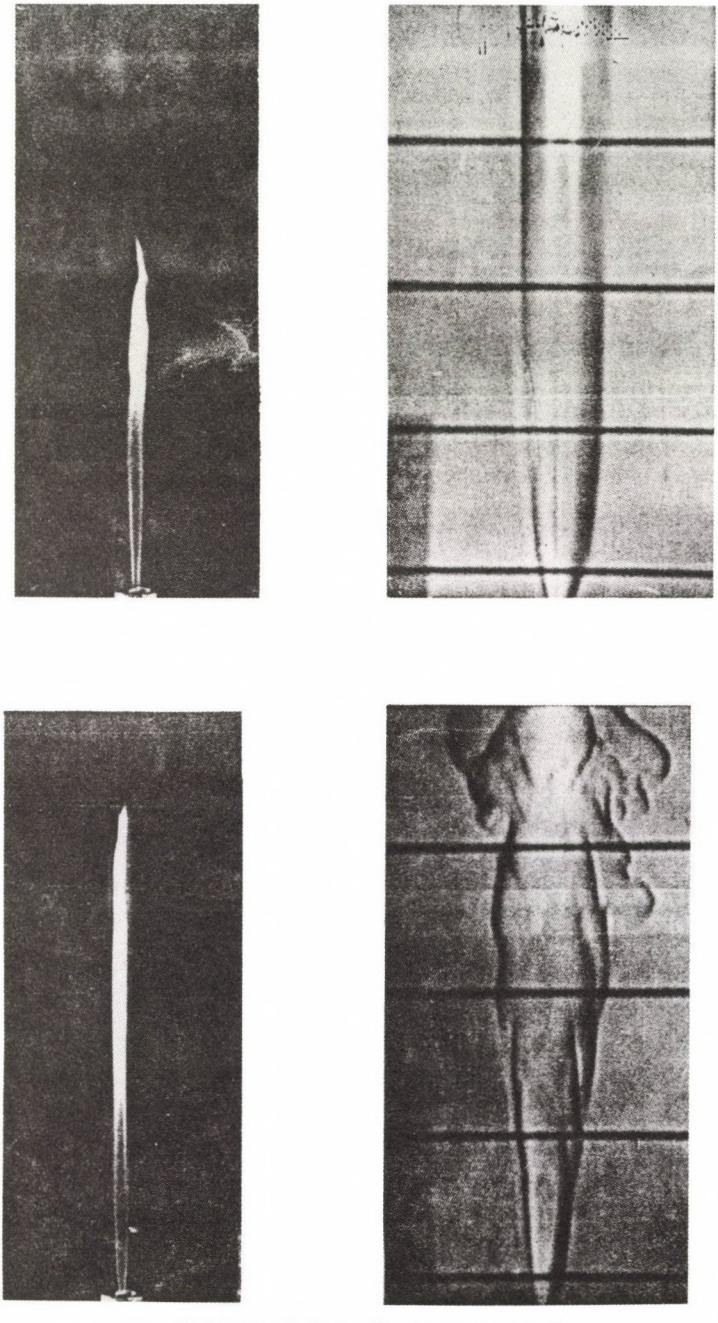

Fig. 7. Photo of flames (in laminar region)

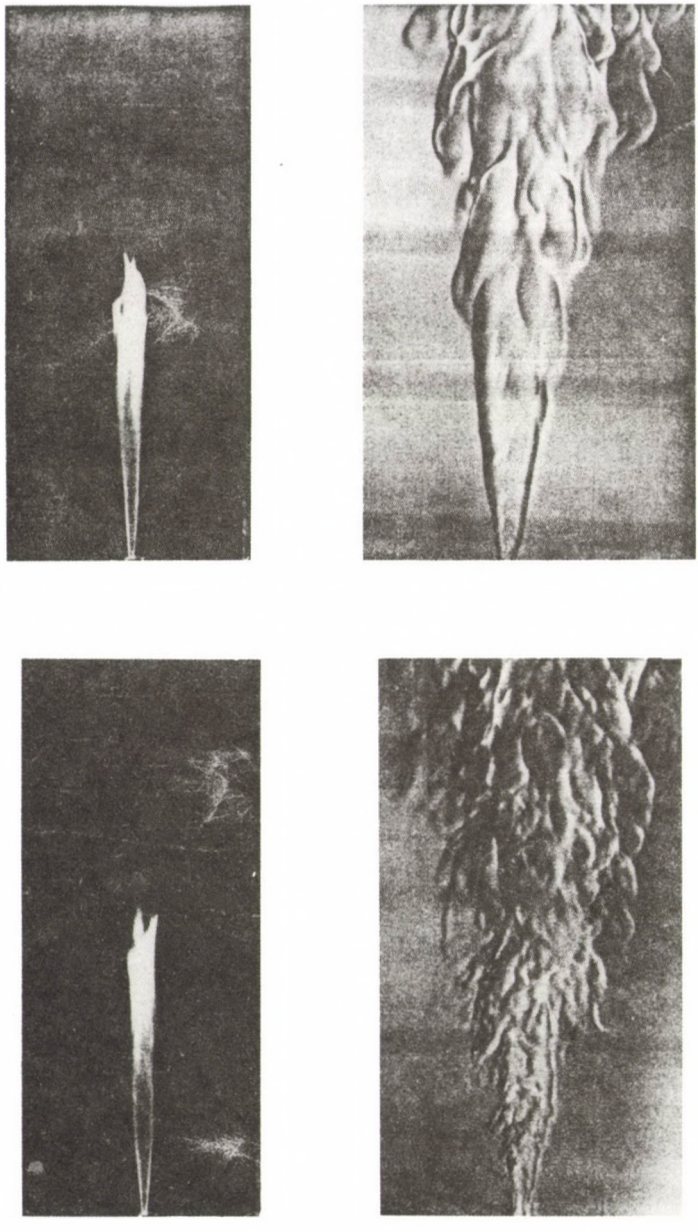

Fig. 8. Photo of flames - a) in transient region, b) in turbulent region

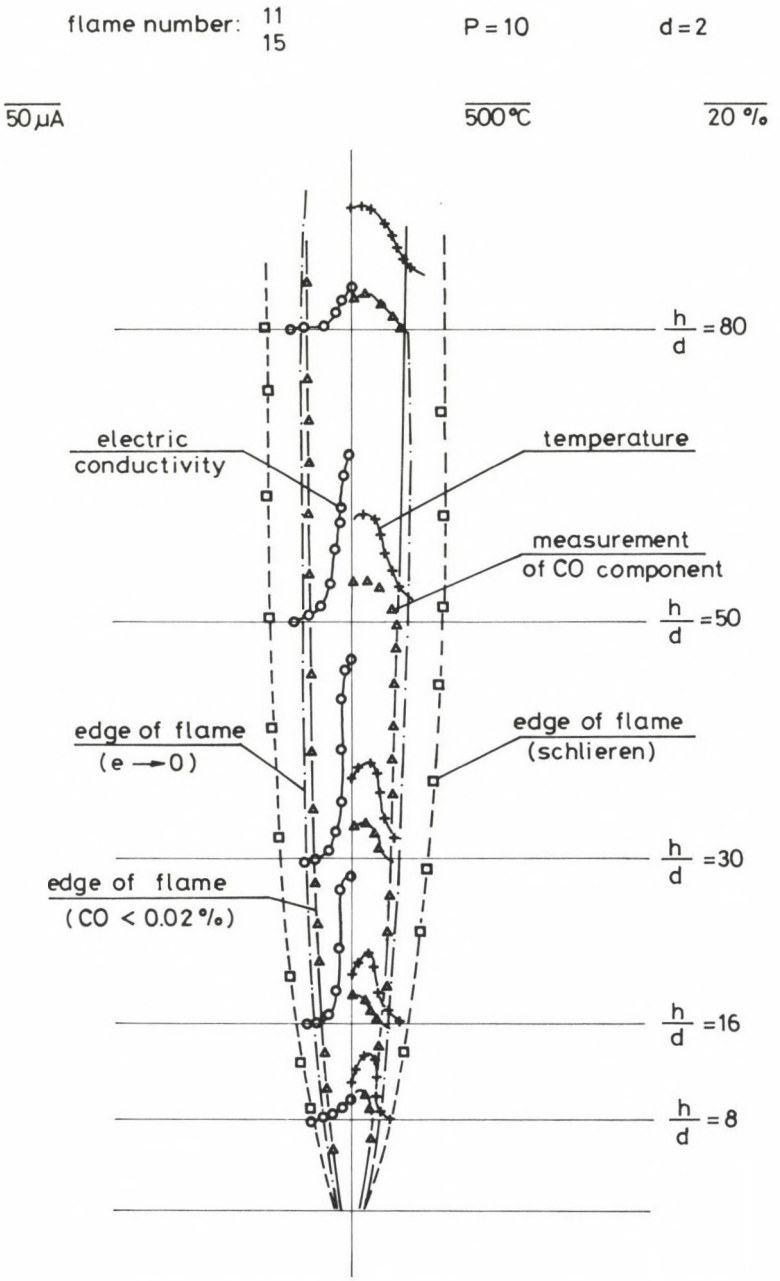

Fig. 9. Distribution of temperature CO, CO_2 and electric conductivity in different cross-sections along the flame-length

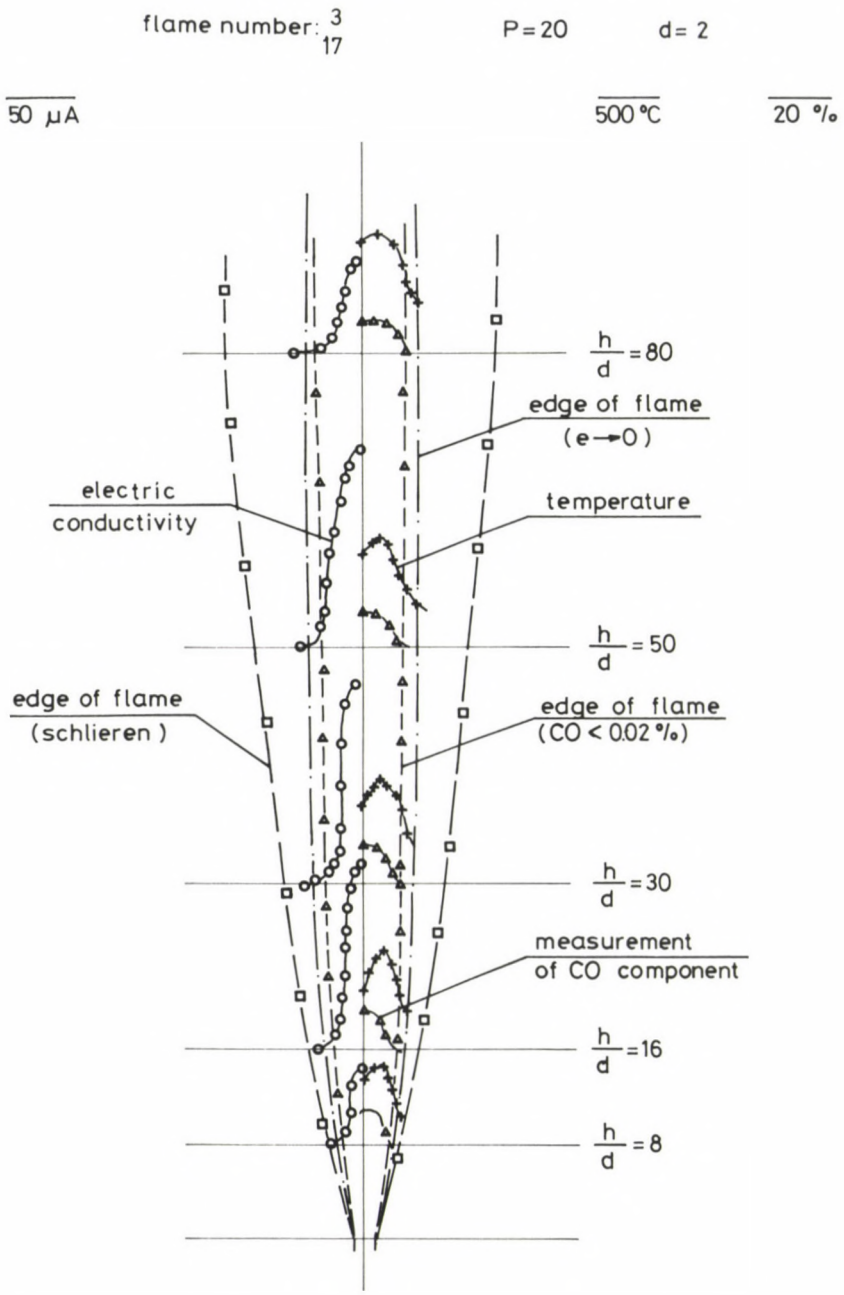

Fig. 10. Distribution of temperature CO, CO_2 and electric conductivity in different cross-sections along the flame-length

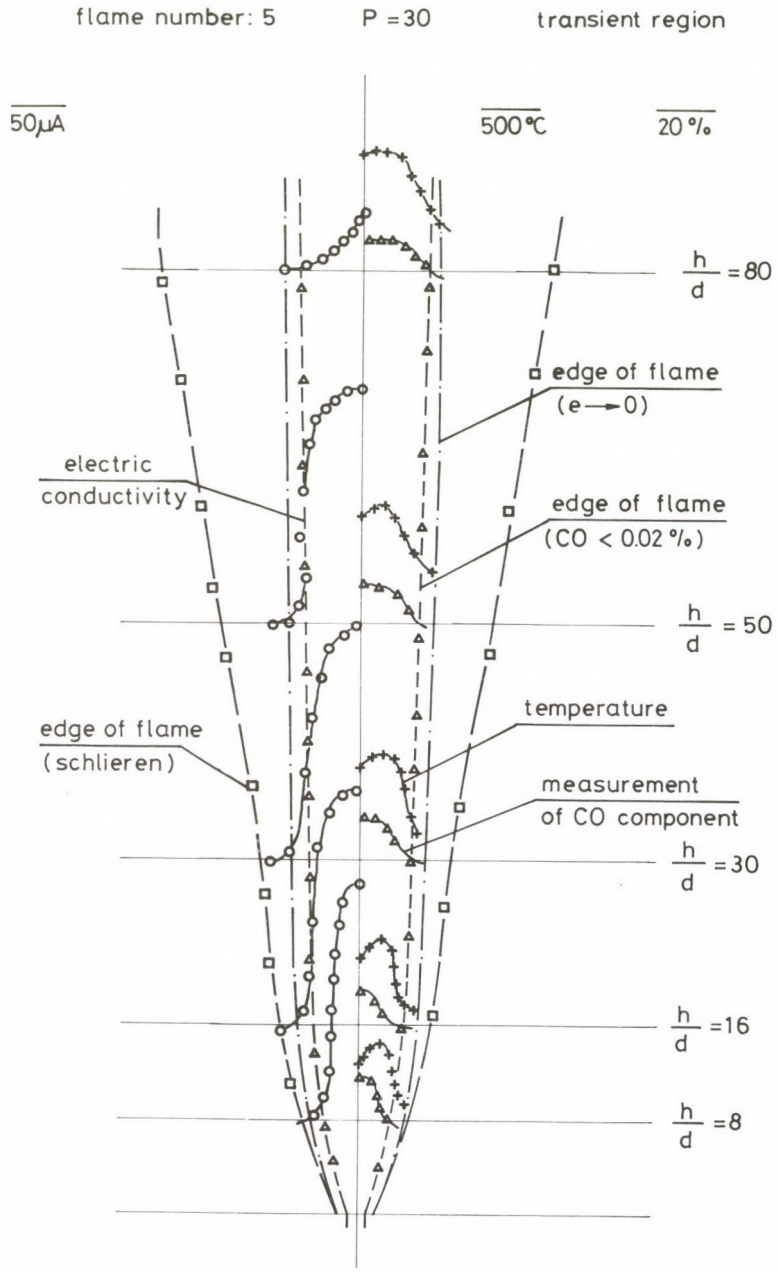

Fig. 11. Distribution of temperature CO, CO_2 and electric conductivity in different cross-sectiions along the flame-length

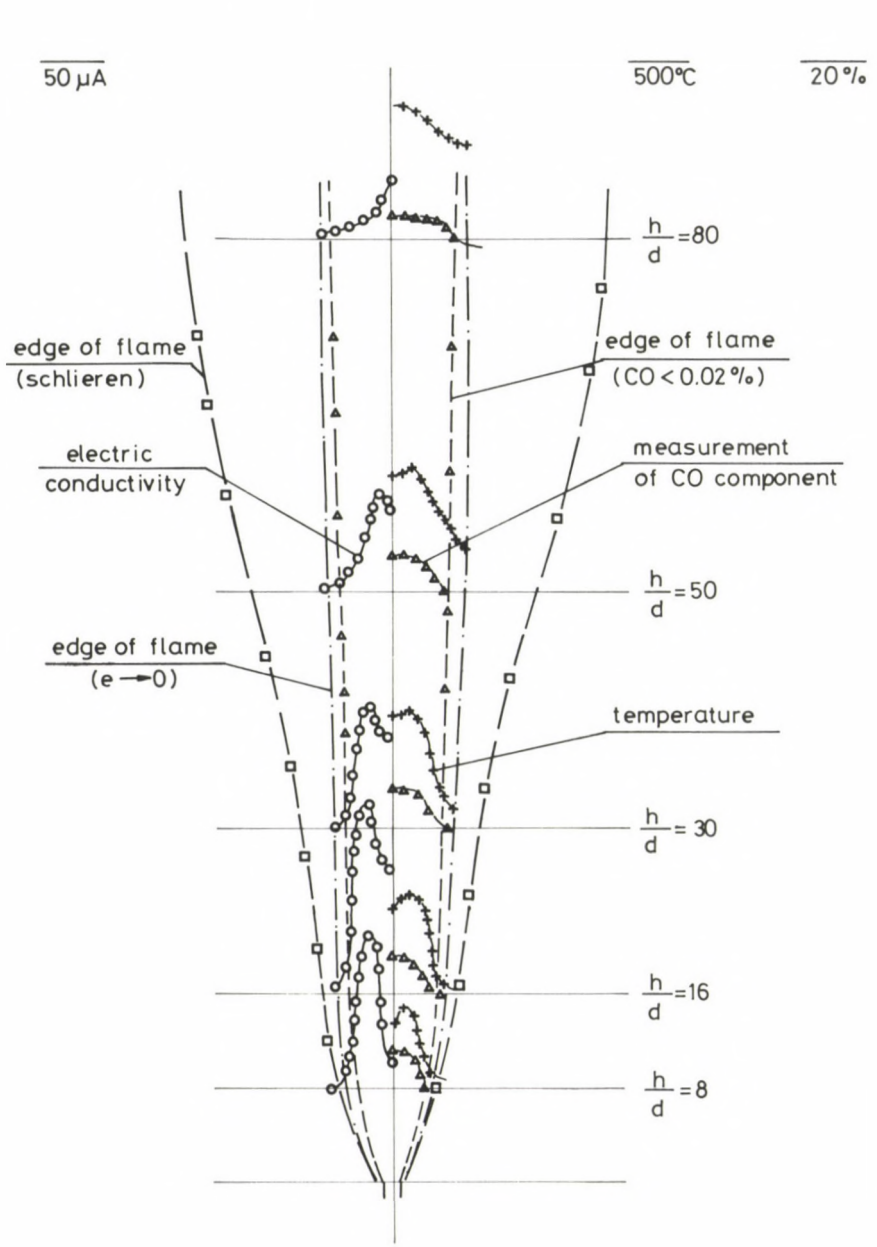

Fig. 12. Distribution of temperature CO, CO_2 and electric conductivity in different cross-sections along the flame-length

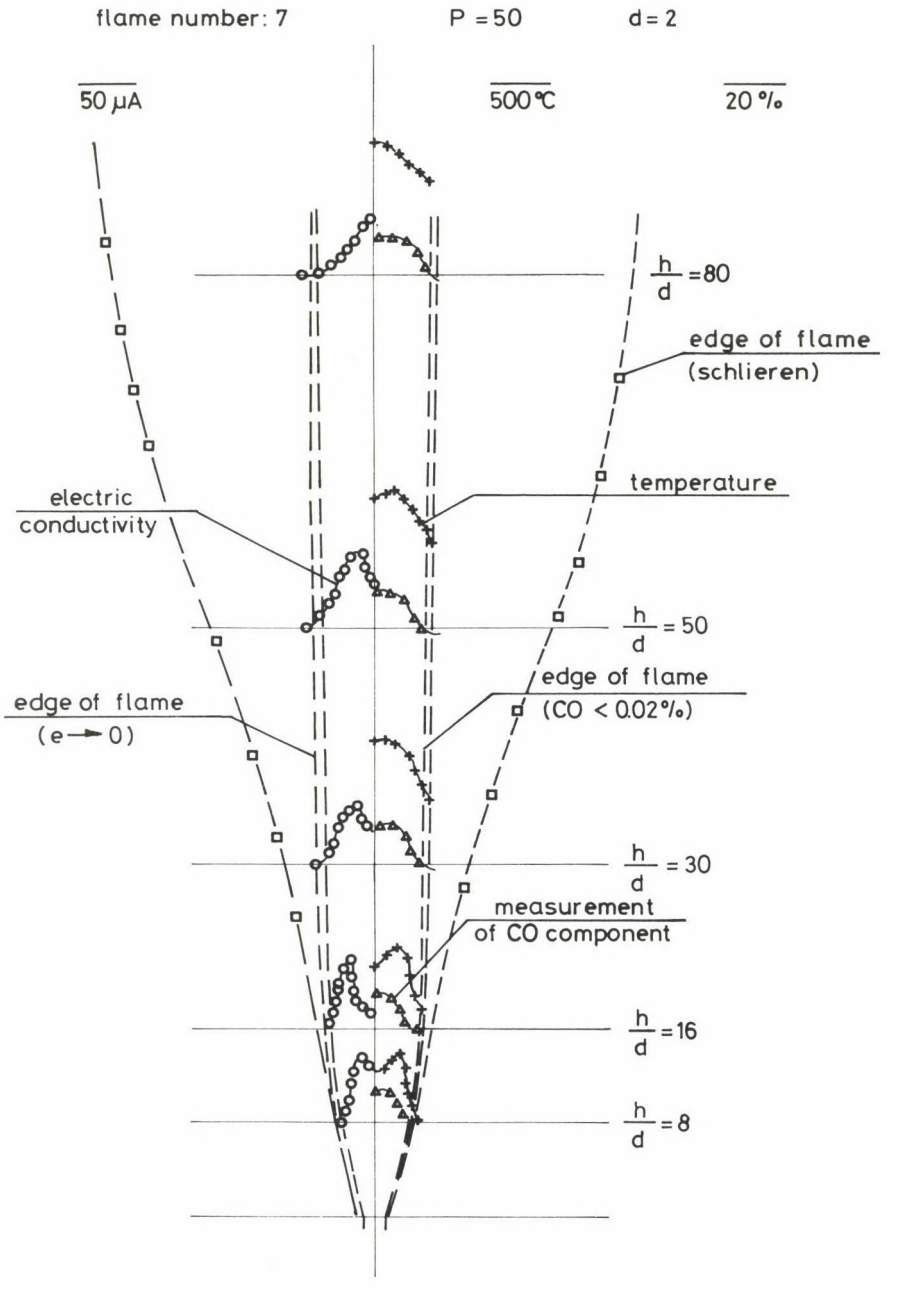

Fig. 13. Distribution of temperature CO, CO_2 and electric conductivity in different cross-sections along the flame-length

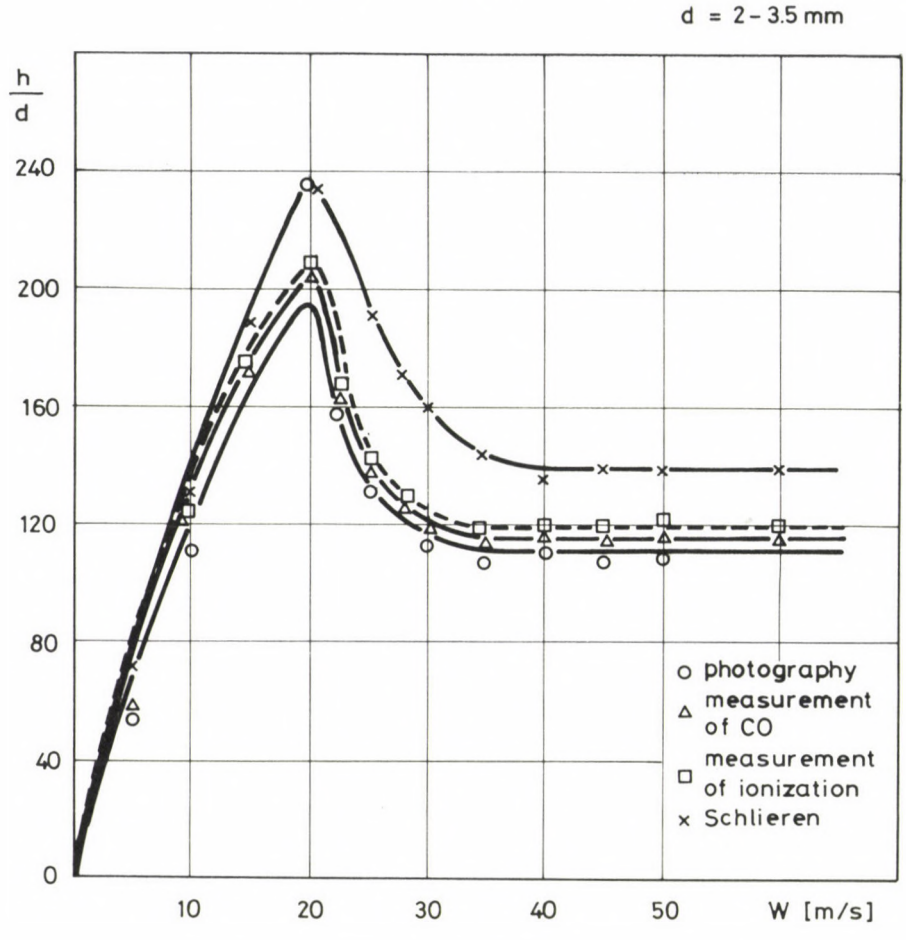

Fig. 14. Length of flames as a function of output velocity

the individual diffusion flames, the construction of nozzles and the flow characteristics are dealt with successively below.

Length of flames

As a result of our experiments, the length of diffusion flames is shown in Fig. 14 as a function of the nozzle diameter and the output velocity of the gas leaving the nozzle. From the diagrams it can be seen that in the laminar region, the length of flames is increasing proportionally with the increase in the nozzle diameter and the output velocity of the jet.

On the basis of our experiments, the approximate formulae to be

applied to the calculation of the flame-length were established with the help of the method of approximate calculation. These formulae can be expressed in the following form:

Within laminar region

$$\frac{h}{d_o} = k_1 \left[1 + L_{min}\right] w^{n_1}$$

where:

h — flame-length

d_o — diameter of nozzle

L_{min} — theoretical air-demand

w — output velocity of gas leaving the nozzle

k_1 — coefficient to be determined experimentally

$k_1 = 2.58$ by photo

$k_2 = 2.81$ by the measurement of CO component

$k_1 = 2.98$ by measurement of ionization

$k_1 = 3.5$ on the basis of Schlieren exposure

n_1 — exponent to be determined also experimentally

$n_1 - 0.94$ by photo

$n_1 - 0.923$ by measurement of CO component

$n_1 - 0.918$ by measurement of ionization

$n_1 - 0.89$ on the basis of Schlieren exposure

It can be seen that the diffusion flame-length is yielded the shortest by using the method of photography, and it is yielded the longest by using the method of Schlieren exposure, and as a consequence, an average value belongs to the measurement of CO component and electric conductivity.

In transient region, the length of flame is inversely proportional with the output velocity. On the basis of our experiments, the length of flames can be calculated by using the following formula:

$$\frac{h}{d_o} = k_2 \left[1 + L_{min}\right] w^{n_2}$$

where:

k_2 — coefficient to be determined experimentally

$k_2 = 1985$ by photo

k_2 = 1982 by measurement of CO component
k_2 = 1892 by measurement of ionization
k_2 = 1846 on the basis of Schlieren exposure

n_2 — exponent to be determined also experimentally
n_2 = -1.31 by photo
n_2 = -1.29 by measurement of CO component
n_2 = -1.26 by measurement of ionization
n_2 = -1.22 on the basis of Schlieren exposure

As it was proved by our experiments, in turbulent region the diffusion flame-length remains nearly unchanged with the increase in output velocity, which can be expressed by the following formula:

$$\ell = k_3 \left[1 + L_{min}\right] d_o$$

where:

k_3 — coefficient to be determined experimentally
k_3 = 18 by photo
k_3 = 20 by measurement of CO component
k_3 = 21 by measurement of ionization
k_3 = 24 on the basis of Schlieren exposure

Diameter of flames

One of the important values determining the geometrical characteristics of flames is the diameter of it. As it can be seen from the experimental data, the diameter of flames is dependent upon the diameter of the nozzle mouth and the output velocity. Within the different regions, the diameters of flames are also different. The relation between the maximum diameter of flames and the dimension of nozzle-mouth, as well as the output velocity is shown in Fig. 15. On the basis of diagrams, the formula applied to the calculation of the maximum diameter of flames was established with the help of the method of approximate calculation according to the following.

In laminar region:

$$d_{max} = k_4 \left[1 + L_{min}\right] w^{n_4} d_o$$

where:

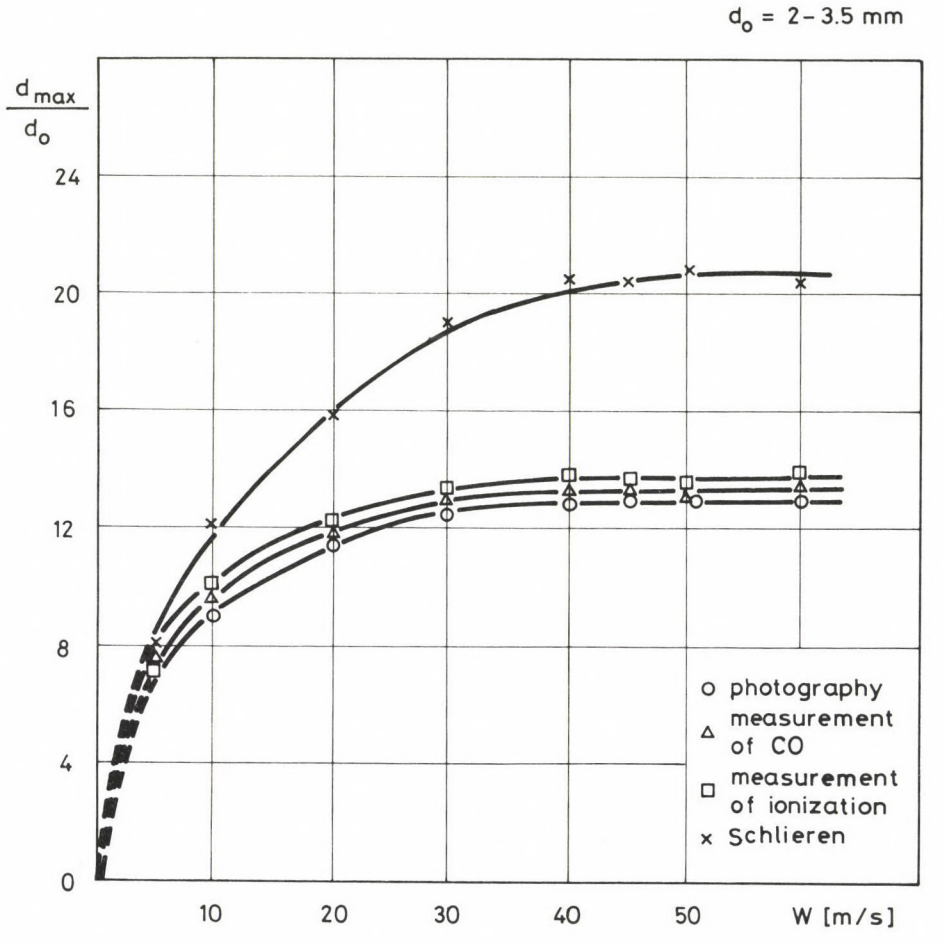

Fig. 15. Maximum diameter of flames as a function of output velocity

k_4 — coefficient to be determined experimentally

$k_4 = 0.80$ by photo

$k_4 = 0.86$ by measurement of CO component

$k_4 = 0.94$ by measurement of ionization

$k_4 = 0.79$ on the basis of Schlieren exposure

n_4 — exponent to be determined also experimentally

$n_4 = 0.328$ by photo

$n_4 = 0.315$ by measurement of CO component

$n_4 = 0.299$ by measurement of ionization

$n_4 = 0.447$ on the basis of Schlieren exposure

In turbulent region, the maximum diameter of flames is almost independent from the output velocity, which can be written as follows:

$$d_{max} = k_5 \left(1 + L_{min}\right) d_o \quad ,$$

where:

k_5 — coefficient to be determined experimentally

$k_5 = 2.25$ by photo

$k_5 = 2.33$ by measurement of CO component

$k_5 = 2.38$ by measurement of ionization

$k_5 = 3.97$ on the basis of Schlieren exposure

In transient region, the maximum diameter of flames varies in a complicated way with the increase of output velocity as shown in Fig. 15.

Enveloping surface of flames

With the knowledge of the flame-length and diameter, the surface of flames can be calculated theoretically, and this fact plays an important role in heat radiation- and heat release-calculations of the flames, nevertheless the surface of flames can be determined directly, too, in an experimental way. On the basis of our experimental results, it can be seen that the surface of flames is a function of the nozzle-diameter and the output velocity. The relations between the surface of flames and the output velocity are shown in Fig. 16. On the basis of the experimental diagrams, the formulae used in the calculation of flame surfaces were deducted with the help of approximate calculation, as seen below.

In laminar region:

$$F = k_6 \left[1 + L_{min}\right] w^{n_6} F_o \quad ,$$

where:

F — the enveloping surface of flames

F_o — cross-section of nozzle

$$F_o = \frac{\pi}{4} d_o^2$$

k_6 — coefficient to be determined experimentally

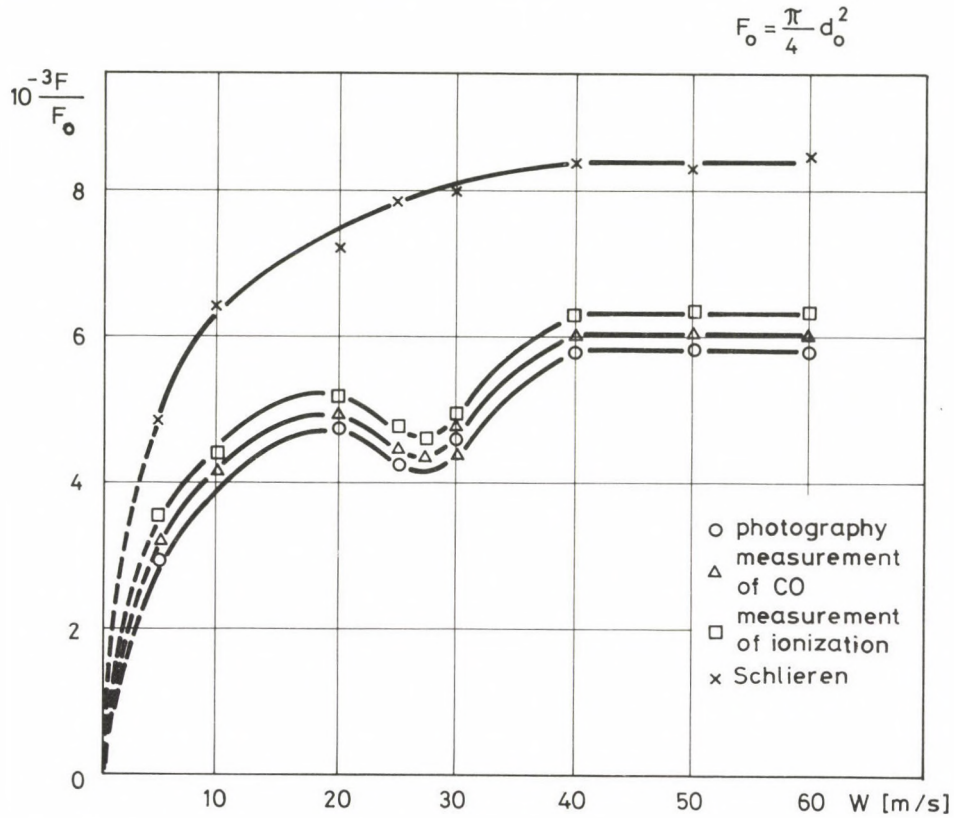

Fig. 16. Enveloping surface of flames as a function of output velocity

k_6 = 297 by photo
k_6 = 333 by measurement of CO component
k_6 = 399 by measurement of ionization
k_6 = 501 on the basis of Schlieren exposure

n_6 – exponent to be determined also experimentally

n_6 = 0.352 by photo
n_6 = 0.326 by measuring CO component
n_6 = 0.278 by measurement of ionization
n_6 = 0.537 on the basis of Schlieren exposure

In fully turbulent region: the enveloping surface of flames (practically independent from the output velocity) can be calculated by means of the below formula:

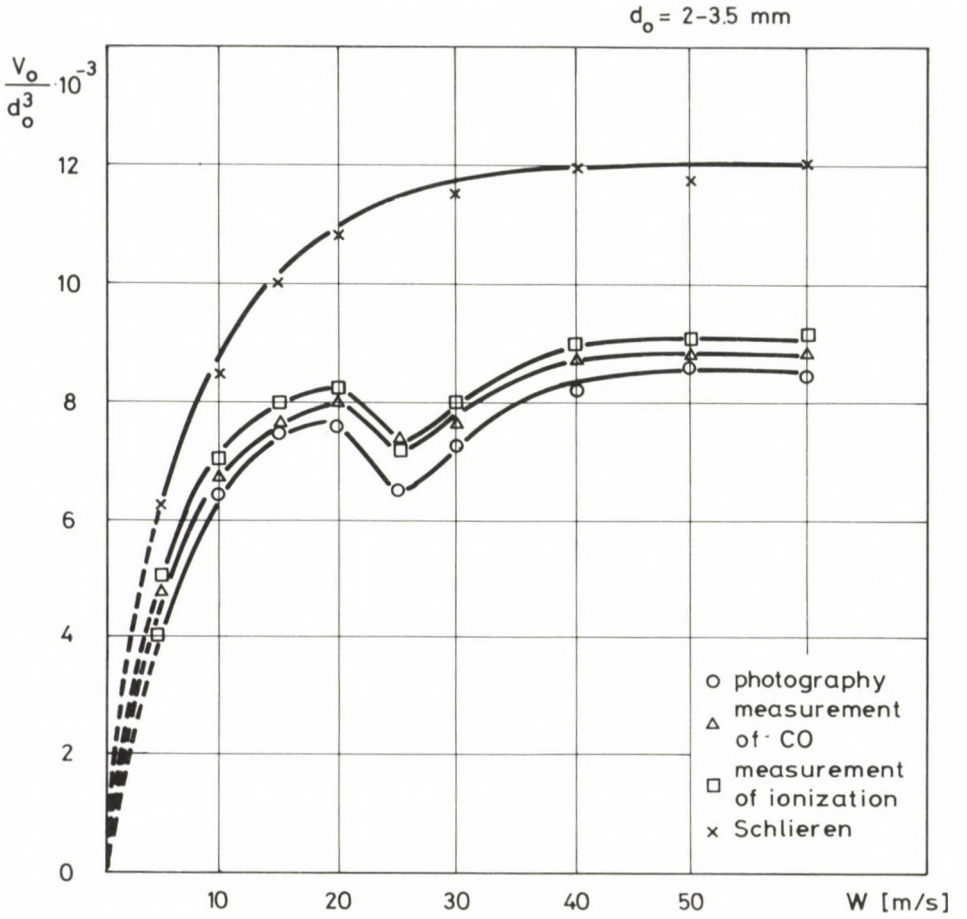

Fig. 17. Volume of flames as a function of output velocity

$$F = K_7 \left[1 + L_{min}\right] F_o \quad ,$$

where:

k_7 — coefficient to be determined experimentally

$k_7 = 1.00 \times 10^3$ by photo

$k_7 = 1.04 \times 10^3$ by measurement of CO component

$k_7 = 1.09 \times 10^3$ by measurement of ionization

$k_7 = 1.45 \times 10^3$ on the basis of Schlieren exposure

It should be noted here that the surface of flames is dependent not only on the length of flames but also on their diameter, therefore the change of the transient region can be seen in the diagrams of Fig. 16.

Volume of flames

The calculation of the volume of flames can be carried out similarly to that of the flame surface. On the basis of our experimental results and with the help of approximate calculation method, the relationships between the volume of flames, the dimension of nozzle and the output velocity were established as seen in Fig. 17.

In laminar region: the volume of flames is increasing proportionally with the increase of output velocity, which can be expressed by the following formula:

$$v = k_8 \left[1 + L_{min}\right] w^{n_8} d_o^3 \quad ,$$

where:

v — the volume of flames

k_8 — coefficient to be determined experimentally

$k_8 = 332$ by photo

$k_8 = 406$ by measurement of CO component

$k_8 = 478$ by measurement of ionization

$k_8 = 555$ on the basis of Schlieren exposure

n_8 — exponent to be determined also experimentally

$n_8 = 0.486$ by photo

$n_8 = 0.425$ by measurement of CO component

$n_8 = 0.384$ by measurement of ionization

n_8 (0.416 on the basis of Schlieren exposure

In fully turbulent region: the volume of flames is nearly unchanged in case the output velocity increases. These relations can be calculated by the following formula:

$$v = k_9 \left[1 + L_{min}\right] d_o^3 \quad ,$$

where:

k_9 — coefficient to be determined experimentally

$k_9 = 1468$ by photo

$k_9 = 1520$ by measurement of CO component

$k_9 = 1563$ by measurement of ionization

$k_9 = 2073$ on the basis of Schlieren exposure

The above diagrams and formulae can be applied to the free-jet diffusion flames, as well as in the case of town gas and natural gas.

In a closed space, there is another characteristics involved, i.e. recirculation due to which the jet can absorb more of the surrounding substances than was admitted into it in the form of combustion air from outside. The recirculation delays the mixing of the fuel and air, and owing to it, the flame will be extended in length. According to our experimental results and foreign researchers, the difference between the dimensions of the free-jet flames and those of the closed-jet ones can be expressed by the following relationships:

$$\ell_{cl} = \left[1.1 - 1.3\right] \ell_f$$

$$F_{cl} = \left[1.25 - 1.5\right] F_f$$

$$v_{cl} = \left[1.3 - 1.6\right] v_f$$

where subscripts: cl and f refer to the closed and free-jet flames, resp.

REFERENCES

1. Mao, S.N.: Examination of flows in flames within the combustion chamber of steam generators, (In Hungarian) Candidate dissertation, MTA 1979

2. Si Mao, S.N. - Zentai, K.: Examination of the shape of gas-flames (In Hungarian), Energiagazdálkodás, Budapest, 1979/XII

3. Medgyes, B.: Adaptation of Schlieren Method, Study (In Hungarian) OKGT-GKVÁ Budapest, 1979

Acta Technica Acad.Sci.Hung., 101(3), pp. 259–280 (1988)

EFFECT OF MATERIAL INTENSITY AND ENERGY INTENSITY ON THE EFFICIENCY OF DEVELOPMENT OF THE NATIONAL ECONOMY

ERDŐSI, P.*

(Received: 1 June 1987)

This is a contribution of the author to a conference on 'Importance of the economic utilization of materials and energy in technical development' held on May 4, 1987, organized by the Department of Technical Sciences of the Hungarian Academy of Sciences.

Adopting a combined technical-economic approach, the author presents a macro-economic situation report on the enormous field referred to in the title. By means of some diagrams, the author casts light upon the most important relationships which have determined the events of world economy in the recent 15 years and on the other hand, he evaluates the Hungarian conditions as a function of international changes called also 'changeover to a new era in world economy'.

Introduction, background, the problem posed

The problem of material intensity and energy intensity** has come to the front in the world's interest more recently as a result of repeated oil price explosions as a problem having both technical and economic implications. At that time, international actions started to hold ground against the rapid increase of production costs, efforts which resulted in the last analysis, at least in some top industrialized countries of a market-controlled economy, in favourable economic changes based on high tech of the present days. These changes are essentially an unprecedented rapid economic restructuring accompanied a rapid reduction of the material and energy intensity in production.

Although the problem has been recognized everywhere, the change has taken place in different ways and at a different rate in the different countries or groups of countries in effort to adjust the economy to the new conditions.

A typical example of this effort is an increase by about 30 to 50% of net production (or GDP) in the industrialized countries as compared with

---

*Erdősi, P., H–1025 Budapest, Felsőzöldmáli u. 3/b, Hungary

**Specific material and energy consumption per unit production (GDP)

Akadémiai Kiadó, Budapest

the value before the oil crisis while the consumption of material and energy remained more or less unchanged.

Indirectly, the same is suggested by the change in energy intensity in IEA countries (included in the organization of International Energy Agency) in the period between 1973 and 1984. According to Fig. 1 /1/, a reduction of approximately 20% occurred in this period in total energy intensity and that of oil intensity amounted to 30%. However, as seen in the Figure, the improvement occurred in majority in the period after the second oil price explosion.

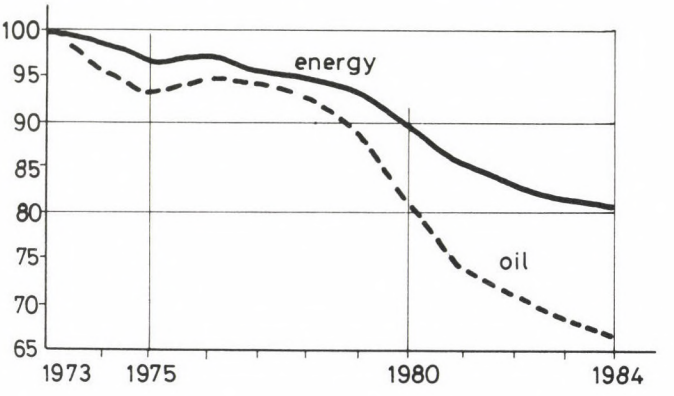

Fig. 1. Energy and oil intensity in total IEA 1973 to 1984 /1/

A reduction of energy consumption or, in other words, a reduced energy intensity necessarily implies a rationalized use of materials, first of all basic materials as the difference of some orders of magnitude (tenfold, twentyfold or even fiftyfold) between the energy intensity figures of basic material industry and processing industry is a well known fact. Hence, the energy demand and energy intensity of the national economy is fundamentally determined by the basic material producer sector in spite of the fact that the contribution of this sector to income is 'insignificant'. The conditions of home industrial production are demonstratively illustrated by the figures tabulated in Table 1 (indicating only approximate numerical values for the most important characteristics). On the basis of the Table, the difference between basic material industry (AIP) on the average and manufacturing industry (FIP) on the average is appreciable.

Tabulated in columns s_i of the Table are approximate values of contribution to GDP while in the second column, the approximate share in

Table 1.

	$s_i = P_i/P$ %	E ratio %	E/s_i %/%	Ratio
AIP	15	70	4.5	15
FIP	85	30	0.3	

energy consumption, the other columns indicating the ratio between these contributions and shares. Conspicuously,

— the contribution of AIP to GDP is about 15% only while its share in energy consumption amounts to 2/3 of total consumption

whereas

— the manufacturing sector with its contribution of about 85% to GDP has a share of only 30% in total energy consumption.

— The quotients of the index numbers show how did the change of the ratio of the different sectors in production affect the energy demand and/or energy intensity. The role of economic restructuring, the magnitude of the effect of changes are demonstrated by these figures.

The tabulated figures are more or less applicable also to international conditions. (According to a Japanese analysis /2/, within the industrial sector, the contribution of basic material industry to GDP is 24%, its share in energy consumption being 67% while within the manufacturing sector, 40% of total industrial production comes from machine industry, highly developed and most up-to-date in Japan, its share in energy consumption amounting to 3% only.)

The significant effect of reduction of material and energy intensity on the efficiency of production is reflected by this situation alone as suggested by the Table unanimously.

Namely, the capital intensity of the energy sector is well known. That means that the capital demand of the energy sector is disproportionately high as compared with the narrow resources available in general.

Moreover, the high energy intensity is usually combined with a high capital intensity. That means that in sectors of a high energy demand, also the capital demand is significant while at the same time the contribution of these sectors to income is relatively small.

Hence, the material intensity and energy intensity of production, denoted hereinafter by α and ε, respectively, affect the efficiency of

production directly. That is the absolute and specific income of the national economy depends fundamentally on these factors. It is therefore a fundamental requirement that the material and energy intensity be reduced with a view to increase the efficiency of production of the national economy. However, this requirement implies more than a conventional rationalization and conservation effort; it also implies a sectoral and production restructuring.

Methodological considerations, definitions

Before some diagrams of a global character are presented, let us see the simplified formula used in production efficiency analysis based essentially on the conventional equation,

$$c + v + m = x \gtreqless p \text{ (price)} \qquad (1)$$

of the value-creating process. According to the formula, costs c+v required to produce a product and at least the assumed (or expected) net income, m, shall be refunded in the course of marketing ($p \geqq x$). Should, however, the price be $p < x$ which means that the product is sold at a reduced price, not only net income m will not be realized but after an additional price reduction, part of the expenditures will not be refunded either.

The relationship applies to individual products and to the production of the national economy alike.

In the present analysis, the simplified formula given above shall be extended.

In so doing, material cost c is broken down to different components and, in addition to energy c_e, the most important groups of material consumption (basic material for metallurgy, chemical industry, agriculture, other materials and components, up-to-date equipment etc. and amortization) are used as an independent component each (c_{Fe}, c_{Al}, c_{Vi}, c_{mg}, ... etc.).

The GDP value added which is essentially the source of final output including private and communal consumption, increase in stocks for investment (and payment for losses due to unfavourable terms of trade and repayment of debts, a serious trouble today) is given as the difference between gross production x (or market price $p \gtreqless x$) and material expenditures c, the ultimate aim of production being an absolute and relative increase of GDP.

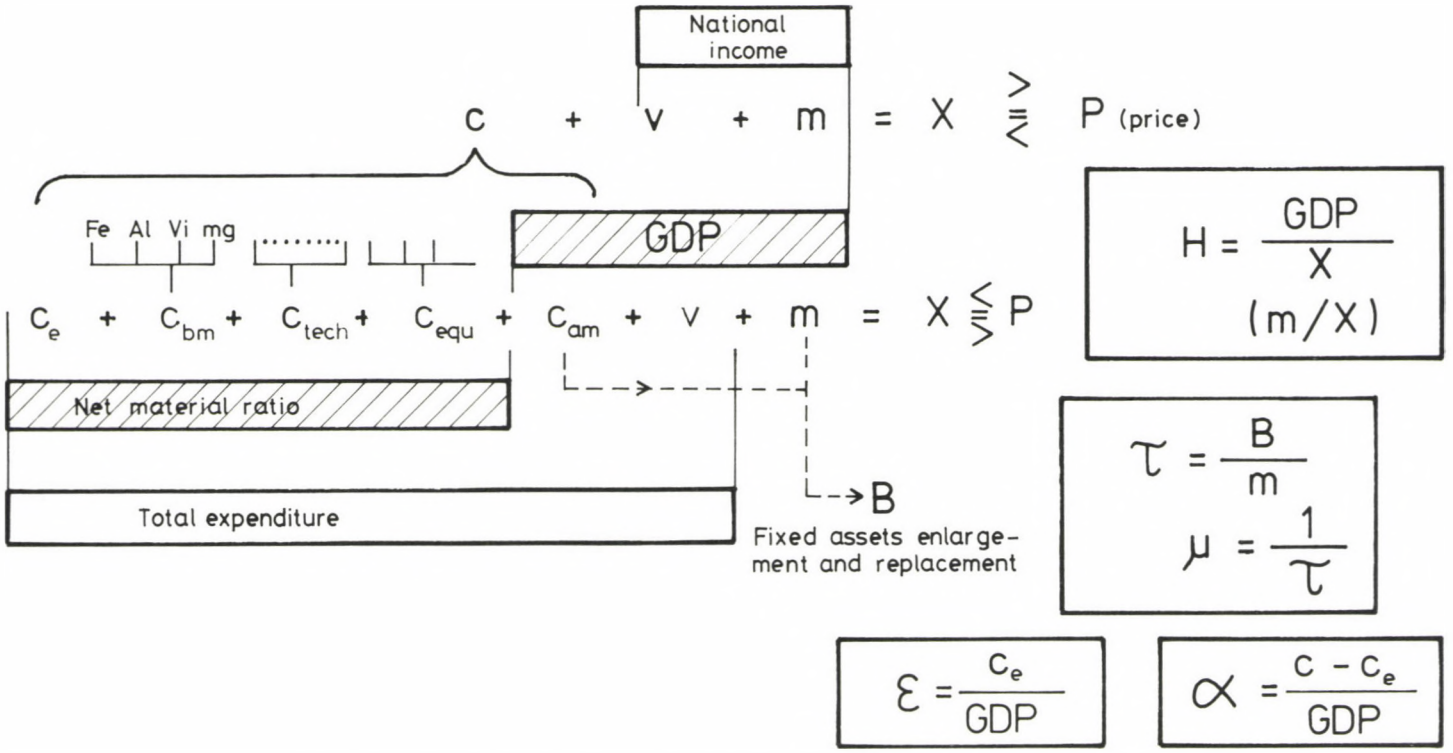

Fig. 2. Basic equations of the value-creating process, most important characteristics

In cost and income analysis, the equations for value creation shall reasonably be related to specific, unit production (as shown by Figs 4 and 5 given later in this work).

The detailed formula permits the following basic relationship, a matter of fact indeed, to be gathered:

For given (e.g. unit) x, the lower the net material consumption, the higher the GDP or in other words, as the energy and material intensity improves, the efficiency of the national production (H) increases accordingly.

Investment B (increase of fixed assets), resulting from amortization and part of net income m, is also included among the relationships given in Fig. 2, which as a certain 'fixed' ratio of GDP serves for simple and progressive reproduction. The specific value of this investment B, related usually to net social income m (or occasionally to GDP (is essentially the 'capital intensity' (τ), its reciprocal (μ) being the specific capital efficiency (taking into consideration also earlier investments).

The efficiency of the national production can be evaluated first of all on the basis of absolute and relative quantities of GDP (or of m); it is essentially index numbers GDP/x or m/x that can be used to describe the macroeconomic efficiency.

The index number defined above and index number

$$\eta_{ng} = \frac{K}{E}$$

describing the efficiency of the national energy system /3/ have much in common. In the above formula, K is the output for utilization in production and in private consumption from total energy input E of the energy system.

In Fig. 3, the above efficiency index numbers of the national economy are illustrated graphically, making use of what is offered by the input-output model. Here

— the mutual inputs (current expenditures on production) and outputs of the sectors are included in quadratic field C,

— the creation of GDP being represented by dark field T (to which import sources I are added) while

— the utilization of GDP appears as field K on the right (completed with field Ex representing export to compensate for import).

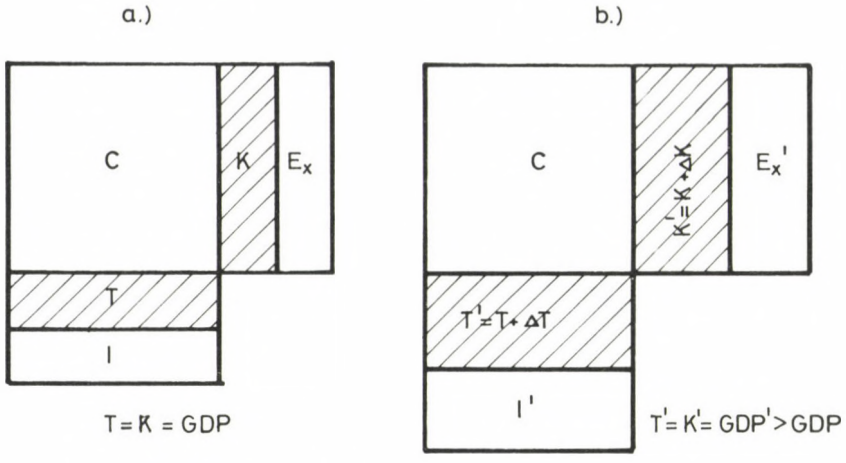

Fig. 3. The ratio between the areas in the input-output balance model is characteristic of the efficiency of production

Efficiency can be characterized essentially by areas, the ratio between their sizes being different. It can be seen without any detailed analysis that e.g. alternative 'b' represents a more favourable production situation i.e. a production of higher efficiency. Namely, a higher output K obtained for C of identical size but of a different (better) sectoral structure means higher efficiency on the basis of relationship $H = \frac{K}{C+K}$. (Analogously, for an identical K, the production is more efficient where C is smaller.) Within a theoretical range $0 < H < 1.0$, the magnitude of the efficiency index depends on whether $K \lessgtr C$ (the extremes being $C \gg K$ or $K \gg C$, respectively.)

The relationships formulated above assuming that K = T become more complicated because of inequalities $I \neq Ex$ resulting from the magnitude and structure of import I and export Ex (increasing losses due to terms of trade, including also compulsory debt repayments).

The significance of material and energy intensity in respect of efficiency of the national production (H) is quite obvious provided the fact that the material and energy consumption increases the size of quadratic field C in first line is accepted.

Since GDP is characteristic of the efficiency, energy intensity index ε and material intensity index α shall also be expressed as a specific value related to GDP.

Different cost and income structure, material and energy intensity of the sectors

On the basis of the simplified formulae for cost and income structure (formula 1, Fig. 2), it is easy to plot column diagrams to illustrate the most important, extremely divergent, efficiency characteristics of the different producer sectors. Two diagram types are presented, based on 1985 statistics.

One of them serves for the distribution of costs and incomes in % or in fillér/Ft within the price (x=p=100%) of the product (different components of cost c of Fig. 4, using the symbols and definitions of Fig. 2). The cost and income relations are indicated separately for the average of basic material industry and for that of manufacturing industry in addition to the average characteristics of total industry. (Detailed analyses went down to special branches of industry /4/.)

To contribute to the success of comparative efficiency calculations, the column diagrams indicate also

— the different economic sectors' 'own' capital intensity that is investment or fixed assets per unit net income (B/m) and

— the fixed assets development demand of the energy sector, required for operation of these sectors as a sectoral 'additional' energetic investment (B_E/m).

The other type of column diagrams (Fig. 5) is designed to show expenditures on production of GDP of Ft 1.0 for the most important industrial sectors, that is the material and energy intensity in Ft/Ft. Essentially, the column diagrams illlustrate also H=GDP/x type sectoral efficiency index numbers directly but in a reciprocal sense (that is the Figures are x/GDP Figures). It is enough to look at these diagrams to see what a different expenditure is required to produce unit income in the various producer activities. The difference between their energy and material costs is conspicuous. Moreover, the instability of energy costs as a function of time is significant due to the instable energy prices. Approximate values for the sectors' 'own' (B/m) and 'additional' (B_E/m) capital intensity are indicated also in these Figures.

Summed up below are the most important conclusions that can be drawn from both Figures.

According to the diagrams given in Fig. 4,

— the average industrial GDP ratio amounts to 26%, the share of net income m within this value being about half,

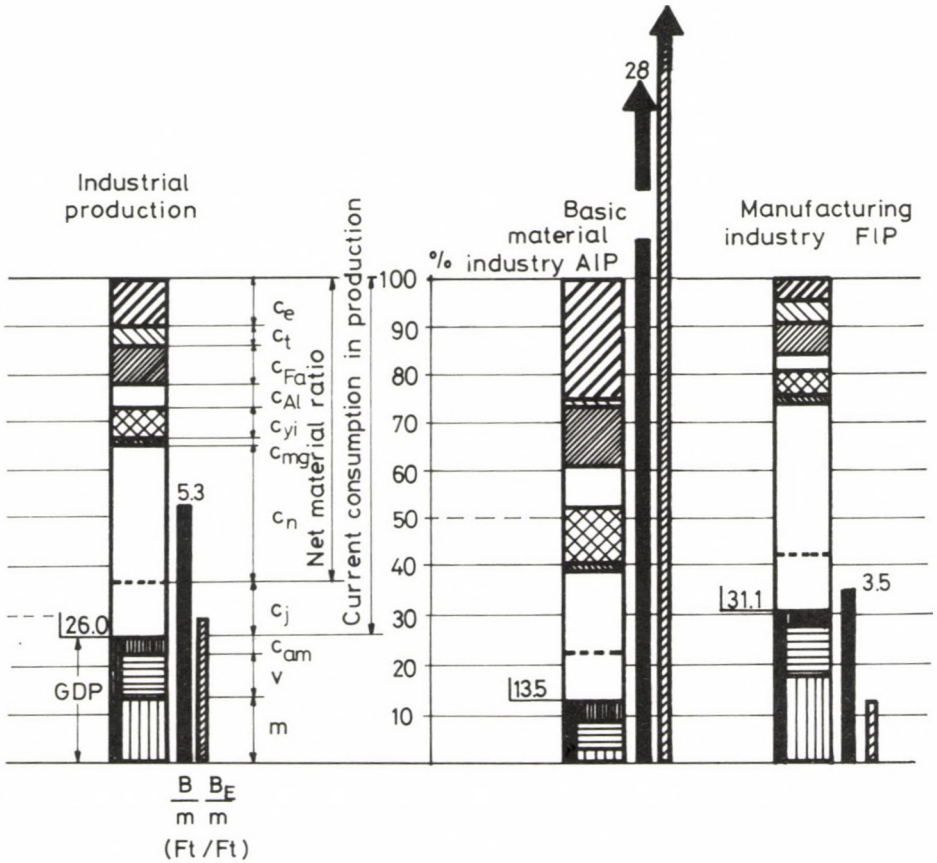

Fig. 4. Sectoral expenditure and income structures (1985) /4/

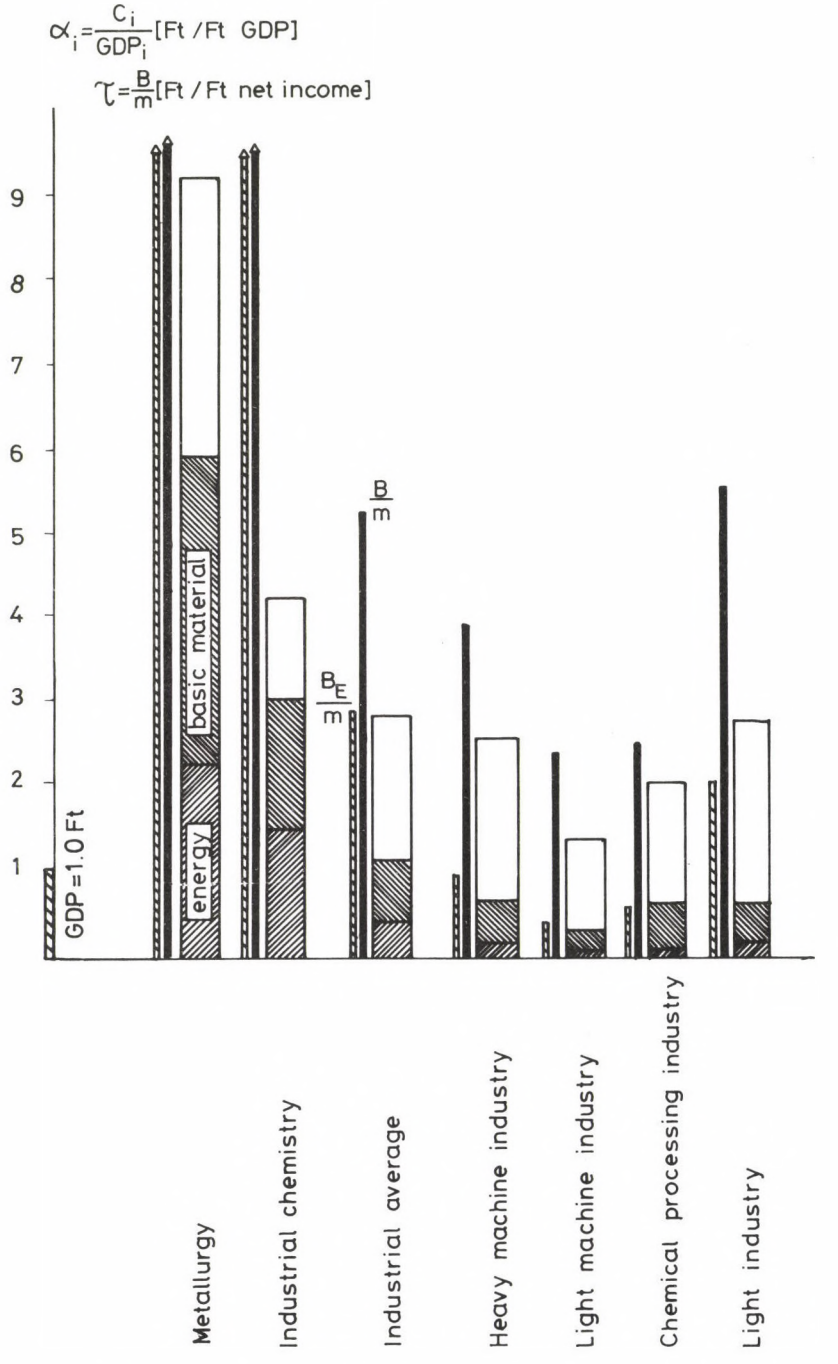

Fig. 5. Sectoral material and energy intensities (1985) /4/

— the ratio of energy costs among the other costs is conspicuous (about 10% of gross production),

— an 'additional' energetic investment of a ratio of about 50% is added to 'own' sectoral capital intensity of about 5 Ft/Ft on the average (resulting in combination in a capital intensity of 7—8 Ft/Ft),

— the average index numbers of AIP and FIP differ significantly from the industrial average and between the two sectors, the difference in some factors is multiple (5fold, 10fold or even 20fold or higher). The variation of the index numbers of the different sectors or special branches is still more significant.

The high capital intensity with an inherently high current expenditure demand (and low income ratio) of the basic material industry on the one hand, and the relatively low capital intensity and high income ratio of the processing industry on the other hand alone indicate the significant effect of different sectoral developments on the efficiency of production of the national economy.

Figure 6 shows clearly that capital intensity (τ) is incidental to energy intensity (ε) in a sector, indicating also approximate values for capital efficiency (μ) for the purpose of information.

Fundamental conformity condition between economy and energy

The most important relationships to describe the role of energy (inclusive of material intensity) more exactly but still on a global scale are summed up below.

The basic formula expressing the close relation between economy and energy (P and E, respectively) is well known:

$$E = P \cdot \varepsilon \quad . \tag{2}$$

Contrary to accepted opinion, this close relationship is by no means a close correlation between E and P as energy intensity index ε responsible for the relation is a factor varying within wide limits, the magnitude of which being determined first of all by the production structure of the economy.

The production, income, energy demand of any (aggregated) economic unit of a reasonably large size can be algebraically simply summed up as the sum of production, income, energy demand of units of a lower level in economic hierarchy. At the same time, the different technica-economic index

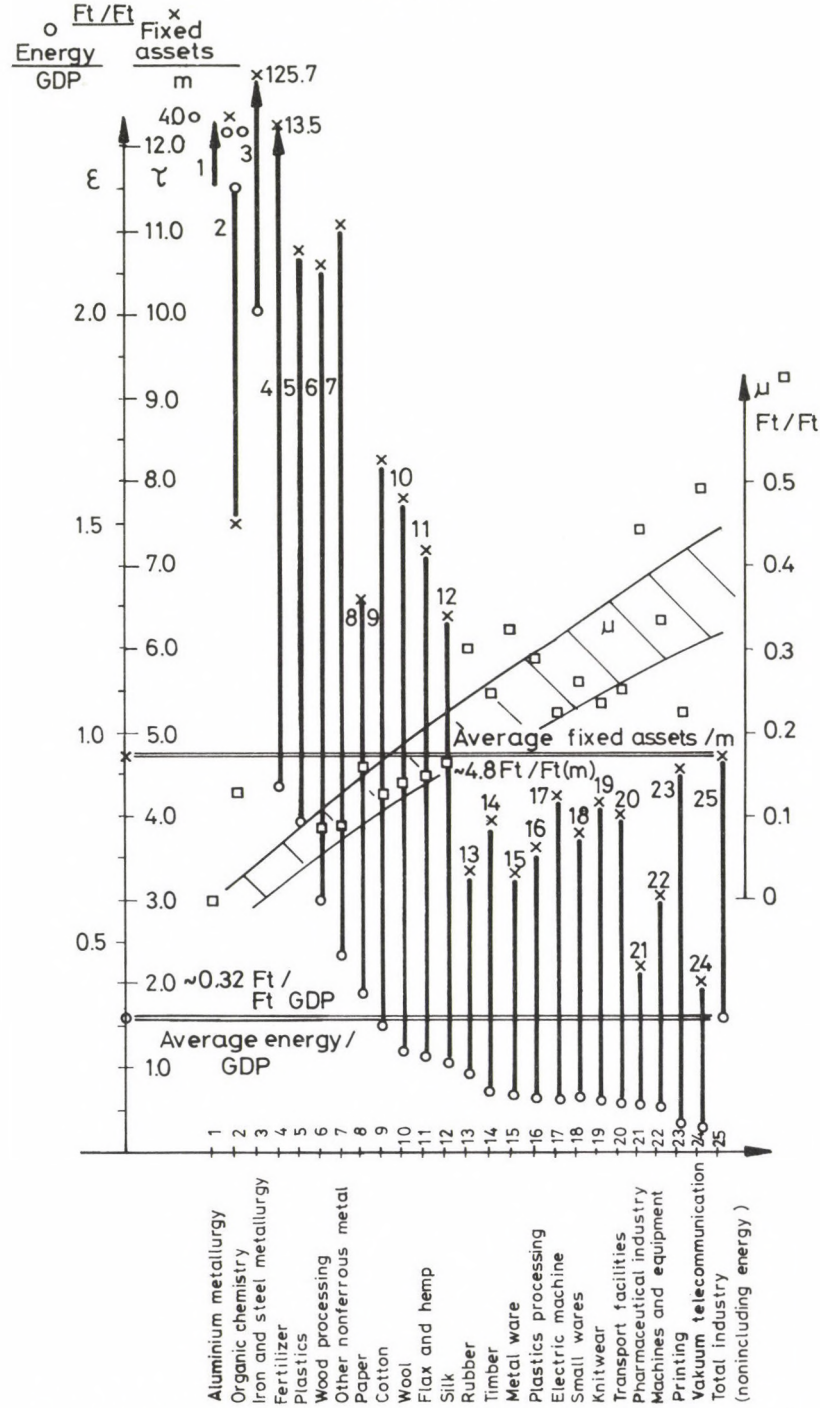

Fig. 6. Sectoral energy intensity, capital intensity and capital efficiency /4/

numbers (like energy intensity ε, economy or energy growth rate ν, fuel-electricity ratio φ, material intensity α etc.) can always be determined as the weighted average of component units i.

$$P = \sum_i P_i \qquad s_i = P_i/P$$

$$E = \sum_i E_i \qquad s_i^E = E_i/E$$

$$\varepsilon = \sum_i s_i \cdot \varepsilon_i$$

$$\nu_P = \sum_i s_i \cdot \nu_{Pi} \quad ; \quad \nu_E = \sum_i s_i^E \cdot \nu_{Ei}$$

On the basis of these general principles, the basic formula of energy demand (2) can be written with different subscripts (for past, future, increment) as

$$E = P \sum s_i \cdot \varepsilon_i \tag{3}$$

where factor s_i stands for P_i/P, the ratio of the different sectors i within total production (GDP).

Should a factor φ expressing the global ratio, calculable on the basis of fixed sectoral ratio φ_i between fuel and electricity consumption, be added to the above formulae according to formula

$$\varphi = \frac{E_V}{E_t} = \frac{\varepsilon_V}{\varepsilon_t} = \frac{\sum_i s_i \cdot \varepsilon_i \cdot \varphi_i}{\sum_i s_i \cdot \varepsilon_i} ,$$

then the following, relatively meaningful formulae are obtained for the growth in energy consumption and growth rate of energy demand:

$$\Delta E = E_1 - E_o = E_o^t \cdot \left[(1+\nu_P)(1+\varphi_1)(1+\lambda_t) - (1+\varphi_0)\right] \tag{4}$$

and

$$_{\mu}E = (1+\nu_P)(1+\lambda_t)\cdot\frac{1+\varphi_1}{1+\varphi_0} - 1 \quad , \tag{5}$$

respectively, where λ_t (not defined yet) is the rate of improvement of 'fuel energy intensity' $\Delta\varepsilon_t/\varepsilon_t$ without electricity.

In the formulae, each factor is a function of production structure s_i. Accordingly, the following conclusions, which are occasionally quite obvious but often not realized in everyday practice, can be drawn from what has been said above:

— the energy plan can not be independent; it should be always integrated with national economic plans,

— 'accuracy' and validity of an energy plan can only be interpreted, when consistent with the national economic plan; it can not exist alone,

— when forecasting the economy only in global, macroeconomical trends, there is not any possibility to prepare a reliable energy plan at all,

— the magnitude of the energy demand is fundamentally determined, in addition to the economic growth (change of P), by the economic structure characterized by s_i. Because of the multiple, sometimes extremely great difference, between the energy intensities of the different producer units (10fold, 20fold, or even 50fold), this structural effect is decisive in average energy intensity of the national economy (industry) and thus in energy demand $E = P \cdot \varepsilon$ in accordance with $\varepsilon = \sum s_i \cdot \varepsilon_i$.

The contribution of the increase in value resulting from technical development (denominator of the fraction describing energy intensity) to improvement of the individual energy intensity, $\varepsilon_i = E_i/P_i$, is more significant. As compared with this, the effect of energy conservation in the conventional sense (reduction in energy consumption E in the numerator) is little. In other words, there is no choice but to produce products marketable at the highest possible price on the basis of a definite (possibly limited) energy consumption although energy conservation is not negligible either. In this way, the energy intensity of production reduces 'automatically' and significantly.

Note that, considering what has been said above (formulae 3 thru 5), the elasticity index often used in planning for future economy and energy is methodologically unsuited for this purpose. As suggested obviously by formula

$$r = \nu_e / \nu_p = \frac{\Delta E/E_o}{\Delta P/P_o} ,$$

this index is also structure dependent, a function of the level of economic development and of energy consumption as well as of the absolute value of their growth rate. (E.g. an index r = 0.5 = 1.0/2.0 has different implications than and index r = 0.5 obtained for a growth rate of e.g. 1.5% or 3.0%, especially if, moreover, it is associated with a different value of E_o or P_o.) Hence, an elasticity index as a future requirement to be realized would necessitate that 'millions' of economic parameters be specified simultaneously. (The elasticity index can be calculated subsequently, either statistically for the past or in planning for the future as a subsequent checkup or additional information.)

Resources equilibrium condition

It follows from what has been said that, once the trend, magnitude and structure of economic development have been decided, we have no freedom any more in assuming the magnitude of energy demand and at the same time in determining the national economic resources (investment, import) required for energetic purposes. Namely, the resources demands of sectoral and energetic developments shall be closely co-ordinated. Writing the fundamental, but rather simplified, consistence relationship for investment (leaving private energy consumption here out of consideration), the total investment for production purposes will be

$$B_T = \sum_i B_i + B_E = \sum_i (B_i + e_i \cdot B_i) = \sum_i B_i \cdot (1 + e_i)$$

where

$$0.3 - 0.4 < e_i < 1.0 - 3.0 .$$

Depending on the energy intensity of the sectors, the specific values of sectoral 'additional' energetic investment factors vary within wide limits. Accordingly, also the distribution between total sectoral investment $\sum B_i$ and energetic investment B_E may vary significantly, depending on the structure of economic development and as a result, the variation of productivity of the economy may be similarly significant, depending on the produc-

Table 2. Combined effect of energy and capital intensity upon efficiency of production

	h GDP/en		a Fixed assets /GDP				h.a Fixed assets /en.					h' (u/z) GDP/fixed assets FIP:AIP		A_{en} / ΣA		$A_i/\Sigma A$
	Ft/Ft	FIP:AIP (u)	i	en*	Σ	Σ	i	en	FIP:AIP (z)							
	Ft/Ft						Ft/Ft		Σ	i	en	Σ	i	%	FIP: AIP	%
	1	2	3	4	5=3+4	6=7+8	7	8	9=10+11	10	11	12	13	14=8:6	15	16
AIP	0.55	17.1	7.3	10.7	18.0	9.9	4.0	5.9	2.4	4.5	1.0	[7.1]	3.8	~60	~0.4	[40]
FIP	9.4		1.9	0.6	2.5	23.8	17.9	5.9						25		[75]
Metallurgy	0.48	23.7	8.7	10.3	19.0	9.1	4.2	4.9	2.3	3.8	1.0	[10.3]	6.2	54	~0.4	[46]
Light machine industry	11.4		1.4	0.4	1.8	20.9	16.0	4.9						23		[77]

*Approximate figures

Note: The tabulated income figures include only sectoral incomes without those of energy sectors

tion structure. At the same time, it is suggested by the relationship that the ratio of resources engaged by energetic investment (B_E/B_T) can not be assumed or varied freely because distribution of investment allocation between the energy sector and other sectors is strictly determined by the economic (industrial) development structure.

An example given below (Table 2) gives a comprehensive picture of the combined effect of energy intensity and capital intensity upon efficiency, taking into consideration indirectly that, in accordance with the directives of the economic development concept, the growth of energy can take place at a limited rate only. In this example, a comparison of the most important characteristics of basic material industry (AIP) and manufacturing industry (FIP), two poles of industrial production, is given, taking the average of both sectors as a basis. (Average values for metallurgy and light machine industry are also tabulated down in the Table.) The most important numerical values, worth to memorize, are discussed below:

— Essentially, the reciprocal of energy intensity index number, the so-called energy utilization factor denoted by h, is suited to describe the efficiency of production directly from an energetic point of view as a 'GDP/energy' index number expressing income per unit energy. Taking this factor as a measure, there is a 15 to 20fold difference between average basic material industry and average manufacturing industry in favour of the latter according to h (columns 1, 2 in Table 2). Because of the variation in both sectors, the difference between the extremes may be even 50fold. (Differences of 1:80 within industrial activities are mentioned in a similar Japanese study /2/.)

— The difference in 'own' sector fixed assets per unit GDP is about fourfold, again in favour of manufacturing sectors. The ratio of total investments increases to about 7fold by additional energy investments where the difference between the two latters is about 18fold (see columns /fixed assets/GDP/ 3,5 and 4).

— Interesting information is supplied by columns 6 thru 11 denoted by 'h.a', containing the possibilities and distribution of sectoral and total investment for the same (limited) energy consumption. The difference is only 4.5fold between the extremes for sectoral investment while about 2.4-fold for total investment. (Much investment is required in manufacturing industry to consume the envisaged quantity of energy, but it generates much more income simultaneously.)

— However, in case of identical investment magnitude, also the income resulting from average development in manufacturing industry is much higher, 7.1fold, as shown by ratio h' (u/z) (columns 12—13). The difference is especially significant in the distribution of investment allocation (columns 14—16), the development in manufacturing industry requiring only about 1/4 of total investment for energy investments as compared with 2/3 in basic material industry.

As shown also by the numerical results of comprehensive model studies /5/, even a very small shift in a favourable or unfavourable direction as compared with the present sectoral structure results in a deviation one and a half to two times as much in the net national product. Similar input-output balance studies confirmed numerically the fundamental economic rule according to which

reduction of material and energy intensity results in increasing efficiency of production of the national economy.

Classification of possibilities to improve efficiency

In summing up, let us go back to formula $E = P \sum s_i . \varepsilon_i$ (3) again. Adopting the logic of this formula, effects increasing the efficiency can be classified on the basis of the numerical values presented. Assuming identical economic growth, the lower the average energy intensity of production ($\varepsilon = \sum s_i . \varepsilon_i$), the lower the energy consumption (E) that is the higher the efficiency of production. This criterion will be met if,

— on the one hand, the economic structure is favourable (s_i) that is the ratio of low-energy (low ε_i) activities in production is high. In this case, the production is at the same time less capital intensive and results in a much higher specific income.

— On the other hand, the above criterion will be met if the individual, sectoral energy intensity (ε_i) and specific energy consumption improve significantly. This can be achieved in two ways, index number ε_i being a fraction in each case, namely

= by increase of the denominator of the fraction that is the value produced (GDP) by way of technical development or production restructuring to arrive at $P + \Delta P$ instead of P or

= by reduction of the numerator of the fraction by energy conservation and specific improvement ($E - \Delta E$ instead of E).

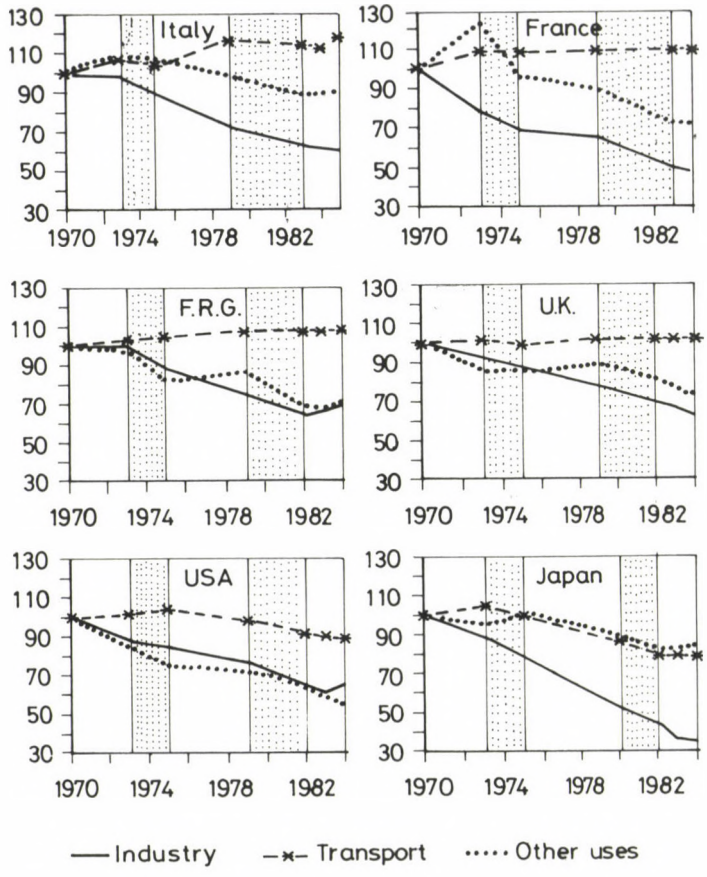

Fig. 7. Non-electric energy intensities in some industrialized countries (1970 = 100) /6/

According to calculations, the improvement in energy intensity resulting from modernization of the production is multiple as compared with the results of direct energy conservation.

International results

And what happened in the world in the recent period of 15 years? Just the most typical phenomena:

— The growth in GDP in the industrialized countries, accompanied with a significant restructuring, has been typically 20 to 60%. All the high-energy industrial activities (iron and steelmaking, production of cement,

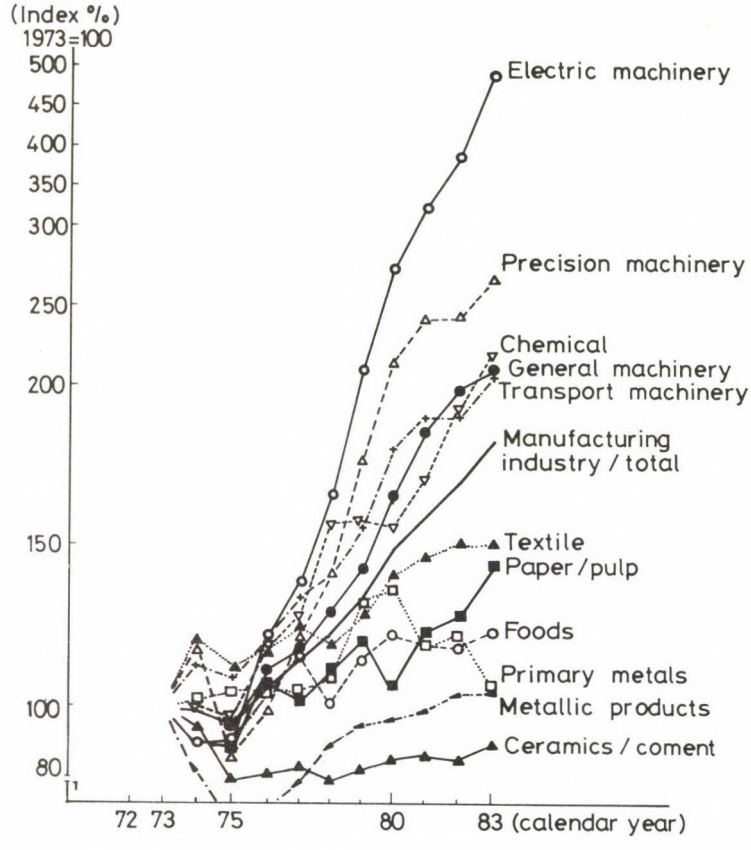

Fig. 8. Trends of GDP by industry /2/

plastics etc.) have been kept at, or below, the rate before the oil crisis. This is responsible first of all for a significant reduction in energy intensity in the six top capitalist countries after the oil crisis as shown in Fig. 7 /6/. (Note that the electricity intensity of industry increased in general in the same period in most countries except for the USA and Japan where a reduction of 40% occurred.)

A most typical sectoral restructuring has taken place in Japan where, according to Fig. 8, the increase in GDP of the so-called pulling sectors (electronics, instrument engineering) amounts to 300 to 500% while the production of energy intensive sectors is stagnant or reducing (see Fig. 8).

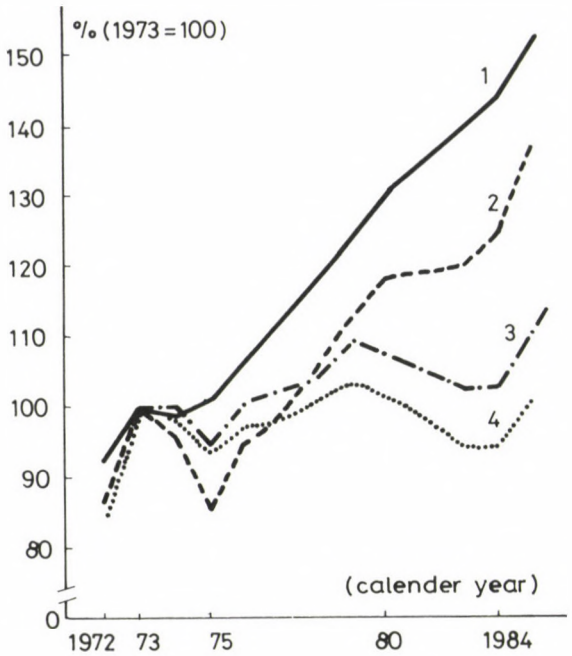

Fig. 9. Trends of GNP, IIP and energy supply and demand /2/
1-Real GNP, 2-IIP, 3-Total primary energy supply, 4-Total final energy consumption

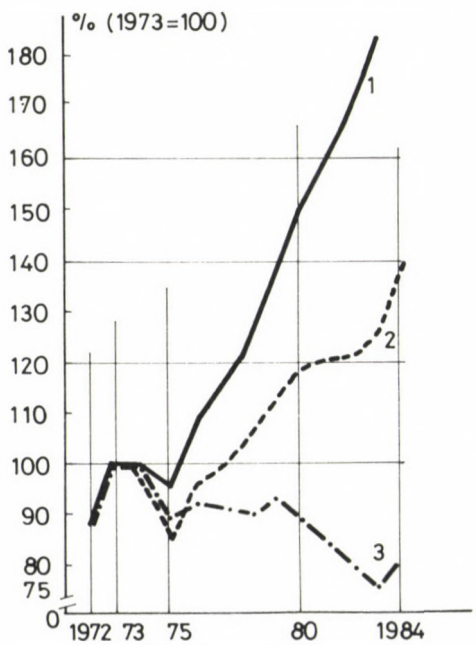

Fig. 10. Trends of industrial energy consumption /2/
1-GNP in manufacturing industry,
2-IIP in the manufacturing industry,
3-Total final energy consumption in the manufacturing industry

As a result of this deliberate restructuring, there is practically no change in total energy consumption (see Fig. 9 /2/) while the energy consumption of the industry reduced in absolute value in spite of the rapid economic growth (Fig. 10 /2/), hence its ratio within total consumption decreased from 61.5% to 30.4% in this period.

Characteristically of the structural shifts in Japanese economy, an improvement of about 15% occurred in the FIP/AIP ratio in contribution to GDP within only a few years after the oil crisis. (Note that the home ratio has not displaced from the earlier value but it is more or less stable. Moreover, as a result of debt repayment obligation, even a change in reverse direction occurred in some years.)

National tasks

Similar results to be achieved are still among future expectations in Hungary. To meet these expectations, a radical restructuring of both the sectoral structure and production is unavoidable, resulting at the same time in a definite significant reduction of the material and energy intensity. Otherwise no improvement of the efficiency of production is expectable. Quite obviously, restructuring involves 'setbacks' and thus distressing social problems like unemployement, retraining etc. that have to be controlled simultaneously with a view to increase the overall efficiency of production. This cimplex approach shall be adopted in formulating the public interests while in the way out, improvement of the efficiency is a key issue which, however, can never be achieved without a significant reduction of material and energy intensity.

REFERENCES

1. WEC 1986 1.2.1.14: Energy Situation in IEA Countries
2. WEC 1986 2.1.12: The Structural Changes in Energy Demand and Economy since the Oil Crises — the Japanese Case
3. Comparison of efficiency, loss and resources demand of different energy systems (energy production-conversion I-O model tests). Institute of Industrial Economy, Budapest 1985
4. Expenditure intensity of production, investigation of ppogrammes effecting expenditure intensity. Institute of Industrial Economy, Budapest 1987
5. Dynamic model for comparison of the efficiency of sectoral developments of different energy intensity. Institute of Industrial Economy, Budapest 1983
6. WEC 1986 1.1.16: Distrubances Induced by Oil Crises in Energy-Economy Relationship

Acta Technica Acad.Sci.Hung., 101(3),.pp. 281—294 (1988)

RESULTS OF INTERFERENCE MEASUREMENTS ON 400 AND 750 kV TRANSMISSION LINES

JERMENDY, L. - TIMASHOVA, L.V.

(Received: 30 May 1988)

The results of interference measurements on 400 and 750 kV transmission lines at frequencies above 30 MHz are presented. Instruments meeting technical characteristics of the CISPR requirements were used. Frequency spectra of interference and interference attenuation along the line and in the lateral direction were gained.

The rates of interference intensity growth for artificial gaps of different sizes were determined.

The results of laboratory measurements of audible noise for bundle conductors with different diameters and for different conductor surface gradients are given. Frequency spectra of audible noise from a 750 kV transmission line using various instruments and microphones were obtained.

Introduction

Until recently relatively little attention was paid to interference from transmission lines above 30 MHz. In the meantime, this frequency range is very important because this is the frequency range on which TV channels operate.

Interference generated by transmission lines reduces reception quality and reliability, decreases areas of assured TV reception.

Observation carried out in one region of the USSR have shown that TV reception degradation in the areas of transmission line routes caused most complaints, up to 90% in total, and only 10% of complaints were related to radio reception degradation, below 30 MHz.

Sources of interference from transmission lines in the higher frequency range are line fittings and insulator strings with loose contacts and sharp elements as well as thrown metal wires on conductors. Reasons for such increased interference can be detected and eliminated during operation of the transmission line. Current impulses, taking place during the breakdown of a gap, have a high amplitude and a short rise time. The shape of current impulse frequency spectra of gap discharges is not determined by

---

Jermendy, L., Institute for Electrical Power Research H— 1368 Budapest, P.O.B. 233, Hungary; Timashova, L.V., All-Union Electric Power Research Institute, SU—115201 Moscow, Kashyrskoe Chaussée 22, USSR

Akadémiai Kiadó, Budapest

the discharges themselves, but it is determined by the external circuit. That is why there is no typical frequency spectrum of interference occurring during a gap discharge /1/.

With increasing rated voltage of the transmission lines a new interference source appeared — corona on conductors. This interference source is not a local one and practically cannot be eliminated on operating transmission lines. It is impossible from the economical point of view to escape corona on EHV and UHV lines, where intensive corona occurs during foul weather conditions. Intensity of interference generated by corona on conductors rapidly decreases with increasing frequency, the shape of a frequency spectrum being determined by physical mechanism of discharge.

Measurements have shown /2/ that the effect of weather conditions on an interference level is determined to a great extent by an interference source. When interference is caused by corona on transmission line conductors the interference level in fair weather is low, but in rain and snow it strongly increases and can exceed a fair weather level by 24 dB in individual cases.

If an interference source is a gap discharge, effects of weather are different. With an internal gap discharge interference is not affected by weather conditions.

The value of interference generated by an open gap discharge is significant in fair weather, but under precipitation a conducting channel occurs in the gap and the discharge is stopped.

The electrical discharges which cause corona will also produce audible noise. Below 400 kV the noise levels are of little concern. At this voltage level if the line has an acceptably low radio noise, there normally is no audible noise problem. In foul weather a great number of corona sources are present on the conductor, the audible noise being more intense. Generally for laboratory test heavy rain is used because this artificial rain and the heavy rain noise values for transmission lines can relatively be well reproduced and compared. Beside this the influence of different surface conditions of the conductor diminish with increasing rain intensity. The important variables in production of audible noise e.g. the subconductor diameter, the maximum surface gradient, the number of the subconductor can well be investigated in a wide range by way of model tests.

Television interference

Laboratory tests

Interference levels from discharges in gaps of different sizes were investigated in the laboratory. For measurements the meter used met the prescription of CISPR and had a bandwidth of 120 kHz. The reported values are dB above 1 μV/m. During the tests air temperature, humidity and pressure were unchanged. It was registered that bad contacts (gaps) caused interference up to 500—600 MHz.

In case of large gaps interference is higher, but it occurs at higher voltages. For high relative air humidity and also with graphitizing a gap a conducting channel occurs across the gap and the discharge is stopped.

Figure 1 shows frequency spectra of interference from gaps of different sizes.

The frequency spectra have a number of maxima and minima, caused by the presence of reflected waves.

Interference intensity rises with increasing test voltage. Figure 2 shows the rate of the growth of television interference (TVI) generated by air gaps and adjusted to 150 kHz.

For large gaps the TVI growth is decreased with increasing voltage. With an accuracy of about 6% the TVI growth is 15 dB for a gap of 0.09 mm, 6 dB — for a gap of 0.3 mm, 1.2 dB — for a gap of 1 mm at voltage increase of 100 kV.

Measurements on 400 and 750 kV transmission lines

To decide problems of electromagnetic compatibility of transmission lines with different receiving devices it is very important to know the characteristics of interference attenuation in the direction perpendicular to the line. Figure 3 shows frequency spectra of interference generated by a gap discharge on a 400 kV transmission line at various distances from the line (the measurements were made at the midspan). Measured field strength of TVI is a result of adding direct waves and reflected ones. TVI intensity decreases with frequency. At high frequencies interference attenuates in the direction perpendicular to the line more rapidly than it does at lower frequencies.

Similar frequency spectra of interference at four distances from 20

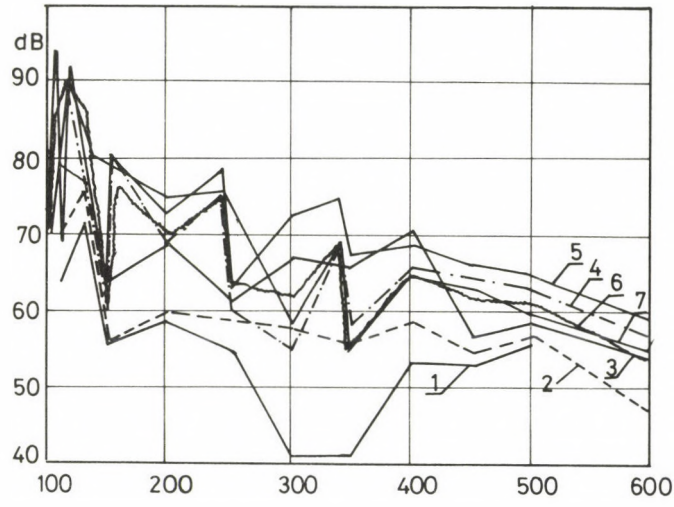

Fig. 1. Frequency spectra of television interference for air gaps of a different size
1,2,3 - a gap of 0.09 mm, test voltage of 70 kV, 100 kV, 150 kV, respectively;
4,5 - a gap of 0.3 mm, test voltage of 90 kV, 150 kV, respectively;
6,7 - a gap of 1 mm, test voltage of 150 kV, 200 kV, respectively

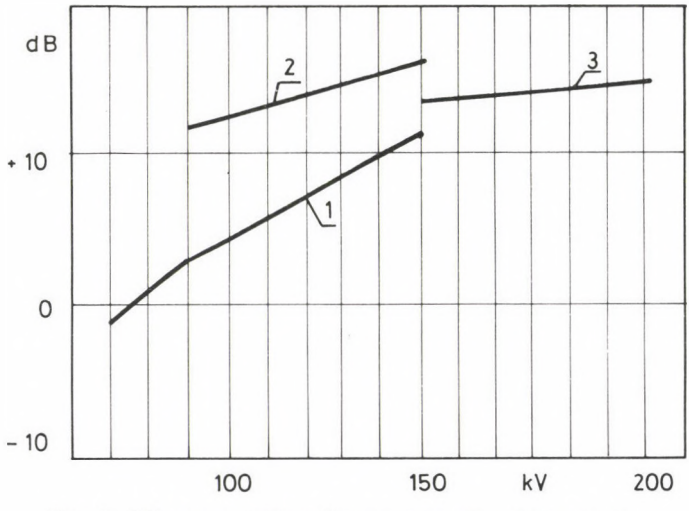

Fig. 2. TVI versus voltage for air gaps of a different size
1 - gap of 0.09 mm; 2 - a gap of 0.3 mm; 3 - a gap of 1 mm

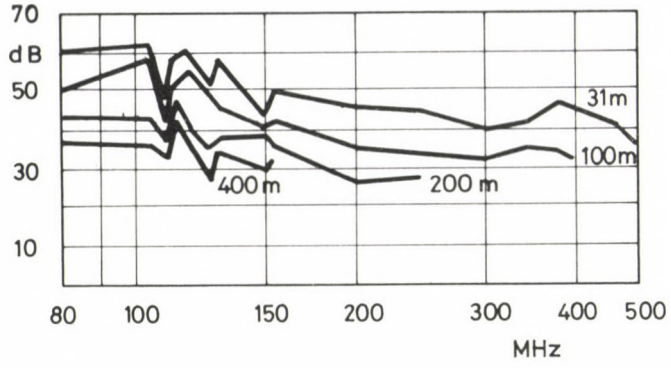

Fig. 3. Frequency spectra of TVI generated by gap discharges on the 400 kV transmission line

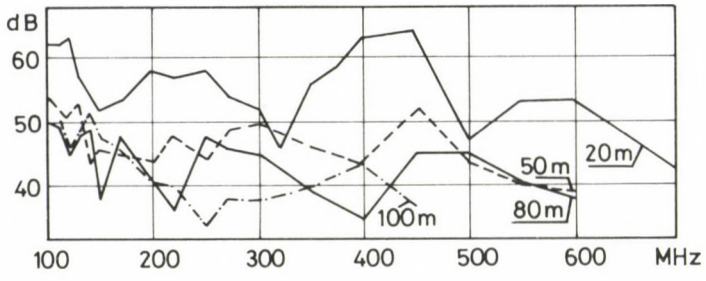

Fig. 4. Frequency spectra of TVI generated by gap discharges in the midspan of the 750 kV transmission line

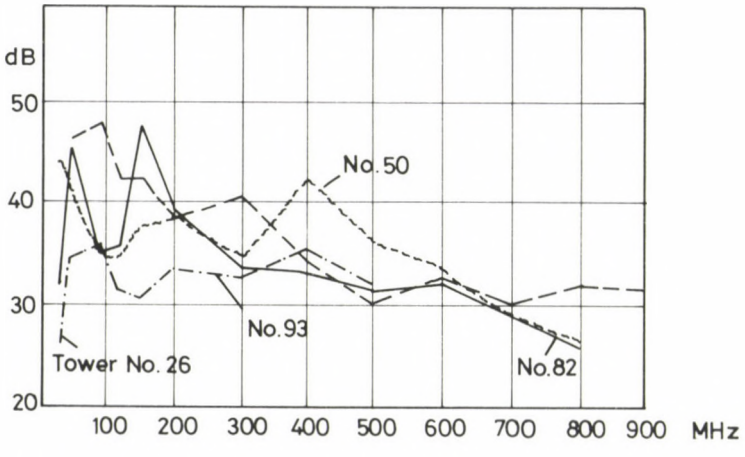

Fig. 5. Frequency spectra of TVI generated by different towers of the 750 kV transmission line in fair weather

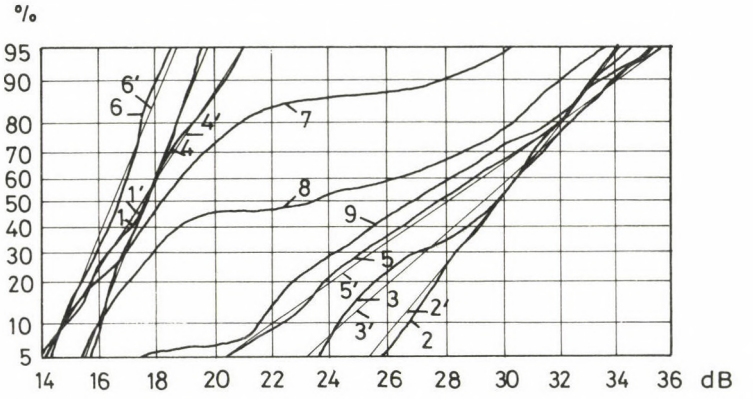

Fig. 6. Integral distribution curves of TVI on the 750 kV transmission line at 300 MHz
1,3,5 - fair weather, rain, snow, respectively; gap discharge;
2,4,6 - fair weather, rain, snow, respectively; gap discharge;
7,8,9 - fair weather, rain, snow, respectively; corona on conductors and gap discharge

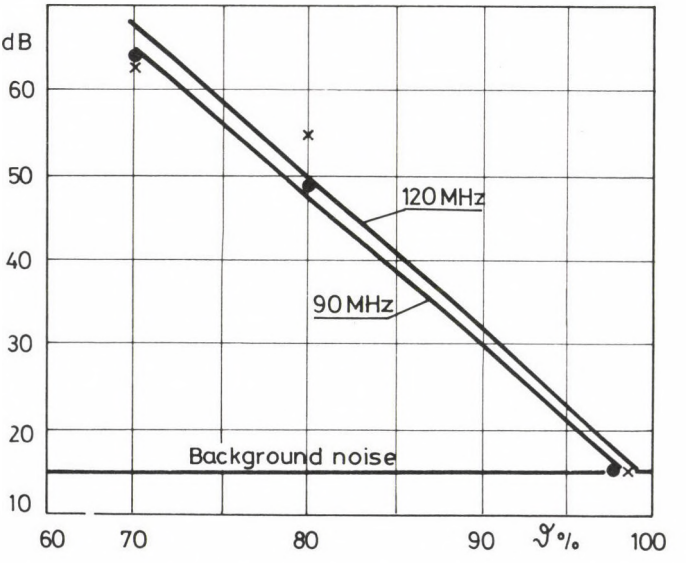

Fig. 7. TVI change as a function of relative air humidity

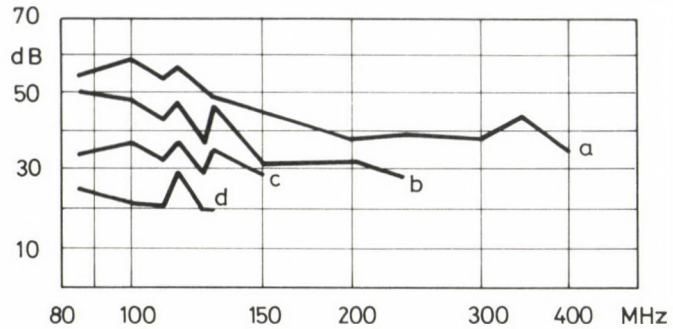

Fig. 8. Frequency spectra of TVI from the 400 kV double-circuit transmission line a - local sources on both circuits; b - local sources only on one circuit; c - antenna is placed at a distance of 180 m along the line from the last interference source; d - antenna is placed at a distance of 500 m along the line from the last interference source

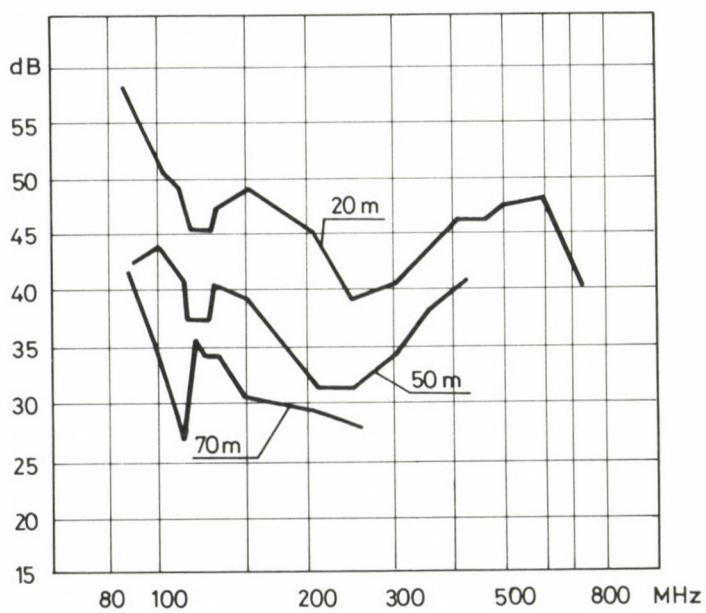

Fig. 9. Frequency spectra of TVI generated by artificial sources

to 100 m from the transmission line were obtained at the midspan of a 750 kV line, see Fig. 4.

It should be noted, that interference values from the 750 kV line seemed to be commensurate with interference from the 400 kV line.

Figure 5 shows frequency spectra of interference obtained near towers of the 750 kV line. TVI attenuation is about 23 dB at ten times frequency increase. Furthermore, on the 750 kV line long-term measurements of interference generated by gap discharges and corona on conductors at 300 MHz were carried out (thousands of points). The test results for different weather conditions are shown in Fig. 6.

It can be seen that interference due to gap discharges in rain and snow has a level which is close to interference from corona on conductors in fair weather.

The straight lines in Fig. 6 correspond with integral normal distribution curves drawn on the basis of calculated mean values and standard deviations. Interference distribution for each type of interference sources during any weather conditions is close to normal one. Combination of interference from different types of sources results in a distribution strongly differing from normal one.

At the midspan of the 400 kV transmission line measurements of TVI were carried out at frequencies of 90, 120 MHz at various relative air humidity. An interference source is a gap discharge. Above 70% relative humidity if the relative humidity is increased by 10% an interference decrease is about 20 dB. At relative humidity higher than 95% the interference commensurates with the inherent noise of a measuring instrument, see Figure 7.

Several local interference sources were detected on a double — circuit 400 kV transmission line. During measurements an antenna was directed perpendicular to the line /3/. As seen in Fig. 8 interference intensity considerably decreases along the line, interference attenuation being about 17—20 dB/km. The number of upper frequencies of interference spectrum reduces approximately by 100 MHz per each kilometer along the line. If local sources occur on both circuits the interference level is about 10 dB higher than if sources are on one circuit.

Measurements of interference from artificial sources were carried out on the double-circuit 400 kV line with 4 bundle conductor. Before tests the presence of interference sources on a selected section of the line was

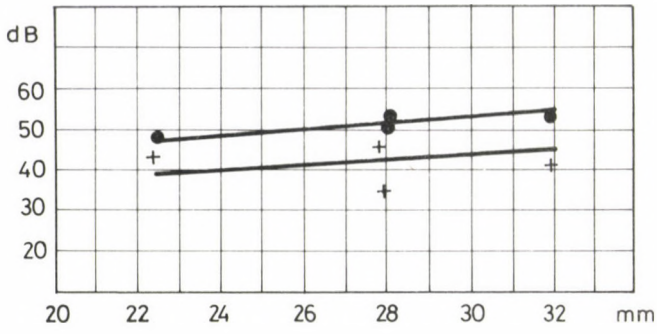

Fig. 10. Audible noise as a function of a conductor diameter for a 3 bundle conductor
● - rain; + - fair weather

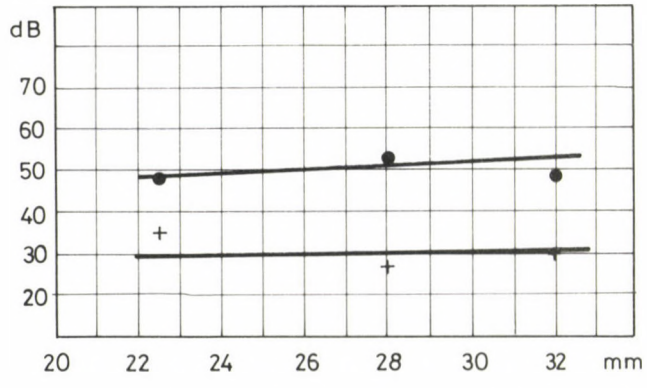

Fig. 11. Audible noise as a function of a conductor diameter for a 4 bundle conductor
● - rain; + - fair weather

checked. Interference was not detected. Following this some artificial source were set at the middle of the span.

Figure 9 shows frequency spectra of interference at different lateral distances from the line. Interference propagated along the line up to 1.5 km from a source, with ten times distance increase interference decrease is about 14 dB.

Audible noise

Laboratory tests

Audible noise levels caused by corona on conductors of 12 m long with 3 and 4 bundle, conductor being different diameters, were investigated in the laboratory.

Audible noise was measured with a noise meter of RFT—102 type, using third—octave filters and a 1—inch diameter microphone. The microphone was located 5 m from the conductor. The mean values at frequencies of 2.5 kHz — 10 kHz were taken, as in this frequency range a frequency spectrum of audible noise is relatively flat. Audible noise dependences on a conductor diameter for 3 and 4 bundle conductor are shown in Fig. 10 and 11.

Maximum electric field strength at the conductor surface was about 25-28 kV/cm. The rate of artificial rain exceeded 1 mm/min. In heavy rain interference is practically identical for different conductor number at the same gradients. In fair weather interference is different. It is related with different surface conditions of the conductor used.

Dependences of audible noise on maximum conductor surface gradients for 3 and 4 bundle conductor are given in Fig. 12.a and b.

It can be seen, with increasing gradients a difference between interference in rain and in fair weather decreases, for gradients higher than 25 kV/cm interference levels are practically commensurate.

Measurements on the 750 kV transmission line

On the 750 kV line audible noise measurements were carried out using various instruments and microphones with different characteristics. Frequency spectra of audible noise at different distances from the transmission line are shown in Fig. 13. a, b, and c. As seen in the figures, the

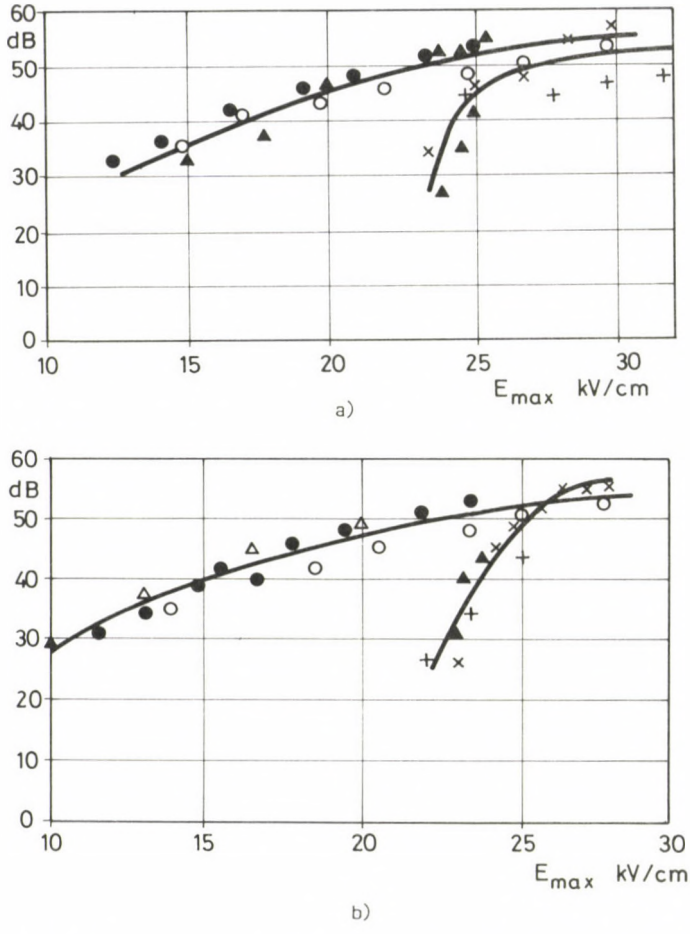

Fig. 12. Audible noise as a function of maximum conductor surface gradient
+ - fair weather, o - rain, d = 22.4 mm
x - fair weather, ● - rain, d = 27.9 mm
▲ - fair weather, △ - rain, d = 31.8 mm
a) for a 3 bundle conductor
b) for a 4 bundle conductor

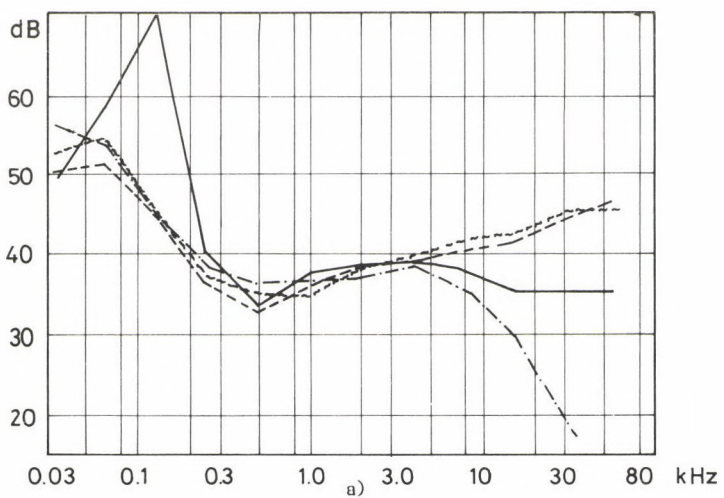

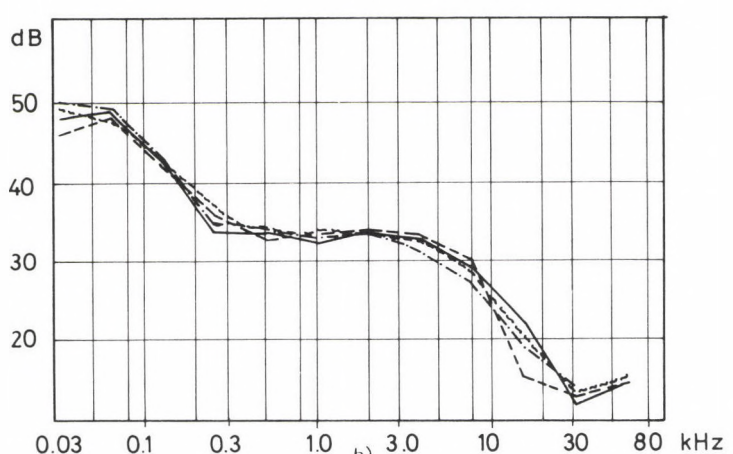

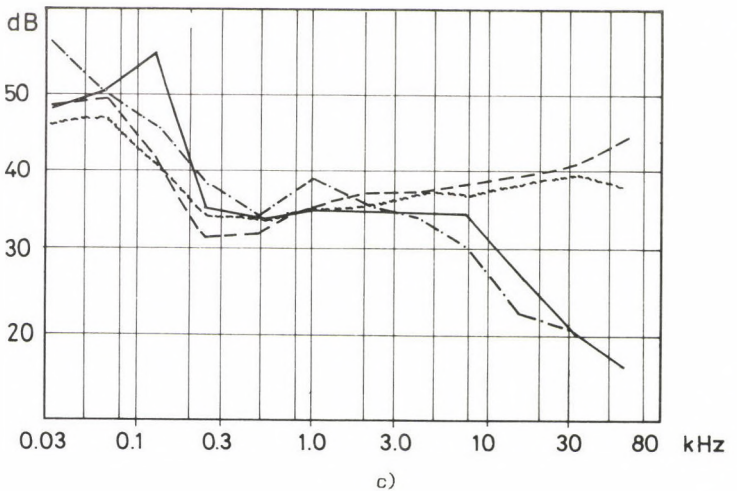

Fig. 13. Frequency spectra of audible noise of the 750 kV transmission line

—·—·— B & K

——— RFT - 102

∼ ∼ ∼ RFT - 102, the membrane is soldered to the microphone body

– – – RFT - 102, a cone type microphone

a) under the outermost phase

b) 10 m from the outermost phase

c) 20 from the outermost phase

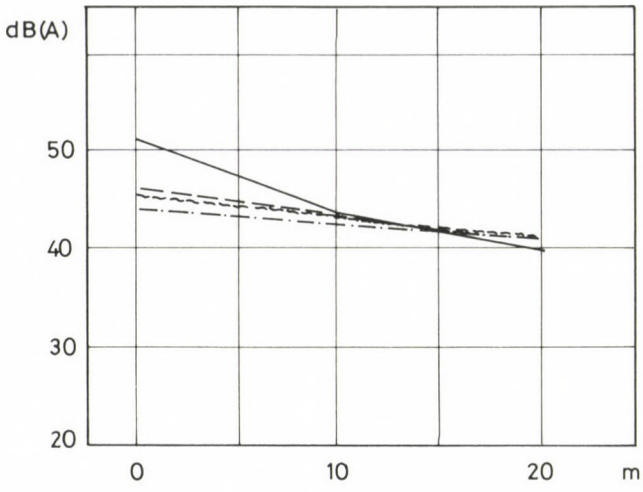

Fig. 14. Noise level in dB(A), versus a distance to the line

—·—·— B & K

——— RFT - 102

– – – RFT - 102, the membrane is soldered to the microphone body

~ ~ ~ RFT - 102, a cone type microphone

shape of frequency spectra at distance near the line depends on microphone characteristics. At the distance of 20 m from the line the shape of frequency spectra of noise generated by corona on conductors is practically the same with measuring instruments of different types and using microphones with different characteristics. Evidently, it is related with electric field effects on characteristics of different microphones used for measurements /4/.

Figure 14 shows noise levels in dB(A) at different distances from the line.

It can be seen, as in the previous case, noise levels at 20 m from the line are practically the same for measurements with instruments of different types and microphones with different characteristics.

Conclusions

1. The highest TVI takes place for corona on conductors in foul weather and for gap discharges in fair weather.

2. The same interference source generates higher TVI values at higher voltages.
3. Interference at frequencies above 30 MHz attenuates along the line at distances up to 3—4 spans in both directions from a source. Attenuation is about 14 dB for ten times distance increase.
4. In the direction perpendicular to the line interference attenuation is about 23 dB for ten times distance increase.
5. For ten times frequency increase interference attenuation is about 23 dB.
6. TVI levels generated by a gap discharge in rain and snow are approximately equal to an interference level due to corona in fair weather and commensurate with inherent meter noise.
7. For relative air humidity of about 95% a TVI level is commensurate with the inherent meter noise.
8. In heavy rain audible noise does not depend on the conductor number at the same gradients.
9. At gradients more than 25 kV/cm audible noise in rain and fair weather is practically the same.
10. At distances of 20 m and above from the transmission line where the electric field is less than 4 kV/m, audible noise levels are the same when measurement were made with instruments of different types and microphones with various characteristics were used.

REFERENCES

1. Bourgsdorf, V.V., Yemelyanov, N.P., Timashova, L.V.: "Radio and television interference from a 750 kV line with 5-conductor bundles", Paper 232-08 presented at the CIGRE Symposium on Transmission Lines and the Environment, Stockholm, June 23-25, 1981

2. Emelyanov, N.P., Kostyushko, V.A., Tomasov, A.I., Timashova, L.V., Zitzer, M.M.: "Investigation of corona effects on EHV and UHV transmission lines", Paper 36-11 presented at CIGRE Session, Paris, 29 August - 6 September, 1984

3. Jermendy, L., Roestel, T.: "Television Interference Caused by Capacitive Discharges on High Voltage Transmission Lines, Paper 83-16 presented at the Fifth International Symposium on High Voltage Engineering, Braunschweig, 24-28 August, 1987

4. Jermendy, L., Miklós, V., Paulusz, M.: "Study of radio interference, acoustic noise and electric field of extra high voltage lines", Paper 233-03 presented at the CIGRE Symposium on Transmission Lines and the Environment, Stockholm, June 23-25, 1981

Acta Technica Acad.Sci.Hung, 101(3), pp. 295–304 (1988)

THERMAL CONVERSION OF PARAFFINS

MIKHAIL, S. - ELBADRAWY, S. - BARAKAT, Y. - FARAG, A.*

(Received: 1 October 1988)

The objective of this study is the examination of the effect of thermal conversion on paraffins. The conversion of individual normal paraffins such as C_8, C_{10}, C_{12} and C_{14} was carried out thermally in a bench scale unit designed to work under atmospheric pressure. The examinations were carried out in the temperature range from 400° to 600°C and at water/n-paraffin ratio of 50–100/100.

The results indicate a significant increase in olefin content by the effect of increase in carbon chain length from n-C_8 to n-C_{14}. The amount of olefinic products attain a maximum value at a reaction temperature of 600°C and water/n-paraffin ratio of 100/100.

By the application of the optimum thermal conditions to a kerosine fraction of boiling range from 140° to 220°C, a considerable amount of liquid aromatics was obtained in addition to olefinic gases due to cracking.

From the viewpoint of boiling point distribution, the products contain 80% components having boiling points up to 190°C.

Introduction

The olefins obtained from normal paraffins are now important for the production of detergents as well as intermediates for synthesis /1/. Knaus et al. earliest dealt with the study of the product yields in the decomposition of liquid hydrocarbon mixtures /2, 3/ by thermal treatment of individual hydrocarbons of various structures containing six carbon atoms, with model mixtures of two and four components, and with the straight napthas of various compositions.

More recently, Shah et al. /4/ investigated the thermal decomposition of an octane-nonane mixture.

In another work by Csikós, R. on the decomposition of paraffin waxes and wax distillates by thermal treatment giving olefins increased in yields by recirculation, individual n-paraffins as well as mixtures of hydrocarbons in kerosine fraction were studied by thermal decomposition.

---

*Dr. Samir Elbadrawy, Egyptian Petroleum Research Institute, Nasr city, Cairo, Egypt

Akadémiai Kiadó, Budapest

Experimental

Pure saturated hydrocarbons such as, n-C_8, n-C_{10}, n-C_{12} and n-C_{14} were subjected to thermal treatment in the presence of heated steam. The experiments were carried out in a reactor (115 cm long and 0.8 cm in diameter packed with inert quartz and placed horizontally through two separate tubo furnaces. The examination was carried out in the temperature range from 400 to 600°C and at water to n-paraffin ratio of 50-100/100. Both the reactants and heated steam were fed into the reactor through a metering pump.

The gaseous and liquid products were collected simultaneously and analysed by gas-liquid chromatography and fluorescence indicator analysis (FIA), respectively.

The optimum thermal conditions were applied to kerosine fraction with a b.p. from 140 to 220°C, having the following characters:

Refractive index, at 20°C	1.4523
Aniline point	64°C
Component analysis:	
saturate, wt%	54
olefin, wt%	28
aromatic, wt%	18

Results and discussion

1. Effect of water/n-octane ratio

The effect of the variation in the volume ratio of water/n-octane ranging from 50:100 and 100:100 was investigated in the temperature range of 350 to 550°C (Table 1).

Data in Figure 1 show that with the increase in reaction temperature from 350 to 550°C, the yield of olefins wt% increases, and consequently, the yield of saturates decreases. At the same time, the amount of aromatic is zero. In all cases, and at any reaction temperature, the product yield was one hundred percent. This means that with a decrease in the saturates from 100 to 85, the olefin amount increases from 0 to 15 wt%, for example, at 550°C.

In the Figure, it is also shown that the amount of olefins shows a remarkable increase as the ratio of water vapour increases from 50 to 100 at all reaction temperatures. The increase in the yield of olefins with a

Table 1. Effect of water/normal octane ratio on the yield of olefins

Reactor temp. ^{o}C	Water/C_8 ratio	Yield of olefins wt%
350	50/100	1.0
350	100/100	2.5
400	50/100	2.0
400	100/100	4.5
450	50/100	4.0
450	100/100	5.5
500	50/100	7.0
500	100/100	9.5
550	50/100	12.0
550	100/100	15.0

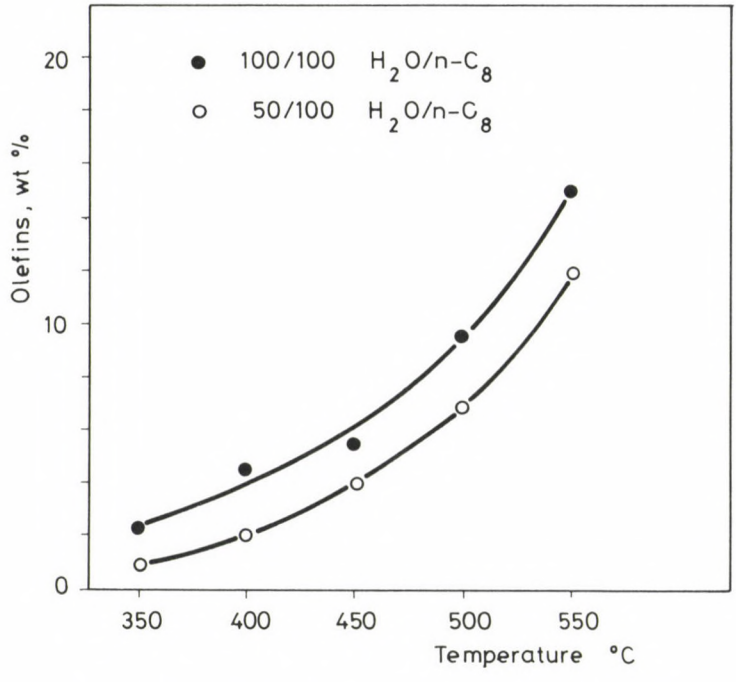

Fig. 1. Effect of water/n.C_8 - ratio on the yield of olefin

simultaneous increase in vapour may be attributed to the lesser formation of coke deposits at a higher ratio (100:100) of water vapour/n-octane, which facilitates the formationof olefins and increases its amount.

2. Effect of chain length of n-paraffins

From the previous results, it is obvious that the olefin-content attains its maximum value at 100/100 water/n-octane ratio and at 550°C.

It is of interest to study the effect of chain length of the feed n-paraffin on the yield of olefin. For this purpose, n-octane, n-decane, n-dodecane and tetradecane were used within the temperature range of 350–550°C and water vapour n-paraffin ratio of 100:100.

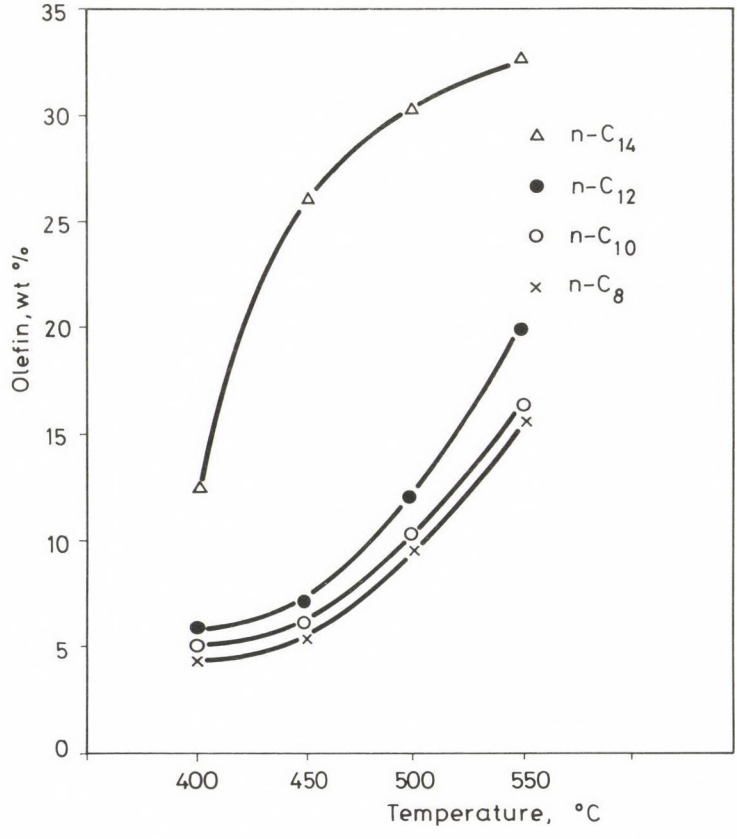

Fig. 2. Effect of temperatures on the conversion with changes of chain length of the n-paraffins

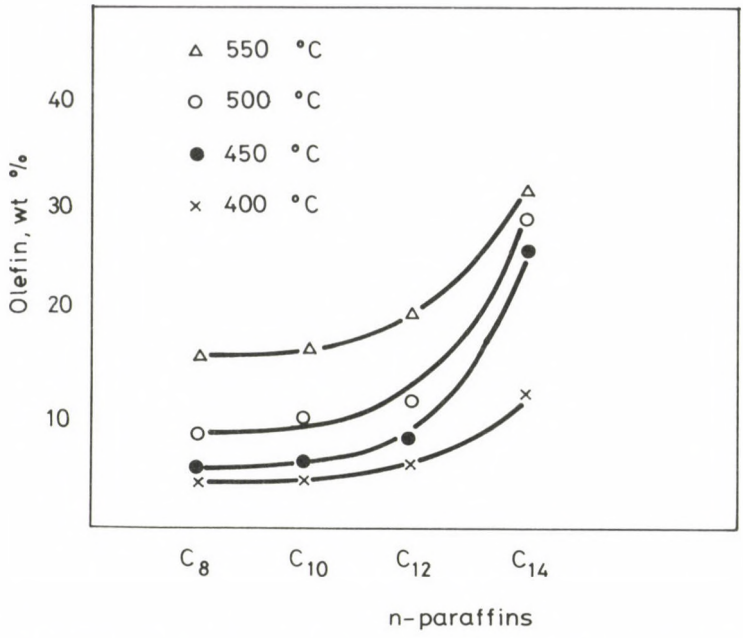

Fig. 3. Relation between the amount of olefins and the chain length of n-paraffins

Table 2. Effect of chain length of the normal paraffin on the conversion into olefins

n-paraffin chain length	wt.% yield of olefin at reactor temperature °C 400	450	500	550
C_8	4.5	5.5	9.5	15.5
C_{10}	5.0	6.0	10.0	16.0 + traces arom.
n-C_{12}	6.0 +aromatics traces	7.0 +aromatics traces	12.0 +aromatics traces	20.0 +aromatic 1.0wt.%
n-C_{14}	12.5 +aromatics traces	26.0 +aromatics traces	30.0 +aromatics 2.0 wt.%	32.5 +aromatics 2.0 wt.%

As shown in Fig. 2, the total conversion of all n-paraffins, n-C_8, n-C_{10}, n-C_{12} and n-C_{14} increases continuously with the increase of reaction temperature. The conversion wt% of any of the n-paraffins studied increases with the increase in the chain length from C_8 to C_{14} as illustrated in Fig. 3. Thus, the obtained results indicate that the percentage conversion into olefin compounds decreases in the following order: n-C_{14} > n-C_{12} > n-C_{10} > n-C_8.

On the other hand, the percentage conversion of n-paraffins into the corresponding olefins increases with the increase in the molecular weights i.e. as the number of carbon atoms increases.

Analysis of the reaction products (Table 2) shows that in all cases aromatics are formed in traces. Such traces of aromatics increase with the increase in the number of carbon atoms of the n-paraffins.

It can be concluded that the reaction proceeds through free radicals intermediate mechanism, and consequently, with the increase in the number of carbon atoms also the freedom to the formation of free radicals increases, i.e. the intermolecular rearrangement and consequently, the increase in the yield of olefins are facilitated.

3. Application of the investigated conditions to the kerosine fraction with b.p. from 140 up to 220°C

When using the kerosine fraction, the investigation was carried out with the help of two furnaces. Products obtained at 250°C in the first furnace, are then subjected to reaction at 400°C in the second furnace. From the data obtained, (Table 3 and Fig. 4), small changes are observed in the component distribution of the products by changing the reaction temperature from 250 to 400°C as compared with that of feed.

The gaseous products obtained, consist mainly of C_1-C_6 having a considerable amount of butene and pentene. But, by varying the reaction temperature from 400 to 550°C in the first furnace and fixed at 600°C in the second one, it is clear that, the yield of aromatic compounds increases and the yield of olefinic ones decreases with the increase in the reaction temperatures up to 550°C. On the other hand, the yield of the overall saturated hydrocarbons gradually decreases, as illustrated in Fig. 4.

The distribution of gaseous products is similar to that obtained at 400°C reaction temperature (second furnace) with a considerable increase in the amount of olefinic gases.

On the basis of the above results, it can be seen, too that the continuous increase in the amount of aromatics is equivalent to the continuous decrease in the amount of olefins at each reaction temperature, or at a temperature rise to 50°C. This behaviour may be due to the dehydrogenation of the saturated compounds to olefinic ones, through free radical intermediate mechanism, and immediately, the olefinic ompounds cyclize to give rise to a higher amount of aromatic compounds with the in-

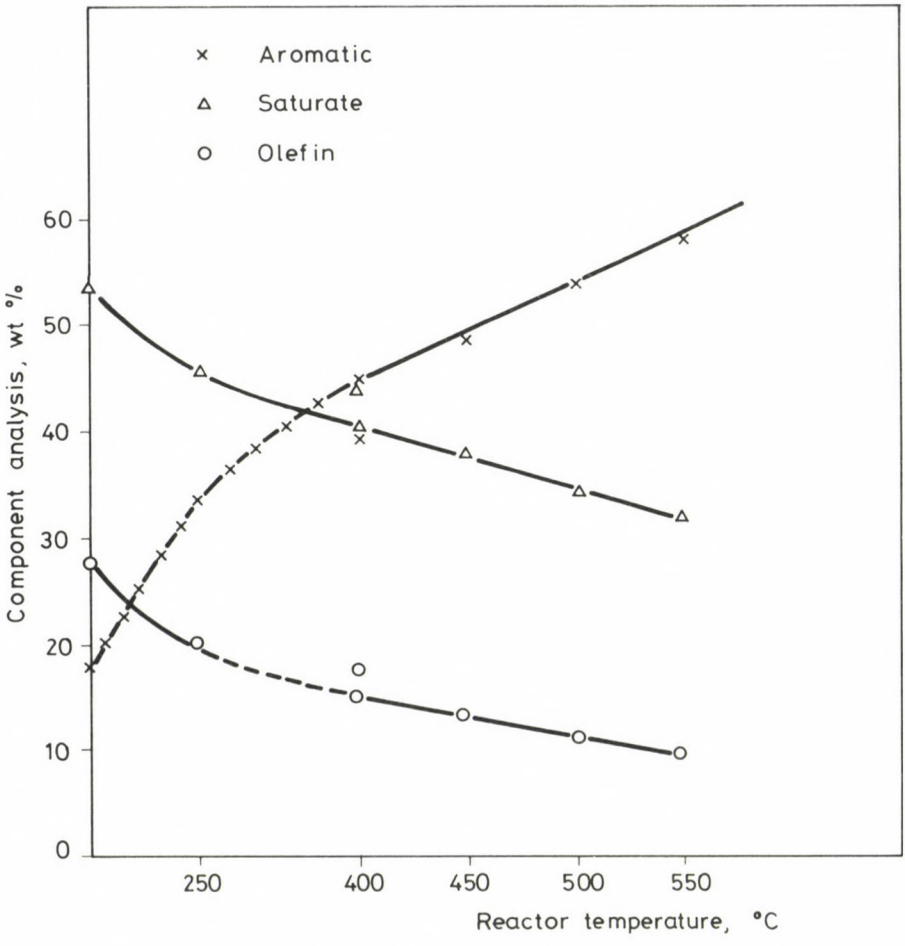

Fig. 4. Component analysis of the produced kerosine at different reaction temperatures

creasing of the reaction temperature up to 550°C, and this explanation may be confirmed also by the decrease in the yield of olefinic compounds.

The increase in the yield of aromatic compounds as resulting from the thermal conversion occurring in the course of feed, may be also due to the fact that the aromatic compounds already present in the feed, act as initiators facilitating the direction of aromatics formation and increasing its amount.

The results of the ASTM distillation are shown in Fig. 5. It indicates that the boiling point distribution of the product is lower than that

Table 3. Effect of the reaction temperature on the component distribution and physical characteristics of the products from kerosine

Temp. of furnace °C		Component distribution wt.%			Refractive	Aniline
1st furnace	2nd furnace	Saturates	Olefins	Aromatics	index, 20°C	point, °C
Feed -	-	54	28	18	1.4523	64
250	400	46	20	34	1.4500	64
400	400	44	18	38	1.4516	64
400	600	40	15	45	1.4552	59
450	600	38	13	49	1.4564	58
500	600	34	11	55	1.4567	55
550	600	32	10	58	1.4568	55

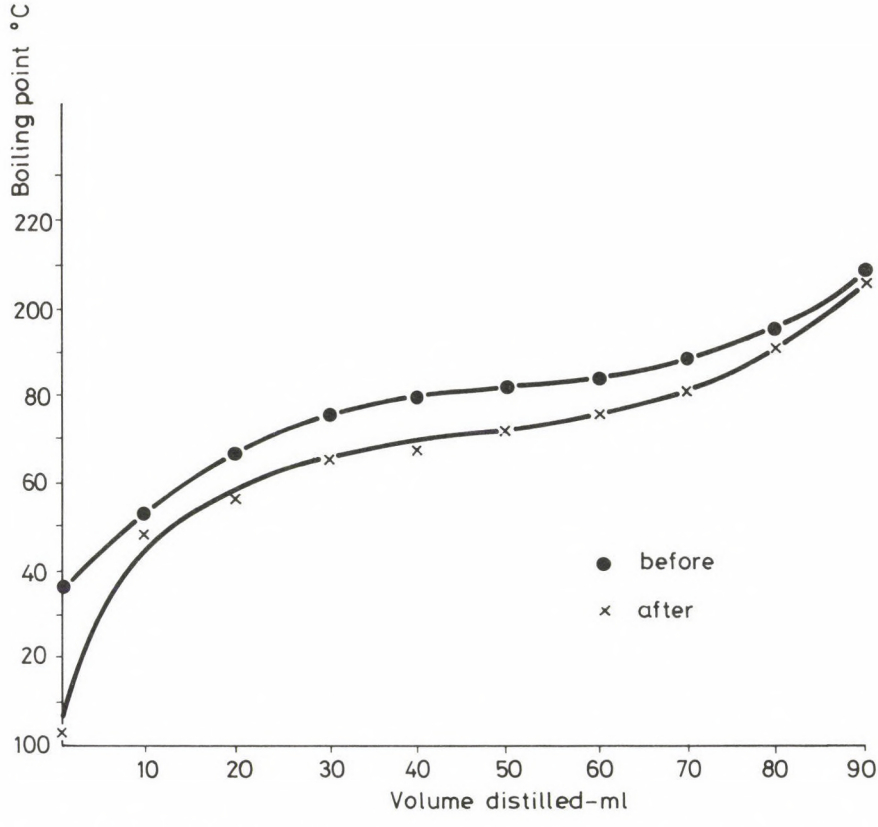

Fig. 5. ASTM-destillation of a kerosine fraction before and after thermal treatment

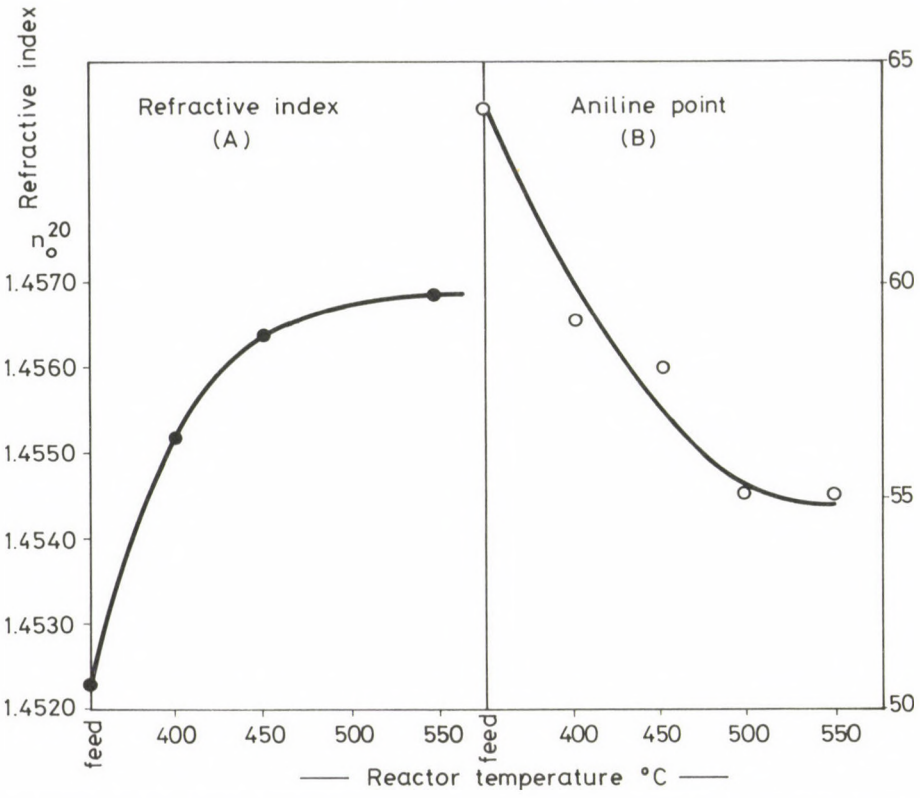

Fig. 6. Effect of reactor temperatures on refractive index (A) and aniline point (B) of the thermal product of kerosine

of the feed. The above findings are in agreement with the data of aniline point and refractive index, as shown in Fig. 6.

REFERENCES

1. Csikós, Cs. - Báthory, H.: Journal of Industrial Chem. 6 (1978), 155-162.

2. Knaus, J.A. - Patton, J.L.: Chem. Eng. Prog., 57 (1961), 57.

3. Knaus, J.A. - Yarze, J.C. - Campbell, W.M.: Sixth World Petroleum Congress, Frankfurt/Main, 163 Section IV, paper 31.

4. Shah, Y.T. - Stuart, E.B. - Kunzru, D.: Ind. Eng. Chem. Process Des. Develop., 12 (1973), 344.

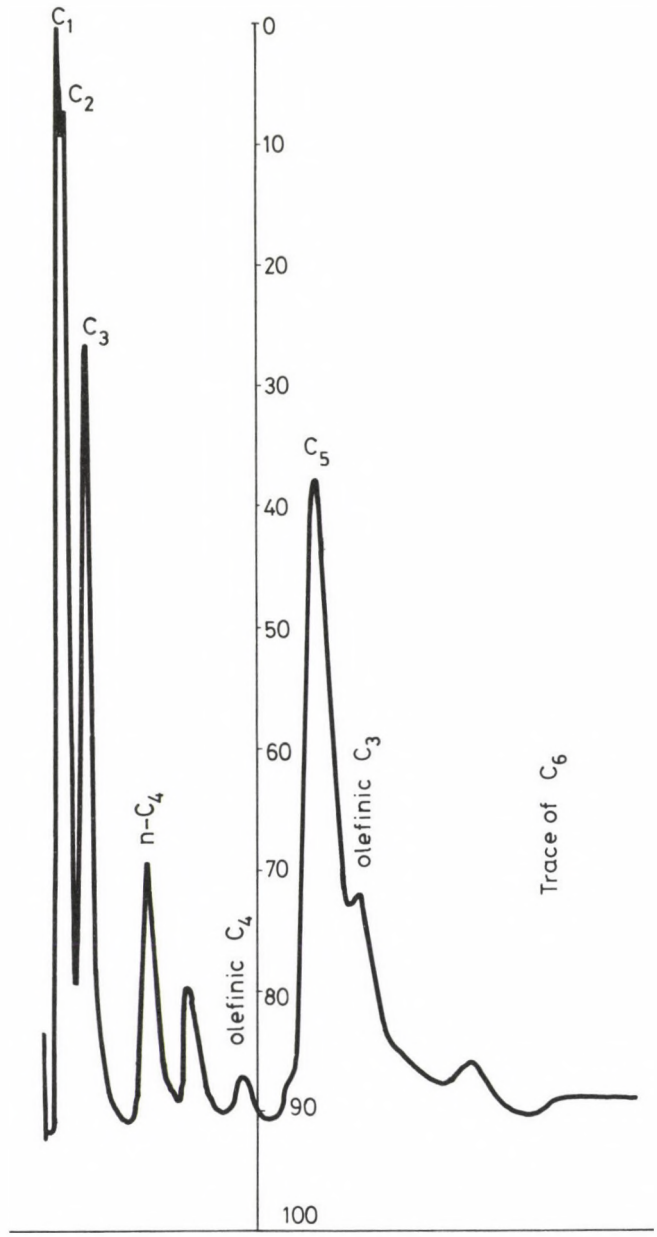

Fig. 7. Gas chromatography of thermally treated kerosine (at 550-600 ^{o}C)

Acta Technica Acad.Sci.Hung., 101(3), pp. 305—321 (1988)

EVENT RECOGNITION BASED ON LINEAR PLANT MODEL

PALÁNCZ, B. - BENEDEK, S.*

(Received: 18 March, 1988)

A method based on identified linear plant-model is recommended for on-line plant surveillance and disturbance analysis. The parameters of the linear model are determined by numerical "experiments" carried out by a comprehensive and verified non-linear dynamic plant-model.

Utilizing the analytical solution of linear, discrete system a so-called event-indicator vector can be defined to detect the reasons of process disturbances.

The present method requires very short computation time, therefore its application is suggested, when the necessary computation has to be achieved as fast as the real process itself in order to evaluate measurement signals and to provide prompt operator's reactions.

For illustration a simplified case study representing malfunction detection in the operation of a nuclear power plant is presented.

NOTATION

A,B	matrices of the linear system
a_{ij}, b_{ij}	elements of matrices
I	residual to be minimized
N	number of considered events
T	duration time of analysis, sec
t	time, s
x	state deviation vector, characterizing the deviation from the steady state
u	event indicator vector

Greek Letters:

ε	noise level of state vector
ΔT	sampling period, sec
Φ	resolvent matrix

Subscripts and superscripts:

i,j	indices of matrix elements
k	k-th sampling (3)
m	measured value
n	n-th numerical experiment (2)

*Palánczy, B., H—1085 Budapest, Salétrom u. 9, Hungary; Benedek, S., H—1368 Budapest, P.O.B. 233, Hungary

Akadémiai Kiadó, Budapest

1. Introduction

Monitoring and surveillance of plant process, detecting the reasons of failures and disturbances in order to avoid malfunctions and accidents, are very important in case of many dangerous and complex processes taking place in chemical as well as in nuclear power industries.

Monitoring the important physical variables and employing effective failure recognition system ensure fast identification and localization of the malfunction sources. In this way the operating staff can react quickly and adequately in order to prevent more serious situations.

In the last years many different methods have been worked out to detect process-ill-behaviour indicated by the presence of abnormal transients. The state estimation and identification procedures /1/, consequence analysis /3/ have been employed mainly for safety study of nuclear power plants /2, 7/. These procedures require dynamical plant-model, which sometimes can be complicated and complex. However, to ensure quick operator's action, the model evaluation time must be about as long as the process time. In this case these procedures have been proved to be slow and clumsy.

There is a good overview about methods employing stochastical signal-technique to investigate linear systems /8/. Abnormalities in the process imply jumping change in the elements of the noise-transfer matrix. On this basis the causes of the process failures can be determined.

In /9/ one may find a good practical summary about the noise analysis of industrial measurements, although the authors do not deal with event recognition.

In this paper we present a fairly new idea to analyse abnormal complex transients and to detect their reasons quickly and in a simple way.

According to our opinion the representation of the effect of the disturbance events must be considered as external control variable, u in the process model. To correct and overcome such characteristical, but not accidental disturbances, the operating staff has to carry out proper actions. However, in case of simultaneous turn up of more disturbances in a short time period, when the situation can be expected to become worse in minutes, even well trained operating personal are in dilemma to decide the proper reaction.

Our method is recommended to support operator actions in such an ambiguous, misleading and overlapping situation.

To illustrate this method a simplified example for analyzing transients of a nuclear power station is presented.

2. Linear Model

Let us consider the following linear, multivariable dynamic model:

$$\dot{x}(t) = Ax(t) + Bu(t) \tag{1}$$

where $\dot{x}(t)$ is measurable state deviation vector characterizing the deviation from the normal steady state, $u(t)$ is so-called event indicator vector. Whenever the j-th event takes place $u_j = 1$, otherwise $u_j = 0$. The elements of the A and B matrices can be identified by the "teaching" process.

3. Teaching Process

The "teaching" of the linear model, the identification of its matrix coefficients can be carried out by numerical experiments employing a complex, sophisticated and verified nonlinear model, which describes adequately the dynamic of the process to be supervised. During this identification process the events to be recognized are numerically simulated one by one and the matrix elements a_{ij} and b_{ij} can be computed on the basis of the $\dot{x}(t)$ trajectories provided by the nonlinear model by minimizing the following multivariable nonlinear function:

$$I(a_{ij},b_{ij}) = \sum_{n=1}^{N} \int_{0}^{T} (\dot{x}_m^n - Ax_m^n - Bu_m^n)^2 \, dt \tag{2}$$

where $x_m^n(t)$ is the trajectory computed by the nonlinear model in the n-th experiment, when only the n-th element of the u_m^n vector differs from zero. This minimization task with a_{ij} and b_{ij} as unknown variables leads to the solution of a linear multivariable algebraic system /4/.

4. Event Recognition

The solution of the linear system (1) for discrete time step ΔT in recursive form is /5/:

$$x^{k+1} = \Phi(\Delta T)\, x^k + \frac{\Delta T}{2} B u^{k+1} + \frac{\Delta T}{2} \Phi(\Delta T)\, B u^k \tag{3}$$

where the trapezoidal rule was used and

$$\Phi(\Delta T) = e^{A \Delta T}, \quad x^k = x(t), \quad t = k \Delta T \tag{4}$$

Reordering the equation (3) for the event indicator vector, we get

$$u^{k+1} = \frac{2}{\Delta T} B^{-1} x^{k+1} - \frac{2}{\Delta T} B^{-1} \Phi(\Delta T)\, x^k - B^{-1} \Phi(\Delta T)\, B u^k \tag{5}$$

During the normal working process, $|x(t)| < \varepsilon$, ε is the noise level of the measured variables. In case when the disturbances of the j-th type event has occurred, the x(t) state deviation vector will change accordingly and the value of the event indicator computed by the recursive algorithm (5) will approach to 1. The on-line principle of the event recognition is represented by Fig. 1.

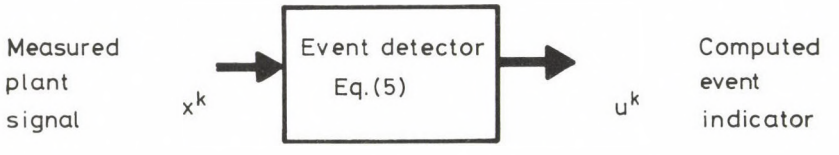

Fig. 1. Principle of the event recognition procedure

Because the linear model estimates the process (more precisely the nonlinear model) in integral or global way (see Eq. (2)), therefore according to our investigations using an integral (global) indicator vector is more effective, namely

$$u(t) = \frac{1}{t} \int_0^t u(\lambda)\, d\lambda \tag{6}$$

In this way the proper indication of an event is much more unique and straightforward especially noisy environment.

The stability conditions for algorithm (5) are given in the Appendix. These conditions were satisfied in our case.

5. Case Study

Our method described in the previous sections was put in a computer code EVENT-1 and applied to the process analysis of a pressurized water nuclear reactor of type WWER-440. To emphasize the significance of the method, the investigated problem was formed in a very simplified way in the paper.

The block diagram of the power station can be seen on Fig. 2.

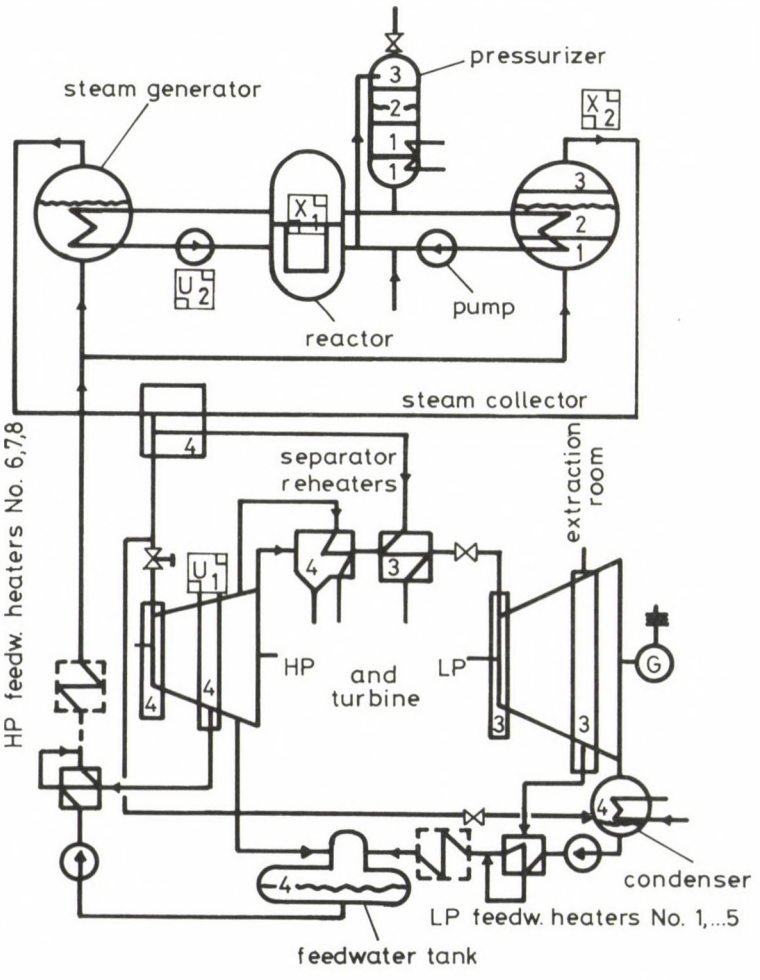

Fig. 2. The block diagram of a WWER-440 nuclear power plant

The identification of the linear model has been carried out by a computer code TRANSILOOP /6/, which was verified through field measurements and provides reliable dynamical simulation of the process.

The state variables and events considered for this example are in Table 1.

Table 1. State variables and disturbance events

x_1: relative power output deviation, dimensionless
x_2: steam generator outlet pressure deviation, bar
u_1: event indicator of malfunction in control valve operation
u_2: event indicator of pump shutdown

Two cases have been studied. In the first case only one event occurs and this is the more realistic case in practice. In the second case two events take place with a certain time-lag between them. This later investigation were interesting because the identification of the linear model was carried out for single events only, and we were eager to know how the method works, when the input signals produced by mixed events of the analyzed nonlinear industrial processes take place.

The identified coefficients of the linear system are in Table 2.

Table 2. Identified coefficients of the Linear Model

$$A = \begin{pmatrix} -0.0948 & 0.00009 \\ 0.02924 & -0.01292 \end{pmatrix} \qquad B = \begin{pmatrix} -0.00285 & -0.0162 \\ 0.0185 & -0.0120 \end{pmatrix}$$

5.1 Recognition of single event

Figure 3 shows the time history of the state deviation variables indicating the effect of the decreasing flow rate in the primary circuit resulted by fault of one main cooling pump.

In Fig. 4 the state deviation variables versus time can be seen in case of malfunction turbine control valve operation causing small change in the steam flow to secondary side.

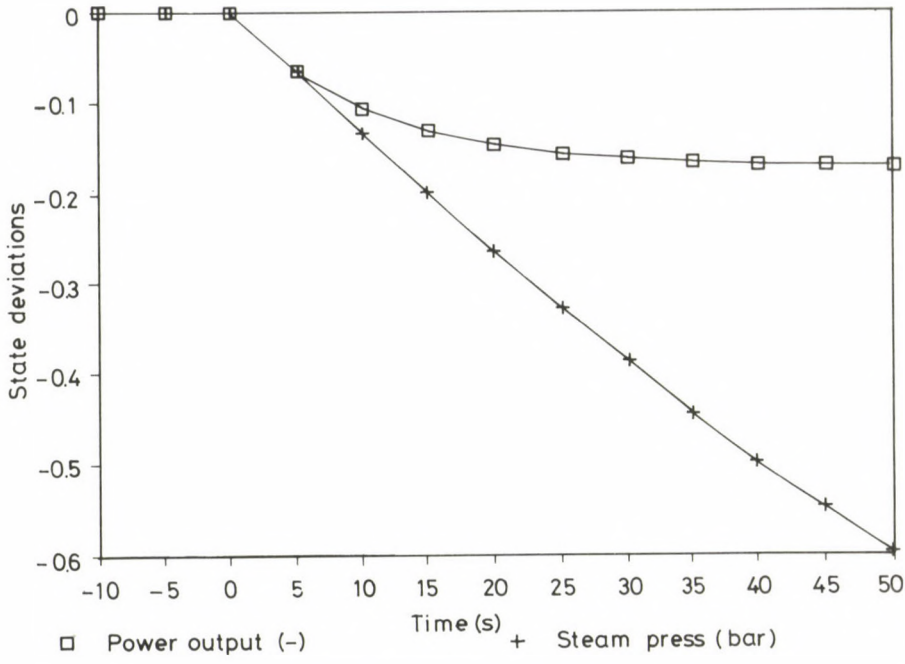

Fig. 3. State change resulted by pump break-down (simulation)

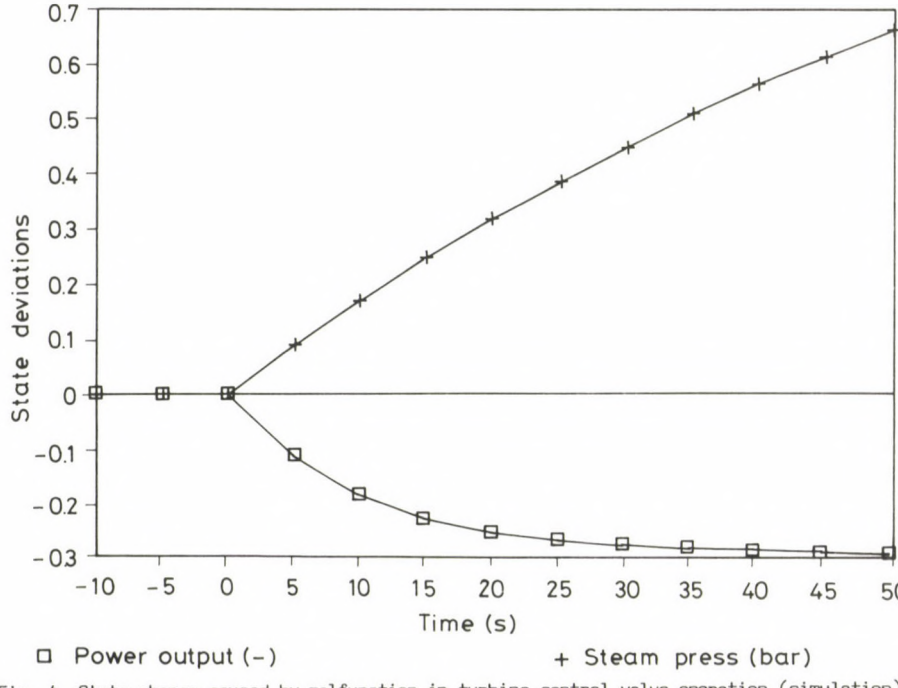

Fig. 4. State change caused by malfunction in turbine control valve operation (simulation)

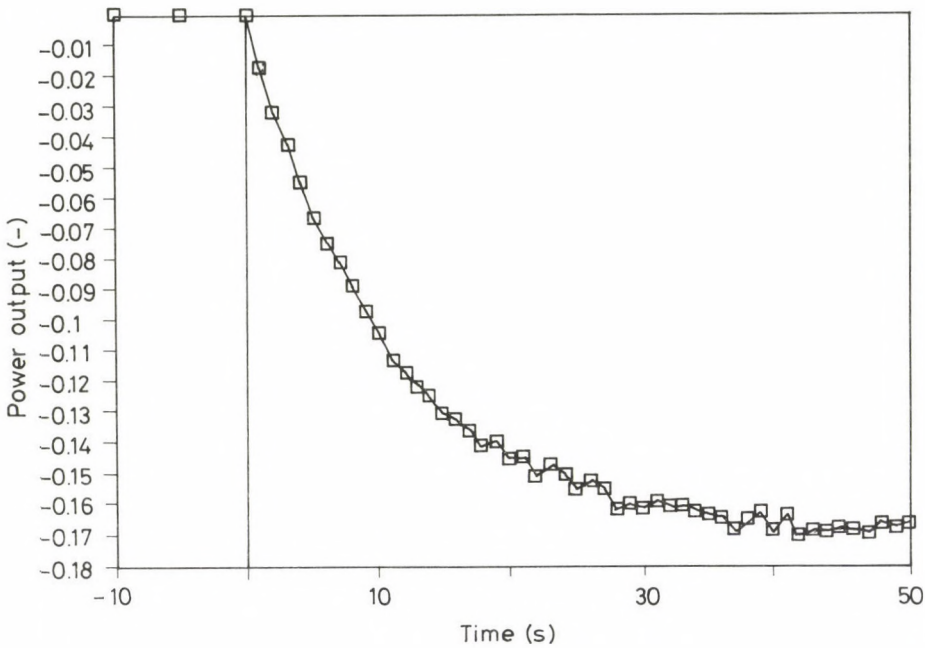

Fig. 5. Transient of decrease in relative power output resulted by pump shut-down (measurement)

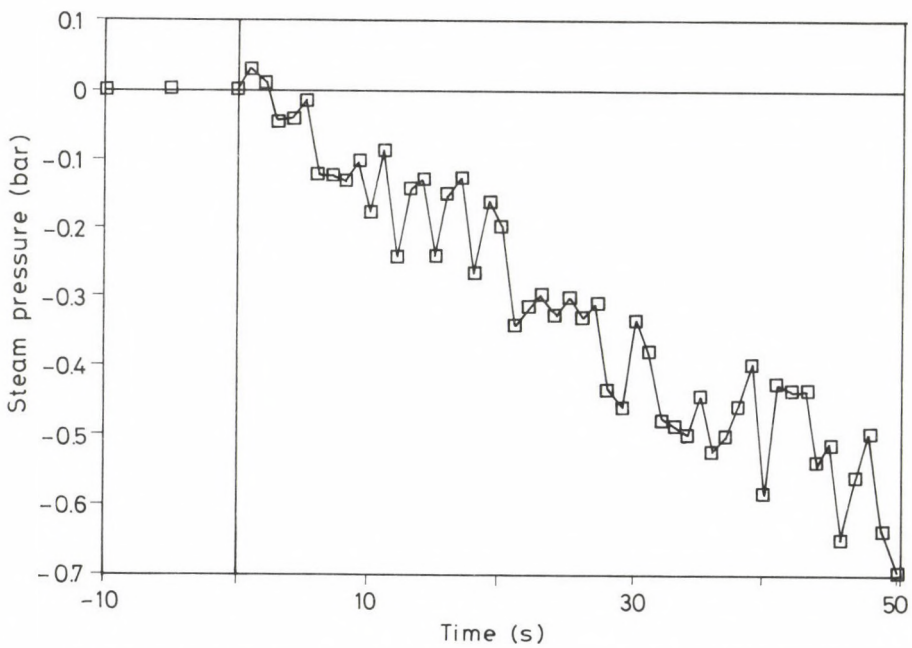

Fig. 6. Transient of decrease in steam pressure resulted by pump shut-down (measurement)

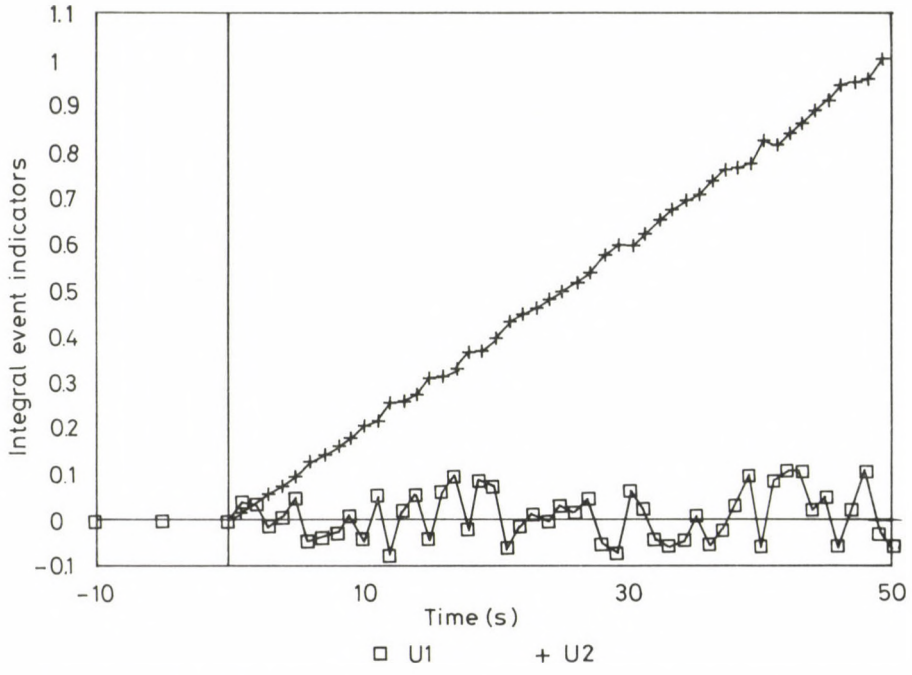

Fig. 7. Change of the components of event indicator vector in time, in case of pump shut-down

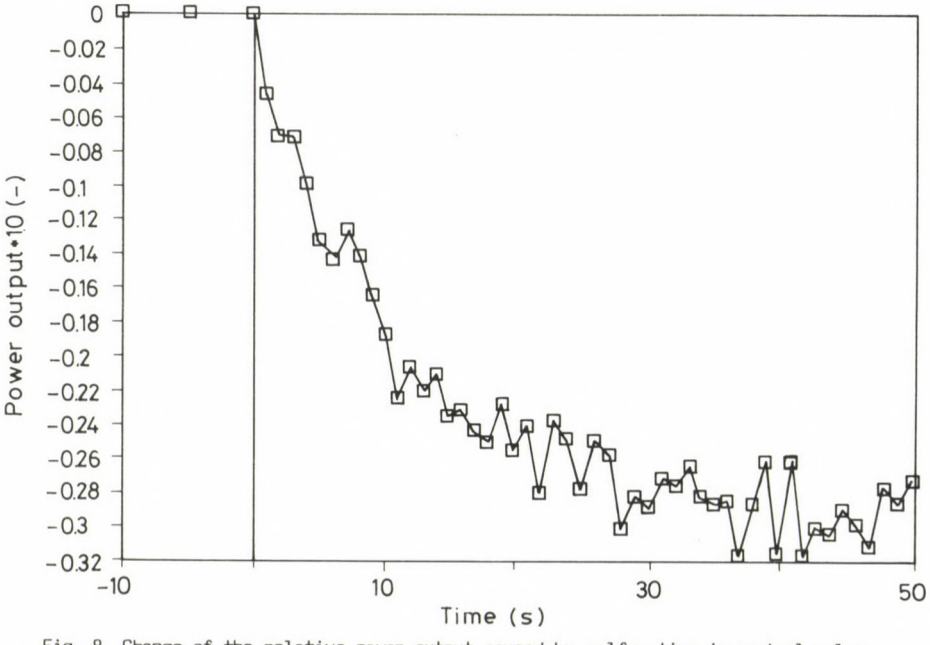

Fig. 8. Change of the relative power output caused by malfunction in control valve operation (measurement)

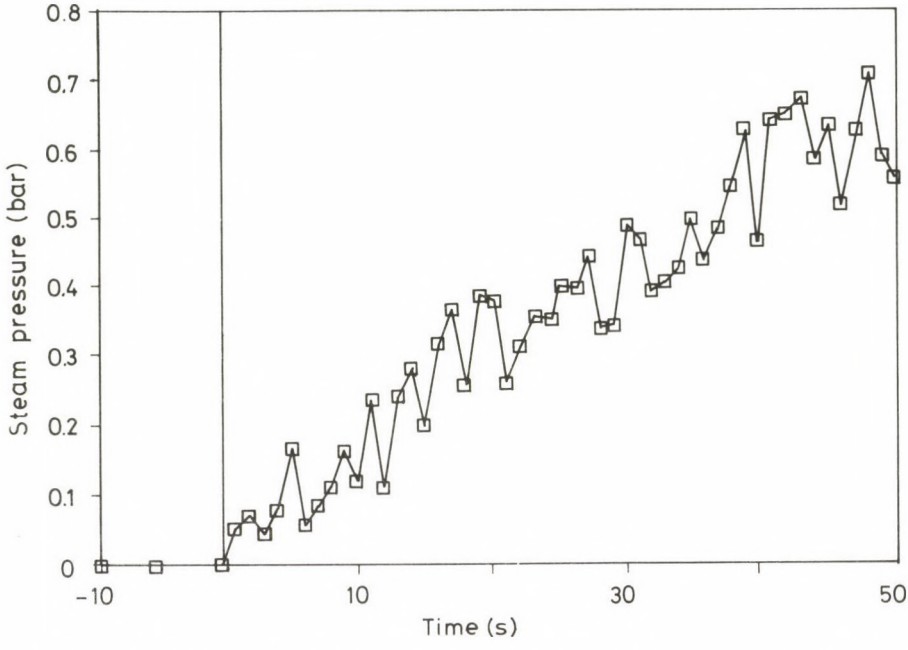

Fig. 9. Change in the steam pressure resulted by malfunction in control valve operation (measurement)

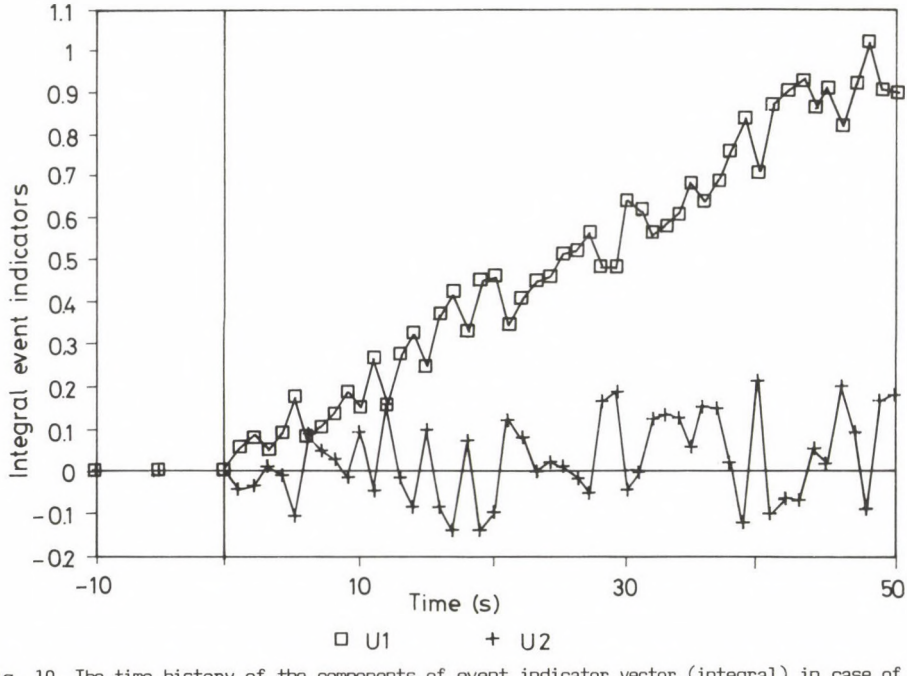

Fig. 10. The time history of the components of event indicator vector (integral) in case of malfunction in control valve operation

These figures represented the state trajectories computed by the TRANSILOOP code, and these have been used for the identification of linear model.

Figure 5 and 6 show field measurements in case of the cooling pump shutdown. One can realize that the noise level of the reactor power output measurement is considerably lower than that of the steam pressure in the steam generator.

The computed event indicators versus time are shown on Fig. 7 as the result of the computation carried out by EVENT-1. The sampling period and computation time step were the same, $\Delta T = 1$ s.

Figures 8 and 9 represent the time history of the two state variables in case of malfunction in control valve operation. The computed integral event indicators are shown in Fig. 10.

According to these figures, our method could recognize disturbance events unambiguously even in very noisy environment.

5.2 Recognition of mixed events

Now, we apply our method to recognizing mixed events existing simultaneously. In this test case the pump break-down is followed by the malfunction in control valve operation in 25 seconds. The measured state variables are shown in Fig. 11.

Figure 12 shows clearly, that our method has recognized both events, although the teaching process was not carried out previously for this mixed case.

6. Sensitivity Study

The ΔT sampling period and noise level dependence sensitivity of our algorithm were investigated in case of mixed events.

On Fig. 13 the result of the event recognition can be seen in case of $\Delta T = 5$ s for measured, noisy trajectories. Figure 12 illustrates the effect of ΔT change, where the results for $\Delta T = 1$ s can be seen. Figures 14 and 15 show the computed event indicators in case of noiseless environment for $\Delta T = 5$ and $\Delta T = 1$ s.

According to these figures the proposed algorithm seems to be fairly robust concerning sample period and computation time step up to about 5 sec in noise environment.

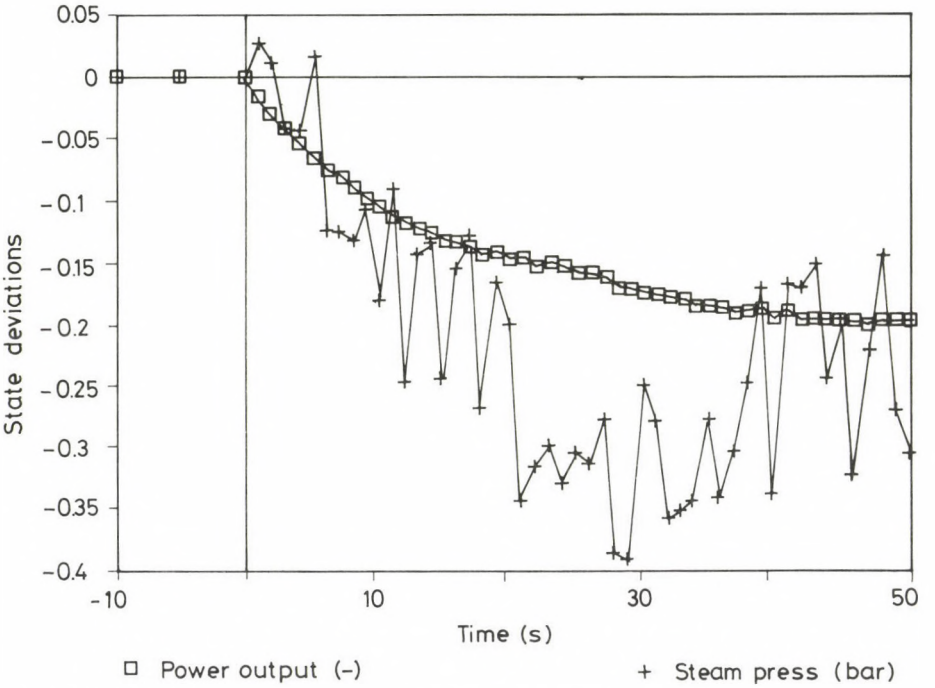

Fig. 11. Changes in relative power output and in steam pressure in case of mixed event (measurement)

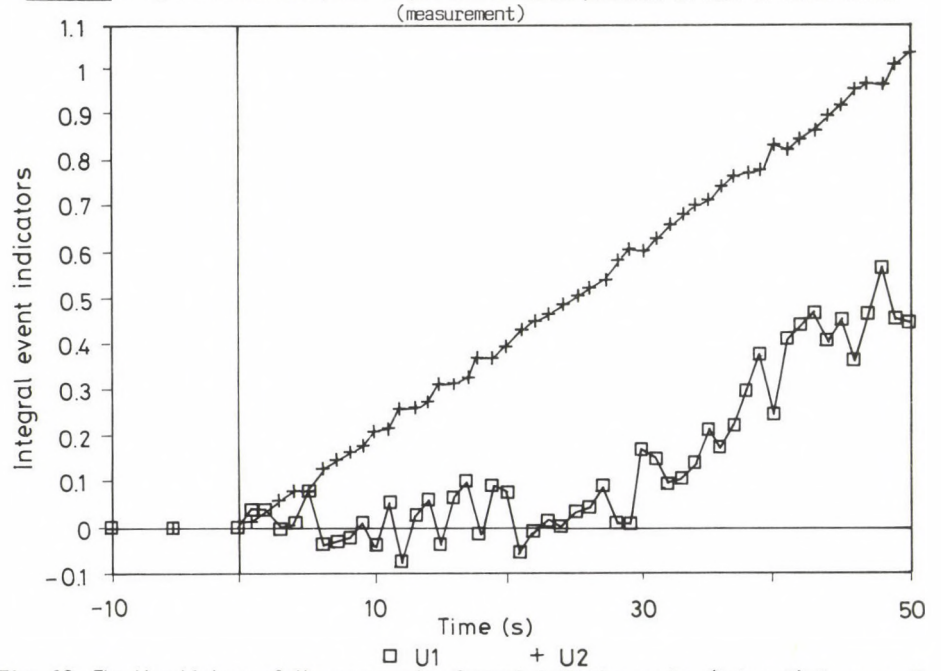

Fig. 12. The time history of the components of event indicator vector (integral) in case of mixed events

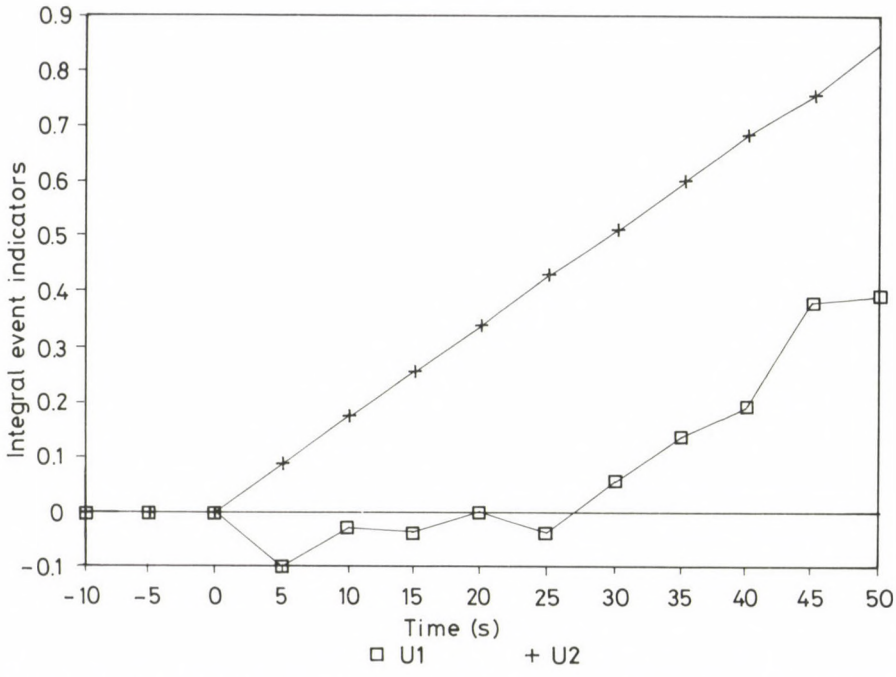

Fig. 13. The time history of the components of event indicator vector (integral) in case of mixed events, at $\Delta T = 5$ s sampling rate

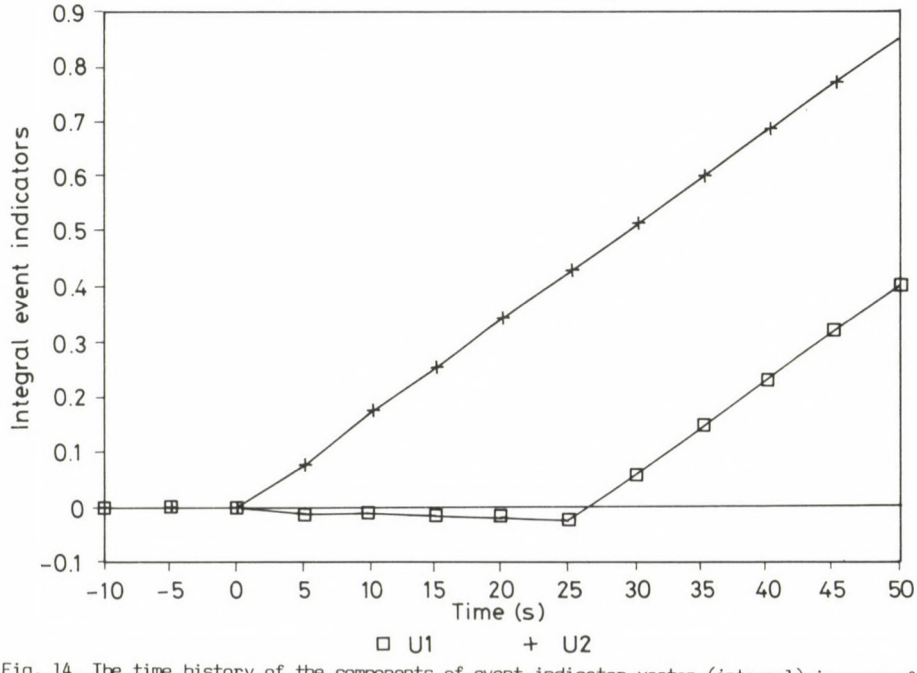

Fig. 14. The time history of the components of event indicator vector (integral) in case of mixed events, at $\Delta T = 5$ s sampling rate, assuming noiseless environment

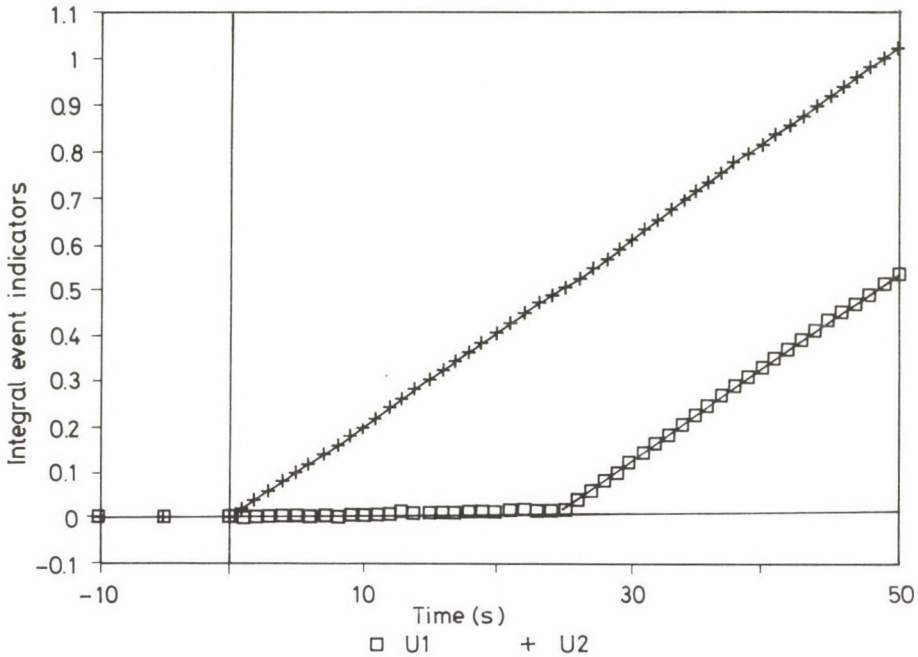

Fig. 15. The time history of the components of event indicator vector (integral) in case of mixed events, at ΔT = 1 s sampling rate, assuming noiseless environment

7. Summary

An event recognition method based on linear plant model has been presented. This method is suitable for on-line process monitoring because its short computation time requirement.

To identify the coefficients of the linear system, a nonlinear model was used, which describes the monitored process precisely. The matching between these two models was achieved in global (integral) instead of local sense.

According to our experiments, the global form of the event indicator is much more preferable.

In case of process with complex dynamics, the application of first order model is not sufficient, consequently higher order models are required. However, these may be also replaced by enlarged first order multivariable system.

Acknowledgement

The authors wish to thank Dr. G. Almásy his useful critical remarks which improved considerably the quality of this publication.

APPENDIX

Stability of the algorithm

The stability of the discrete-time model can be analysed by using concepts of stability of dynamic systems applied to (5). Two general types of stability can be considered: (a) external stability, considered by the excitation and (b) equilibrium stability related to the free evolution of the system starting from some initial conditions, as with Lyapunov, asymptotical and global stability. It is shown that all stability types are assured by conditions related to the modulus of the eigenvalues of matrix $-B^{-1}\Phi B$.

Equilibrium stability

If there is not excitation, three types of stability can be considered for algorithm (5), namely Lyapunov, asymptotical and global. The Lyapunov stability is important to assure that the initial distortions and round-off errors do not increase artificially in the computation process. The asymptotical and global stabilities are important in order to assure that these perturbations damp out in the computation process. If there is not excitation acting on the system, equation (5) reduces to

$$u^{k+1} = -B^{-1}\Phi B\, u^{k} = (-B^{-1}\Phi B)^{k+1}\, u^{0} \qquad (7)$$

It means that the algorithm is stable in the sense of Lyapunov if the moduli of the eigenvalues of matrix $(-B^{-1}\Phi B)$ are $<$ or $=$ 1 and only the eigenvalues belonging to unit-sized Jordan block have moduli =1, and the algorithm (5) is asymptotically and globally stable if all the eigenvalues of $-B^{-1}\Phi B$ have moduli smaller than one.

External stability

The algorithm (5) is externally stable if for any u^{0} with $\|u^{0}\| \leq \delta$ and x^{k} with $\|x^{k}\| \leq \delta$ for $k \geq 0$ there is a positive constant ε in such a

way that $\|u^k\| \leq \varepsilon$ for any k. This stability condition is equivalent to that which states that to any bounded excitation corresponds a bounded response. Therefore this type of stability is important to guarantee the lack of artificial amplifications of the response. To analyse the conditions under which our algorithm is externally stable, it is necessary to express the response at an arbitrary instant k T with the responses at all previous instants. A relation of this kind can be written by recurrently applying Eq. (5) starting from the initial instant. It leads to

$$u^{k+1} = \frac{2}{\Delta T}\left[B^{-1}x^{k+1} - 2\sum_{j=0}^{k-1}(-B^{-1}\Phi B)^j (B^{-1}\Phi)x^{k-j} - \right.$$
$$\left. - (B^{-1}\Phi B)^k (B^{-1}\Phi)\, x^o\right] + (-B^{-1}\Phi B)^{k+1} u^o \tag{8}$$

If all the eigenvalues of matrix $(-B^{-1}\Phi B)$ are inside the unit circle, the following inequality can be written

$$\|(-B^{-1}\Phi B)^m\| < C\,\mu^m \tag{9}$$

where m is a positive integer, and C and μ are positive constant numbers, μ being smaller than one. Employing compatible norms

$$\|u^{k+1}\| \leq \|(-B^{-1}\Phi B)^{k+1}\|\ \|u^o\| + \frac{2}{\Delta T}\left[\|B^{-1}\|\ \|x^{k+1}\| + \right.$$
$$+ 2\sum_{j=0}^{k-1}\|(-B^{-1}\Phi B)^j\|\ \|B^{-1}\Phi\|\ \|x^{k-j}\| + \tag{10}$$
$$\left. + \|(-B^{-1}\Phi B)^k\|\ \|B^{-1}\Phi\|\ \|x^o\|\right]$$

Applying the inequality (8) and considering the preconditions of external stability, we get

$$\|u^{k+1}\| \leq \delta C\left[\mu^{k+1} + \frac{2}{\Delta T}\,\frac{\|B^{-1}\|}{C} + \frac{4}{\Delta T}\|B^{-1}\|\,\|\Phi\|\right.$$
$$\left.(1 + \mu + \mu^2 + \ldots + \mu^k)\right] \tag{11}$$

Then

$$\| u^{k+1} \| \leq \varepsilon$$

where

$$\varepsilon = \vartheta C K \left(\frac{2}{\Delta T} \frac{\| B^{-1} \|}{C K} + \frac{1}{1 - \mu} \right) \tag{12}$$

and

$$K = \max \left(\frac{4}{\Delta T} \| B^{-1} \| \| \Phi \|, 1 \right) \tag{13}$$

Consequently, the necessary conditions for external stability of the algorithm (5) are:

a) the original system Eq. (3) has equilibrium stability,

b) $\det B^{-1} \neq 0$,

c) the all eigenvalues of $-B^{-1} \Phi B$ are inside the unit circle.

REFERENCES

1. Himmelblau, D.M.: Fault Detection and Diagnosis in Chemical and Petrochemical Processes. Elsevier Scientific Publ. C. Amsterdam, 1978.

2. Meijer, C.H., Frogner, B. and Long, A.B.: A Disturbance Analysis System for on-line Power Plant Surveillance and Diagnosis presented paper at IAEA-NPPCI Specialist Meeting, Munich, Dec. 5-7, 1979.

3. Amendola, A. and Reina, G.: DYLAM-1: A Software Package for Event Sequence and Consequence Spectrum Methodology, EUR 9224, N, JRC, ISPRS (1984)

4. Paláncz, B.: Controllability Test on Flowthrough Drying Process with Linearization of the Distributed Model, Hung. J. of Ind. Chemistry, 3 (1975), 127-140.

5. Rosko, J.S.: Digital Simulation of Physical Systems, Addison-Wesley, (1972).

6. Benedek, S.: TRANSILOOP - a computer code for transients in nuclear plants with pressurized water reactors, Atomkernenergie/Kerntechnik, 49 (1986), 21-28.

7. Nelson, W.R.: REACTOR - an expert system for diagnosis and treatment of nuclear reactor incidents, Proceedings AAAI-82 (1982), 296-301.

8. Turkey, A.A.: On the Problem of Sensor Validation and Fault Detection in Dynamic Systems, Working Paper IF/22, MTA SZTAKI (1988).

9. Volgin, V.V. - Karimov, R.N.: Correlation methods in Industrial Control. Műszaki Könyvkiadó (1984), Engineering (in Hungarian).

Acta Technica Acad.Sci.Hung., 101(3), pp. 323—337 (1988)

SOLUTION OF INVERSE HEAT CONDUCTION PROBLEM BY ORTHOGONAL COLLOCATION TECHNIQUES

PALÁNCZ, B. - SZABOLCS, G.*

(Received: 15 September, 1987)

A numerical method based on orthogonal collocation techniques for solving inverse heat conduction problems is presented. This method offers a possibility of determining temperature distributions as well as of computing boundary values by using measured temperature records at an internal point of a solid body. A very modest computation demand, high stability and robustness qualify this method as a successful candidate for on-line applications. Applying the proposed method to conjugated heat transfer problems, the heat transfer coefficient can be estimated on the basis of the measured fluid bulk temperature.

NOTATIONS

a	heat conductivity, m^2/s
$a_{0,1,2}$	coefficients
A,B	collocation matrices
C	system matrix
C	specific heat kJ/kg,K
e	vector
L	thickness, m
t	time, s
T	temperature, K
X	space coordinate, m
r	relative location of the temperature sensor, see Eq. (9)
q	temperature change, see Eq. (23), K

Greek Letters

Δt	time step, s
$\eta\xi$	dimensionless space coordinates
λ	heat conduction coefficient, W/m,K
ϱ	density, kg/m^3

*Palánczy, B., H—1085 Budapest, Salétrom u. 9, Hungary; Szabolcs, G., H—1133 Budapest, Bessenyei u. 25/a, Hungary

Akadémiai Kiadó, Budapest

Indices

I	first section
II	second section
k	k-th measurement
m	measurement point
s	solid phase
w	interface

1. Introduction

In contrast with the classic direct heat conduction problem where the internal temperature distribution has to be determined under specified boundary conditions, the inverse problem arises from applications for which temperature data are not available on the boundary, but are given instead at internal points /1/.

There are many industrial processes where the inverse problem may turn up. The knowledge of surface temperature, heat flux rate or internal temperature distribution of a working industrial equipment is often necessary. Unfortunately, neither surface temperatures can be measured directly nor internal temperature sensors can be built in without destruction of the structural material. Therefore the temperature distribution shall be determined by means of internal thermocouples of minimum number (possibly one).

Such problems arise in case of chemical reactors, where the surface temperature of the reactor wall shall be kept under a specified limit in order to avoid certain poisoning side-reactions /2/. To prevent thermal overstresses or to estimate and predict changes in material properties caused by periodical temperature variation in the structural materials of turbines, steam generators and of certain equipment of nuclear power stations, the unsteady internal temperature distribution should be known /3/. Also the temperature control of distributed parameter systems can be considered to be an inverse problem /4/.

Two important difficulties unknown in case of normal heat conduction have to be overcome to cope with inverse problems. The first is the ill-posed nature of this problem. This means that, because of measurement errors, the measured values of temperature do not belong to the same solution of the heat conduction equation /5/.

The second difficulty is that the experimental data are available only at certain times. On one hand, the time between two observations should be short enough to ensure the stability of the numerical procedure

and to avoid the loss of important informations about the process during dead-time. On the other hand, the time between two measurements should be long enough to permit the measured values to be evaluated /6/.

There are two ways to overcome the first difficulty. The first is to use filtering and smoothing methods well known in control theory and practice /7/.

The other possibility is to integrate a regression type minimizing procedure used in system identification and parameter estimation into the algorithm solving inverse problems /8/.

Methods of a more or less analytical character may successfully overcome the second difficulty /9/. In this paper, a computation method is presented, based on orthogonal collocation techniques which, according to our experiments, reduce both difficulties considerably. This method can be considered as a hybrid of the differential and analytical methods.

2. Mathematical Modell

Let us consider a flat plate having finite thickness and direct contact with liquid phase at one side, X=0. The bulk liquid temperature $T_L(t)$ changes with time. Convective heat transfer takes place between the liquid phase and the flat plate surface, X=0, while the other side of the plate is perfectly insulated at X=L. The point of temperature measurement, $X=L_m$, divides thickness L of the plate into two sections, see. Fig. 1.

Considering the first section, $0 < X < L_m$:

$$\frac{\partial T}{\partial t} = \frac{a}{L_m^2} \frac{\partial^2 T}{\partial \eta^2} \qquad \text{if} \quad 0 < \eta < 1 \tag{1}$$

where

$$\eta = \frac{X}{L_m} \quad \text{and} \quad a = \frac{\lambda_s}{C_s \varrho_s} \tag{2}$$

Boundary condition at X=0:

$$-\frac{\partial T}{\partial \eta} = Nu_m (T_L - T_w) \qquad \text{if} \quad \eta = 0 \tag{3}$$

where

$$Nu_m = \frac{\alpha_w L_m}{\lambda_s} \tag{4}$$

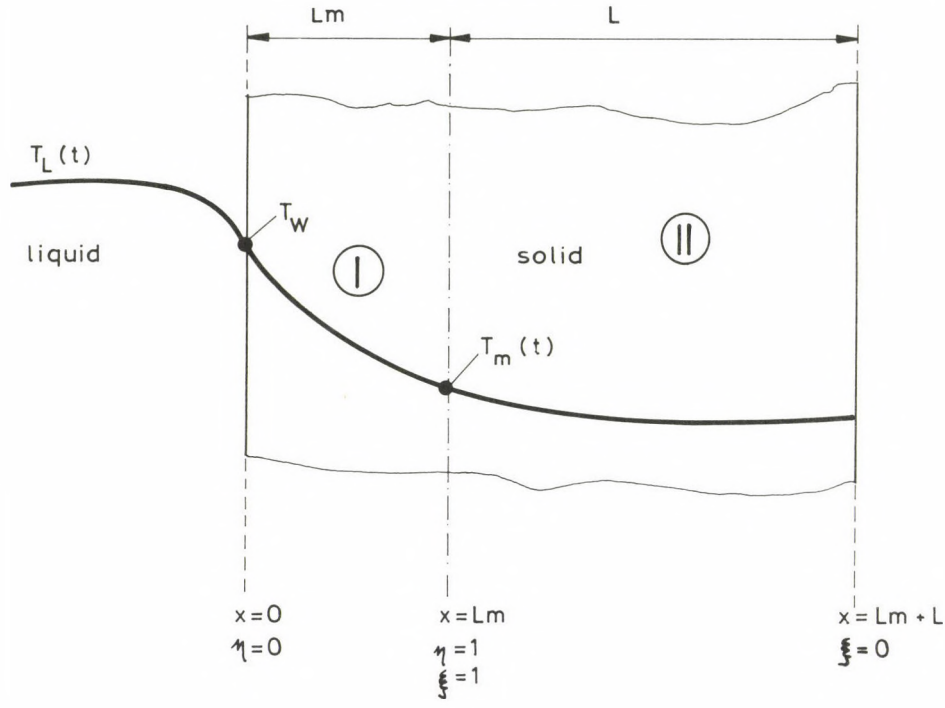

Fig. 1. Physical Modell

Considering the second section, $L_m < X < L_m + L$

$$\frac{\partial T}{\partial t} = \frac{a}{L^2} \frac{\partial T}{\partial \xi_2} \qquad \text{if} \qquad 0 < \xi < 1 \tag{5}$$

where

$$\xi = 1 - \frac{X - L_m}{L} \tag{6}$$

Boundary condition at $X=L_m+L$:

$$\frac{\partial T}{\partial \xi} = 0 \qquad \text{if} \qquad \xi = 0 \tag{7}$$

Joint boundary condition at $X=L_m$:

$$\frac{\partial T}{\partial \eta} = r \frac{\partial T}{\partial \xi} \qquad \text{if} \qquad \eta = \xi = 1 \tag{8}$$

where

$$r = -\frac{L_m}{L} \tag{9}$$

3. Solution to the second section

Using orthogonal collocation techniques, the solution of Eq. (1) can be expressed as a function of measured temperature T_m at $X=L_m$. Considering internal collocation points of number N, the temperature distribution can be approximated by the following polynomial function, see Fig. 2.

$$T_{II}(\xi, t) = \sum_{i=1}^{N+1} d_{II,i}(t)\,\xi^{2(i-1)} \tag{10}$$

Applying this approximation, the following differential equation system is obtained for the collocation points /11/:

$$\frac{dT_{II,i}}{dt} = \frac{a}{L^2}\left(\sum_{k=1}^{N} B_{ik}\,T_{II,k} + B_{i,N+1}\,T_m\right) \tag{11}$$

$$i = 1,2,\ldots,n$$

The boundary condition (7) is satisfied automatically because of the odd order of the polynomial function.

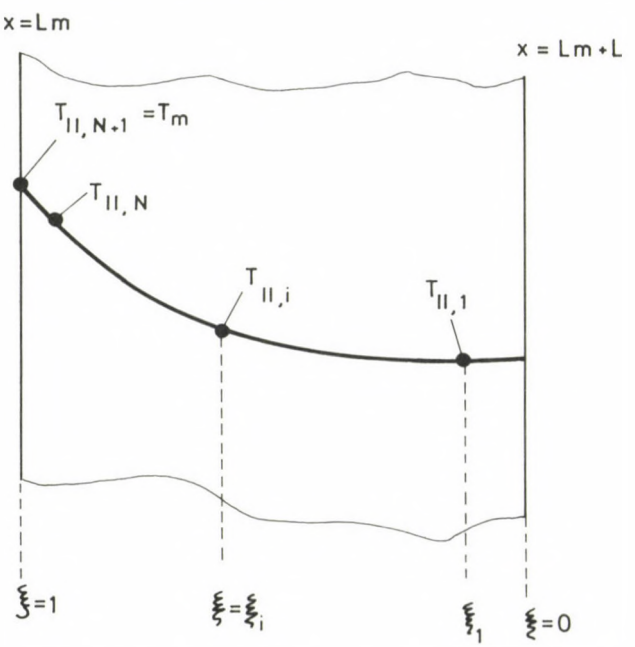

Fig. 2. Location of the collocation points in Section II

In matrix form

$$\dot{T}_{II} = CT_{II} + eT_m(t) \tag{12}$$

where

$$c_{ik} = \frac{a}{L^2} B_{ik} \qquad i,k = 1,2,\ldots,N \tag{13}$$

and

$$e_i = \frac{a}{L^2} B_{i,N+1} \qquad i = 1,2,\ldots,N \tag{14}$$

Solution of Eq. (12) for Δt discrete time:

$$T_{II}^{k+1} = \exp(C\,\Delta t)\, T_{II}^{k} + \frac{\Delta t}{2}\, eT_m^{k+1} + \frac{\Delta t}{2} \exp(C\,\Delta t)\, eT_m^{k} \tag{15}$$

where

$$T_{(\,)}^{k} = T_{(\,)}(k\,\Delta t) \tag{16}$$

Because the eigenvalues of matrix C are different:

$$\exp(C\,\Delta t) = \sum_{i=1}^{N+1} e^{\lambda_i \Delta t} \prod_{\substack{j=1 \\ j\neq i}}^{N+1} \frac{C - \lambda_j I}{\lambda_i - \lambda_j} \tag{17}$$

The recursive formula (15) requires a very short computation time because its coefficients are constant.

4. Solution to the first section

While the solution to the second section is independent of the temperature distribution in the first section, the situation is quite different in the opposite case. Although the use of orthogonal collocation techniques again seems to be quite consequent, the second order polynomial approximation used in differential methods /10/ has proved successful according to numerical experiments.

Let us approximate the temperature profile in the first section by a second order polynomial representing a particular solution of Eq. (1):

$$T_I(\eta,t) = a_0 + a_1 \quad + a_2 \left(\frac{L_m^2}{2a} \eta^2 + t \right) \tag{18}$$

Then the coefficients associated with the solution at $t = k \Delta t$ can be determined as follows:

Values of temperature at location $\eta = 1$, at time $t = k \Delta t$ and $t = (k+1) \Delta t$

$$T_m^k = a_0^k + a_1^k + a_2^k \left(\frac{L_m^2}{2a} + k \Delta t \right) , \tag{19}$$

$$T_m^{k+1} = a_0^k + a_1^k + a_2^k \left[\frac{L_m^2}{2a} + (k+1) \Delta t \right] \tag{20}$$

respectively, and therefore

$$a_2^k = \frac{T_m^{k+1} - T_m^k}{\Delta t} . \tag{21}$$

At $\xi = \eta = 1$, coefficient a_1^k can be determined on the basis of boundary condition (8):

$$\left(\frac{\partial T}{\partial \eta} \right)^k = r \left(\frac{\partial T}{\partial \xi} \right)^k = r \left(\sum_{p=1}^{N} A_{N+1,\,p} T_{II,p}^k + A_{N+1,N+1} T_m^k \right) \tag{22}$$

Introducing

$$q_m^k = r \left(\frac{\partial T}{\partial \xi} \right)^k \tag{23}$$

and considering Eq. (18), we get

$$a_1^k + a_2^k \frac{L_m^2}{a} = q_m^k , \tag{24}$$

then a_1^k can be computed as

$$a_1^k = q_m^k - \frac{T_m^{k+1} - T_m^k}{\Delta t} \frac{L_m^2}{a} . \tag{25}$$

Assuming that the temperature profile described by Eq. (18) is valid also at the point of measurement, that is

$$T_m^k = a_0^k + a_1^k + a_2^k \left(\frac{L_m^2}{2a} + k \Delta t \right) \tag{26}$$

then

$$a_0^k = T_m^k - q_m^k + \left(\frac{1}{2}\frac{L_m^2}{a} - k\right)(T_m^{k+1} - T_m^k) \quad , \tag{27}$$

and the surface temperature:

$$T_w^k = a_0^k + a_2^k \, k \, \Delta t = T_m^k - q_m^k + \frac{1}{2}\frac{L_m^2}{a} \quad . \tag{28}$$

If the bulk temperature of the liquid phase is measured, the Nusselt-number, Nu_m, can also be determined on the basis of boundary condition given in Eq. (3):

$$Nu_m \, (T_L^k - T_w^k) = - a_1^k \quad , \tag{29}$$

therefore

$$Nu_m = \frac{\dfrac{T_m^{k+1} - T_m^k}{\Delta t}\dfrac{L_m^2}{a} - q_m^k}{T_L^k - T_w^k} \tag{30}$$

5. Numerical example

The proposed procedure is illustrated by the following numerical example:

Data used for computation:

L_m = 2.8 mm
L =25.2 mm
a = 1.15 . 10^{-5} m^2/s^2
N = 2

In this case, matrices A and B are /11/:

$$A = \begin{bmatrix} -1.753 & 2.508 & -0.7547 \\ -1.371 & -0.6535 & 2.024 \\ 1.792 & -8.791 & 7 \end{bmatrix}$$

$$B = \begin{bmatrix} -4.74 & 5.677 & -0.9373 \\ 8.323 & -23.26 & 14.94 \\ 19.07 & -47.07 & 28 \end{bmatrix}$$

The initial condition: $T(X,0) = 51^{o}C$ for $0 \leq X \leq L_m + L$

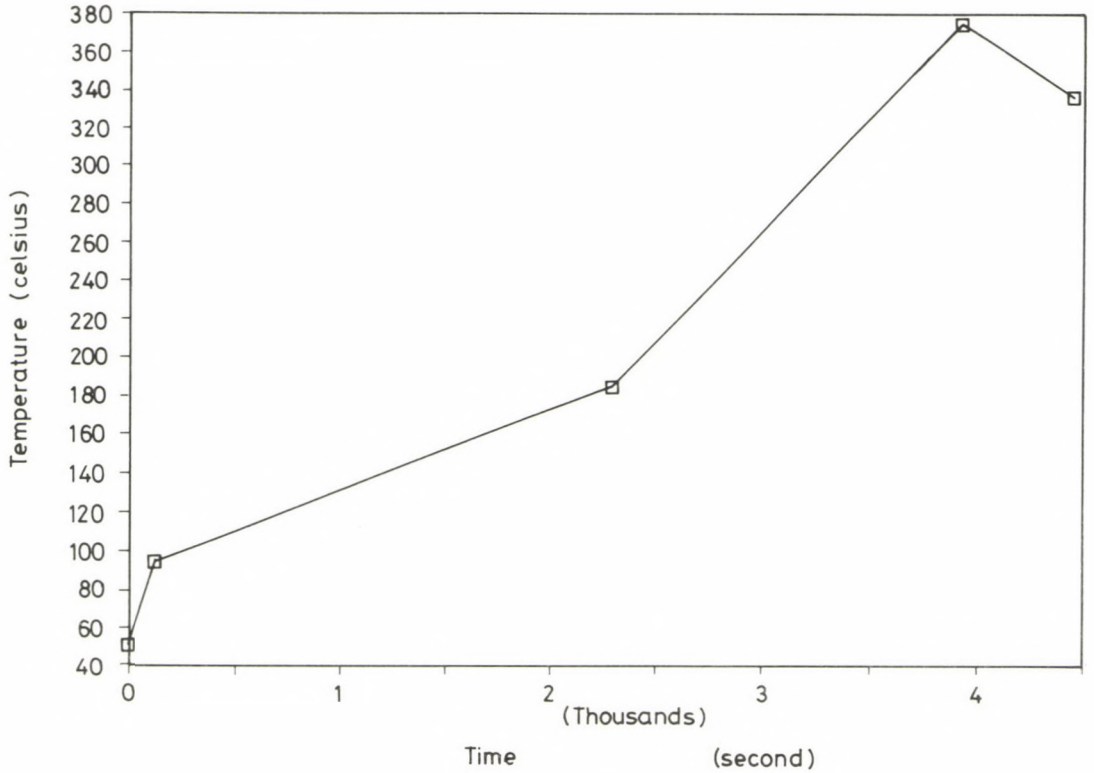

Fig. 3. Bulk temperature of liquid phase versus time

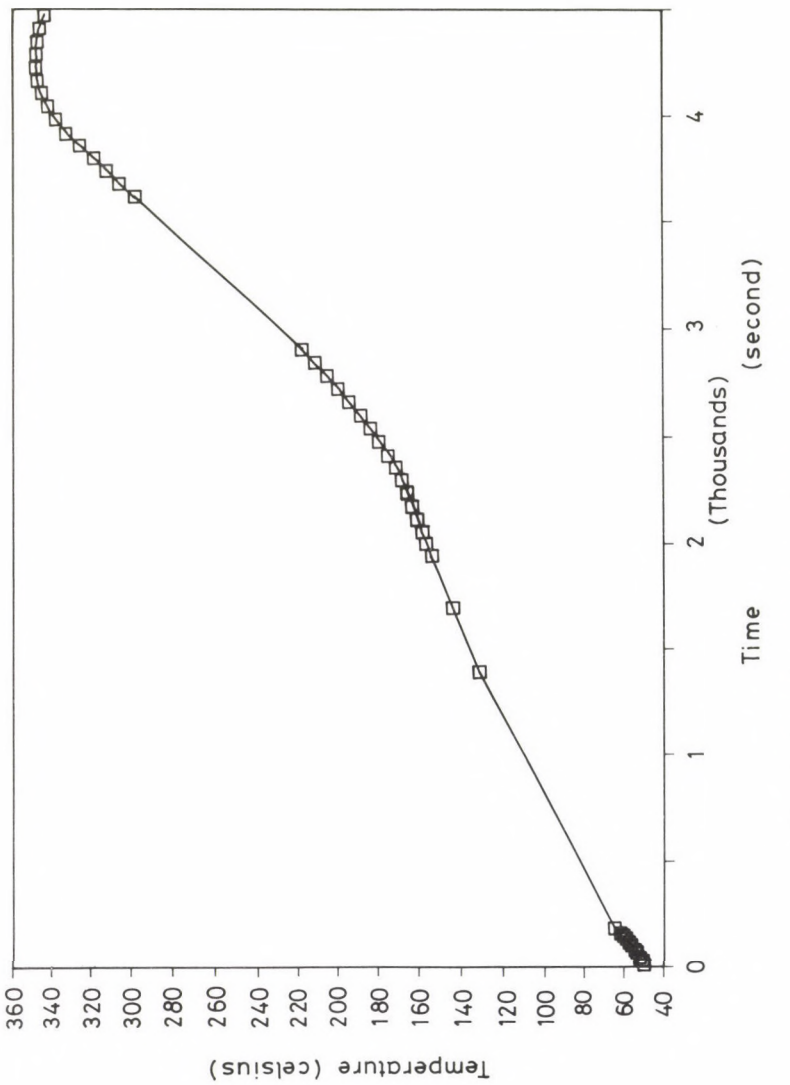

Fig. 4. Measured temperature in the wall (x = 2.8 mm)

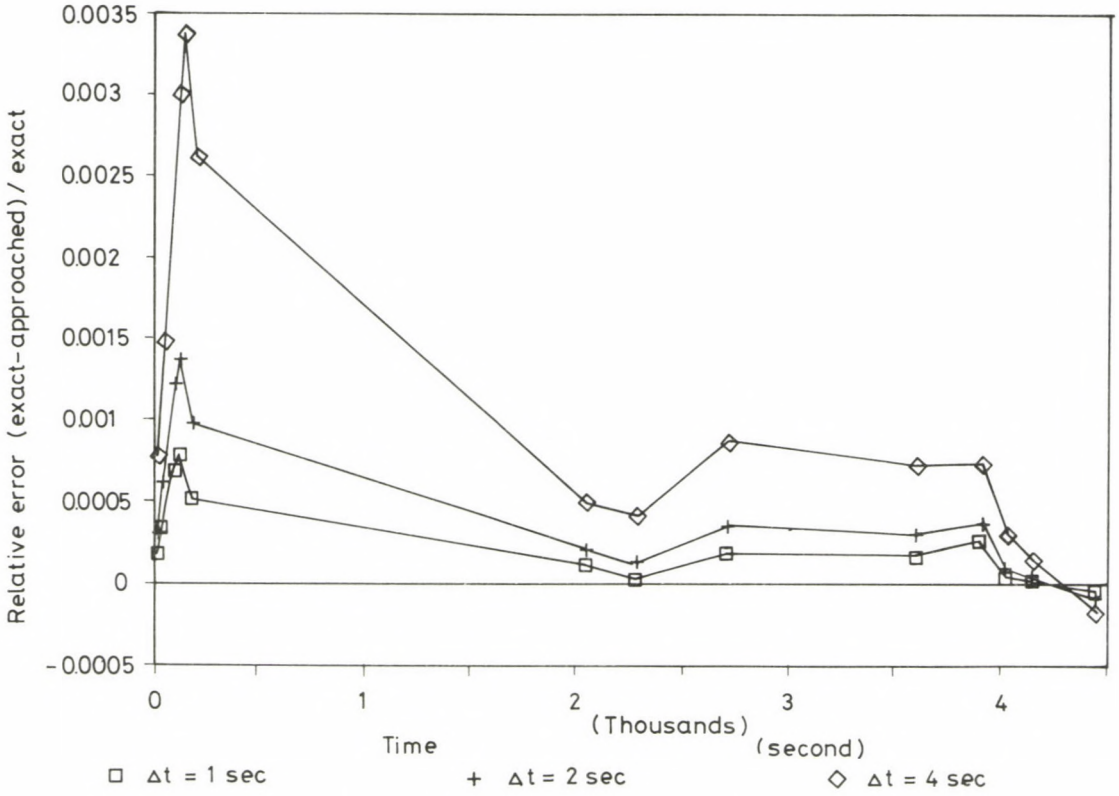

Fig. 5. Relative deviation between computed and actual surface temperatures in case of different time steps

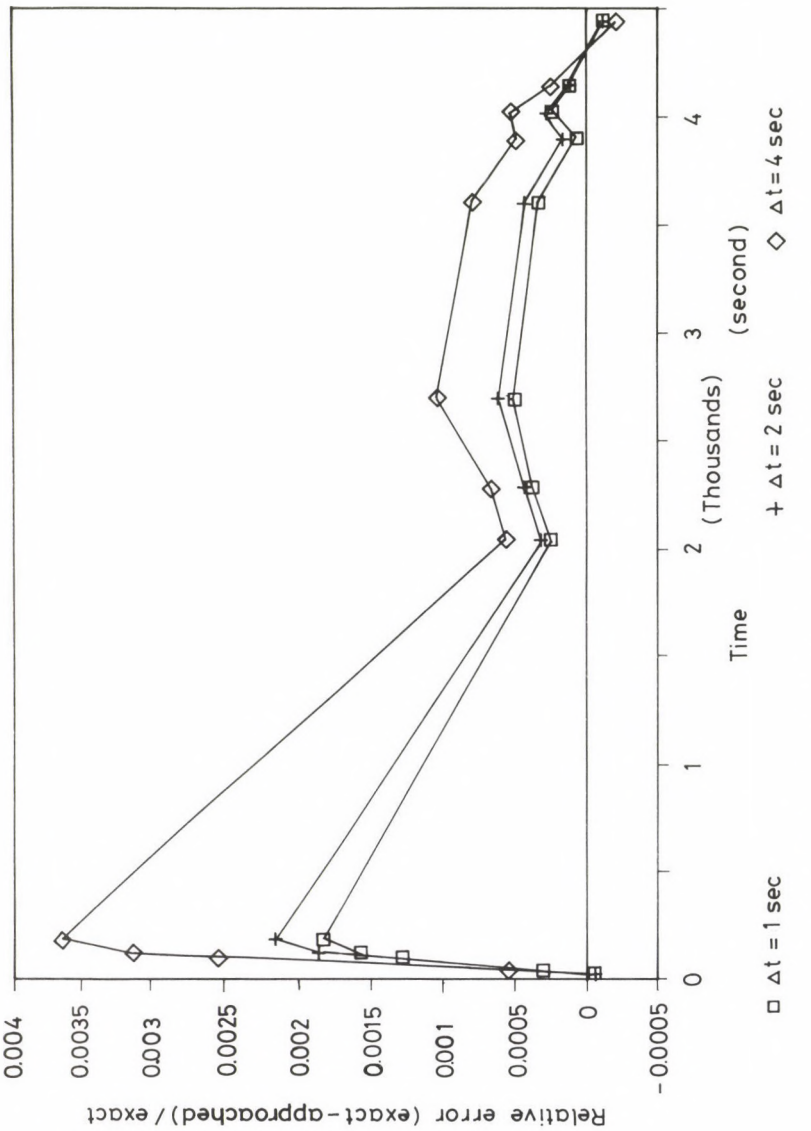

Fig. 6. Relative error of average temperature at different time steps

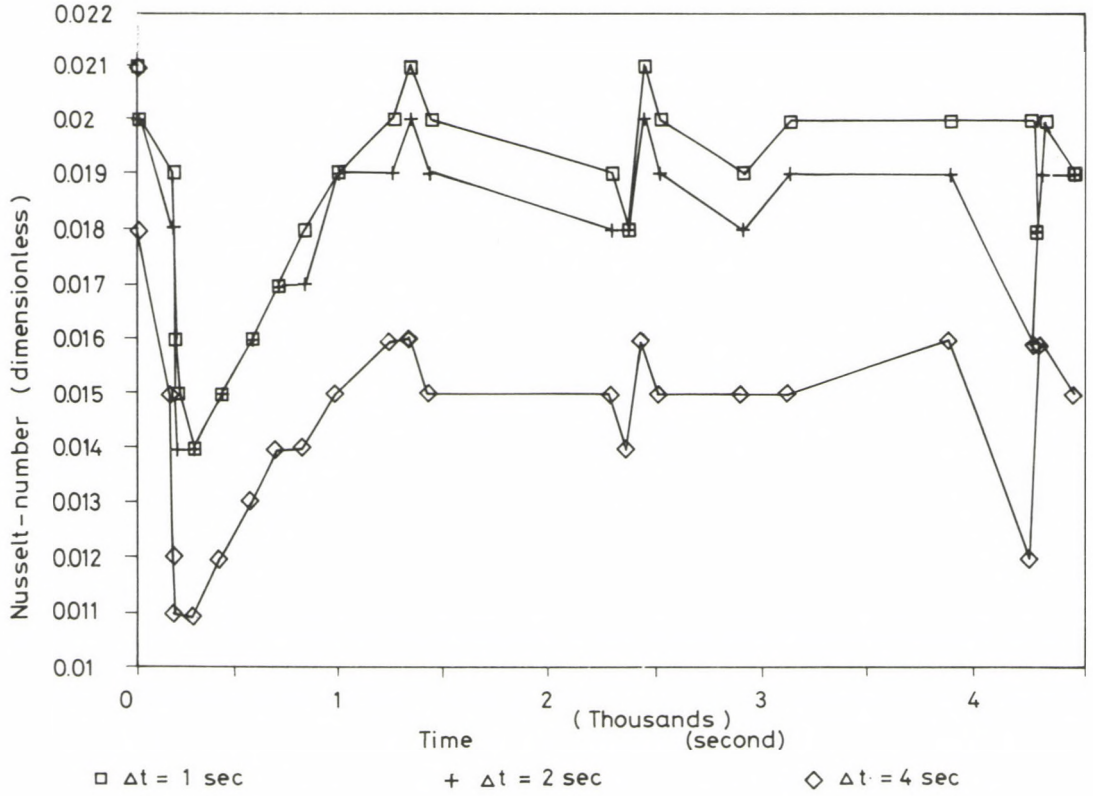

Fig. 7. Estimated Nusselt-number versus time at different time steps (exact value: 0.021)

Figure 3 shows the bulk temperature of the liquid phase versus time. The temperature records at the point of measurement can be seen in Figure 4. Time between two subsequent measurements: 1, 2 and 4 seconds. In practice, using interpolation techniques, this time can be even longer. In case of a very high noise level in the environment, spline smoothing can be used /12/.

The results of the numerical analysis are presented in Figs 5—7. The relative error in both surface and average temperature is practically negligible. However, the estimation of the Nusselt number was satisfactory only for $\Delta t = 1$ s.

6. Summary

Numerical procedure based on orthogonal collocation techniques has been proposed for solving inverse heat conduction problems. The main advantage of this method is the fast and robust recursive algorithm suited for on-line monitoring.

"Noisy" measurement can be smoothed by means of Bezier-splines and interpolation techniques provide smaller computation time step than that is used for measurements. In case of conjugated heat conduction problem, the heat transfer coefficient can be estimated on the basis of the measured bulk temperature of the liquid phase.

REFERENCES

1. Courant, R. - Hilbert, D.: Method of mathematical physics, I, New York Interscience Publishers (1953).
2. Borckel, D. - Graf, R.: "Ein numerisches, mathematisch - physikalisches Lösungsverfahren zur Bestimmung instationär Temperaturfelder zwecks Ermittlung von Temperaturdifferenzen mittels einer Messtelle", VGB Kraftwerkstechnik,9 (1984), 808—815.
3. Pesti, L. - Szabolcs, G.: "Stress Analysis of the boyler downcomer tubes and the pressurized pipebend of the Power Plant Pécs", (in Hungarian). Sci. Report of the Institute for Electrical Power Research, AHF 240, Budapest (1985).
4. Gilles, E.D.: Systeme mit verteilten Parametern, R. Oldenbourg Verlag, München (1973).
5. Weber, C.F.: "Analysis and Solution of the Ill-Posed Inverse Heat Conduction Problem", Int. J. of Heat and Mass Transf.24 (1981), 1783—1792.
6. Rosko, J.S.: Digital Simulation of Physical Systems, Addison-Wesley, London (1972).
7. Ray, W.H.: Advanced Process Control, McGraw-Hill, New York (1981).
8. Beck, J.V.: "Nonlinear Estimation Applied to the Nonlinear Inverse Heat Conduction Problem, Int. J. of Heat and Mass. Transf. 13 (1970), 703—716.

9. Alnajem, N.M. - Özisik, M.N.: "A direct analytic approach for solving two-dimensional linear inverse heat conduction problems" Wärme und Stoffübertragung, 20 (1986), 89—96.

10. Woelk, G.: "Verbesserung von Differenzenverfahren durch Teilgebietslösungen" Wärme- und Stoffübertragung 7 (1974), 208—214.

11. Finlayson, B.A.: Nonlinear Analysis in Chemical Engineering. McGraw-Hill, New York (1980).

12. Enns, S.: "Free-Form Curves on Your Micro", BYTE (1986), 225—230.

Acta Technica Acad.Sci.Hung., 101(3), pp. 339—344 (1988)

ECONOMIC GROWTH AS A FUNCTION OF CHANGES IN ENERGY INTENSITY AND PRODUCTION RESTRUCTURING*

SZERGÉNYI, I.**

(Received: 5 March, 1988)

Energetic development of the national economy should be co-ordinated with the development of energy consumption. A method for an improved co-ordination is suggested by the author, uses estimates based on international comparison, captures technical development and historical data of energy intensity for different industries. The suggested method can be better treated by the consumers than the conventional planning methods (global energy elasticity).

Comparisons on an international scale show that in Hungary, the energy consumption per unit GDP lies well above the same value in the industrialized countries. No need to say that a remedy to this disadvantageous situation would be desirable. A production restructuring is necessary as a result of which the rate of reduction of energy-intensity would be the same, or even higher, than in industrialized countries. Some considerations outlined below are designed to contribute to improvement of the situation, first of all in the field of industry.

In the ten-year period after the first oil crisis, the energy intensity reduced at an annual rate of 2.7% in Japan while 1.8% in West-Europe and an annual improvement of 2.5% was planned by EEC countries for the period until 1995.

In Hungary, the annual average growth rate fo 4.1% of GDP and 2.5% of total energy consumption in the period between 1970 and 1985 resulted in an annual reduction of 1.6% in energy intensity on the average over 15 years, a value lying below the rate of reduction of energy intensity in industrialized countries.

In case of an annual average growth rate of 1% of total energy consumption, a reduction of 1.6% in energy intensity would result in a growth rate of 2.5%/year of GDP in Hungary in the long run.

*This paper is based on the author's contribution to 13th World Energy Conference, Cannes, October 8, 1986

**Szergényi, I., Counsellor of the Central Planning Board, H—1051 Budapest, Roosevelt tér 7, Hungary

Akadémiai Kiadó, Budapest

At the same time, a significant improvement of the energy intensity offers theoretically a fair chance of increasing economic growth (e.g. 3.5% in case of a reduction of 2.5%/year in energy intensity) even in case the growth rate of energy consumption remains unchanged. In this sense, reduction in energy intensity is a factor affecting the range of economic growth.

Considering that production restructuring and changes in energy intensity are taking place simultaneously, a conscious utilization of reduction in energy intensity as a motive power in this joint process may theoretically speed up restructuring. Namely, reduced energy consumption resulting from a reasonably low energy intensity requires reduced energy investment and thus allocation of capital for more efficient production becomes possible. Of course, a realization of this theory in practice can be expected only if anybody contributing to production is interested in realization. The developments will then be investigated increasingly from this point of view while the most important informations, available for those responsible for national-scale energy planning through sectoral channels, can be included in the forecast. (Note that, hopefully, there comes a time when the efficiency of production will not be evaluated in sectoral 'pigeonholes'. A more differentiated approach is necessary for different reasons, among them because some sectors are rather inhomogeneous also in this respect. However, evaluation on a national economic scale will never be successful without a certain aggregation as otherwise one has to rely upon only sectoral energy-intensity analysis.)

Essentially, the energy consumption of the national economy is the sum of energy consumption of the productive and non-productive sectors including also losses resulting from energy conversion (relationship 1 in Fig. 1).

Considering that industry is the top energy consumer within the national economy, the effect of industrial development on the energy consumption of the national economy is investigated at present. Tabulated below are values indicating the share of industry, other producer sectors as well as the private and communal sector in the energy consumption of the national economy in the period between 1970 and 1985:

	Total energy consumption		Industry	Other producers	Private and communal sector
	PJ	%	%	%	%
1970	917	100	43	28	29
1985	1324	100	38	24	38

Reduction of the energy intensity on a national economic scale requires that also energy intensity in the industrial sector be improved. Required for this improvement is a sectoral restructuring or more precisely, restructuring within the different sectors by increase of the production of less energy-intensive products.

Relationship 2 and 3 describe the relation between industry and the different industrial sectors in respect of energy intensity and energy consumption, respectively. (Of course, the relationships apply also to the other producer sectors.) The values of energy intensity at different times can be correlated according to relationship 4. (No doubt, a more complicated equation system would certainly better describe the relation between the energy sector and other sectors in the long run. However, practical calculations require simple methods and the formulae presented here are a reasonable simplification.)

Table 1. Production restructuring in industry and growth in sectoral production in the period between 1970 and 1985

	1970		1985		Annual average growth rate of GDP
	$GDP^{*}(a)$	%	$GDP^{*}(a)$	%	%/year (r_a)
Total national economy	448.1	-	819	-	4.1
Total industry	128	100	238	100	4.2
Mining	45.9	35.8	42.4	17.9	-0.5
Electricity	4.8	3.8	11.3	4.8	5.9
Metallurgy	9.9	7.7	9.4	4.0	-0.3
Machine industry	31.7	24.8	86.3	36.3	6.9
Chemical industry	11.0	8.6	39.0	16.4	8.8
Light industry	22.5	17.6	43.3	18.2	4.5
Other industry	2.2	1.7	5.7	2.4	6.6
Other producers	141.4	-	246.8	-	3.8

*at invariable 1981 prices

The difference in growth rate of GDP between the sectors determines the sectoral structure (or restructuring) numerically. In the period between 1970 and 1985, the growth rate of all sectors except for mining and metallurgy exceeded the industrial average (4.2% per year) and the share of these sectors within industry increased (Table 1). The energy intensity of the sectors is either a priori low (light industry, machine industry) or reducing (chemical industry), or, possibly, both low and reducing (machine industry, see Table 2). Accordingly, the reduction of energy intensity of

Table 2. Energy consumption, energy intensity and annual average rate of change in energy intensity in the period between 1970 and 1985

	1970		1985		Annual average rate of change in energy intensity 1970-1985 (r_c)
	energy consumption PJ* (b)	energy intensity kJ(Ft/c)	energy consumption PJ*	energy intensity kJ(Ft/c)	%/year
Total energy consumption	916.9	2046	1323.9	1394	- 1.6
Total consumption of industry	394.9	3085	501.7	2113	- 2.5
Mining	38.8	845	42.1	993	+ 1.1
Electricity	4.6	958	6.9	611	- 3.0
Metallurgy	147.8	14929	157.4	16745	+ 0.8
Machine industry	50.8	1603	55.7	645	- 5.9
Chemical industry	108.3	9845	191.6	4913	- 4.5
Light industry	41.1	1827	45.6	1053	- 3.6
Other industry	3.5	1591	2.4	421	- 8.5
Other producers**	258.2	1826	318.2	1289	- 2.3
Private and communal consumers	263	-	504.0	-	-

*10^{15} J

**Food economy, building economy, communication, post, telecommunication

industry takes place at a more dynamic rate than the average reduction in the national economy. Nevertheless, industrial development without increase of energy consumption that is, a more dynamic reduction of energy intensity and thus a better adjustment of the national economy to the global trend prevailing in industrialized countries are desirable in the future.

How can this effort be expedited?

Most important relationships of the simplified method for calculation of energy demand per GDP

$$B = b_{ip} + b_{et} + b_{nt} = \sum_{i=1}^{n} b_i + b_{et} + b_{nt} \qquad (1)$$

where

b_{ip} energy consumption of industry on a national economic scale

b_i energy consumption of industrial sector i

b_{et} total productive energy consumption outside industry on a national economic scale

b_{nt} non-productive (private and communal) energy consumption

n number of industrial sectors

$$c_{ip} = \sum_{i=1}^{n} \frac{b_i}{\alpha i} \frac{a_i}{\alpha ip} = \sum_{i=1}^{n} c_i q_i \qquad (2)$$

where

c_{ip} energy intensity of industry

a_{ip} GDP by industry

a_i GDP by industrial sector i

c_i energy intensity of industrial sector i

q_i share of industrial sector i in GDP by industry

$$b_{ip} = \Sigma\, b_i = \Sigma\, a_i\, c_i \qquad (3)$$

$$c_t = c_0 \left(1 + \frac{r_c}{100}\right)^{*t} \qquad (4)$$

where

c_o energy intensity of the year taken as a basis for comparison

r_c annual rate of change in energy intensity

Relationships 1 thru 4 permit the lumped sectoral information on the sectoral units to be integrated on a national economic scale. Tables 1 and 2 show such a synthesis of data on the past.

The global rate of reduction of energy intensity diversified for the different sectors may be a useful information on integration of sectoral energy intensity and its change in time with that of the national economy.

Another, still more important, possibility offered by these relationships is that, based on data supplied by the sectoral units on planned increase of production and modernization of the structure of production including also reduction of energy intensity, calculations to estimate the future energy demand of the national economy can also be made (provided the scope of information supply is sufficiently wide and that missing information can be replaced with estimate). The more complete the information

---

*The relationship applies also to average growth rate of GDP and energy consumption (r_a and r_b, respectively) with a or b used in place of c in the formula.

supply by the sectoral units, the more reliable the energy forecast as compared with the present quality.

Integration is not a simple summing-up but also iterative work, a synthesis of national economic approach and professional knowledge. An iterative step can be carried out in the way described below:

— In planning for the national economy, a production development and energy-intensity-reduction programme shall be worked out first for the national economy as a whole and for the most important sectors, based on analysis of the past, macro-economic considerations and international comparison.

— The production and energy-intensity-reduction index numbers formulated on a sectoral scale shall be compared with, and checked up against, the professional concepts of the sectoral units.

— The energy demand of the national economy and of the different sectors can then be estimated on the basis of new corrected data including also comments of the sectoral units. This is the point where missing information shall be replaced with estimate. The effect of information supplied by enterprises included in the investigation on sectoral estimates of which the picture of industry as a whole can be set up shall be predicted. The first iterative cycle is thus completed.

New iteration will be necessary if the difference between the first and second estimate of the energy demand of the national economy is significant or the national economic requirement changes.

Reduction of the electricity intensity is of unique importance because the electricity sector is developing at a more dynamic rate as compared with the other energy sectors and thus also the investment demand of the electricity sector is higher. Here also, modernization of the structure of production is important since, as shown by international comparison, the electricity consumption per GDP in Hungary is significantly higher than in industrialized countries. Therefore, additional improvement of the rate of reduction of electricity intensity is necessary as compared with the rate of reduction over the recent period of 16 years.

It is easy to admit that a more reliable prediction of electricity consumption, a decisive factor in the growth of total energy demand, is possible when restructuring is taken into consideration as a mirror of the development objectives of sectoral units aware of the possibilities offered by technical development. The relationships 1 thru 4 can be used also in this work.

Acta Technica Acad.Sci.Hung., 101(3), pp. 345 (1988)

BOOK REVIEW

Retter, G.J.: Matrix and spacephasor theory of electrical machines. Akadémiai Kiadó, Budapest, 1987

The author's book is a summary of up-to-date theories of electrical machines designed, according to the author's intention, to couple the matrix method and the Park-vector method and to direct the English-speaking readers' attention to the Park-vector method as this method has come from the English domain of language but unfortunately, it is not used there.

The book consists of five parts, each part consisting of two chapters. The first part deals with the physics and steady-state operation of the machines and within this, with moment build-up and energy considerations.

Commutator transformation as basic transformation is discussed in the second part, presenting an introduction into the unified theory of electrical machines and describing the relationship between basic electrical machines and commutator transformation.

The system of the tree basic transformations is described in the third part, the first chapter dealing with phase and symmetrical component transformation while the second chapter with the 'a priori' derivation of basic transformations.

Discussed in the fourth part are the partial asymmetry and 'non-transformation' methods, including semisymmetrical and partially symmetrical machines as well as the partitioning method.

Part Five describes the use of three-phase vectors (or spacephasors), the first chapter discussing the method of three-phase vectors while the second chapter the application of this method.

Ample literature and examples of application are provided for each of the ten chapters of the five parts at the end of the different chapters.

Given in appendix are the harmonic analysis of some functions, the rules of Laplace transformation, transforms of some functions as well as the fundamental relationships of matrix algebra and analysis.

An additional chapter at the end of the book is devoted to solutions of applications examples. Like any successful technical-scientific work, the book offers ample illustration including about 230 figures.

More or less, the theory of electrical machines is a 'domestic science' in Hungary as said by the author: he refers to top scientists of this field from Jedlik to Benedikt in the past as well as to the present school in Hungary founded by K.P. Kovács and I. Rácz, University Professors, in asymmetric and transient states of a.c. engines. G. Kron, also Hungarian, was the first to use the matrix method or tensor method widely used in the domain of English language. This method is coupled by the author with the spacephasor method developed by K.P. Kovács and I. Rácz.

Professor Retter ranges among the most productive authors of the Hungarian scientific-technical literature. His present work is a synthesis of educational experiences collected over many years. What is new in the book are the efforts to present the reasonable applications of both methods selectively and, on the other hand, the synthesis that is application of both methods in combination. The book is outstanding in that it offers an useful and, although sometimes sophisticated but enjoyable reading for both university students and engineers engaged in research and practical work.

K. Karsai

Akadémiai Kiadó, Budapest

PRINTED IN HUNGARY
Akadémiai Kiadó és Nyomda Vállalat, Budapest

NOTICE TO CONTRIBUTORS

Papers in English* are accepted on condition that they have not been previously published or accepted for publication.

Manuscripts in two copies (the original type-written copy plus a clear duplicate one) complete with figures, tables, and references should be sent to

Acta Technica
Münnich F. u. 7. I. 111 A
Budapest, Hungary
H-1051

Although every effort will be made to guard against loss, it is advised that authors retain copies of all material which they submit. The editorial board reserves the right to make editorial changes.

Manuscripts should be typed double-spaced on one side of good quality paper with proper margins and bear the title of the paper and the name(s) of the author(s). The full postal address(es) of the author(s) should be given in a footnote on the first page. An abstract of 50 to 100 words should precede the text of the paper. The approximate locations of the tables and figures should be indicated on the margin. An additional copy of the abstract is needed. Russian words and names should be transliterated into English.

References. Only papers closely related to the author's work should be referred to. The citations should include the name of the author and/or the reference number in brackets. A list of numbered references should follow the end of the manuscript.

References to periodicals should mention: (1) name(s) and initials of the authors(s); (2) title of the paper; (3) name of the periodical; (4) volume; (5) year of publication in parentheses; (6) numbers of the first and last pages. Thus: 5. Winokur, A., Gluck, J.: Ultimate strength analysis of coupled shear walls. American Concrete Institute Journal 65 (1968), 1029–1035.

References to books should include: (1) author(s) name; (2) title; (3) publisher; (4) place and year of publication. Thus: Timoshenko, S., Gere, J.: Theory of Elastic Stability. McGraw-Hill Company, New York, London 1961.

Illustrations should be selected carefully and only up to the necessary quantity. Black-and-white photographs should be in the form of glossy prints. The author's name and the title of the paper together with the serial number of the figure should be written on the back of each print. Legends should be brief and attached on a separate sheet. Tables, each bearing a title, should be self-explanatory and numbered consecutively.

Authors will receive proofs which must be sent back by return mail.

Authors will receive 50 reprints free of charge.

*Hungarian authors can submit their papers also in Hungarian.

Periodicals of the Hungarian Academy of Sciences are obtainable at the following addresses:

AUSTRALIA
C.B.D. LIBRARY AND SUBSCRIPTION SERVICE
Box 4886, G.P.O., *Sydney N.S.W. 2001*
COSMOS BOOKSHOP, 145 Ackland Street
St. Kilda (Melbourne), Victoria 3182

AUSTRIA
GLOBUS, Höchstädtplatz 3, *1206 Wien XX*

BELGIUM
OFFICE INTERNATIONAL DES PERIODIQUES
Avenue Louise, 485, *1050 Bruxelles*
E. STORY-SCIENTIA P.V.B.A.
P. van Duyseplein 8, *9000 Gent*

BULGARIA
HEMUS, Bulvar Ruszki 6, *Sofia*

CANADA
PANNONIA BOOKS, P.O. Box 1017
Postal Station "B", *Toronto, Ont. M5T 2T8*

CHINA
CNPICOR, Periodical Department, P.O. Box 50
Peking

CZECHOSLOVAKIA
MAD'ARSKA KULTURA, Národni třida 22
115 66 Praha
PNS DOVOZ TISKU, Vinohradská 46, *Praha 2*
PNS DOVOZ TLAČE, *Bratislava 2*

DENMARK
EJNAR MUNKSGAARD, 35, Nørre Søgade
1370 Copenhagen K

FEDERAL REPUBLIC OF GERMANY
KUNST UND WISSEN ERICH BIEBER
Postfach 46, *7000 Stuttgart 1*

FINLAND
AKATEEMINEN KIRJAKAUPPA, P.O. Box 128
00101 Helsinki 10

FRANCE
DAWSON-FRANCE S.A., B.P. 40, *91121 Palaiseau*
OFFICE INTERNATIONAL DE DOCUMENTATION ET LIBRAIRIE, 48 rue Gay-Lussac
75240 Paris, Cedex 05

GERMAN DEMOCRATIC REPUBLIC
HAUS DER UNGARISCHEN KULTUR
Karl Liebknecht-Straße 9, *DDR-102 Berlin*

GREAT BRITAIN
BLACKWELL'S PERIODICALS DIVISION
Hythe Bridge Street, *Oxford OX1 2ET*
BUMPUS, HALDANE AND MAXWELL LTD.
Cowper Works, *Olney, Bucks MK46 4BN*
COLLET'S HOLDINGS LTD., Denington Estate,
Wellingborough, Northants NN8 2QT
WM DAWSON AND SONS LTD., Cannon House
Folkstone, Kent CT19 5EE
H. K. LEWIS AND CO., 136 Gower Street
London WC1E 6BS

GREECE
KOSTARAKIS BROTHERS INTERNATIONAL BOOKSELLERS, 2 Hippokratous Street, *Athens-143*

HOLLAND
FAXON EUROPE, P.O. Box 167
1000 AD Amsterdam
MARTINUS NIJHOFF B. V.
Lange Voorhout 9–11, *Den Haag*
SWETS SUBSCRIPTION SERVICE
P.O. Box 830, 2160 Sz Lisse

INDIA
ALLIED PUBLISHING PVT. LTD.
750 Mount Road, *Madras 600002*
CENTRAL NEWS AGENCY PVT. LTD.
Connaught Circus, *New Delhi 110001*
INTERNATIONAL BOOK HOUSE PVT. LTD.
Madame Cama Road, *Bombay 400039*

ITALY
D. E. A., Via Lima 28, *00198 Roma*
INTERSCIENTIA, Via Mazzé 28, *10149 Torino*
LIBRERIA COMMISSIONARIA SANSONI
Via Lamarmora 45, *50121 Firenze*
SANTO VANASIA, Via M. Macchi 58
20124 Milano

JAPAN
KINOKUNIYA COMPANY LTD.
Journal Department, P.O. Box 55
Chitose, *Tokyo 156*
MARUZEN COMPANY LTD., Book Department
P.O. Box 5050 Tokyo International, *Tokyo 100-31*
NAUKA LTD., Import Department
2-30-19 Minami Ikebukuro, Toshima-ku, *Tokyo 171*

KOREA
CHULPANMUL, *Phenjan*

NORWAY
TANUM-TIDSKRIFT-SENTRALEN A.S.
Karl Johansgata 43, *1000 Oslo*

POLAND
WĘGIERSKI INSTYTUT KULTURY
Marszałkowska 80, *00-517 Warszawa*
CKP I W, ul. Towarowa 28, *00-958 Warszawa*

ROUMANIA
D. E. P., *Bucuresti*
ILEXIM, Calea Grivitei 64–66, *Bucuresti*

SOVIET UNION
SOYUZPECHAT — IMPORT, *Moscow*
and the post offices in each town
MEZHDUNARODNAYA KNIGA, *Moscow G-200*

SPAIN
DIAZ DE SANTOS Lagasca 95, *Madrid 6*

SWEDEN
ESSELTE TIDSKRIFTSCENTRALEN
Box 62, *101 20 Stockholm*

SWITZERLAND
KARGER LIBRI AG, Petersgraben 31, *4011 Basel*

USA
EBSCO SUBSCRIPTION SERVICES
P.O. Box 1943, *Birmingham, Alabama 35201*
F. W. FAXON COMPANY, INC.
15 Southwest Park, *Westwood Mass. 02090*
MAJOR SCIENTIFIC SUBSCRIPTIONS
1851 Diplomat, P.O. Box 819074,
Pallas, Tx. 75381-9074
READ-MORE PUBLICATIONS, INC.
140 Cedar Street, *New York, N. Y. 10006*

YUGOSLAVIA
JUGOSLOVENSKA KNJIGA, Terazije 27, *Beograd*
FORUM, Vojvode Mišića 1, *21000 Novi Sad*

HU ISSN 0001-7035

Index: 26.025

ACTA TECHNICA

ACADEMIAE SCIENTIARUM HUNGARICAE

EDITOR-IN-CHIEF: P. MICHELBERGER

VOLUME 101
NUMBER 4

MECHANICAL ENGINEERING — M/1

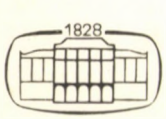

AKADÉMIAI KIADÓ, BUDAPEST 1988

ACTA TECHNICA

A JOURNAL OF THE HUNGARIAN ACADEMY OF SCIENCES

Acta Technica publishes original papers, preliminary reports and reviews in English, which contribute to the advancement of engineering sciences.
Acta Technica is published by

AKADÉMIAI KIADÓ
Publishing House of the Hungarian Academy of Sciences
H-1450 Budapest, Alkotmány u. 21.

Subscription information

Orders should be addressed to

KULTURA Foreign Trading Company
H-1389 Budapest P.O. Box 149

or to its representatives abroad

Acta Technica is abstracted/indexed in Applied Mechanics Reviews, Current Contents–Engineering, Technology and Applied Sciences, GeoRef Information System, Science Abstracts.

CONTENTS

Gausz, T. - Czédli, Gy.: Examination of flow developing in supersonic diffusers 347

Tatár, I.: Chordal thickness and span measurement of helical gears 361

Tatár, I.: Chordal thickness and span measurement of conjugate surfaces 379

Váradi, K. - Poller, R.: Analysis of gear teeth contact by the finite element method 397

Yosry, W. - Balogh, I. - Molnár, F.: Experimental study of wear of slip differential units 419

Acta Technica Acad.Sci.Hung., 101(4), pp. 347–360 (1988)

EXAMINATION OF THE FLOW DEVELOPING IN SUPERSONIC DIFFUSERS

GAUSZ, T.* - CZÉDLI, G.**

(Received: 2 October 1987)

In this paper, the possibility of a numerical solution to Euler's equation transformed to a two-dimensional, rectangular domain is examined. The approximate solution is sought with the use of the finite difference method. In the calculations, the so-called "smearing" technique is applied.

As an example, the velocity- and pressure-distributions developing in supersonic diffusers are examined with the help of this procedure.

It should be noted that the calculation procedure introduced in this paper should be developed further in several points.

Introduction

In everyday practice it is widespread that the tubular profiles and fitting-parts of pipe-lines of continuously increasing cross-section, i.e. diverging into the direction of flow are called diffusers. However, this technical term can be considered correct only up to the point where the so-called Mach-number characterizing the flow velocity of the compressible fluid remains under 1 (here incompressible fluids are not dealt with because in engineering practice the flow velocity of fluids is lower by an order of magnitude in every case than the propagation velocity of the sound in the given fluid). For the case of the steady-state flow of non-viscous (ideal) gases flowing within an adiabatic nozzle, the following relationship can be written:

$$\frac{dA}{A} = (M^2 - 1)\frac{dc}{c}$$

where:

A is the cross-section of the nozzle at a certain place

dA is the variation in the cross-section of the nozzle in the direc-

*Gausz, Tamás, H-1111 Budapest, Budafoki u. 9, Hungary

**Czédli, György, H-1332 Budapest, Kresz Géza u. 16, Hungary

Akadémiai Kiadó, Budapest

c is the velocity of the fluid flowing through a certain cross-section

dc is the variation in the velocity of the flowing fluid

M is Mach-number calculated across a given cross-section

From the above equation it can be seen that in case $M > 1$, a positive dA belongs to a positive dc, i.e. in the case of the so-called supersonic flows having a velocity exceeding that of the sound, velocity c of the fluid will increase provided that cross-section A increases simultaneously. Consequently, a device serving for the decrease in velocity of a fluid flowing at a subsonic velocity will increase the supersonic flow, i.e. a subsonic diffuser will turn into a supersonic confuser with the geometric conditions unchanged. The way of decelerating the supersonic flows, too, can be concluded from the equation: in case $M > 1$, a negative dA belongs to a negative dc, i.e. in a converging nozzle the flow velocity of the supersonic fluid decreases.

Those said above are valid also for the flow of real (viscous) fluids. The best example of it is the Laval (jet) nozzle, in which the fluid is accelerated first in a converging section up to the sound velocity limit, and then a further increase in the velocity is achieved by applying a diverging nozzle. In short, supersonic diffusers are called the converging devices applied in flow technique for the deceleration of flows having a velocity higher than that of the sound. The intention of using those devices generally is to decelerate the fluid down to subsonic velocity with the simultaneous possible highest pressure-rise. As it will be seen, such a requirement can be satisfied only at the expense of much difficulty.

1. Classical methods

The deceleration of supersonic flows is practically feasible in the simplest way since any kind of disturbation (e.g. a central cone, or wire grid) gives rise to shock waves decreasing the velocity and increasing the pressure of the fluid passing through them.

In straight-line pipe-lines within which a real (viscous) fluid is flowing at a supersonic velocity, the friction itself (together with the swollen boundary layer) represents the disturbation leading in each case to the so-called normal shock waves, and passing through them the flow is always decelerated to subsonic velocity. However, this passage through the normal shock wave involves an enormous increase in entropy, and as a result

of this, the efficiency of the so-called dynamic compression will be small, and the available terminal (final) pressure will be low – in contrast to the task envisaged.

Good result can be achieved only if more oblique shock waves of low intensity are excited, and then the fluid decelerated in this way to the vicinity of the sound velocity limit is further decelerated by a normal shock wave now of low intensity down to subsonic velocity. The diffusers used today follow this principle without exception. In the course of investigations, the best solution available theoretically set as an aim is the deceleration by means of an infinite series of elementary oblique (Mach) waves (isentropic nozzles are called the diffusers made with the purpose of carrying out this kind of deceleration).

Researchers are in charge of finding a geometric form (diffuser-contour) corresponding to the given supersonic parameters (Mach-number, mass-flow, temperature etc.) and the required subsonic velocity which can ensure the highest pressure-rise. However, this problem has not been solved so far despite of applying the most up-to-date computers, and the developments are mainly based upon experimental results, which are considerably more expensive as compared with the use of computer-aided methods.

But nowadays the solution of the inverse problem is facilitated by computer-aided methods: in the case of applying a given geometric configuration by way of a diffuser, what output subsonic parameters are determined by a group of input supersonic parameters, and what the available pressure-rise will be.

The classical methods have been worked out in detail during this century. Due to the relative simplicity of equations describing the laws of one-dimensional flows, it has become feasible to deal with the effect of normal shock waves by applying simple methods and graphic representation. Such methods have been developed for the case of two-dimensional flows, as well, assuming frictionless flow of fluids. By using these methods, the calculation of oblique shock waves excited by the edge of an infinite wedge, and the graphic representation of their parameters, i.e. shock-polar curve (strophoid curve) are rendered possible. However, the system of shock waves excited in the course of two-dimensional flows deviates basically from that developing, e.g. around a body of rotational symmetry (e.g. a cone). When a wedge of an angle of 20° is put into a flow of $M = 1.5$, then a so-called detached shock wave will be produced but when a cone of an angle of 20° is put into a flow of the same kind, then a regular, attached conical shock

wave will be generated whose axis is parallel with that of the cone, and whose constituent is generated starting from the peak of the cone, i.e. the two systems of shock waves are decisively differing from each other not only in their structure, though the planar representation (section) of the wedge and cone, respectively, were identical in our example. Consequently, the methods elaborated for the so-called two-dimensional (planar) flows, e.g. the hodograph-method, or the method of characteristics applicable well for the solution of problems in isentropic two-dimensional flows can not be applied to the case of the three-dimensional supersonic flows, or else their applications represents a good approximation even in favourable cases.

The solution is provided by applying numerical methods. The fundamental equations describing the flow of the fluid (energy-equations, momental equations and certain equations of state) are not transformed by means of different assumptions reducing at the same time the scope of application, instead, they are applied in a general sense without any restriction. Naturally, this method involves a great deal of calculations due to which it can be applied only with the aid of computers – if there is a computer of sufficiently quick operation and properly great capacity of storage available.

2. Mathematical model describing the flow

The fluid entering the diffuser is decelerated from supersonic velocity into a subsonic one. In the course of deceleration, an intensive shock wave is generated simultaneously whose intensity is dependent upon the lay-out of the diffuser. The flow characteristics of the intensive shock wave undergo an abrupt change, and they can be reckoned with properly by taking into consideration the principle of conservation (continuity of material, momental – Euler's equations, energy).

There are several forms of the principle of conservation known. In the flows of this kind, the most favourable application of it is its so-called "conservative" form /1, 2/.

In our examinations, the fluid is assumed to be frictionless. With respect to the cylinder-symmetry of the diffuser, from among the principles of conservation, the conservation of mass and the momentum can be written in the following concise form – with the variation in polar angle considered as zero in the cylindrical co-ordinate system:

$$\frac{\partial \underline{f}}{\partial t} + \frac{\partial \underline{F}}{\partial x} + \frac{\partial \underline{G}}{\partial r} + \underline{H} = 0 \qquad (2.1)$$

where:

$$\underline{f} = \begin{bmatrix} \varrho \\ \varrho u \\ \varrho v \end{bmatrix} \qquad \underline{F} = \begin{bmatrix} \varrho u \\ \varrho u^2 + p \\ \varrho uv \end{bmatrix}$$

$$\underline{G} = \begin{bmatrix} \varrho v \\ \varrho uv \\ \varrho v^2 + p \end{bmatrix} \qquad \underline{H} = \begin{bmatrix} \varrho v/r \\ \varrho uv/r \\ \varrho u^2/r \end{bmatrix}$$

Here: ϱ – the density of fluid

u – is the axial velocity component

v – is the radial velocity component

p – is the pressure

r – is the radial co-ordinate

x – is the axial co-ordinate

It should be noted that equation (2.1) differs from the classical equations plotted in the system if right-angled co-ordinates only in "H", and the interpretation of the co-ordinates and velocities, respectively.

Equation of energy is written in the following form according to the simpler method adopted in technical literature:

$$e = \frac{u^2 + v^2}{2} + \frac{\varkappa p}{\varrho(\varkappa - 1)} = \text{constant.} \qquad (2.2)$$

In this equation it is expressed, on the one hand, that the total energy of the flowing fluid is constant in each point examined, and on the other hand, that no energy is imparted by the surroundings, i.e. the flow is adiabatic.

With the help of the cylindrical co-ordinate system, the problem has been reduced to a two-dimensional one. The examined domain is the plane section of the diffuser, or more precisely, only half of it since the flow is symmetrical with respect to the centre-line. This is, of course, an enormous advantage, and in addition, the cylindrical co-ordinate system (similar to that of right-angled co-ordinates) is an orthogonal one, too.

Although this domain is not sufficiently simple any more but according to the computing-technique methods, additional transformation will

be applied. With the help of this, the original domain (Fig. 1/a) is mapped into a rectangle (Fig. 1/b):

$$x = x \ ,$$

$$y = m(r - r_a) \ ,$$

where:

$$m = \frac{1}{r_f - r_a} \ .$$

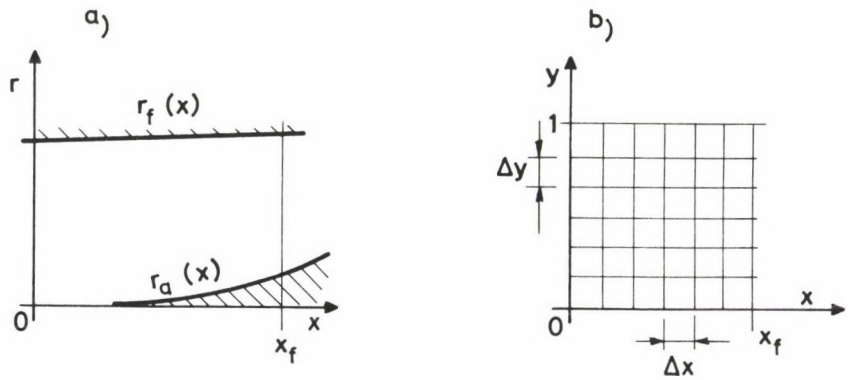

Fig. 1.

The rectangular domain can be covered by a uniform grid, and the calculation of the boundary conditions is much simpler, as well, than in the case of a more irregular domain since in the case of curved boundary-lines, the grid-points do not generally fit onto the boundary-line, and as a consequence, when the boundary conditions are taken into consideration, either interpolation is required /2/ (presuming the existence of grid-points beyond the domain), or a so-called distorted distribution should be applied, i.e. in the point last but one towards the boundary the step-intervals (distances between grid-points) should be chosen in a way that the last grid-point be simultaneously a boundary point.

Both possibilities involve considerable difficulty in calculations; it is also a hard problem to insert particular procedures (subroutines) serving for the purpose mentioned above into the computing routine. Due to this, both the time required for the elaboration of the program, and the transit time will be increased as compared to the application of transformation leading to Fig. 1/b.

In fact, one of the main advantages of finite-element method also lies in the fact that the calculation for the single elements is carried

out in a local-co-ordinate system, and only the final summarization is calculated – after a proper transformation, or inverse transformation, respectively, – within the original, global co-ordinate system.

The inverse of transformation can be written simply like this:

$$x = x$$

$$r = \frac{y}{m} + r$$

The function-determinant of transformation can be calculated in a simple way, as well:

$$J = \frac{\partial(x,y)}{\partial(x,r)} = \begin{vmatrix} 1 & 0 \\ a & m \end{vmatrix} = m$$

where: (2.3)

$$a = a(x,y) = \frac{\partial}{\partial x}\left(\frac{y}{m} + r_a\right)$$

It should be noted here that the value of J can never be zero in practice (it would require $r_f \longrightarrow \infty$), neither can it be infinite (it would require $r_f = r_a$). Due to this, the mapping is a bijection, i.e. it covers all the examined points, and it is mutually unequivocal.

The domain of Fig. 1/b is also called the domain of calculation, and the transformed quantities of the velocities are:

$$U = x_x u + x_r v = u$$

$$V = y_x u + y_r v = au + mv$$

Naturally, (2.1) should also be transformed, paying attention to the fact that the new (x,y) co-ordinate system is not an orthogonal one. The transformed set of differential equations will be:

$$\frac{\partial \underline{\tilde{f}}}{\partial t} + \frac{\partial \underline{\tilde{F}}}{\partial x} + \frac{\partial \underline{\tilde{G}}}{\partial y} + \underline{\tilde{H}} = 0 \qquad (2.4)$$

where:

$$\underline{\tilde{f}} = \frac{1}{J}\underline{f} = \frac{1}{m}\underline{f}\ ;$$

$$\underline{\tilde{F}} = \frac{1}{J}\left(\underline{f}U + p - \begin{bmatrix} 0 \\ x_x \\ x_r \end{bmatrix}\right) = \frac{1}{m}\begin{bmatrix} \varrho \\ \varrho u^2 + p \\ \varrho uv \end{bmatrix} = \frac{1}{m}\underline{F}$$

$$\underline{\tilde{G}} = \frac{1}{J}\left(\underline{f}V + p\begin{bmatrix} 0 \\ y_x \\ y_r \end{bmatrix}\right) = \frac{1}{m}\begin{bmatrix} \varrho(au+mv) \\ \varrho u(au+mv) + ap \\ \varrho v(au+mv) + mp \end{bmatrix}$$

$$\underline{\tilde{H}} = \frac{1}{J}\underline{H} = \frac{1}{m}\underline{H} \quad .$$

Quantities "a" and "m" can be determined with the knowledge of geometric conditions. Further on, the calculation will be carried out within domain according to Fig. 1/b but using quantities more familiar for us physically (ϱ, u, v, p).

This essentially means that the values of the physical variables are stored in the grid-points by the computer, and when it is required, the transformed quantities are calculated with the knowledge of those, as well as quantities "a" and "m".

Similarly, the values of the physical variables are taken into consideration even with the boundary conditions since our fundamental statements (e.g. constancy of energy, the velocity component perpendicular to the wall is zero etc.) are related to those conditions.

The steady-state solution is to be found as the asymptotic solution of the non-steady state model. Let it be assumed that the flow is fully known at a fixed point of time. Now the flow pattern is to be found developing in a certain sufficiently short time-interval. This can be calculated with the help of the following two-step difference-scheme:

$$\begin{aligned} \underline{\tilde{U}}^{n+1}_{j,k} = \frac{1}{4}\left(\underline{\tilde{U}}^{n}_{j+1,k} + \underline{\tilde{U}}^{n}_{j-1,k} + \underline{\tilde{U}}^{n}_{j,k+1} + \underline{\tilde{U}}^{n}_{j,k-1}\right) \\ - \Delta t\left(\frac{\underline{\tilde{F}}^{n}_{j+1,k} - \underline{\tilde{F}}^{n}_{j-1,k}}{2\Delta x} + \frac{\underline{\tilde{G}}^{n}_{j,k+1} - \underline{\tilde{G}}^{n}_{j,k-1}}{2\Delta y}\right) \\ + \frac{\Delta t}{4}\left(\underline{\tilde{H}}^{n}_{j+1,k} + \underline{\tilde{H}}^{n}_{j-1,k} + \underline{\tilde{H}}^{n}_{j,k+1} + \underline{\tilde{H}}^{n}_{j,k-1}\right) \end{aligned} \qquad (2.5)$$

$$\tilde{U}^{n+2}_{j,k} = \tilde{U}^{n}_{j,k} - \Delta t \left(\frac{\tilde{F}^{n+1}_{j+1,k} - \tilde{F}^{n+1}_{j-1,k}}{\Delta x} + \frac{\tilde{G}^{n+1}_{j,k+1} - \tilde{G}^{n+1}_{j,k-1}}{\Delta y} \right) + 2\,\Delta t\, \tilde{H}^{n+1}_{j,k}$$

It should be noted that to achieve the stability of the scheme, it is generally not sufficient to satisfy the Courant-Friedrichs-Leny (CFL) criterion but in addition to it, a further completion (e.g. artificial viscosity) will be also necessary /1/.

With difference equation (2.5) examined thoroughly, the quaternion of values (ϱ, u, v, p) of the internal grid-point can be calculated for a subsequent moment of time $t_0 + 2\Delta t$ from values (ϱ, u, v, p) known for each grid-point (on the boundary, too) at some moment of time t_0.

The calculation on the boundary points requires special attention despite the uniform scheme. The energy need not any attention or treatment because it is identical, constant in each point and at any moment of time.

On the entry line, the calculation of the velocity and pressure is very simple, as well since those are constant quantities. This is the physical basis of the asymptotic solution. This is the constant ensuring convergence, at least in principle, of the variable interpreted in other points towards the asymptotic solution.

The triad (u, v, p) is unknown on the lower and upper boundaries, respectively. But with the knowledge of one of them (e.g. v), the other two ones can be calculated — u can be calculated from the condition of the resultant velocity parallel with the wall, and p from the equation of energy.

If either of the three could be assumed as continuous, then with the knowledge of the internal points, any of them could be extrapolated onto the outer boundary, and could be interpolated onto the inner one. However, this condition can not be fulfilled.

There is a technique applicable to the solution when the shock wave is captured (capturing). In this case, the interpolation or extrapolation does not involve any difficulty if the place of discontinuity is known — since, as it is known, the velocity component parallel with the shock wave undergoes no change within the shock wave.

In this case, another technique adopted as the so-called "smearing" was chosen. Here the shock wave is modified by means of aritificial viscosity so that the flow characteristics should be changing along a longer section, i.e. there should no abrupt discontinuity take place.

After all, if v is interpolated or extrapolated on the lower or upper

boundary, respectively, on the basis of smearing, no major fault is committed. There is an ad nal point of view that due to $v < u$, the change of v becomes smaller, too. With the knowledge of v-s on the boundary points, u and p can be calculated.

It remains to examine the boundary-line of co-ordinate x_f corresponding to the exit cross-section. Here, it should be taken into consideration that the exact direction of the flow is unknown, therefore both velocity components should be extrapolated. However, according to the recommendation of technical literature, the extrapolation can be rendered more accurate with the consideration of the constant mass flow since the requirement is that exactly as much fluid should leave the flow as has entered it. With the knowledge of the exit surface and the mass flow, the absolute value of exit velocities should be modified accordingly.

Hereby, the numerical method is completed, and practical calculations are enabled.

3. Practical utilization

The mathematical model introduced above was applied in the course of project-work connected with the development of supersonic diffusers. Utilizing the cylinder-symmetry, the equations should be solved within the domain assigned by the contour of the diffuser. The domain was divided into equal distances in the direction of longitudinal axis x, and radius r, according to Fig. 2. In the course of solution, the flow characteristics (velocities, pressure, temperature and density) are calcualted in each grid-point. However, the boundary conditions involve difficulty in the course of solution, since the usage of the difference-scheme requires the knowledge of characteristics in the adjacent grid-points.

The boundary conditions are not complete because the specified values of the density and pressure are lacking on the boundary, i.e. the contour. However, the boundary provides a relationship between the axial and radial velocity components: the resultant velocity can not have a velocity component normal to the contour, i.e. if the contour is a straight line subtending an angle α with longitudinal axis x (which is the longitudinal section of a cone having a straight constituent), then velocity components v_x of axial, and v_r of radial direction should satisfy condition

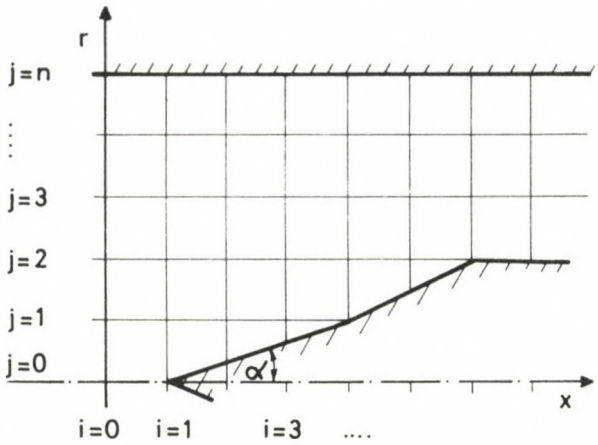

Fig. 2.

$v_r = v_x \cdot tg\alpha$. This condition can be used also in the case of contours of continuous curvature considered as a broken line (e.g. in the course of examination of isentropic nozzles).

An example of the shock wave defined by the mathematical model is shown in Fig. 3. In the figure, the shock wave having its origin in the peak of the cone can be identified on the basis of variation in radial velocities. The half-cone angle and the intensity of the shock-wave cone exhibit a good agreement with the result obtainable by means of analytical solution (because the first shock-wave cone can be defined also analytically with the help of relatively simple devices while the other ones can not be defined any more). The entry (initial) parameters are plotted in the Figure, the flowing fluid is an overheated water vapour. The shock wave is traced in dashed line. The Figure is based upon the results of the steady-state model as obtained in 327 steps. In the Figure, the effects of artificial viscosity used for ensuring the stability can be displaced well:

- in cross-section 1, the radial velocities are still of zero value outside the shock wave according to the realty but in the other cross-sections (lying behind with respect to flow), the radial velocity is not of zero value any more outside the shock wave due to the moment-transport inserted into the computational procedure by artificial viscosity,
- when moving away from the wall, the intensity of the shock wave is decreasing in accordance with the linear increase in artificial

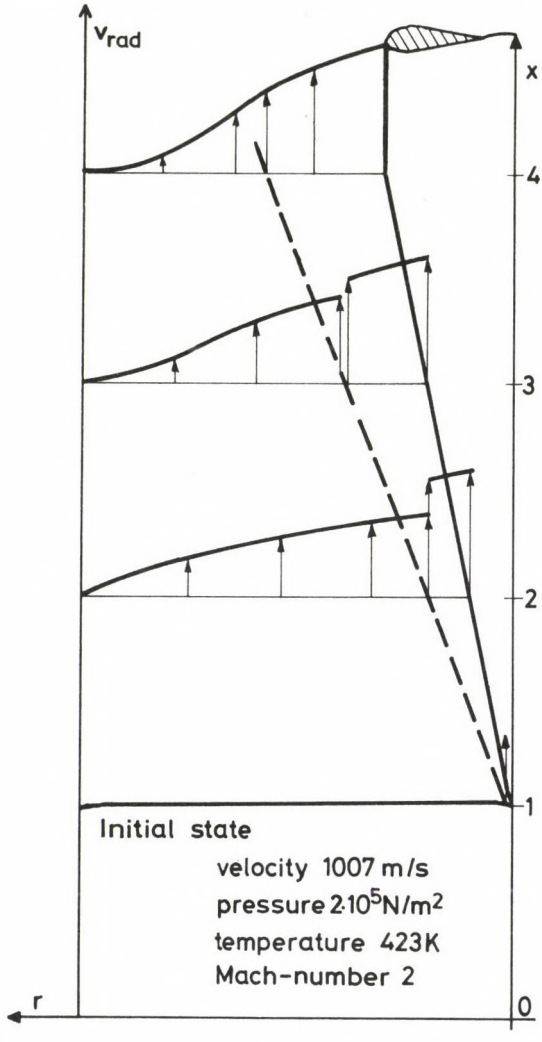

Fig. 3.

viscosity. Hence the denomination: "smearing" of the shock wave has been given to this procedure.

Obviously, the mathematical model can be treated only with the aid of computers. On the basis of our experience so far, the following points should be observed in the course of selecting the proper kind of computers:

- it should have a sufficiently great capacity of storage,
- aerodynamic investigations were characterized by some hundreds of

unknown in 1950-ies; the number of the unknown had run up to a hundred thousands by 80-ies in the leading research centres of the world – naturally, in the case of computer-aided background work. In our country, the desk-type computers are the most widespread. A computer of type Commodore C64 can ensure the reception of about 4.000 unknowns; in case of a planar problem, this means about 60x60 grids while in case of a spatial problem only a grid of dimension 15x15x15 can be envisaged – therefore it is useful to transform the problem into one to be solved within a co-ordinate system of cylinder-symmetry. The great capacity of the storage equipment has a very important influence upon the application of models using real (viscous) fluids where, for the sake of stability, the so-called mesh-Reynold's-number should be kept on a low value, and to this end, the grid-points should be spaced out close to each other, which – in turn – requires a large storage capacity.

According to our examinations, the capacity of storage equipment in a computer C64 does not enable the application of a sufficiently dense grid, and the too loose grid-spacing endangers the convergence of the solution in the case of certain contour-shapes, or initial parameters, respectively,

- the operational speed of the machine should be sufficiently high. To determine the very simple partial result shown in Fig. 3, about five hours are required in the case of a program of a machine code run in a C64, while in the case of more complex problems, the desk-type computers have proved to be very slow,
- the number representation of the computer should enable the application of arithmetic of high precision. One of the important conditions of numerical stability is represented by the computational error due to the quotients of the differences between large numbers. To examine the supersonic flows within diffusers, a number-representation computer of 32 bites is required being able to compute with arithmetic of double precision. Such requirements are generally not met by machines of category HC.

The observation of the above points is important also for the reason because if our procedure of great operational demand is to be "conformed" to the available machine of small storage capacity and low speed of operation, introducing at the same time simplifications and loose spacing out of

grids, then the solution will lose its stability, and can not provide appreciable results.

Summarization

It can be stated that due to the development of computing-technique devices, nowadays new vistas open up as far as the numerical examination of the most complex aerodynamic problems is concerned. Thus the majority of experimental examinations can be substituted which are practically more expensive by an order of magnitude. In this way, the number of the indispensable examinations can be reduced essentially.

However, further theoretical examinations, too, are required for the development of procedures most suitable for out possibilities. Thus, e.g. one direction of our investigations is represented by the development of a proper model of boundary layer, or the practical evaluation of the models developed so far with respect to the serviceability of them in computing technique, then the examination of the efficiency of the aids (e.g. artificial viscosity) applied to ensure the numerical stability, or again, changing over to the so-called conservative variables promising an interesting development the value of which is continuous even within shock waves, i.e. by means of which the numerical work can be simplified essentially by means of examining the sets of differential equations written for the continuous functions.

REFERENCES

1. Peyret, R. - Tayler, T.D.: Computation Methods for Fluid Flow, Springer Verlag,1983
2. Roache, P.J.: Computational Fluid Dynamics Hermasa, Pub. Albuquerque, 1976
3. Németh, E.: Hydromechanics, Tankönyvkiadó, Budapest, 1963
4. Landau, L.D. - Lifsic, E.M.: Theoretical Physics VI, Tankönyvkiadó, Budapest, 1980
5. Faragó, I. - Gáspár, Cs.: Numerical Methods for the solution of partial differential equations for hydrodynamic applications, BME MTI, 1982

Acta Technica Acad.Sci.Hung., 101(4), pp. 361–378 (1988)

CHORDAL THICKNESS AND SPAN MEASUREMENT OF HELICAL GEARS

TATÁR, I.*

(Received: 8 September 1987)

A model close to reality but theoretically erroneous has been taken as a basis so far for calculation of the chordal thickness of symmetric teeth confined by helicoidal surfaces. In the worst case, the error of approximation may be as high as a few tenth mm. Probably, the surface normals associated with the end points of the measurable chord are intersecting. With this condition applied to helicoidal surfaces, a transcendent equation is obtained between the parameters of the surface. A quickly convergent simple solution is presented in this paper for calculation of the chordal thickness of constant-lead helicoidal teeth of arbitrary profile and applied then to involute gears. The span measurement (base tangent length or tooth distance) can be considered to be a special tooth chord and thus the expressions developed can also be applied for the calculation of span measurement.

NOTATION

b	face width
d_y	diameter of an arbitrary cylinder coaxial with the axis of rotation
d_M	diameter of measuring pin or ball
$\underline{e}$	direction of the axis of symmetry
$\bar{e}_a$	chordal space width
$\bar{h}_a$	chordal addendum
$\bar{h}_q$	chordal addendum in measurement over pins or balls (see Fig. 4a)
$\underline{i},\underline{j},\underline{k}$	unit vectors
k	number of teeth in the span
$m,\underline{m}$	line of intersection and direction of the pair of tangential surfaces
m_n	normal module
$\underline{n}$	direction of surface normal
p_z	lead
$\underline{r}$	position vector
r_a	radius of addendum circle
r_b	radius of base circle

*Tatár, Iván, H-3529 Miskolc, Középszer u. 78, Hungary

Akadémiai Kiadó, Budapest

r_y radius of an arbitrary cylinder coaxial with the axis of rotation

r_X, r_Y distance of intersection of gear

$\underline{s}_a$ chordal thickness

s_q distance between the centres of pins or balls

v auxiliary variable (for definition see /4/)

x,y,z scalar co-ordinates

x profile shift coefficient

z number of teeth

M measurement over pins or balls, for a gear with an even number of teeth

0 origin of fixed system of coordinates

0_1 origin of moving system of coordinates

P_b, P_j end points of the chord

W(k) span measurement over k teeth

α_n normal rack profile angle

α_t transverse rack profile angle

α_{yt} transverse profile angle

α_X, α_Y half of the angle between the pair of tangential planes

α_{Xt}, α_{Yt} half of the angle between the pair of tangential planes in transverse section

β inclination angle at pitch cylinder

β_b inclination angle at base cylinder

β_y inclination angle at a cylinder of radius r_y

β_X, β_Y angle between the axis and the intersection line of tangential planes (tooth space angle)

ε_i auxiliary variable (see Eqs 29, 32)

η_y transverse profile angle referring to the space

ϑ parameter

ϑ_1 solution of normal helix-chord

μ' angle between the profile angle and the position vector in the transverse plane

μ complementary angle of μ'

ϱ radius of curvature of caliper

τ angular spacing

ψ_y angular position of a tooth point in the transverse plane

1. Introduction

Cylindric gears and worms with helical teeth are a typical example of toothed wheels having a helicoidal surface. The tooth or the tooth space of these toothed wheels is flanked by two helicoidal surfaces as is suggested also by the name of teeth of this type. In case of symmetric teeth, the two helicoidal surfaces are a mirror image of each other with respect to the axis of symmetry.

Two helices (tooth direction lines) are cut out of the pair of helicoids by a cylinder coaxial with the axis of rotation (Fig. 1a). Typically, the lead of any helix cut out of constant-lead helicoid by a cylinder is identical while the inclination angle of the tooth (angle included by the tangent of the helix and the centreline) is different, depending on the selected radius of the cylinder:

$$r_y = \cot \beta_y = p_z = \text{const} \tag{1}$$

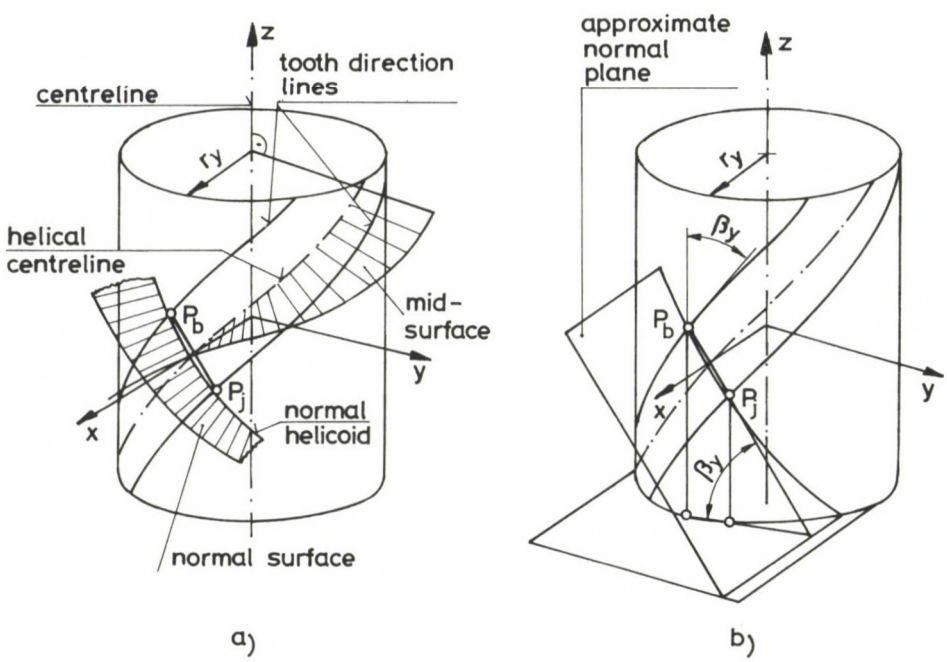

Fig. 1.

According to Fig. 1a, a centreline of the helicoid can be defined over a cylinder having similarly a radius r_y between the tooth direction lines arranged symmetrically with respect to the helicoid centreline. Straight lines starting from points of the helicoid centreline, intersecting the centreline at right angles, constitute a sharp helicoidal surface that is the surface of symmetry (mid-surface) of the tooth. Each radius of the mid-surface is the axis of symmetry of the tooth and therefore the result of measurement is not affected by a displacement of the caliper along the length of the tooth in case of such surfaces (assuming a theoretically accurate surface).

The surface perpendicular to the tooth direction lines is called normal surface, again a sharp helicoidal surface with the radii intersecting the centreline similarly at right angles. Its line of intersection with the mid-surface is a straight line with axis x being the common radius in Fig. 1a. The trace of the normal surface on the cylinder is the normal helical line, the intersections of the tooth direction lines and the normal helical line determining the chord of the normal helical line denoted by P_bP_j /1/.

The normal surface is usually replaced with the approximate normal plane perpendicular to the centreline of the helicoid (Fig. 1b). A so-called chord of normal inclination is cut out of the tooth direction lines by the approximate normal plane, which includes with the transverse plane an angle corresponding to the angle of inclination of the tooth direction lines.

It follows from the mentioned properties of the helicoidal surface that, while the normal surface is independent of the selected radius, r_y, the angle of inclination of the approximate normal plane varies as a function of the radius according to /1/. Therefore, by approximate normal section, the section constituted with the normal plane of the helical centreline of the surface of division in a narrow sense.

2. A correct method of computation of cordal space width and chordal thickness

2.1 Chordal thickness

In calculating for the chordal dimension of symmetric teeth, it has been shown /5/ that the normals associated with the end points of the

measurable chord are intersecting:

$$[\underline{r}\ \underline{n}\ \underline{e}] = 0 \qquad (2)$$

where $\underline{r}$ position vector of one of the end points of the chord

$\underline{n}$ normal at the same point

$\underline{e}$ direction of the axis of symmetry.

The model of normal-inclination chord is used to determine the chordal dimension of helicoidal teeth (e.g. DIN 3960) although Eq. 2 is not satisfied for either normal-inclination or normal-helicoid chords. The two chords mentioned are usually a good approximation to the measurable chord but in an unfavourable case, the error might be as high as a few tenth mm.

To write Eq. 2 in detail, let the surface be produced by helical motion of transverse profile $r_y = r_y(\psi_y)$. Let $r_y(\psi_y)$ in right-handed Cartesian co-ordinate system $O_1(x_1y_1z_1)$ stand for e.g. the left transverse profile where independent variable $\psi_y > 0$ is just the tooth angle (Fig. 2). Let axis of symmetry x_1 of the profile coincide with axis x of fixed co-ordinate system O(xyz). With system O_1 caused to move helically to the right, axis x_1 describes the mid-surface and the tooth surface is obtained as an envelope surface of front sections of infinite density:

$$\underline{r} = r_y \begin{bmatrix} \cos(\psi_y - \vartheta) & -\sin(\psi_y - \vartheta) & \vartheta\cot\beta_y \end{bmatrix}, \qquad (3)$$

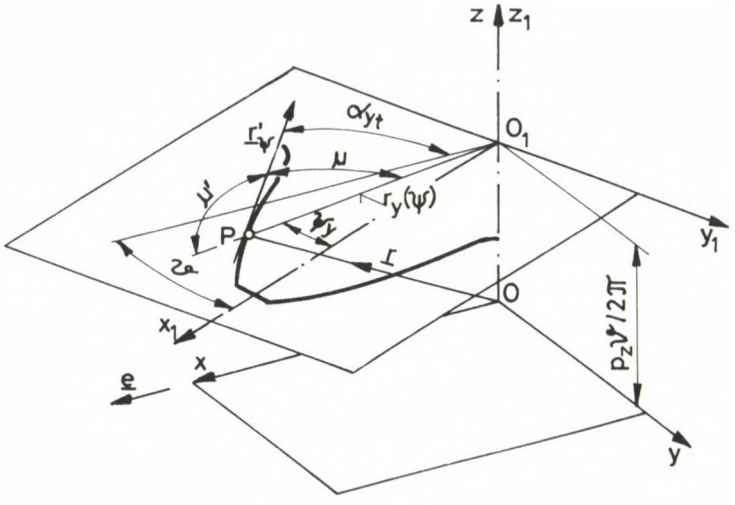

Fig. 2.

wnere ϑ angle of rotation and Eq. 1 characteristic of helicoidal surfaces has been used in writing co-ordinate z.

To make it simple, let notation

$$v = \psi_y - \vartheta \tag{4}$$

be introduced. With this notation, Eq. 3 can be written as

$$\underline{r} = r_y \begin{bmatrix} \cos v & -\sin v & \vartheta \cot \beta_y \end{bmatrix} . \tag{5}$$

With surface Eq. 3 differentiated with respect to parameters ϑ and ψ_y, the directions of the tangents of the parameter lines are obtained:

$$\underline{r}'_\vartheta = \frac{\partial \underline{r}}{\partial \vartheta} = r_y \begin{bmatrix} \sin v & \cos v & \cot \beta_y \end{bmatrix} , \tag{6}$$

$$\underline{r}'_\psi = \begin{bmatrix} \dot{r}_y \cos v - r_y \sin v \\ -\dot{r}_y \sin v - r_y \cos v \\ 0 \end{bmatrix} \quad ; \quad \dot{r}_y = \frac{dr_y}{d\psi_y} . \tag{7}$$

Let angle μ' included by the transverse profile tangent and the radius vector in section, defined by relationship $\tan \mu' = r_y/\dot{r}_y$ (Fig. 2) be introduced. Since in practice the tooth thickness is reducing towards the addendum circle, let the complementary angle of μ' be taken into account instead of μ':

$$\tan \mu = \tan(\pi - \mu') = -r_y/\dot{r}_y . \tag{8}$$

From Eq. 8 substituting r_y into Eq. 7, the direction of the profile tangent in the transverse plane will be

$$\underline{r}'_\psi = \lambda \begin{bmatrix} \cos(\mu - v) & \sin(\mu - v) & 0 \end{bmatrix}, \quad \lambda = \dot{r}_y/\cos \mu . \tag{9}$$

The normal of the surface is perpendicular to the tangents of the parameter lines. Factors that can be taken out from all the three components can be omitted from the vectorial product of Eq. 6 and Eq. 9 as the direction of the normal is not affected by these factors. Thus, after rearranging

$$\underline{n} = \begin{bmatrix} \sin(\mu - v) & -\cos(\mu - v) & \cos \mu \tan \beta_y \end{bmatrix} . \tag{10}$$

With the position vector and the normal substituted into Eq. 2 and with $\underline{e} = \underline{i}$ taken into consideration, relationship

$$\tan^2\beta_y \cdot \sin v \cdot \cos\mu/\cos(\mu - v) - \vartheta = 0 \qquad (11)$$

must exist between the parameters at the end point of the chord. In this case, the tangential points (end points of the chord) lie on the cylinder of radius r_y.

In calculation of the chordal thickness, radius r_y shall reasonably be assumed in such a way that the tangential points will lie between the limit circle and addendum circle near the tooth center. Now the procedure is, as follows: β_y shall be calculated for r_y, ψ_y and μ from function $r_y(\psi_y)$ and finally, ϑ from relationship Eq. 11. Since here $\mu = \mu(\psi_y)$, $v = v(\psi_y, \vartheta)$, the equation can not be resolved for by means of elementary methods in a closed form in general. With ψ_y and ϑ

$$\bar{s}_a = 2\sqrt{y^2 + z^2} = d_y\sqrt{\sin^2 v + \vartheta^2 \operatorname{ctg}^2\beta_y} \quad , \qquad (12)$$

$$\bar{h}_a = r_a - x = r_a - r_y\cos v \quad , \qquad (13)$$

where $d_y = 2r_y$

r_a radius of the addendum circle.

2.2 Introduction of new variables

Let the acute angle between tangent of profile $\underline{r}\psi$, and the axis of symmetry indicated in Fig. 2 written:

$$\cos\alpha_{Yt} = \frac{|\underline{r}'\psi \cdot \underline{e}|}{|\underline{r}'\psi|} = \cos(\mu - v) \quad ,$$

that is

$$\alpha_{Yt} = \mu - v = \mu - \psi_y + \vartheta \quad . \qquad (14)$$

The two normals belonging to the end points of the chord and the tangential plane have been plotted in Fig. 3. For the time being, possible intersection of the tangential plane and the surface or the fact that no external plane touches the surface shall be left out of consideration. The pair of tangential planes is essentially an imaginary module saddle which is in contact with the tooth surface at points P_b, P_j. Semi-apex angle

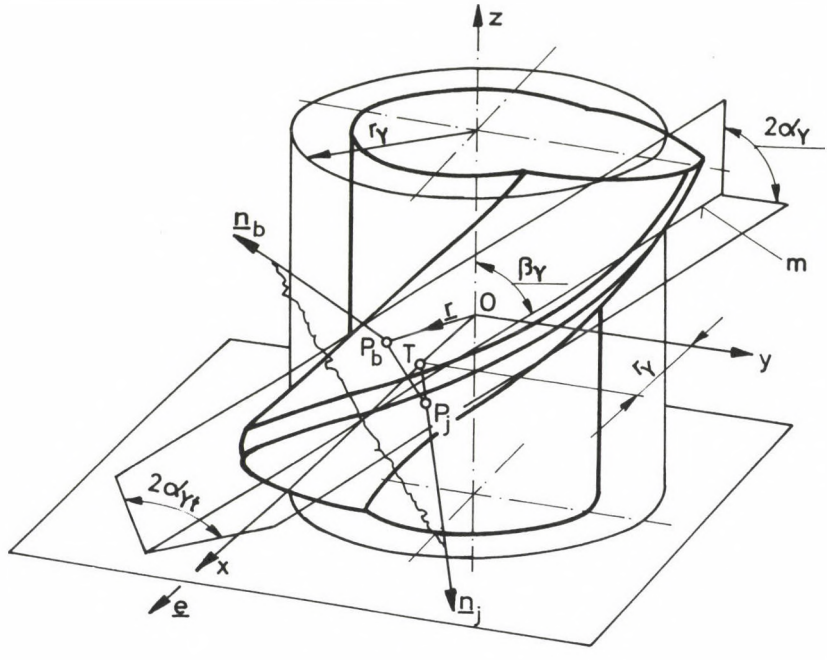

Fig. 3.

characteristic of the pair of planes:

$$\sin \alpha_Y = \frac{|\underline{n}\,\underline{e}|}{|\underline{n}|} = \sin \alpha_{Yt} / \sqrt{1 + \cos^2 u \tan^2 \beta_y} \quad . \qquad (15)$$

It can be seen in Fig. 3 that an angle $2\alpha_{Yt}$ is included by the lines of intersection of tangential planes and transverse plane.

Axis of symmetry $\underline{e} = \underline{i}$ is contained by the plane of intersecting normals assigned to the end points of the chord, thus the plane contains also position vector $\underline{r}$ of point P_b. Therefore, the direction of line of intersection m of the pair of tangential planes can be written also in a form $\underline{m} = \underline{r} \times \underline{e}$. The angle of inclination of the axis of rotation and line of intersection is at the same time an angle characteristic of the inclination of the module saddle:

$$\cos \beta_Y = \frac{\underline{m}\,\underline{k}}{|\underline{m}|} = \frac{[\underline{r}\,\underline{e}\,\underline{k}]}{|\underline{r} \times \underline{e}|} = \sin v / \sqrt{\sin^2 v + \vartheta^2 \cot^2 \beta_y} \quad . \qquad (16)$$

Using Eq. 11, eliminate parameter ϑ from the denominator of the fraction. After transformation,

$$\tan \beta_Y = \cos \mu \cdot \tan \beta_y / \cos \alpha_{Yt} \quad . \tag{17}$$

is obtained.

Relationship

$$\tan \alpha_Y = \tan \alpha_{Yt} \cdot \cos \beta_Y \tag{18}$$

is found between the semi-apex angle of the module saddle and its transverse section angle in a comparison of equations Eq. 15 and Eq. 17.

With parameters α_Y and β_Y introduced, the chordal thickness can be written in a more 'elegant' form and, on the other hand, the new variables permit the tooth caliper dimension measured by means of a spherical or cylindric feeler to be calculated. To write an 'elegant' tooth dimension, let the denominator of the right side of Eq. 16 be expressed and substituted into Eq. 12:

$$\bar{s}_a = d_y \sin v / \cos \beta_Y \quad . \tag{19}$$

To illustrate the chordal thickness measurable by means of a spherical or cylindric feeler, the plane of normals shall be rotated around the axis of symmetry into the transverse plane (Fig. 4a). Closed position of the feelers is considered to be zero dimension on the tooth caliper. Thus the instrument reads

$$\bar{s}_q - 2\varrho = \bar{s}_a + 2\varrho (1 - \cos \alpha_Y) \quad , \tag{20}$$

with a height

$$\bar{h}_q = \bar{h}_a - \varrho \sin \alpha_Y \tag{21}$$

between feeler center and addendum circle associated with it. Here $\bar{s}_q$ is the distance of feeler centers and ϱ is the radius of the feelers. For (20), (21), angle α_Y shall be calculated by use of value ψ_y, ϑ which has been determined for the chordal thickness according to (14), (15).

In addition to calculation of the chordal thickness make sure that the chordal thickness is measurable. The contact can be considered to be undisturbed if the surfaces in contact are not penetrating

into each other and they have no common points beside the tangential point (or contact curve), there is no 'measurement interference'. In case of an edge gauge, the normal curvature of the surface shall be determined on the basis of the normal plane passing through the edge (the edge being parallel to line of intersection m of the tangential planes) while in case of a spherical feeler, it is enough the compare the smaller main bend radius and the radius of the ball. In case of a cylindric feeler, a more complicated investigation is required /6/.

The point of intersection (T) of the normals is a characteristic point of the plane plotted in Fig. 4a. On the basis of the Figure, the distance between point T and the centreline can be expressed as the chordal thickness:

$$r_Y = x - \frac{\bar{s}_a}{2} \tan \alpha_Y \quad ,$$

where $x = r_y \cos v$ is co-ordinate x of the end point of the chord. Using the expressions Eq. 14, 18, and 19, the right side can be contracted to obtain r_Y in a simpler form:

$$r_Y = r_y \cos \mu / \cos \alpha_{Yt} \quad . \tag{22}$$

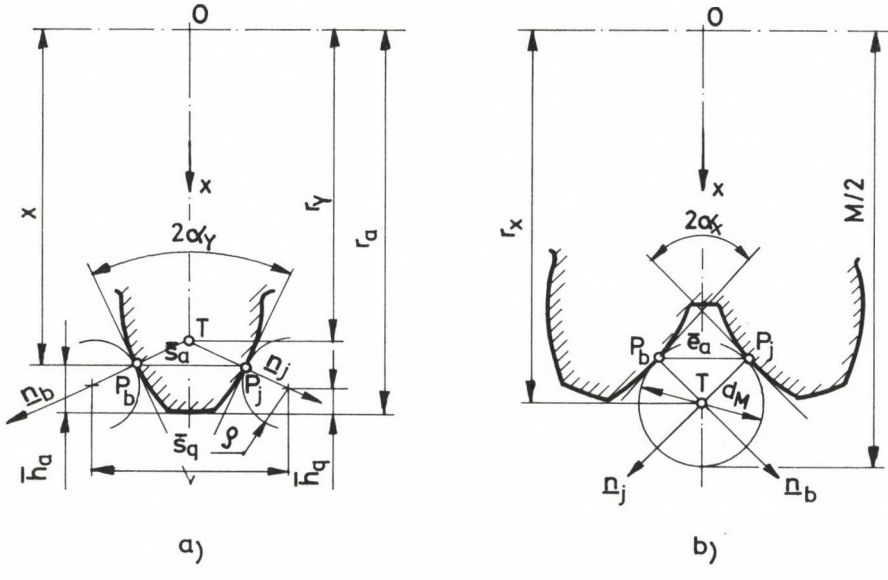

Fig. 4.

The tooth inclination angle measurable along radius r_Y complies with β_Y because, according to Eq. 1, $r_Y \cot \beta_Y = r_y \cot \beta_y$ = const. from Eq. 22 and Eq. 18. Therefore, the inclination of the module saddle as compared with the centreline (or the angle of angular displacement of the tooth caliper measured from the face plane) complies with the tooth inclination angle defined over the cylinder passing through the intersection of the normals.

2.3 Chordal space width

Let vector Eq. 3 be transformed so that $\underline{r}$ will be the surface flanking on the tooth space while the axis of symmetry of the tooth space will remain axis x. Now in Eq. 5, relationship

$$u = \eta_y - \vartheta \tag{23}$$

stands for v while relationship

$$\alpha_{Xt} = \mu + \eta_y - \vartheta = \mu + u \tag{24}$$

stands for Eq. 14, where η_y is the tooth space angle in the transverse plane. Now the pair of tangential planes is considered to be an imaginary module wedge that can be placed into the tooth space, being in contact with the tooth surface at the end points of the chord. For the sake of distinction, subscript X is used to denote the semi-apex angles of the module wedge (Fig. 4b). Taking into consideration what has been said above, relationship between the parameters will then be

$$\tan^2 \beta_y . \sin u . \cos \mu / \cos (\mu + u) - \vartheta = 0 \tag{25}$$

Equations 15 through 17 for angles still apply but now with subscript X, the formula for the chordal space width being similar to Eq. 12 or Eq. 19:

$$\bar{e}_a = d_y \sqrt{\sin^2 u + \vartheta^2 \cot^2 \beta_y} = d_y \sin u / \cos \beta_X \quad . \tag{26}$$

Note that, starting from the chordal space width, calculation of the ball or pin size for teeth of any arbitrary profile is rather simple. It can be seen in Fig. 4b that $M/2 = r_X + d_M/2$, $r_X = r_y \cos \mu / \cos \alpha_{Xt}$

being the distance of the center of the ball or of the axis of the pin from the axis of rotation while d_M the diameter of the gauge. Because of the assumed radius r_y, diameter d_M can not be selected optionally as $d_M = \bar{e}_a/\cos\alpha_x$ according to the Figure.

Here dimension M is exactly the ball or pin size for toothed wheels of even tooth number provided the gauges are located opposite to each other in the same face plane. Starting from dimension M, the ball size can be written also for toothed wheels of odd tooth number depending on the number and arrangement of gauges.

2.4 Approximate calculation for chordal thicknesses

Solution of transcendent Eq. 11 or Eq. 25 is required for determination of the chordal thickness or chordal space width at diameter d_y selected. As has been mentioned, the normal helix chord is in most cases a good approximation to the measurable chord. Fortunately, it is relatively easy to determine the intersection of the normal helix and tooth direction line. The parameter ϑ_1 of the end point of the normal helix on the cylinder of radius r_y of surface Eq. 5 can be produced in a closed form /1/. For the tooth chord,

$$\vartheta_1 = \psi_y \sin^2\beta_y \quad , \quad \text{or} \quad v_1 = \psi_y \cos^2\beta_y \quad . \tag{27}$$

With ν_1 or v_1 assumed to be the initial value of iteration, the solution can be gradually improved using Newton' a method by means of recursion formula

$$v_{i+1} = v_i + \frac{\vartheta_i - \varepsilon_i \tan\beta_y . \sin v_i}{\varepsilon_i^2 + 1} \quad , \tag{28}$$

$$\vartheta_{i+1} = \psi_y - v_{i+1} \quad ; \qquad i = 1, 2, 3, \ldots$$

The first expression in Eq. 28 converges quickly with the second term on the right side (increment of v) approaching to zero, where

$$\varepsilon_i = \tan\beta_y . \cos\mu/\cos(\mu - v_i) \quad . \tag{29}$$

Because of Eq. 23 and Eq. 24, the starting parameters for the chordal space width contain tooth space angle:

$$\vartheta_1 = \eta_y \sin^2 \beta_y \quad , \qquad \text{or} \qquad u_1 = \eta_y \cos^2 \beta_y \quad . \tag{30}$$

Instead of Eq. 28 of the improved solution, relationship

$$u_{i+1} = u_i + \frac{\vartheta_i - \varepsilon_i \tan \beta_y . \sin u_i}{\varepsilon_i^2 + 1} \quad ,$$

$$\vartheta_{i+1} = \eta_y - u_{i+1} \quad ; \qquad i = 1, 2, 3, \ldots \tag{31}$$

shall now be used, where

$$\varepsilon_i = \tan \beta_y \, . \, \cos \mu / \cos (\mu + u_i) \quad . \tag{32}$$

3. Span measurement

Let the span measurement be measured over teeth k. Use the results of chordal thickness of teeth for derivation. For this purpose, write the equation of tooth surface in contact with the micrometer instead of Eq. 5.

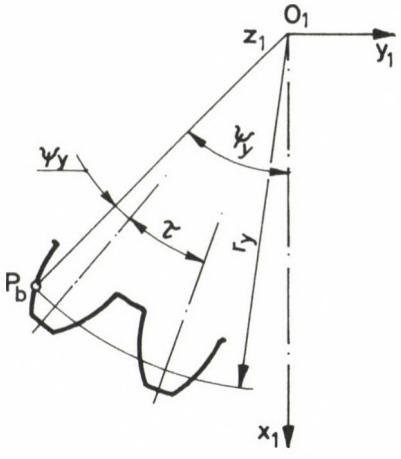

Fig. 5.

In Fig. 5, the teeth are arranged symmetrically as compared with axis x_1 in the transverse plane illustrated. With angular division $\tau = 2\pi/z$ introduced, it can be seen that $\Psi_y = (k-1)\tau/2 + \psi_y - t$ shall be formally written instead of ψ_y in (3) that is, in the formulae for the chord

$$v = \Psi_y - \vartheta = (k-1)\tau/2 + \psi_y - \vartheta \ , \tag{33}$$

$$\alpha_{Yt} = \mu - v = \mu - (k-1)\tau/2 - \psi_y + \vartheta \ . \tag{34}$$

The jaws of the caliper used for measurement in this case are parallel planes. That means that the semi-apex angle of the module angle is $\alpha_Y = 0$ or $\alpha_{Yt} = 0$. Taking this into consideration, the parameters determining the point of contact are given by the solution of Eqs 34 and 11 for a definite k. With ϑ eliminated, equation

$$\tan^2 \beta_y \ . \ \sin\mu \ . \ \cos\mu + \mu - \psi_y - (k-1)\tau/2 = 0 \tag{35}$$

is a function of only ψ_y which yields a different solution for each k. From among the solutions, only those for the applicable tooth surface can be taken into account. This can be tested e.g. by calculation of radius $r_y(\psi_y(k))$. Span measurement W(k) can be calculated using parameter ψ_y determined from Eq. 35 on the basis of Eq. 12 or Eq. 19 where $\vartheta = (k-1)\tau/2 + \psi_y - \mu$.

Another condition for measurement of the span is that the toothed wheel be sufficiently wide. Angle β_Y in Fig. 6 shall be calculated for $\alpha_{Yt} = 0$ from Eq. 17. It can be seen in the Figure that, because of the safe bearing of the feelers and chamfering, it is necessary that

$$b > W(k) \ . \ \sin\beta_Y \ . \tag{36}$$

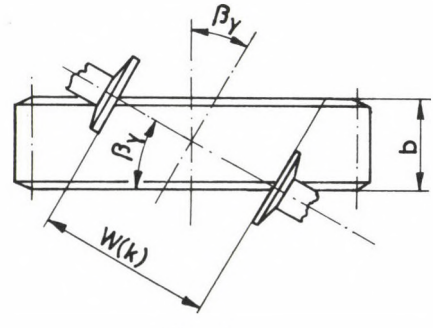

Fig. 6.

4. Application

Involute tooth profile is provided for the decisive majority of helical gears used in mechanical engineering. In case of gears of involute teeth, r_y and ψ_y are known as a function of profile angle α_{yt}:

$$r_y = r_b/\cos\alpha_{yt} = \frac{zm_n}{2}\,\frac{\cos\alpha_t}{\cos\beta\,.\,\cos\alpha_{yt}}\quad , \tag{37}$$

$$\psi_y = \frac{\pi/2 + 2x\tan\alpha_n}{z} + \operatorname{inv}\alpha_t - \operatorname{inv}\alpha_{yt}\quad , \tag{38}$$

where r_b – radius of base circle
x – profile shift coefficient
α_n – normal rack profile angle
z – number of teeth
m_n – normal module
β – inclination angle at pitch cylinder
α_t – transverse rack profile angle and
$\operatorname{inv}\alpha = \tan\alpha - \widehat{\alpha}$.

To determine angle μ, let the two equations be differentiated with respect to the profile angle:

$$\frac{dr_y}{d\alpha_{yt}} = r_y \operatorname{tg}\alpha_{yt}\quad ;\quad \frac{d\psi_y}{d\alpha_{yt}} = -\operatorname{tg}^2\alpha_{yt}\quad .$$

Using these relationships,

$$\operatorname{tg}\mu = -r_y/\dot{r}_y = -r_y\,\frac{d\psi_y}{d\alpha_{yt}}\left(\frac{dr_y}{d\alpha_{yt}}\right)^{-1} = \operatorname{tg}\alpha_{yt}\quad ,$$

that is $\mu = \alpha_{yt}$. Thus factor ε_i required for iteration will be

$$\varepsilon_i = \tan\beta_y \cos\alpha_{yt}/\cos(\alpha_{yt} - v_i)\quad .$$

4.1 Let the theoretical chordal thickness be calculated for a gear of involute teeth of known geometry. Starting data including those previously calculated are, as follows:

Number of teeth	$z = 26$
Normal module	$m_n = 5$ mm
Tooth inclination angle at pitch cylinder	$\beta = 25^0$
Profile shift coefficient	$x = 0.428$
Normal rack profile angle	$\alpha_n = 20^0$
Diameter of addendum circle	$d_a = 157.6$ mm
Test diameter	$d_y = 147.6$ mm
tooth inclination angle	$\hat{\beta}_y = 0.4473853$
angular position of the tangent point of caliper jaw in the transverse plane	$\hat{\psi}_y = 0.0597830$
transverse profile angle	$\hat{\alpha}_{yt} = 0.4468671$

About a module is selected as the height of measurement. That means that the test diameter, $d_y = d_a - 2m_n = 147.6$ mm.

Take care to use radian as a unit for angles in the formulae.

Initial values of iteration according to Eq. 27:

$$v_1 = \psi_y \cos^2 \beta_y = 0.0485945, \quad \vartheta_1 = \psi_y - v_1 = 0.0111885 \ .$$

To make it clear, the intermediate results of calculation are tabulated below:

i	ϑ_i	v_i	$\bar{s}_a$(mm)	Δv_i	ε_i
1	0.0111885	0.0485945	7.9530	-	0.469461
2	0.0109867	0.0487963	7.9532	$2.02 \cdot 10^{-4}$	0.469421
3	0.0109867	0.0487963	7.9532	$3.2 \cdot 10^{-9}$	-

With the parameters of the second line, chordal addendum of measurement is $\bar{h}_a = 5.0878$ mm. At the same circle, $\eta_y = \pi/z - \psi_y = 0.0610475$ for the chordal dimension of the tooth groove and thus the values to be used as starting values in iteration are

$$u_1 = \eta_y \cos^2 \beta_y = 0.0496224, \quad \vartheta_1 = \eta_y \sin^2 \beta_y = 0.0114251 \ .$$

For chordal thickness, the results tabulated below are obtained in a similar way:

i	ϑ_i	u_i	$\bar{e}_a$(mm)	Δu_i	ε_i
1	0.0114251	0.0496224	8.1211	-	0.4921377
2	0.0116571	0.0493904	8.1215	$-2.32 \cdot 10^{-4}$	0.4920759
3	0.0116571	0.0493904	8.1215	$-5.7 \cdot 10^{-9}$	-

Tabulated in the third column of the Tables are chordal thicknesses calculated with the actual i-th pair of values. As seen in the fourth column, the difference between two subsequent parameters ($\Delta v_i = v_i - v_{i-1}$) lies in an order of magnitude as high as 10^{-9} and it is therefore not worth the trouble to continue iteration and thus calculation of ε_i. It can also be seen that for small modules, even the accuracy of chordal thickness $\bar{s}_{al}$ or chordal space width $\bar{e}_{al}$ calculated with the initial value is sufficient.

4.2 Let the chordal thickness of involute helical gears be determined!

Since in case of involute teeth $\mu = \alpha_{yt}$, it follows from (34) because of $\alpha_{Yt} = 0$ that $v = \mu = \alpha_{yt}$. At the same time, $\tan \beta_Y = \cos \alpha_{yt} \cdot \tan \beta_y = \tan \beta_b$ that is $\beta_Y = \beta_b$ according to Eq. 17. Accordingly, the micrometer for measurement of the span shall be turned off through the tooth inclination angle at the base cylinder. Thus and with Eq. 37 as well as on the basis of Eq. 19,

$$W(k) = d_y \sin \alpha_{yt} / \cos \beta_b = z m_n \frac{\cos \alpha_t \cdot \tan \alpha_{yt}}{\cos \beta \cdot \cos \beta_b} .$$

Profile angle α_{yt} is unknown in the formula for the chordal dimension measurable over more teeth and it shall be determined on the basis of Eq. 35.

It is well known that $\tan \beta_y = \tan \beta_b / \cos \alpha_{yt}$ in case of involute profiles. Substituting this and Eq. 38 into Eq. 35, the equation can be resolved for α_{yt}:

$$\tan \alpha_{yt} = \cos^2 \beta_b \left[\frac{\pi(k-0.5) + 2x \tan \alpha_n}{z} + \operatorname{inv} \alpha_t \right] .$$

The right side of the expression is a function of the number of teeth in the span according to the basic data for teeth and thus a different profile angle α_{yt} and a different test diameter are obtained for each k.

With the expression of tan α_{yt} substituted again into the formula of W(k) and taking into consideration relationship cos α_t . cos β_b = = cos α_n . cos β existing between base profile angles and tooth inclination angles, the well known relationship is obtained for the span measurement over k teeth:

$$W(k) = m_n \cos \alpha_n \left[(k-0.5)\,\pi + z \text{ inv } \alpha_t + 2x\tan \alpha_n \right] .$$

REFERENCES

1. Drahos, I.: Geometrical basis of chordal thickness of helical gears (presented at the 4th Conference on Gears held in Budapest, May 12-14, 1980)

2. Korhammer, A.: Berechnung der Zahnstärke im Teilzylinder bei Schrägverzahnung, Werkstatt u. Betrieb, Vol. 85 (1952), 138-139

3. Niemann, G., Winter, H.: Maschinenelemente. Band II. Zweite Auflage. Springer-Verlag, Berlin-Heidelberg-New York-Tokyo, 1983

4. Weinhold, H.: Die Zahndickensehne bei Stirnrädern als Rechnungsgrösse, Maschinenbautechnik, Vol. 6 (1957), Nr. 11, 616-621

5. Tatár, I.: Chordal thickness of symmetric teeth (manuscript in Hungarian)

6. Litvin, F.L.: Theory of gear engagement, Műszaki Könyvkiadó, Budapest, 1972

Standards:

DIN 3960 Begriffe und Bestimmungsgrössen für Stirnräder (Zylinderräder) und Stirnradpaare (Zylinderpaare) mit Evolventenverzahnung. Zusammenstellung der Gleichungen, 1980

Acta Technica Acad.Sci.Hung, 101(4), pp. 379–396 (1988)

CHORDAL THICKNESS AND SPAN MEASUREMENT OF CONJUGATE SURFACES

TATÁR, I.*

(Received: 8 September 1987)

For determination of the test dimensions of teeth, it is necessary that the equation of the surface confining the tooth be known. According to experience, the calculation is difficult even in case of teeth of a relatively simple surface because of the complexity of transformed equations. A simple calculation process is presented in this study, permitting the chordal thickness and the span measurement to be determined on the basis of the conjugate surface without knowledge of the transformed tooth surface. The relationships derived apply to any symmetric teeth. In this study, the method is applied to a Wildhaber-Novikov gear.

NOTATION

a, $\underline{a}$	length (axial distance) and vector of normal transversal
b	face width
b_1	co-ordinate of centre of curvature of base profile
$\underline{e}_2$	unit vector of the direction of axis of symmetry
h_a	chordal addendum
$\underline{i}$, $\underline{j}$, $\underline{k}$	unit vectors of co-ordinate axes
i_{12}	ratio
k	number of teeth (tooth spaces) in the span
m_n	normal module
$\underline{n}$	direction of surface normal
$n_{x,y,z}$	scalar components of the normal
$\underline{r}$	position vector of a point of the surface
r_2	radius of pitch cylinder (non standard)
r_a	radius of addendum circle
r_y	distance of a point of the surface from the centreline
r_Y	distance of intersection of normals from the centreline
s_a	chordal thickness
u, v	surface parameters

*Tatár, Iván, H-3529 Miskolc, Középszer u. 78, Hungary

Akadémiai Kiadó, Budapest

$\underline{v}_{12}$ relative velocity

x, y, z co-ordinate axes, scalar co-ordinates

0 origin of the co-ordinate system

P travelling point of the characteristic, end point of the chord

T intersection of normals associated with the end point of the chord

R_1, R_2 main radii of curvature

W(k) span measurement over k teeth

α_y semi-apex angle of module saddle

β tooth inclination angle at the non-standard

β_Y angle between the chord and pitch circle the transverse plane

ϑ parameter

ϱ radius of curvature of base profile

τ angular spacing

φ angular displacement

$\underline{\omega}$, ω angular velocity vector, and its absolute value

$\underline{\omega}_{12}$ relative angular velocity

Σ shaft angle

Φ_2 auxiliary variable (for definition see Eq. 24)

1. Introduction

Cylindric gears are usually finish-machined by means of tools of a symmetrical or asymmetrical geometry of the cutting edge (e.g. milling or grinding). In the course of machining, the tool edges skim the generating surface which is in general a simple surface such as a plane, cylindric surface of a directrix characteristic of the teeth or a surface of rotation of a simple meridian curve or, possibly, a helical surface.

The position of the tool as compared with the workpiece keeps varying in the course of machining. Kinematically, this relative motion is limited depending on the type and geometry of the gear and tool as well as on the technology. The tool surface produced will become the envelope surface of the instantaneous positions of the tool surface in the course of its relative motion. That means that the tooth surface is mapped by the tool surface. With the function of the two terms interchanged, mapping is interchangeable, mutual and unambiguous. The surfaces so associated are called conjugate surfaces. Conjugate surfaces tangent each other along a common curve, a characteristic, at any instant.

Assume that singular points are contained neither the tool surface nor the conjugate surface and that the law of motion is known for both members.

2. Derivation of conjugate surfaces

Consider a general machining practice when the shafts of gear blank and the tool are non-intersecting and non-parallel and the angle between them is Σ (Fig. 1). The tool and system O_1 associated with it are rotating at angular velocity ω_1 within stationary system O having axis z in common with system O_1. Similarly, the workpiece and along with it, system O_2 are rotating at angular velocity ω_2 within stationary system O_0. The positive directions of axes z comply with the directions of the angular velocity

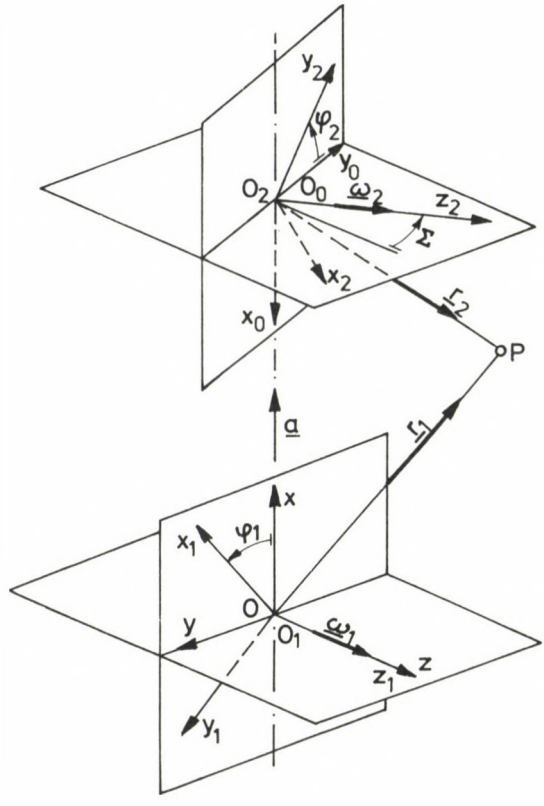

Fig. 1.

vectors, the origins of the co-ordinate systems being the feet of the normal transversal of the axes of rotation. Unit vectors $\underline{i}$, $\underline{j}$, $\underline{k}$ of axes x, y, z, respectively constitute a right-handed system, their index complying with the index of their origin.

Let a be the length of the normal transversal. The equation and the direction of the normal of the surface of member 1 (tool) in system O_1 are known:

$$\underline{r}_1^{(1)}(u,v) = \left[x_1^{(1)}(u,v) \quad y_1^{(1)}(u,v) \quad z_1^{(1)}(u,v) \right] , \tag{1}$$

$$\underline{n}_1^{(1)}(u,v) = \left[n_{x1}^{(1)}(u,v) \quad n_{y1}^{(1)}(u,v) \quad n_{z1}^{(1)}(u,v) \right] . \tag{2}$$

The motion of the two members is linked by constant velocity ratio

$$i_{12} = \omega_1 / \omega_2 = \varphi_1 / \varphi_2 . \tag{3}$$

The envelope surface is determined by means of the kinematic method /1/. Since the surfaces are neither separating nor penetrating into each other, the relative displacement or relative velocity along the characteristic will always take place at right angles to the normal that is

$$\underline{n}_1^{(i)} \, \underline{v}_{12}^{(i)} = 0 \tag{4}$$

where the superscript (i) refers to that Eq. 4 can be written in any co-ordinate system.

Let system 0 without index be selected as a reference system. In case of angular displacement φ_1 or member 1

$$\underline{r}_1 = \begin{bmatrix} x_1^{(1)} \cos\varphi_1 - y_1^{(1)} \sin\varphi_1 \\ x_1^{(1)} \sin\varphi_1 + y_1^{(1)} \cos\varphi_1 \\ z_1^{(1)} \end{bmatrix} = \begin{bmatrix} x_1 \\ y_1 \\ z_1 \end{bmatrix} \tag{5}$$

$$\underline{n}_1 = \begin{bmatrix} n_{x1}^{(1)} \cos\varphi_1 - n_{y1}^{(1)} \sin\varphi_1 \\ n_{x1}^{(1)} \sin\varphi_1 + n_{y1}^{(1)} \cos\varphi_1 \\ n_{z1}^{(1)} \end{bmatrix} = \begin{bmatrix} n_{x1} \\ n_{y1} \\ n_{z1} \end{bmatrix} \tag{6}$$

It is possible to use the position vector of the contact point P of the tool and the centre distance to express $\underline{r}_2$. This possibility shall be utilized in writing relative velocity $\underline{v}_{12} = \underline{v}_1 - \underline{v}_2 = \underline{\omega}_1 \times \underline{r}_1 - \underline{\omega}_2 \times \underline{r}_2$. According to the definition in Fig. 1, $\underline{r}_2 = \underline{r}_1 - \underline{a}$. Accordingly,

$$\underline{v}_{12} = \underline{\omega}_1 \times \underline{r}_1 - \underline{\omega}_2 \times (\underline{r}_1 - \underline{a}) = \underline{\omega}_{12} \times \underline{r}_1 + \underline{\omega}_2 \times \underline{a} \tag{7}$$

where $\underline{\omega}_{12} = \underline{\omega}_1 - \underline{\omega}_2$ is the vector of the relative angular velocity while $\underline{a} = a\underline{i}$ is the position vector of the origin of system O_1. Also,

$$\underline{\omega}_1 = \omega_1 \underline{k} = i_{12} \omega_2 \underline{k} \quad , \tag{8}$$

$$\underline{\omega}_2 = \omega_2 \begin{bmatrix} 0 & -\sin\Sigma & \cos\Sigma \end{bmatrix}. \tag{9}$$

in expression (7). With these and with vectors Eq. 5 and Eq. 6 substituted, the following condition is obtained for engagement:

$$n_{x1}\left[z_1 \sin\Sigma - y_1(i_{12} - \cos\Sigma)\right] + n_{y1}\left[i_{12} x_1 + (a - x_1)\cos\Sigma\right] + n_{z1}(a - x_1)\sin\Sigma = 0 . \tag{10}$$

Eq. 10 corresponds to a function $f_1(u, v, \varphi_1) = 0$ which is a linkage between the three parameters. With one of the parameters epxressed for any arbitrary, but fixed, value $\varphi_1 = c$ and substituted back into Eq. 5 of the surface, the instantaneous contact curve of the tool displaced angularly through angle φ_1 and gear displaced angularly through angle $\varphi_2 = \varphi_1/i_{12}$ is obtained in the stationary system. With φ_1 varied, family of characteristics $\underline{r}_1\left[u, v(u, \varphi_1)\right]$ can be determined which as a whole give the engagement surface. With the surface of action transformed into system O_2 rotating along with term 2 we obtain the mapped (transformed) surface.

3. Chordal thickness of conjugate surfaces

To write condition $\left[\underline{r}_2^{(2)}\ \underline{n}_2^{(2)}\ \underline{e}_2^{(2)}\right] = 0$ for the end points of the chord in detail, each factor of the mixed product shall be produced in system O_2 while to write the position vector, transformation $\underline{r}_2^{(2)} = \underline{\underline{M}}_2\underline{r}_1$ is required, where $\underline{\underline{M}}_2$ is the transfer matrix from system O to system O_2. Surface $\underline{r}_2^{(2)}$ contains four variables (u, v, φ_1, φ_2) but $\varphi_2 = \varphi_1/i_{12}$ because of the known law of motion while $\varphi_1 = \varphi_1(u, v)$ according to Eq. 10 and thus, in fact, it is only a function of parameters u, v. Hence, direction of the normal of the mapped (transformed) surface:

$$\underline{n}_2^{(2)} = \frac{\partial \underline{r}_2^{(2)}}{\partial u} \times \frac{\partial \underline{r}_2^{(2)}}{\partial v} \quad .$$

The direction of axis of symmetry $\underline{e}_2^{(2)}$ can be written relatively simply if the co-ordinate system is selected adequately. This will be later discussed in detail.

As it can be seen, it is rather tiresome to write the vectors in system O_2 and the chances of an error are considerable. Transformed equations are rather complicated even in case of relatively simple surfaces. Another difficulty comes from the fact that angle φ_1 can not always be expressed from relationship Eq. 10 and therefore the differentiation required for determination of the normal can be made only by means of an intermediate parameter.

A much simpler method is presented below. Here we take as a starting point that the knowledge of the equation of the conjugate surface is not necessary; it is enough to know discrete points of the surface and the normals associated with these points and to investigate which of these points satisfies the condition for the chord. These known points are points of the characteristic. Since the surfaces touch each other, they have a normal in common and thus $\underline{n}_2^{(2)}$ need not be determined at all.

Investigation is made in stationary system O. At the beginning when ($\varphi_1 = \varphi_2 = 0$), axes x_1 and x_2 are just coincident with the normal transversal. Let axis x_1 be the symmetry line of the tooth space of term 1 while $\underline{r}_1$ one of the surfaces flanking on the tooth space in system O_1. In this case, axis x_2 will be the symmetry line of one tooth of the generated gear. According to what has been said, the following condition applies to the chord:

$$\left[\underline{r}_2\underline{n}_2\underline{e}_2\right] = \left[(\underline{r}_1 - \underline{a})\underline{n}_1\underline{e}_2\right] = 0 \qquad (11)$$

The only unknown in the equation is direction $\underline{e}_2$. To determine the direction of the axis of symmetry, consider that while the tool turns through an angle φ_1 in the stationary system, its conjugate pair and thus also the axis of symmetry of it displaces through angle φ_2. This direction is the direction of the unit vector of axis x_2 in system 0:

$$\underline{e}_2 = \left[-\cos\varphi_2 \qquad -\cos\Sigma\cdot\sin\varphi_2 \qquad -\sin\Sigma\cdot\sin\varphi_2\right] . \qquad (12)$$

Considering that $\underline{a} = a\underline{i}$ and making use of vectors Eq. 5, Eq. 6 and Eq. 12, the result of expansion of the mixed product will be

$$n_x\sin\varphi_2\,(y\sin\Sigma - z\cos\Sigma) + n_y\left[(a-x)\sin\Sigma\cdot\sin\varphi_2 + z\cos\varphi_2\right] -$$

$$- n_z\left[(a-x)\cos\Sigma\sin\varphi_2 + y\cos\varphi_2\right] = 0 . \qquad (13)$$

In the equation, x, y, z and n_x, n_y, n_z are a function of the tool surface and angle φ_1. Thus Eq. 13 satisfies a new condition, $f_2(u,v,\varphi_1)=0$. The existence of equality of Eq. 10 means that the point is a contact point that is at the same time a point of the contact surface as well while Eq. 13 suggests that it is at the same time the end point of the chord. The two equations contain three unknowns and therefore we have the freedom to stipulate one parameter. Since the tool data are known, it is reasonable to find the conjugate of the point lying on the cylinder of radius r_{y1} of the tool. From Eq. 5

$$r_{y1}^2 = x_1^2 + y_1^2 = x^2 + y^2 , \qquad (14)$$

and the distance of the same point from axis of rotation $z_2 = z$

$$r_{y2}^2 = (a-x)^2 + (y\cos\Sigma + z.\sin\Sigma)^2 . \qquad (15)$$

Vector Eq. 5, the end point of the chord, is determined by the solution of equation system Eq. 10, Eq. 13 and Eq. 14 for u, v, φ_1. Eq. 15 can be used to verify whether the point is on the usable tooth surface of the machined gear. The poisiton of the end point of the chord can be modified by varying r_{y1}.

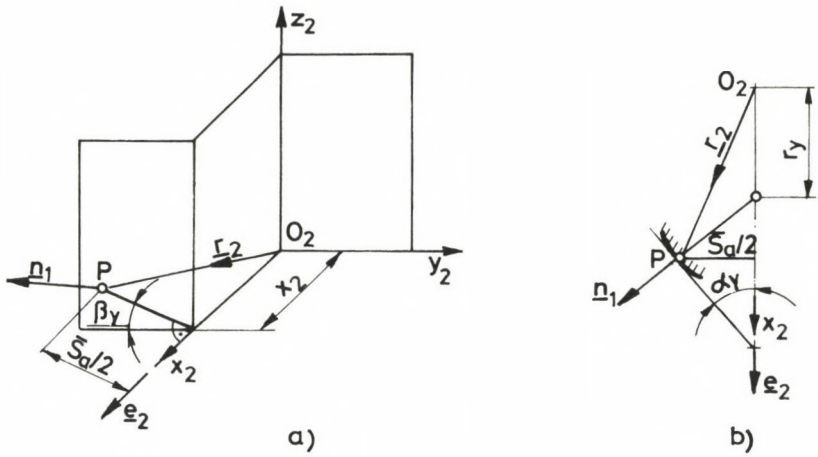

Fig. 2.

System O_2 is privileged in Fig. 2a but we continue defining the vectors in system O. On the basis of the Figure, only directives are given for calculation of the chordal thickness and chordal addendum:

$$\left(\frac{\bar{s}_{a2}}{2}\right)^2 = \underline{r}_2^2 - (\underline{r}_2\,\underline{e}_2)^2 \quad , \tag{16}$$

$$\bar{h}_{a2} = r_{a2} - \underline{r}_2\,\underline{e}_2 \quad . \tag{17}$$

The angle of inclination of the chord as compared with transverse plane x_2y_2 complies with the angle of inclination between the faceplane and the plane containing the chord and vectors $\underline{n}_1$, $\underline{e}_2$. Here the normal of the transverse plane is unit vector $\underline{k}_2$ of axis z_2 while that of the plane containing the chord is $\underline{n}_1 \times \underline{e}_2$. Let $0 \leq \beta_\gamma < \pi/2$ according to our definition. Hence

$$\cos\beta_\gamma = \frac{|(\underline{n}_1 \times \underline{e}_2)\underline{k}_2|}{|\underline{n}_1 \times \underline{e}_2|} = \frac{|[\underline{n}_1 \underline{e}_2 \underline{k}_2]|}{|\underline{n}_1 \times \underline{e}_2|} \quad , \tag{18}$$

where in system O

$$\underline{k}_2 = \begin{bmatrix} 0 & -\sin\Sigma & \cos\Sigma \end{bmatrix} . \tag{19}$$

The plane of $\underline{r}_2$, $\underline{n}_1$, $\underline{e}_2$ has been turned into the plane of the drawing in Fig. 2b. Semi-apex angle of the imaginary module saddle touching the

tooth surface at end-point P of the chord is

$$\sin \alpha_Y = \frac{|\underline{n}_1 \; \underline{e}_2|}{|n_1|} \quad , \qquad 0 \leq \alpha_Y < \pi/2 \quad . \tag{20}$$

In the knowledge of the above quantities, the distance of intersection T of the normal and the axis of symmetry from centreline z_2 can be written e.g. in the following way:

$$r_Y = \underline{r}_2 \; \underline{e}_2 - \frac{\bar{s}_{a2}}{2} \tan \alpha_Y \quad . \tag{21}$$

In relationships Eq. 16 thru Eq. 21, $\underline{r}_2 = \underline{r}_1 - \underline{a}$ and solution u, v, φ_1 of equation system Eq. 10, Eq. 13 and Eq. 14 shall be used for calculation of the vectors.

The equations will take a simpler form if the axes are arranged parallel ($\Sigma = \pm\pi$, $\sin\Sigma = 0$, $\cos\Sigma = -1$) or normal shaft arrangement ($\Sigma = \pm\pi/2$, $\sin\Sigma = \pm 1$, $\cos\Sigma = 0$) to each other. In the latter case, the sign of Σ is important. The definition of the angle can be read in Fig. 1.

3.1 The common chord

Theoretically, there is no clearance between the tooth surfaces and the two surfaces flanking on the tooth groove contact their conjugate pair at once. Investigation of engagement of a tooth-space and a tooth shows that two independent contact curves can be observed at any instant. In case of engagement of symmetric teeth, the contact curves will lie as a mirror image of each other along the common axis of symmetry if the centreline of the tooth-space of one of the gears coincides with the centreline of the tooth of the mating gear. The two end points of the chord associated with position $\varphi_1 = \varphi_2 = 0$ lie on the common contact curve that is the chord belongs both to the surface of the tool (as a toot-space chord) and to the surface of such a special position is called common chord. Common chord is e.g. the constant chord in case of gears of involute teeth.

Angle φ_1 is one of the independent parameters of equation system Eq. 10, Eq. 13 and Eq. 14. At the beginning of the investigation $\varphi_1 = \varphi_2 = 0$ and in the special case, Eq. 13 for the chord takes the following simple form:

$$n_y^z - n_z^y = 0 \quad . \tag{22}$$

It can be seen from the Eq. 5 — Eq. 6 transformation, the position vector and the normal of surface Eq. 1 comply with the form transformed into the stationary system: ($\underline{r}_1^{(1)} = \underline{r}_1$, $\underline{n}_1^{(1)} = \underline{n}_1$). Therefore, instead of the scalar components of the surface and the normal, tool data with superscript (1) known in system O_1 can be written immediately into Eq. 10 and Eq. 22. In the two independent equations, only parameters u, v are unknown because of $\varphi_1 = 0$ and thus condition Eq. 14 can not be stipulated. It may occur that, with pair of values u, v obtained as a solution of the equation system, r_{y1} is not incident with the surface of term 1 suited for measurement and accordingly, r_{y2} is not suitable either. In this case, the common chord can not be used to check the gear.

3.2 The tooth-space chord

Let vector Eq. 1 be the position vector of the surface flanking on one of the teeth of the tool, the symmetry line of which being axis x_1. Since it is the tooth space of the gear which is formed by the tooth of the tool, the solution of equation system Eq. 10, Eq. 13 and Eq. 14 will result now in parameters required to determine the chordal thickness of the tooth space of the gear. The method used for calculation is perfectly identical with what has been said in relation to the tooth chord.

Here again, note that the tooth-space chord, angle α_y and distance r_Y are used for calculation of the ball or pin size of the gear as has been shown in /3/. Perfect contact between the surface of the tooth space and the caliper shall be tested especially in case of a measuring pin. A simple method and useful directives for determination of the main curvatures of derived surfaces are given e.g. by Litvin /1/.

4. Span measurement

As it has been shown, the span measurement is a special dimension measured for teeth k where the normal and the axis of symmetry intersect at right angles that is $\underline{n}_1\underline{e}_2 = 0$ and accordingly

$$n_x \cos\varphi_2 + n_y \cos\Sigma \cdot \sin\varphi_2 + n_z \sin\Sigma \cdot \sin\varphi_2 = 0 \quad . \tag{23}$$

To write the equations, one of the surfaces flanking on tooth space k of member 1 and its normal shall be determined in system O_1 in such a way that axis x_1 will be the symmetry line of the flanked tooth space (Fig. 3). Eqs 10, 13 and 23 suited for calculation of span measurement contain the scalar components of this modified surface and normal. The wanted parameter, u, v, φ_1, is supplied by solution of the equation system for fixed k.

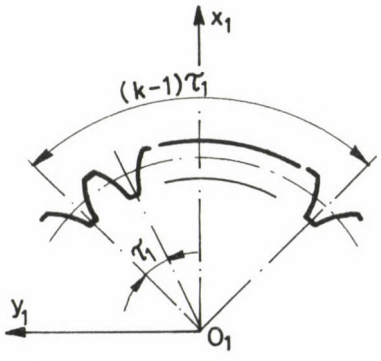

Fig. 3.

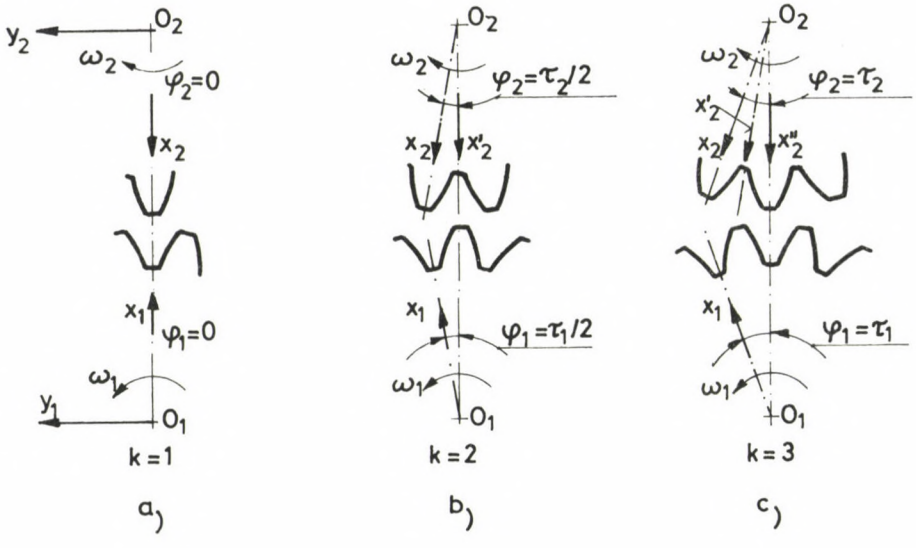

Fig. 4.

Thick line has been used to draw the surface of the tooth space in Fig. 3 where the number of tooth spaces flanked symmetrically to axis x_1 is exactly k. Although this means only angular displacement of member 1 as compared with the model used for calculation of the chordal thickness of the tooth (the tooth chord model is obtained for k = 1), a somewhat different procedure is selected for practical reasons.

To understand the principle applied in calculation, consider Fig. 4. For the sake of lucidity, the two gears engaging have been pulled apart and their transverse planes have been turned into the plane of the Figure. Fig. 4a shows the model used for calculation of the chordal thickness of the tooth. As seen, the 'tooth thickness along the pitch circle' measurable for one tooth will be found in the range of $-\tau_1/2 < \varphi_1 < \tau_1/2$ or $-\tau_2/ < \varphi_2 < \tau/2$ because in case of $|\varphi_1| > \tau_1/2$, the next tooth 'enters the picture' and the new axis of symmetry will be x_2' while the number of clamped teeth 2 (Fig. 4b). For the sake of simplicity, rotation is investigated only in positive direction and thus $\tau_1/2 < \varphi_1 < \tau_1$ for k = 2 because k will increase by one again and the new axis of symmetry will be x_2'' if angle φ_1 reaches τ_1 (fig. 4c) and so on. The calculation is thus somewhat tiresome because both φ_1 and φ_2 contain the number of teeth clamped. To make it simple, let model a) be kept and the changes of k be taken into consideration in the directions of axes x_2, x_2', x_2'' ... It can be seen the angle included by two adjacent symmetry lines is half of the angular spacing ($\tau_2/2$) and the symmetry lines 'rotate' in a direction opposite to ω_2 as k increases. Therefore,

$$\Phi_2 = \varphi_2 - (k-1)\ \tau_2/2 = \varphi_2 - (k-1)\,\pi/z_2 \qquad (24)$$

appears in unit vector $\underline{e}_2$, Eq. 12 instead of φ_2/z_2 is the number of teeth while the surface remains the same as th at used for calculation of the tooth chord. This means that Eq. 10 applies invariably while in Eq. 13 and Eq. 23, Φ_2 shall be written formally in place of φ_2.

The span measurement shall be calculated by means of parameter u, v, φ_1 satisfying both Eq. 10 and the modified Eqs 10 and 23 simultaneously, similarly to the chordal thickness (writing only W(k) in place of $\bar{s}_{a2}$ in the formula) while the position of the tangential point shall be verified by means of Eq. 15. Should r_{y2} fail to fall within the tooth surface suited for measurement, the value of k shall be changed. Usually more solu-

tions are obtained from among which that where the tangential point lies about in the centre of the tooth shall be kept.

The number of usable solutions may be limited also by the width of the gear. Inequality

$$b > W(k) \cdot \sin \beta_Y \tag{25}$$

shall be satisfied by all means. Here angle β_Y can be calculated in a way simpler than Eq. 18. Since in case of span measurement, the chord clamped and the normal are co-linear,

$$\sin \beta_Y = \frac{|\underline{n}_1 \underline{k}_2|}{|\underline{n}_1|} \quad . \tag{26}$$

5. Practical suggestions for computation

Parameter φ_1 is often contained in a transcendent form in the equation system defining the chordal thickness or the span measurement. The most practicable way of solution is decided by the actual equations. In the most unfavourable case, none of the parameters can be eliminated and e.g. in calculating for the chordal thickness, the procedure is, as follows:

Use reasonable polar co-ordinates to write the surface of member 1 because the assumed value of r_{y1} appears in place of x, y in Eqs 10 and 14 in this case. Assume $\varphi_1 = 0$ (the value of φ_1 being usually low, amounting to a few degrees only) and determine the missing parameter of the surface from Eq. 10 (this is possible only by iteration in general). The parameters so calculated ensure that the point will be a coupling point. Test then whether Eq. 13 for the chord is satisfied by the parameters. If not, change the value of φ_1 and note whether the left side of Eq. 13 approaches to zero. This is an instruction for a further change of φ_1. φ_1 shall be changed until Eq. 13 is satisfied to the required accuracy.

Because of the trigonometric functions in the equations, values associated with each other of quite a number can be found. φ_1 may be also negative and of course, also φ_2 will be negative in this case. Note that a solution of φ of lowest absolute value is required for calculation of the chordal thickness or span measurement.

Use of a computer is advisable for solution of the equation system

because the calculations are rather complicated. The computer not only speeds up calculation but it is advantageous also in that the calculation can be repeated with different input parameters more times or a programme can be assembled permitting the chordal thickness associated with the specified chordal addendum, $\bar{h}_{a2}$, or the ball size associated with given ball diameter, to be calculated e.g. by double iteration.

6. Application

The method to determine the chordal thickness and the span measurement presented here can be applied to any teeth confined by symmetric surfaces provided the conjugate pair of the tooth surface is known. This is the surface of the finishing tool or in case of conjugate pairs, the tooth surface of the mating-gear. In case of gears where the contact is theoretically point-like, it is always the tooth surface (generating surface) that shall be taken as a starting point.

An example is given to illustrate what has been said. In the example, the relationships required for determination of the chordal thickness and the span measurement are derived for the gear of convex teeth of a pair of Wildhaber-Novikov helical gears engaging with each other.

The profile of the tool applied to produce the tooth is shown in Fig. 5b /1/, the generating surface being a cylinder with a directrix lying in plane x_1y_1 and with generatrices parallel to axis z_1. The plane of action of the generating surface tangents the non-standard pitch cylinder of radius r_2 of the gear. The motion of system O_2 rotating along with the gear to be machined and system O_1 associated with the tooth surface is investigated in system O without subscript (Fig. 5a). System O_1 inclined through tooth inclination angle β moves in the direction of axis y at a constant velocity of $\underline{v}_1 = r_2 \frac{d\varphi_2}{dt} \underline{j} = r_2 \omega_2 \underline{j}$, its displacement being $r_2 \varphi_2$ in case of angular displacement φ_2 of the gear. The effective surface of the tooth is developed by a cylindric surface of radius ϱ. The generating surface in its own system:

$$\underline{r}^{(1)} = \begin{bmatrix} r_2 + \varrho \sin\vartheta & -b_1 + \varrho\cos\vartheta & u \end{bmatrix} . \tag{27}$$

With surface Eq. 27 transformed into the stationary system,

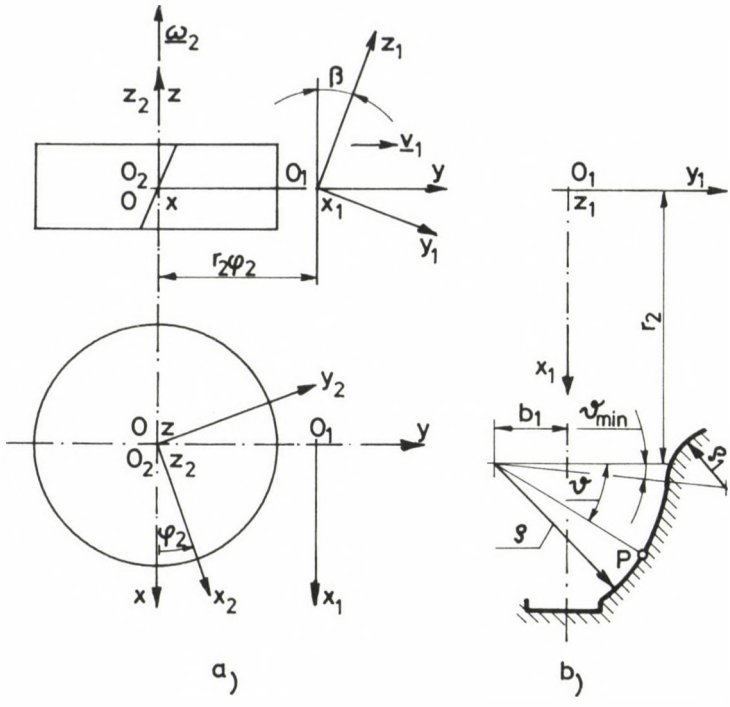

Fig. 5.

$$\underline{r} = \begin{bmatrix} r_2 + \varrho \sin\vartheta \\ u.\sin\beta + (\varrho\cos\vartheta - b_1)\cos\beta + r_2\varphi_2 \\ u.\cos\beta - (\varrho\cos\vartheta - b_1)\sin\beta \end{bmatrix} \tag{28}$$

is obtained. $\underline{r}(u, \vartheta, \varphi_2)$ is the family of surfaces while in a fixed position φ_2, $\lambda\underline{n} = \frac{\partial\underline{r}}{\partial u} \times \frac{\partial\underline{r}}{\partial u}$ is the normal where $\lambda \neq 0$ is the norming factor. After differentiation and multiplication,

$$\underline{n} = \begin{bmatrix} \sin\vartheta & \cos\beta\cos\vartheta & -\sin\beta\cos\vartheta \end{bmatrix}. \tag{29}$$

For determination of the relative velocity, we use that $\underline{v}_2 = \underline{\omega}_2 \times \underline{r}$ where $\underline{\omega}_2 = \omega_2 \underline{k}$. Thus

$$\underline{v}_{12} = \underline{v}_1 - \underline{v}_2 = 2 \begin{bmatrix} u\sin\beta + (\varrho\cos\vartheta - b_1)\cos\beta + r_2\varphi_2 \\ -\varrho\sin\vartheta \\ 0 \end{bmatrix}$$

Equation of engagement according to relationship $\underline{nv}_{12} = 0$:

$$u \sin\beta + r_2 \varphi_2 - b_1 \cos\beta = 0 \quad . \tag{30}$$

Direction of the symmetry line as a function of the number of flanked teeth clamped:

$$\underline{e}_2 = \left[\cos\Phi_2 \ \sin\Phi_2 \ 0\right] , \tag{31}$$

where, according to Eq. 24, $\Phi_2 = \varphi_2 - (k-1)\ \tau_2/2$. Using vectors Eq. 28, Eq. 29 and Eq. 31, equation $\left[\underline{r}\ \underline{n}\ \underline{e}\right] = 0$ for span measurement can be written in detail

$$r_2 \sin\beta \ . \cos\vartheta \ (\sin\Phi_2 - \varphi_2 \cos\Phi_2) + b_1 \sin\beta \ . \sin\vartheta . \sin\Phi_2 +$$

$$+ u\,(\cos\beta . \sin\vartheta . \sin\Phi_2 - \cos\vartheta . \cos\Phi_2) = 0 \quad . \tag{32}$$

If $\Phi_2 = \varphi_2$ in the Eq. 32, the equation suited for calculation of the chordal thickness will be obtained. With parameter u eliminated, transcendent equation

$$(\tan\vartheta . \tan\varphi_2 - \cos\beta)\ (r_2\varphi_2 \cos\beta - b_1) - r_2 \sin^2\beta . \tan\varphi_2 = 0 \tag{33}$$

is obtained for φ_2.

The end point of the chord lies on a cylinder of radius r_{y2} and the radius of the cylinder can be determined on the basis of co-ordinates x and y of surface Eq. 28. Because of the special position of systems 0 and 0_2, $r_{y2}^2 = x_2^2 + y_2^2 = x^2 + y^2$. If parameter u is eliminated using Eq. 30 in co-ordinate y,

$$r_{y2} = \sqrt{(r_2 + \varrho\sin\vartheta)^2 + (\varrho\cos\beta . \cos\vartheta)^2} \quad . \tag{34}$$

This relationship shows for which radius r_{y2} of which cylinder the point transformed by the point of parameter ϑ of the basic profile is found. The radius of the limit circle for ϑ_{min} indicated in Fig. 5b can be calculated from Eq. 34. With the radius of the addendum circle written in the relationship in place of r_{y2}, the largest parameter, ϑ_{max}, of the active profile can be determined.

In calculation of the chordal thickness of the tooth, proceed, as follows:

Assume a mean value for ϑ in the range of $\vartheta_{min} \ldots \vartheta_{max}$ and determine the value of φ_2 on the basis of Eq. 30 and then the chordal thickness and the chordal addendum on the basis of relationships Eqs 16, 17 for this.

Another possible way of calculation is to assume r_{y2} and to determine ϑ on the basis of Eq. 34 while φ_2 on the basis of Eq. 33 and so on.

To calculate the span measurement, write equation $\underline{n}\,\underline{e} = 0$ expressing perpendicularity of the normal and the symmetry line:

$$\sin\vartheta \cdot \cos\Phi_2 + \cos\beta \cdot \cos\vartheta \cdot \sin\Phi_2 = 0 \quad . \tag{35}$$

Parameters u and ϑ can be eliminated from Eqs 30, 32 and 35 available. After rearranging and transformation, transcendent equation

$$\tan^2\beta \cdot \sin\Phi_2 \cdot \cos\Phi_2 - \frac{b_1}{r_2\cos\beta} + \varphi_2 = 0 \tag{36}$$

is obtained. Remember: $\Phi_2 = \varphi_2 - (k-1)\ \tau_2/2$ and thus the number of teeth clamped is contained in Eq. 36. With k = 2, 3, ..., try to find the solution for φ_2, then determine parameters ϑ and u for every φ_2 on the basis of Eq. 35 and Eq. 30. With the value of parameters φ_2, ϑ, u associated with a selected k substituted into Eq. 28 again, the contact point of the micrometer used for span measurement and the tooth surface and from Eq. 34, radius r_{y2} are obtained. From among the solutions, only that where r_{y2} falls between the limit circle and addendum circle of where inequality $\vartheta_{min} < \vartheta(k) < \vartheta_{max}$ is satisfied for ϑ associated with k is satisfied is measurable. More values of this type offer themselves in general from among which that most approximating the arithmetic mean of ϑ_{min} and ϑ_{max} shall reasonably be selected.

Finally, verify on the basis of the calculated span measurement whether the width of the gear is sufficient. According to Eq. 26, $\sin\beta_Y = \sin\beta \cdot \cos\vartheta$ that is

$$b > W(k)\ \sin\beta \cdot \cos\vartheta \quad .$$

Assume a gear where

$z_2 = 9$,
$m_n = 8$ mm,
$\beta = 30^0$,

r_2 = 41.5692 mm,
r_a = 51.170 mm,
b = 80 mm

(see notation), the basic profile specifications being

ϱ = 1.5 m_n = 12 mm,
ϑ_{min} = 5°40',
b_1 = 0.529037 m_n = 4.232296 mm.

From equation 34 ϑ_{max} = 49.75° for r_{a2}. Assume ϑ = 25° and determine the value of φ_2 from Eq. 33. Omitting the details of calculation, $\bar{\varphi}_2$ = 0.087042 and thus

$$\bar{s}_{a2} = 12.473 \text{ mm}, \qquad \bar{h}_{a2} = 3.887 \text{ mm}.$$

Maximum number of teeth in the span: k_{max} = Int (z_2/2) (integer part of half of the tooth number). The solutions of Eq. 36 and the results calculated are tabulated below:

k	$\hat{\varphi}_2$(rad)	ϑ(°)
2	0.1745598	8.681
3	0.2481206	22.702
4	0.2840652	39.635

It can be seen that the contact point lies near the fillet and therefore k = 3 shall be selected. Here the radius associated with the end point of the chord is r_{y2} = 47.185 mm, the theoretical span measurement being W(3) = 64.758 mm. The width of the gear is sufficient because b > W(3) $\sin\beta \cdot \cos\vartheta$ = 29.870 mm.

Since the main radii of curvature of the conjugate surface /1/,

$$R_1 = \frac{r_2}{\sin\vartheta \cdot \sin^2\beta} + \varrho \quad \text{and} \quad R_2 = \varrho \ ,$$

are of identical sign, the surface consists of elliptic points. Hence, a common tooth caliper and a micrometer with flat (jaws) can be used for the measurement.

REFERENCES

1. Litvin, F.L.: Theory of engagement of gears, Műszaki Könyvkiadó, Budapest, 1972
2. Tatár, I. Chordal thickness of symmetric teeth, Manuscript
3. Tatár, I.: Chordal thickness and span measurement of helical gears, Manuscript

Acta Technica Acad.Sci.Hung., 101(4), pp. 397–416 (1988)

ANALYSIS OF GEAR TEETH CONTACT BY THE FINITE ELEMENT METHOD

VÁRADI, K.* - POLLER, R.**

(Received: 18 April 1989)

Contact of machine parts such as gears may require complicated investigations because of the high load in a relatively narrow contact area comparing with the bulk of the bodies. Here a numerical algorithm based upon the "coefficient matrix" theory and the results of a previous FEM analysis is presented as a solution of the contact problem between spur gears where the surface roughness and the rotating approach of the contacting teeth is taken into consideration. Contact pressure distribution, rigid and elastic body motion, as well as the size of the contact area are calculated at different loads. Having these also the stress and strain state throughout the contacting teeth is given including the subsurface and bending stresses. It is shown according to other investigations in contact mechanics that the initial gap essentially affects the contact state so the surface finish of spur gear teeth is important.

The traditional, approximate analysis of the contact state of cylindrical gears is based upon the Hertzian contact theory (see, e.g. in /1/). For the reckoning of the real state of contact between the meshing teeth (e.g. profile error, corrugation and/or surface roughness, the expectable state of friction, wear etc.), such contact algorithms are required which contain essentially fewer approximate assumptions.

First, let the assumptions of the Hertzian contact theory be surveyed from the aspect of real contact between the meshing teeth:

a) The theory of small deformations is in force.

The assumption remains valid since the arising displacements are smaller by an order of magnitude than the dimensions of the teeth.

b) The surfaces of the bodies may be represented by quadratics in the surrounding of the contact area.

The dimensions of the contact area are essentially smaller than those of the teeth, consequently, in the case of an involute profile, the replacing quadratic surface involves a negligibly small error. The effect of the profile error, corrugation and/or surface roughness should not be taken into consideration. The contact theory of the bodies bounded by non-quadratic sur-

*Váradi, Károly, H-1118 Budapest, Torbágy u. 8, Hungary

**Poller, Rudolf, H-1041 Budapest, Szigeti József u. 25, Hungary

Akadémiai Kiadó, Budapest

faces is amazingly rich (see, e.g. /1/). A part of those was developed for the contact state of roller bearings to be analyzed (e.g. /2, 3/ etc.).

c) The system of forces distributed among the bodies is of normal direction.

Except the small surroundings of point C (pitch-point), there is a considerable slide arising on the contact surface of the meshing teeth; consequently, in addition to the distributed force system of normal direction, there occurs a tangential force system, too. The real state of friction is influenced also by the presence of lubricant. Consequently, instead of analysing the "dry" friction state, the analysis of the boundary and complete lubrication state is required. In these theories of contact friction, the liquid friction state is examined on the basis of EHD lubrication theory. On the basis of contact pressure distribution and the slide parameters, the loss-power developing along the contact region /4, 2/, and, in turn, the heat release, too, can be determined numerically.

d) The material of the bodies in contact is homogenous and isotropic, and it obeys Hooke's law.

From among these assumptions, the assumption of the linearly elastic material-law is opposed to the fact that plastic deformation and wear occur in the surroundings of roughness peaks on the surface of real teeth. The wear process — owing to its complexity — is often analysed on the basis of experiments, measurements /5/, or else, by means of approximate models /6/.

e) The surface of the bodies is perfectly smooth. The dimensions of the contact region are essentially smaller than those of the meshing teeth; as for its order of magnitude, it is commensurable with the surface roughness. The initial gap between the bodies in contact (which is often equal to some microns) is directly commensurable with the surface roughness of teeth.

The experimental and numerical analyses of the bodies in contact having rough surfaces are dealt with, e.g. in /7, 8, 9/.

f) The displacements of the points in contact can be calculated from the problem of the elastic infinite half-space (half-plane) loaded by distributed force system.

In the case of meshing teeth, the deflection of the teeth is considerable, it can be even greater than the local elastic deflection /10/. The model of the infinite half-space (half-plane) is suitable only for the analysis of local elastic deflections.

g) The elastic displacement of the contact region points coincides with the direction of the rigid-body displacement of the bodies.

The direction of the rigid-body displacement of the meshing teeth is determined by the angular displacement of the gears. These directions do not coincide with the common normal of the meshing teeth /11/.

h) The contact pressure distribution is proportional to the ordinates of a semi-ellipsoid.

This condition is fulfilled for the bodies bounded by quadratic surfaces. In case of profile error, corrugation and/or surface roughness, the arising pressure distribution is built up differently.

In the past decades, a number of such contact algorithms were developed which contain essentially fewer assumptions than the Hertzian ones /1/, ... /11/. While with the spreading over of the computational technique, such numerical contact procedure have emerged due to which all the Hertzian assumptions can be omitted theoretically (e.g. /1, 2, 6/ etc.). In a portion of those the finite element method is also used.

The analysis of the state of contact between the meshing teeth is treated in a number of publications, too, analysing the wear process from experimental aspect in each case individually. See, e.g. publications /5, 12/ and /13/. In the course of experimental examinations, the variation in surface roughness is measured during the running-in period in /14/.

1. Coefficient-matrix solution to contact problems

One of the most widespread methods of the numerical solution to contact problems is represented by the procedure based upon the coefficient-matrix /1/. Let this method be summarized according to Fig. 1. The position of the initial point-contact between the two bodies is visualized by a thin line. Due to the load applied, the two bodies are shifted into the position indicated by dashed line, while they perform a "rigid-body" displacement of magnitude δ, and in this way, the contact region of indicated width will be developed, within which the contact pressure distribution will be built up. In Fig. 1a, – for the sake of better visualization of contact relationships – the deformed shape of the two bodies in a state "stretched" to distance δ is indicated by a thick line, whereas the contact pressure distribution is going on to act upon the two bodies. In Fig. 1a, the gap between the couple of points in contact indicated by symbol i is equal to

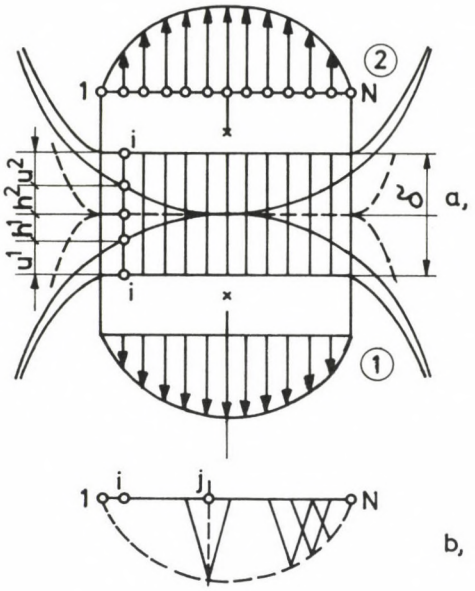

Fig. 1. Geometric condition of contact

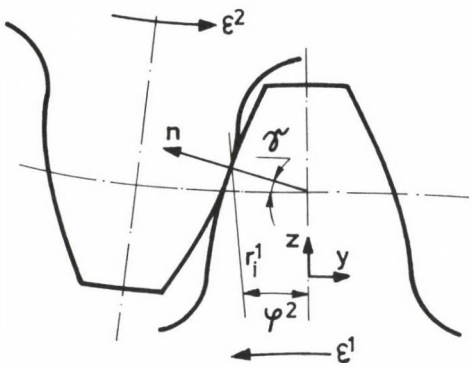

Fig. 2. Contact of gear teeth

$h_i^1 + h_i^2$. Here, h_i^1 and h_i^2 represent the distance of the points positioned on body No. 1 and No. 2, respectively, as measured from the common tangent. Let the elastic displacement of the points be designated by u_i^1 and u_i^2.

The geometric condition of contact expresses that the rigid-body displacement between the contacting bodies is in accordance with the sum of the initial gap and the elastic displacements in all points of the contact area, i.e.

$$\delta_i = u_i^1 + h_i^1 + h_i^2 + u_i^2 \quad (i = 1, \ldots, N) \quad . \tag{1}$$

The equation of the contact stress in the inner points of contact area is:

$$p_i > 0 \quad , \qquad (1 < i < N) \tag{2}$$

while in the initial and terminal points of the contact region, it is:

$$p_1 = 0 \qquad \text{and} \qquad p_N = 0 \tag{3}$$

During the contact of cylindrical gears, the direction of the rigid-body displacement does not coincide with that of the elastic displacement of the points in contact, therefore, the geometric equation of contact should be written vectorially /11/.

In the case of cylindrical gears, "rigid-body" displacement δ_i can be interpreted like this:

$$\delta_i = r_i^1 \varepsilon^1 \cos(\varphi^1 + \gamma^1) + r_i^2 \varepsilon^2 \cos(\varphi^2 + \gamma^2) \tag{4}$$

where r_i^1 is the radius of the nodal point of symbol i positioned within the contact area (Fig. 2) as measured from the centre of the gear, while ε^1 is the "rigid-body" angular displacement of the gear of symbol 1. The angle setting the direction of the normal is γ^1, while φ^1 is the angle between the point in contact and axis z. Symbols r_i^2, ε^2 and γ^2 can be interpreted similarly. (In case of gears, "rigid-body" displacement δ_i can be derived from the "rigid-body" angular displacements.) Let it be assumed for the ratio of ε^1 and ε^2 that it is identical with the ratio of displacements belonging to the unit pressure profiles acting on the middle of the contact area of the two teeth.

Elastic displacement u_i of the points in contact can be derived analitically or numerically; e.g. with the use of finite element method /5/.

Elastic displacement u_i in body No. 1, as indicated in Fig. 1, arises by the effect of contact pressure distribution p_j ($j = 1, \ldots N$). It is the same case with u_i^2. These elastic displacements can be produced on Cauchy's superposition theorem so that the pressure distribution is resolved into parts, and their effects exerted on the displacement are summed up then. As it can be seen in Fig. 1, triangular pressure distributions are used, the sum of which (the section-wise linear pressure function) yields the required pressure distribution with a good approximation. Consequently, the elastic displacement of point i can be derived in a way that the individual displacements resulting from the single pressure distributions are taken, and they are, in turn, summed up. Let w_{ij} denote the displacement of nodal point i caused by the triangular unit pressure distribution contained in j. With the knowledge of the effect of each pressure distribution exerted upon the displacement in nodal point i, it can be written that

$$u_i^1 = \sum_{j=1}^{N} w_{ij}^1 \, p_j \qquad (i = 1, \ldots N) \tag{5}$$

Quite similarly, u_i^2 can be derived on the basis of w_{ij}^2. Geometric equation (1) of the contact, after the corresponding substitutions, will be:

$$r_i^1 \; \varepsilon^1 \cos(\varphi^1 + \gamma^1) + r_i^2 \; \varepsilon^2 \cos(\varphi^2 + \gamma^2) =$$
$$= \sum_{j=1}^{N} (w_{ij}^1 + w_{ij}^2) \, p_j + h_i^1 + h_i^2 \qquad (i \; (\; 1,\ldots N) \tag{6}$$

Let the sum of the coefficient-matrix of the two bodies be designated by symbol w_{ij}, while its inverted by symbol $(w_{ij})^{-1}$. Accordingly, after rearranging equation (6), the following is yielded:

$$p_j = \sum_{i=1}^{N} (w_{ij})^{-1} (r_i^1 \; \varepsilon^1 \cos(\varphi^1 + \gamma^1) +$$
$$+ r_i^2 \; \varepsilon^2 \cos(\varphi^2 + \gamma^2) - h_i^1 - h_i^2) \tag{7}$$

On the basis of coefficient-matrix w_{ij}, or initial gaps h_i^1 and h_i^2 received from its inverted, the contact pressure distribution arising in case of

given δ_i can be calculated according to (7). Let equation (7) be written for the case i = 1 and i = N, with equation (3) taken into consideration, as follows:

$$p_1 = \sum_{i=1}^{N} (w_{1i})^{-1}(r_i^1\ \varepsilon^1 \cos(\varphi^1 + \gamma^1) + r_i^2\ \varepsilon^2 \cos(\varphi^2 + \gamma^2) - h_i^1 - h_i^2) = 0$$

$$p_N = \sum_{i=1}^{N} (w_{Ni})^{-1}(r_i^1\ \varepsilon^1 \cos(\varphi^1 + \gamma^1) + r_i^2\ \varepsilon^2 \cos(\varphi^2 + \gamma^2) - h_i^1 - h_i^2) = 0 \qquad (8)$$

The coefficient-matrix solution algorithm for contact problems can be used according to the following. Let the maximum possible contact area be assigned on both bodies, then in the nodal point within those, let the unit triangular pressure distributions act, and then coefficient-matrices w_{ij}^1 and w_{ij}^2 should be generated with the help of the finite element method.

Afterwards, the initial point of the contact area is assumed within the maximum possible contact area, and the terminal point of the contact area is searched on the basis of relationship (8). Finally, the contact pressure distribution can be directly calculated from (7).

The coefficient-matrix can be generated during a single run by the finite-element program packages suitable for taking more loading cases into consideration.

In the course of the analysis of contact problems, the resultant load to be transferred between the two bodies is often given. In this case, the above calculations should be repeated starting from different initial points, and in this way, the pressure distribution the resultant of which approximates the resultant load to be transferred as close as possible can be received.

In case of discrete (detached) contact areas, the above procedure should be applied to each of those individually, with the fact taken into consideration, that in this case, too, the rigid-body displacement is common for the individual bodies in contact.

2. The contact state of teeth of ideal geometry

The following analyses are carried out for the contact of cylindrical gears having tooth number $z_1 = z_2 = 21$ and module $m = 6$. The load on gear drive is 1280 N. The length of the contact area is $2b = 800\ \mu m$, and the maximum of the contact pressure is $p_{max} = 2050\ N/mm^2$ calculated according to the Hertzian theory. (Similar data were used in the course of measurements and analyses in /13/. In this way, we can rely directly on the measurements concerning the surface roughness in the following chapters.)

The finite element meshes (Fig. 3) were assumed with respect to the requirement that sufficient nodal points should be positioned within the contact area. It is advisable to maintain a dense mesh below the contact area because the state of stress in the surroundings of the contact area reaches its maximum at a certain depth below the contact area. Symbols B, C and D in Fig. 3 mark out the region of single tooth-pair meshing, while points A and E indicate the boundaries of the multi-tooth-pair meshing.

In the course of generating the coefficient-matrix, first the displacements belonging to the triangular unit pressure distributions of normal direction acting individually on the 21 characteristic nodal points were determined, then the orthogonal (normal) projections were formed from the former.

In Fig. 4, the contact pressure distribution between points C-C is shown, as well as the initial gap between the two teeth. The initial gap corresponds to the quadratic surfaces replacing the involute profile. The maximum deviation in the contact pressure distribution as compared to that calculated according to Hertz comes to max. 2%. The present procedure taking into consideration even the deflection of teeth yields an essentially different result as for the rigid-body displacement of the bodies in contact is concerned, nevertheless an identical result is received for the contact pressure distribution due to quadratic surfaces.

The state of stress below the contact area is shown in Fig. 5. In Figs 5a and 5b, the sub-surface stresses as resulting from the optical stress analysis, or else from the present calculations can be seen, while in Fig. 5c, the reduced stresses below the contact area are shown. The sub-surface stresses deviate only by a few %-s from the corresponding results in /1/.

In the case of the teeth meshing in points B-D or A-E, respectively, the Hertzian contact pressure distribution remains similarly unchanged.

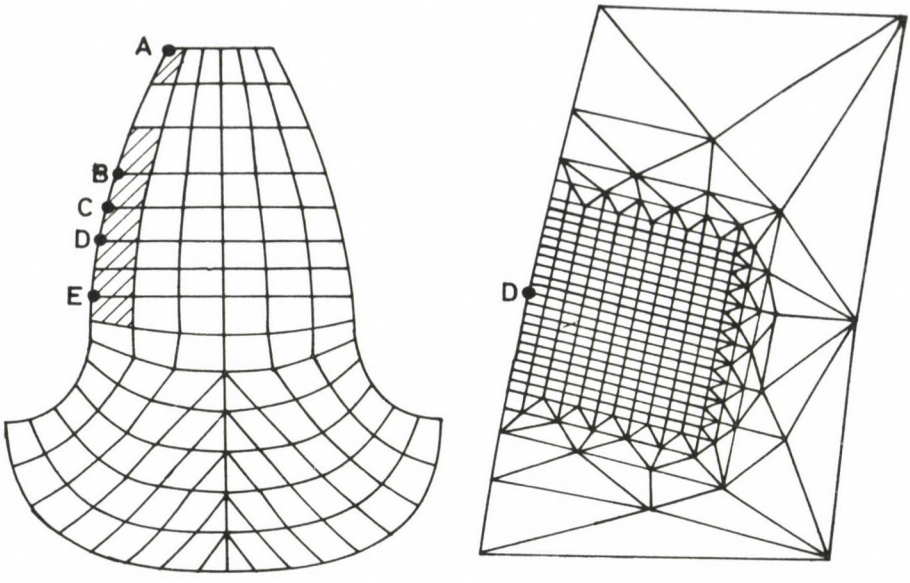

Fig. 3. Finite-element mesh of teeth and the environment of point D, as an example

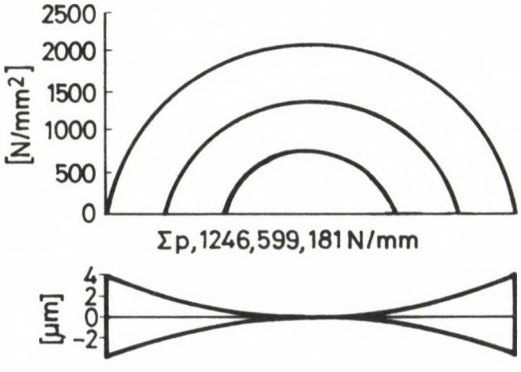

Fig. 4. Contact pressure distribution between points C-C

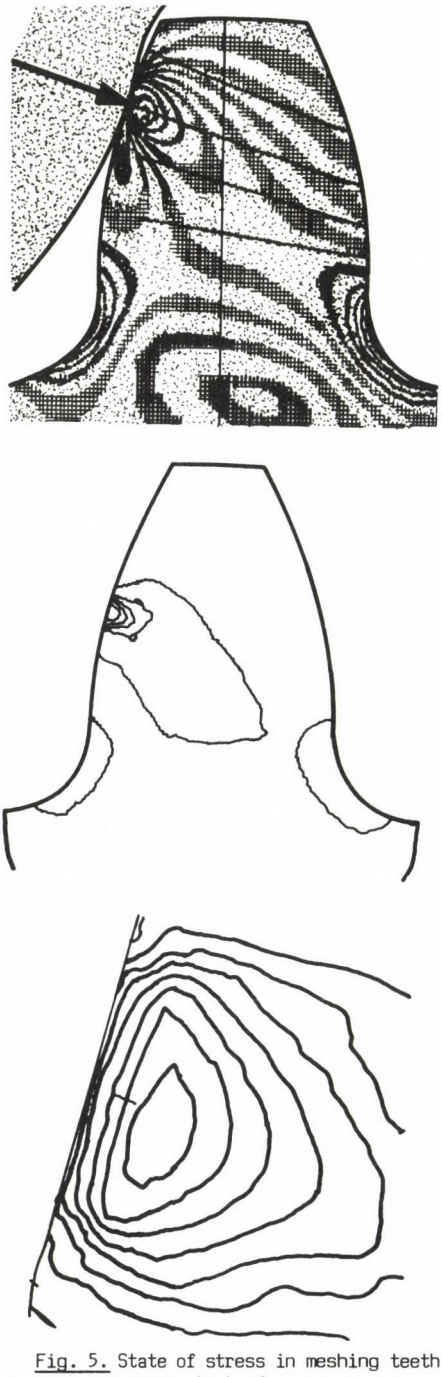

Fig. 5. State of stress in meshing teeth
a) according to optical stress analysis /16/; b) reduced stresses according to von Mises;
c) reduced stresses below the contact region according to von Mises

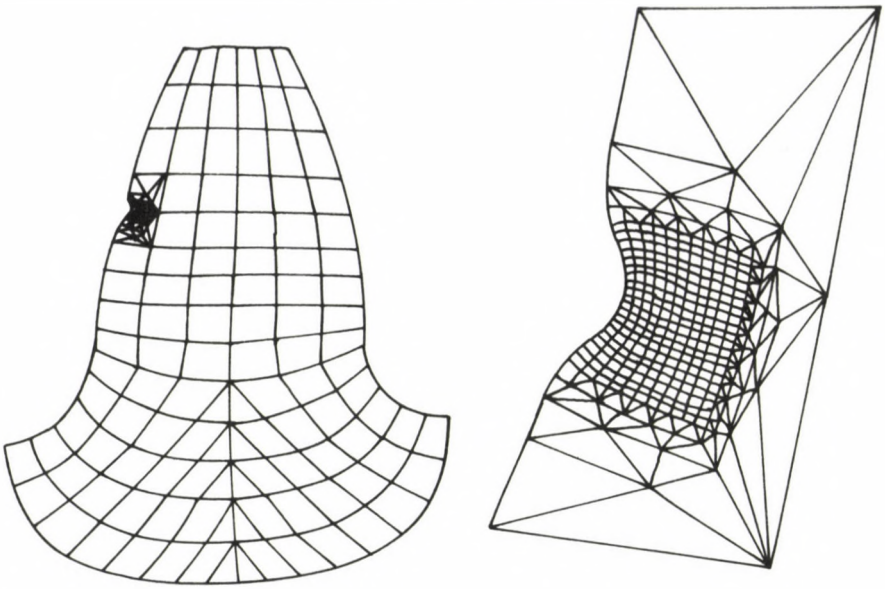

Fig. 6. Displacements arising by the effect of the contact pressure distribution acting in the environment of C (in a 50-fold enlargement)

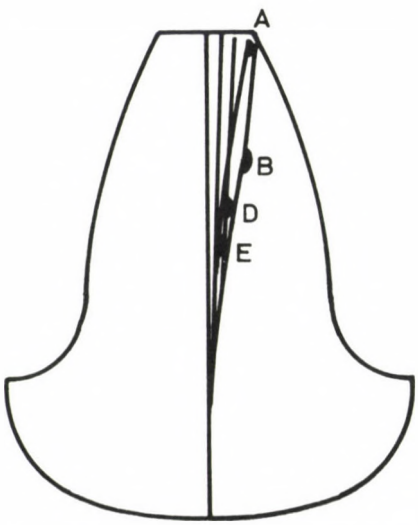

Fig. 7. The displacements of tooth centre-line, as well as the environment of the contact region in cases of A, B, D and E (in a 50-fold enlargement)

Owing to the deflection of teeth, the centre of the contact area will be shifted from its initial point-contact position during loading, nevertheless in the new position neither the involute profile nor the radius of curvature of the quadratic surfaces replacing the former will practically change due to the small distance. There is an essential deviation in the rigid-body displacements owing to the deflection of teeth (Fig. 7).

In Fig. 6, the joint effect of the tooth deflection and the elastic surface deformation is shown in the surroundings of point C. The concave character of the contact area is brought about by the enlargement of displacements.

In Fig. 7, the displacements in the surroundings of meshing points A, B, D and E are summarized, and besides, the centre-line of the driving tooth is also indicated.

3. The effect of the real surface (profile error, surface roughness, wear etc.) upon the state of contact

The machined tooth surface is rough and deviates essentially from the perfectly smooth surface considered as ideal. Due to the wear caused by repeated loads, the original initial surface is subject to changes. According to experiences, the surface roughness generally becomes more favoruable (smaller) during the running-in period (the roughness peaks wear off), while later on, surface fatigue occurs at places (e.g. "grey stains", cracking, pitting formation etc.) /12, 13, 14/.

The quality of the initial surface can be influenced by more exact machining and the reduction in surface roughness, while the fatigue process (first of all, the fatigue wear) depends on the state of lubrication, too. It is essential to know whether the EHD oil film will develop or not between the teeth.

The effectiveness of EHD lubrication state is most often decided upon on the basis of the ratio of minimum oil film thickness h_o and equivalent surface roughness R_e. If this ratio is greater than 4, then the state of fluid friction will develop, while on the contrary, mixed lubrication, or boundary lubrication, respectively, will occur according to Fig. 8. According to /12/, the average surface roughness of the ground teeth most often is: $R_a = 0.5\ \mu m$, and the developing minimum thickness of the oil film is: $h_o = 0.2, \ldots, 0.8\ \mu m$. As a consequence, it can be calculated that the

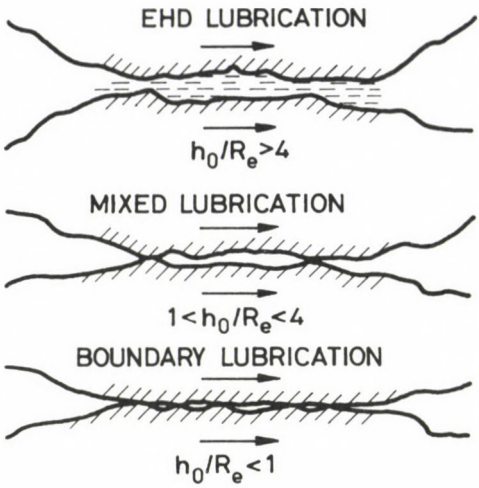

Fig. 8. Interpretation of different states of friction

friction interfaces are not perfectly separated from each other by the EHD oil film.

In the state of mixed lubrication, the contact pressure distribution remains essentially unchanged in comparison to the state of dry friction (boundary lubrication), consequently, the same mechanical models can be used with the difference that the friction coefficient of the mixed lubrication is smaller (instead of 0.1 – 0.15, it is 0.06). Naturally, the state of mixed lubrication is essentially more favourable in practice than the dry friction, but at the same time, it does not reach the favourable life-increasing effect of the fluid friction state (see, EHD technical literature).

Now, let the measurement result be considered first, as given in /13/. In Fig. 9, the shape of the tooth surface is shown in its original state and in the course of a repeated load-cycle number 10^7. In the section enlarged, the profile error can be seen well together with the individual contact positions examined. In the further parts of Fig. 9, the contact pressure distribution built up in the individual positions is shown together with the pressure distribution between the corresponding ideal surfaces. It can be stated that the contact pressure distribution and the subsurface stress state will be modified depending on the width and depth of the profile error. It is likely that the vibration-exciting dynamic effect of the profile error is much more unfavourable than that above.

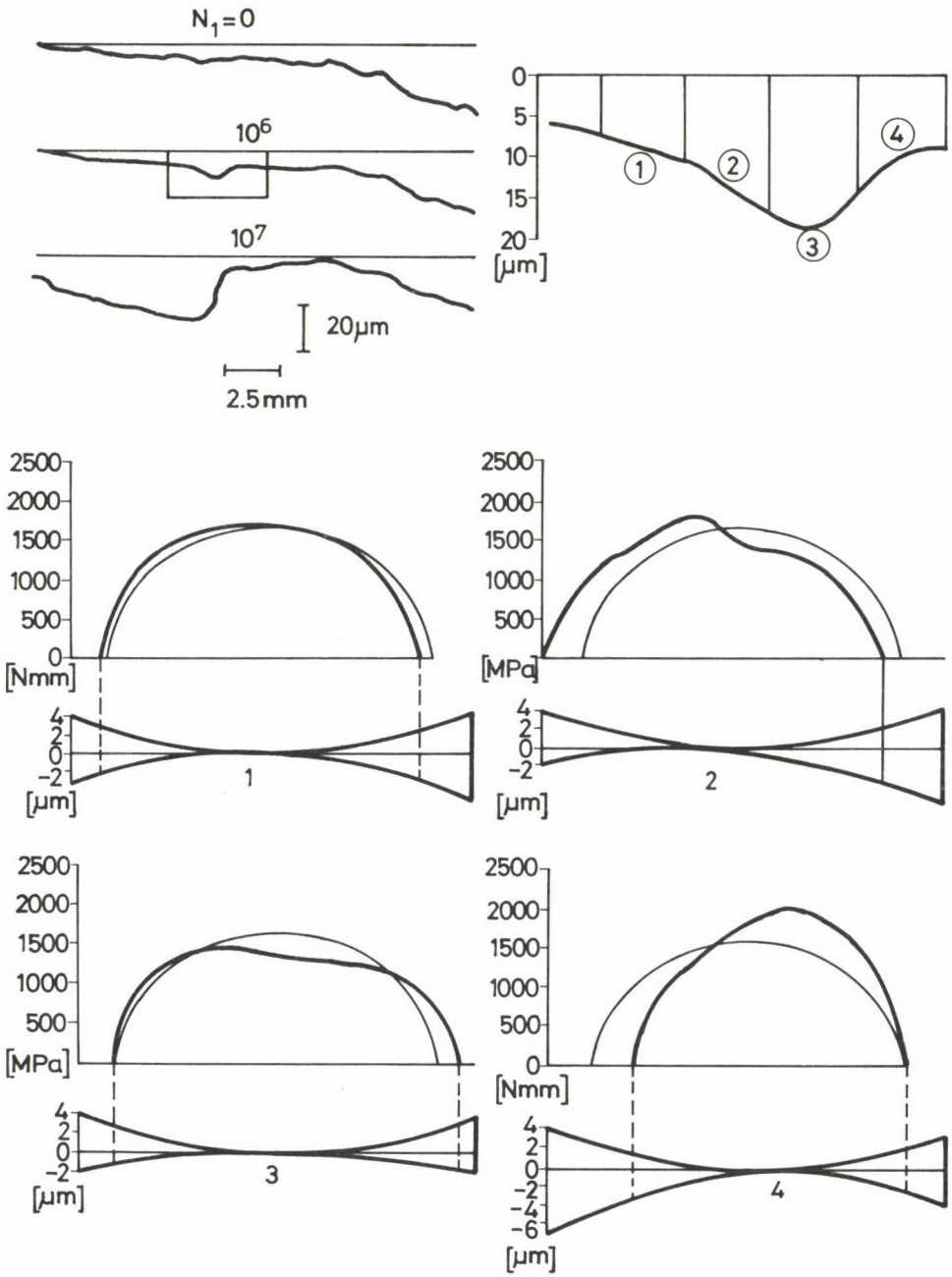

Fig. 9. Profile error produced by the effect of repeated stress-cycles, and the contact pressure distributions developed there

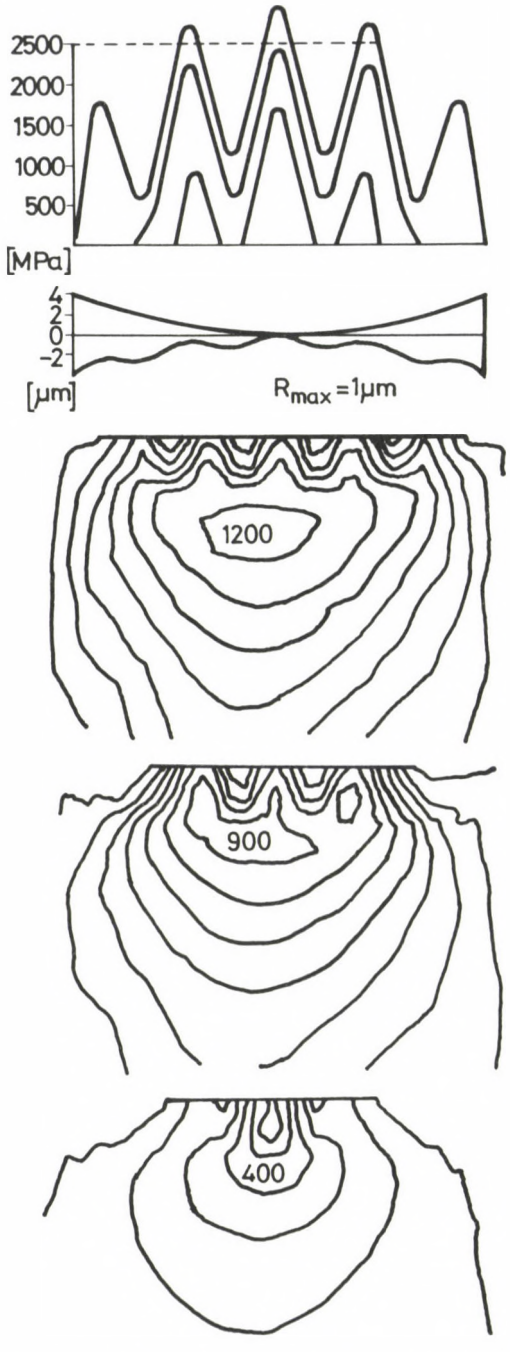

Fig. 10. Contact pressure distribution and reduced stress contours for different loads in case of R_{max} = 1 μm

Now let us change over to the analysis of surface roughness. In the technical literature, there are a lot of models available for the approximate or relatively exact analysis of the interaction between the rough surfaces and the contact state (e.g., one of the chapter in /13/, further on papers /8, 9/ etc.). Surface roughness is simulated most frequently by sine-waves, and these sine-waves are superimposed on the ideal surface. The contact surface of the other body is generally ideally smooth. Johnson, Greenwood, Higginson /17/ examine the contact state of regular-wave surfaces, too, in one- and two-dimensional cases. Kragelszkij /5/ analyses the contact of rough surfaces in an experimental way and with the help of approximate models. It is stated that local plastic regions are formed in the small environment of the roughness peaks even in case of relatively low load. In this paper, the cases of partial and total contacts are also interpreted. Wear process is analysed, and the quantity of worn-off material (debris) is measured in an experimental way by a lot of scientists; thus, the wear process and the factors effecting them (e.g., surface roughness, lubricant etc.) are graded /14/.

In the following, let the coefficient-matrix contact procedure be applied to the contact interfaces shown in Fig. 10. The contact surface of one of the bodies should remain ideal, while on the contact surface of the other one, the rough surface should be replaced by sine-waves within the maximum contact area. Let the expected contact pressure distribution be determined along the contact area of maximum dimensions, as well as for low loads. In Fig. 10, the contact pressure distributions, the resultant forces, as well as the stress contours reduced according to von Mises and characterizing the subsurface stress state are shown in case of $R_{max} = 1\ \mu m$. In all the three cases, these contours follow truly the character of the contact pressure distribution (i.e., the initial gap) directly below the surface, while in the depth where the maximum number of the contours can be found for ideal surfaces, the effect of surface roughness can be detected no longer. In the course of the running-in period, when plastic deformation and wear occur in the environment of surface roughness peaks, the state of stress depending on the surface roughness changes essentially in a shallow depth below the surface. At the same time, the maximum of the reduced subsurface stresses (which can be found in this depth also with ideal surfaces) changes only to a small extent due to the fact that in the course of plastic deformation and wear, the dimensions of the contact region are subject to changes.

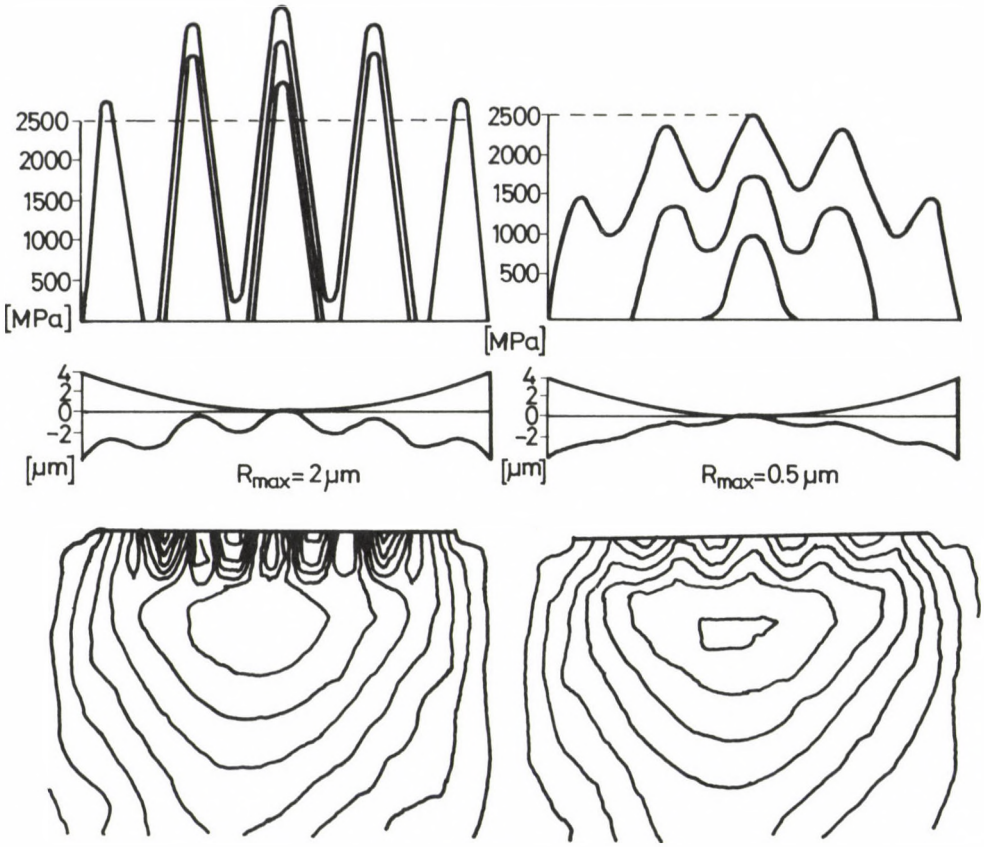

Fig. 11. Contact pressure distribution and reduced stress contours in case of different surface roughnesses

In Fig. 11, the cases of different surface roughnesses are shown with the roughness wavelength unchanged. The essentially deviating effect of surface roughnesses R_{max} = 0.5 μm and R_{mx} = 2 μm can be seen clearly. In the latter case, the maximum of the contact pressure is nearly 4000 N/mm^2, which pressure peak is unbearable for the surface with reversible deformations present, and in this way, a local plastic deformation develops in this small environment. This effect of surface roughness is verified also by experiments in a number of publications (e.g. /13/).

By the effect of permanent deformation and a more intensive wear occuring in the case of a greater surface roughness, a fraction of roughness peaks is abraded, and in this way, it can be imagined that after the running-in period, the state of contact becomes elastic again. One of the

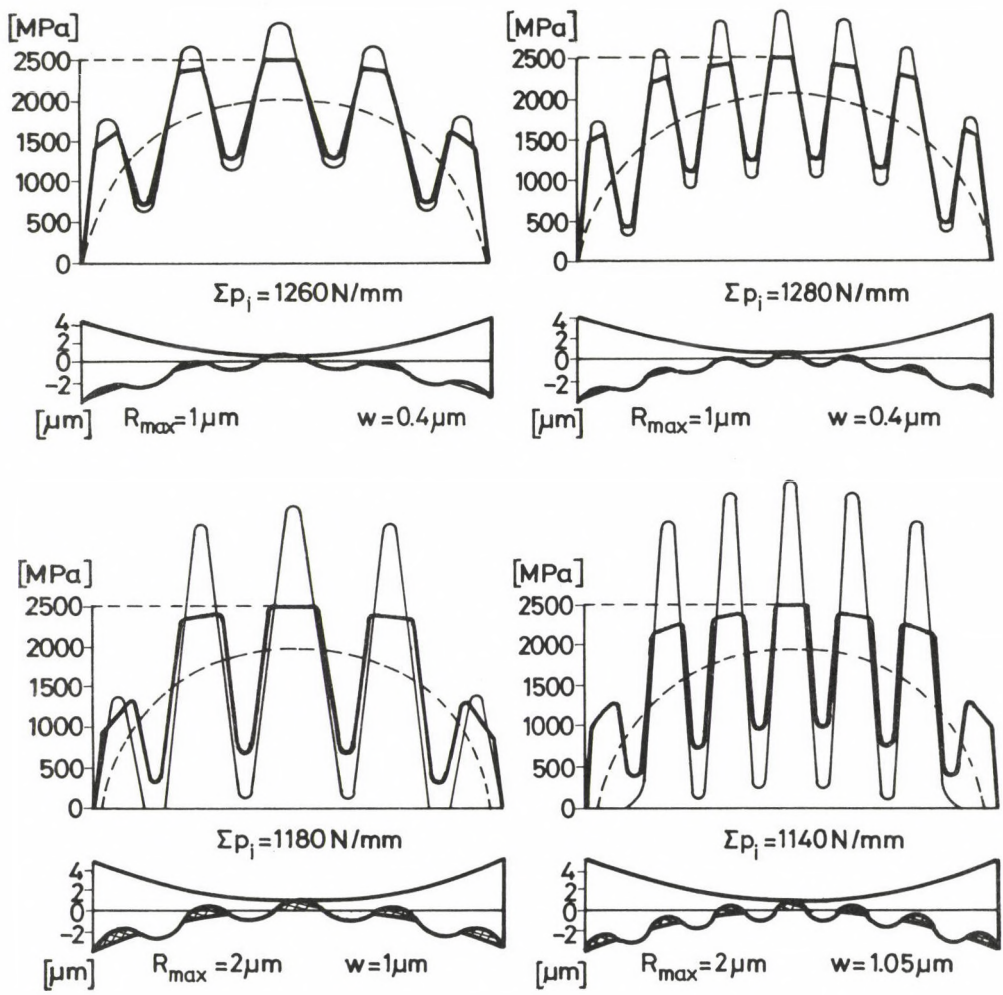

Fig. 12. Simulation of contact pressure distributions and wear in case of different surface roughnesses and roughness wavelengths

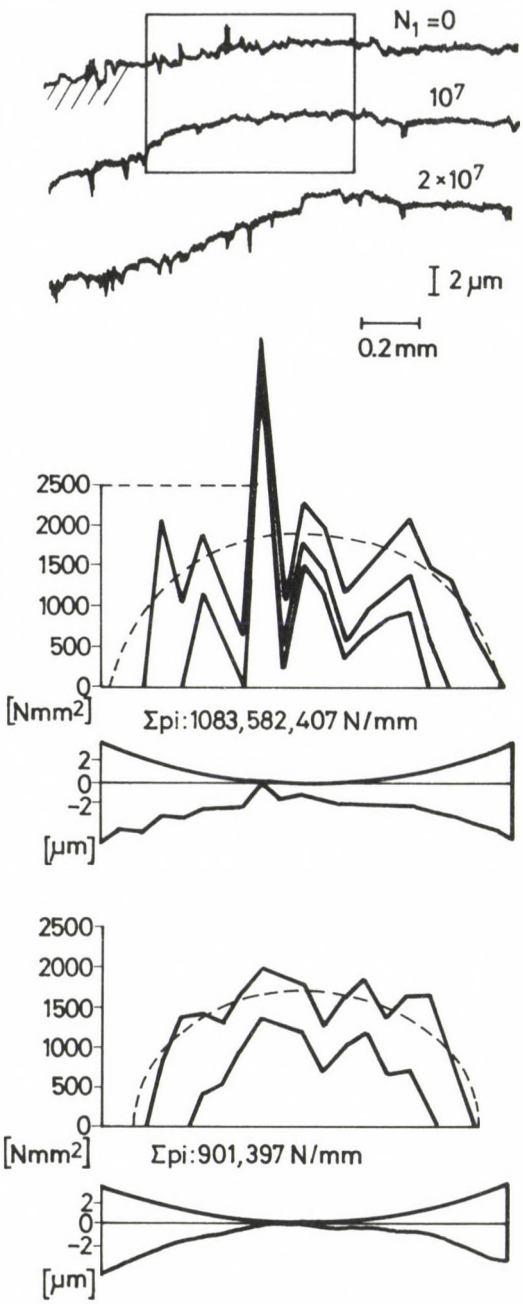

Fig. 13. Surface roughness (R_{max} = 2 µm) in /13/, and contact pressure distribution in case of different loads for the initial profile and for that worn to a small extent

conditions required for this is that the surface pressure should not exceed a critical value (e.g., p_{max} = 2500 N/mm^2). The critical surface pressure depends on the material, heat treatment etc. With this condition prescribed, and uniform wear (e.g., flattening) assumed, the reduction in the roughness height can be concluded for which the condition p_{mx} = 2500 N/mm^2 is fulfilled. In Fig. 12, an example of this is given in cases of two roughness wavelengths with surface roughness R_{max} = 2 μm and R_{max} = 1 μm. It can be stated that the contact state is not influenced essentially by the change in the roughness wavelength, while the role of the surface roughness height can be determined.

According to the Figs simulating the wear process, the width of the contact pressure peaks is nearly identical with the dimensions of the flattened wave-peaks. It can be seen that the minimum of the contact pressure is increased, and the contact area became wider.

The simulation of surface roughness by means of sine-waves serves for the purpose of introducing the phenomenon in principle. Further on, let the interaction between the real surface roughness and the contact pressure distribution be examined. The effect of the real surface roughness is analysed on the basis of the measurement results given in /13/. In Fig. 13, the measurement results are shown on the one hand, and the contact pressure distributions belonging to those for the initial tooth profile, and after 10^7 repeated stress cycles for the tooth profile developed by the effect of small-scale wear, on the other hand. It is very probable that after the wear-off of roughness peaks, a more favourable state of lubrication will be established, and at the same time, the subsurface stress state will be more favourable, too.

Conclusions

The coefficient-matrix process of the contact introduced here is suitable for the analysis of the contact state between the bodies of arbitrary shape, and among them, for the analysis of cylindrical gears, too.

In the course of calculations, the effect of the tooth deflection, profile error, corrugation and surface roughness can be taken into consideration, and the initial phase of the wear process can be traced on the basis of the simplified model.

It can be stated that the contact state of cylindrical gears are

essentially effected by surface roughness. A similar statement is made in /13/ as for the interaction between the surface roughness and surface fatigue.

This procedure is suitable for the analysis of interaction between most different surface roughnesses and the contact state.

REFERENCES

1. Johnson, K.L.: Contact Mechanics, Cambridge University Press, 1985
2. Mul, M.J. - Kalker, J.J. - Fredriksson, B.: The contact between arbitrarily curved bodies of finite dimensions, Transactions of the ASME, Journal of Tribology, January, 1986, Vol. 108, 140-148
3. Váradi, K.: Analysis of the pressure distribution in deep-groove ball bearings, Periodica Polytechnica, Vol. 26, No. 4, 203-221
4. Váradi, K.: Contact and friction state of single-row deep groove ball bearings, Publ. Tech. Univ. for Heavy Industry, Miskolc, Series C. Machinery, Vol. 40 (1983), 71-108
5. Kragelszkij, I.V. - Mihin, H.M.: Friction and wear calculation in engineering structures, Hungarian translation, Műszaki Könyvkiadó, 1987
6. Páczelt, I.: Analysis of the contact problem of elastic systems (in Hungarian), Dr. Sci. Techn. Thesis, Miskolc, 1981
7. Mirski, W. - Stupnicki, I.: Effect of surface roughness on the state of stress of solids in contact, Institute of Aeronautical Technology and Applied Mechanics Warsaw, Technical University
8. Francis, H.A.: The accuracy of plane strain models for the elastic contact of three-dimensional rough surfaces, Wear, 85 (1983), 239-256
9. Tangena, A.G. - Wijnhoven, P.J.M.: Finite element calculation on the influence of surface roughness on friction, Wear, 103 (1985), 345-354
10. Tobe, T. - Kato, M. - Inoue, K.: True stress and stiffness of spur gear tooth, Proc. of the Fifth World Congress on Theory of Machines and Mechanisms - 1979, 1105-1108
11. Poller, R. - Váradi, K.: Analysis of the geometrical condition of contact, Periodica Polytechnica, Mechanical Engineering, Vol. 32. No. 1, 1988, 37–49.
12. Lynwander, P.: Preventing gear tooth scoring, Machine Design, March 20, 1980, 45-48
13. Ariura, Y. - Veno, T. - Nakanishi, T.: An investigation of surface failure of surface-hardened gears by scanning electron microscopy observations, Wear, 87 (1983), 305-316
14. Kimura, Y. - Okado, K. - Yamamoto: Wear during lubricated rolling contact, ASLE/ASME Lubrication Conference, Dayton, Ohio, October 16-18, 1979
15. Váradi, K. - Molnár, L. - Kollár, Gy. - Gara, P.: Analysis of some engineering contact problems by FEM (in Hungarian), GÉP, XXXIX. évf. 1987. 1, 10-16
16. Juvinal, R.C.: Fundamentals of machine component design, John Wiley, New York, 1983
17. Johnson, K.L. - Greenwood, J.A. - Higginson, J.G.: The contact of elastic regular wavy surfaces, Int. J. Mech. Sci. Vol. 27, No. 6, 383-396 (1985)

Acta Technica Acad.Sci.Hung., 101(4), pp. 419-429 (1988)

EXPERIMENTAL STUDY OF WEAR OF SLIP DIFFERENTIAL UNITS

WAHEED YOSRY, A.[*] - BALOGH, I.[**] - MOLNÁR, F.[***]

(Received: 25 November 1987)

The wear of slip differential units of three 154 kW trucks was measured by gamma ray spectrometry of neutron activated wear debris. Wear was expressed in terms of iron content of the wear debris found in the used oil. When the iron content in the used oil exceeded 125 mg/liter, the used oil was drained off and fresh oil was supplied to the unit. The lubrication properties of the used oil were tested by Amsler testing machine. Test results show that the wear of the slip differential unit is affected by solid and liquid contaminants and loss of antiwear properties of the used oil. The used oil can be renewed by filtration and dispersion with solid lubricant additives. A chelate type metal-organic compound gave the most satisfactory results as solid lubricant additive.

1. Introduction

In addition to the solid contaminants found in the new fresh oils, the slip differential unit lubricant is contaminated by contaminants built up during assembly and maintenance, and external contaminants entering the unit in service through the defective seal of the axles, as well as contaminants generated internally during operation and removed from the surface of gear teeth, synchronizing clutches, and other mating surfaces. Much of these contaminants settles to the bottom of the unit casing but a sufficient amount of them circulates with the oil and causes damage, particularly to the roller bearings incorporated in the unit /1, 2/. Water contaminated in the lubricating oil may react with oil vapours or oil additives to produce a highly corrosive atmosphere /3/. The change in wear of the engine as a function of driving distance was measured by the used oil analysis /4/. The change in lubricating properties of vehicle engine oil was studied in /5, 6/ as a function of driving distance. In this paper, the wear of the slip differential units in three 154 kW trucks was measured

[*]Waheed Yosry, Aly, 22 Haret El-Ramah, El-Nassria, El Sayeda Zainab, Cairo, EGYPT P.N. 11461

[**]Balogh, István, H-1194 Budapest, Csiky u. 66, Hungary

[***]Molnár, Ferenc, H-5000 Szolnok, Várkonyi tér 20, IX/6, Hungary

Akadémiai Kiadó, Budapest

every 5000 km of the driving distance, and the lubrication properties of the used oil were studied by using Amsler testing machine.

2. Description of experiment

2.1 Oil samples

Hy-K80 SAE 80 EP transmission oil was used as lubricant for the slip differential unit of three trucks running in urban areas. This is a normal sulphur-phosphorus-type EP gear oil. A sample of 50 ml of the used oil was taken from the unit at running distance interval of 5000 km. The used oil samples were filtered through a 3 μm membrane, ashed, and the ash was neutron irradiated. From the mixture of the created radioisotopes the Fe was determined through the characteristic γ line of ^{59}Fe radioisotope. The sensitivity of wear measurement is 10^{-7} g Fe, the accuracy of the measurement is $\pm$15% /7/. During the test, when the Fe content in the used oil exceeded 125 mg/l, the used oil was drained off and fresh oil was supplied to the unit. The used oils drained from the three trucks will be referred to in the text, as A, B and C.

2.2. Lubrication tests

Lubrication tests were carried out by an Amsler testing machine. The test specimens, in form of discs, were of St. 50 (carbon steel of 0.35% carbon, 173 kp/mm^2 Brinell Hardness, and 0.7 μm surface roughness, R_a). The coefficient of friction was determined by measuring the frictional torque using a pendulum device, which is a part of Amsler machine. Wear was measured by the reduction in test specimen weight. The test specimens were keyed on the upper and lower shaft of the Amsler machine, the speed of which were 175 and 193 r/min, respectively. With the surface speeds of the two specimens v_1 = 0.37 m/s for the upper test specimen and v_2 = 0.40 m/s for the lower one, the relative sliding speed was found to be 0.77 m/s, as shown in Fig. 1.

The test conditions are summarized in Table 1.

The lubrication tests were carried out to examine the antiwear properties of the following oil samples:

(a) Drained used oils A, B and C.

(b) The drained used oils filtered by 5.0 μm membrane. It will be referred to as filtered oil.

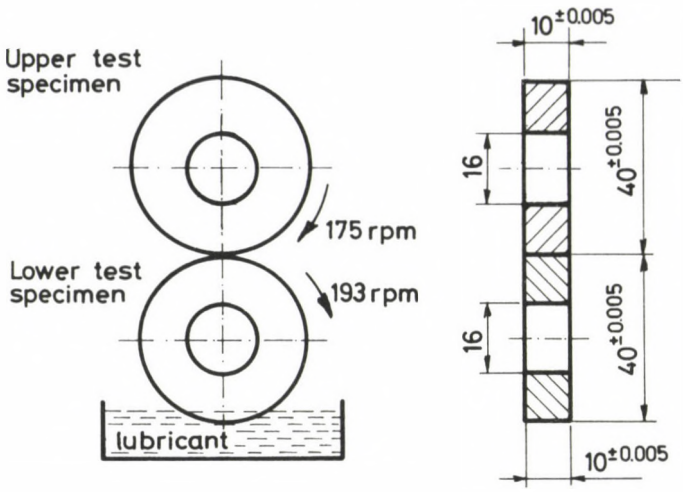

Fig. 1. Operating conditions and specimen dimensions

Table 1

Lubrication tests conditions

Load and speed	1000 N, 0.77 m/s
Temperature	25°C
Test duration	300 min

(c) Filtered oils heated at 105°C for 2 hours to evaporate water contaminants. It was found that the water contents evaporated were 0.52, 0.58 and 0.98 wt% for oil samples A, B and C, respectively.

(d) Filtered oils dispersed with 5 wt% of different solid lubricant additives. The solid lubricant additives used in tests are MoS_2 of particle size of 0.3–0.5 μm, PTFE powder, calcium hydroxide-type white matter of particle size of 5–10 μm /8,9/, and an additive of a chelate type metal-organic compound; in the text, this will be referred to as CMOC. Thermal decomposition of the compound takes place as a result of frictional heating at the sliding interface. The resultant deposits or coatings have excellent sliding characteristics /10, 11/.

3. Results and discussion

The wear of the slip differential unit as expressed in terms of iron content of the used oil is shown in Fig. 2 as a function of running distance. The results show that the iron content generally increases proportionally with running distance. When the concentration of iron content in the used oil exceede 125 mg/liter, the oil was drained off, and fresh oil was supplied. The oil was changed for truck A, B and C after running distances of 40 000, 33 000 and 15 000 km, respectively. The relatively higher water content in used oil C may be responsible for the wear rate. This confirms that the oil change period is more affected by oil contaminants than the running distance. The antiwear properties of used oils A, B and C obtained by using Amsler machine are shown in Fig. 3. The wear resulted from used oils was higher than that resulted from filtered

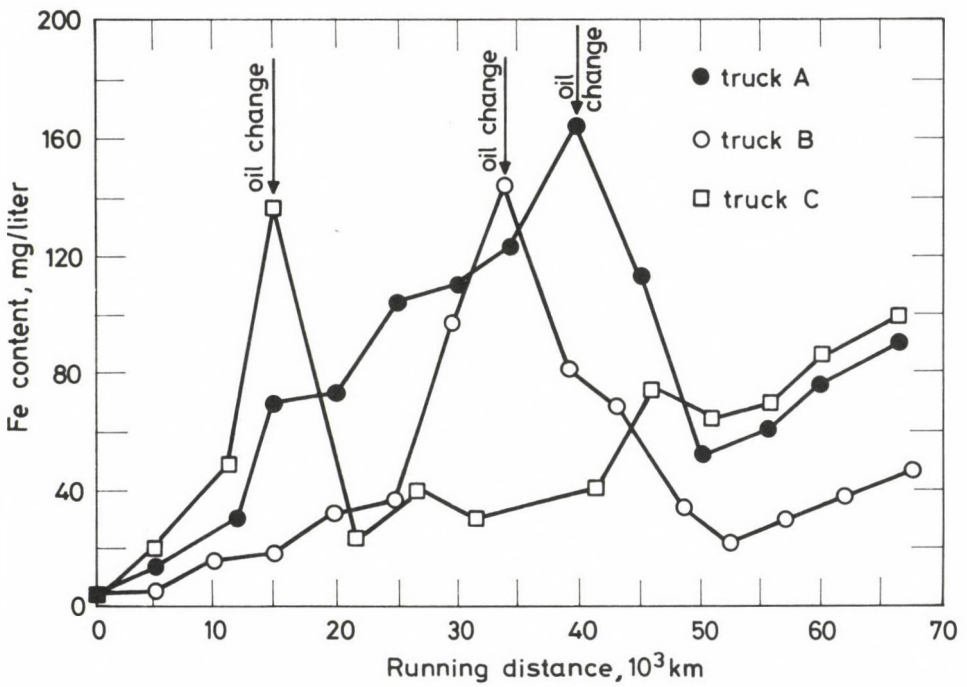

Fig. 2. Wear of slip differential unit as a function of running distance

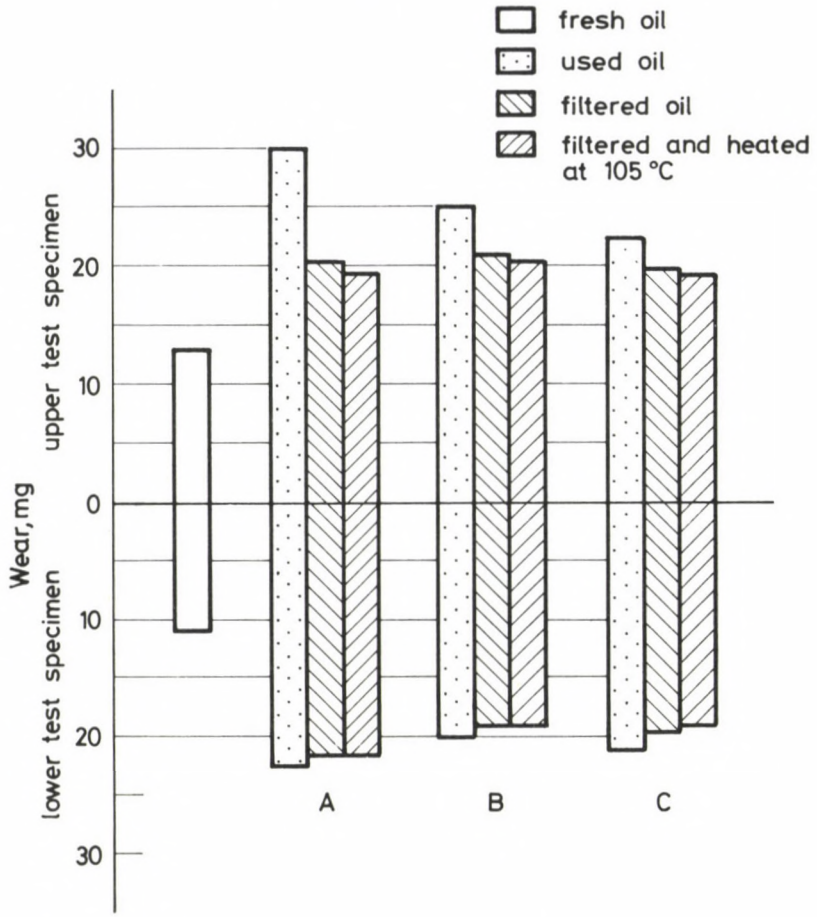

Fig. 3. Wear resulted from fresh, used, filtered, and filtered and heated at 105°C oil samples (Experimental conditions: Lubricant: SAE 80 EP of 25°C, Load: 1000 N, speed: 0.77 m/s, experiment duration: 300 min. A, B and C are referring to the used oils drained from truch A, B and C, respectively)

ones. Slight decrease in wear occurred with the used oil that had been filtered and heated at 105°C. The fresh oil showed lower wear rate as compared with that of the filtered and heated used oil. This difference may be due to the loss of antiwear properties of the used oil. Filtered and heated at 105°C oil samples taken from used oil A were prepared by adding 5.0 wt% of different, solid lubricant additives.

Generally, the dispersion of the above mentioned additives increased the antiwear properties of the used oil. The CMOC additive gave the most satisfactory results, as shown in Fig. 4. The coefficient of friction —

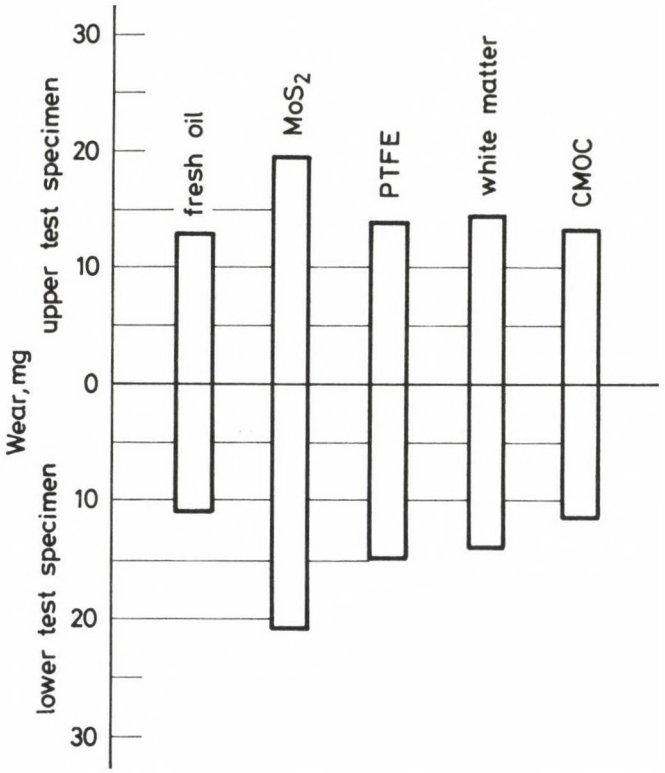

Fig. 4. Wear resulted from used oil samples filtered and dispersed with differential solid lubricant additives as compared with those resulted from fresh oil (Experimental conditions: as in Fig. 3.)

time recordings during the first hour of five hours tests are shown in Fig. 5.

With the used oil, the coefficient of friction not only increased but the trace became erratic. For filtered and heated oils, the erratic trace decreased. A remarkable decrease in coefficient of friction was obtained when the filtered and heated oil samples were dispersed with PTFE. Fig. 6 shows photomicrographs of Ferrograms of fresh oil, used oil as well as filtered oil samples of type A. In the used oil, the existence of wear particles consisting of iron and iron oxide up to 30 μm in size was observed. Besides, it is shown that filtration of the used oil removed a lot of relatively big wear particles. As shown in Fig. 4, the CMOC additive gave the most satisfactory results in reducing wear, which fact may be due to the additive heteropolar character since the organic radical resulting

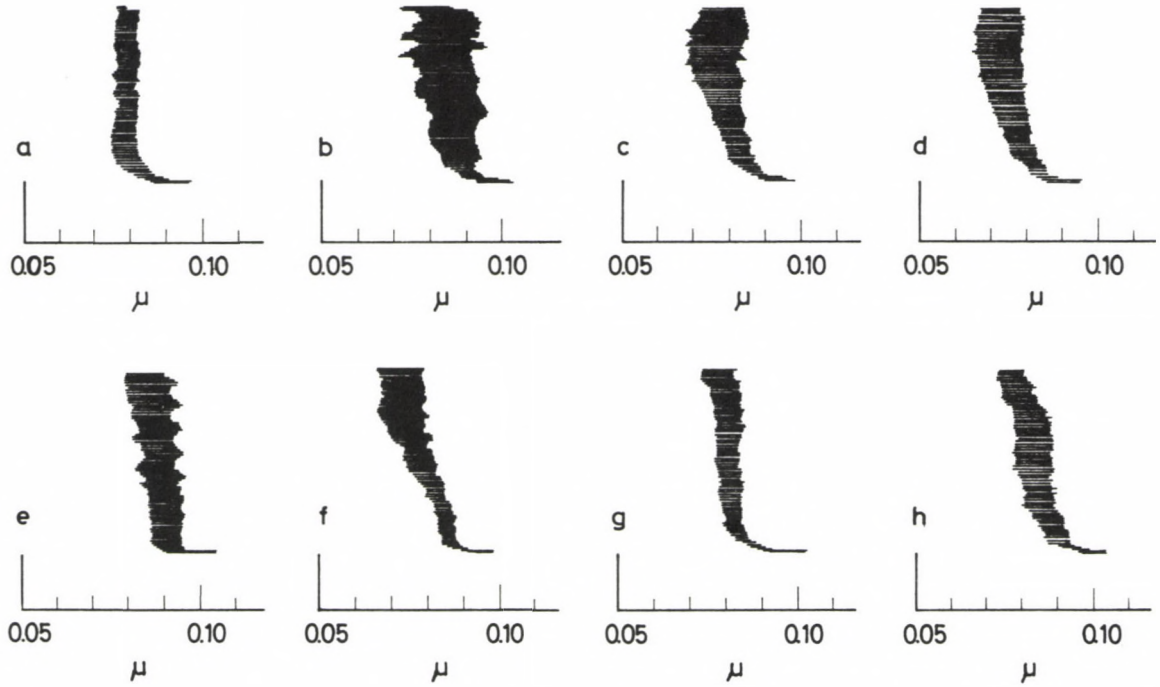

Fig. 5. Coefficient of friction-time recordings during the first hour of five hours tests ((a) fresh oil, (b) used oil, (c) filtered oil, (d) filtered and heated at 105 °C, and filtered oil dispersed with (e) MoS_2, (f) PTFE, (g) white matter, (h) CMOC; Experimental conditions: as in Fig. 3.)

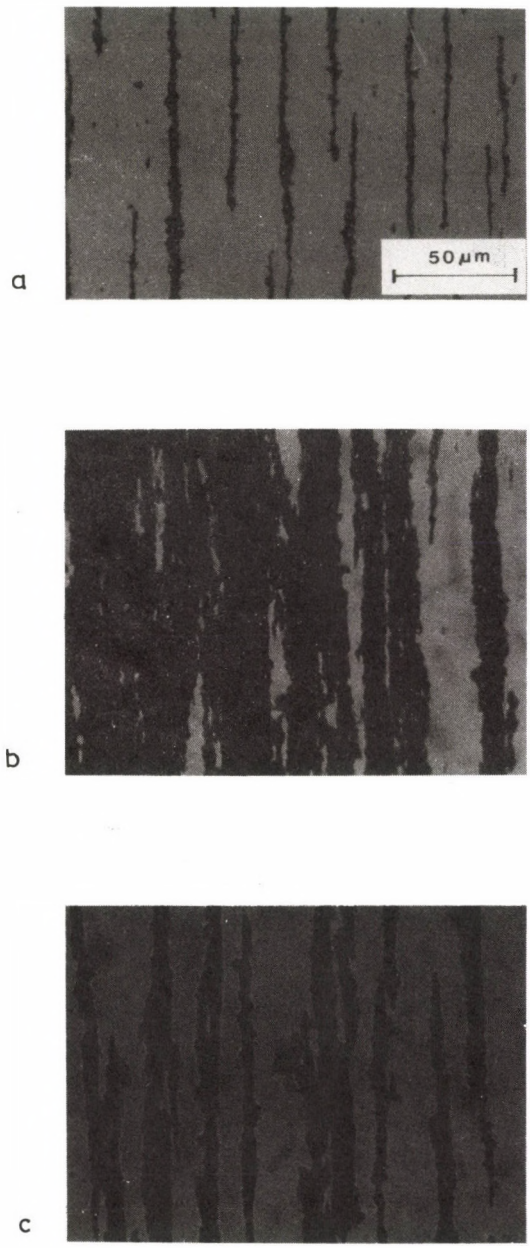

Fig. 6. Ferrograms of fresh, used and filtered oil samples
(a) fresh oil, (b) used oil type A, (c) used oil type A filtrated through 5 µm membrane

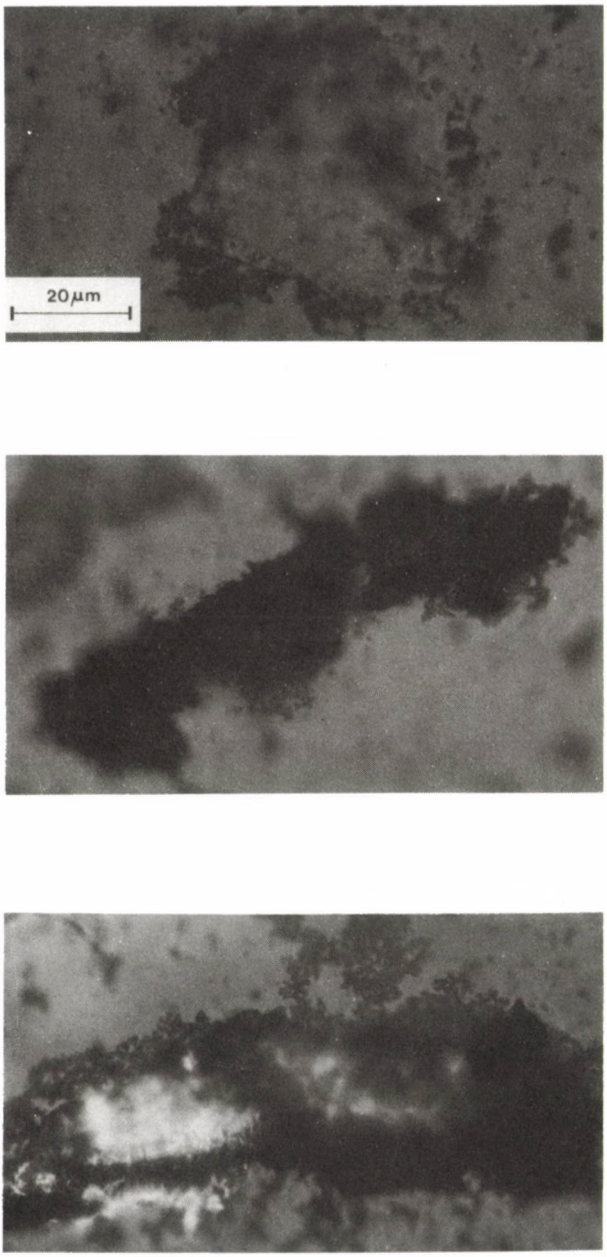

Fig. 7. Ferrograms prepared from an oil sample contaminated with solid contaminants and dispersed with CMOC additive
(a) quartz particle, (b) large particles of iron and iron oxide, (c) large particles of Aluminium

from the decomposition process adheres to the friction surfaces and forms a protective coating preventing the solid contaminants from sticking easily to metal. The CMOC particles smaller in size than 1.0 μm stick to the surfaces of wear and the solid particles contaminated in the oil, and make them less abrasive, as shown in Fig. 7.

Wear experiments were repeated five times and the average was plotted. The difference between the maximum and minimum values was less than 30% of the minimum value.

4. Conclusion

The wear of slip differential units during use was measured by gamma ray spectrometry of neutron activated wear debris found in the used oil.

The change in the lubrication properties of used oils was tested by using Amsler machine. The following results were obtained:

(1) The wear was affected by both solid and water contaminants as well as the loss in the oil antiwear properties.

(2) The used oil can be renewed by filtration through 5 μm membrane and dispersion with CMOC solid lubricant additive of 5 wt% concentration.

ACKNOWLEDGEMENTS

This work was carried out at the Department of Tribology, Research and Development Company of Automotive Industry, Budapest, Hungary.

The helpful assistance of Mrs. Gizella Szilasi and Mrs. Margit Balog is gratefully acknowledged.

REFERENCES

1. Greene, A.B.: Lubrication and lubricants, Braithwaite, E.R. (ed.) Elsevier Publishing Co., Amsterdam (1967), 463

2. Fitzsimmons, B. - Cave, B.J.: Lubricant contaminants and this effects on tapered roller bearing performance, Tribology international, 10 (2) (1977), 93-100

3. Ellis, E.E. - Hill, R.L. - Downs, E.M.: Breakdown of EP gear lubricants in pinion bearings, Presented at the 16th ASLE Annual Meeting, Philadelphia, 1961

4. Balatoni, F. - Fodor, J. - Monori, G. - Noeh, G.: Monitoring of the manufacturing process, Condition monitoring 84, Swansea, U.K., M.H. Jones (ed.), 1984

5. Kawamura, M. - Fujita, K. - Ninomiya, K.: The lubrication properties of used engine oil, Wear (1982), 77, 195-202

6. Fujita, K. - Esaki, Y. - Kawamura, M.: The antiwear property of zink dialkyldithio-phosphates in used engine oils, Wear (1983), 89, 323-331

7. Fodor, J.: Tribodiagnostics in internal combustion engines by using gamma-ray spectrometry of wear, C40/78, Swansea Symposium, 1978

8. Wochnowski, H. - Knappwost, A. - Wustefeld, B.: Calciumhydroxis als Festschimerstoff, Schmiertechnik und Tribologie, 23, 1 (1976)

9. Zakar, A. - Vamos, E. - Somfai, K. - Somogyi, M.: The employment of solid lubricants in plasting forming, EUROTRIB 81, Warsaw, Poland, 1981

10. Fodor, J. - Ling, F.F.: Friction reduction in an I.C. engine through improved filtration and a new lubricant additive, ASLE/ASME Conference, San Diego, USA, 22-24. 11. 1984, 84-LC-6B-1, 1-4

11. Lubricant composition, U.K. Patent 20902878, 1984

PRINTED IN HUNGARY
Akadémiai Kiadó és Nyomda Vállalat, Budapest

NOTICE TO CONTRIBUTORS

Papers in English* are accepted on condition that they have not been previously published or accepted for publication.

Manuscripts in two copies (the original type-written copy plus a clear duplicate one) complete with figures, tables, and references should be sent to

Acta Technica
Münnich F. u. 7. I. 111 A
Budapest, Hungary
H-1051

Although every effort will be made to guard against loss, it is advised that authors retain copies of all material which they submit. The editorial board reserves the right to make editorial changes.

Manuscripts should be typed double-spaced on one side of good quality paper with proper margins and bear the title of the paper and the name(s) of the author(s). The full postal address(es) of the author(s) should be given in a footnote on the first page. An abstract of 50 to 100 words should precede the text of the paper. The approximate locations of the tables and figures should be indicated on the margin. An additional copy of the abstract is needed. Russian words and names should be transliterated into English.

References. Only papers closely related to the author's work should be referred to. The citations should include the name of the author and/or the reference number in brackets. A list of numbered references should follow the end of the manuscript.

References to periodicals should mention: (1) name(s) and initials of the authors(s); (2) title of the paper; (3) name of the periodical; (4) volume; (5) year of publication in parentheses; (6) numbers of the first and last pages. Thus: 5. Winokur, A., Gluck, J.: Ultimate strength analysis of coupled shear walls. American Concrete Institute Journal 65 (1968), 1029–1035.

References to books should include: (1) author(s)' name; (2) title; (3) publisher; (4) place and year of publication. Thus: Timoshenko, S., Gere, J.: Theory of Elastic Stability. McGraw-Hill Company, New York, London 1961.

Illustrations should be selected carefully and only up to the necessary quantity. Black-and-white photographs should be in the form of glossy prints. The author's name and the title of the paper together with the serial number of the figure should be written on the back of each print. Legends should be brief and attached on a separate sheet. Tables, each bearing a title, should be self-explanatory and numbered consecutively.

Authors will receive proofs which must be sent back by return mail.

Authors will receive 50 reprints free of charge.

*Hungarian authors can submit their papers also in Hungarian.

Periodicals of the Hungarian Academy of Sciences are obtainable at the following addresses:

AUSTRALIA
C.B.D. LIBRARY AND SUBSCRIPTION SERVICE
Box 4886, G.P.O., *Sydney N.S.W. 2001*
COSMOS BOOKSHOP, 145 Ackland Street
St. Kilda (Melbourne), Victoria 3182

AUSTRIA
GLOBUS, Höchstädtplatz 3, *1206 Wien XX*

BELGIUM
OFFICE INTERNATIONAL DES PERIODIQUES
Avenue Louise, 485, *1050 Bruxelles*
E. STORY-SCIENTIA P.V.B.A.
P. van Duyseplein 8, *9000 Gent*

BULGARIA
HEMUS, Bulvar Ruszki 6, *Sofia*

CANADA
PANNONIA BOOKS, P.O. Box 1017
Postal Station "B", *Toronto, Ont. M5T 2T8*

CHINA
CNPICOR, Periodical Department, P.O. Box 50
Peking

CZECHOSLOVAKIA
MAD'ARSKA KULTURA, Národni třida 22
115 66 Praha
PNS DOVOZ TISKU, Vinohradská 46, *Praha 2*
PNS DOVOZ TLAČE, *Bratislava 2*

DENMARK
EJNAR MUNKSGAARD, 35, Nørre Søgade
1370 Copenhagen K

FEDERAL REPUBLIC OF GERMANY
KUNST UND WISSEN ERICH BIEBER
Postfach 46, *7000 Stuttgart 1*

FINLAND
AKATEEMINEN KIRJAKAUPPA, P.O. Box 128
00101 Helsinki 10

FRANCE
DAWSON-FRANCE S.A., B.P. 40, *91121 Palaiseau*
OFFICE INTERNATIONAL DE DOCUMENTATION ET LIBRAIRIE, 48 rue Gay-Lussac
75240 Paris, Cedex 05

GERMAN DEMOCRATIC REPUBLIC
HAUS DER UNGARISCHEN KULTUR
Karl Liebknecht-Straße 9, *DDR-102 Berlin*

GREAT BRITAIN
BLACKWELL'S PERIODICALS DIVISION
Hythe Bridge Street, *Oxford OX1 2ET*
BUMPUS, HALDANE AND MAXWELL LTD.
Cowper Works, *Olney, Bucks MK46 4BN*
COLLET'S HOLDINGS LTD., Denington Estate,
Wellingborough, Northants NN8 2QT
WM DAWSON AND SONS LTD., Cannon House
Folkstone, Kent CT19 5EE
H. K. LEWIS AND CO., 136 Gower Street
London WC1E 6BS

GREECE
KOSTARAKIS BROTHERS INTERNATIONAL BOOKSELLERS, 2 Hippokratous Street, *Athens-143*

HOLLAND
FAXON EUROPE, P.O. Box 167
1000 AD Amsterdam
MARTINUS NIJHOFF B. V.
Lange Voorhout 9–11, *Den Haag*
SWETS SUBSCRIPTION SERVICE
P.O. Box 830, 2160 Sz Lisse

INDIA
ALLIED PUBLISHING PVT. LTD.
750 Mount Road, *Madras 600002*
CENTRAL NEWS AGENCY PVT. LTD.
Connaught Circus, *New Delhi 110001*
INTERNATIONAL BOOK HOUSE PVT. LTD.
Madame Cama Road, *Bombay 400039*

ITALY
D. E. A., Via Lima 28, *00198 Roma*
INTERSCIENTIA, Via Mazzé 28, *10149 Torino*
LIBRERIA COMMISSIONARIA SANSONI
Via Lamarmora 45, *50121 Firenze*
SANTO VANASIA, Via M. Macchi 58
20124 Milano

JAPAN
KINOKUNIYA COMPANY LTD.
Journal Department, P.O. Box 55
Chitose, *Tokyo 156*
MARUZEN COMPANY LTD., Book Department
P.O. Box 5050 Tokyo International, *Tokyo 100-31*
NAUKA LTD., Import Department
2-30-19 Minami Ikebukuro, Toshima-ku, *Tokyo 171*

KOREA
CHULPANMUL, *Phenjan*

NORWAY
TANUM-TIDSKRIFT-SENTRALEN A.S.
Karl Johansgata 43, *1000 Oslo*

POLAND
WĘGIERSKI INSTYTUT KULTURY
Marszalkowska 80, *00-517 Warszawa*
CKP I W, ul. Towarowa 28, *00-958 Warszawa*

ROUMANIA
D. E. P., *Bucuresti*
ILEXIM, Calea Grivitei 64–66, *Bucuresti*

SOVIET UNION
SOYUZPECHAT — IMPORT, *Moscow*
and the post offices in each town
MEZHDUNARODNAYA KNIGA, *Moscow G-200*

SPAIN
DIAZ DE SANTOS Lagasca 95, *Madrid 6*

SWEDEN
ESSELTE TIDSKRIFTSCENTRALEN
Box 62, *101 20 Stockholm*

SWITZERLAND
KARGER LIBRI AG, Petersgraben 31, *4011 Basel*

USA
EBSCO SUBSCRIPTION SERVICES
P.O. Box 1943, *Birmingham, Alabama 35201*
F. W. FAXON COMPANY, INC.
15 Southwest Park, *Westwood Mass. 02090*
MAJOR SCIENTIFIC SUBSCRIPTIONS
1851 Diplomat, P.O. Box 819074,
Pallas, Tx. 75381-9074
READ-MORE PUBLICATIONS, INC.
140 Cedar Street, *New York, N. Y. 10006*

YUGOSLAVIA
JUGOSLOVENSKA KNJIGA, Terazije 27, *Beograd*
FORUM, Vojvode Mišića 1, *21000 Novi Sad*

HU ISSN 0001-7035

Index: 26.025